



The
University
Of
Sheffield.

**STUDY OF CLOSED-CYCLE GAS TURBINE FOR
APPLICATION TO SMALL MODULAR REACTORS
(SMRs) AND COAL-FIRED POWER GENERATION
THROUGH MODELLING AND SIMULATION**

By:

Olumide Olumayegun

Supervisor: Prof Meihong Wang

A thesis submitted in partial fulfilment of the requirement for the degree of
Doctor of Philosophy

The University of Sheffield
Faculty of Engineering
Department of Chemical and Biological Engineering

November 2017

Acknowledgement

I would like to express my deep appreciation to my thesis supervisor, Professor Meihong Wang, for his guidance, help and support throughout the period of this study. Special thanks to Dr Mathew Aneke for agreeing to serve as my second supervisor. I would also like to appreciate Dr Eni Oko for creating time to read through the thesis and making corrections. I am especially grateful to my industrial supervisor, Mr Greg Kelsall from GE Power, for his support and for facilitating this study. Other people at GE Power who made technical contributions to this work at various times include Dr Mark Tothill, Mr Johann Quenaut, Dr Andrew Pike and Dr Friederike Mund. I am grateful for their comments and suggestions, which greatly contributed to the quality of this thesis.

I would like to thank all my friends and colleagues in the Process & Energy Systems Engineering Group, both at University of Hull and The University of Sheffield. Our numerous discussions, though not necessarily related to this thesis, immensely contributed to my learning process and comprised an essential part of the evolution of this thesis.

I am also grateful to everyone at RCCG Amazing Grace Chapel for their friendship and for providing an amazing community for me and my family. Thank you Pastor and Pastor (Mrs) Aleshinloye for your prayers and care.

I would have found it difficult to cope with the rigour of PhD research without the understanding, support and dedication of my darling wife, Atinuke Olumayegun. Dear, you are wonderful and I really appreciate you for going along this journey with me. Of course, I cannot forget my prince and princess, David and Daniela, for always cheering me up at home.

Financial supports from GE Power (formerly Alstom Power Ltd) and EU FP7 Marie Curie research staff exchange programme are gratefully acknowledged.

Abstract

Closed-cycle GT has the potential for improved efficiency of electricity generation, compact and simple design, and reduced CO₂ emissions and therefore could complement conventional power conversion systems (PCSs). However, power generation from closed-cycle GT needs to be demonstrated to establish the integrity, operation and performance of the plant before commercial deployment can be realised. This thesis provides an understanding, through modelling and simulation, of the thermodynamic performance and component design parameters, and the dynamic behaviours, operation and control of closed-cycle GTs for the purpose of assessing their feasibility for near-term demonstration.

A systematic, full-scope study was performed for nitrogen closed-cycle GT coupled to small modular sodium-cooled fast reactor (SM-SFR) and supercritical carbon dioxide (s-CO₂) closed-cycle GT coupled to small modular pressurised water reactor (SM-PWR). The study included selection between alternative plant designs, steady state performance analysis, preliminary design of components, dynamic model development and simulation of plant transients, and design of control systems. Additionally, performance evaluation was performed for s-CO₂ closed-cycle GT for application to coal-fired power generation integrated with solvent based PCC.

Intercooled closed-cycle GT using nitrogen as working fluid and with a single shaft configuration has been one common PCS option for possible near-term demonstration of SFR. In this work, a new two-shaft nitrogen cycle with parallel turbines was proposed to further simplify the design of the turbomachinery and reduce turbomachinery size without compromising the cycle efficiency. Mathematical models in Matlab were developed for steady state thermodynamic analysis of the cycles and for preliminary design of the heat exchangers, turbines and compressors. The study indicated that the new configuration has the potential to simplify the design of turbomachinery, reduce the size of turbomachinery and provide opportunity for improving the efficiency of the turbomachinery.

Dynamic model of the new two-shaft nitrogen cycle power plant was developed in Matlab/Simulink. Control schemes, which enables the plant to satisfy the operational requirements under load-following and loss-of-load conditions, were implemented. Inventory control is unable to keep the generator speed within the specified ± 30 rpm of the synchronous speed during normal load-following operation. However, bypass valve control is able to maintain the generator speed within ± 17 rpm of the synchronous speed. Maximum generator shaft overspeed is below 105% during sudden loss-of-load condition, which is below the 120% maximum limit. Hence, stable and controllable operation of the two-shaft nitrogen GT power plant is possible.

Matlab models were developed for thermodynamic performance analysis and preliminary design of components for s-CO₂ closed-cycle GTs coupled to SM-PWR. Recompression s-CO₂ layout is the most common configuration for s-CO₂ cycle power plant. However, the performance assessment of the recompression s-CO₂ cycle for application to PWR shows that temperature of the turbine exhaust is too low to allow any meaningful recuperation in the high temperature recuperator. Hence, a new layout, the single recuperator recompression layout, is suggested. The efficiency of the new layout is comparable to that of the recompression cycle and higher than that of the simple recuperated cycle layout. Investigation of the impact of heat exchanger design on plant performance showed that the recompression cycles have higher pressure losses than the simple recuperated cycle. Therefore, if the heat exchanger design and pressure loss is considered in performance evaluation, the recompression cycles might not be that superior to the simple cycle. However, parametric analysis indicated that the new layout is the most promising for application to PWR.

Dynamic modelling, simulation and control system design was also carried out for the single recuperator recompression cycle coupled to SM-PWR. Inventory/pressure control is not considered to avoid issues associated with the rapid variation of CO₂ properties around the critical point. To effectively control the plant, flow split control and throttle valve were added to the normal control systems (bypass valve, control rod, coolant pump and cooling water control). The change in shaft speed during load-following operation is about ± 27 rpm while shaft overspeed during loss-of-load is about 107% of the synchronous speed. These are all within the allowable shaft speed limit.

Aspen Plus simulation was performed to evaluate the thermodynamic performance of cascaded s-CO₂ cycles coupled to coal-fired furnace and integrated with 90% post-combustion CO₂ capture. Three bottoming s-CO₂ cycles were investigated: simple recuperated cycle, partial heating cycle and the newly proposed single recuperator recompression cycle. Results for a 290 bar and 593 °C power cycle without CO₂ capture showed that the configuration with single recuperator recompression cycle as bottoming cycle has the highest plant net efficiency of 42.96% (HHV), followed by the simple recuperated, 42.46% and the partial heating, 42.44%. Integration of CO₂ capture reduced the efficiencies of the single recuperator recompression, the simple recuperated and the partial heating configurations to 31.76%, 31.22% and 31.13% respectively. Without CO₂ capture, the efficiencies of the coal-fired supercritical CO₂ cycle plants were about 3.34-3.86% point higher than the reference steam cycle plant and about 0.68-1.31% point higher with CO₂ capture. The findings so far underscored the promising potential of cascaded s-CO₂ power cycles for coal-fired power plant application.

Publications and Presentations

Part of this thesis has been published in the following peer reviewed journal:

- Olumayegun, O., Wang, M., and Kelsall, G. (2016). Closed-cycle gas turbine for power generation: A state-of-the-art review. *Fuel*, Vol. 180, pp. 694-717.
- Olumayegun, O., Wang, M., and Kelsall, G. (2017). Thermodynamic analysis and preliminary design of closed Brayton cycle using nitrogen as working fluid and coupled to small modular Sodium-cooled fast reactor (SM-SFR). *Applied Energy*, Vol. 191, pp. 436-453.

The author contributed to publication of this journal paper:

- Meng, H., Wang, M., Aneke, M., Luo, X., **Olumayegun, O.**, & Liu, X. (2018). Technical performance analysis and economic evaluation of a compressed air energy storage system integrated with an organic Rankine cycle. *Fuel*, Vol. 211, pp. 318-330.

Also part of the research described in this thesis was presented by the author at the 11th European Conference on Coal Research and its Application (ECCRIA 11), 5-7 September 2016, Sheffield, UK. The journal article is currently in preparation:

- Olumayegun, O., Wang, M. and Oko, E. (2016). Thermodynamic performance evaluation of supercritical CO₂ closed Brayton cycles for coal-fired power generation with post-combustion carbon capture. Available at <http://www.maggichurchosevents.co.uk/ferf/downloads/1B3%20Olumayegun%20Olu mide.pdf>

Other planned publications from this thesis are:

- Olumayegun, O. and Wang, M.. Dynamic modelling, simulation and control of a two-shaft nitrogen closed-cycle gas turbine coupled to small modular sodium cooled fast reactor.
- Olumayegun, O. and Wang, M.. Thermodynamic performance evaluation with heat exchangers design for supercritical CO₂ Brayton cycle coupled to small modular Pressurised Water Reactor (SM-PWR) for power generation.
- Olumayegun, O. and Wang, M. Dynamic modelling, simulation and control of supercritical CO₂ closed-cycle gas turbine coupled to small modular Pressurised Water Reactor (SM-PWR).

Table of Contents

Acknowledgement	iii
Abstract.....	v
Publications and Presentations.....	vii
List of Figures.....	xvii
List of Tables	xxv
Nomenclature.....	xxix
Abbreviations.....	xxxii
1 Introduction.....	1
1.1 Background and motivations	1
1.2 Overview of closed-cycle GT technologies	2
1.3 Aim and objectives of this research.....	5
1.4 Plant design choices.....	6
1.5 Predicted novel contributions.....	9
1.6 Research methodology and scope of this study	10
1.7 Software tools used for the study.....	11
1.7.1 Matlab [®] /Simulink [®]	11
1.7.2 Aspen Plus [®]	12
1.8 Outline of the thesis	12
2 Literature Review.....	15
2.1 Introduction.....	15
2.2 Historical development of closed-cycle GT.....	15
2.3 Review of relevant concepts and major features.....	18
2.3.1 Fuel/Heat sources.....	18
2.3.1.1 Fossil fuels	19
2.3.1.2 Nuclear heat source.....	20
2.3.1.3 Concentrated solar power heat source.....	21
2.3.1.4 Biomass fuel.....	22
2.3.1.5 Waste heat recovery	22
2.3.2 Working fluids	22

2.3.2.1 Helium and other noble gas mixture.....	23
2.3.2.2 Nitrogen working fluid.....	23
2.3.2.3 Supercritical CO ₂ working fluid.....	24
2.3.3 Compact heat exchangers.....	26
2.3.4 Physical layouts/configurations of closed-cycle GT.....	28
2.3.4.1 Recuperated, intercooled and reheated cycle.....	28
2.3.4.2 Layouts for S-CO ₂ cycle.....	28
2.3.5 Horizontal versus vertical configuration.....	30
2.3.6 Integrated versus distributed configuration.....	30
2.3.7 Single shaft versus multi-shaft configuration.....	31
2.4 Important R&D programmes and experimental/pilot plants, and commercially operated plants.....	31
2.4.1 R&D programmes and experimental/pilot facilities worldwide.....	32
2.4.1.1 The AK-36 test plant.....	32
2.4.1.1.1 Participants and purpose.....	32
2.4.1.1.2 Description of facilities.....	32
2.4.1.1.3 Activities.....	32
2.4.1.2 Feher (supercritical CO ₂) cycle test module.....	36
2.4.1.2.1 Participants and purpose.....	36
2.4.1.2.2 Description.....	36
2.4.1.2.3 Activities.....	37
2.4.1.3 HHV.....	37
2.4.1.3.1 Participants and purpose.....	37
2.4.1.3.2 Description of facility.....	37
2.4.1.3.3 Activities.....	37
2.4.1.4 GT-MHR.....	38
2.4.1.4.1 Participants and purpose.....	38
2.4.1.4.2 Description.....	38
2.4.1.4.3 Activities.....	39
2.4.1.5 PBMR.....	40

2.4.1.5.1	Participants and purpose	40
2.4.1.5.2	Description	40
2.4.1.5.3	Activities	41
2.4.1.6	GTHTR300	41
2.4.1.6.1	Participants and purpose	41
2.4.1.6.2	Description	42
2.4.1.6.3	Activities	42
2.4.1.7	JAEA s-CO ₂ cycle test loop	42
2.4.1.7.1	Participants and purpose	42
2.4.1.7.2	Description of facilities	43
2.4.1.7.3	Activities	43
2.4.1.8	SNL s-CO ₂ Brayton cycle loops	44
2.4.1.8.1	Participants and purpose	44
2.4.1.8.2	Description of facilities	44
2.4.1.8.3	Activities	45
2.4.1.9	HTR-10GT	45
2.4.1.9.1	Participants and purpose	45
2.4.1.9.2	Description	46
2.4.1.9.3	Activities	46
2.4.1.10	ANTARES	46
2.4.1.10.1	Participants and purpose	46
2.4.1.10.2	Description	47
2.4.1.10.3	Activities	47
2.4.1.11	BG demonstration plant	48
2.4.1.11.1	Participants and purpose	48
2.4.1.11.2	Description of facilities	48
2.4.1.11.3	Activities	48
2.4.2	Commercially operated closed-cycle GT plants	49
2.5	Summary of modelling and simulation studies, operation and control strategies	50
2.5.1	Steady state thermodynamic performance studies	50

2.5.1.1 Performance comparison with conventional plants.....	51
2.5.1.2 Studies based on cycle configuration	52
2.5.2 Dynamic modelling and simulation studies.....	53
2.5.2.1 Modelling studies and computer codes for research programmes.....	53
2.5.2.2 Non project specific modelling studies and codes.....	55
2.5.2.3 1-D, 2-D and CFD modelling of closed-cycle GT.....	55
2.5.3 Operation and control options for closed-cycle GTs.....	56
2.6 The need for closed-cycle GT demonstration plant.....	57
2.7 Summary.....	57
3 Steady State Model Development for Closed-cycle GTs Coupled to Nuclear Reactor and Methodology for Preliminary Design of Components	59
3.1 Introduction	59
3.2 Steady state modelling of closed-cycle GT and its implementation in Matlab®	59
3.3 Fluid thermodynamic and transport properties implementation in the Matlab®	62
3.4 Verification of the steady state model	63
3.5 Heat exchanger design and sizing methodology	65
3.6 Turbomachinery design and sizing methodology.....	69
3.7 Summary.....	75
4 Thermodynamic Performance Analysis of Nitrogen Brayton Cycle Coupled to SM-SFR and Preliminary Design of Components	77
4.1 Introduction	77
4.2 Plant configurations and description of the nitrogen Brayton cycles	78
4.2.1 Reference single-shaft intercooled CBC	78
4.2.2 Two-shaft intercooled CBC with parallel turbines.....	79
4.2.3 Assumptions and settings	80
4.3 Results of thermodynamic performance evaluation	81
4.4 Results of heat exchanger design.....	87
4.5 Results of turbomachinery design	89
4.5.1 Turbomachinery design simplification.....	90
4.5.2 Size reduction of the turbomachinery.....	90

4.5.3 Efficiency improvement.....	91
4.6 Summary	95
5 Thermodynamic Performance Analysis of S-CO ₂ Brayton Cycle Coupled to SM-PWR and Preliminary Design of Components.....	97
5.1 Introduction.....	97
5.2 Description of the s-CO ₂ Brayton cycle nuclear power plants and performance evaluation	98
5.2.1 Assumption and settings for PWR/s-CO ₂ nuclear power plant performance evaluation	98
5.2.2 Simple recuperated s-CO ₂ Brayton cycle for SM-PWR plant	100
5.2.3 Recompression s-CO ₂ Brayton cycle for SM-PWR plant.....	102
5.2.4 Single recuperator recompression s-CO ₂ Brayton cycle for SM-PWR plant.....	103
5.3 Heat exchangers design and its impact on the performance and size of the SM-PWR/s-CO ₂ power plant.....	107
5.3.1 Results of precoolers design	108
5.3.2 Results of IHXs design	114
5.3.3 Results of recuperators design	116
5.3.4 Impact of heat exchanger design on plant performance and size.....	119
5.4 Parametric analysis of s-CO ₂ Brayton cycles.....	121
5.4.1 Effect of precooler outlet conditions on thermal efficiency.....	121
5.4.2 Effect of maximum operating pressure on thermal efficiency	123
5.4.3 Effect of TIT on thermal efficiency	124
5.4.4 Effect of recuperator's minimum TTD	125
5.5 Selection of suitable s-CO ₂ Brayton cycle for PWR application	127
5.6 Turbomachinery design for s-CO ₂ Brayton cycle for SM-PWR.....	130
5.7 Summary	133
6 Dynamic Model Development for Closed-Cycle GTs Coupled to Nuclear Reactors.....	135
6.1 Introduction.....	135
6.2 Plant components' dynamic model development	135
6.2.1 Nuclear reactor model.....	136
6.2.2 Reactor coolant pump model	139

6.2.3 Compressor and turbine models	143
6.2.3.1 Compressor model.....	143
6.2.3.2 Turbine model.....	145
6.2.4 Heat exchanger model	146
6.2.5 Rotating shafts and generator model	148
6.2.6 Control valve and actuator model.....	149
6.2.7 Mixing junction model	151
6.2.8 Splitting junction model	152
6.2.9 PID controller model	153
6.3 Fluid thermodynamic properties for dynamic modelling	153
6.4 Model integration in Matlab®/Simulink®	154
6.5 Summary.....	154
7 Control System Design.....	155
7.1 Introduction	155
7.2 Control options for closed-cycle GTs coupled with nuclear reactors.....	155
7.2.1 Principles of closed-cycle GT control	155
7.2.2 Inventory/pressure control method.....	156
7.2.3 Bypass control method	157
7.2.4 Temperature/Reactor control method.....	158
7.2.5 Comparison of the control options	159
7.3 Control system requirements and objectives	161
7.4 Tuning of the PID controllers.....	163
7.5 Summary.....	164
8 Dynamic Performance Analysis of the SM-SFR Coupled with Nitrogen Cycle (SM-SFR/Nitrogen) Plant.....	165
8.1 Introduction	165
8.2 Automatic control system configurations for the SM-SFR/Nitrogen nuclear power plant	166
8.3 Plant's design point conditions and components parameters	171
8.4 Open loop step response of the SM-SFR/Nitrogen plant model	172

8.5 Normal load following between 100% and 50%	175
8.5.1 Control strategy 1: Bypass valve control only	176
8.5.2 Control strategy 2: Bypass valve control and reactor control	185
8.5.3 Control strategy 3: Inventory regulation and reactor controls	190
8.5.4 Control strategy 4: Bypass valve control and inventory regulation with reactor control	196
8.6 100% instantaneous loss of grid load.....	199
8.7 Summary	205
9 Dynamic Performance Analysis of the SM-PWR with s-CO ₂ cycle (SM-PWR/s-CO ₂) Plant	207
9.1 Introduction.....	207
9.2 Operation, control and simulation challenges for s-CO ₂ cycle	207
9.3 Design point conditions and components parameters for the SM-PWR/s-CO ₂ cycle nuclear power plant.....	210
9.4 Automatic control configuration for the SM-PWR/s-CO ₂ nuclear power plant	211
9.5 Normal load following between 100% and 50% of the SM-PWR/s-CO ₂ plant.....	214
9.6 100% instantaneous loss of grid load of the SM-PWR/s-CO ₂ plant.....	220
9.7 Summary	226
10 Thermodynamic Performance Evaluation of Supercritical CO ₂ CBC for Coal-Fired Power Generation with Solvent-based PCC.....	227
10.1 Introduction.....	227
10.2 Description of the supercritical CO ₂ Brayton cycles for pulverised coal-fired application	228
10.2.1 Coal-fired furnace and the main s-CO ₂ CBC	228
10.2.2 Utilisation of flue gases residual heat	229
10.2.3 Overall plant configuration and integration with PCC.....	230
10.3 Steady state simulation of coal-fired s-CO ₂ cycle power plant in Aspen Plus®	233
10.3.1 Aspen Plus® software and thermo-physical property method.....	234
10.3.2 Coal combustion and furnace simulation.....	235
10.3.3 s-CO ₂ CBCs simulation in Aspen Plus®	236
10.3.4 Preheater, ash removal and flue gas desulfurization simulation	237

10.3.5 Performance calculation	237
10.4 Solvent-based post-combustion CO ₂ capture	239
10.4.1 Description of MEA-based CO ₂ capture process	239
10.4.2 Rate-based simulation of the CO ₂ capture system in Aspen Plus®	240
10.5 Verification of the Aspen Plus® model of the s-CO ₂ Brayton cycle.....	242
10.6 Baseline boundary conditions and design point parameters.....	243
10.7 Performance comparisons among Case A, Case B and Case C of the coal-fired s-CO ₂ Brayton cycle power plants	244
10.8 Choice of configuration and parametric study.....	250
10.8.1 Effect of turbine inlet operation conditions	251
10.8.2 Effect of precooler outlet/MC inlet operating conditions.....	252
10.8.3 Effect of minimum TTD of the recuperators.....	253
10.9 Summary.....	254
11 Conclusions and Recommendations for Future Work.....	257
11.1 Conclusions	257
11.1.1 SM-SFR/nitrogen closed-cycle GT power plant	257
11.1.2 SM-PWR/s-CO ₂ closed-cycle GT power plant	258
11.1.3 Coal-fired/s-CO ₂ closed-cycle GT power plant.....	259
11.2 Recommendations for future work	260
References	263
Appendices	283
Appendix A Turbomachinery Design Data.....	283
A.1 Turbomachinery design data for the SM-SFR/ Nitrogen plant.....	283
A.1.1 Turbomachinery design data for the single-shaft nitrogen cycle.....	283
A.1.2 Turbomachinery design data for the single-shaft nitrogen cycle.....	287
A.2 Turbomachinery design data for the single recuperator recompression s-CO ₂ cycle .	293
Appendix B Integration of Plant Components Dynamic Models in Simulink	300

List of Figures

Figure 1-1 Global energy production by fuel (Courtesy of The British Petroleum Company Plc)	1
Figure 1-2 Gas turbine classification	4
Figure 1-3 Open and closed-cycle GTs schematic and T-S diagram (Brenes, 2014)	4
Figure 1-4 Gas turbine firing temperature trends (McDonald, 1995)	5
Figure 1-5 Overview of the selection of design study options for nuclear closed-cycle GTs	8
Figure 1-6 Overview of research methodology	10
Figure 2-1 Aerojet Rocketdyne's oxy-combustion coal-fired s-CO ₂ Brayton cycle (Vega et al., 2014)	19
Figure 2-2 Indirect and direct nuclear GT cycles (Wang and Gu, 2005)	21
Figure 2-3 Comparison of turbine sizes for steam, helium and s-CO ₂ (Dostal, 2004)	26
Figure 2-4 The recompression s-CO ₂ cycle	29
Figure 2-5 The Escher Wyss AK-36 test plant (Keller, 1978)	33
Figure 2-6 Sketch of the Feher 150 kWe S-CO ₂ power cycle (Hoffmann and Feher, 1971)	36
Figure 2-7 Schematic of HHV test circuit (Weisbrodt, 1995)	38
Figure 2-8 GT-MHR layout (Armentrout, 2011)	39
Figure 2-9 Simplified diagram of the PBMR Brayton cycle system (Koster et al., 2003)	41
Figure 2-10 Layout of GTHTR300 (Courtesy of JAERI)	42
Figure 2-11 JAEA s-CO ₂ cycle test loop (Kisohara et al., 2008)	43
Figure 2-12 S-CO ₂ split flow recompression CBC test assembly at SNL (Courtesy of SNL)	45
Figure 2-13 Schematic of HTR-10GT (Wu and Yu, 2007)	46
Figure 2-14 Schematic of the V/HTR ANTARES plant (Gauthier et al., 2006)	47
Figure 2-15 BG demonstration facility (McDonald, 2012)	48
Figure 3-1 Single intercooling layout with recuperation (Ahn and Lee, 2014)	64
Figure 3-2 PCHE construction (courtesy of Heatric)	66
Figure 3-3 Nodalization of heat exchanger	68
Figure 3-4 Axial turbine stator-rotor arrangement and velocity diagram	71
Figure 3-5 Axial compressor rotor-stator arrangement and velocity diagram (Saravanamuttoo et al., 2009)	72
Figure 4-1 Reference single-shaft intercooled CBC (Alpy et al., 2011)	79
Figure 4-2 Temperature-Entropy diagram for intercooled CBC	79
Figure 4-3 Proposed two-shaft CBC with turbines in parallel	80
Figure 4-4 Cycle efficiency as a function of LPC inlet pressure and LPC outlet pressure for both configurations	83
Figure 4-5 Thermodynamic state points of the single-shaft configuration	84
Figure 4-6 Thermodynamic state points of the two-shaft configuration	85

Figure 4-7 Fluid temperature profiles along the heat exchangers length (all counter-current flow)	88
Figure 4-8 Effects of recuperator TTD on overall cycle efficiency and recuperator volume.....	89
Figure 4-9 Effect of turbomachinery efficiencies on overall cycle efficiency	95
Figure 5-1 Schematic diagram of a conventional PWR nuclear power plant (NRC, 2017).....	97
Figure 5-2 s-CO ₂ cycle compressor and turbine specific work as function of precooler outlet pressure at 32 °C precooler outlet temperature.....	99
Figure 5-3 Flowsheet, state point values and performance results of simple recuperated s-CO ₂ Brayton cycle coupled to PWR	101
Figure 5-4 Temperature-Entropy (T-S) diagram of simple recuperated s-CO ₂ Brayton cycle..	102
Figure 5-5 Flowsheet, state point values and performance results of recompression s-CO ₂ Brayton cycle coupled to PWR	104
Figure 5-6 Temperature-Entropy (T-S) diagram of recompression s-CO ₂ Brayton cycle.....	105
Figure 5-7 Flowsheet, state point values and performance results of single recuperator recompression s-CO ₂ Brayton cycle coupled to PWR.....	106
Figure 5-8 Temperature-Entropy (T-S) diagram of single recuperator recompression s-CO ₂ Brayton cycle.....	107
Figure 5-9 Flow area versus (a) velocity (b) Reynolds number (c) Nusselt number (d) HTC (e) pressure loss and (f) volume of precooler	109
Figure 5-10 Precooler hot and cold streams temperature profile.....	111
Figure 5-11 Temperature difference between the hot and cold stream within the precooler	112
Figure 5-12 Hot and cold stream specific heat capacity values within the precooler.....	112
Figure 5-13 Hot and cold stream density values within the precooler	113
Figure 5-14 Variation of HTCs within the precooler	113
Figure 5-15 IHX hot and cold stream temperature profiles for the (a) simple cycle layout (b) recompression cycle layout and (c) single recuperator recompression cycle layout.....	115
Figure 5-16 IHX hot and cold side HTCs and the overall HTC for the (a) simple cycle layout (b) recompression cycle layout and (c) single recuperator recompression cycle layout.....	116
Figure 5-17 Recuperator hot and cold stream temperature profile for the (a) simple cycle layout (b) LTR of the recompression cycle layout (c) HTR of the recompression cycle layout and (d) single recuperator recompression cycle layout.....	118
Figure 5-18 Recuperator hot and cold sides HTC and the overall HTC for the (a) simple cycle layout (b) LTR of the recompression cycle layout (c) HTR of the recompression cycle layout and (d) single recuperator recompression cycle layout	119
Figure 5-19 Comparison of total pressure losses for the simple, recompression and single recuperator recompression cycle	120
Figure 5-20 Comparison of the previous and the new thermal efficiency after heat exchanger design for the different s-CO ₂ cycle layouts.....	120

Figure 5-21 Comparison of the total heat exchanger volume including the volume of the recuperator, IHX and precooler for the different s-CO ₂ cycle layouts.....	121
Figure 5-22 Effect of precooler outlet temperature and pressure on the thermal efficiency of simple s-CO ₂ Brayton cycle	122
Figure 5-23 Effect of precooler outlet temperature and pressure on the thermal efficiency of recompression s-CO ₂ Brayton cycle	122
Figure 5-24 Effect of precooler outlet temperature and pressure on the thermal efficiency of single recuperator recompression s-CO ₂ Brayton cycle.....	123
Figure 5-25 Effect of maximum cycle pressure on thermal efficiency for the simple, recompression and single recuperator s-CO ₂ Brayton cycles	124
Figure 5-26 Effect of TIT on the thermal efficiency for the simple, recompression and single recuperator recompression s-CO ₂ Brayton cycles.....	125
Figure 5-27 Effect of changes in recuperator minimum TTD on the recuperator effectiveness of the simple, recompression and single recuperator recompression cycles	126
Figure 5-28 Effect of changes in recuperator minimum TTD on the thermal efficiencies of the simple, recompression and single recuperator recompression cycles	126
Figure 5-29 Effect of changes in recuperator minimum TTD on the recuperator volumes of the simple, recompression and single recuperator recompression cycles.....	127
Figure 5-30 State point values and performance results of single recuperator recompression s-CO ₂ Brayton cycle coupled to PWR based on the selected optimum boundary conditions	129
Figure 6-1 Dimensionless performance curves of pump (Walas, 1990).....	142
Figure 6-2 Heat exchanger regions	147
Figure 6-3 Control valve.....	150
Figure 6-4 Linear, equal percentage and quick opening valve characteristics.....	151
Figure 6-5 Mixing junction.....	152
Figure 6-6 Splitting junction.....	152
Figure 7-1 Simple CBC plant with inventory (pressure) control.....	157
Figure 7-2 Simple CBC with bypass control method showing three possible location of the bypass valve (A, B or C).....	158
Figure 7-3 Effect of the different control methods on the cycle efficiency	161
Figure 8-1 Control scheme for the SM-SFR/Nitrogen nuclear power plant.....	169
Figure 8-2 Block diagram of the implemented control methods	170
Figure 8-3 Plant's open loop transient response to step change in bypass valve opening showing the mass flow rate through the bypass valve, the free turbine power output supplied to the generator, the reactor fission power and the turbine-generator shaft speed.....	173
Figure 8-4 Plant's open loop transient response to step change in mass inventory setting showing the mass flow rate of nitrogen, the TIP, the FPT output supplied to the generator, the turbine-generator shaft speed and the IHX terminal temperatures	174

Figure 8-5 Plant's open loop transient response to step change in control rod reactivity showing the turbine inlet and reactor outlet temperatures, the FPT output supplied to the generator, the reactor fission power and the turbine-generator shaft.	175
Figure 8-6 Load demand, turbine power output supplied to the generator and reactor fission power during normal load following with bypass valve control only	179
Figure 8-7 FPT-generator shaft speed during normal load following with bypass valve control only	179
Figure 8-8 Bypass mass flowrate FPT mass flowrate during normal load following with bypass valve control only	180
Figure 8-9 FPT outlet pressure and pressure ratio during normal load following with bypass valve control only	180
Figure 8-10 Precooler and intercooler cooling water flowrates manipulated by the cooling water controller during normal load following operation	181
Figure 8-11 LPC and HPC inlet temperatures maintained at the design value by the cooling water controllers during load following operation	181
Figure 8-12 Temperature transients at reactor outlet, turbine inlet, recuperator hot side inlet, reactor inlet and Na/N ₂ IHX cold side inlet during load following with bypass valve control only	182
Figure 8-13 Average fuel and coolant temperature during load following operation with bypass valve control only	182
Figure 8-14 Changes in reactor reactivity during load following operation with bypass valve control only	183
Figure 8-15 Variation of the plant efficiency during load following operation with bypass valve control only	183
Figure 8-16 Turbomachinery power during load following operation with bypass valve control only	184
Figure 8-17 Compressor shaft speed variation during load following with bypass valve control only	184
Figure 8-18 Load demand, turbine power output and reactor fission power during normal load following with bypass valve and reactor controls	186
Figure 8-19 Variation of the plant efficiency during load following operation with bypass valve control and reactor control	186
Figure 8-20 FPT-generator shaft speed during normal load following with bypass valve and reactor controls	187
Figure 8-21 Control rod reactivity adjustment along with fuel and coolant reactivity during load following operation with bypass valve and reactor control	187

Figure 8-22 Adjustment of the coolant pump torque along with the variation of the pump speed and coolant mass flow rate during load following operation with bypass valve control and reactor control.....	188
Figure 8-23 Temperature transients at reactor outlet, turbine inlet, recuperator hot side inlet, reactor inlet and Na/N ₂ IHX cold side inlet during load following with bypass valve control and reactor control.....	188
Figure 8-24 Turbomachinery power during load following operation with bypass valve control reactor control.....	189
Figure 8-25 Compressor shaft speed variation during load following with bypass valve control and reactor control.....	189
Figure 8-26 Load demand, turbine power output and reactor fission power during normal load following with inventory control and reactor controls.....	191
Figure 8-27 Plant efficiency during load following operation with inventory control and reactor controls.....	192
Figure 8-28 Mass inventory of nitrogen gas in the PCS during load following operation with inventory and reactor controls.....	192
Figure 8-29 Transient responses of nitrogen, sodium and cooling water mass flowrate during load following operation with inventory control and reactor controls.....	193
Figure 8-30 Control rod reactivity adjustment along with fuel and coolant reactivity during load following operation with inventory control and reactor control.....	193
Figure 8-31 Control adjustment of the coolant pump torque and speed during load following operation with inventory control and reactor control.....	194
Figure 8-32 Variation of turbine inlet and outlet pressure and pressure ratio during load following operation with inventory control and reactor controls.....	194
Figure 8-33 Variation of turbomachinery power during load following with inventory control and reactor controls.....	195
Figure 8-34 Temperature transient responses during load following with inventory control and reactor controls.....	195
Figure 8-35 Transient response of FPT-generator shaft speed during load following operation with inventory control and reactor controls.....	196
Figure 8-36 Responses of turbine output power and reactor fission power to load demand changes during load following operation with bypass valve control and inventory control.....	197
Figure 8-37 Plant efficiency during load following operation with bypass valve control and inventory control.....	198
Figure 8-38 Total Brayton cycle and bypass valve mass flowrate during load following operation with bypass valve control and inventory control.....	198
Figure 8-39 FPT-generator shaft speed during load following operation with bypass valve control and inventory control.....	199

Figure 8-40 Grid load change from full load to zero and transient responses of the turbine power output and reactor fission power	201
Figure 8-41 Transient responses of the bypass valve and FPT mass flowrates during loss of load event	201
Figure 8-42 Transient response of the FPT-generator shaft rotational speed during loss of load event	202
Figure 8-43 Transient responses of the reactor reactivity during loss of load event.....	202
Figure 8-44 Control of the coolant pump torque along with the pump speed and coolant mass flowrate during loss of load event	203
Figure 8-45 Transient responses of the precooler and intercooler water flowrates and the LPC and HPC inlet temperatures during loss of load event	203
Figure 8-46 Variation of the CDT, the LPC and the HPC power during loss of load.....	204
Figure 8-47 Transient response of compressor shaft rotational speed during loss of load.....	204
Figure 8-48 Transient responses of plant temperatures during loss of load	205
Figure 9-1 CO ₂ phase diagram showing the critical point.....	209
Figure 9-2 CO ₂ isobaric specific heat capacity around the critical point	210
Figure 9-3 Control scheme for the SM-PWR/s-CO ₂ cycle nuclear power plant.....	213
Figure 9-4 Load demand, turbine net power output and reactor power during normal load following of the SM-PWR/s-CO ₂ plant.....	214
Figure 9-5 Shaft speed of the SM-PWR/s-CO ₂ plant during normal load following transient .	215
Figure 9-6 Bypass valve mass flow rate and turbine mass flow rate of the SM-PWR/s-CO ₂ plant during normal load following operation.....	215
Figure 9-7 Turbine outlet pressure during normal load following operation of the SM-PWR/s-CO ₂ plant	216
Figure 9-8 MC inlet temperature and adjustment of the cooling water mass flow rate during normal load following of the SM-PWR/s-CO ₂ plant.....	216
Figure 9-9 Adjustment of the coolant pump torque, speed and coolant mass flow rate to maintain the TIT at 290 °C during normal load following of the SM-PWR/s-CO ₂ plant.....	217
Figure 9-10 Fuel reactivity, coolant reactivity and modulation of control rod reactivity during normal load following of the SM-PWR/s-CO ₂ plant.....	217
Figure 9-11 Reactor core outlet, turbine inlet, reactor inlet, turbine outlet/recuperator hot inlet and IHX cold inlet temperature during normal load following of the SM-PWR/s-CO ₂ plant ..	218
Figure 9-12 Average fuel temperature and average coolant temperature during normal load following of the SM-PWR/s-CO ₂ plant.....	218
Figure 9-13 MC, RC and turbine power during normal load following of the SM-PWR/s-CO ₂ plant	219
Figure 9-14 Adjustment of flow split fraction during normal load following of the SM-PWR/s-CO ₂ plant	219

Figure 9-15 Variation of plant efficiency during normal load following of the SM-PWR/s-CO ₂ plant	220
Figure 9-16 Grid load change from full load to zero and transient responses of the turbine net power output and reactor fission power of the SM-PWR/s-CO ₂ plant	221
Figure 9-17 Transient response of the turbomachinery-generator shaft rotational speed during loss of load event of the SM-PWR/s-CO ₂ plant.....	221
Figure 9-18 Transient responses of the bypass valve and turbine mass flowrates during loss of load event of the SM-PWR/s-CO ₂ plant	222
Figure 9-19 Turbine outlet pressure during loss of load event of the SM-PWR/s-CO ₂ plant...	222
Figure 9-20 Transient responses of the MC inlet temperature and precooler water flowrates during loss of load event of the SM-PWR/s-CO ₂ plant	223
Figure 9-21 Transient responses of the reactor reactivity during loss of load event of the SM-PWR/s-CO ₂ plant.....	223
Figure 9-22 Control of the coolant pump torque along with the pump speed and coolant mass flowrate during loss of load event of the SM-PWR/s-CO ₂ plant	224
Figure 9-23 Transient response of reactor outlet, turbine inlet, reactor inlet, recuperator hot inlet and IHX cold inlet temperature during loss of load event of the SM-PWR/s-CO ₂ plant.....	224
Figure 9-24 Transient response of average fuel and coolant temperature during loss of load event of the SM-PWR/s-CO ₂ plant	225
Figure 9-25 Transient response of the MC, RC and turbine power during loss of load of the SM-PWR/s-CO ₂ plant.....	225
Figure 10-1 Main single reheat recompression cycle integration with coal-fired furnace.....	229
Figure 10-2 Case A - Simple recuperative bottoming cycle	231
Figure 10-3 Case B - Partial heating bottoming cycle	232
Figure 10-4 Case C - Single recuperator recompression bottoming cycle.....	232
Figure 10-5 Integration of coal-fired s-CO ₂ Brayton cycle with PCC unit.....	233
Figure 10-6 Simplified block diagram of the coal-fired s-CO ₂ cycle power plants.....	234
Figure 10-7 Simplified process flow diagram for MEA-based PCC unit (IPCC, 2005).....	240
Figure 10-8 Cycle efficiencies of the topping cycle and Case C bottoming cycle as a function of the flow split fractions	245
Figure 10-9 Distribution of the input heat value among the different heaters	246
Figure 10-10 Comparison of the overall plant net efficiency of Case A (simple recuperative cycle as bottoming cycle), Case B (partial heating cycle as bottoming cycle) and Case C (single recuperator recompression cycle as bottoming cycle) with the supercritical steam plant (from Olaleye (2015)) as the benchmark	249
Figure 10-11 Plant net efficiency as a function cycle maximum pressure from 200 bar to 500 bar for the three configurations (Case A – simple recuperative cycle as bottoming cycle, Case B –	

partial heating cycle as bottoming cycle and Case C – single recuperator recompression cycle as bottoming cycle).....	250
Figure 10-12 Plant net efficiency as a function of cycle maximum pressure at different TIT for the single recuperator recompression bottoming cycle configuration (i.e. Case C) with no carbon capture and with carbon capture integrated.....	252
Figure 10-13 Effect of precooler outlet temperature on plant net efficiency of the single recuperator recompression bottoming cycle configuration with no carbon capture with precooler outlet pressure varying from 60 bar to 110 bar.....	253
Figure 10-14 Plot of CO ₂ pressure against density in the critical region showing the rapid rise in density at pseudo-critical pressures corresponding to different CO ₂ temperatures	253
Figure 10-15 Plant net efficiency as a function of recuperators minimum TTD for the single recuperator recompression bottoming cycle s-CO ₂ plant	254
Figure B-1 Simulink integration of the dynamic models of the SM-SFR/nitrogen closed-cycle GT components (two-shaft parallel turbines layout).....	300
Figure B-2 Simulink integration of the dynamic models of the SM-PWR/s-CO ₂ closed-cycle GT components (Single recuperator recompression layout).....	301

List of Tables

Table 1-1 Overview of the scope of this study	11
Table 2-1 Historical development of closed-cycle GT	17
Table 2-2 Advantages and disadvantages of closed-cycle GT working fluids (Lee et al., 1981)	25
Table 2-3 Features of compact heat exchangers	27
Table 2-4 Research programmes and test facilities technical information	34
Table 3-1 Correlations for computing liquid sodium properties (Sobolev, 2011).....	63
Table 3-2 Input parameters for the verification of the nitrogen CBC. Data taken from Ahn and Lee (2014).....	64
Table 3-3 Verification of cycle model with the literature value	65
Table 3-4 Selected PCHE specifications	66
Table 4-1 Steady state thermodynamic performance result.....	86
Table 4-2 Design parameters of the heat exchangers.....	88
Table 4-3 Turbines design parameters and main features for the nitrogen cycles	92
Table 4-4 LPC design parameters and main features for the nitrogen cycles.....	93
Table 4-5 HPC design parameters and main features for the nitrogen cycles	94
Table 5-1 Design parameters and assumed boundary conditions for the PWR/s-CO ₂ cycle power plant	99
Table 5-2 Precoolers conditions and design parameters for the simple, the recompression and the single recuperator recompression s-CO ₂ cycle for SM-PWR application	110
Table 5-3 IHX conditions and design parameters for the simple, the recompression and the single recuperator recompression s-CO ₂ cycle for SM-PWR application	114
Table 5-4 Recuperator conditions and design parameters for the simple, the recompression and the single recuperator recompression s-CO ₂ cycle for SM-PWR application	117
Table 5-5 Heat exchangers design result for the selected single recuperator recompression cycle for PWR application	130
Table 5-6 MC and RC design parameters and main features for the single recuperator recompression s-CO ₂ cycle	132
Table 5-7 Turbine design parameters and main features for the single recuperator recompression s-CO ₂ cycle	133
Table 6-1 Feedback reactivity coefficients, prompt-neutron life time and delayed neutron parameters for the SFR (Ragusa and Mahadevan, 2009).....	138
Table 6-2 Feedback reactivity coefficients, prompt-neutron life time and delayed neutron parameters for the PWR (Thomas, 1999; Naghedolfeizi, 1990).....	138
Table 7-1 Features of the control methods.....	161
Table 8-1 Pairing of the manipulated inputs and controlled output for plant automatic control system	166

Table 8-2 Summary of plant's design point conditions and parameters	172
Table 8-3 Proportional, integral and derivatives gain parameters of the PID controllers	176
Table 9-1 Summary of design point conditions and parameters for the SM-PWR/s-CO ₂ plant	211
Table 10-1 Proximate and ultimate analysis of Illinois No 6 coal (Fout et al., 2015).....	235
Table 10-2 Validation of s-CO ₂ Brayton cycle model against literature value	243
Table 10-3 Boundary conditions and design parameters.....	244
Table 10-4 Summary of the main stream values for the three cases calculated with baseline boundary conditions and design parameters.....	246
Table 10-5 Parameters and performance results of the PCC unit.....	248
Table 10-6 Comparison of plant performances with and without PCC for Case A (simple recuperative cycle as bottoming cycle), Case B (partial heating cycle as bottoming cycle) and Case C (single recuperator recompression cycle as bottoming cycle).....	248
Table A-1 Overall design requirements and parameters for the LPC of the single shaft nitrogen cycle.....	283
Table A-2 Total/stagnation properties in the three stages of the LPC of the single-shaft nitrogen cycle.....	283
Table A-3 Static properties in the three stages of the LPC of the single shaft nitrogen cycle ..	284
Table A-4 Stage geometry and parameters for the LPC of the single-shaft nitrogen cycle	284
Table A-5 Overall design requirements and parameters for the HPC of the single shaft nitrogen cycle.....	284
Table A-6 Total/stagnation properties in the four stages of the HPC of the single-shaft nitrogen cycle.....	285
Table A-7 Static properties in the four stages of the HPC of the single shaft nitrogen cycle ...	285
Table A-8 Stage geometry and parameters for the HPC of the single-shaft nitrogen cycle.....	285
Table A-9 Overall design requirements and parameters for the turbine of the single-shaft nitrogen cycle	286
Table A-10 Total/stagnation properties in the three stages nozzle leading (NLE), nozzle trailing edge (NTE) and rotor trailing edge (RTE) of the turbine of the single-shaft nitrogen cycle	286
Table A-11 Static properties in the three stages nozzle leading (NLE), nozzle trailing edge (NTE) and rotor trailing edge (RTE) of the turbine of the single-shaft nitrogen cycle	286
Table A-12 Stage geometry and parameters for the turbine of the single-shaft nitrogen cycle	287
Table A-13 Overall design requirements and parameters for the LPC of the two-shaft nitrogen cycle.....	287
Table A-14 Total/stagnation properties in the one stage of the LPC of the two-shaft nitrogen cycle.....	288
Table A-15 Static properties in the one stage of the LPC of the two-shaft nitrogen cycle	288
Table A-16 Stage geometry and parameters for the LPC of the two-shaft nitrogen cycle.....	288

Table A-17 Stage geometry and parameters for the LPC of the two-shaft nitrogen cycle	289
Table A-18 Total/stagnation properties in the two stages of the HPC of the two-shaft nitrogen cycle	289
Table A-19 Static properties in the two stages of the HPC of the two-shaft nitrogen cycle.....	289
Table A-20 Stage geometry and parameters for the HPC of the two-shaft nitrogen cycle.....	290
Table A-21 Overall design requirements and parameters for the CDT of the two-shaft nitrogen cycle	290
Table A-22 Total/stagnation properties in the one stage nozzle leading (NLE), nozzle trailing edge (NTE) and rotor trailing edge (RTE) of the CDT of the two-shaft nitrogen cycle.....	290
Table A-23 Static properties in the one stage nozzle leading (NLE), nozzle trailing edge (NTE) and rotor trailing edge (RTE) of the CDT of the two-shaft nitrogen cycle.....	291
Table A-24 Stage geometry and parameters for the CDT of the two-shaft nitrogen cycle.....	291
Table A-25 Overall design requirements and parameters for the FPT of the two-shaft nitrogen cycle	291
Table A-26 Total/stagnation properties in the four stages nozzle leading (NLE), nozzle trailing edge (NTE) and rotor trailing edge (RTE) of the FPT of the two-shaft nitrogen cycle.....	292
Table A-27 Static properties in the four stages nozzle leading edge (NLE), nozzle trailing edge (NTE) and rotor trailing edge (RTE) of the FPT of the two-shaft nitrogen cycle	292
Table A-28 Stage geometry and parameters for the FPT of the two-shaft nitrogen cycle.....	292
Table A-29 Overall design requirements and parameters for the MC of the single recuperator recompression s-CO ₂ cycle	293
Table A-30 Total/stagnation properties in the eight stages of the MC of the single recuperator recompression s-CO ₂ cycle	293
Table A-31 Static properties in the eight stages of the MC of the single recuperator recompression s-CO ₂ cycle	294
Table A-32 Stage geometry and parameters for the MC of the single recuperator recompression s-CO ₂ cycle	294
Table A-33 Overall design requirements and parameters for the RC of the single recuperator recompression s-CO ₂ cycle	295
Table A-34 Total/stagnation properties in the seventeen stages of the RC of the single recuperator recompression s-CO ₂ cycle	295
Table A-35 Static properties in the seventeen stages of the MC of the single recuperator recompression s-CO ₂ cycle	296
Table A-36 Stage geometry and parameters for the RC of the single recuperator recompression s-CO ₂ cycle	297
Table A-37 Overall design requirements and parameters for the turbine of the single recuperator recompression s-CO ₂ cycle	298

Table A-38 Total/stagnation properties in the three stages of the turbine of the single recuperator recompression s-CO₂ cycle..... 299

Table A-39 Static properties in the three stages of the turbine of the single recuperator recompression s-CO₂ cycle..... 299

Table A-40 Stage geometry and parameters for the turbine of the single recuperator recompression s-CO₂ cycle..... 299

Nomenclature

A	Area (m ²)
AR	Aspect ratio
b_H	Blade height (m)
c	Blade chord (m)
C	Absolute velocity (m/s) or specific heat capacity (J/(kg.K))
C_i	Concentration of delayed neutron precursor of i th group (neutron per m ³) or Concentration of the i th component (mol/m ³)
C_L	Lift coefficient
C_p	Specific heat capacity at constant pressure (J/(kg.K))
C_v	Constant valve construction coefficient (m ²)
D	Diameter (m)
DF	Diffusion factor
$dHaller$	de Haller number
E	Activation energy (J/mol)
$e(t)$	Error signal
f	Darcy friction factor
g	Gravitational acceleration (m/s ²)
H	Head (m)
HHV	Higher heating value (J/kg)
h	Specific enthalpy (kJ/kg) or convective heat transfer coefficient [W/(m ² .K)]
I	Inertia (kg.m ²)
K	Constant of proportionality or experimental heat transfer coefficient
K_d	Derivative gain of PID controller
K_i	Integral gain of PID controller
K_p	Proportional gain of PID controller
k	Thermal conductivity [W/(m.K)] or Pre-exponential factor
k_e	Reactor core multiplication factor
L	Length (m)
$LMTD$	logarithmic mean temperature difference (K)
\ln	Natural logarithm
M	Mass (kg)
\dot{m}	Mass flow rate (kg/s)
min	Minimum
N	Shaft speed (rad/s)
n	Neutron density (neutron per m ³)
N_b	Number of blade
Nu	Nusselt number
op	Optimum value
P	Pressure (Pa or N/m ²) or Perimeter (m)
Pr	Prandtl Number
\dot{Q}	Volumetric flow rate (m ³ /s)
Q	Heat transferred or duty (watt or J/s)
R	Universal gas constant (J/(K.mol))
r	Radius (m) or reaction rate (mol/(s.m ³))
Re	Reynold number
S	Strength density of an external constant neutron source (neutron/m ³ .s) or Entropy (J/(kg.K))
s	Blade spacing (m)
T	Temperature (K)
t	time
TTD	Terminal temperature difference
t	Conduction length (m)

U	Overall heat transfer coefficient [W/(m ² .K)] or blade velocity (m/s)
$u(t)$	Control signal
V	Velocity (m/s) or volume (m ³)
W	Power (W or J/s) or relative velocity (m/s)
y	Fraction

Greek Symbols

α	Absolute velocity angle (degree) or reactivity coefficient (1/°C)
β	Relative velocity angle (degree) or total fraction of delayed neutrons
β_i	Fraction of delayed neutron emitted by the i th precursor group
γ	Specific heat ratio
Δ	Change in quantity
δ	Fluid deflection through blade
ε	Effectiveness or pipe roughness
η	Efficiency
Λ	Reaction or neutron mean generation time (s)
λ_i	Decay constant of the i th precursor (s ⁻¹)
μ	Viscosity (Pa-s)
ξ	Relative pressure loss or friction loss coefficient (m ⁻⁴) or blade nominal loss coefficient
Π	Product operator
π	Pressure ratio or pi
ρ	Density (kg/m ³) or reactivity ($\Delta k/k$)
Σ	Sum operator
σ	Blade solidity
ϕ	Flow coefficient
ψ	Stage loading coefficient

Subscripts

0	Stagnation property or steady state
1	Turbine or compressor stage inlet
2	Turbine rotor or compressor stator inlet
3	Turbine or compressor stage exit
<i>ad</i>	Adiabatic
<i>aux</i>	Auxilliary
<i>C</i>	Cold stream
<i>c</i>	Compressor or coolant
<i>cdt</i>	Compressor driving turbine
<i>ef</i>	Effective
<i>elec</i>	Electrical
<i>f</i>	Reactor fuel or fission
<i>fpt</i>	Free power turbine
<i>gen</i>	Generator
<i>H</i>	Hot stream
<i>h</i>	Hydraulic
<i>hpc</i>	High pressure compressor
<i>hpt</i>	High pressure turbine
<i>HX</i>	Heat exchanger
<i>i</i>	inlet
<i>is</i>	Isentropic
<i>L</i>	Electric load demand
<i>lpc</i>	Low pressure compressor
<i>lpt</i>	Low pressure turbine
<i>m</i>	Melting or mean-line

<i>max</i>	Maximum
<i>mc</i>	Main compressor
<i>min</i>	Minimum
<i>nor</i>	Normalised value
<i>o</i>	Outlet
<i>P</i>	Pump
<i>r</i>	Nuclear reactor
<i>rc</i>	Recompression compressor
<i>ref</i>	Reference value at design point
<i>s</i>	Specific
<i>T</i>	Temperature
<i>t</i>	Turbine
<i>th</i>	Thermal
<i>tt</i>	Total-to-total
<i>W</i>	Metal wall
<i>wf</i>	Working fluid
<i>x</i>	Axial component
θ	Tangential component

Superscripts

<i>n</i>	Temperature exponent of reaction rate constant
<i>a_i</i>	Exponent of the <i>i</i> th component of the reaction rate kinetic

Abbreviations

2-D	Two-dimensional
ASTRID	Advanced Sodium Technological Reactor for Industrial Demonstration
ANTARES	AREVA New Technology Advanced Reactor Energy Supply
ANL	Argonne National Laboratories
PBMR	Pebble Bed Modular Reactor
CBC	Closed Brayton cycle
CCGT	Combined cycle gas turbine
CCS	Carbon capture and storage
CEA	French Atomic Energy Commission
CDT	Compressor-driving turbine
CHE	Compact heat exchanger
CSP	Concentrated solar power
DOE	Department of Energy
EDF	Electricité de France
ESP	Electrostatic precipitator
FBC or AFBC	Fluidized bed combustion or atmospheric FBC
FD	Forced draft
FGD	Flue gas desulfurization
FPT	Free power turbine
GA	General Atomics
Gen IV	Generation IV
GT	Gas turbine
GT-MHR	Gas Turbine-Modular Helium Reactor
GTHTR300	Gas Turbine High Temperature Reactor 300
HHT	High temperature reactor Helium gas turbine
HHV	High temperature helium turbomachinery test facility or higher heating value
HPC	High pressure compressor
HTC	Heat transfer coefficient
HTGR	High temperature gas-cooled reactor
HTR	High temperature recuperator
HTR/VHTR	High Temperature Reactor/Very High Temperature Reactor
HTR-10GT	10 MW helium cooled High Temperature Reactor Gas Turbine
ID	Induced draft
IHX	Intermediate heat exchanger
INET	Institute of Nuclear and New Energy Technology
INL	Idaho National Laboratories
JAERI	Japan Atomic Energy Research Institute
LMTD	Logarithmic mean temperature difference
LPC	Low pressure compressor
LTR	Low temperature recuperator
MC	Main compressor
MEA	Monoethanolamine
MGR-GT	Modular High-temperature Gas-cooled Reactor Gas Turbine
Na/N ₂ IHX	Sodium/nitrogen intermediate heat exchanger
NIST	National Institute of Standards and Technology
ORC	Organic Rankine Cycle
PA	Primary air
PCC	Post-combustion CO ₂ capture
PCHE	Printed Circuit Heat Exchanger
PCS	Power conversion system
PCU	Power conversion unit
PID	Proportional-Integral-Derivative

PSD	Particle size distribution
PWR	pressurised water reactor
RC	Recompression compressor
s-CO ₂	Supercritical carbon dioxide
SISO	Single-input single-output
SFR	Sodium cooled fast reactor
SM-PWR	Small modular pressurised water reactor
SM-SFR	Small modular sodium-cooled fast reactor
SMR	Small modular reactor
SNL	Sandia National Laboratories
TIP	Turbine inlet pressure
TIT	Turbine inlet temperature
TTD	Terminal temperature difference
USC	Ultra-supercritical

1 Introduction

1.1 Background and motivations

Closed-cycle gas turbine (GT) power plant has the potential to complement the conventional coal-fired power plant and open cycle GT power plants. As shown in Figure 1-1, global energy production has been increasing and it is projected to continue to increase in the future due to increasing world population and economic growth (Meter, 2008; Barner, 2006; Wang, 2009). Associated with the increased energy demand is the increase in fuel prices (Behar et al., 2013). Although there is currently a drop in the price of crude oil, the future is still unknown. It is expected that the percentage of power generated by renewable sources and possibly nuclear energy will increase in an attempt to reduce carbon dioxide (CO₂) emission (Behar et al., 2013). A unique feature of closed-cycle GT is its potential to serve as power conversion system (PCS) for non CO₂ emission energy sources such as nuclear reactor, concentrated solar power (CSP), biomass, geothermal and fuel cell (Najjar and Zaamout, 1992; Al-attab and Zainal, 2015; Kim et al., 2012). Therefore, the current global efforts geared towards the generation of electricity in a more efficient and environmentally benign manner through the research and development of alternative energy sources and PCSs will provide more market for closed-cycle GT.

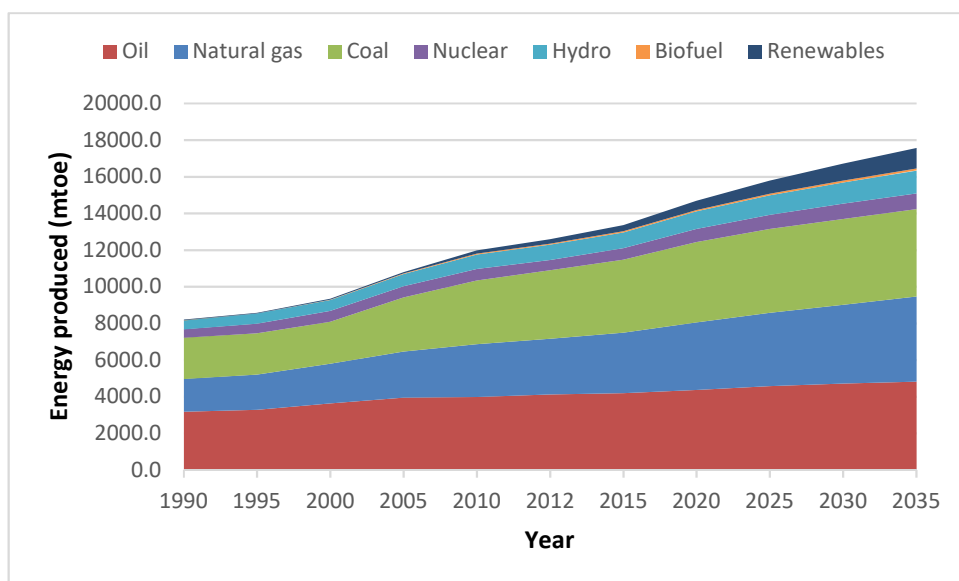


Figure 1-1 Global energy production by fuel (Courtesy of The British Petroleum Company Plc)

One previous drawback of the closed-cycle GT has been the lack of suitable heat source since light water reactor could not meet the high temperature requirement necessary for the cycle to be competitive. Similarly, the closed cycle GT was not well suited for conventional fossil-fired heat sources (Sarkar and Bhattacharyya, 2009; Dostal, 2004). Therefore, early popularity of the closed-

cycle GT from the 1950s to the 1970s was soon over shadowed by the more matured open cycle GT, which gives higher efficiency due to its higher firing temperature.

However, in the recent past, there has been a revival of interests in the study of closed-cycle GT as an alternative or as an additional PCS. Contributing to the renewed interest are the enormous achievement in the areas of high temperature small modular reactors (SMRs), the development of next generation nuclear reactors by Generation IV consortium and the improvement of solar receivers. While these new promising heat sources share the common features of moving to higher operating temperatures, the conventional PCSs cannot be adapted to exploit some of these higher temperatures. Hence, the door is open for the closed-cycle GT to be more competitive and will have billions of US dollars of commercial market

Furthermore, other previous hindrances to the commercialisation of closed-cycle GT such as material limitations for the high temperature and high pressure applications, the non-availability of suitable compact heat exchangers (CHEs) and the lack of sufficient turbomachinery experience are no longer major concerns (Sarkar and Bhattacharyya, 2009; Gibbs, 2008). For instance, the high pressure and high temperature are no longer considered as a drawback since power plant operators have acquired much experience with supercritical and ultra-supercritical (USC) steam units with operating conditions up to 320 bar and 600/610 °C. CHEs such as the printed circuit heat exchanger (PCHE) with high effectiveness and ability to withstand high pressure and temperature are now available as replacement for the classical shell and tube design (Heatric, 2015; Gibbs, 2008).

In the field of gas turbomachinery, introduction of magnetic bearing in 1985 means heavy rotor can be sustained and oil ingress in nuclear reactor eliminated (Kikstra, 2001; McDonald, 1994). The development of solid state frequency converters removes the restriction to always design the gas turbomachinery for synchronous speed and allows optimisation of turbomachinery performance on common shaft with the generator (Yan, 1990). The availability of advanced numerical computational tool now allows improved design of the heat exchangers and the turbomachinery aerodynamics.

It seems the next stage in the development of closed-cycle GT is the demonstration of the technologies. Therefore, conceptual studies of steady state and dynamic performances as well as preliminary design of plant components is required in order to assess the feasibility of different application options for near-term demonstration.

1.2 Overview of closed-cycle GT technologies

All GTs operate on the thermodynamic cycle called the Brayton cycle to produce mechanical power. Based on the path of the gases, GTs can be classified as shown in Figure 1-2 as: (a) open

cycle with air as the working fluid; (b) closed cycle with air or other fluids as the working fluid and (c) Semi closed cycle. Furthermore, closed-cycle GT can be characterised by the heat source and the working fluid. Applicable heat sources include fossil fuel, nuclear, solar and biomass while working fluids include air, s-CO₂, nitrogen, helium and other noble gases (Figure 1-2).

In a closed cycle GT or closed Brayton cycle (CBC), the turbine exhausts are not thrown out but recirculated. The layout and Temperature-Entropy (T-S) diagram of a simple regenerative closed cycle GT is shown in Figure 1-3(b). The working fluid is compressed in the compressor from point 1 to 2. Then it enters the recuperator where some of the heat content of the turbine exhaust is regenerated (points 2 to 3). After regeneration the fluid passes through the heat source, which could either be a nuclear reactor core, an intermediate heat exchanger (IHX) or a gas heater (points 3 to 4). In the heat source, the fluid achieves the highest temperature within the cycle. This is followed by an expansion in the turbine (points 4 to 5). The turbine provides the work for the compressor and generator. The turbine exhaust is then used to preheat the fluid coming out of the compressor in the recuperator (points 5 to 6). Finally, heat is rejected from the cycle in the cooler, where the fluid is cooled to the initial conditions.

Several authors (Saravanamuttoo et al., 2009; Bathie, 1996; Keller, 1978; Najjar and Zaamout, 1992) have highlighted the benefits of closed-cycle GT for power generation which include:

- Closed-cycle GT can achieve higher efficiency than the steam cycle at high temperature.
- Simpler than steam Rankine cycle which has many heat exchangers and pumps as well as a lot of piping.
- The possibility of operating at higher pressure gives compact components and smaller plant footprint compared to steam turbine plant. Higher power-to-size ratio and reduced capital cost can then be achieved.
- Unlike open cycle GT that can only use clean fuel, CBC can use solid fuels like coal and biomass as well as solar, nuclear and waste heat.
- Use of different working fluids with favourable thermal and transport properties (e.g. helium, nitrogen, CO₂, argon, neon and gas mixtures).
- No fouling and corrosion of system components and no need for air filtration in contaminated environment.

Despite the many benefits of closed-cycle GT, the open cycle has been more popular due to its capability to achieve very high turbine inlet temperature (TIT) making it more efficient, more compact and less costly. Figure 1-4 produced by McDonald (1995) shows the trends of the increase in firing temperature of open cycle and closed-cycle GTs. While closed-cycle GT firing temperature is limited by the allowable maximum temperature of the metallic heat exchanger,

open cycle GT takes advantage of increase in firing temperature and the availability of natural gas in abundance. Therefore, closed-cycle GT might not be able to replace open cycle GT with the current technology but it could still find usefulness in applications where open cycle GT cannot be deployed such as nuclear. Closed-cycle GT also has the potential to operate at higher temperature than steam Rankine cycle.

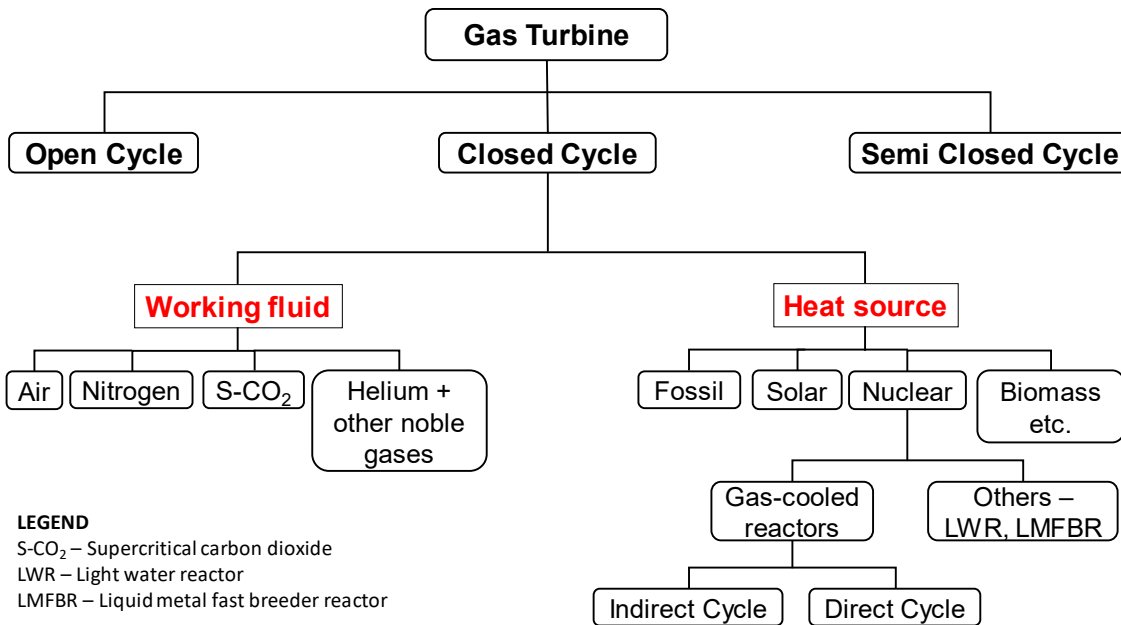
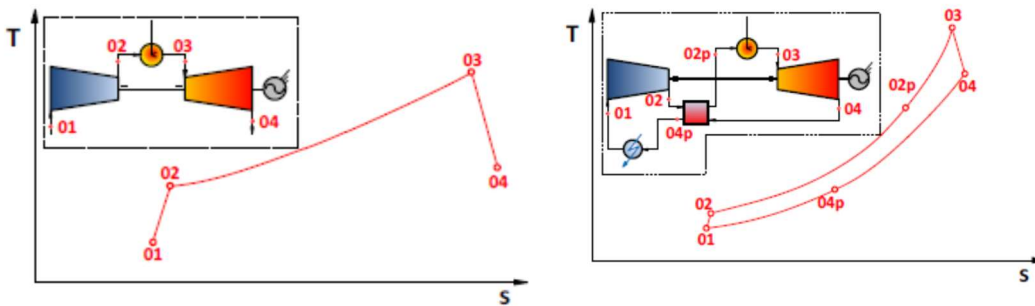


Figure 1-2 Gas turbine classification



(a) Open cycle gas turbine

(b) Closed cycle gas turbine

Figure 1-3 Open and closed-cycle GTs schematic and T-S diagram (Brenes, 2014)

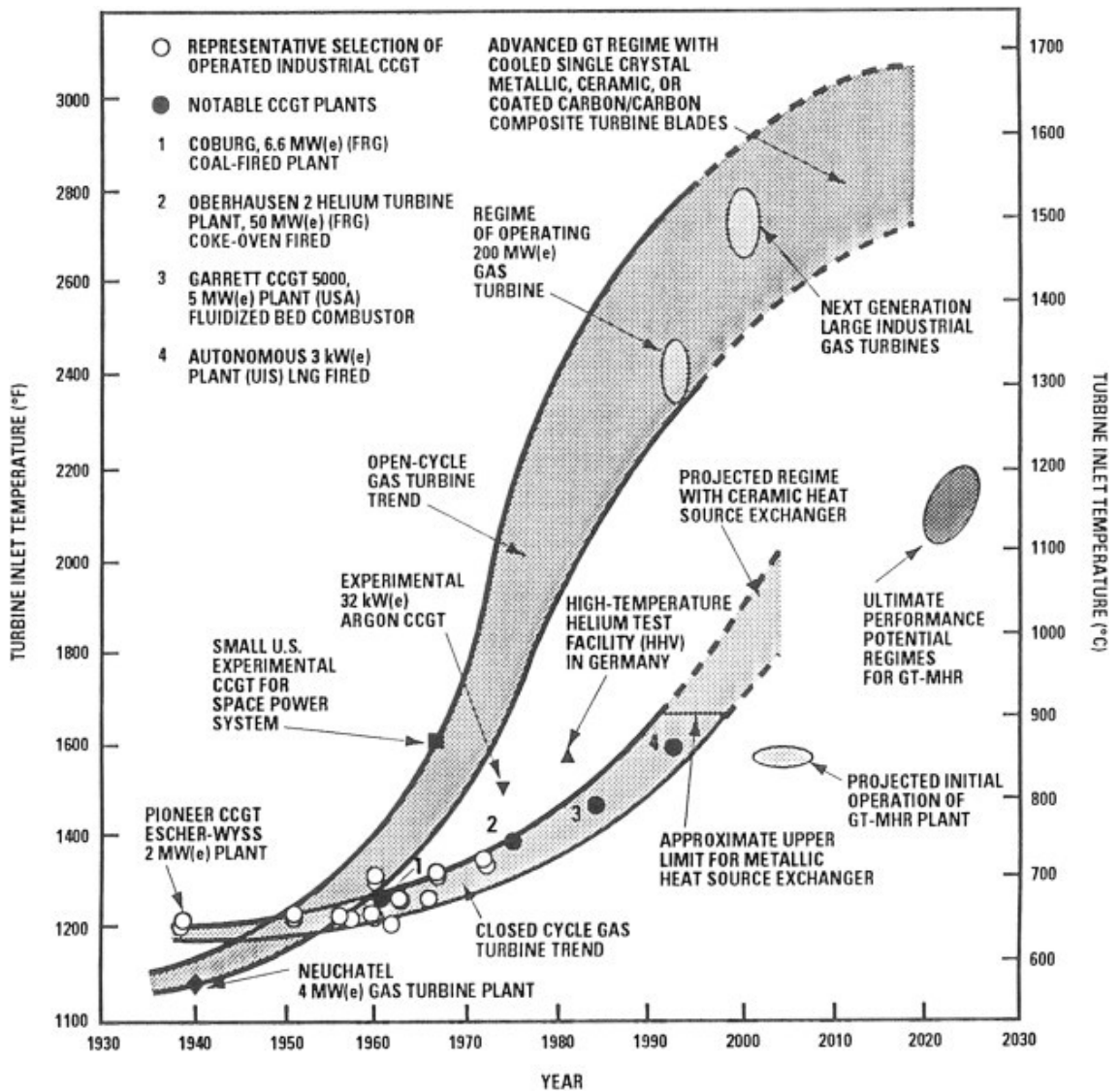


Figure 1-4 Gas turbine firing temperature trends (McDonald, 1995)

1.3 Aim and objectives of this research

The aim of this research is to adequately understand, through modelling and simulation, the steady state performance, the component design parameters and the dynamic behaviours, operation and control of closed-cycle GTs for the purpose of assessing their feasibility for near-term demonstration.

This research aim will be achieved through the following objectives:

- To provide comprehensive review of previous research, programmes and operating experience on closed-cycle GTs
- To carry out steady state thermodynamic performance analysis of closed-cycle GTs coupled to small modular sodium cooled fast reactor (SM-SFR), small modular

pressurised water reactor (SM-PWR) and coal-fired furnace with solvent-based carbon capture

- To perform preliminary design and sizing of the heat exchangers, compressors and turbines of the closed-cycle GTs coupled to the SMRs
- To develop dynamic models of closed-cycle GTs coupled to nuclear reactors
- To implement control systems for closed-cycle GTs coupled to the SM-SFR and SM-PWR
- To carry out dynamic performance analysis of closed-cycle GTs coupled to the SM-SFR and SM-PWR

1.4 Plant design choices

The selection of plant designs to be studied include the choice of heat sources, the selection of appropriate working fluids and the most suitable Brayton cycle configurations for different applications. In the selection of heat source, consideration is given only to mature technologies so that development efforts can be focused on the closed-cycle GT PCS. The heat sources chosen for design and performance study in this work are pressurised water reactor (PWR), sodium cooled fast reactor (SFR) and coal-fired furnace.

For the nuclear reactor heat sources, SMRs are considered. SMRs are defined as nuclear reactors with size less than 300 MWe. The UK Department of Energy & Climate Change (DECC) plans to invest at least £250 million toward the commercialisation of SMRs in the UK over five years from 2015 (WNA, 2015). The interest in SMRs is driven by the following benefits:

- Reduced impact of capital costs and hence viewed to have less financial risk
- Enhanced safety from simplified designs
- Can be deployed faster as most of them could be factory-built and then assemble on site
- Easier to operate and maintain compared with the larger nuclear reactors
- Flexible with respect to electricity generation and hence can help cope with the challenges of intermittent renewable energy by rapidly increasing or decreasing power output
- More flexible siting. Can be sited in off-grid areas requiring small power and future growth can be accommodated by simply adding extra units
- Cheaper when mass produced

The choice of working fluids and cycle configuration for each heat source results in three stream of studies in this work. An overview of study options for the nuclear closed-cycle GT is shown in Figure 1-5.

- 1) **SM-PWR application:** PWR is the most common type of nuclear reactor representing about 60% of all nuclear reactors in the world. Hence, SM-PWRs are the most matured of the SMRs as they are based on existing technology and years of design and operational experience. In this study, supercritical carbon dioxide (s-CO₂) is chosen as the CBC working fluid for the SM-PWR application. S-CO₂ cycle gives better efficiency than other closed-cycle GT at low/medium temperature (Dostal, 2004). It also provides compact design and smaller plant footprint. The s-CO₂ cycle might not be competitive in term of efficiency at the PWR temperature when compared with the steam Rankine cycle, which is the state-of-the-art PCS for nuclear power reactors. However, s-CO₂ cycle offers the advantages of compact design and smaller components, which is compatible with the modularity of the reactor (Dostal, 2004). The most common s-CO₂ layout is the recompression configuration. However, a new modified layout is investigated in this work for PWR application.

- 2) **SM-SFR application:** In addition to larger SFRs, SM-SFRs are also under consideration by Generation IV International Forum, which is developing the next generation of nuclear reactors with temperature higher than current reactors (GIF, 2014). The Generation IV nuclear reactors (Gen IV reactors) are the next step in the deployment of nuclear power generation to meet the world's future energy demand (Damiani et al., 2014). Of all the six Gen IV reactors, SFR has been identified as the most matured and hence the most suitable for near-term demonstration (Pérez-Pichel et al., 2012; Merk et al., 2015; Carre et al., 2010).

The PCS implementation is critical to the successful commercialization of the SM-SFR power plant technology. The current SFRs (e.g. Phenix, SuperPhenix, BN 600, BN 800, etc.) adopt the proven steam Rankine cycle as PCS (Pérez-Pichel et al., 2011; Seo et al., 2016). However, there are concerns over the coupling of steam cycle to SFR. The challenges include: (a) safety concern because of the possibility of hazardous sodium-water reaction (b); high capital cost because of additional secondary sodium circuit and large plant footprint; and (c) low efficiency. Also, for s-CO₂ Brayton cycle, sodium-CO₂ reaction could be of safety concern at some temperatures and requires further investigation to understand the nature of the chemical reaction (Sienicki et al., 2010; Eoh et al., 2013). Helium gas does not react with sodium but helium CBC is not promising for SFRs due to its low thermal efficiency (Pérez-Pichel et al., 2011). Hence, in this study, nitrogen Brayton cycle is considered as the PCS for the SM-SFR application.

The nitrogen CBC option is attractive because nitrogen is inert, thus eliminating the risk of sodium-water or sodium-CO₂ reactions. Furthermore, design of nitrogen PCS is anticipated to be less challenging since years of experience from air GT engines can be applied (Sun et al., 2000). After all, nitrogen properties are similar to those of air. Hence, the nitrogen cycle is perceived as the only potential option for short-term demonstration while the s-CO₂ cycle could be a suitable option for long-term applications (Alpy et al., 2011; Pérez-Pichel et al., 2011). The popular cycle layout for nitrogen CBC is the intercooled single shaft configuration. A two-shaft option is also investigated in this study as means of simplifying the turbomachinery design.

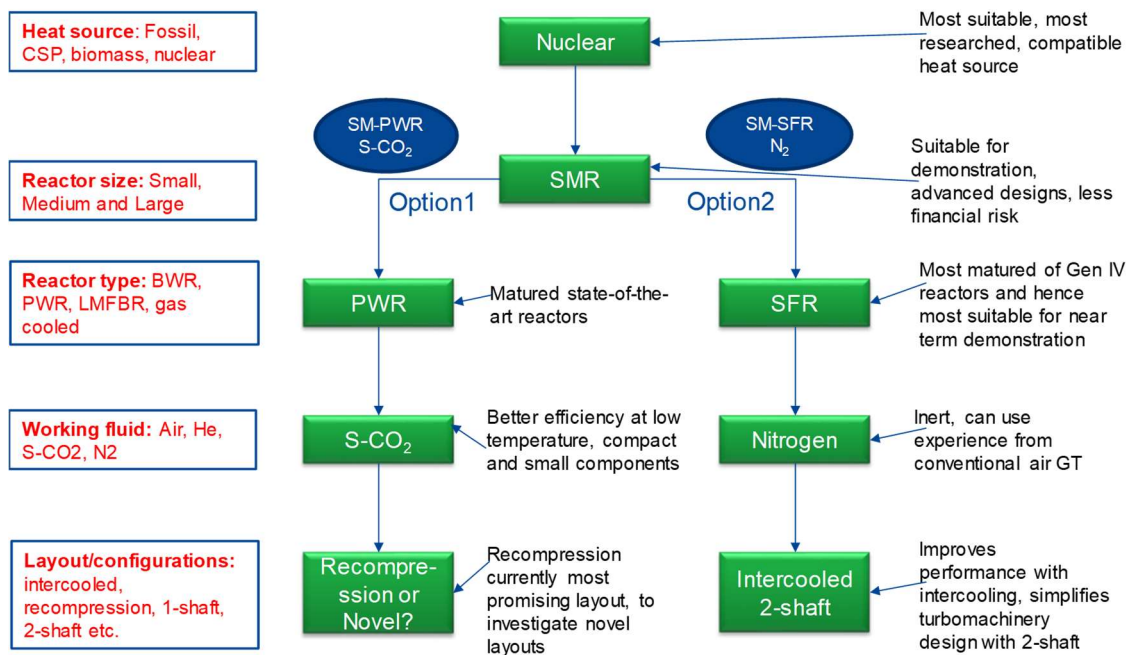


Figure 1-5 Overview of the selection of design study options for nuclear closed-cycle GTs

- 3) **Coal-fired power generation application:** Coal-fired power generation is expected to remain a key component of the global energy mix into the future due to its reliability, security of fuel supply, cheap fuel and competitive cost of electricity (Cau et al., 2015; IEA, 2016). In addition, coal-based electricity generation is a matured and well-developed technology compared to alternative energy sources. In 2014, about 40.8 % of the world total electricity was generated by coal combustion in coal-fired power stations and coal's share of the world total primary energy supply reached 29%, its highest level since 1971 (IEA, 2016). However, one prime concern about continued use of fossil fuels like coal for power generation is the emission of CO₂ to the atmosphere.

Two options that have been identified for mitigating CO₂ emissions from fossil fuel power plants are CCS (carbon capture and storage) systems and efficiency improvement. Post-combustion CO₂ capture (PCC) by chemical absorption with aqueous

monoethanolamine (MEA) solvent is currently the most preferred CCS option (IPCC, 2005; Arachchige and Melaaen, 2012). The second approach to reducing CO₂ emissions, which is by efficiency improvement, usually requires increased main steam temperature and pressure. Therefore, the state-of-the-art technology for coal-fired power generation, the USC steam plant, now operates at a steam pressure up to 300 bar and temperature up to 600 °C with reheat.

However, CCS systems and efficiency improvement through increased temperature and pressure have their limitations. Firstly, integration of PCC system with fossil fuel power plants leads to significant efficiency penalty and increased cost of electricity generation. Secondly, lack of advanced materials to withstand harsh operating conditions limits further improvement in efficiency through main steam temperature and pressure increase (Mecheri and Le Moullec, 2016).

Therefore, in this work, to improve the efficiency of coal-fired power plants, s-CO₂ Brayton cycle is considered as an alternative to the conventional steam Rankine cycle. Additionally, CO₂ capture is facilitated by integrating an MEA-based PCC system with the s-CO₂ cycle power plant.

1.5 Predicted novel contributions

Despite the substantial previous research carried out on closed cycle GTs for power generation, an extensive study to investigate the near-term feasibility options for different applications and that which performs a full-scope assessment covering the choice of designs, thermodynamic performance analysis and optimisation, preliminary design of components, dynamic performance analysis and control strategy development is rare. Most studies tend to focus either on a single application involving only a particular heat source and working fluid, or limit studies to only steady state thermodynamic analysis, or on a component design independent of the cycle, or on dynamic performance and control for the PCS without including the heat source dynamics.

The main novel contributions of this work are:

- Critical review of closed-cycle GT, important R&D programmes and studies and update of major demonstration and test facilities
- The development of three closed-cycle GT options (SM-SFR/Nitrogen, SM-PWR/s-CO₂ and coal-fired/s-CO₂), each of which could be pushed forward for near-term demonstration
- New two-shaft nitrogen CBC with parallel turbines as a promising alternative to the single-shaft configuration to simplify the design of the turbomachinery. To the best of

our knowledge, no one has investigated a two-shaft configuration option for nitrogen cycle coupled to SFR.

- Preliminary design of main cycle components of nuclear closed-cycle GTs
- New layout concept, the single recuperator recompression layout, as the most promising s-CO₂ Brayton cycle layout for PWR and suitable for low temperature heat sources
- Development of cascaded s-CO₂ Brayton cycles for efficient utilisation of flue gas heat from coal-fired furnace
- Integration of solvent-based PCC to a coal-fired s-CO₂ Brayton cycle power plant
- Development of dynamic models based on first principle for nuclear closed-cycle GTs, which incorporate the dynamics of both the reactor side and the PCS
- Design of suitable control scheme for the selected nuclear closed-cycle GT layouts

1.6 Research methodology and scope of this study

The coupling of closed-cycle GT to either nuclear reactor or coal-based heat source with carbon capture is yet to be commercialised. There are a number of challenges regarding the performance, components design, operation and control of the plant. Figure 1-6 illustrates the research methodology followed in this study to achieve the research objectives. Table 1-1 shows the scope of the studies carried out on three applications of closed-cycle GTs deemed suitable for near-term demonstration.

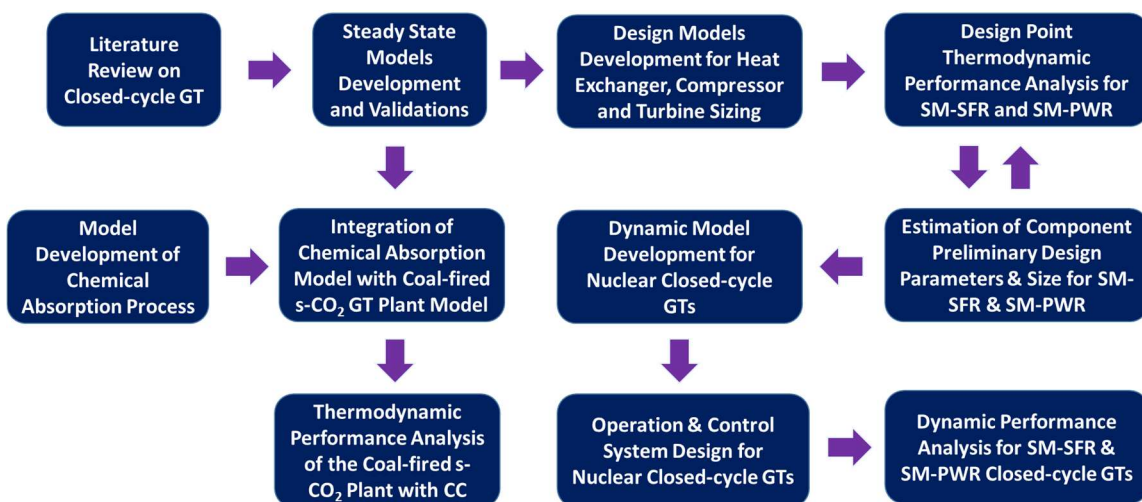


Figure 1-6 Overview of research methodology

Table 1-1 Overview of the scope of this study

	SM-SFR/Nitrogen	SM-PWR/s-CO ₂	Coal-fired/s-CO ₂
Literature Review	✓ (Ch. 2)	✓ (Ch. 2)	✓ (Ch. 2)
Development of steady state models & validation	✓ (Ch. 3)	✓ (Ch. 3)	✓ (Ch. 10)
Model development of chemical absorption process	Not applicable	Not applicable	✓ (Ch. 10)
Development of heat exchanger & turbomachinery design models	✓ (Ch. 3)	✓ (Ch. 3)	X
Steady state thermodynamic performance analysis	✓ (Ch. 4)	✓ (Ch. 5)	✓ (Ch. 10)
Preliminary design and sizing of heat exchangers, compressors and turbines	✓ (Ch. 4)	✓ (Ch. 5)	X
Dynamic model development	✓ (Ch. 6)	✓ (Ch. 6)	X
Operation & control system design	✓ (Ch. 7 & 8)	✓ (Ch. 7 & 9)	X
Dynamic performance analysis	✓ (Ch. 8)	✓ (Ch. 9)	X

1.7 Software tools used for the study

1.7.1 Matlab®/Simulink®

Matlab® (**matrix laboratory**) is a high-level programming language and interactive environment for numerical computation and visualisation. Matlab® allows development of algorithms, creation of models and user interfaces, plotting of functions and data, and interfacing with programs written in other languages (MathWorks, 2014). Simulink® is an additional package that adds multi-domain simulation and model-based design. Simulink provides a graphical editor, customisable block libraries and solvers for modelling and simulation of dynamic systems (MathWorks, 2015).

Matlab®/Simulink® is used for the modelling, design and simulation of the nuclear closed-cycle GT power plants (i.e. the SM-SFR/Nitrogen and SM-PWR/s-CO₂ plants). It is referred to in Chapter 3 and Chapter 6 in the development of the steady state, component design and dynamic model of nuclear closed-cycle GTs. Matlab®/Simulink® is used because it is a more general and flexible numerical computation and visualisation tool. It has a large mathematical library and a very powerful control toolbox. In this study, a REFPROP (version 9.1) program of the National

Institute of Standards and Technology (NIST) is embedded in the Matlab[®]/Simulink[®] software for obtaining fluid thermodynamic and physical properties.

1.7.2 Aspen Plus[®]

Aspen Plus[®] is process modelling, simulation and optimisation software that possess model libraries of various unit operations encountered in chemical, petrochemical and power generation plants. The added Aspen Properties[®] software equipped Aspen Plus with a relatively large physical property database (Dyment and Mantrala, 2015).

Aspen Plus[®] is used for the simulation of the coal-fired/s-CO₂ power plant with solvent-based PCC. It is mentioned in Chapter 10 in the development of steady state simulation of coal-fired s-CO₂ power plant and rate-based simulation of CO₂ capture system. Aspen Plus[®] is used because it is very powerful for simulating processes involving chemical reactions, heat and mass transfer.

1.8 Outline of the thesis

Chapter 2 presents the review of closed-cycle GTs for power generation. It provides a state-of-the-art assessment of the research activities and development of closed cycle GTs. Relevant concepts necessary for an understanding of closed-cycle GT is explained. An overview of important R&D programmes and experimental/pilot plants, and commercially operated plants is provided. Research activities on the modelling and simulation of closed-cycle GT are discussed. Finally, the need for demonstration plant for closed-cycle GT is highlighted.

Chapter 3 describes the steady state model development for closed-cycle GTs coupled to nuclear reactor heat sources and its implementation in Matlab[®]. The implementation of the fluid thermodynamic and transport properties is also described. Verification of the steady state model with results of numerical model from the literature is presented. In addition, heat exchanger and axial turbomachinery design methodology are presented.

Chapter 4 presents the steady state thermodynamic performance analysis of the SM-SFR/Nitrogen cycle (i.e. the SM-SFR coupled to nitrogen CBC) power plant. Also presented are the results of the preliminary design of the heat exchangers and turbomachinery for the plant. A reference single-shaft Brayton cycle is compared with a newly suggested two-shaft configuration with regard to performance and turbomachinery design optimisation.

Chapter 5 presents the steady state thermodynamic performance analysis and preliminary design of heat exchangers and turbomachinery for the SM-PWR/s-CO₂ cycle (i.e. the SM-PWR coupled to supercritical CO₂ cycle) power plant. The performance and preliminary design of the

components of a newly proposed s-CO₂ layout is compared with simple recuperated and recompression s-CO₂ layout.

Chapter 6 describes the dynamic model development for closed-cycle GT coupled to nuclear reactor. The chapter presents the mathematical model for nuclear reactor, coolant pump, compressor, turbine, heat exchanger and other cycle components. Model integration in Matlab[®]/Simulink[®] is also explained.

In Chapter 7, the control system design for nuclear closed-cycle GT is described. The principles of control of closed-cycle GT are explained. Control system requirements and objectives are highlighted and the tuning of the controller is explained.

Chapter 8 presents the dynamic performance of the SM-SFR/Nitrogen nuclear plant. Automatic control system configuration for the plant is described. The plant transient response and control system performance under normal load following and loss of grid load are investigated.

In Chapter 9, the dynamic performance analysis of the SM-PWR/s-CO₂ nuclear power plant is presented. Also, operation, control and simulation challenges for s-CO₂ cycle power plant are described. Automatic control configuration for the plant is presented and transient responses of the plant under load following and loss of grid load events are presented.

Chapter 10 describes the thermodynamic performance of coal-fired s-CO₂ Brayton cycle power plant with solvent-based PCC. Simulation of coal-fired s-CO₂ cycle plant and chemical absorption process in Aspen Plus[®] are described as well as the validation of the s-CO₂ CBC model. Performance comparison of three cases of coal-fired s-CO₂ power plant is presented.

Chapter 11 provides conclusions for the study and recommendation for future work.

2 Literature Review¹

2.1 Introduction

The aim of this chapter is to provide a state-of-the-art assessment of the research activities and development of closed-cycle GT. For those with little knowledge of closed-cycle GT, the chapter will give an introduction of the relevant concepts necessary to achieve basic understanding. For those already acquainted with the technology, this chapter will review past experiences, recent progress and give an outlook of the future research directions based on current developments.

The distinctions between the discussions in this chapter and previous review work such as Keller (1978) and Frutschi (2005) are:

- This chapter provide an update of major demonstration and test facilities worldwide
- It provides a critical review of important research programmes and research studies in modelling and simulation, and operation and control of closed-cycle GTs and

The historical development of closed- cycle GT is enumerated. The relevant technology concepts (e.g. heat sources, working fluids, configuration and layout) for the understanding of closed-cycle GT is reviewed. Then the major power plants, demonstration and experimental test facilities, and research activities worldwide are reviewed. This is followed by an overview of the various studies based on modelling, simulation, operation and control. Also highlighted is the need for demonstration plant.

2.2 Historical development of closed-cycle GT

Table 2-1 shows the historical development of closed-cycle GT in chronological order. In 1935, at a time when the development of GT technologies was just emerging, Ackeret and Keller patented the closed-cycle GT (Frutschi, 2005; McDonald, 2012). Four years later, the pioneering closed-cycle GT, the AK-36 test plant, was built. However, no industrial plant was built until about a decade later as a result of the Second World War and the following economic recession (McDonald, 2012). In 1949, the first industrial closed-cycle GT power plant reported in the literature was commissioned in the city of Coventry, UK (Frutschi, 2005). By the early 1970s, about 20 fossil-fired air closed-cycle GT plants had been constructed in Europe with a total operating time of about 750,000 hours (Bammert and Groschup, 1977; Frutschi, 2005; McDonald,

¹ Most of this chapter has been published in Olumayegun, O, Wang, M. and Kelsall, G. (2016). Closed-cycle gas turbine for power generation: A state-of-the-art review. *Fuel*, Vol. 180, pp. 694-717

2012). The ability to operate on different fuels and the possibility for the cogeneration of heat and power contributed to the popularity of the power plants at that time (McDonald, 2012).

With the successful operation of the small air closed-cycle GT power plants in Europe, efforts were directed toward the design of plants with larger rated power output (Keller, 1978). However, above 30 MW, helium was considered a more suitable working fluid than air and it can serve as coolant in high temperature gas-cooled reactors (HTGRs). The first helium closed-cycle GT, albeit with no output power generation, was developed in 1962 by James La Fleur for driving a cryogenic air separation process in the USA (La Fleur, 1963). Earlier in 1942, Ackeret and Keller proposed the application of helium closed-cycle GT to HTGR with direct cycle (Keller, 1978). In the following four decades, various conceptual design studies were done on the possibility of coupling helium CBC to HTGR in the USA, Germany, the UK and France. This is as a result of recognising that its adaptability to HTGR would contribute to future acceptance. The first of the German-Swiss High Temperature Reactor Helium GT (HHT) project, the coke oven gas fired Oberhausen II helium turbine cogeneration plant, was built in 1974. The second demonstration facility for the HHT project, the high temperature helium turbomachine test facility (HHV), was built in 1981. These large nuclear GT power plant concepts were not pursued further due to lack of technology readiness. Hence, from 1981, investigation of nuclear GT was limited to paper studies only (McDonald, 2012).

Research focus on helium GT was shifted to the high temperature SMR GT system from the early 1980s. By 1987, studies at MIT resulted in a conceptual design of the Modular High-temperature Gas-cooled Reactor Gas Turbine, MGR-GT (Yan, 1990). General Atomics (GA) of USA developed the first design of the Gas Turbine-Modular Helium Reactor (GT-MHR) in 1990 (Baxi et al., 2008). ESKOM Company of South Africa in 1994 started the development of a 400 MWth Pebble Bed Modular Reactor (PBMR) with direct helium Brayton cycle. The Japan Atomic Energy Research Institute (JAERI) started in 2001 the Gas Turbine High Temperature Reactor 300 (GTHTR300) programme (Yan et al., 2003). In China, the Institute of Nuclear and New Energy Technology (INET) at Tsinghua University in 2003 started the experimental 10 MW helium cooled High Temperature Reactor Gas Turbine (HTR-10GT) project (Wu and Yu, 2007). In mid 2003, development began on the French High Temperature Reactor/Very High Temperature Reactor (HTR/VHTR) project, the ANTARES (AREVA New Technology Advanced Reactor Energy Supply) combined cycle cogeneration concepts, comprising a topping helium/nitrogen mixture CBC (Gauthier et al., 2006).

Table 2-1 Historical development of closed-cycle GT

Date	Development
1935	Prof Curt Keller and Prof J. Ackeret patented the closed-cycle GT in Berne, Switzerland
1939	The AK-36, the pioneer closed-cycle GT, was built by Escher Wyss AG in Zurich, Switzerland.
1949	An industrial closed-cycle GT with waste heat source and using air as working fluid was commissioned in Coventry UK
1950	G. Sulzer patented a partial condensation CO ₂ Brayton cycle
1960	In Germany, the Oberhausen I air closed-cycle GT cogeneration plant was commissioned
1962	The US Army's ML-1, the only nuclear reactor coupled CBC ever built, was built for mobile power generation. In the USA, the pioneering helium closed-cycle GT was built for air liquefaction by James La Fleur
1970	A 150 kWe S-CO ₂ loop was designed by Hoffman and Feher to investigate the possibility of using S-CO ₂ cycle for small terrestrial nuclear reactor
1972	The biggest and the last air closed-cycle GT was built by Escher Wyss for the City of Vienna
1974	The first HHT project, the Oberhausen II, started operation in German. Operation stopped in 1988.
Early 1980s	GA conducted an assessment of a large size (2000 MWth) HTGR-GT OKBM in USSR investigated the replacement of steam cycle with CBC for their 1000 MWth nuclear power plant
1981	The second HHT project, the HHV test facility, was built in Germany
1987	Years of studies at MIT resulted in a conceptual design of the MGR-GT
1994	The South African company, ESKOM, started the development of PBMR helium GT plant. Later changed to indirect steam Rankine cycle in 2009.
1995	A joint programme for the development of the GT-MHR was started by GA of USA and Minatom of Russia with the support of the Russian and U.S. Department of Energy (DOE). Framatone (France) and Fuji Electric (Japan) later joined the programme In Britain, a natural gas-fired closed cycle GT test facility using mixture of nitrogen and oxygen (2%) as working fluid was installed by British Gas.
2000	MIT in collaboration with INL, SNL and ANL revived interest in SCO ₂ cycle study
2001	The GTHTR300 programme was started by the JAERI in partnership with Toshiba and Mitsubishi
2003	The experimental HTR-10GT project was started in China by INET A 1/3-scale test model of the GTHTR300 compressor was designed and fabricated in Japan to investigate the performance and design Development of ANTARES (France) combined cycle cogeneration plant concept with a topping CBC.
2012	After previous installation of small S-CO ₂ compression test loops and the CBC test bed (SBL-30), SNL contractor Barber-Nichols Inc. completed the design and installation of a megawatt class S-CO ₂ recompression cycle test assembly
2014	Echogen announced the commercialisation of 8 MW EPS100 heat engines, that uses S-CO ₂ as working fluid for waste heat recovery

In 1950, a partial condensation CO₂ closed-cycle GT was patented by G. Sulzer (Sulzer, 1950). In the 1960s and early 1970s, the benefits of the unique features of CO₂ gave rise to increased interest in its potential use as working fluid among researchers (Gokhstein and Verkhivker, 1971; Angelino, 1968; Feher, 1967; Strub and Frieder, 1970). After this period, development of s-CO₂ cycle was delayed with no deployment of the plant taking place because of the lack of technology maturity for the high pressure and high temperature system. However, in the late 1990s and early 2000s, a renewal of interest in the s-CO₂ cycle was kindled by research at institutions such as the MIT in collaboration with Sandia National Laboratories (SNL), the Idaho National Laboratories (INL) and the Argonne National Laboratories (ANL) (Gibbs, 2008; Dostal et al., 2001). Other institutions included the Czech Technical University in 1997 and the Tokyo Institute of Technology (Kato et al., 2001; Dostal et al., 2001).

2.3 Review of relevant concepts and major features

The fundamental concepts and features relating to the design consideration of close-cycle GT involve:

- Selection of heat source
- Choice of working fluid and
- Adoption of a physical layout/configuration for the cycle.

An understanding of the cycle components is also required.

2.3.1 Fuel/Heat sources

The closed-cycle GT is applicable to most thermal heat sources for power generation. Hence its potential markets include (McDonald, 1985; Anheden, 2000):

- Electric power generation from nuclear, CSP, biomass, geothermal, waste heat and energy storage system
- Power plants with CCS
- Space exploration power systems
- Marine and underwater propulsion and power systems
- Terrestrial transportation systems

2.3.1.1 Fossil fuels

All the early operational closed-cycle GTs were fossil fuel fired (Fruttschi, 2005). After some time it was clear that the fossil-fired closed-cycle plants using air as working fluid could not compete with open cycle due to the small rated power and low firing temperature (below 700 °C). Hence, the Oberhausen II plant was built in 1974 to prepare the ground for nuclear closed-cycle GT and demonstrate the use of helium in high temperature large-scale plant. The plant was fired by coke oven gas to give hot helium temperature of 750 °C. A detailed description of these plants and others will be presented later.

Closed-cycle GT can be integrated with combustion systems that have low emissions such as fluidized bed combustion (FBC). CO₂ emission can be mitigated by either enabling the GT to operate on a CO₂-neutral fuel like biomass, or using a fossil fuel and then capturing the CO₂ instead of venting it to the atmosphere. Under the US DOE (Department of Energy) programme, Aerojet Rocketdyne and Southwest Research Institute have been evaluating s-CO₂ closed-cycle GT using fossil fuels with CCS (Johnson et al., 2012; McClung et al., 2014). The Aerojet Rocketdyne's Zero Emission Power and Steam (ZEPS™) plant using FBC is an oxy-coal power plant with s-CO₂ Brayton cycle (Figure 2-1). A technical-economic evaluation of a coal-fired s-CO₂ closed-cycle GT plant with PCC by Le Moullec (2013) showed 15% reduction in cost of electricity compared to supercritical steam plant equipped with CO₂ capture.

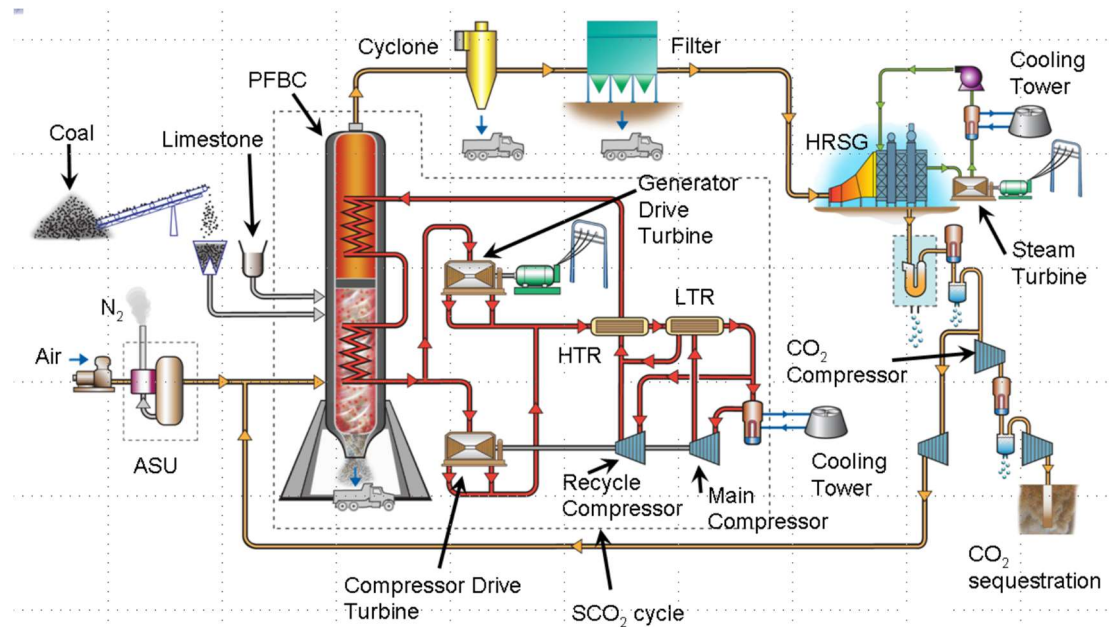


Figure 2-1 Aerojet Rocketdyne's oxy-combustion coal-fired s-CO₂ Brayton cycle (Vega et al., 2014)

2.3.1.2 Nuclear heat source

Closed-cycle GT is well suited for nuclear heat sources as it prevents release of contaminated fission material to the environment unlike open cycle GT. Also, with efficiency up to 50% at about 1000 °C reactor outlet temperature and the benefit of smaller plant footprint, the closed-cycle GT can compete with steam cycle (Golovko et al., 2000).

Escher Wyss suggested coupling of closed-cycle GT to the Dragon helium cooled reactor and GHH suggested coupling to the Beach Bottom reactor (Keller, 1978). GA assessed a large 2000MWth HTGR GT and OKBM in the USSR investigated the replacement of steam cycle with CBC for their 1000MWth VG-400 nuclear reactor (Brey, 2000; Golovko et al., 1995). However, the only nuclear reactor coupled closed-cycle GT ever built was the ML-1 for mobile power generation (Wright et al., 2005).

In order to achieve inherent safety, most modern HTGR design adopts SMR concept limited to below 600 MWth (Golovko et al., 2000). Some recent designs of HTGR-coupled CBC are GT-MHR (Russia and USA), ANTARES (France), GT-HTR300 (Japan), HTR-10GT (China) and PBMR (South Africa). They all use helium as reactor coolant. The Generation-IV consortium, established in 2000, is developing six categories of next generation nuclear reactors expected to be fully matured for commercialisation in the period between 2020 and 2030 or beyond (Abram and Ion, 2008; Kelly, 2014). These reactors, for electricity generation and hydrogen production, would be operating at higher temperature than the current reactors. Various researches on the power cycles for these next generation reactors indicated closed-cycle GTs as promising alternatives to the current steam turbine cycles (Dostal, 2004; Zhao and Peterson, 2008; Cha et al., 2009; Parma et al., 2011).

The CBC can be coupled to the reactor in either a direct cycle (in the case of gas-cooled reactors) or an indirect cycle configuration as shown in Figure 2-2.

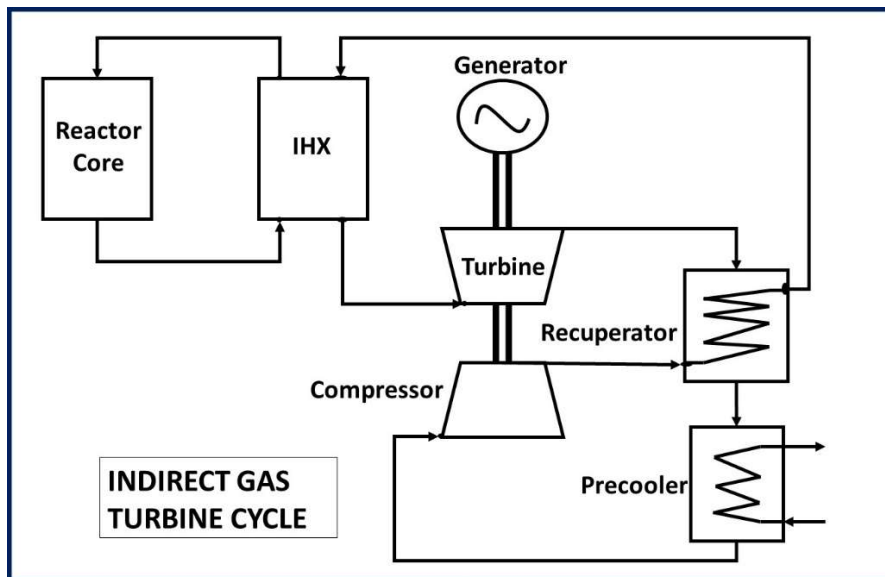
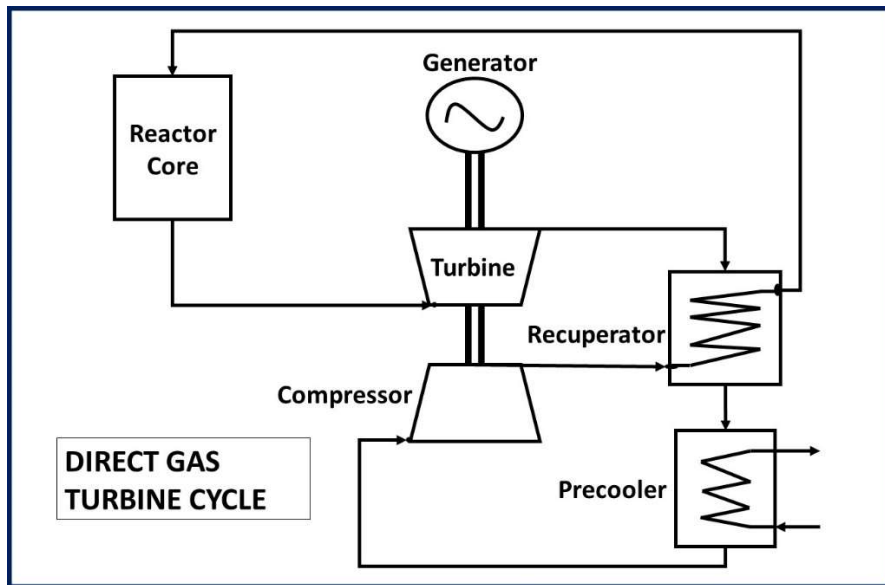


Figure 2-2 Indirect and direct nuclear GT cycles (Wang and Gu, 2005)

2.3.1.3 Concentrated solar power heat source

CSP can provide renewable thermal power at temperature up to and above 1000 °C with the current receiver technologies to drive a power conversion cycle for the generation of electricity (Al-attab and Zainal, 2015; Ma and Turchi, 2011).

Many researchers are now investigating closed-cycle GT as alternative cycle for CSP offering increased efficiency by taking advantage of the higher temperature (Chacartegui et al., 2011a; Ma and Turchi, 2011; Forsberg et al., 2006; Garg et al., 2013; Muto et al., 2014). According to Ma and Turchi (2011), the use of a single-phase fluid like s-CO₂ as both solar heat transfer fluid and the PCS working fluid will give a simpler plant and is compatible with sensible heat thermal energy storage. Economic and technical analysis of CSP s-CO₂ cycle seems to suggest 5–10 MW

as the optimal capacity (Ma and Turchi, 2011; Casella and Colonna, 2011). Southwest Research Institute has just received a grant of USD 4.9 million (EUR 4.4m) from the US DOE through the SunShot Initiative to fabricate and test the turbine and CHEs of an s-CO₂ closed cycle for CSP plant. The plant is estimated to reduce the cost of CSP power to USD 0.06 per kWh and raised the efficiency to over 50% (current steam cycle based CSP plant efficiency is less than 35%). The project, running from December 2014 through to mid-2016, involved other industrial partners like Aramco Services Co, Bechtel Marine Propulsion Corp, Electric Power Research Institute (EPRI), General Electric (GE) and Thar Energy.

2.3.1.4 Biomass fuel

The non-availability of biomass fuel in large quantity at a single location limits the use of large-scale steam cycles or integrated gasification combined cycles to achieve higher efficiencies. Hence, most biomass plants are usually small-scale plants that are based on internal combustion engines and Organic Rankine Cycles (ORCs) having low efficiencies (Manente and Lazzaretto, 2014). Therefore, the possibility of efficiently exploiting a solid renewable source like biomass at the point of fuel production without the need for transportation has increased the potential market of small modular closed-cycle GT (Traverso et al., 2006).

2.3.1.5 Waste heat recovery

Global opportunity exists for low-grade waste heat recovery in industrial processes, GTs exhaust, diesel engines, renewables etc. S-CO₂ power cycles have been investigated and developed as a good option for recovering waste heat (Wang et al., 2010; Persichilli et al., 2011; Mohagheghi and Kapat, 2014; Di Bella, 2011; Wright et al., 2014; Held, 2014). In December 2014, Echogen became the first to commercialise s-CO₂ power cycle with the introduction of their 8 MW EPS100 waste heat recovery unit that uses s-CO₂ working fluid to convert waste heat into power (Reuters, 2014).

Also receiving attention among researchers (Bhinder et al., 2011; Munoz et al., 2011; Sánchez et al., 2011b) are hybrid systems comprising of high temperature fuel cells and bottoming closed-cycle GTs. The closed-cycle GT generates extra electric power by recouping some of the thermal energy in the fuel cell exhaust gases and thereby improve the system efficiency.

2.3.2 Working fluids

The choice of working fluid for closed cycle GT will strongly affect the size, geometry and performance of the plant. Some working fluids usually considered for CBCs include air, nitrogen, CO₂, helium and other noble gases. Table 2-2 summarises the relative advantages and

disadvantages of the working fluids. Currently, the most popular working fluids are helium, nitrogen and s-CO₂.

2.3.2.1 Helium and other noble gas mixture

Helium CBC is one of the most mature of the closed-cycle GTs. It was chosen as the working fluid in HTGR designs such as the GT-MHR and the PBMR. Helium cycles requires turbine outlet temperatures around 900 °C in order to achieve attractive efficiencies (about 45-48%). Hence, this high temperature may prove difficult to accommodate especially when very high goals are set for the plant capacity factor (Dostal, 2004).

Pérez-Pichel et al. (2011) investigation using helium-nitrogen, helium-argon and helium-xenon mixtures showed that there is drastic reduction in efficiency of the plant as the molecular weight increases but the turbo-machines and shaft length will be significantly smaller than those designed to operate with pure helium. El-Genk and Tournier (2008b) investigated the attributes and limitations of noble gases and binary mixtures as potential coolant for reactor and working fluid for the CBCs. Wang and Gu (2005) studied helium, nitrogen and air Brayton cycles for a HTGR and their results indicated comparable efficiencies for the gases. However, the helium turbomachinery has more stages than those of nitrogen and air while helium and nitrogen have shorter blade length than air.

For power generation in space, Tarlecki et al. (2007) analysed Ar, He, Xe, Ar-Xe, He-Xe, N₂ and H₂ closed-cycle GTs and found that the diatomic gases (N₂ and H₂) gave higher efficiencies than the monoatomic gases. Najjar and Zaamout (1992) compared the performance of closed-cycle GT using He, combustion gases, air and CO₂ as working fluid for heat recovery. Different helium and s-CO₂ cycle layouts for fusion reactors involving intercooling, recuperation, combined cycle and dual cycle with ORC and steam Rankine cycle were studied by Linares et al. (2011). Results indicated that higher efficiency can be obtained with helium, albeit with complex cycle layouts. However, s-CO₂ cycle achieved the improved performance with less complex layouts.

2.3.2.2 Nitrogen working fluid

The nitrogen CBC option is attractive because nitrogen is inert, thus eliminating the risk of sodium-water or sodium-CO₂ reactions in SFRs. Furthermore, design of nitrogen PCS is anticipated to be less challenging since years of experience from air GTs can be applied (Sun et al., 2000). After all, nitrogen properties are similar to those of air.

The nitrogen gas CBC is mainly been developed in France under the ASTRID (Advanced Sodium Technological Reactor for Industrial Demonstration) SFR project (Saez et al., 2008; Alpy et al., 2011; Cachon et al., 2012). Cachon et al. (2012) presented different feasibility studies and heat

exchanger design for innovative PCSs for ASTRID SFR. The result led to the selection of nitrogen gas Brayton cycle. Alpy et al. (2011) performed a comparison in terms of the thermodynamic performance and preliminary components sizing between nitrogen and s-CO₂ cycle for the ASTRID SFR. The s-CO₂ cycle has a higher efficiency (about 44%) than the nitrogen cycle (about 38%). However, the nitrogen cycle was chosen for near-term demonstration of electricity generation from CBC coupled to SFR. Recently, Seo et al. (2016) investigated the adoption of nitrogen PCS for a SM-SFR. Nitrogen working fluid was chosen ahead of s-CO₂ and helium considering both safety and thermal performance as well as the elimination of intermediate sodium loop. Sensitivity studies were performed to optimise the system and the effect of the elimination of intermediate (secondary) sodium loop on the thermodynamic efficiency of the plant was studied. The study showed that the elimination of the intermediate loop increased the thermodynamic efficiency by 3% point.

2.3.2.3 Supercritical CO₂ working fluid

Early work to compare several real gases for supercritical Brayton cycles by Feher (1967) as well as Hoffmann and Feher (1971) favoured CO₂. s-CO₂ power cycles are currently being widely investigated as PCS for application in nuclear, fossil, CSP, biomass, and waste heat recovery systems because of its advantages (Kim et al., 2016; Pham et al., 2015; Neises and Turchi, 2014; Hu et al., 2015; Mecheri and Le Moullec, 2016; Le Moullec, 2013; Dostal, 2004; Bae et al., 2014). s-CO₂ Brayton cycle has been found to have higher cycle efficiency than steam Rankine cycle and other gas Brayton cycles in the medium to high temperature range (above 450 °C). Other potential benefits of s-CO₂ cycle compared to steam cycle include:

- Reduced capital cost due to smaller size of the components
- Less complex system layout
- Fewer problems with material than water as there is less risk of corrosion and scaling and no formation of water droplets that could damage the turbine blades (Bae et al., 2014; Feher, 1967)
- Reduced water consumption and could likely achieve better performance compared to steam cycle at dry cooling conditions (Cheang et al., 2015; Ahn et al., 2015)

Kato et al. (2004) presented the result of a comparative design study of turbo-machinery between helium and CO₂ cycles. The CO₂ cycles gas turbo-machinery volume (or weight) was estimated to be about one-fifth compared with helium cycles. Figure 2-3 shows the comparison between the sizes of steam turbine, helium turbine and s-CO₂ turbine. The use of mixture of CO₂ with additive gases (O₂, He, Ar, Kr, butane and cyclohexane) as working fluid to improve the performance of s-CO₂ cycle of a nuclear reactor was investigated by Hu et al. (2015). The results showed that CO₂-He and CO₂-Kr mixtures could improve the cycle performance. SNL is demonstrating

supercritical CO₂ closed-cycle GT for power generation. The results obtained in this project demonstrated stable and controllable operation near the critical point over a range of conditions and confirmed the performance potential of these cycle (Wright et al., 2010).

Table 2-2 Advantages and disadvantages of closed-cycle GT working fluids (Lee et al., 1981)

Working fluid	Advantages	Disadvantages
Air	<ul style="list-style-type: none"> Considerable design experience available Air is abundant and inexpensive 	<ul style="list-style-type: none"> High pressure loss Requires high TIT to achieve attractive efficiency Poor heat transfer coefficient compared to helium Likely oxidation of materials at high temperature Limited plant capacity
Nitrogen	<ul style="list-style-type: none"> Composition and properties partly similar to air, can use experience from conventional air GT 	<ul style="list-style-type: none"> High pressure loss Requires high TIT Poor heat transfer property Likely nitriding and embrittlement of material at high temperature
Helium	<ul style="list-style-type: none"> Low pressure loss Good heat transfer coefficient Inert and non-toxic No Mach number restriction in turbomachinery design 	<ul style="list-style-type: none"> More number of turbomachinery stages High leakage Limited turbomachinery design experience Requires high TIT
s-CO ₂	<ul style="list-style-type: none"> Good efficiency at moderate TIT Non-toxic, relatively good thermal stability and inertness Low leakage rate Good critical point (7.3773 MPa, 30.978 °C) Compact and small turbomachinery 	<ul style="list-style-type: none"> More corrosive than helium at high temperature Limited design experience Likely operation and design challenges due to rapidly varying property near the critical point Possibility of energetic chemical reaction with sodium in sodium cooled reactor

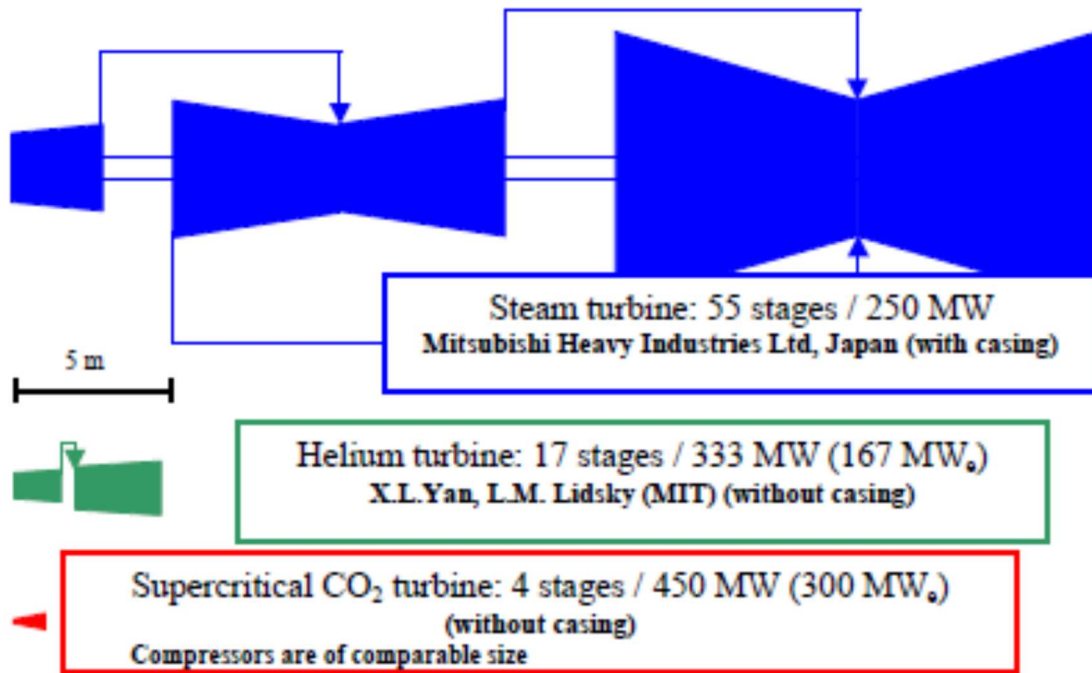


Figure 2-3 Comparison of turbine sizes for steam, helium and s-CO₂ (Dostal, 2004)

2.3.3 Compact heat exchangers

Heat exchange devices for closed-cycle GT must have superior performance providing very close temperature approaches and reliable mechanical characteristics at high pressure and temperature to guarantee the cycle efficiency and safety. Selection of potential CHE technologies is based upon their abilities to cope with the operating condition parameters and other parameters such as fouling, nuclear irradiation, corrosion, compactness, weight, maintenance and reliability (Tochon et al., 2004; Li et al., 2011).

A survey of CHE technologies to determine their suitability is presented in Table 2-3. The designs that meet more requirements of closed-cycle GT are the diffusion bonded Plate Fin Heat Exchanger (PFHE) and PCHE. In spite of high pressure drop and other limitations, PCHE is best rated compared to other CHEs in terms of reliability, mechanical resistance, compactness and simultaneous operation at high pressure and high temperature. For high pressure applications, the high pressure drop is not a constraint, but for low or moderate pressure applications, the pressure loss will be the main barrier to the use of PCHE (Li et al., 2011).

Table 2-3 Features of compact heat exchangers

Type	Maximum Pressure (bar)	Maximum Temperature (°C)	Compactness (m ² /m ³)	Hydraulic diameter (mm)	Comment
Spiral heat exchanger	25	200-540	200	10-50	Temperature limit depends on gasket material. Easy to clean.
Plate heat exchanger	2-40	200-400	120-660	2 - 10	Operating limits determined by the technology (gasketed, brazed or welded). Generally restricted to low temperature and pressure application.
Brazed PFHE	80-120	200-550	800-1500	1-2	Selected for GT-MHR recuperator (Shenoy and Potter, 1996). Operating limits depend on the materials (aluminium, stainless steel)
Diffusion bonded PFHE	620	800	700-800	1-2	Can tolerate higher pressures than other PFHE
Printed circuit HE	500-1000	900	2500	0.5-2	Selected for SNL S-CO ₂ loop (Pasch et al., 2012). No gaskets or brazing material, hence reduce risk of leakage, fluid incompatibility and temperature limitations.
Marbond	400	900	10000	<PCHE	Novel with little information on its application.
Ceramic HE	10	1300	-	-	Novel heat exchanger primarily constructed by replacing parts of existing CHEs with ceramic.

2.3.4 Physical layouts/configurations of closed-cycle GT

The arrangement of the closed-cycle GT components, usually the heat exchangers and the turbomachinery, gives the physical layout and configuration of the system. Modification of the simple cycle layout in an effort to improve the cycle efficiency can lead to cycle with recuperation, intercooling and reheating as well as other unique configurations for supercritical CO₂ cycle. Also, the design choice can be classified based on the plant orientation as either vertical or horizontal layout; based on the number of rotor shaft as either single shaft or multi-shaft configuration; and based on the interconnection of the components as either integrated or distributed layout.

2.3.4.1 Recuperated, intercooled and reheated cycle

A fundamental design choice for improving the efficiency of closed-cycle GT is the addition of recuperative/regenerative heat exchanger in which heat is transferred from the turbine hot exhaust gas to the compressor discharge stream. Addition of the usually large regenerator will increase the cost of the plant. However, almost all design of closed-cycle GT employs regeneration because the loss of efficiency in a non-regenerative cycle is prohibitive (Shin, 1975). Alternatively, a heat recovery steam generator can be placed in the turbine exhaust instead of the recuperator for increased utilisation of the heat input. The heat recovery steam generator then produces steam for either cogeneration of heat or for a steam turbine bottoming cycle in a combined cycle arrangement.

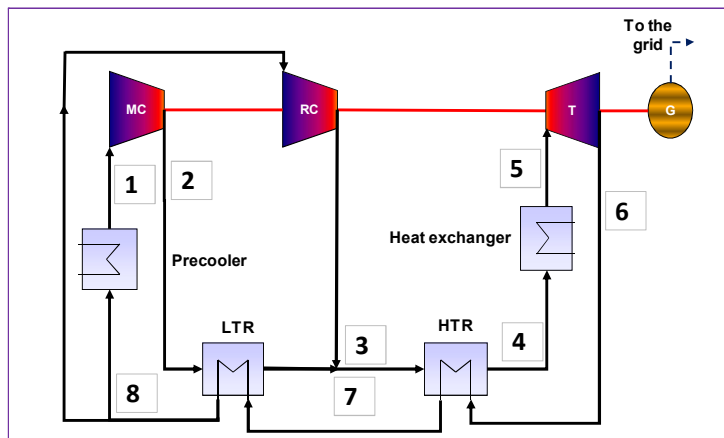
For intercooled cycles, efficiency is improved by reducing the average temperature of heat rejection from the cycle. On the other hand, reheating increases cycle efficiency by increasing the average temperature of heat addition to the cycle. The optimal number of inter-cooling and reheating is selected by the trade-off between a merit of cycle efficiency increase and a demerit of capital cost increase (Ishiyama et al., 2008). Some HTGRs like the HTR-10GT and the GT-MHR include inter-cooling in their configurations while others like the GTHTR300 ruled out the use of inter-cooler despite the 2% efficiency gain because of the added complexity to the turbomachinery (Herranz et al., 2009).

2.3.4.2 Layouts for S-CO₂ cycle

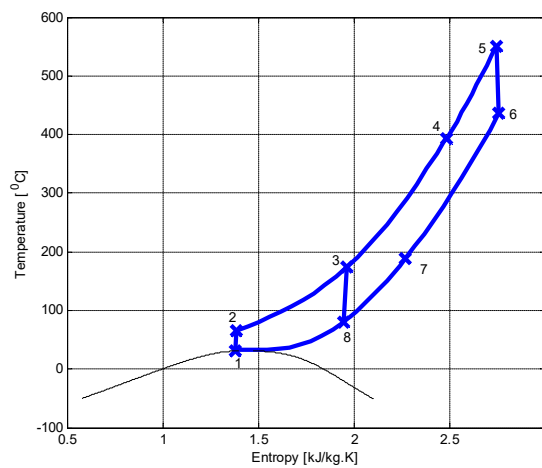
In order to take advantage of the reduced compression work around the critical point, the selection of cycle conditions for s-CO₂ is radically different compared to other fluids. For s-CO₂ cycles, the compressor inlet conditions are selected to be around the critical point (30.978

°C, 73.773 bar) and a turbine inlet pressure (TIP) much higher than other Brayton cycle is chosen. Also, it is difficult to achieve high efficiency with the usual simple cycle and cycle with intercooling and reheating because heat transfer is not effective in the recuperators due to pinch point problem.

Therefore, several other configurations have been proposed for CO₂ power cycle in an attempt to achieve higher efficiency (Feher, 1967; Angelino, 1968; Dostal, 2004; Kulhanek and Dostal, 2011). Such alternative layouts include the recompression, the precompression, the split expansion, the partial cooling and the partial heating layouts. The recompression layout, shown in Figure 2-4, seems to be the most promising.



(a) Recompression s-CO₂ Brayton cycle layout



(b) T-S diagram

Figure 2-4 The recompression s-CO₂ cycle

The drawback to a recompression cycle configuration is the addition of a compressor and a second recuperator, adding more complexity and capital cost to the system (Parma et al., 2011). Ahn et al. (2015) compared the performance of various s-CO₂ cycle layouts. Review of s-CO₂ cycle by Crespi et al. (2017) focused on the categorisation of the various layouts and comparison of their reported performances.

2.3.5 Horizontal versus vertical configuration

A primary reason for the choice of horizontal orientation of GT is the ease of maintenance as both ends of the plant will be accessible. Also in the event of bearing failure, the weight of the rotor is shared by two or more radial auxiliary bearings. In contrast, the weight is usually concentrated on a single axial auxiliary bearing in vertical machines (Penfield Jr and Rodwell, 2000). The auxiliary bearing must be able to withstand the initial impact and the heat generated. With the use of horizontal bearing, years of experience with combined cycle gas turbine (CCGT) and steam turbine system can be applied to the closed-cycle GT system (Driscoll and Hejzlar, 2004).

One benefit of vertical system is that the turbine thrust, which poses a problem in horizontal machines, can be balanced by gravitational force. Also, in horizontal system, the turbomachine shaft is bent by few millimetres because of gravitational force causing loss of efficiency. This problem is not present in vertical configuration because there is no bowing of the shaft under gravity (Baxi et al., 2008). Both PBMR and GT-MHR turbomachines adopted the vertical orientation. These machines are large in size and therefore the design of the auxiliary bearings is challenging as there is only a limited experience with vertical turbomachines (Penfield Jr and Rodwell, 2000).

2.3.6 Integrated versus distributed configuration

Design choice selected for the GT-MHR is the integral configuration in which all the components of the power conversion unit (PCU) are bundled into a single pressure vessel. This eliminates complicated ductworks, minimise pressure losses and saves cost (Baxi et al., 2008). On the down side, it is difficult to accommodate valves inside an integral vessel, and access for inspection and maintenance could be difficult (Gibbs et al., 2006; Driscoll and Hejzlar, 2004). Also, integral PCU in a conventional steel pressure vessel puts a limit on the power rating due to differential and transient temperature gradient in the vessel.

In contrast, distributed (multi-module or fully-dispersed) configuration is the most common design choice for CBC (Gibbs et al., 2006). In this case, the PCU components are dispersed and individual components connected by ducts. Distributed configuration requires larger

volume for the ductworks than integral design because of the distances between the components (Wright et al., 2006).

2.3.7 Single shaft versus multi-shaft configuration

Decision to employ either a single shaft or a multi-shaft turbomachinery train is also a fundamental design consideration. In single shaft arrangement, the turbines, compressors and generator are mounted on a single rotor shaft. In multi-shaft, two or more independent turbomachinery-generator rotor shafts are employed. The GT-MHR and the GTHTR300 employ single shaft arrangement while the PBMR employs three shafts. Single shaft is inherently easier to control in the event of loss of load and usually have smaller footprint than multi shaft configuration (Wright et al., 2006). Problems of single shaft include the difficulty with isolating different pressure zones and the problem associated with the dynamics of the long rotor shaft.

Adopting a multi shaft turbomachine provides the benefit of improved performances in the plant compared to one-shaft option (Golovko et al., 2000). For instance, the augmented shaft stiffness as a result of the smaller length of the shafts will improve the dynamic performance of the rotating shaft. Also multi shaft arrangement provides more flexibility for part-load operation and the rotational speed of the turbomachinery can be optimised independently (Gibbs et al., 2006; Carstens, 2007; Kaikko, 1998). However, there are problems of control and protection of the turbomachine during loss of load (El-Genk and Tournier, 2008a).

Rousseau and Van Ravenswaay (2003) compared single and three-shaft closed-cycle GT configurations based on steady state and transient simulations. The cycle efficiency and specific power of the two configuration were found to be similar at full power operation. However, their transient performance differs, with the single shaft requiring ten times more power for start-up than the three-shaft configuration.

2.4 Important R&D programmes and experimental/pilot plants, and commercially operated plants

This section gives a brief review of some important research programmes and pilot/demonstration plants worldwide for closed-cycle GT. Also, an overview of some of the early commercially operated plants will be provided.

2.4.1 R&D programmes and experimental/pilot facilities worldwide

Over the years and particularly in the last two decades, R&D efforts have been growing in the USA (DOE, SNL, ANL, INL, MIT), China, Japan, Korea and Europe. This has led to the construction of some experimental/pilot plants for investigating thermal performance, component testing and to demonstrate the feasibility of closed-cycle GT. Table 2-4 gives some technical data of these programmes and facilities.

2.4.1.1 The AK-36 test plant

2.4.1.1.1 Participants and purpose

In 1939, Escher Wyss in Zurich, Switzerland built this first closed-cycle GT installation (Keller, 1978; McDonald, 2012). The plant was used to test the operation of closed-cycle GT and hence opened the door for the construction of commercial fossil-fired closed-cycle GT with air as working fluid in Europe.

2.4.1.1.2 Description of facilities

The recuperated closed cycle with air as working fluid was externally fired by light oil and the TIT was 650 °C. The plant adopted two-shaft configuration with three compressors and two intercoolers. The high-pressure turbine and the compressors were on one shaft rotating at 8000 rpm while the low-pressure turbine and the generator were on the second shaft rotating at 3000 rpm. The two shafts were connected with gears to improve dynamic performance and to mitigate shaft over speed during load shedding (Fruttschi, 2005). Figure 2-5 shows a picture of the AK-36 plant.

2.4.1.1.3 Activities

The 2 MWe plant was operated for about 6000 hours during the Second World War for supplying electricity to the Escher Wyss factory in Zurich. Initial test results confirmed the need to change the turbomachinery design. Hence, all compressors stages were changed into axial type instead of the previous design with radial end stages. An efficiency of 31.6 % was recorded in test conducted at a higher TIT of 700 °C in 1944 by Prof Quiby of ETH Zurich (Fruttschi, 2005).

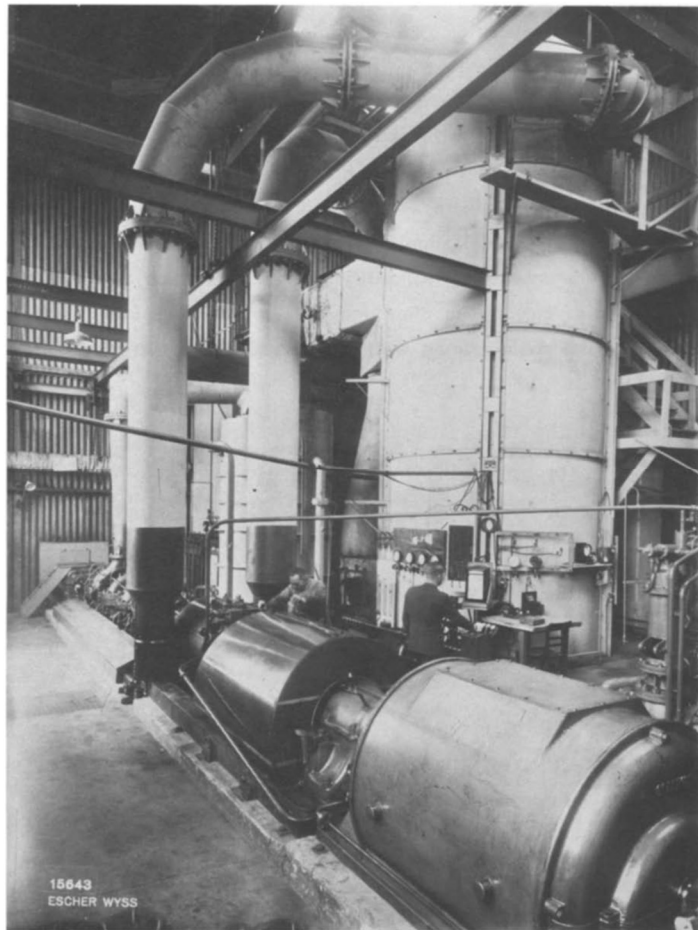


Figure 2-5 The Escher Wyss AK-36 test plant (Keller, 1978)

Table 2-4 Research programmes and test facilities technical information

Programme/ Plant	Country	Developer	Development Phase/Status	Rating	Working fluid	Fuel/Heat source	TIT (°C)	TIP (bar)	Description	Eff	Reference
AK-36	Switzerland	Escher Wyss	Test plant	2 MWe	Air	Light oil	650	24	2 shaft, 2 speed connected by gears	31.6 % at 700 °C	(Fruttschi, 2005)
ML-1	USA	US Army	Test plant	350 kWe	Nitrogen	Nuclear	650	-	Mobile trailer mounted	-	(Fruttschi, 2005)
La Fleur	USA	La Fleur Enterprises	Test plant	2 MW	Helium	Natural gas	650	18	Closed cycle GT cryogenic process for air liquefaction	-	(Fruttschi, 2005; McDonald, 2012)
Feher Module	USA	John R. Hoffmann and Ernest G. Feher	Design	150 kWe	CO ₂	Helium-cooled reactor	732	114	Indirect cycle, two-shaft PCS	-	(Hoffmann and Feher, 1971)
HHV	Germany	KFA Juelich	Test facility	-	Helium	-	850	51	No external heat, compressor, turbine & motor on one shaft	-	(Weisbrodt, 1995)
Garrett CCGT 5000	USA	Garrett Corporation	Demonstration	9 MWe (5 MWe + 4 MWe)	Air	Petroleum coke	788	41	Combined cycle & non-recuperated closed cycle GT fired with AFBC	24%	(Mason et al., 1984; McDonald, 1995)
SBL-30	USA	SNL/BNI	Test facility	30 kWe	N ₂ , Air, CO ₂ , He, Mixtures	Electric	-	-	Uses a modified Capstone C-30 gas-micro-turbine	-	(Wright, 2007)
MHTGR-IGT	China	INET	Concept design	200 MWth	Nitrogen	Helium HTGR	850	60	Indirect cycle, three compressor, two intercooler	48%	(IAEA, 2001)
ACACIA	The Netherlands	Nuclear Research and consultancy Group (NRG)	Concept design	40 MWth	Helium	HTGR	800	22.8	Cogeneration, recuperated CBC	-	(Kikstra and Verkooijen, 2000)
BPCU (Brayton Power Conversion Unit)	USA	NASA	Test facility	2 kWe	Helium-Xenon	Electric heater	723	-	Integrated PCS Turbine/Alternator/Compressor, recuperators, and gas cooler)	-	(Johnson and Hervol, 2006)
SNL S-CO₂ loop	USA	SNL/BNI	Test plant	260 kWth, 780 kWth	CO ₂	Electric heater	-	-	Modular & reconfigurable hardware unit	-	(Wright et al., 2010; Wright, 2012)
GTHTR300	Japan	JAERI	Design	600MWth	Helium	HTGR	850	70	Direct cycle, horizontal single shaft	45.8%	(Kunitomi et al., 2004)

Table 2-4 (continued)

Programme/ Plant	Country	Developer	Development Phase/Status	Rating	Working fluid	Fuel/Heat source	TIT (°C)	TIP (bar)	Description	Eff	Reference
PBMR	South Africa	PBMR Pty (Ltd)	Conceptual design	400 MWth/165 MWe	Helium	HTGR	900	70	Direct cycle	42.7% (net)	(Koster et al., 2003)
MPBR	USA	MIT & INEEL	Concept design	250 MWth/120 MWe	Helium	HTGR	879	78	Indirect cycle, modular components, three shaft arrangement	48%	(Wang, 2009)
GT-MHR	USA & Russia	GA & MINATOM	Design	600MWth/2 86 MWe	Helium	HTGR	850	70	Intercooled and recuperated direct cycle; integrated, vertical and single shaft configuration	> 47%	(Kiryushin et al., 1997)
GT-HTGR	USA	GA	Concept design	2000 MWth/800 MWe	Helium	HTGR	850	81.6	Direct cycle with two heat transport loops, single-shaft turbomachinery	40%	(Moore et al., 1982)
BG Demonstrator	UK	British Gas	Test facility	1 MWth	Nitrogen/ Oxygen mixture	Natural gas	900	-	Two turbocharger arrangement, no generator	-	(McDonald, 2012)
HTR-10GT	China	INET	Test facility	10MWth/2.2 MWe	Helium	HTGR	750	-	Intercooled & recuperated single shaft direct cycle	22%	(Xu et al., 2005)
NR IST	USA	Naval Reactors (NR), KAPL & Bettis Lab	Test facility	779kWth/10 0 kWe	s-CO ₂	Electric heater	300	160	Simple recuperated CBC, two shaft arrangement	-	(Kimball, 2011)
ANTARES	France	AREVA	Concept design	600 MWth	Nitrogen/ Helium mixture	VHTR	950	70	Indirect cycle cogeneration combined cycle	-	(Gauthier et al., 2006)
JAEA loop	S-CO ₂ Japan	JAEA	Test loop	30 kWth	s-CO ₂	Electric heater	-	130	No electric output	-	(Kisohara et al., 2008)
ASTRID	France	CEA	Concept design	1500 MWth	Nitrogen	SFR	515	180	Indirect intercooled & recuperated CBC, single shaft turbomachine	37.8 %	(Alpy et al., 2011)
STAR-LM	USA	ANL	Concept design	400 MWth/181 MWe	s-CO ₂	LFR	560	200	Single shaft split flow recompression cycle	45%	(Moissev et al., 2008)

2.4.1.2 Feher (supercritical CO₂) cycle test module

2.4.1.2.1 Participants and purpose

Ernest G. Feher patented the supercritical cycle heat engine in 1966 and later reported on a fully supercritical CO₂ power cycle (Feher, 1966; Feher, 1967). In 1970, Hoffmann and Feher designed a 150 kWe s-CO₂ test module shown in Figure 2-6. The purpose was to investigate the possibility of using s-CO₂ cycle for advanced ground nuclear reactors for the US Army.

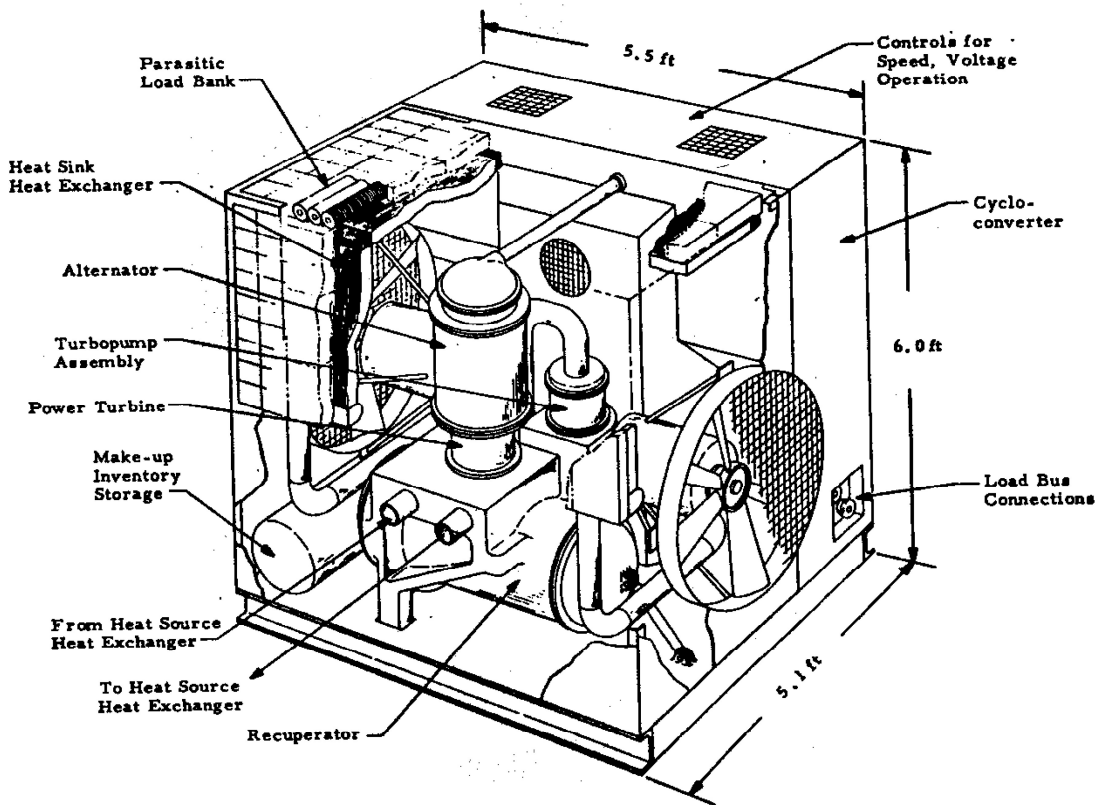


Figure 2-6 Sketch of the Feher 150 kWe S-CO₂ power cycle (Hoffmann and Feher, 1971)

2.4.1.2.2 Description

A helium HTGR with core outlet of 760 °C and 350 bar was proposed as the heat source for the cycle. In order to independently optimise the rotational speed of the pump and turbine, a two-shaft arrangement was adopted. The generator shaft rotational speed was optimised as 40,000 rpm. CO₂ was chosen as the working fluid due to its many favourable properties. The working fluid in this recuperative cycle was maintained above the critical pressure throughout the cycle but temperature in the compression process was below the critical temperature. Hence cooling the CO₂ to liquid phase will require a year-round supply of cold water between 10 – 15 °C which might be difficult to obtain. The schematic of the module is shown in Figure 2-6.

2.4.1.2.3 Activities

The cycle components such as pump, turbine and recuperators were designed. The pump, the turbine driving the pump and the power turbine were designed with efficiency of 75%, 88% and 85% respectively. Also, the start-up and control strategies for the plant were suggested. Parasitic load bank was suggested for part-load operation instead of turbine bypass valve control because of demanding requirements on bypass valve.

2.4.1.3 HHV

2.4.1.3.1 Participants and purpose

The HHV helium test system was built in 1981 at Research Centre Juelich (KFA) in Germany as part of the HHT project in an international cooperation between Germany, Switzerland and the United States (Weisbrodt, 1995).

The purpose of the HHV test rig was to carry out a 1:1 scale test of helium turbomachinery, pipes, heat exchangers and valves at extreme temperatures similar to HTGR-coupled closed-cycle GT plant (Frutschi, 2005).

2.4.1.3.2 Description of facility

The turbine, compressor and electric motor are on a single shaft rotating at 3000 rpm (Figure 2-7). Helium is circulated around the system by the turbomachinery at about 200 kg/s. The 90 MW compressor power is jointly supplied by the electric motor (45 MW) and the turbine. The compression process was able to raise the temperature of the helium gas up to 850 °C and hence no external heater was employed. The hot gas leaving the compressor then passed through a test bed section after which it is cooled to about 829 °C and expanded in the turbine.

2.4.1.3.3 Activities

Initial issues encountered during commissioning are oil ingress into the helium circuit and leakage of helium at the operating temperature of 850 °C. These problems were resolved by redesigning the labyrinth seal, and the buffer and helium cooling system (McDonald, 2012). The facility was operated for about 1100 hour and test results indicated that the turbomachinery has better efficiency than the design value. Important test data were obtained for validation of blade performance, rotor cooling, seal system, controls and rotor dynamic stability (McDonald, 2014). In late 1981, the HHT project was stopped and the test facility was shutdown.

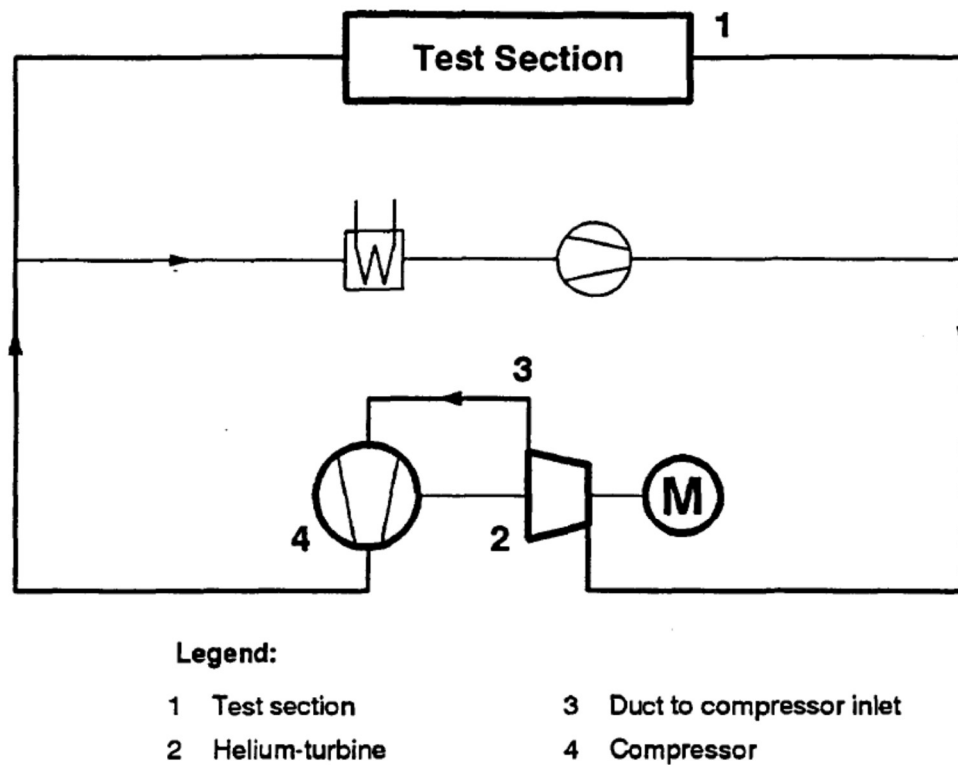


Figure 2-7 Schematic of HHV test circuit (Weisbrodt, 1995)

2.4.1.4 GT-MHR

2.4.1.4.1 Participants and purpose

In 1995, GA (USA) and MINNATOM (Russia) jointly signed an agreement to develop and design the GT-MHR (Kiryushin et al., 1997). The facility is to be constructed in Russia at the Siberian Chemical Combine in Seversk. FRAMATONE (France) and Fuji Electric (Japan) later joined the project in 1997 (Brey, 2000).

The goal of the programme was to construct a facility for the destruction of Russian weapons-grade plutonium and use the heat generated to produce electricity in a direct cycle GT and with the future prospect of serving as commercial nuclear plant burning uranium fuel.

2.4.1.4.2 Description

The GT-MHR consist of a 600 MWth helium-cooled reactor with a core outlet temperature of 860 °C directly coupled to a closed-cycle GT PCS (Figure 2-8). The reactor and the PCS are enclosed in two separate vertical steel vessels connected with a horizontal vessel. The PCS has a single-shaft turbomachine that is oriented vertically and supported by electromagnetic and protective bearings. The generator, turbine, and two compressors are connected to the turbomachine shaft rotating at 3000 rpm. Also included in the surrounding annulus of the PCS

2.4.1.5 PBMR

2.4.1.5.1 Participants and purpose

PBMR Pty (Ltd), a subsidiary of the South African power utility company, ESKOM started the design and construction of a prototype closed cycle helium GT plant using a PBMR as heat source (Koster et al., 2003). Between 1999 and 2009, about US\$ 1.3 billion was invested in the project by the South African government, ESKOM, Westinghouse, and the Industrial Development Corporation of South Africa. Local and international companies that participated in the project included Mitsubishi Heavy Industries of Japan (turbomachinery), Nukem of Germany (fuel technology), SGL of Germany (graphite), Heatric of UK (recuperator), IST Nuclear of South Africa (nuclear auxiliary system), Westinghouse of USA (instrumentation), ENSA of Spain (pressure boundary) and Sargent & Lundy of USA (Architect/Engineer services).

The purpose of the PBMR project is to build a commercial reference plant capable of meeting the requirements set for commercialisation such as being located at the centre of load growth in South Africa, capital and operation cost being within cost achieved by large coal-fired plants, reduced CO₂ emission etc. (Brey, 2000).

2.4.1.5.2 Description

The PBMR is a direct cycle helium Brayton cycle with a core outlet temperature of 900 °C. The design was changed many times. The initial design consist of three rotating shafts – the low pressure (LP) turbo-compressor, the high pressure (HP) turbo-compressor and the power turbine-generator shaft (Figure 2-9). Other components include the recuperators, intercooler and a precooler. All the rotors were oriented vertically, housed in separate vessels and sustained on magnetic bearings due to the cold welding nature of helium preventing the use of mechanical bearing. The power turbine-generator shaft rotates at 3000 rpm synchronous speed while the LP turbo-compressor rotates at 15,000 rpm and the HP turbo-compressor at 18,000 rpm. The helium inventory tank will permit power control from 20% to 100% of full load. Below 20%, reactor bypass valve control are used (Kumar et al., 2000).

In later designs, reactor thermal power was scaled up to 400 MWth and the configuration was changed to a single shaft horizontal arrangement. The shaft then rotates at 6000 rpm and a gear was used to reduce the speed to 3000 rpm for the generator (No et al., 2007).

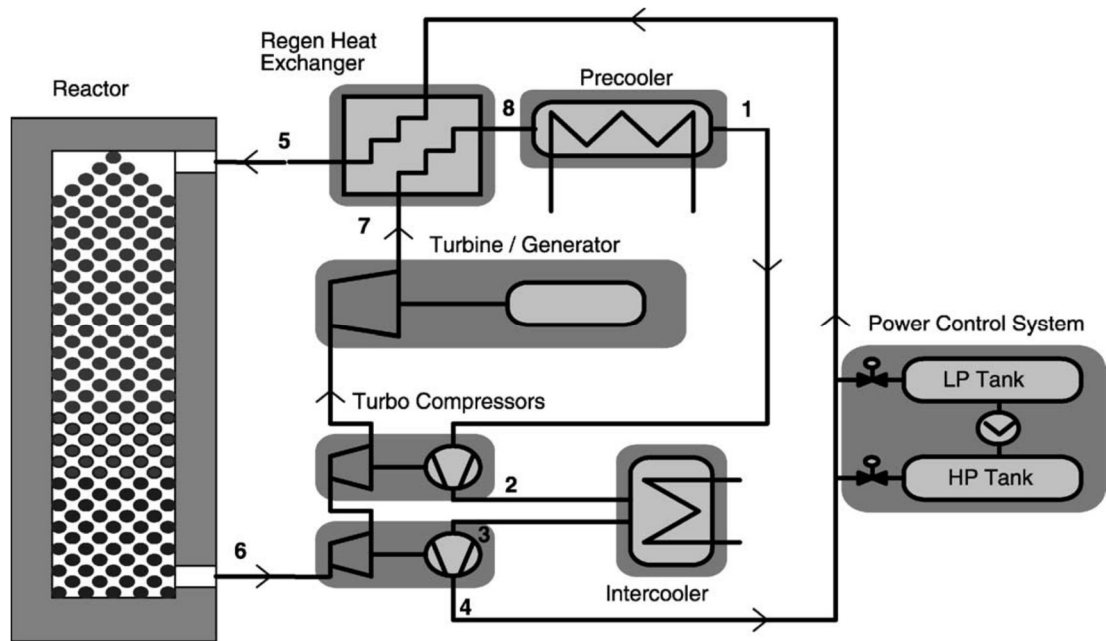


Figure 2-9 Simplified diagram of the PBMR Brayton cycle system (Koster et al., 2003)

2.4.1.5.3 Activities

Conceptual design of the plant was carried out and computational simulations were used to predict the performance of the GT plants (Kumar et al., 2000; Walter et al., 2006; Janse van Rensburg and Kleingeld, 2011). Several experimental tests were also conducted to support the design (Rousseau and van Staden, 2008; du Toit et al., 2014).

Challenges include limited experience with helium gas turbomachinery, rise in fuel temperature, economic competitiveness, development costs and funding, and the lack of customer to place order (Thomas, 2011). In 2009, the PCS was changed to an indirect Rankine steam cycle with cogeneration due to its less technical challenges. The project was terminated in 2010 due to financial difficulty.

2.4.1.6 GTHTR300

2.4.1.6.1 Participants and purpose

In 2001, the GTHTR300 programme was proposed by the JAERI to design and carried out R&D on a closed-cycle helium GT system (Yan et al., 2003; Kunitomi et al., 2004; Takizuka, 2005).

The objective of the GTHTR300 is to establish the feasibility of a simple design that will significantly lower the technical requirement and cost for near-term deployment with a demonstration plant in the 2010s and commercial plant in the 2020s (IAEA, 2001; Takizuka, 2005; Kunitomi et al., 2004).

2.4.1.6.2 Description

The plant is designed with a reactor power of 600 MWth at 850 °C core outlet temperature and electrical output of 275 MWe. The key features of GTHTTR300 are (Figure 2-10): inherently safe modular reactor design, non-intercooled Brayton cycle, horizontal single-shaft turbomachine with compressor, turbine and generator on magnetic bearings, and three separate steel vessels (reactor pressure vessel, power conversion vessel and heat exchanger vessel) connected by coaxial double pipes. The turbomachine shaft rotates at 3600 rpm. The disadvantage of this configuration is the need for a large building for the horizontal PCS (No et al., 2007).

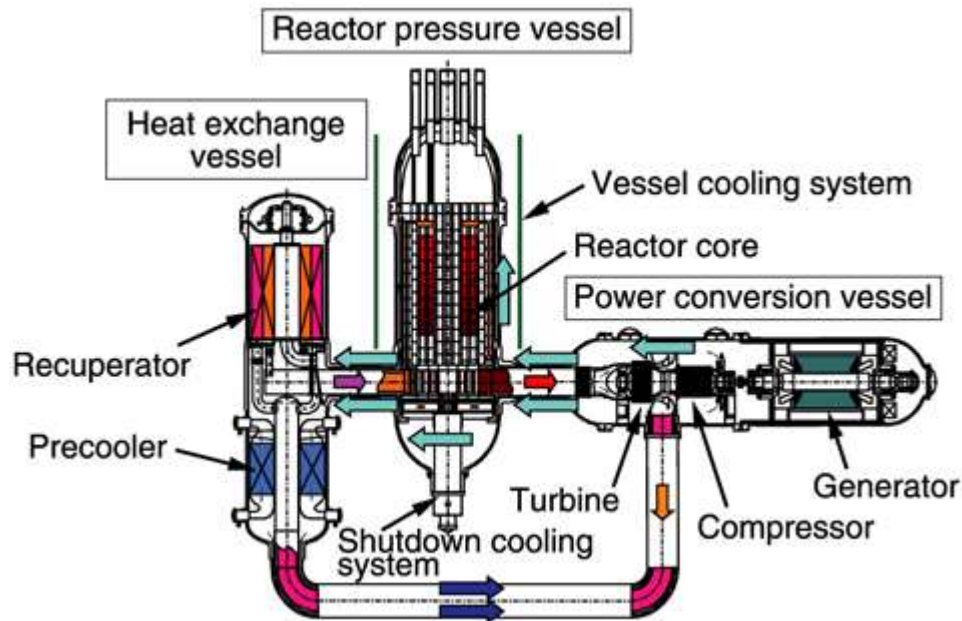


Figure 2-10 Layout of GTHTTR300 (Courtesy of JAERI)

2.4.1.6.3 Activities

R&D activities include design of the helium turbomachinery, 1/3-scale model tests, aerodynamics performance test, magnetic bearing development test, and closed-cycle GT operation and control test (Takada et al., 2003; Takizuka et al., 2004; Yan et al., 2008).

Although several R&D work has been done, the prototype demonstration plant is yet to be constructed.

2.4.1.7 JAEA s-CO₂ cycle test loop

2.4.1.7.1 Participants and purpose

The test loop was fabricated by JAEA (Japan Atomic Energy Agency) and its objectives are to determine the performance of CO₂ compressor near the critical point, to confirm the thermal-hydraulic performance of PCHE recuperator and to determine the operational stability of s-CO₂ cycle coupled to SFR (Kisohara et al., 2008).

2.4.1.7.2 Description of facilities

A view of the s-CO₂ test loop is shown in Figure 2-11. The test loop consists of three compressors (LP, HP and bypass compressor), two PCHE recuperators, an expansion valve to simulate turbine, a 30 kWth electrical heater to represent sodium/CO₂ heat exchanger, a pre-cooler and an intercooler.

The electrical heater heats the CO₂ to 300 °C and the thermal power is only about 1/20000 of the actual IHX power. Reciprocating CO₂ compressors were employed because the CO₂ flow rate (about 200-400 kg/hr) is too low for centrifugal or axial compressor. The cooler is located before the expander because the expander cannot be used at temperature above room condition. The pre-cooler and intercooler are used to condition the CO₂ temperature to the supercritical condition (Kisohara et al., 2008; Sienicki et al., 2009; Sienicki et al., 2010).

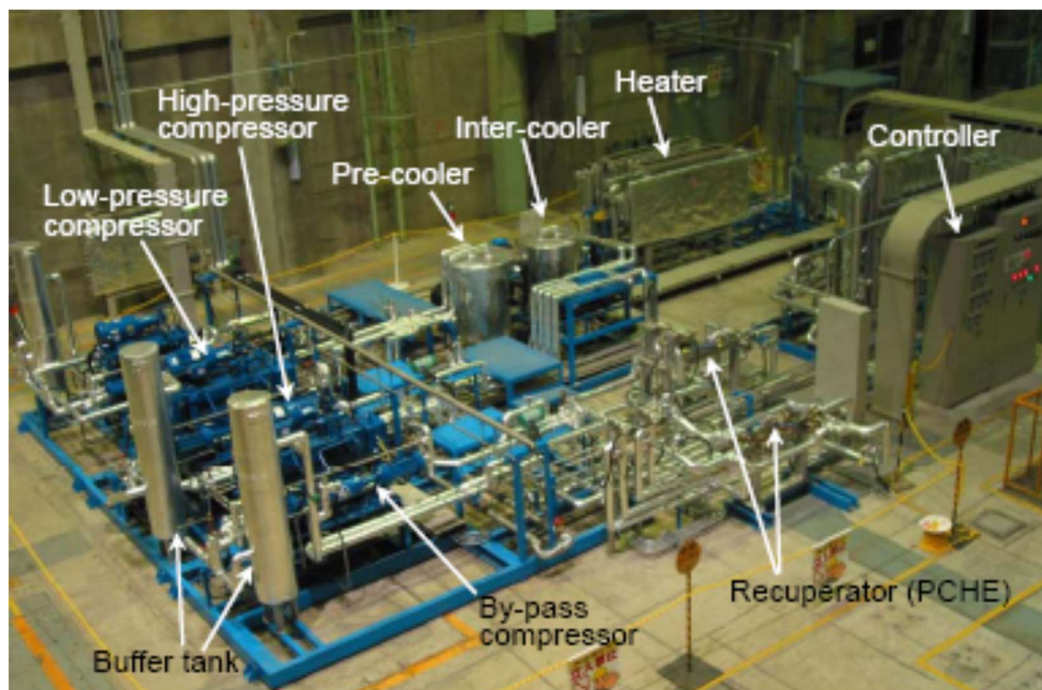


Figure 2-11 JAEA s-CO₂ cycle test loop (Kisohara et al., 2008)

2.4.1.7.3 Activities

Compressor efficiency tests were carried out with test data obtained at different conditions both further from the critical point and around the critical region. Test results confirmed that compressor efficiency increased significantly around the supercritical region. Recuperator thermal-hydraulic tests were conducted with two types of PCHE, one with zigzag fin and another with a new S-fin type. Thermal-hydraulic properties of the different fin were evaluated by means of CFD analysis. The two recuperator types showed similar thermal performance but the S-fin type is better in term of pressure drop which is about 1/6 of the zigzag type. Finally, both transient and steady state operation stability tests were performed by changing the compressor condition

from subcritical to supercritical and then maintained at steady state afterward. Test results showed no instability during the transient and steady state operations (Kisohara et al., 2008; Sienicki et al., 2009; Sienicki et al., 2010).

A full-scale test to simulate an actual cycle was suggested for a more precise investigation of s-CO₂ cycle (Kisohara et al., 2008).

2.4.1.8 SNL s-CO₂ Brayton cycle loops

2.4.1.8.1 Participants and purpose

SNL constructed the s-CO₂ cycle loops with funding from the US DOE's Office of Nuclear Energy and the Laboratory Directed Research & Development (LDRD) programme (Wright et al., 2010). Barber-Nichols Incorporated (BNI) was contracted to design, manufacture and assemble the loops. Modification of the initial compression loop to a heated un-recuperated Brayton loop was contracted by Knolls Atomic Power Laboratories (KAPL).

The purpose of the programme is to investigate s-CO₂ Brayton cycle that could be used with nuclear (and solar, fossil or geothermal) heat sources by constructing small scale s-CO₂ Brayton cycle loops. The loops are for studying the important issue of operation and control near the critical point and to obtain test data for validating s-CO₂ cycle models and turbomachinery design tools (Wright et al., 2010).

2.4.1.8.2 Description of facilities

SNL fabricated two s-CO₂ cycle loops:

- A s-CO₂ compression loop with a centrifugal compressor driven by a 50 kWe motor/alternator at 75,000 rpm with a flow rate of 3.51 kg/s was constructed in 2008. This loop uses ball bearings and has no heat source and no turbine but uses orifice valve for reducing pressure instead. In 2009, the loop was modified to a heated but un-recuperated Brayton loop and the turbomachine reconfigured as a turbo-alternator-compressor unit with addition of gas-foil bearings. The CO₂ is heated by two Watlow electric heaters supplying 130 kW each. The turbine was included to assist the motor in supplying part of the compression power. However, net output power can be produced if the TIT is sufficiently high (Wright et al., 2010).
- A power producing s-CO₂ split flow recompression CBC test assembly (Figure 2-12) started test operation at BNI site in Arvada, Colorado in 2010 with potential of generating up to 250 kWe (Pasch et al., 2012; Wright, 2012). The facility was later relocated to SNL in 2012. The loop uses gas-foil bearing, permanent magnet motor/generator and Heatric's PCHEs. The heaters supplied about 780 kW to the cycle at 538 °C.



Figure 2-12 S-CO₂ split flow recompression CBC test assembly at SNL (Courtesy of SNL)

2.4.1.8.3 Activities

The s-CO₂ compression loop was operated in the liquid region, vapour region and in the saturation curve, all around the critical point with over 80 tests. Tests included measuring leakage flow rates, windage losses, compressor performance and balancing thrust loads (Wright et al., 2010). Also investigated are bearing type and sealing technologies. The loop was modelled with the SNL's RPCSIM (Reactor Power and Control SIMulation) Simulink code. Test data agrees with the design and model performance predictions. Results also showed stable and controllable operation in the region of the critical point.

The next phase is the development of a large industrial demonstration s-CO₂ GT plant capable of generating more than 10 MWe.

2.4.1.9 HTR-10GT

2.4.1.9.1 Participants and purpose

In China, INET of Tsinghua University started the construction of a 10 MWth pebble-bed HTR-10 test facility in 1995 under the China High Technology Programme. The reactor reached criticality in 2000 and full power was achieved in 2003 (Xu et al., 2005). In the second phase of the programme, the HTR-10GT project was started in 2002 to test the coupling of CBC to the HTR-10. In 2000, OKBM of Russia signed agreement with INET for the conceptual design of the GT PCS.

The purpose of the HTR-10GT project is to carry out R&D on HTR-coupled GT power generation system and demonstrate the feasibility (Sun et al., 2000).

2.4.1.9.2 Description

The components of the direct closed-cycle GT system include the HTR-10 heat source, low pressure compressor (LPC) and high pressure compressor (HPC), turbine, recuperator, intercooler and precooler (Figure 2-13). The single shaft turbomachine rotor is supported by active magnetic bearing (Wu and Yu, 2007). The reactor core outlet temperature is about 750 °C and the thermal efficiency is about 22%.

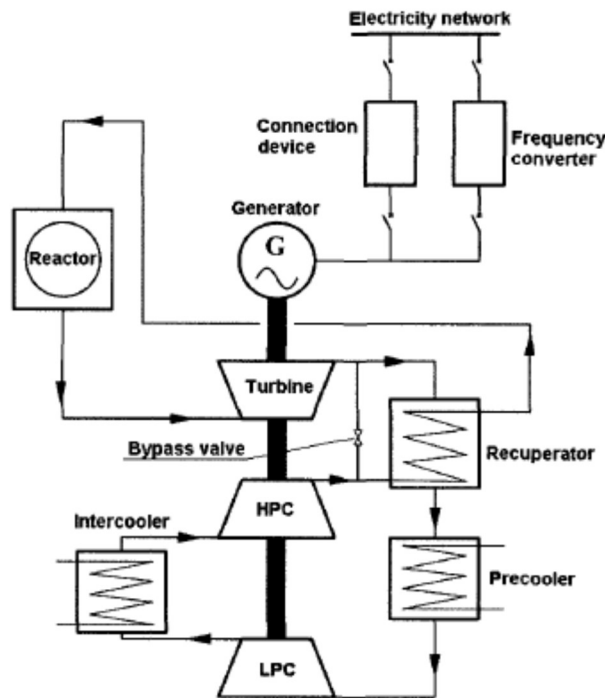


Figure 2-13 Schematic of HTR-10GT (Wu and Yu, 2007)

2.4.1.9.3 Activities

Safety demonstration tests of the HTR-10 reactor were completed. Studies were made on the design of the turbomachinery and heat exchangers, and the conceptual design of the PCS by OKBM and INET was completed in 2002 (Sun et al., 2000; Xu et al., 2005). Different test rigs were established to test the turbocompressor and the active magnetic bearing (Wu and Yu, 2007; Yang et al., 2008; Yang et al., 2014). The HTR-10GT project is still ongoing.

2.4.1.10 ANTARES

2.4.1.10.1 Participants and purpose

In France, Framatone ANP, a company jointly owned by AREVA and Siemens, developed the ANTARES concept for the production of hydrogen and generation of electricity.

The aim of the ANTARES programme is to create a commercially competitive advanced HTR to meet the future industrial requirement for carbon free electricity generation and fossil free process heat supply.

2.4.1.10.2 Description

The VHTR ANTARES plant employed an indirect cycle and distributed layout. It is design for cogeneration of high temperature process heat (for hydrogen production) and high efficiency electricity generation with combined cycle components (Figure 2-14). The reactor thermal power is 600 MWth and helium is circulated in the primary circuit at 1000 °C reactor outlet temperature (Gauthier et al., 2006). Heat is transferred to the PCS through the IHX. The topping closed-cycle GT uses mixture of helium and nitrogen as working fluid to obtain fluid property similar to air for derivative GT design technology. The plant efficiency is improved with a bottoming steam turbine cycle facilitated with steam generator. The GT turbomachine, the steam turbine and the generator rotate on a single shaft.

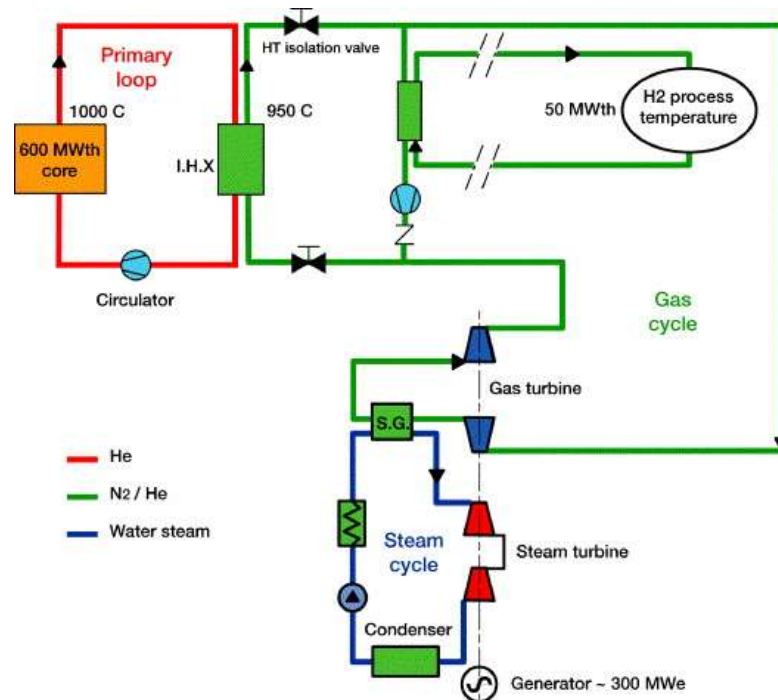


Figure 2-14 Schematic of the V/HTR ANTARES plant (Gauthier et al., 2006)

2.4.1.10.3 Activities

Manufacturing feasibility for the large components was established and in 2006 the conceptual design phase was completed (Carre et al., 2010).

2.4.1.11 BG demonstration plant

2.4.1.11.1 Participants and purpose

In the UK, British Gas (BG) developed a closed-cycle GT demonstration facility at Coleshill near Birmingham in 1995 (McDonald, 2012). The aim of the facility was to serve as test plant for larger closed-cycle GT power plant using helium as working fluid and higher TIT than previous fossil-fired closed-cycle GTs (McDonald, 2012; Al-attab and Zainal, 2015).

2.4.1.11.2 Description of facilities

The facility used mixture of nitrogen and 2% oxygen as working fluid. The cycle is fired with natural gas through advanced gas-fired heater rated at about 1 MWth. The advanced gas-fired heat exchanger is a major feature of the facility. It can raise the working fluid temperature to about 1000 °C, which is much higher than the temperature of previously operated fossil-fired closed-cycle GT plants.

2.4.1.11.3 Activities

The construction of the facility was completed (Figure 2-15). However, demonstration activities could not progress beyond initial development phase as a result of changes in the company (McDonald, 2012).



Figure 2-15 BG demonstration facility (McDonald, 2012)

2.4.2 Commercially operated closed-cycle GT plants

Some fossil-fired closed-cycle GT plants were built and operated mostly in Europe in the 1950s, 1960s and 1970s. A comprehensive description of these plants is given by Keller (1978), Frutschi (2005) and McDonald (2012). A few of them were highlighted as follows:

- **Coventry plant:** As a result of encouraging test results from AK-36 installation, a 700 kWe closed-cycle GT was built in Coventry, UK in 1949. It used waste heat as heat source and air as working fluid. With about 25% efficiency, the power output doubles those obtained from conventional steam turbine plants of that era.
- **Paris plant:** In 1952, EDF (Electricite de France) contracted Escher Wyss to build the 12 MWe plant at St. Denis in Paris. The air working fluid is heated to about 660 °C by burning light or heavy oil. The plant adopted a rather complex layout with two shafts, four compressors, three intercoolers, and two turbines as well as the precooler, recuperator, intermediate gas heater and the primary side flue gas circulating equipment. However, stable and reliable operation was attained. The plant was replaced by a 250 MWe steam turbine plant after operating for about 7000 hours.
- **Toyotomi plant:** Fuji Electric under the license of Escher Wyss built a natural gas fired air closed-cycle GT plant at Toyotomi, Japan for the Hokkaido electricity company in 1957. It produced 2 MWe of electricity with a TIT of 660 °C and 26% efficiency. After operating successfully for about 125,000 hours, the plant was shut down due to non-availability of fuel (Frutschi, 2005).
- **Oberhausen I:** GHH Sterkrade AG built the cogeneration plant for the municipal works of Oberhausen, Germany in 1960 under the license of Escher Wyss. It was fired by bituminous coal and uses air as working fluid. The plant was operated for more than 100,000 hours with about 14 MWe electrical power output and 28 MWth district heating. It was later modified for coke oven gas firing in 1971 and stopped operation in 1982. Technical challenges included failures of the compressor rotor and stator blades due to corrosion and vibration.
- **Kashira plant:** Escher Wyss of Zurich was contracted by the Institute of Thermal Engineering, Technical University of Moscow in 1961 to build a 12 MWe closed-cycle GT at Kashira. The plant burned coal to generate electricity and produce heat energy for district heating with a TIT of 680 °C and 28% efficiency. Difficulties included un-solidified ash resulting in excessive slag formation and the high content of pyrite in the coal causing the plates of the coal crusher to wear out fast.

- **Gelsenkirchen plant:** Starting from 1967, the Gelsenkirchen plant was successfully operated for nearly 100,000 hours generating 17 MWe of electricity plus heat energy for district heating. The plant used blast furnace gas and light oil as fuel. It stopped operation due to a crack in the blast furnace. This was the last closed-cycle GT with air as working fluid to be commercially operated. It became obvious during this time that the fossil-fired closed-cycle GT could no longer compete with open cycle GT (McDonald, 2012).
- **Oberhausen II:** In 1974, the second closed-cycle GT plant at Oberhausen was built for commercial production of electricity (50 MWe) and district heating (53.5 MWth). It also served as a demonstration plant for the HHT nuclear project providing information on dynamic behaviour and integrity of components. It used helium as working fluid and was fired with coke oven gas. The plant was only able to produce 30 MWe instead of the rated 50 MWe due to poor turbomachinery design and excessive pressure losses (Frutschi, 2005). Operation was terminated in 1988 due to non-availability of fuel. Problems encountered are axial movement of rotor leading to labyrinth seals damage, blade failure and vibrations causing bearing damage.

Other constructed fossil-fired closed-cycle GT reported in the literature are: Clydebank test facilities, UK (1950 & 1951); Dundee plant, UK (1954); TUCO 52, Switzerland (1955); Ravensburg, Germany (1956); Altnabreac, UK (1959); Rothes, UK (1960); Coburg, Germany (1961); Nippon Kokan, Japan (1961); Haus Aden, Germany (1963); Phoenix helium turbine for nitrogen liquefaction, USA (1966) and Vienna, Austria (1972).

2.5 Summary of modelling and simulation studies, operation and control strategies

A number of researchers through modelling and simulation has studied the steady state thermodynamic performance, dynamics and control of closed-cycle GT. This section will provide an overview of the literatures on steady state thermodynamic analysis and dynamic modelling as well as suggested operation and control schemes for closed-cycle GT. Highlights of modelling/simulation tools employed for closed-cycle GT will also be provided.

2.5.1 Steady state thermodynamic performance studies

Various closed-cycle GT heat sources, working fluids and layouts have been studied in literature in order to determine their thermodynamic performances.

2.5.1.1 Performance comparison with conventional plants

Angelino performed thermodynamic evaluation of four configurations of s-CO₂ condensation cycle and concluded that s-CO₂ power cycle has the potential to perform better than reheat steam cycle on account of efficiency, simplicity and compactness (Angelino, 1968).

Sánchez et al. (2011b) compared the performance of molten carbonate fuel cell (MCFC) hybrid system using s-CO₂ closed-cycle GT to a reference hybrid system using air in open cycle configuration. Results indicated that the MCFC-s-CO₂ hybrid system yielded about 10% efficiency increase with respect to the reference system as a result of improved performance specifications of s-CO₂ components (turbine, compressor and heat exchanger). Dekhtiarev (1962) studied condensing reheated s-CO₂ cycles as a good alternative to steam cycle for fossil fuel plant. Technical-economic analysis of coal-fired s-CO₂ Brayton cycle with carbon capture by Le Moullec (2013) showed promising results with net plant efficiency of 41.3% as well as reduction in levelized cost of electricity and reduction in cost of avoided CO₂ compared to superheated steam power cycle with carbon capture. Hanak and Manovic (2016) proposed s-CO₂ cycle instead of the conventional steam cycle for electricity generation from the high-grade heat of calcium looping process. The calcium looping plant was used to capture 90% of CO₂ from the flue gas of coal-fired power plant. Results of retrofitting the calcium looping process with s-CO₂ recompression cycle indicated that a gain in efficiency of about 1-2% point over that of the steam cycle could be obtained. Modelling results of biomass to PCSs based on cascaded s-CO₂ cycle showed a 10% efficiency increase above the convention biomass plant PCS based on ORC or reciprocating internal combustion engines (Manente and Lazzaretto, 2014).

Ishiyama et al. (2008) examined steam Rankine cycle, helium and s-CO₂ closed-cycle GT for nuclear fusion reactor and recommended the s-CO₂ cycle based on its reasonable efficiency, reduced volume and the ease of permeated tritium separation. The coupling of small modular light water reactor to s-CO₂ Brayton cycle was investigated by Yoon et al. (2012). Preliminary results showed comparable efficiency to the conventional steam cycle and potential for further reduction of capital cost of SMR plant due to the small size of s-CO₂ cycle components. Santini et al. (2016) investigated the adoption of s-CO₂ cycle for a far lower temperature (about 260 °C) of an existing PWR. The results indicated that a reheated recompression s-CO₂ cycle achieved a net cycle efficiency of about 34% compared to 33.5% of the existing steam cycle and the plant footprint was 10 times smaller than the steam cycle plant.

In Chacartegui et al. (2011a), s-CO₂ cycles were investigated for CSP plants as alternative to the conventional steam cycle. Performance results showed that s-CO₂ cycle has the potential to compete with the steam cycles based on efficiency and cost. Similarly, Sasol Technology of South Africa benchmarked three s-CO₂ cycles layouts and a supercritical steam cycle against a

superheated steam cycle for CSP plants with molten salt storage system (Cheang et al., 2015). In this instance, results showed that s-CO₂ cycles cannot compete with the current steam cycle technology in term of efficiency and cost. The conflict between the conclusions of the two studies can be attributed to the differences in assumed TITs, gearbox and generator/motor efficiencies, and costs associated with material selection.

2.5.1.2 Studies based on cycle configuration

Herranz et al. (2009) investigated helium direct Brayton cycle with single and three-shaft configurations with emphasis on the effects of intercooling and reheating using the parameters and conditions of PBMR. Thermodynamic and economic assessment indicated that intercooling produces substantial improvement in efficiency, reheating produces no remarkable improvement in performance other than allowing flexibility of operation and use of multi-shaft configuration tends to increase cost of plant without any efficiency improvement.

PhD thesis by Dostal at MIT provided a detailed steady state analysis of s-CO₂ cycles for next generation nuclear reactors based on thermodynamic performance (Dostal, 2004). The study settled on the recompression s-CO₂ cycle layout as the preferred option for reactor core outlet temperature above 500 °C because of its simplicity, compactness, cost and thermal efficiency. Al-Sulaiman and Atif (2015) compared the performance of five different s-CO₂ Brayton cycle configurations (simple, regenerative, recompression, pre-compression and split expansion cycle) for CSP application and the recompression cycle was found to give the best efficiency. Recompression and partial cooling cycles were compared by Neises and Turchi (2014) for CSP, highlighting the potential reduction in cost and improvement of CSP receiver efficiency with the partial cooling cycle.

Recently, Wang et al. (2017) reviewed and compared the main s-CO₂ cycle configurations integrated with molten salt solar power towers having both the main heater and a reheater. Intercooling was introduced into the main compressor of the recompression cycle to further improve the performance. S-CO₂ cycles and the various configurations have also been investigated as bottoming cycles for fuel cell (Bae et al., 2014) and GT system (Kim et al., 2016) as well as an alternative PCS for other waste heat recovery process (Persichilli et al., 2011; Banik et al., 2016) and biomass plants (Manente and Lazzaretto, 2014). Bae et al. (2014) investigated s-CO₂ cycle configurations comprising an s-CO₂ Brayton-steam Rankine cycle cascade, a recompression cycle and two simple recuperated cycle (a supercritical and a trans-critical cycle) as bottoming cycles for molten carbonate fuel cell. The different layouts were compared in terms of cycle efficiency, the net electric power output of the hybrid system and physical size.

Kim et al. (2016) compared the performance of nine s-CO₂ cycle layouts together with three newly developed concept as bottoming cycles for GT plant. It was concluded that although the recompression cycle has a good cycle efficiency, it is not suitable as a bottoming cycle due to its poor heat recovery factor. Pham et al. (2015) carried out the mapping of thermodynamic performance and exergy analysis for different s-CO₂ cycle configurations and operating conditions. The study concluded that the recompression cycle in condensing mode is the most fitting configuration for PWR application due to system simplicity and compactness, and for SFR application due to improved efficiency and optimal IHX inlet temperature. Sakar (2009) performed exergetic analysis of s-CO₂ recompression cycle and found the exergetic efficiency more sensitive to the isentropic efficiency of turbine and the effectiveness of the high temperature recuperator (HTR) than compressor efficiency and low temperature recuperator (LTR) effectiveness respectively.

2.5.2 Dynamic modelling and simulation studies

Closed-cycle GT plants are expected to experience transient/dynamic conditions like start-up, shutdown and load changes more frequently than base-load plants. Therefore, accurate prediction of the dynamic characteristics of the plant through modelling and simulation is required for stable operation, fault diagnosis and control system design. Hence, following the efforts to develop closed-cycle GT is the numerical modelling of its dynamic behaviour under various operating and accident conditions.

2.5.2.1 Modelling studies and computer codes for research programmes

Dynamic models of closed-cycle GT developed at the Institute for Turbomachinery, University of Hannover were validated with measured data from the Oberhausen I plant (Bammert and Krey, 1971; Bammert and Poesentrup, 1980). The Swiss Federal Institute for Reactor Research in collaboration with Brown Boveri-Sulzer Turbomachinery Ltd (BST) developed the TUGSIM-10 computer code for transient analysis of a large nuclear closed-cycle GT cycle and the code was validated with measurement data from a 30 MWe fossil-fired closed-cycle GT using air as working fluid (Dupont et al., 1977). In 1980, GA developed a FORTRAN transient analysis computer code, called REALY2, for the dynamic and control modelling of the GT-HTGR plant (Bardia, 1980). The REALY2 model was used for design of control and instrumentation, plant configuration studies, performance selection and design of plant components. The GTSim transient simulation program was developed by Yan (1990) to investigate the dynamic characteristics and for control system design for an advanced nuclear GT plant.

Dynamic simulation studies were also performed for most of the recent closed-cycle GT programmes. Verkerk and Van Heek (2000) used Panthermix (for reactor core) and RELAP5 (for

PCS) code to model the ACACIA pebble bed HTR coupled directly to helium closed-cycle cogeneration plant and analysed transients related to Loss of Coolant Incident (LOCI) and Loss of Flow Incident (LOFI). The transient simulation indicated that a LOCI or LOFI was not the worse-case scenario for the maximum reactor temperature. Different control options and the effect of design choices on dynamic behaviour of the ACACIA plant was investigated with Aspen Custom Modeller by Kikstra and Verkooijen (2000). Later, Verkerk and Kikstra (2003) compared RELAP5 and Aspen Custom Modeller modelling of load rejection and part-load transients of the ACACIA plant. Also, RELAP5-3D was used for analysis of CBC coupled to gas-cooled reactor for spacecraft propulsion (McCann, 2007), and transient simulation of lead-cooled reactor coupled to s-CO₂ cycle (Nikiforova et al., 2009) and fusion reactor coupled to s-CO₂ cycle (Batet et al., 2014). At ANL, Vilim developed the Gas Plant Analyser and System Simulator for Hydrogen production (GAS-PASS/H) for dynamic modelling of gas cooled reactor cycles (Vilim et al., 2004). The code was later modified for modelling of s-CO₂ recompression cycle by Carstens at MIT (Carstens, 2007).

Flownex network simulation code was developed as the primary simulation software for the South African PBMR project (van Ravenswaay et al., 2006). The code can be linked with Simulink[®] for control system design (Carstens, 2007). Closed Cycle System Simulation (CCSS) code for transient simulation of CBC was validated with experimental data from the NASA BPCU (Johnson and Hervol, 2006). CATHARE2 code (Geffraye et al., 2011), developed by CEA (French Atomic Energy Commission), EDF, IRSN (Radio-protection and Nuclear Safety Institute) and AREVA-NP originally for French PWR, was adapted by researcher at CEA for transient analysis of the CEA Gas Fast Reactor (GFR) coupled to closed-cycle GT (Tauveron et al., 2005; Tauveron and Bentivoglio, 2012). The code was validated for CBC with data from Oberhausen I and II plants (Bentivoglio et al., 2008). TRACE, a code developed by the United States Nuclear Regulatory Commission (NRC), was modified and used for transient analysis and control system design of the s-CO₂ Brayton cycle IST facility at Bettis Atomic Power Laboratory (Hexemer and Rahner, 2011; Hexemer, 2014). Aimed at HTR-10GT project, INET at Tsinghua University developed HTR-GTsim transient analysis software (Wenlong et al., 2012). More test data are needed to verify the accuracy of the code but good agreement exist between the code and simulation results from THERMIX code.

At ANL, the Plant Dynamics Code (PDC) was created specifically for transient analysis of s-CO₂ recompression cycle and the coupled reactors (Moisseytsev and Sienicki, 2009a). Previously, the code has been employed to investigate behaviour of s-CO₂ cycle coupled to Lead-cooled Fast Reactor (LFR) like SSTAR (Small Secure Transportable Autonomous Reactor) and STAR-LM (Secure Transportable Autonomous Reactor with Liquid Metal coolant) developed at ANL, and SFR like the ABR-1000 and the French ASTRID plant (Moisseytsev and Sienicki, 2008;

Moisseytsev and Sienicki, 2010; Floyd et al., 2013). The PDC code is currently been validated with experimental data from the SNL s-CO₂ loop (Moisseytsev and Sienicki, 2014; Moisseytsev and Sienicki, 2011).

2.5.2.2 Non project specific modelling studies and codes

Modelling tools mentioned above are mostly developed for specific projects and applications. Modelling studies of closed-cycle GT with commonly available software have been reported in the literature as well. Wright and Sanchez (2005) used Simulink[®] to perform dynamic modelling and control of a space reactor coupled to CBC. Matlab[®] model and simulation of transient behaviour of HTGR helium turbine plant was presented by Xie (2011). Studies of dynamic behaviour and control of geothermal s-CO₂ Brayton cycle during startup, heat addition, changes in cooling medium temperature and mass flow, and changes in loop mass was implemented in DYMOLA simulation environment by Singh et al. (2011). Modelica non-proprietary modelling language was employed by Casella and Colonna (2011) for dynamic modelling and control studies of solar s-CO₂ Brayton cycle plant. At Korea Atomic Energy Research Institute (KAERI), MMS (Modular Modelling System) was used for modelling KALIMER-600 SFR coupled with s-CO₂ closed-cycle PCS.

Part load analysis of MCFC-s-CO₂ hybrid system by Sánchez et al. (2011a) showed good performance and efficient control system as well as highlighted the impact of heat exchanger effectiveness on system efficiency. Ablay (2013) investigated a simple dynamic modelling approach and control strategies under load following operation for an advanced molten salt reactor coupled to CBC. Iverson et al. (2013) presented the transient response of s-CO₂ Brayton cycle to a reduction in solar heat input for short duration in CSP and found that the system could continue to operate effectively until thermal input is restored. The computer model was validated with data from the SNL recompression s-CO₂ experimental loop.

2.5.2.3 1-D, 2-D and CFD modelling of closed-cycle GT

Models of closed-cycle GT are usually based on turbomachinery performance maps (a 0-dimensional quasi-steady state approach) to simulate the dynamic characteristics and control of the plant (Tauveron et al., 2007). Use of performance maps is sufficient in most cases for simplified dynamic performance studies and control system designs. However, its implementation is prone to interpolation errors and usually limited to normal operating range as it cannot simulate very low speed, heat exchange with wall, surge, stall or reverse flow conditions. More detailed analysis of extreme transients will sometimes requires either a 1-D, 2-D or even 3-D CFD model of system components.

A 1-D turbomachinery modelling approach was applied by Tauveron et al. (2007) to gas cooled reactor GT to investigate transient behaviour during pipe rupture accident event. Kim et al. (2008) and Kim et al. (2009) simulated load transients in GTHTR300 with a 2-D turbomachinery model implemented into GAMMA-T code. Brenes (2014) performed CFD simulation of s-CO₂ compressor with ANSYS Fluent® taking into consideration the unique features s-CO₂ cycle such as rapid property variation near critical point and possibility of condensation in the compressor. Based on similar reason, Pecnik et al. (2012) and Suo-Anttila and Wright (2011) used data from SNL s-CO₂ loop for CFD modelling of s-CO₂ radial compressor and for simulation of flow in the test loop respectively. Other CFD studies included the work of Munroe et al. (2009) for s-CO₂ centrifugal compressor and Van Abel et al. (2011) for pressure drops and heat transfer in s-CO₂ PCHEs.

2.5.3 Operation and control options for closed-cycle GTs

An area that needs to be proven in order to determine the overall success of closed-cycle GT relates to its operation and control. Theoretically, the power output of closed-cycle GT is determined by the mass flow rate, the compressor inlet temperature, the TIT, the turbomachinery efficiencies and the pressure ratio (Yan, 1990). Hence, typical control options for modulating the power output of closed-cycle GT include inventory/pressure control, bypass control and temperature/thermal input control.

Changing the mass flow rate of the working fluid, usually called inventory or pressure control, is the most attractive option as power level can be varied without changing the plant efficiency (Dostal, 2004). This method uses inventory tanks to store the working fluid for power reduction, and releases working fluid into the cycle during power increase. Disadvantages of inventory control are that it requires an inventory tank whose size can be quite large depending on the power range to be controlled. Also, the rate of change of power level is limited by the size of the control valves. Hence, while the 50 MWe Oberhausen II plant utilized multi-vessel inventory control, the large 800 MWe GT-HTGR project developed by GA did not use inventory control because of the large helium inventory that would be required and expected to be transferred between the tank and the power conversion circuit (Yan, 1990). HTGR-GT adopted only bypass and TIT control.

In bypass control, the turbine pressure ratio is manipulated by controlling the mass flow rate through the heat source and turbine through the regulation of the bypass valve and hence a reduction in the power output. A significant advantage of bypass control over inventory control is its capability to deal with rapid power changes. For temperature control, the TIT is controlled by varying the amount of heat transferred in the IHX or reactor.

2.6 The need for closed-cycle GT demonstration plant

Before commercial deployment, a number of technologies remain to be proven and these will be largely addressed in a demonstration facility. A number of experimental and pilot test studies have been carried out for closed-cycle GT but they are usually too small to incorporate all the features and technologies typical of a commercial size plant. Also, the newly developed enabling technologies for closed-cycle GT were never tested in the early operated fossil-fired closed-cycle GT power plants. Hence, demonstration plants with scales of 10s of MWe will be required to evaluate the operation and performance of closed-cycle GT. McDonald (1997) suggested a demonstration plant with power rating in the range 25-50 MWe for meaningful demonstration of helium closed-cycle GT plant. SNL is currently proposing a minimum size of 10 MWe for demonstration of commercial-scale S-CO₂ Brayton cycle plant (Sienicki et al., 2011).

The demonstration plant will permit the verification of the performance and integrity of turbomachinery and rotor assembly, heat exchangers, bearings, seals, and control systems under operating conditions identical to commercial plant. Similarly, the whole operating range (start-up, shutdown, full load and part load operations) of the plant can be tested. The demonstration plant will be adequately instrumented to obtain data for validation of both steady state and dynamic models of the plant.

To this end, this thesis investigates the feasibility of near-term demonstration of closed-cycle GT by studying the steady state and dynamic performances and perform preliminary design of components for different suitable CBC configurations coupled to two mature nuclear heat sources viz-a-viz SFR and PWR. In addition, thermodynamic performance of s-CO₂ Brayton cycles coupled to coal-fired furnace is investigated.

2.7 Summary

Closed-cycle GT has the potential for improved efficiency of electricity generation, compact and simple design, and reduced CO₂ emissions and therefore could complement conventional power plants. A state-of-the-art assessment of the plant and research work carried out so far is provided in this chapter. These include its historical development, major concepts and features of the plant, important research programmes worldwide, experimental facilities, commercially operated plants, and studies through modelling and simulation. The experimental and pilot test facilities are usually too small for investigating all the features and technologies applicable to commercial size plant. Therefore, the need for closed-cycle GT demonstration plant to establish the integrity, operation and performance of the plant before commercial deployment was emphasised. Carrying out studies through modelling and simulation could provide an understanding of the steady state

and dynamic performances as well as the operation and control of the closed-cycle GT plants as a way of assessing their feasibility for near-term demonstration.

3 Steady State Model Development for Closed-cycle GTs Coupled to Nuclear Reactor and Methodology for Preliminary Design of Components²

3.1 Introduction

In this chapter, the development of the steady state models to be employed for the thermodynamic performance analysis of nuclear closed-cycle GTs is presented. The main components having significant impact on the performance and size of CBC are the heat exchangers and turbomachinery. Therefore, this chapter also describes the methodology for their preliminary design and sizing. Design of the primary circuit components such as the reactor and sodium pump was not considered. Also piping design was not examined.

3.2 Steady state modelling of closed-cycle GT and its implementation in Matlab[®]

For the purpose of steady state performance analysis, a cycle analysis code was developed in Matlab environment for nitrogen and s-CO₂ closed-cycle GTs coupled to SFR and PWR respectively. The cycle calculation code consists of models of the reactors, pumps, IHXs, recuperators, precoolers, intercoolers, compressors, turbines and pipes. Models of the individual component were derived based on steady state mass and energy balances, thermodynamic relations and characteristic equations of the components.

The known input variables are reactor thermal power; core outlet temperature and pressure; cycle maximum pressure; hot side outlet temperatures of IHX, precooler and intercooler; turbomachinery isentropic efficiencies; minimum terminal temperature difference (TTD) or effectiveness of heat exchangers; generator efficiency; and relative pressure losses of pipes and heat exchangers. Consequently, the mass flow rates, fluid thermodynamic states, heat transferred, mechanical power delivered or absorbed, generator output and cycle efficiency were evaluated. In the case of the intercooled nitrogen cycle, the whole cycle calculation process begins with initial guesses for the LPC and HPC pressure ratios. The iteration is continued until optimum values of compressor ratios in term of the maximum cycle efficiency are obtained. Note that any

² Most of this chapter has been published in Olumayegun, O., Wang, M. and Kelsall, G. (2017). Thermodynamic analysis and preliminary design of closed Brayton cycle using nitrogen as working fluid and coupled to small modular sodium-cooled fast reactor (SM-SFR). *Applied Energy*, Vol. 191, pp. 436 – 453. See Section 3 and 4

thermodynamic property can be obtained from the fluid thermodynamic property sources if two independent properties are known.

The reactor was modelled as a heat source. For a given reactor thermal power, the primary circuit coolant mass flow rate was calculated using equation (3-1). The full meaning of the equation symbols can be found in the Nomenclature section.

$$Q_r = \dot{m}_{coolant}(h_{ro} - h_{ri}) \quad (3-1)$$

The coolant is recycled by the pump. The external power input in the pump is given as:

$$W_p = \dot{m}_{coolant}(h_{po} - h_{pi}) \quad (3-2)$$

The pump isentropic efficiency is:

$$\eta_{p,is} = \frac{h_{po,is} - h_{pi}}{h_{po} - h_{pi}} \quad (3-3)$$

For an isentropic process in the pump, it follows that the first law for closed system undergoing reversible process becomes:

$$h_{po,is} - h_{pi} = \frac{P_{po} - P_{pi}}{\rho_{pi}} \quad (3-4)$$

The compressors were modelled using their pressure ratios and isentropic efficiencies. The compressor outlet conditions were computed from equation (3-5) and (3-6):

$$P_{co} = P_{ci}\pi \quad (3-5)$$

$$\eta_{c,is} = \frac{h_{co,is} - h_{ci}}{h_{co} - h_{ci}} \quad (3-6)$$

The power consumption of the compressors, W_c is calculated as the product of working fluid mass flow rate, \dot{m}_{wf} and enthalpy rise between the inlet and outlet of the compressors.

$$W_c = \dot{m}_{wf}(h_{co} - h_{ci}) \quad (3-7)$$

Similarly, the turbines were modelled using the pressure ratios and isentropic efficiencies. The pressure, enthalpy and power were calculated by using equation (3-8), (3-9) and (3-10).

$$P_{to} = \frac{P_{ti}}{\pi} \quad (3-8)$$

$$\eta_{t,is} = \frac{h_{ti} - h_{to}}{h_{ti} - h_{to,is}} \quad (3-9)$$

$$W_t = \dot{m}_{wf}(h_{ti} - h_{to}) \quad (3-10)$$

The IHX, recuperator, precooler and intercooler were modelled as counter-flow heat exchangers. Two calculation options are available. The first option is to assume that the minimum TTD is known while the second option is to assume that the effectiveness is known. Using the TTD approach, the minimum TTD can occur either at the hot end (hot stream inlet/cold stream outlet) or at the cold end (cold stream inlet/hot stream outlet). As an initial guess, the minimum TTD was assumed to occur at the hot end, then:

$$T_{Co} = T_{Hi} - TTD_{min} \quad (3-11)$$

Therefore, the heat exchanger duty (heat transferred), Q_{HX} is:

$$Q_{HX} = \dot{m}_C(h_{Co} - h_{Ci}) \quad (3-12)$$

Then the hot stream outlet enthalpy is:

$$h_{Ho} = h_{Hi} - \frac{Q_{HX}}{\dot{m}_H} \quad (3-13)$$

If the temperature difference at cold end is discovered to be lower than the minimum TTD, equation (3-11) is replaced with equation (3-14). Then the above calculation is repeated but starting with cold end.

$$T_{Ho} = T_{Ci} + TTD_{min} \quad (3-14)$$

However, if the effectiveness approach is to be used, the exchanger effectiveness, ε_{HX} is defined as:

$$\varepsilon_{HX} = \frac{\dot{m}_C(h_{Co} - h_{Ci})}{Q_{max}} = \frac{\dot{m}_H(h_{Hi} - h_{Ho})}{Q_{max}} \quad (3-15)$$

The maximum theoretical heat transfer rate in counter flow heat exchanger of infinite heat transfer surface area, Q_{max} , is given as follows:

$$Q_{max} = \min\{(\dot{m}_C(h_{CoTHi} - h_{Ci})); (\dot{m}_H(h_{Hi} - h_{HoTCi}))\} \quad (3-16)$$

Where h_{CoTHi} is the outlet enthalpy of cold stream at the temperature of the hot stream inlet and h_{HoTCi} is the outlet enthalpy of the hot stream at the cold stream inlet temperature

Inlet or outlet pressures of heat exchangers and pipes were calculated from the relative pressure losses defined as:

$$\xi = \frac{P_i - P_o}{P_i} \quad (3-17)$$

The cycle thermodynamic states of pressure, temperature and enthalpy at all component inlet and outlet were obtained by solving the equations (3-1) - (3-17). Then the electrical power supplied to the grid or load demand, W_L was calculated as:

$$W_L = \eta_{gen} \left(\sum W_t - \sum W_c \right) - W_P \quad (3-18)$$

Note that pump power was not considered negligible in the cycle calculation. This will reduce the plant efficiency. The thermal efficiency, η_{th} is defined as the ratio of electrical power output to the reactor thermal power:

$$\eta_{th} = \frac{W_L}{Q_r} \quad (3-19)$$

The cycle analysis code is further integrated with the heat exchanger preliminary design code/program. Heat exchanger design was performed based on the mass flow rates and fluid conditions determined through the cycle calculation, and a chosen maximum pressure loss constraint. Then the initial heat exchanger pressure losses used for cycle calculation are replaced with the actual pressure losses obtained from the preliminary design code. The process is repeated iteratively until there is convergence of the mass flow rates and fluid conditions. On the other hand, the turbomachinery design code determined the number of stages and size of the turbines and compressors.

3.3 Fluid thermodynamic and transport properties implementation in the Matlab®

The liquid sodium or pressurised water in the primary circuit carries the heat energy to be transferred to the PCS, nitrogen gas or s-CO₂ is the working fluid in the PCS while liquid water in the cold side of the precoolers and intercoolers is used for heat rejection to the environment. Hence, the cycle analysis and the preliminary design codes must be able to simulate the fluid properties of liquid sodium, nitrogen gas, s-CO₂ and water. Fluid thermodynamic properties to be simulated include: enthalpy, density, heat capacity and speed of sound. Transport properties include the dynamic viscosity and thermal conductivity.

Since Matlab® does not have any thermodynamic and transport property function, a Matlab® code was written to compute the properties of liquid sodium. The computations were based on correlations recommended by Sobolev (2011). A summary of the correlations used to generate property values of liquid sodium is given in Table 3-1. The effect of pressure on the thermodynamic and transport properties of liquid sodium was neglected. However, properties of nitrogen gas, s-CO₂ and water were obtained from NIST REFPROP (version 9.1) program. The REFPROP program has been reported to be accurate and widely applicable to a variety of pure fluid and mixtures (Lemmon et al., 2013; Carstens, 2007). Any unknown properties can be requested from the REFPROP program by supplying two known independent properties. Both the Matlab® code for liquid sodium property and the NIST REFPROP program were used as subroutines in the cycle analysis and preliminary design codes.

Table 3-1 Correlations for computing liquid sodium properties (Sobolev, 2011)

Property	Correlations (T is in Kelvins)	Units
Enthalpy	$h = 164.8(T - T_m) - 1.97 \times 10^{-2}(T^2 - T_m^2) + 4.167 \times 10^{-4}(T^3 - T_m^3) + 4.56 \times 10^5(T^{-1} - T_m^{-1}); T_m = \text{melting temperature}$	J/kg
Density	$\rho = 1014 - 0.235T$	kg/m ³
Specific heat capacity	$C_p = -3.001 \times 10^6 T^{-2} + 1658 - 0.8479T + 4.454 \times 10^{-4} T^2$	J/kgK
Viscosity	$\ln \mu = \frac{556.835}{T} - 0.3958 \ln T - 6.4406$	Pa-s
Thermal conductivity	$k = 110 - 0.0648T + 1.16 \times 10^{-5} T^2$	W/mK

3.4 Verification of the steady state model

The steady state model was verified with results of numerical model reported for nitrogen CBC by Ahn and Lee (2014). Figure 3-1 shows the layout of the intercooled nitrogen CBC, which is composed of precooler (PC-1), intercooler (PC-2), recuperator (RCP), IHX, LPC (C1), HPC (C2) and turbine (T1). The input parameters used for the verification are shown in Table 3-2. In Table 3-3, the main results of the cycle model are compared with the literature values. The results of the cycle model agreed well with the results obtained from literature to within 0.86%. The small dissimilarities in the results could be due to the thermodynamic properties calculations and the round-off error in the input parameters. Therefore, the developed Matlab® cycle model is deemed accurate enough for simulating the performance of CBCs.

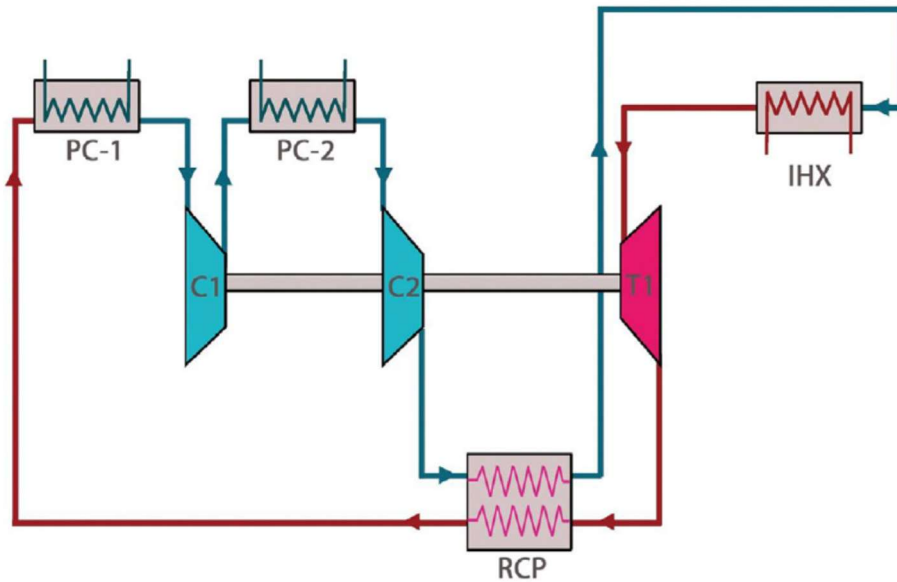


Figure 3-1 Single intercooling layout with recuperation (Ahn and Lee, 2014)

Table 3-2 Input parameters for the verification of the nitrogen CBC. Data taken from Ahn and Lee (2014)

Parameters	Value
Cycle maximum pressure	181.5 bar
LPC/HPC inlet temperature	27 °C
TIT	500 °C
IHX Na side inlet temperature	526 °C
IHX Na side outlet temperature	450 °C
Recuperator minimum TTD	14.2 °C
Turbine efficiency	90%
LPC/HPC efficiency	85%
Thermal work	150 MW

Table 3-3 Verification of cycle model with the literature value

Parameters	Literature value	Simulation value	Relative difference (%)
Precooler inlet temperature	90.7 °C	90.6 °C	0.11
LPC outlet temperature	59.4 °C	59.4 °C	0
HPC outlet temperature	76.5 °C	76.5 °C	0
IHX N ₂ side inlet temperature	348.7 °C	348.6 °C	0.03
Turbine outlet temperature	373.3 °C	373.4 °C	0.03
Recuperator effectiveness	95%	95.1%	0.11
Nitrogen mass flow	2510.0 kg/s	2508.9 kg/s	0.04
Thermal efficiency	34.9%	35.2%	0.86

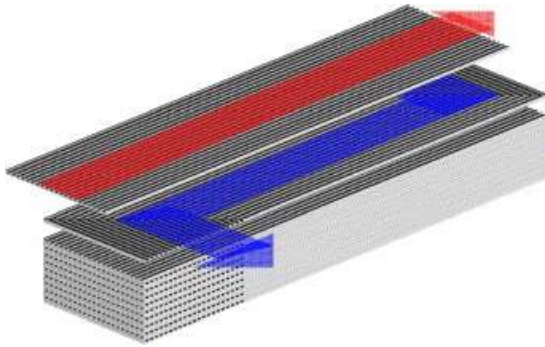
3.5 Heat exchanger design and sizing methodology

Preliminary design and sizing was done for the following heat exchangers: IHX, recuperator, precooler and intercooler. Appropriate selection and design of heat exchangers for CBC is important because (Fourspring and Nehrbaauer, 2011):

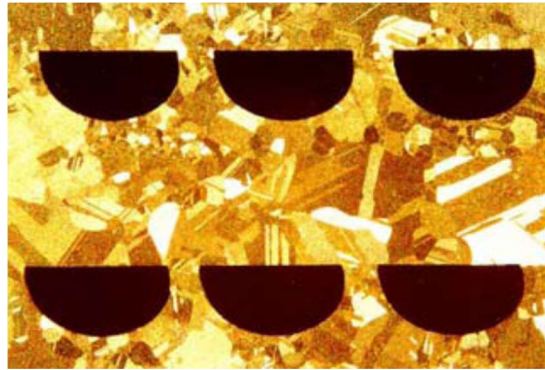
- The volume of the heat exchangers will largely determine the footprint of the CBC and hence the capital cost
- The effectiveness and pressure losses through the heat exchangers will impact the cycle efficiency and hence the operating cost
- Reliable heat exchangers that is able to withstand the CBC's high pressure and temperature will guarantee the safety of the plant.

All the heat exchangers in this work were assumed to be of the PCHE type. Most previous studies settled on the PCHE as the heat exchanger of choice for CBC (Dostal, 2004; Floyd et al., 2013; Wright et al., 2006). This is due to its compactness, reliable mechanical characteristics at high pressure and temperature and the high effectiveness (Shah and Sekulic, 2003). Heatric Ltd (UK) has been the sole manufacturer of PCHE since 1985. PCHEs are constructed from flat metal plates into which fluid flow channels are photo-chemically etched into one side of the plate. The etched-out plates are then stacked and diffusion bonded together to form strong, compact, all-metal heat exchanger module as shown in Figure 3-2. The etched channels are usually semi-circular in cross-section with typical diameter of 1.0 – 5.0 mm and depth of 0.5 – 2.5 mm (Le Pierres et al., 2011). According to Heatric, it is possible to manufacture PCHE module with size up to 900 mm (width) by 900 mm (height) by 2500 mm (length) if desired (Alpy et al., 2011). The calculations in this work were based on the standard plate and flow channel specifications shown in Table 3-4. The

hot and cold plate specifications were assumed to be the same. Straight flow channels with counter-current flow arrangement was also assumed in the design. Depending on the required thermal duty, a number of identical modules are then welded together to form the complete heat exchanger unit (Li et al., 2011).



a. PCHE plate stacking



b. Micrograph section through diffusion bonded core

Figure 3-2 PCHE construction (courtesy of Heatric)

Table 3-4 Selected PCHE specifications

Specification	Value
Material	316L Stainless steel
Channel diameter	1.5-2 mm
Channel pitch	1.9 - 2.4 mm
Plate thickness	1-1.5 mm
Module width	900 mm
Module height	about 900 mm
Module length	≤ 2500 mm

A heat exchanger preliminary design code, which can be integrated with the cycle calculation code, was developed in Matlab[®]. The cycle calculation provided some of the initial design conditions such as the fluid types, mass flow rates, inlet and outlet enthalpies, inlet pressures and effectiveness. The heat exchanger design code then uses the given initial design conditions, the PCHE plate specifications and the desired maximum pressure drop to estimate the size and mass of the heat exchanger. The code calculates the flow frontal cross section area (width X height) and the length of the heat exchanger that meet the required effectiveness while satisfying the maximum pressure loss requirement. The design was carried out based on the logarithmic mean temperature difference (LMTD) method. For proper determination of fluid properties within the

heat exchanger, the flow paths along the heat exchanger is discretised into N number of thermal nodes as shown in Figure 3-3. The specific heat capacity of the fluid can be assumed to be constant within the thermal nodes such that the LMTD can be calculated as follows (Lienhard IV and Lienhard V, 2008):

$$LMTD = \frac{(T_{Ho} - T_{Ci}) - (T_{Hi} - T_{Co})}{\ln \frac{(T_{Ho} - T_{Ci})}{(T_{Hi} - T_{Co})}} \quad (3-20)$$

The heat transferred is given by:

$$Q = \dot{m}_C(h_{Co} - h_{Ci}) = \dot{m}_H(h_{Hi} - h_{Ho}) = U.A.LMTD \quad (3-21)$$

The overall heat transfer coefficient (HTC), U was determined from the convective HTCs and conduction through the heat exchanger material as follows (Dostal, 2004):

$$\frac{1}{U} = \frac{1}{h_H} + \frac{t}{k} + \frac{1}{h_C} \quad (3-22)$$

Convective HTCs were determined based on the Nusselt number formula (Lienhard IV and Lienhard V, 2008):

$$Nu = \frac{hD_h}{k} \quad (3-23)$$

The hydraulic diameter, D_h , was calculated from the area of flow, A, and the wet perimeter, P, of the flow channel section (Kothandaraman and Rudramoorthy, 2007):

$$D_h = \frac{4A}{P} \quad (3-24)$$

The area and perimeter of the semi-circular flow channel of PCHE is given by equation (3-25) and (3-26) respectively:

$$A = \frac{\pi D^2}{8} \quad (3-25)$$

$$P = D \left(1 + \frac{\pi}{2}\right) \quad (3-26)$$

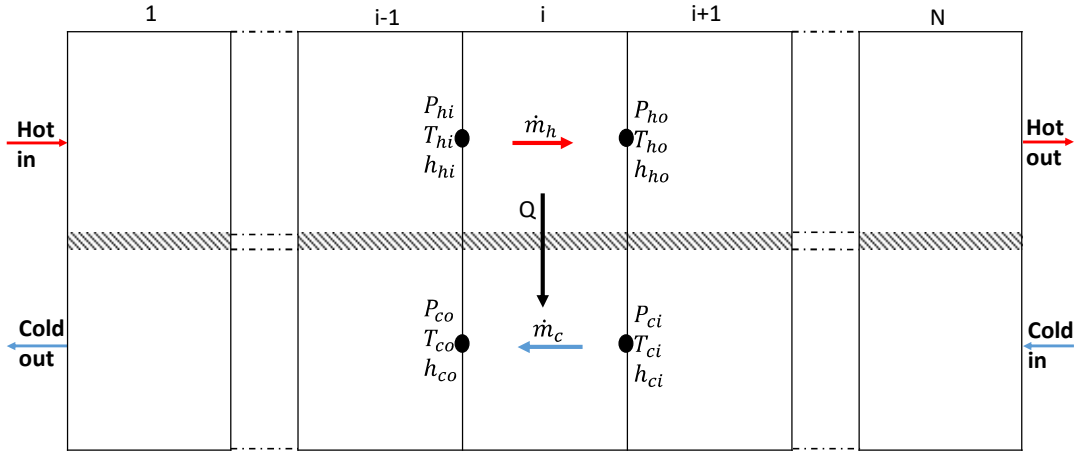


Figure 3-3 Nodalization of heat exchanger

For nitrogen, CO₂ and water, the heat transfer behaviour was estimated by using the Hesselgraves' recommendation for laminar flow and Gnielinski's correlation for turbulent flow as follows (Hesselgreaves, 2001; Dostal, 2004):

- Laminar flow ($Re \leq 2300$)

$$Nu = 4.089 \quad (3-27)$$

- Turbulent flow ($Re \geq 5000$)

$$Nu = \frac{\frac{f}{8}(Re - 1000)Pr}{1 + 12.7(Pr^{2/3} - 1)\sqrt{\frac{f}{8}}} \quad (3-28)$$

Where f is the friction factor that can be obtained from the Moody chart or the Colebrook-White correlation (Colebrook, 1939):

$$\frac{1}{\sqrt{f}} = -2.0 \log \left(\frac{\varepsilon/D_h}{3.7} + \frac{2.51}{Re\sqrt{f}} \right) \quad (3-29)$$

- Transition region ($2300 < Re < 5000$)

$$Nu = 4.089 + \frac{Nu_{Re=5000} - 4.089}{5000 - 2300}(Re - 2300) \quad (3-30)$$

For liquid sodium, the Nusselt number was calculated from the Lockart-Martinelli correlation (Seong et al., 2009):

$$Nu = 5.0 + 0.025(RePr)^{0.8} \quad (3-31)$$

Pressure loss, ΔP inside the channel of length L and hydraulic diameter D_h can be determined with the Darcy-Weisbach equation (Dostal, 2004):

$$\Delta P = f \frac{L}{D_h} \frac{\rho V^2}{2} \quad (3-32)$$

Where the Darcy friction factor, f , for laminar flow is given by (Dostal, 2004):

$$f = \frac{64}{Re} \quad (3-33)$$

For fully turbulent flow, the Darcy friction factor is given by the Colebrook-White correlation in equation (3-29).

The heat exchanger thermal-hydraulic design is an iterative process done to achieve the specified effectiveness (or thermal duty) while ensuring that the desired pressure loss was maintained. The total thermal duty is divided equally among the thermal nodes and uniform heat flux is assumed in each node. The calculation can start from either the cold end or the hot end with an initial guess of flow frontal area. Equations (3-20) to (3-33) are then applied to determine the fluid conditions, HTC's, pressure losses and length of each node. Subsequently, the heat exchanger length and pressure losses on the hot and cold sides are calculated. The calculated pressure loss is compared to the desired pressure loss and if different, a new guess value for the frontal area is selected. The calculation process is repeated until the desired pressure loss is obtained. However, if the calculated length is more than the maximum permissible channel length, a new desired pressure loss is set. Finally, the height, number of module, volume, surface area and mass of the heat exchanger are calculated.

3.6 Turbomachinery design and sizing methodology

The boundary conditions and component parameters selected for the thermodynamic cycles will influence the characteristics and size of the turbomachinery. Hence, preliminary design and sizing was done for the compressors and the turbines in order to highlight the effects of the cycle specifications on the turbomachinery, besides their impact on cycle efficiency. All the turbomachinery was assumed to be of the axial type due to the large volume flow. Thermodynamic cycle calculation results and specifications such as shaft power or mass flow rate, inlet temperature and pressure, pressure ratio and isentropic efficiency will serve as input design requirements.

The similarity concept is a very common approach for conceptual/preliminary design of turbomachinery (Wright et al., 2006; Bae et al., 2015; Sienicki et al., 2011; Gong et al., 2006; Cha et al., 2009; Fuller and Batton, 2009). It is based on the selection of two dimensionless numbers, specific speed (N_s) and specific diameter (D_s), in conjunction with the use of Balje's N_s - D_s diagrams (Balje, 1981). N_s and D_s can be determined from equations (3-34) and (3-35):

$$N_s = \frac{N\sqrt{\dot{Q}}}{(gH_{ad})^{3/4}} \quad (3-34)$$

$$D_s = \frac{D(gH_{ad})^{1/4}}{\sqrt{\dot{Q}}} \quad (3-35)$$

Where N is shaft rotational speed, \dot{Q} is the volumetric flow rate, g is acceleration due to gravity, H_{ad} is stage adiabatic head and D is the wheel diameter. From the N_s - D_s diagrams, the values of N_s and D_s needed to achieve the desired turbomachinery efficiency can be determined. Since the volumetric flow rate and total adiabatic head are already fixed by the thermodynamic cycle specifications, the only potential for optimising the turbomachinery design lies with the choice of rotational speed and stage adiabatic head (or number of stages). For grid-connected shafts, the rotational speed is also fixed and only the number of stages is available for influencing the specific speed. Moreover, there is restriction on the number of stages that can be utilized for turbomachinery design. On the contrary, two-shaft configurations, in which one of the shaft is not connected to the grid, have the advantage to greatly influence the specific speed and hence optimise the efficiency by changing the rotational speed of the non-grid connected shaft.

However, the similarity concept methodology for turbomachinery design has some setbacks. Even though the concept provides a means to rapidly size the turbomachinery, the N_s - D_s diagrams can only predict the approximate value of efficiency. Also, it is only available for single stage compressors and turbines. Therefore, in this study, a more exact but basic and rational preliminary design methodology based on two-dimensional (2-D) mean-line approach was employed. This is because it is not necessary at this initial stage to pursue a detailed design of the turbomachinery. 2-D mean-line analysis means that the flow through the turbomachinery is described by the magnitude and direction of gas velocity in the axial-tangential coordinate at the mean blade height without considering any radial variation in gas flow. Similarly, the thermodynamic properties of the working fluid were specified only at the mean blade height. Thus, fast design solutions can be obtained at the initial phase of turbomachinery design with the 2-D mean-line approach. It is considered a reasonable first approximation for axial-flow turbomachinery with high hub-to-tip ratios greater than 0.8 (Bathie, 1996; Gorla and Khan, 2003) .

The stator-rotor arrangements for axial-flow turbine and compressor are shown in Figure 3-4(a) and Figure 3-5(a) respectively. Axial-flow turbine extracts energy from the working fluid by first increasing the tangential velocity of the gas in a row of stator (or nozzle) blades then followed by a row of rotor blades that convert the gas swirl into torque for the rotating shaft. On the other hand, axial-flow compressor compresses the working fluid by first imparting kinetic energy to the fluid by a row of rotor blades then followed by diffusion in a row of stator blades to convert a part of the kinetic energy into static pressure. Several stages are usually needed in axial-flow

turbomachinery to attain the required pressure ratio. The relationship among the velocities and flow angles at the inlet and outlet of the rotor is best illustrated with the velocity diagrams at the mean blade height shown in Figure 3-4(b) and Figure 3-5(b). The fluid enters the turbine rotor row with a relative velocity, W_2 at an angle, β_2 and leaves with a relative velocity, W_3 at an angle, β_3 . The rotor blade tangential velocity at the mean blade height is U . Vectorial addition of the relative velocities and blade velocity yields the absolute velocities C_2 and C_3 at rotor inlet and outlet respectively. For the compressor, the fluid enters the rotor with a relative velocity, W_1 at an angle, β_1 and leaves with a relative velocity, W_2 at an angle, β_2 . The corresponding absolute velocities are C_1 and C_2 respectively.

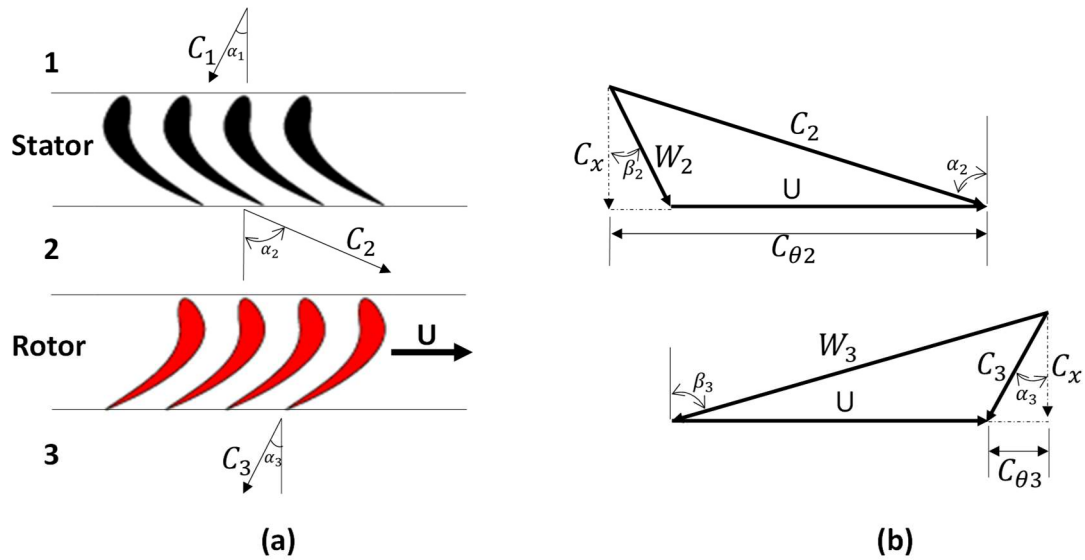


Figure 3-4 Axial turbine stator-rotor arrangement and velocity diagram

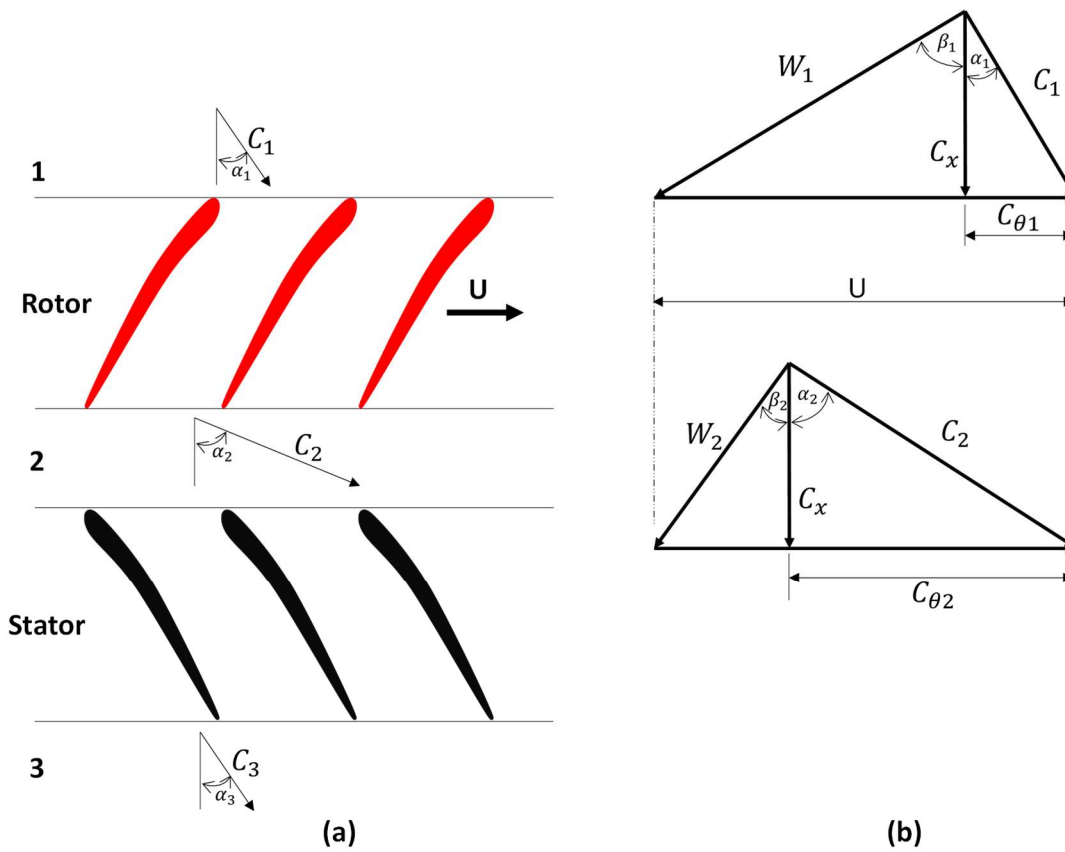


Figure 3-5 Axial compressor rotor-stator arrangement and velocity diagram (Saravanamuttoo et al., 2009)

Subscript x is used to represent the axial component of the gas velocities while subscript θ represents the tangential components.

Turbomachinery design was performed with the following assumptions:

- The process through the rotor and stator is assumed to be adiabatic
- Constant mean-line blade radius, r_m
- Constant axial-flow velocity, C_x throughout the turbomachinery stages
- Equal enthalpy changes per stage
- Repeating stages used except the first stage of the turbine and final stage of the compressor

Euler turbomachinery equation governing the energy transfer in a turbine stage is given as:

$$\Delta h_0 = U(C_{\theta 2} + C_{\theta 3}) \quad (3-36)$$

For compressor stage, the Euler equation is given as:

$$\Delta h_0 = U(C_{\theta 2} - C_{\theta 1}) \quad (3-37)$$

The velocity diagrams can be defined by three parameters: flow coefficient, stage loading coefficient and reaction.

The flow coefficient, ϕ is defined as the ratio of axial flow velocity, C_x to the blade velocity, U :

$$\phi = \frac{C_x}{U} \quad (3-38)$$

The stage loading coefficient, ψ which is a measure of the work done in a stage is defined as:

$$\psi = \frac{\Delta h_0}{U^2} \quad (3-39)$$

Degree of reaction, Λ shows the fraction of the expansion or compression which occurs in the rotor. It is defined as (Dixon, 1998):

$$\Lambda = \frac{\Delta h_{rotor}}{\Delta h_{stage}} \quad (3-40)$$

Where Δh_{rotor} is the difference in static enthalpy between rotor inlet and exit and Δh_{stage} is the difference in static enthalpy between the stage inlet and exit.

Turbine stage performance is specified by total-to-total stage isentropic efficiency, $\eta_{T,tt}$, and the stator loss coefficient, ξ . Turbine stage isentropic efficiency is defined as the ratio of actual work per unit mass to the ideal work per unit mass between the same total pressures:

$$\eta_{t,tt} = \frac{h_{01} - h_{03}}{h_{01} - h_{03,is}} \quad (3-41)$$

The loss coefficient of turbine nozzle blade is determined by the Soderberg's correlation of nominal loss coefficient, ξ , as a function of fluid deflection through the blade, δ :

$$\xi = 0.04 + 0.06 \left(\frac{\delta}{100} \right)^2 \quad (3-42)$$

The loss coefficient is then defined in terms of kinetic energy from the nozzle blade row as (Dixon, 1998) :

$$h_2 - h_{2,is} = \frac{1}{2} C_2^2 \xi \quad (3-43)$$

Compressor stage total-to-total efficiency, $\eta_{c,tt}$ is defined as the ratio of the ideal work to the actual work:

$$\eta_{c,tt} = \frac{h_{03,is} - h_{01}}{h_{03} - h_{01}} \quad (3-44)$$

Since the stage pressure ratios approach unity in this design, the stage efficiency was assumed the same as the polytropic efficiency of the turbomachinery (Mattingly, 2006) .

The compressor blade loading is assessed by the Liebelin's diffusion factor and de Haller number given in equations (3-45) and (3-46) respectively:

$$DF = 1 - \frac{V_o}{V_i} + \frac{\Delta V_\theta}{2\sigma V_i} \quad (3-45)$$

$$dHaller = \frac{V_o}{V_i} \quad (3-46)$$

The blade solidity, σ , is the ratio of the blade chord to blade spacing:

$$\sigma = \frac{c}{s} \quad (3-47)$$

To prevent excessive flow diffusion and potential separation, the diffusion factor should be restricted to below 0.6 and/or the de Haller number should be kept above 0.72. The diffusion factor is used to select the blade solidity which is then used together with the aspect ratio to determine the blade numbers. Aspect ratio, AR is defined the ratio of blade height, b_H to blade chord, c :

$$AR = \frac{b_H}{c} \quad (3-48)$$

For turbine, Zweifel's criterion for optimum lift coefficient, $C_{L,op}$ is used to determine the solidity as follows:

$$C_{L,op} = \left| \frac{2}{\sigma_x} \cos^2 \alpha_o (\tan \alpha_i - \tan \alpha_o) \right| \quad (3-49)$$

Where σ_x is solidity based on axial blade chord.

A value of 0.8 is selected for the optimum lift coefficient.

Annulus flow area, A and blade height, b_H can be calculated with the help of mass continuity in equations (3-50) and (3-51).

$$\dot{m} = \rho A C_x \quad (3-50)$$

$$A = 2\pi r_m b_H \quad (3-51)$$

The mean radius, r_m is obtained from:

$$U = r_m N \quad (3-52)$$

The number of blade, N_b is determined from:

$$N_b = \frac{2\pi r_m}{s} \quad (3-53)$$

Two separate axial-flow turbomachinery design codes were developed in Matlab[®] for the mean-line aerothermodynamic design of the compressors and turbines using the above equations. The design was able to estimate the turbomachinery flowpath geometry, blade heights, gas velocities and flow angles, stage number and volume based on the desired input design requirements obtained from cycle analysis. The main design variables included rotational speed, flow coefficient, stage number, mean blade velocity and inlet flow angle. Thermodynamic properties of the working fluid were obtained from NIST REFPROP program. Static conditions of the fluid were calculated from the stagnation conditions based on the fundamental principle rather than ideal gas approximation. Similarly, calculations for expansion and compression processes were based on enthalpy instead of the use of constant or average specific heat capacity value. Hence, the codes can be applied to working fluid with real gas properties such as s-CO₂. The turbomachinery design outcome can provide a basis for comparison among different cycles as well as highlighting the impact of various choices of design variables. Also in future work, the preliminary design code can be improved further with the capability for blade profile design, span-line design and generation of performance map for off-design analysis and dynamic modelling.

3.7 Summary

This chapter presents the methodology for the development of the steady state models and for the preliminary design of the heat exchanger and turbomachinery of closed-cycle GT for application to nuclear reactor. The steady state modelling equations for the plant components such as the reactor, heat exchanger, pump, turbine and compressor were described. The individual components were modelled based on mass and energy balances, thermodynamic relations and the characteristic equations. The steady state models were implemented in Matlab[®]. The methods for obtaining the thermo-physical properties of fluids were also described. The steady state model was verified with results of numerical model of nitrogen closed-cycle GT reported in the literature.

The Heatric PCHE heat exchangers were selected for the closed-cycle GT to cope with the high pressure of the system and to achieve compact design. The approach for the preliminary design of the heat exchangers were described. Based on cycle conditions at the heat exchanger inlets and PCHE plate specifications, the Matlab[®] code is used to determine the size and geometry of the heat exchangers. In order to capture fluid properties variation within the heat exchanger, it is divided into a number of thermal nodes or sections. Calculations were performed for each node using the LMTD method

The compressors and turbines were designed as axial flow machines. The Matlab[®] codes for preliminary design of the turbomachinery were described. Input requirements for the design of the turbomachinery include mass flow rate, inlet conditions, pressure ratio and isentropic efficiency. The turbomachinery designs are based on mean-line approach in which the flow is represented by mean flow quantities between the blades at the mean blade height without considering any radial variation.

4 Thermodynamic Performance Analysis of Nitrogen Brayton Cycle Coupled to SM-SFR and Preliminary Design of Components³

4.1 Introduction

In this chapter, the thermodynamic analysis and preliminary design of components of CBC using nitrogen as working fluid and coupled to SM-SFR for near-term demonstration of electricity generation from Gen IV reactors was carried out. The often suggested configuration for the nitrogen cycle is the intercooled CBC with single shaft, in which all the compressors, turbine and generator rotates at the grid frequency. However, preliminary design of the turbomachinery indicated that the design of the turbine is especially difficult (CEA, 2012). One solution for simplifying and improving the design of turbomachinery is to change the shaft rotational speed. This requires the use of either a frequency converter or gearbox, both of which will incur efficiency penalty. Moreover, maximum practical power output for which a gearbox is feasible is about 80 MW (Walsh and Fletcher, 2004). Another option is to employ a two-shaft configuration in which the generator and a free power turbine (FPT) rotate at the grid frequency while the compressors and a CDT rotate at an independent shaft speed.

The free selection of a higher compressors shaft speed can then be used to optimise the design of the compressors and the driving turbine. This will result in reduced stage numbers and more compact turbomachinery as well as possible improvement of turbomachinery efficiency. Two layouts are possible for the two-shaft configuration. One is to have the FPT and the CDT in series and the other is to have them in parallel. The two-shaft with parallel turbines layout is adopted in this study as the series turbines layout is known to result in loss of overall cycle efficiency (Lee et al., 2013).

The thermodynamic performances and preliminary designs were evaluated using the Matlab[®] codes developed for cycle analysis, heat exchanger design, axial compressor design and axial turbine design.

³ Most of the results in this chapter have been published in Olumayegun, O., Wang, M. and Kelsall, G. (2017). Thermodynamic analysis and preliminary design of closed Brayton cycle using nitrogen as working fluid and coupled to small modular sodium-cooled fast reactor (SM-SFR). *Applied Energy*, Vol. 191, pp. 436 – 453.

4.2 Plant configurations and description of the nitrogen Brayton cycles

In this study, two nitrogen CBC configurations have been considered: a reference single-shaft intercooled closed-cycle GT configuration and a two-shaft with parallel turbines configuration. The single-shaft intercooled configuration seems to be the most popular design choice for nitrogen CBC. Hence, it will be used as reference case for comparison with the suggested alternative two-shaft configuration.

4.2.1 Reference single-shaft intercooled CBC

The schematic flow diagram of the reference single-shaft intercooled CBC is shown in Figure 4-1. In this configuration, all the turbomachinery rotates on a single shaft. The plant features a 500 MWth SFR coupled indirectly to the PCS through the sodium/nitrogen IHX (Na/N₂ IHX). The primary circuit is made up of the SFR reactor, the primary/hot side of Na/N₂ IHX and the sodium coolant pump. Sodium coolant at 545 °C and 1.15 bar exits the reactor core and flows through the primary/hot side of the IHX. The coolant pump is used to circulate the liquid sodium in the primary circuit. Thus, the reactor core heat is transferred to the PCS via the Na/N₂ IHX. The PCS is connected to the secondary/cold side of the Na/N₂ IHX and uses nitrogen as working fluid. The Brayton cycle consists of two compressors referred to as LPC and HPC, a turbine and four heat exchangers (Na/N₂ IHX, recuperator, precooler and intercooler).

The temperature-entropy (T-S) diagram of the closed Brayton PCS is illustrated in Figure 4-2. High temperature nitrogen leaving the Na/N₂ IHX at 530 °C is expanded in the turbine to produce mechanical power. The power produced by the turbine is used to drive the electrical generator, the LPC and the HPC connected to the same shaft. The shaft rotates at the grid synchronous speed of 3000 rpm since the generator is directly connected to the grid. Part of the residual heat energy in the low-pressure nitrogen exiting the turbine is recovered in the recuperator. The nitrogen gas then enters the precooler where the remaining heat energy is rejected to the surrounding through the cooling water. The cooled nitrogen at 27 °C is compressed in the LPC, cooled again in the intercooler to 27 °C and compressed to the maximum cycle pressure of 180 bar by the HPC. It then enters the high-pressure side of the recuperator where it is preheated with the heat energy recovered from the fluid leaving the turbine. After recuperation, the fluid passes through the secondary side of the Na/N₂ IHX. At the outlet of the Na/N₂ IHX the nitrogen gas achieves the highest temperature within the cycle after absorbing heat from liquid sodium flowing through the primary side. The hot nitrogen gas is then routed to the turbine to repeat the thermodynamic cycle.

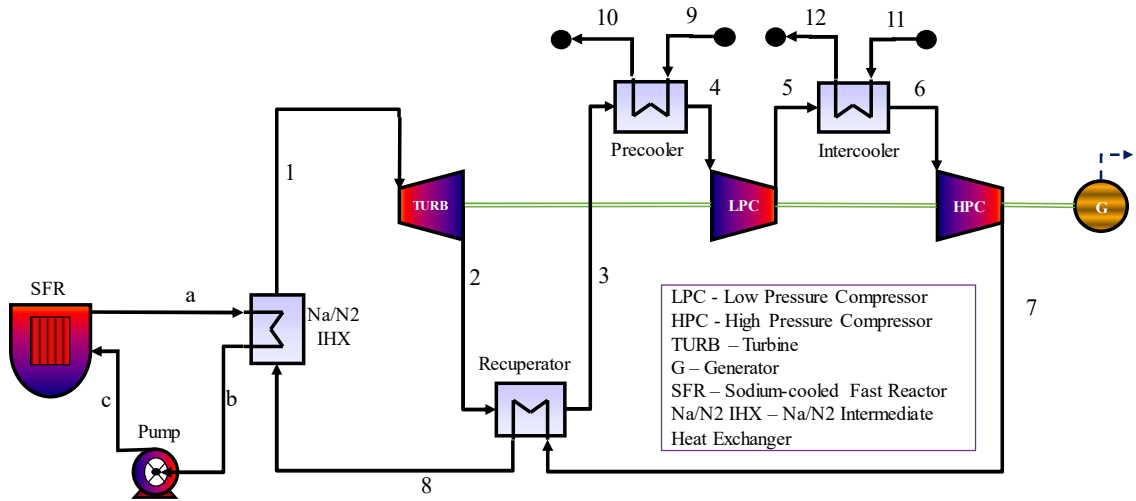


Figure 4-1 Reference single-shaft intercooled CBC (Alpy et al., 2011)

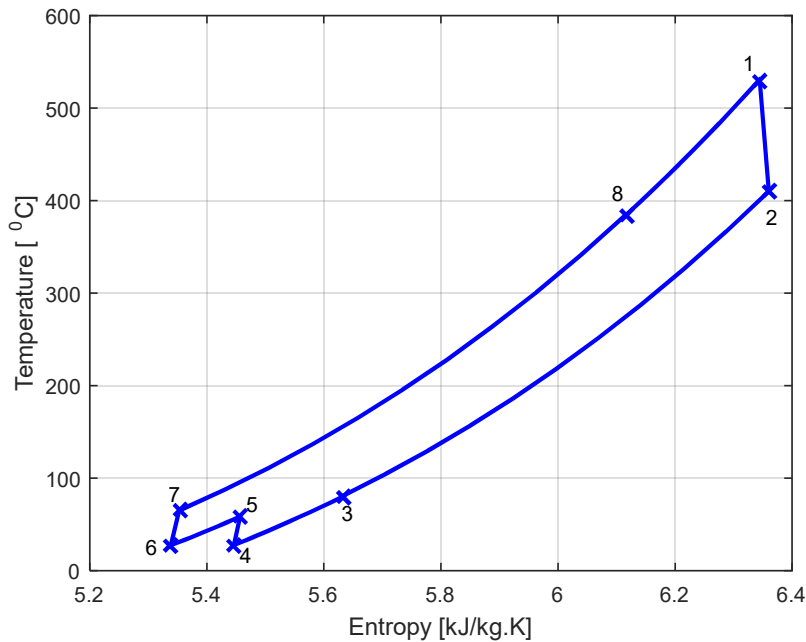


Figure 4-2 Temperature-Entropy diagram for intercooled CBC

4.2.2 Two-shaft intercooled CBC with parallel turbines

The schematic diagram of the proposed alternative two-shaft configuration is shown in Figure 4-3. It is similar to the reference case except that (a) it uses two parallel turbines referred to as CDT and FPT, and (b) it employs two independent rotating shafts referred to as compressor shaft and generator shaft. The CDT drives the LPC and the HPC through the compressor shaft while the FPT drives the electrical generator through the generator shaft. The main nitrogen flow exiting the Na/N₂ IHX is split into two streams at the turbines inlet. The first stream is expanded in the

CDT rotating at speed higher than 3000 rpm. The flow through this turbine is just enough to drive the LPC and the HPC. The second stream flow through the FPT rotating at 3000 rpm to match the grid frequency and generate electric power.

A significant feature of the two-shaft parallel turbines configuration is that the compressor shaft speed can be selected to minimise the technical design challenges of the turbomachines as their design could be optimised for non-grid rotational speed. Also, the use of two parallel turbines instead of series arrangement helps to maintain the thermal efficiency of the PCS (Lee et al., 2013), as well as reduce the volumetric flow through the turbines.

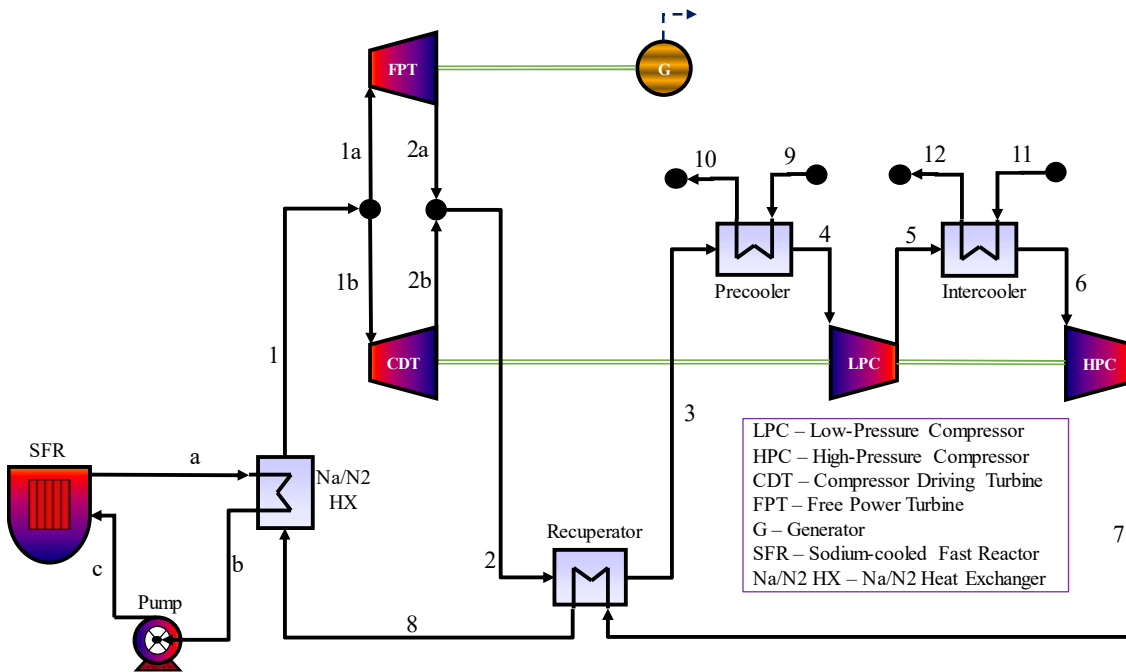


Figure 4-3 Proposed two-shaft CBC with turbines in parallel

4.2.3 Assumptions and settings

Some boundary conditions and parameters have to be set in order to evaluate the thermodynamic performance of the cycles. In this study, the selection of the boundary conditions and parameters were done within the limits allowed by the state-of-the-art in component technologies (e.g. turbine and compressor) and values obtained in the open literature (Pérez-Pichel et al., 2012; Ahn and Lee, 2014; Alpy et al., 2011; Floyd et al., 2013).

Therefore, the following assumptions and settings were used for the thermodynamic performance calculation:

- Steady state full power rating conditions were assumed
- Negligible heat losses to the surrounding except through the cooling water in precooler and intercooler

- The heat source was assumed to be a SM-SFR with a constant reactor thermal input of 500 MW
- A reactor core outlet temperature of 545 °C and pressure of 1.15 bar were selected while IHX Na side outlet temperature was set to 395 °C
- Since pipe design is outside the scope of this study, the pressure losses along the pipes were set to zero
- Pressure loss through the reactor core was set at 3.74 bar
- Turbomachinery were assumed to be adiabatic with isentropic efficiencies of 93%, 89%, 88% and 82% for the turbines, LP compressors, HP compressors and pump respectively. These are based on values that have been reported in the literature.
- LPC and HPC inlet temperatures were set at 27 °C
- Heat exchangers were designed as PCHE type
- Heat exchanger models were based on the TTD (or pinch) approach. Specifying heat exchanger performance in term of minimum TTD or pinch, instead of effectiveness, is considered to be a more realistic measure of what is achievable (Bryant et al., 2011)
- TIT was set to 530 °C. This has been selected higher than the values reported in most literature since this study eliminates the use of intermediate sodium loop
- Recuperator minimum TTD was set to 15 °C
- Precooler and intercooler cooling water inlet temperatures were assumed available at 20 °C. Hence the precooler and intercooler TTD was about 7 °C
- Generator efficiency was taken to be 98.7%
- Maximum cycle pressure at HPC outlet was set at 180 bar
- The compressors inlet pressures were defined by the optimum pressure ratios, which were determined by optimisation to the cycle efficiency

These assumed baseline conditions and parameters only represent a realistic starting point for cycle performance calculation and comparison. Hence, for sensitivity analysis, some of these values could be varied to examine their effects on the cycle performance and component design.

4.3 Results of thermodynamic performance evaluation

Results of the thermodynamic analysis at the baseline boundary conditions and cycle parameters for each of the two cycle configurations studied is presented in this section. The Matlab® cycle analysis code was used to build a thermodynamic model of the CBCs coupled to SFR with the equations listed in Chapter 3. The input variables include reactor thermal power, reactor outlet temperature and pressure, Na/N₂ IHX primary side outlet temperature, TIT, HPC outlet pressure, LPC inlet pressure, LPC and HPC inlet temperature and cooling water temperature. Typical design parameters such as minimum TTD, heat exchanger and reactor pressure losses,

turbomachinery isentropic efficiencies and generator efficiency were used. The input variables and cycle parameters were selected to be the same values for both the single-shaft configuration and the two-shaft alternative. This will ensure a reasonable comparison between the two cycles.

As much as possible, heat balance calculation should aim at achieving the maximum cycle efficiency. Only the compressors' pressure ratios are left as variables for optimising the cycle efficiency. Therefore, optimum pressure ratios of the LPC and HPC, which make each cycle to reach the maximum thermal efficiencies, were determined under the constraints of the specified input variables and cycle parameters. In Figure 4-4, the cycle efficiency as a function of the LPC inlet pressure and the LPC outlet is plotted. The cycle efficiency shows a maximum value at a LPC inlet pressure of 92.11 bar and a LPC outlet pressure of 125.19 bar (i.e. LPC pressure ratio of 1.36 and HPC pressure of 1.44 after taking into consideration the intercooler pressure loss). The optimum pressure ratios are the same for the two configurations. The Matlab[®] code provides the mass flow rate, pressure, temperature and enthalpy of the working fluid at the inlet and outlet of all the cycle components. Also, the heat transferred and power produced or absorbed in each component were calculated. Then the cycles' thermal efficiencies were calculated.

Remarkably, the proposed two-shaft configuration is able to maintain the thermodynamic performance of the nitrogen cycle in addition to the potential for turbomachinery design optimisation with the free compressor shaft speed. It should be noted that previous studies indicated that two-shaft configuration with series turbines usually leads to a deterioration of thermodynamic performance compared to single-shaft configuration due to pressure loss in the connecting duct between the HP turbine and the LP turbine (Lee et al., 2013). Figure 4-5 shows the thermodynamic state points of the reference single-shaft intercooled configuration for the selected optimum conditions while Figure 4-6 shows those calculated for the proposed two-shaft alternatives. Table 4-1 presents the major output variables of the thermodynamic performance analysis. The thermodynamic performance results indicated that the two configuration are similar in every respect except that the two-shaft configuration employed two parallel turbines with the total flow divided between them.

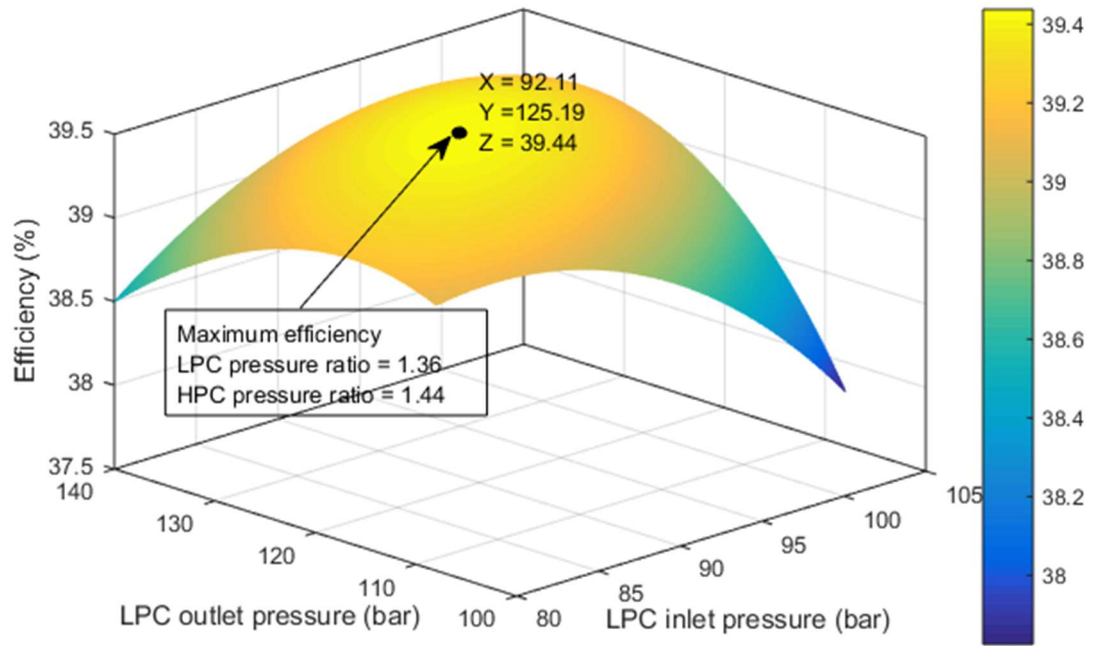


Figure 4-4 Cycle efficiency as a function of LPC inlet pressure and LPC outlet pressure for both configurations

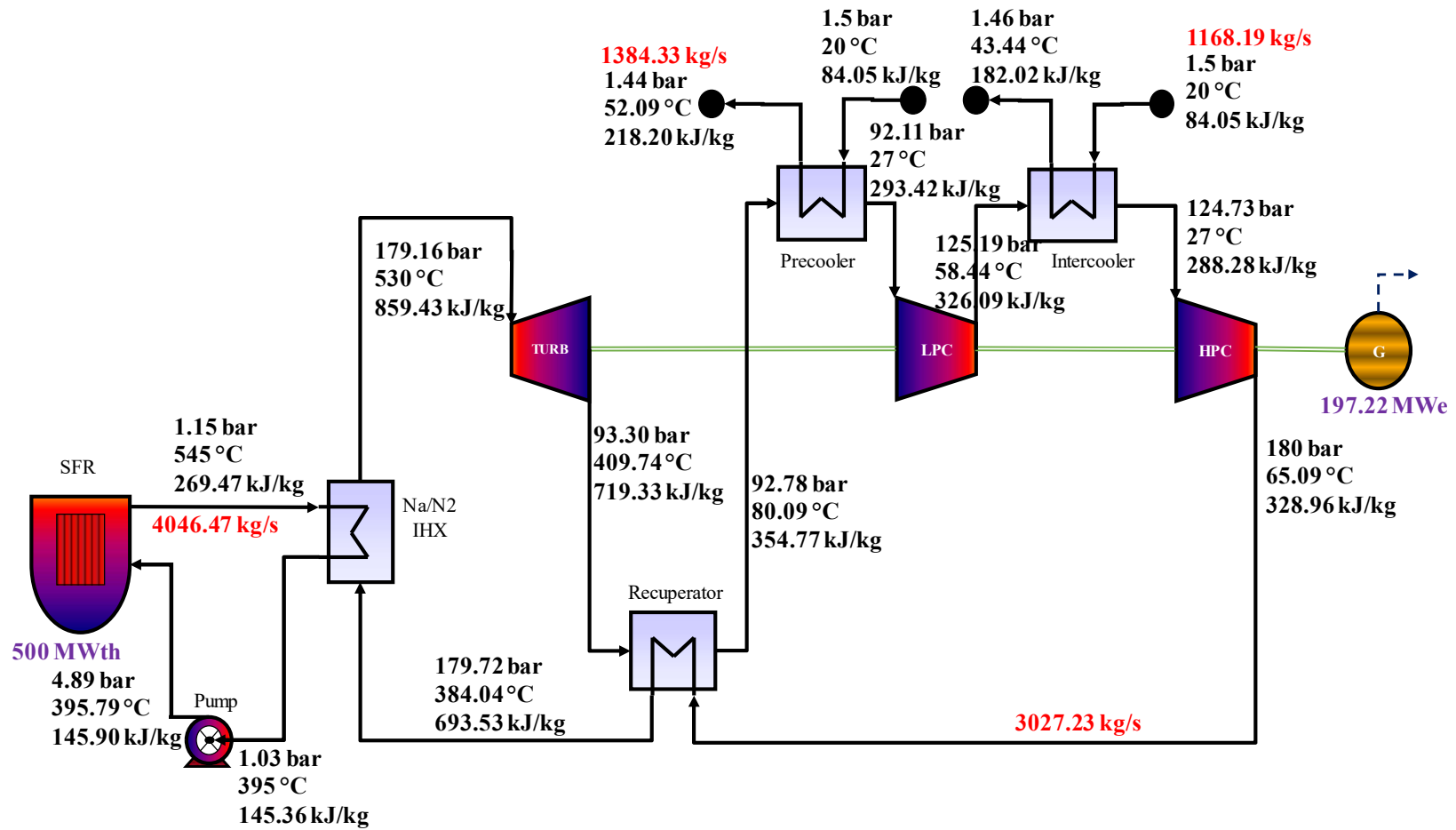


Figure 4-5 Thermodynamic state points of the single-shaft configuration

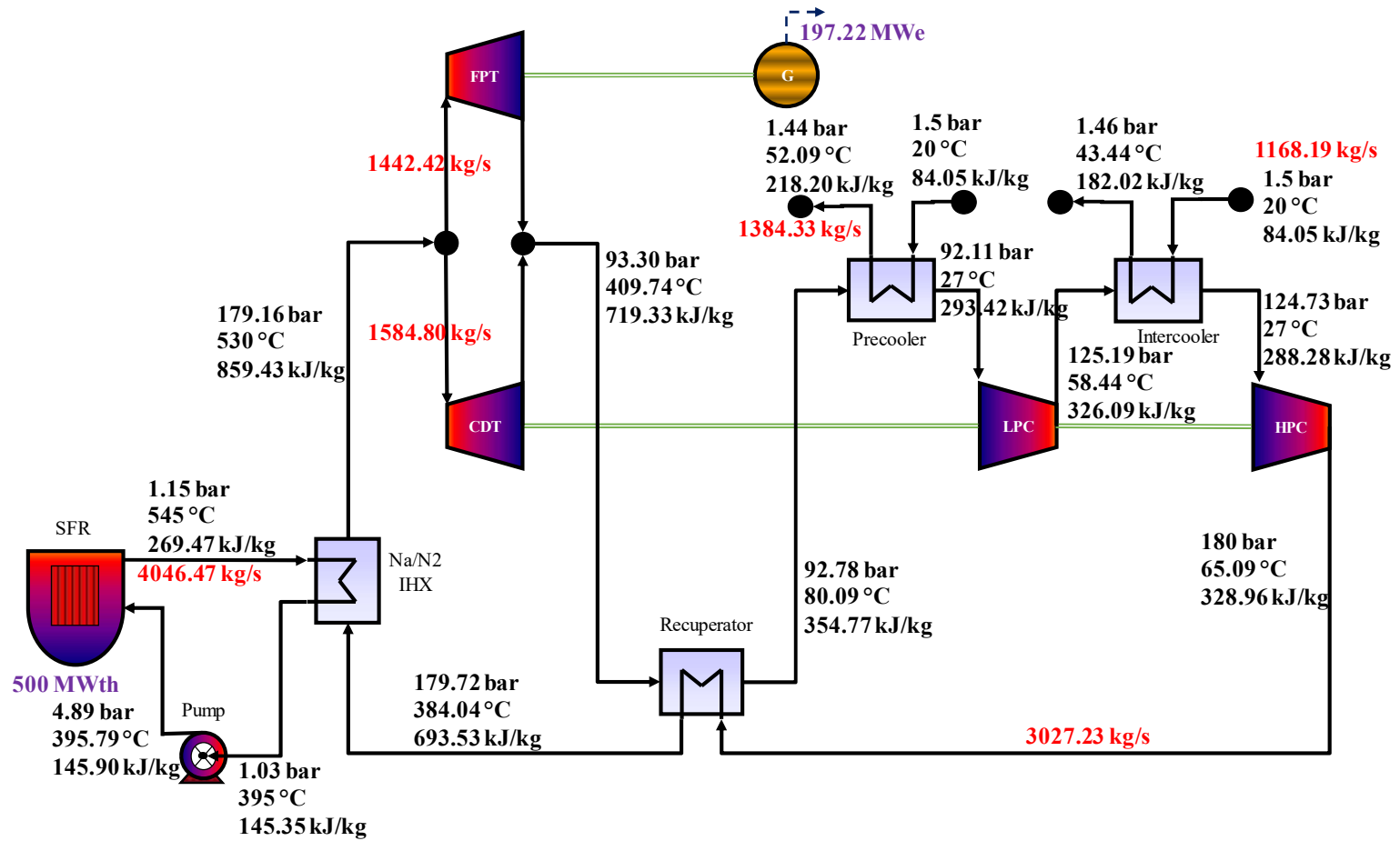


Figure 4-6 Thermodynamic state points of the two-shaft configuration

Table 4-1 Steady state thermodynamic performance result

Description	Single shaft	Two shaft
Mass flow rates		
Reactor coolant mass flow rate	4046.47 kg/s	4046.47 kg/s
FPT	-	1442.42 kg/s
CDT	-	1584.80 kg/s
Total cycle mass flow	3027.23 kg/s	3027.23 kg/s
Precooler cooling water	1384.33 kg/s	1384.33 kg/s
Intercooler cooling water	1168.19 kg/s	1168.19 kg/s
Heat exchanger duty		
Na/N ₂ IHX	502.22 MW	502.22 MW
Recuperator	1103.63 MW	1103.63 MW
Precooler	185.70 MW	185.70 MW
Intercooler	114.45 MW	114.45 MW
Heat exchanger effectiveness		
Na/N ₂ IHX	94.28 %	94.28 %
Recuperator	95.51 %	95.51 %
Precooler	88.06 %	88.06 %
Intercooler	81.41 %	81.41 %
Turbine power		
CDT	-	222.02 MW
FPT	-	202.07 MW
Total turbine power	424.09 MW	424.09 MW
Compressor power		
LPC	98.88 MW	98.88 MW
HPC	123.14 MW	123.14 MW
Total compressor power	222.02 MW	222.02 MW
Pump load (MW)	2.22 MW	2.22 MW
Pressure ratio (-)		
LPC	1.36	1.36
HPC	1.44	1.44
Turbines	1.92	1.92
Net electrical output	197.22 MWe	197.22 MWe
Cycle efficiency	39.44 %	39.44 %

4.4 Results of heat exchanger design

Heat exchangers of the nitrogen cycle include the Na/N₂ IHX, recuperator, precooler and intercooler. Input design conditions used for the preliminary sizing such as the inlet and outlet flow conditions, effectiveness and heat exchanger duties were obtained from the result of thermodynamic performance analysis given in Figure 4-5 or Figure 4-6, and Table 4-1. Since these values were the same for the single-shaft and the two-shaft configurations, the heat exchangers design will also be similar. The heat exchangers were discretised into ten thermal nodes. The results of the preliminary design calculations for the heat exchangers are given in Table 4-2. The temperature profiles of the heat exchangers' hot and cold streams at the inlet and outlet of the thermal nodes are shown in Figure 4-7.

The volume of the recuperator alone constitutes about 68% of the total volume of the heat exchangers, notwithstanding that the compactness of the recuperator has been improved by using smaller channel diameters, pitch and plate thickness. Any effort to reduce plant size and hence cost should therefore consider the selection and design of the recuperator. The relative large volume of the recuperator is due to the large amount of recuperation and poor HTC between nitrogen gas on both sides of the recuperator compared with sodium to nitrogen in the IHX or nitrogen to water in the precooler and intercooler. Also, in this study, conservative design approach was adopted with respect to the channel type, heat conduction length and heat transfer correlation. Thus generally, the sizes of the heat exchangers are likely to be reduced further with a different selection of channel type and a more aggressive design assumption.

The 15 °C baseline minimum TTD chosen for the recuperator seems to be a good compromise between the effect of TTD on recuperator volume and overall cycle efficiency. This is because a slight increase in cycle efficiency by reducing the TTD below 15 °C comes at the cost of very large increase in recuperator volume. The effects of changes in the TTD (or effectiveness) of the recuperator on the overall cycle efficiency and volume of the recuperator are shown in Figure 4-8. It can be seen that lower TTD causes higher cycle efficiency. A reduction of the recuperator TTD from the baseline value of 15 °C to 5 °C results in a cycle efficiency increase of about 3.3% point. However, the TTD has a significant effect on the volume and hence cost of the recuperator. Decreasing the TTD has a non-linear effect on the recuperator size. The same reduction of TTD from 15 °C to 5 °C results in a recuperator volume increase of about 986% above the baseline value. On the other hand, an increase in TTD from 15 °C to 25 °C results in about 62% point reduction in recuperator size.

Table 4-2 Design parameters of the heat exchangers

Description	IHX	Recuperator	Precooler	Intercooler
Heat transfer duty (MW)	502.22	1103.63	185.70	114.45
Fluid, hot side/cold side	Na/N ₂	N ₂ /N ₂	N ₂ /Water	N ₂ /Water
Channel diameter (mm)	2	1.5	2	2
Channel pitch (mm)	2.4	1.9	2.4	2.4
Plate thickness (mm)	1.5	1	1.5	1.5
Number of modules	29	63	23	23
Module width (mm)	900	900	900	900
Module height (mm)	883.56	894.04	885.42	885.05
Module length (mm)	959	2341.9	967.3	878.4
Free flow area (m ²)	5.03	11.79	4	4
Surface area density (m ² /m ³)	714.11	1014.8	714.11	714.11
Thermal density (MW/m ³)	22.70	9.30	10.47	7.11
Hot side pressure loss (kPa)	12	52	67	46
Cold side pressure loss (kPa)	56	28	6	4
Total core volume (m ³)	22.12	118.72	17.73	16.09
Total core mass (kg)	99736	508080	79954	72574

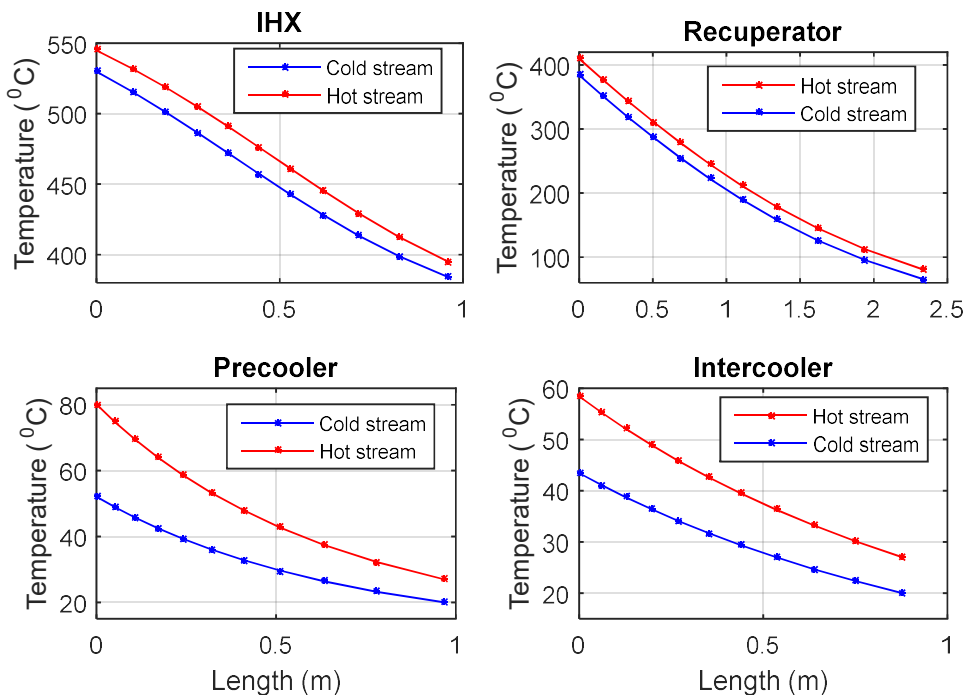


Figure 4-7 Fluid temperature profiles along the heat exchangers length (all counter-current flow)

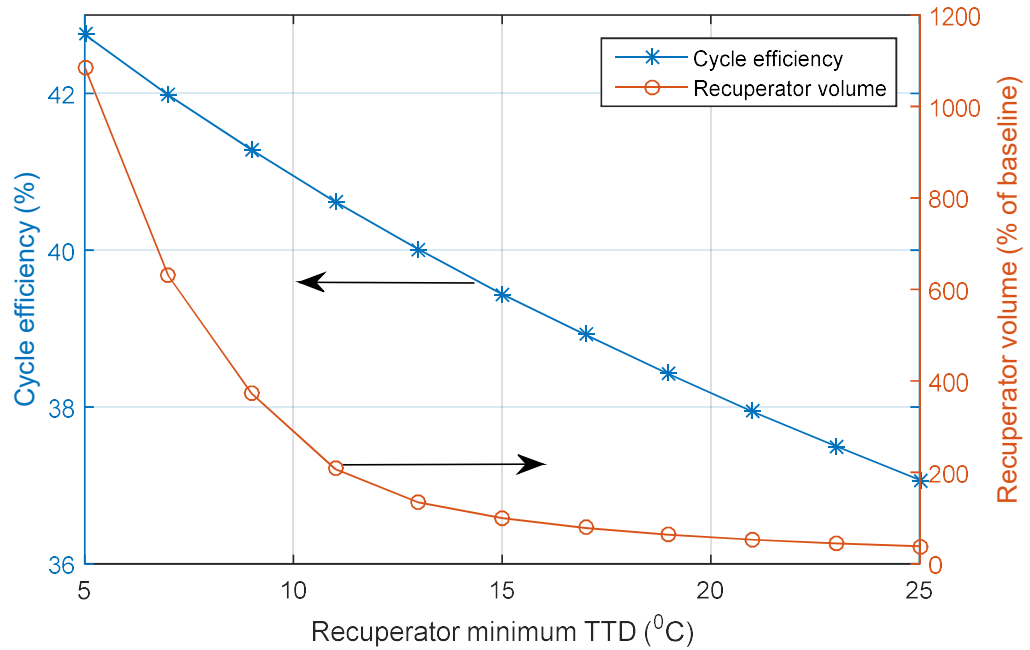


Figure 4-8 Effects of recuperator TTD on overall cycle efficiency and recuperator volume

4.5 Results of turbomachinery design

In this section, the result of the preliminary design and sizing of the turbomachinery based on 2-D meanline design is presented. The result gives the stage numbers and the annular gas flow path geometry of the turbomachinery for the specified input design condition. This provides the basis for assessing the turbomachinery's contribution to the physical size of the plant as well as comparison between the single shaft and the proposed two-shaft configuration. Table 4-3, Table 4-4 and Table 4-5 summarise and compare the respective design parameters for the turbines, the LPCs and the HPCs. These tables provide the number of stages, dimensionless design parameters, blade lengths, maximum diameters and other main features for all the turbomachinery.

The approach taken in this work was to design for approximately the same dimensionless parameters of flow coefficient, loading coefficient and reaction for the turbomachinery of the single shaft and two-shaft configuration while maintaining the hub-to-tip ratio within acceptable limit. The target flow coefficient, stage loading coefficient and stage reaction for the turbines are about 0.6, 1.1 and 0.5 respectively while the respective values for the compressors are about 0.5, 0.3 and 0.55. The turbine dimensionless parameters were selected to be consistent with operation in the 93% efficiency and 60° nozzle outlet angle region of the ϕ - ψ turbine plot. The ϕ - ψ plot was obtained from Saravanamuttoo et al. (2009). In the case of compressor, no such plot was found. Hence, design data from literature was used as a guide in selecting the compressors' dimensionless parameters (Wang and Gu, 2005). Low hub-to-tip ratio will increase secondary losses while too high hub-to-tip ratio will increase the impact of tip clearance losses. Therefore,

as much as possible, the hub-to-tip ratio should be kept between 0.75 and 0.90. For the compressors, a de Haller number greater than 0.72 and a diffusion factor lower than 0.4 are sought. The detailed results of fluid properties, geometry and other parameters for the each stage of the turbomachinery are given in Appendix A.1.

The main reasons for proposing two shaft configuration was to simplify the design of turbomachinery, to reduce turbomachinery size and to provide opportunity for improving cycle efficiency by increasing the efficiency of the turbomachinery if necessary.

4.5.1 Turbomachinery design simplification

The LPC, the HPC and the CDT of the two-shaft layout can be freely designed since there is no requirement for a fixed rotational speed. A shaft speed of 8000 rpm was established as the optimum compressors/CDT rotational speed for the proposed two-shaft configuration. For the reference single-shaft configuration, the rotation speed was set to synchronise with the generator speed of 3000 rpm for a grid frequency of 50 Hz. Therefore, its turbomachinery all rotate at this speed. Also for the proposed two-shaft configuration, the rotational speed of the FPT is fixed at 3000 rpm. The fixing of the generator drive shafts at the synchronous speed will eliminate further losses from the use of gearbox to reduce shaft speed to 3000 rpm or electrical frequency converters to supply electric power at the grid frequency of 50 Hz.

The FPT was designed with one more stage numbers than the stages of the single shaft turbine in order to avoid a hub-to-tip ratio greater than the maximum limit. At a given rotational speed, the number of stages is proportional to the pressure ratio. Thus, the FPT and the single shaft turbine would normally be expected to have the same number of stages since they have the same pressure ratio and rotational speed. However, the hub-to-tip ratio and annular flow area are determined by the flow rate and axial velocity (or blade speed). The FPT's flow rate is lower than the single shaft turbine's flow rate. Therefore, FPT blade speed was reduced to keep the hub-to-tip ratio within acceptable limit while the stage number was increased to bring the loading coefficient to the target value.

4.5.2 Size reduction of the turbomachinery

As indicated in Table 4-3, design calculation indicated that the total turbine volume is reduced from 3.24 m³ in the single shaft configuration to 2.2 m³ (2.0 m³ for FPT and 0.2 m³ for CDT) in the two-shaft configuration due to the reduced tip diameters, although the total number of turbines stages is more for the two-shaft configuration. The size of turbomachinery is a function of both the stage numbers and the tip diameters. For the two shaft CDT, the rotational speed offers extra degree of freedom for design. Hence, the number of stages was reduced to one while appropriate

selection of rotational speed was used to maintain the hub-to-tip ratio within the limits. Also, the high rotational speed of the CDT and the reduced blade speed of the FPT lead to reduced tip diameters of the two-shaft configuration turbines compared to the single-shaft turbine (Table 4-3).

Table 4-4 shows the results of preliminary design of the LPCs while Table 4-5 shows the results for the HPCs. The total compressors volume is reduced from 1.16 m³ (0.59 m³ for LPC and 0.57 m³ for HPC) in the single shaft configuration to 0.2 m³ (0.08 m³ for LPC and 0.12 m³ for HPC) in the two-shaft configuration . The high rotational speed of the proposed two-shaft configuration resulted in reduced number of compressor stages and reduced tip diameters. In addition, the stage loading coefficient of the two shaft HPC is reduced further in order to keep the hub-to-tip ratio above the minimum limit.

4.5.3 Efficiency improvement

Favourable conditions exist in the proposed two-shaft Brayton cycle for improving the turbomachinery efficiencies of the compressors and the CDT. The isentropic efficiencies of the LPC, the HPC and the turbines were assumed in the cycle calculation as 89%, 88% and 93% respectively. These values were also used for the design of the turbomachinery. However, increasing the number of stages and changing the rotational speed are two methods for improving turbomachinery efficiency in a fixed cycle layout (Ahn and Lee, 2014). Therefore, the LPC, the HPC and the CDT of the two-shaft cycle can be redesigned for a higher efficiency by increasing the number of stages and/or by changing the rotational speed. Better turbomachinery efficiencies will further improve the cycle performance. The effects of isentropic efficiencies of the LPC, the HPC and the CDT on the overall cycle efficiency are shown in Figure 4-9. The two shaft Brayton cycle shows about 0.29% point rise in cycle efficiency for each 1% point rise in CDT efficiency, about 0.22% point rise in cycle efficiency for each 1% point rise in LPC efficiency, and about 0.27% point rise in cycle efficiency for each 1% rise in HPC efficiency.

Table 4-3 Turbines design parameters and main features for the nitrogen cycles

Parameters	Single shaft	Two shaft	
		CDT	FPT
Number of stages in turbine	3	1	4
Flow coefficient	0.6	0.6	0.6
Stage loading coefficient	1.08	1.08	1.13
Reaction	0.50	0.50	0.53
Rotational speed, rpm	3000	8000	3000
Maximum tip diameter, mm	1460	926	1210
Maximum tip speed, m/s	229	388	190
Blade height, mm (min/max)	85/135	41/66	56/89
Hub/Tip ratio (min/max)	0.81/0.88	0.86/0.90	0.85/0.90
Blade numbers, (1 st stage stator/rotor)	20/76	25/79	26/103
Blade chord, mm (1 st stage stator/rotor)	264/284	139/177	173/260
Axial length, mm	2007	304	1785
Volume, m ³	3.24	0.2	2.0
Aspect ratio	3	3	3
Solidity	1.25	1.25	1.25
Pressure ratio (-)	1.92	1.92	1.92
Stage efficiency, %	92.60	93	92.55

Table 4-4 LPC design parameters and main features for the nitrogen cycles

Parameters	Single shaft	Two shaft
Number of stages in LPC	3	1
Flow coefficient	0.5	0.5
Stage loading coefficient	0.29	0.29
Reaction	0.55	0.55
Rotational speed, rpm	3000	8000
Maximum tip diameter, mm	1315	880
Maximum tip speed, m/s	207	369
Blade height, mm (min/max)	67/82	63/79
Hub/Tip ratio (min/max)	0.88/0.90	0.82/0.85
Blade numbers, (1 st stage rotor/stator)	64/66	45/50
Blade chord, mm (1 st stage rotor/stator)	73/71	68/61
Axial length, mm	440	140
Volume, m ³	0.59	0.08
Aspect ratio	1.1	1.1
Solidity	1.21	1.21
Pressure ratio (-)	1.36	1.36
Stage efficiency, %	89.32	89
de Haller number	0.75	0.75
Diffusion factor	0.39	0.38

Table 4-5 HPC design parameters and main features for the nitrogen cycles

Parameters	Single shaft	Two shaft
Number of stages in HPC	4	2
Flow coefficient	0.5	0.5
Stage loading coefficient	0.29	0.25
Reaction	0.55	0.55
Rotational speed, rpm	3000	8000
Maximum tip diameter, mm	1257	760
Maximum tip speed, m/s	197	318
Blade height, mm (min/max)	65/52	62/79
Hub/Tip ratio (min/max)	0.90/0.92	0.79/0.83
Blade numbers, (1 st stage rotor/stator)	77/80	37/39
Blade chord, mm (1 st stage rotor/stator)	58/48	70/66
Axial length, mm	461	279
Volume, m ³	0.57	0.12
Aspect ratio	1.1	1.1
Solidity	1.21	1.21
Pressure ratio (-)	1.44	1.44
Stage efficiency, %	88.46	88.31
de Haller number	0.75	0.78
Diffusion factor	0.39	0.34

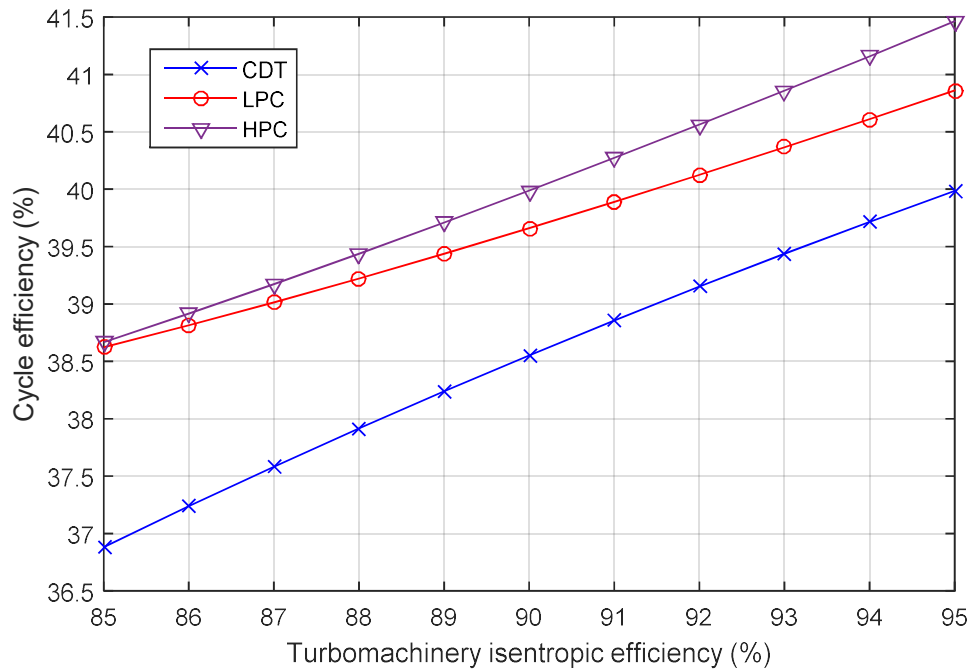


Figure 4-9 Effect of turbomachinery efficiencies on overall cycle efficiency

4.6 Summary

In this chapter, thermodynamic analysis and preliminary design of nitrogen CBCs coupled to a 500 MWth SM-SFR have been presented. A reference single-shaft configuration and a proposed two-shaft configuration with parallel turbines were investigated. Thermodynamic performance assessment of the cycles, preliminary sizing of the heat exchangers and mean-line aerodynamic design of the turbomachinery were performed using models and codes developed in Matlab[®]. Thermodynamically, the single-shaft and the two-shaft configuration are similar. The main significance feature of the two-shaft layout is that the speed of the compressors and the driving turbine can be selected independently to minimise any design challenges associated with adopting a fixed synchronous speed. The preliminary design of the heat exchangers showed that the recuperator made up about 68% of the heat exchangers volume. Therefore, any effort toward reducing the plant size should focus on the selection and design of the recuperator.

The control system design for closed-cycle GT and the dynamic performance of the two-shaft nitrogen closed-cycle GT for application to SM-SFR will be presented later in Chapter 7 and 8 respectively.

5 Thermodynamic Performance Analysis of S-CO₂ Brayton Cycle Coupled to SM-PWR and Preliminary Design of Components

5.1 Introduction

In PWR, the reactor coolant pressure is above the saturation pressure of water corresponding to the highest temperature of coolant in the reactor, so that no coolant boiling occurs in the reactor. It uses ordinary water as both coolant and moderator. A PWR power plant is composed of the primary loop, in which high pressure water flows through the core of the reactor, and the secondary or working fluid loop, which contains the PCS as shown in Figure 5-1. The coolant is heated up in the reactor and the heat is transferred to the working fluid in the steam generator. The generated steam is then used in a steam Rankine cycle to generate electricity. All current nuclear power plants operate on the steam Rankine cycle. However, s-CO₂ power cycle is being investigated as alternative PCS. In a PWR/s-CO₂ cycle nuclear plant, the steam generator is replaced with an IHX and the steam cycle with a s-CO₂ power cycle. S-CO₂ power cycle offers the benefit of smaller components size. This can be significant for SMR where modularity, size and cost is critical for commercial deployment.

This chapter evaluates the steady state thermodynamic performance and preliminary component design of s-CO₂ Brayton cycle for SM-PWR application.

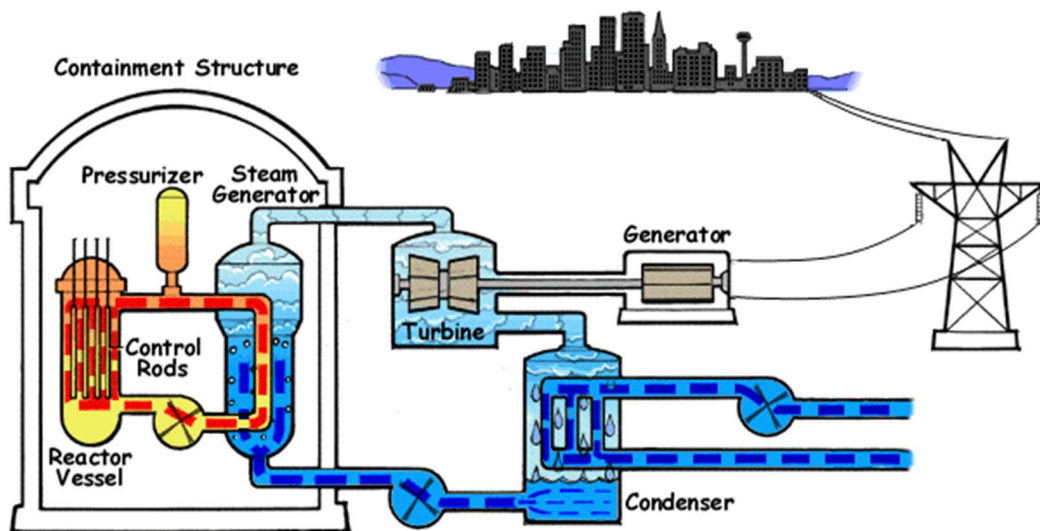


Figure 5-1 Schematic diagram of a conventional PWR nuclear power plant (NRC, 2017)

5.2 Description of the s-CO₂ Brayton cycle nuclear power plants and performance evaluation

5.2.1 Assumption and settings for PWR/s-CO₂ nuclear power plant performance evaluation

The PWR primary loop consists of the reactor, the hot side of the IHX and the coolant pump. The coolant enters the reactor, it then picks up fission heat, and leaves the reactor at about 300 °C. The average temperature rise in the reactor is about 34 °C. The reactor coolant pressure is 155 bar, which is greater than the saturation pressure at the maximum reactor temperature. In this study, the reactor is designed to produce a thermal power of 500 MW. The coolant leaving the reactor enters a Water/CO₂ IHX where it imparts its heat to the s-CO₂ working fluid and leaves the IHX to the coolant pump where it is pumped back to the reactor.

The secondary or working fluid loop consists of the s-CO₂ closed-cycle GT system for power generation. The closed-cycle GT system is made up of turbine, compressor, precooler, recuperator and the cold side of the Water/CO₂ IHX. The heated s-CO₂ working fluid leaves the IHX and enters the turbine at 275 °C. The cycle minimum pressure and temperature at precooler outlet (main compressor inlet) is set to be just above the critical pressure and temperature in order to take advantage of the reduced compression work around the critical point. Figure 5-2 shows the significant reduction in the work needed to compress the fluid at conditions around the critical point. Hence, the precooler outlet conditions is set at 75.75 bar and 32 °C. It is assumed that the cooling water is supplied at about 22 °C. The cycle maximum pressure at compressor outlet is about 200 bar. Impromptu pressure losses of 0.5% are specified for the heat exchangers for initial performance evaluation. The actual pressure losses will be determined after the preliminary design of the heat exchangers. A moderate value of 10 °C is assumed for the recuperator's minimum TTD. Pipes pressure losses are assumed to be negligible.

Table 5-1 summarises the assumptions for component parameters and cycle boundary conditions. These values are typical design values that have been reported in the open literature and documents obtained from industrial partner (Santini et al., 2016; Milani et al., 2017; Padilla et al., 2015; Cheang et al., 2015). The calculations are performed with Matlab® cycle calculation code described in Chapter 3. The thermodynamic and transport properties are obtained from NIST REFPROP program, which uses Span and Wagner equation of state (EOS) for CO₂ with reported uncertainties below 1.5% for pressures up to 300 bar (Lemmon et al., 2013; Span and Wagner, 1996).

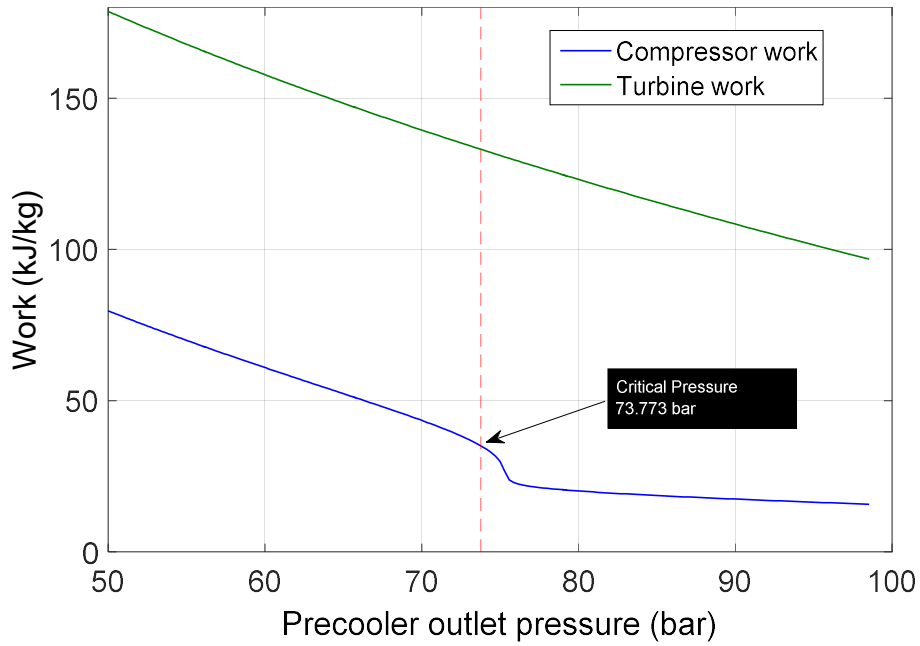


Figure 5-2 s-CO₂ cycle compressor and turbine specific work as function of precooler outlet pressure at 32 °C precooler outlet temperature

Table 5-1 Design parameters and assumed boundary conditions for the PWR/s-CO₂ cycle power plant

Parameters	Value
PWR thermal power	500 MWth
Reactor outlet pressure	155 bar
Reactor outlet temperature	300 °C
Pressure loss in the reactor core	2%
Average temperature rise in reactor	34 °C
Coolant pump efficiency	82%
TIT	275 °C
Precooler outlet pressure	75.75
Precooler outlet temperature	32 °C
Compressor outlet pressure	200 bar
Turbine isentropic efficiency	93%
Main compressor isentropic efficiency	89%
Recompression compressor isentropic efficiency	88%
Heat exchangers pressure loss	0.5%
Precooler and recuperator min TTD	10 °C
Generator efficiency	98.7%

5.2.2 Simple recuperated s-CO₂ Brayton cycle for SM-PWR plant

A unique feature of CO₂ as working fluid is that its critical pressure (7.3773 MPa) and temperature (30.978 °C) are easily achievable. The reduced compression work in the critical region thus enables the achievement of high thermal efficiency. The baseline CBC is the simple recuperated cycle. The flowsheet, state point's values (pressure, temperature and enthalpy) and the results of performance calculation of a simple recuperated s-CO₂ Brayton cycle coupled to SM-PWR are shown in Figure 5-3. The simple Brayton cycle consists of five main components: turbine (1-2), recuperator (2-3 & 5-6), precooler (3-4), compressor (4-5) and IHX (6-1).

The temperature-entropy (T-S) diagram in Figure 5-4 shows the cycle's operation. The s-CO₂ leaving the IHX at pressure of 198.01 bar and temperature of 275 °C is expanded in the turbine to 76.51 bar to produce mechanical power. The turbine power is then used to drive the compressor and the generator. The temperature of the working fluid at the exits of the turbine is about 181.22 °C. This is used in the recuperator to preheat the s-CO₂ coming out of the compressor such that the temperature drops to 77.28 °C at the recuperator exit. Then the remaining heat energy is rejected from the cycle in the precooler where the CO₂ is cooled to 32 °C. After that, the cooled CO₂ is compressed to the maximum cycle pressure of 200 bar. The high-pressure CO₂ leaving the compressor at about 67.28 °C then enters the recuperator where it is preheated with the turbine exhaust to about 120.66 °C. The CO₂ is then returned to the IHX to be heated again to 275 °C by the reactor coolant.

The cycle thermal efficiency of the simple recuperated Brayton cycle is 23.6%. The effectiveness of the recuperator, precooler and IHX are 89.22%, 72.11% and 87.81% respectively. Though the rapidly varying fluid properties around the critical point is a feature that facilitates the reduced compression work of s-CO₂ cycle but it also prevents effective heat transfer in the recuperator. This is because specific heat capacity is strongly dependent on pressure and temperature in the critical region leading to mismatch of heat capacity between the high-pressure CO₂ in the cold side and the low-pressure CO₂ in the hot side of the recuperator. Hence, while the hot side temperature drops by about 104 °C, the cold temperature only rise by about 53 °C. Any attempt to increase the temperature rise in cold side can lead to violation of the minimum TTD specification and temperature cross over in the recuperator (the so-called "pinch point problem"). Consequently, the cold stream cannot be preheated high enough to achieve good recuperator effectiveness. Even with the conventional methods of enhancing thermal efficiency such as reheating and intercooling, it is difficult to achieve high efficiency in simple recuperated s-CO₂ cycle because of the low effectiveness of the recuperator (Muto and Kato, 2008). Some amount of effectiveness and efficiency improvement can be achieved by reducing the minimum TTD specification. However, weight and volume of recuperator will increase.

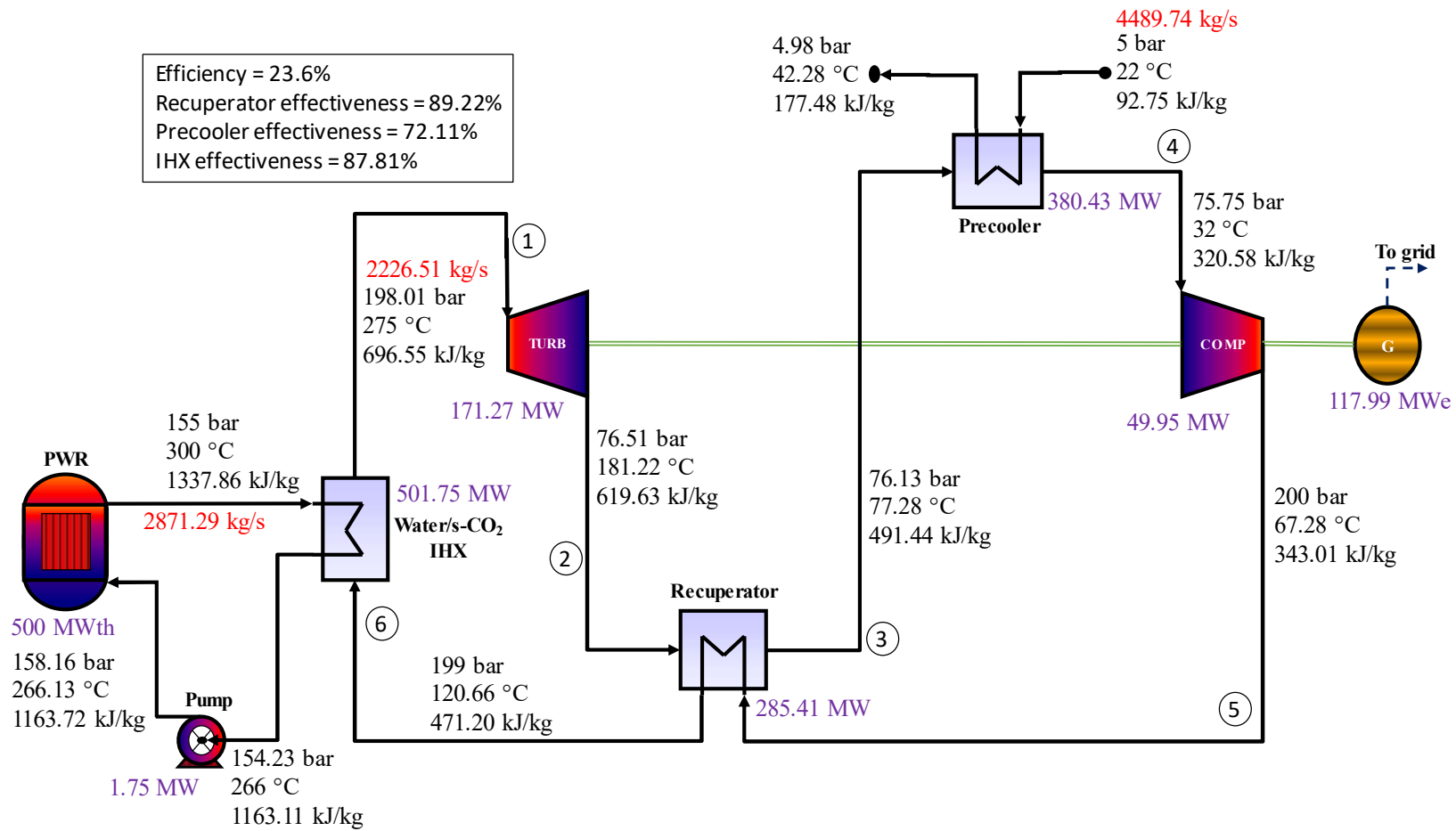


Figure 5-3 Flowsheet, state point values and performance results of simple recuperated s-CO₂ Brayton cycle coupled to PWR

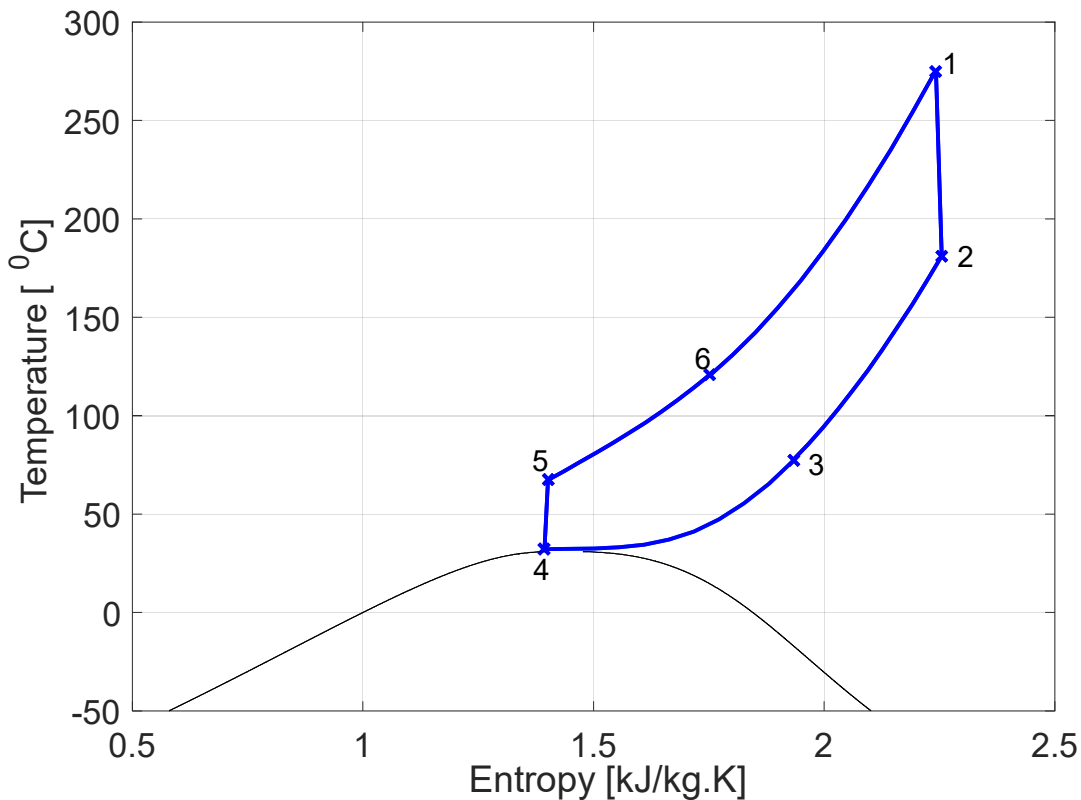


Figure 5-4 Temperature-Entropy (T-S) diagram of simple recuperated s-CO₂ Brayton cycle

5.2.3 Recompression s-CO₂ Brayton cycle for SM-PWR plant

Other layouts to minimise the effect of heat capacity mismatch have been suggested in the literature (Feher, 1967; Dostal, 2004; Angelino, 1968; Kim et al., 2016; Ahn et al., 2015; Moisseytsev and Siemicki, 2009b). Generally, the recompression cycle is considered the most promising layout with the highest thermal efficiency and a relatively simpler configuration than most of the other layouts. In the recompression cycle, the recuperator is divided into two: the HTR and the LTR. The flowsheet, state point values and performance calculation results of recompression s-CO₂ Brayton cycle coupled to SM-PWR are shown in Figure 5-5. The T-S diagram given in Figure 5-6 represents the cycle's operation. The cycle consists of seven major components: turbine (1-2), HTR (2-3 & 9-10), LTR (3-4 & 6-7), precooler (4-5), main compressor, MC (5-6), recompression compressor, RC (4-8) and IHX (10-1).

The problem of heat capacity mismatch is resolved by splitting the flow into two streams at point 4 (Figure 5-5). The main stream is cooled in the precooler to the MC inlet temperature (32 °C). The MC compressed the fluid to maximum cycle pressure of 200 bar and the fluid is then preheated in the LTR. The second stream at point 4 is compressed directly in the RC. It is then mixed with the main stream at the exit of the LTR cold side before entering the cold side of the HTR. The fraction of the flow at point 4 passing through the RC, referred to as recompression

fraction, can be adjusted to make the heat capacity (i.e. the product of mass flow rates and specific heat capacity) of CO₂ on the high-pressure side of the LTR the same as that of the low-pressure side CO₂. Hence, with an optimal selection of recompression fraction, high recuperator effectiveness and consequently high thermal efficiency can be achieved. The optimum recompression fraction is 0.4. The high-pressure CO₂ is now preheated in the recuperators to about 171 °C at the IHX inlet. This is higher than the 121 °C achieved with the simple cycle. Hence, the thermal efficiency of the recompression cycle is about 3% point higher than that of the simple recuperated cycle.

In the medium to high TIT range, the recompression cycle is known to give good thermal efficiency with very effective recuperation in the HTR and LTR. However, for PWR with relatively low TIT, the turbine exhaust temperature is too low to permit any significant recuperation in the HTR. The recuperation takes place mainly in the LTR with more than 97% share of the recuperated heat. The LTR effectiveness is about 93.42% while the HTR effectiveness is about 22%. The cold stream is preheated only by 2 °C (from 169 °C to 171 °C) in the HTR. Therefore, in this study, a new layout in which the HTR is eliminated leaving only the LTR is suggested. It is referred to as single recuperator recompression cycle layout.

5.2.4 Single recuperator recompression s-CO₂ Brayton cycle for SM-PWR plant

The new concept, the single recuperator recompression cycle, is similar to the recompression cycle except that only one recuperator is used. The flowsheet, state point values and performance result of the cycle coupled to SM-PWR are shown in Figure 5-7. The T-S diagram shown in Figure 5-8 represents the cycle's operation. The flow is split into two streams at point 3, just like the recompression cycle. This provides the advantage associated with splitting the flow, that is, a balance of the heat capacity between the cold stream and the hot stream of the recuperator. The main stream is cooled in the precooler, compressed in the MC and preheated in the recuperator. The other stream is compressed in the RC. The two streams are merged together at the outlet of the recuperator. Instead of further preheating the stream in HTR, the stream is routed directly to the IHX to be heated to maximum cycle temperature at turbine inlet.

The single recuperator recompression cycle, with one less component, is simpler than the recompression cycle. The preheated cold stream temperature at the IHX inlet is only about 0.69 °C less than that of the recompression cycle. Moreover, removing the HTR also eliminates the associated pressure losses. The thermal efficiency is about 26.74, which is comparable to that of the recompression cycle for the boundary conditions specified. The cycles' performance comparison under different boundary conditions like TIT will be investigated later.

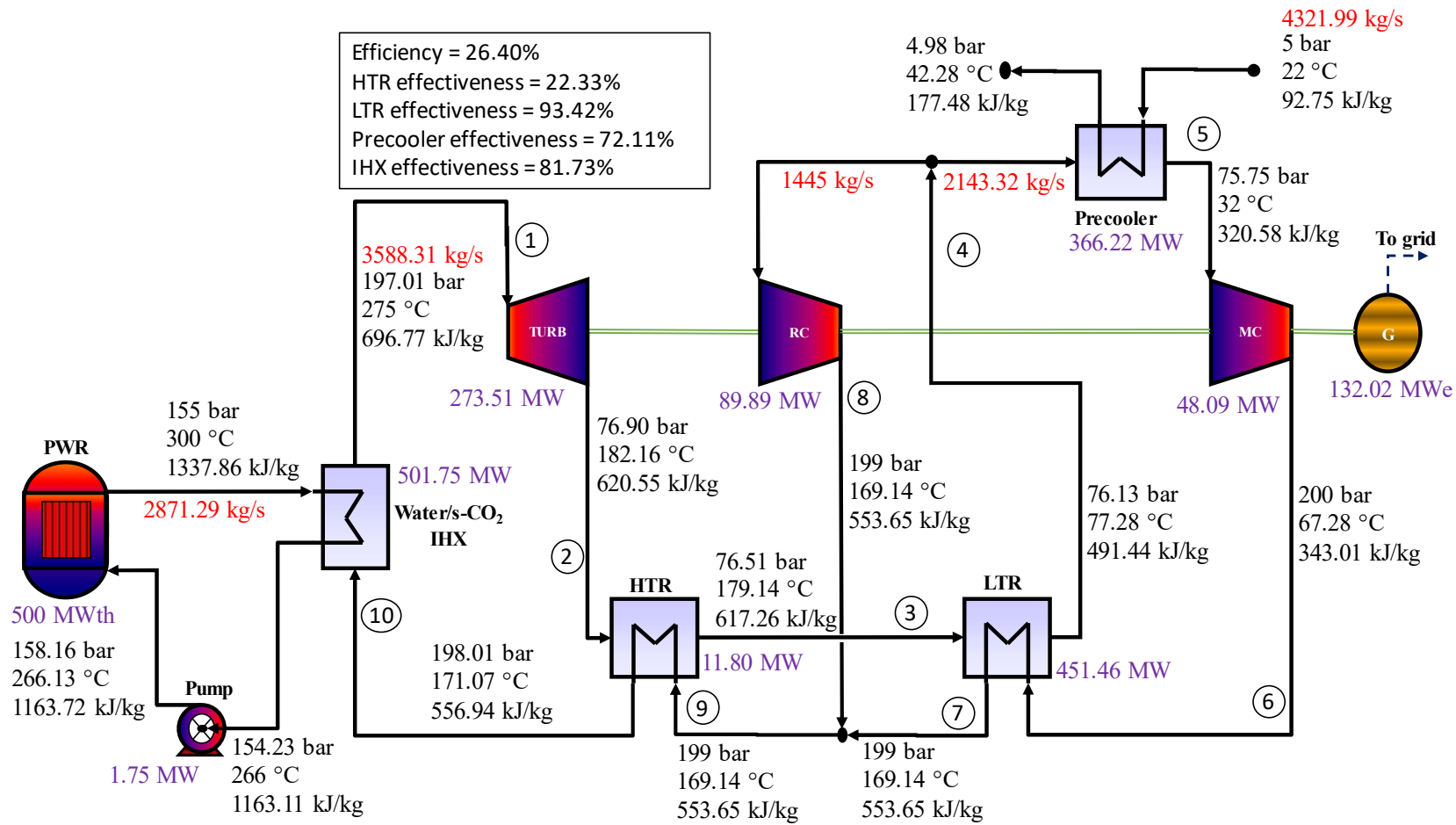


Figure 5-5 Flowsheet, state point values and performance results of recompression s-CO₂ Brayton cycle coupled to PWR

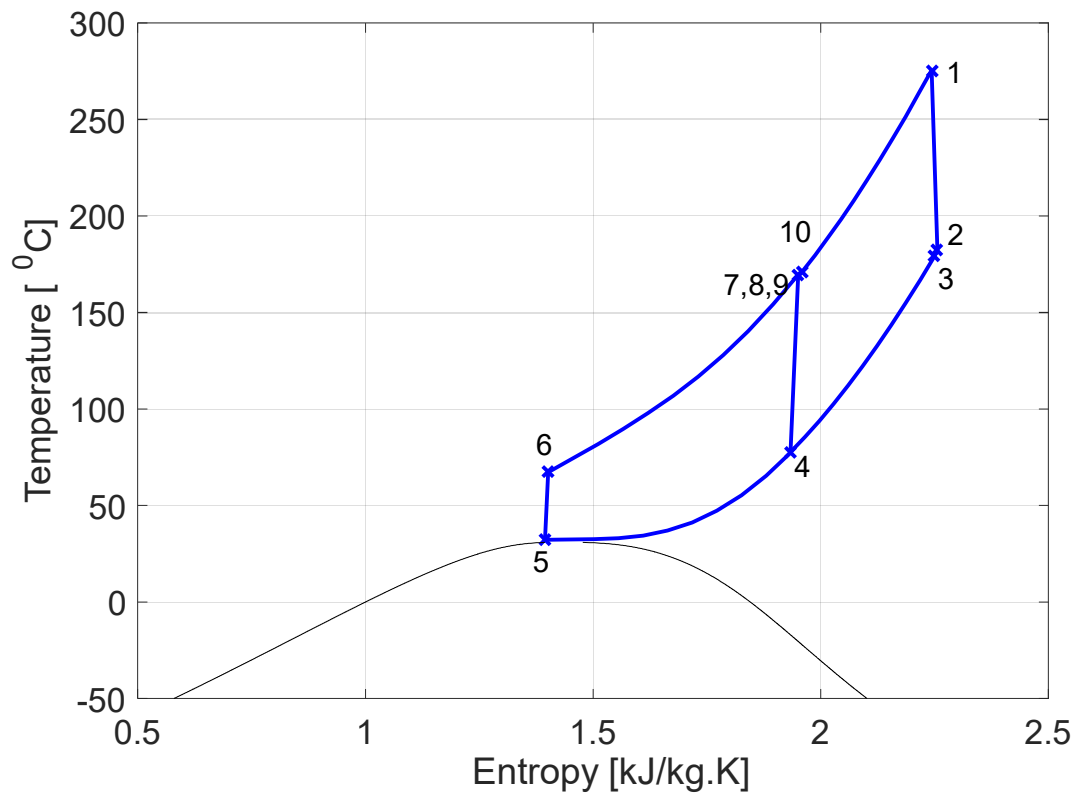


Figure 5-6 Temperature-Entropy (T-S) diagram of recompression s-CO₂ Brayton cycle

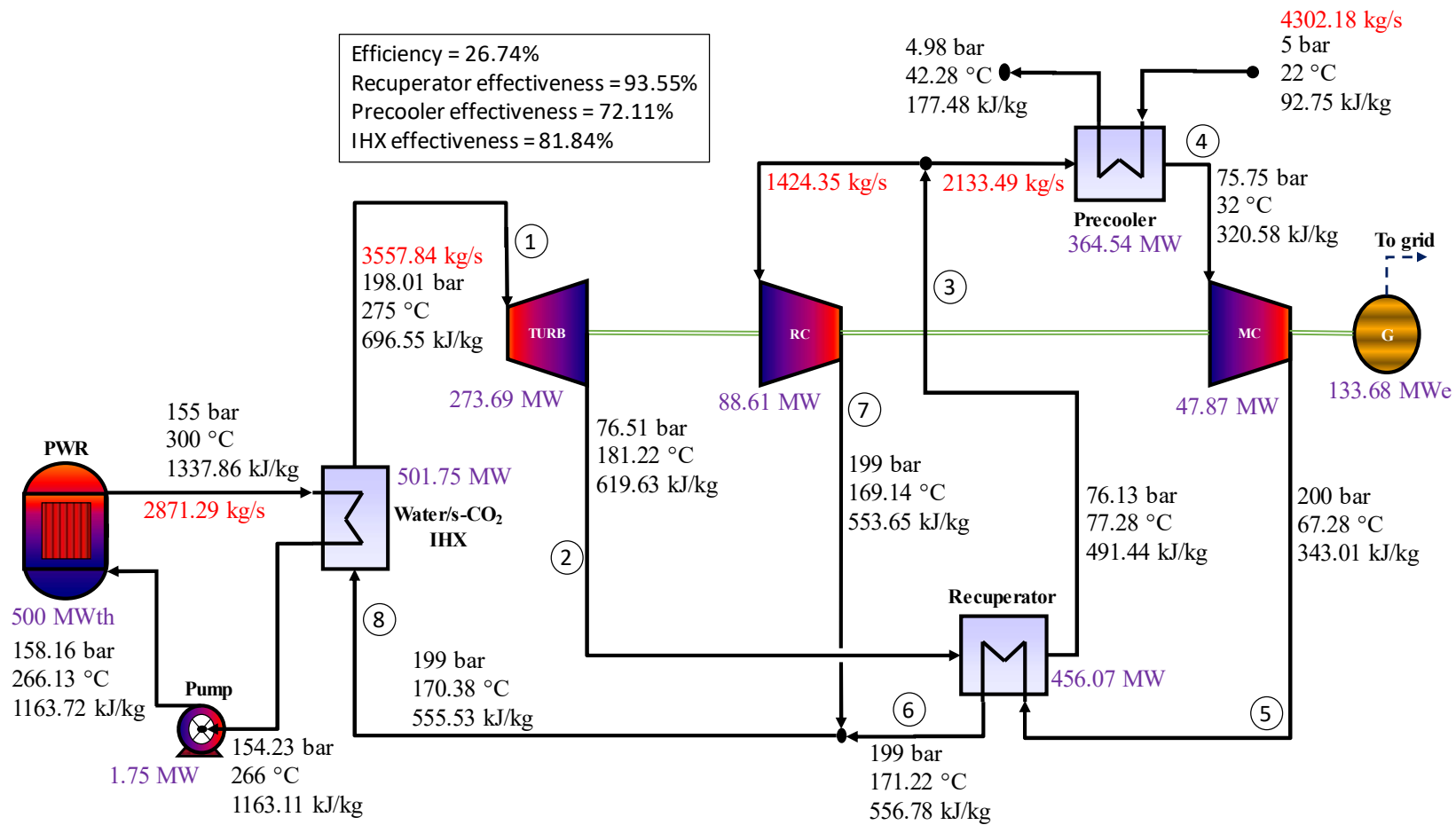


Figure 5-7 Flowsheet, state point values and performance results of single recuperator recompression s-CO₂ Brayton cycle coupled to PWR

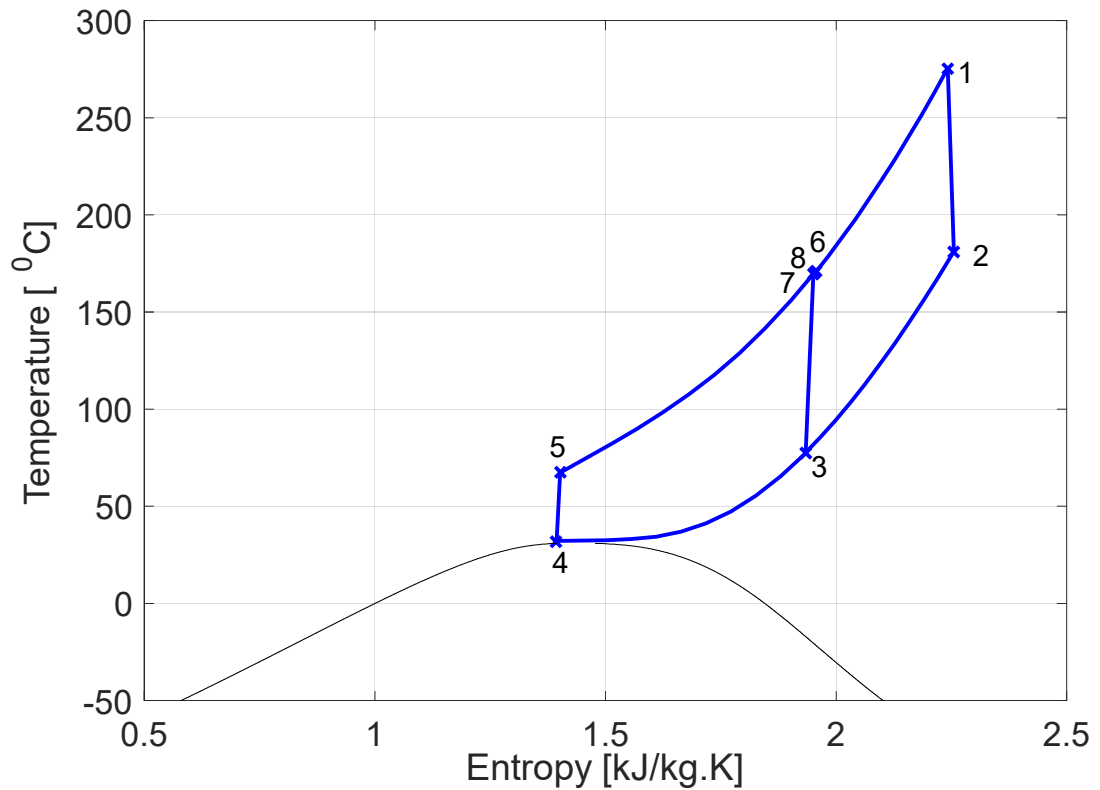


Figure 5-8 Temperature-Entropy (T-S) diagram of single recuperator recompression s-CO₂ Brayton cycle

5.3 Heat exchangers design and its impact on the performance and size of the SM-PWR/s-CO₂ power plant

In this section, the results of the heat exchangers design for the three s-CO₂ Brayton cycles are presented. The reasons for the design of the heat exchangers are:

- To determine the actual pressure losses in the heat exchangers. In the previous heat balance and performance comparison of the s-CO₂ cycles, the pressure losses were assumed as 0.5% in all heat exchangers. However, pressure losses are not expected to be the same for the heat exchangers and for the different s-CO₂ cycle layouts. The pressure drop in a heat exchanger is dependent on the flow conditions and the design choices such as the heat exchanger type and flow area (number of tubes or flow channel). Obtaining the actual pressure losses will allow a more realistic comparison of the thermodynamic performances of the different s-CO₂ cycle layouts.
- To determine the sizes or the relative footprint of the s-CO₂ cycles. Apart from thermal efficiency, the sizes of the plant are equally important in the selection of the most suitable

s-CO₂ cycle layout for the PWR application. The heat exchangers constitute most of the plant footprint because the turbomachinery of s-CO₂ cycle is very small. Therefore, an estimation of the heat exchanger volumes can be used to compare the footprint of the s-CO₂ cycle layouts. The results of the preliminary sizing of the heat exchanger could also provide a basis for economic analysis of the plant.

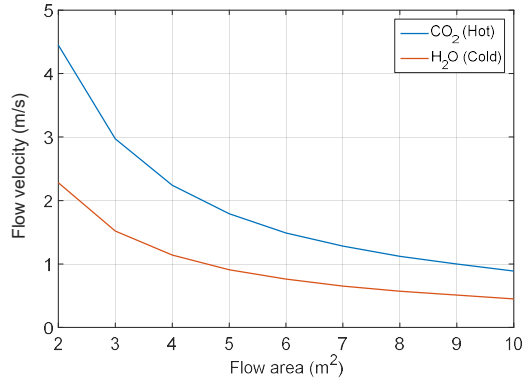
For instance, the specific power (i.e. the ratio of the generated power to the CO₂ mass flow rate) is higher for the simple cycle (about 0.2 kWh/kg) compared to the recompression cycle (about 0.1 kWh/kg). Hence, the total pressure loss and the size of the simple cycle layout is expected to be less than that of the recompression cycle layout. PCHE compact heat exchanger type with counter flow arrangement was utilised for all the heat exchangers. The PCHE geometrical specifications and the preliminary design methodology have been described in Chapter 3. The heat exchanger preliminary design and the cycle performance calculation were performed in an iterative manner with the Matlab[®] program. After an initial cycle performance calculation with the assumed pressure losses, the resulting flow conditions were then used for the preliminary design of the heat exchangers. The initial pressure losses were replaced with the losses obtained from the design and the performance calculation was repeated. The process was repeated until the flow conditions converge. The variation of HTC in the heat exchangers due to the non-linear and rapid variation of CO₂ properties, especially in the vicinity of the critical point, was captured by discretising the heat exchangers into 40 axial nodes. Each node was then evaluated based on the node LMTD and average fluid properties.

5.3.1 Results of precoolers design

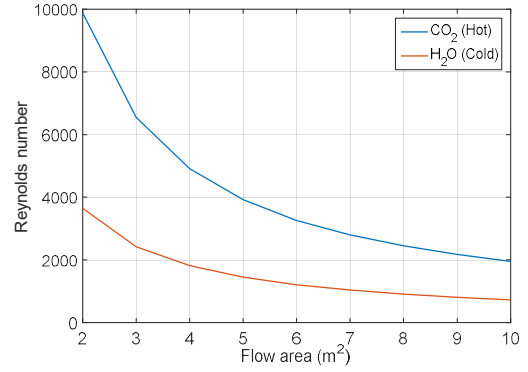
The precooler flow conditions are very similar for the three s-CO₂ cycle layouts. Hence, the results of the preliminary design of the precoolers are very much the same. The precooler cold sink is represented by cold water coming into the precooler at 22 °C. The water cools the s-CO₂ stream on the hot side of the precooler to the 32 °C temperature required at the MC inlet.

The pressure loss and size of a heat exchanger is strongly affected by the flow area (or number of channels) selected, given that the inlet/outlet temperature and mass flow rates are already determined through the cycle heat balance calculation. As such, in the design of the heat exchangers, the flow area must be chosen based on the specified pressure loss constraint. On the other hand, the resulting volume of the heat exchanger must be within acceptable limit. Figure 5-9 shows how the fluid velocity, Reynolds number, Nusselt number, HTC, pressure loss and volume of the precooler vary with the precooler flow area. This trend is similar for all heat exchanger. Larger flow area reduces the velocity of flow and consequently the Reynolds number, the Nusselt number and the HTCs are reduced. Therefore, the volume of the heat exchanger increases as the flow area increases due to the degradation of the HTCs. On the contrary, the

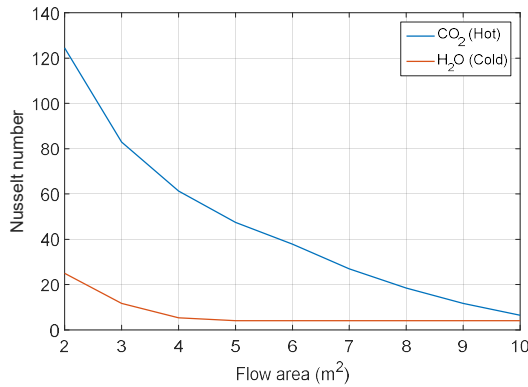
pressure loss reduces with increase flow area because pressure loss is proportional to the square of flow velocity. Therefore, the selection of the appropriate flow area for the heat exchanger design is a compromise between the pressure loss, which will strongly affect the cycle thermal performance, and the volume of the heat exchanger.



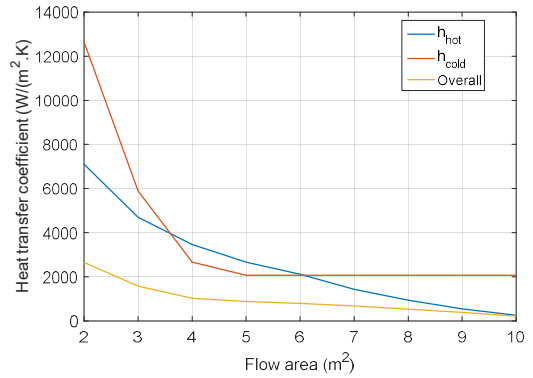
(a) Flow area versus flow velocity



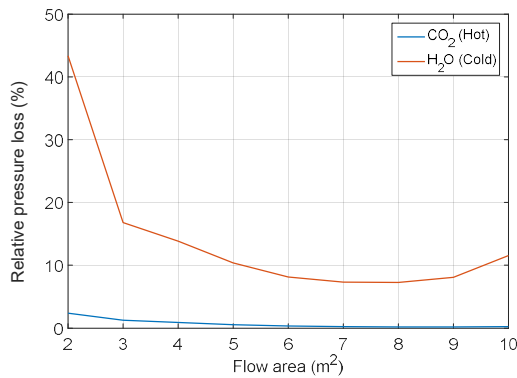
(b) Flow area versus Reynolds number



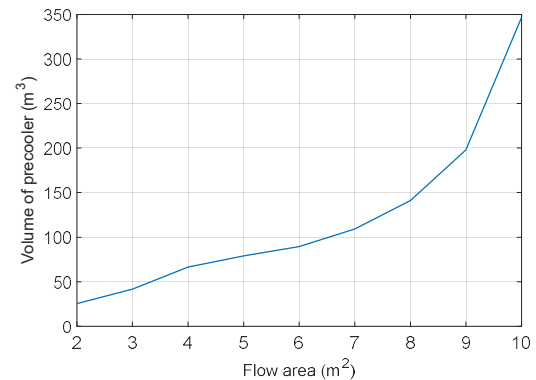
(c) Flow area versus Nusselt number



(d) Flow area versus HTCs



(e) Flow area versus pressure loss



(f) Flow area versus volume

Figure 5-9 Flow area versus (a) velocity (b) Reynolds number (c) Nusselt number (d) HTCs (e) pressure loss and (f) volume of precooler

The precooler design conditions and parameters are given in Table 5-2 for the simple cycle, the recompression cycle and the new concept, the single recuperator recompression cycle layout. A flow area of about 3.6 m² has been chosen to satisfy the pressure loss constraint. This also ensured that the s-CO₂ Reynolds number is above 5000 to maintain turbulence flow. However, the cold side remains laminar in order to satisfy the pressure loss constraint.

The precooler pressure losses, core volumes and core masses are the same for all the s-CO₂ cycle layout. The length of the modules is about 3.5 m, which is above the manufacturing limit (2.5 m). The use of smaller channel diameters (less than the current 2 mm) and reduction of the flow area can be investigated to increase the compactness and hence reduce the module length to within manufacturing limit. However, the pressure loss will increase. Alternatively, each module can be divided into smaller elementary modules whose lengths are within the manufacturing limit.

Table 5-2 Precoolers conditions and design parameters for the simple, the recompression and the single recuperator recompression s-CO₂ cycle for SM-PWR application

Description	Simple cycle	Recompression	New layout
Fluid, hot side/cold side		s-CO ₂ /Water	
Hot side mass flow (kg/s)	2234.43	2209	2209.99
Cold side mass flow (kg/s)	4498.94	4447.76	4449.75
Hot side inlet pressure (bar)		76.52	
Hot side temperature, in/out (°C)		77.28/32	
Cold side inlet pressure (bar)		5/4.26	
Cold side temperature, in/out (°C)		22/42.28	
Heat transfer duty (MW)	380.93	376.60	376.76
Number of modules		21	
Module height (mm)	886.06	875.99	876.38
Module length (mm)		3527	
Free flow area (m ²)		3.61	
Surface area density (m ² /m ³)		714.11	
Thermal density (MW/m ³)		6.45	
Effectiveness (%)		72.07	
Average LMTD (°C)		11.56	
Hot side average Re number		5340	
Cold side average Re number		1980	
Hot side velocity		2.43	
Cold side velocity		1.24	
Hot side pressure loss (kPa)		76.5	
Cold side pressure loss (kPa)		73.5	
Total core volume (m ³)	59.06	58.39	58.42
Total core mass (kg)	266330	263300	263420

The average LMTD between the hot and cold streams along the precooler length is about 11.56 °C. The precooler operates closest to the critical point among the cycle components. Hence, rapid property change is expected in the precooler. Figure 5-10 shows the hot and cold side temperature profile in the precooler while Figure 5-11 shows the temperature difference along the channel length. A pinch point with about 4 °C temperature difference occurs within the precooler. The

temperature difference at the cold end was specified as 10°C while 35 °C was specified for the hot end of the precooler. Attempt to lower these TTDs leads to temperature cross over at the pinch point.

The unusual temperature profile and the occurrence of pinch point within the precooler can be attributed to the rapid and nonlinear variation of the s-CO₂ fluid. Figure 5-12 shows the values of the specific heat capacity along the precooler nodes/sections and Figure 5-13 shows the density variation. The specific heat capacity of the s-CO₂ is about 1.5 kJ/kg-K at precooler inlet sections, which then increases rapidly to about 128 kJ/kg-K at the outlet sections. The s-CO₂ density also increases from about 155 kg/m³ at the precooler inlet to about 522 kg/m³ at the outlet. However, the cold stream properties remain relatively constant from the inlet to the outlet sections. Figure 5-14 shows the hot and cold stream HTC and the overall HTC values in the precooler. The HTC in the hot side rises sharply toward the s-CO₂ stream outlet section due to the rapid change in CO₂ properties.

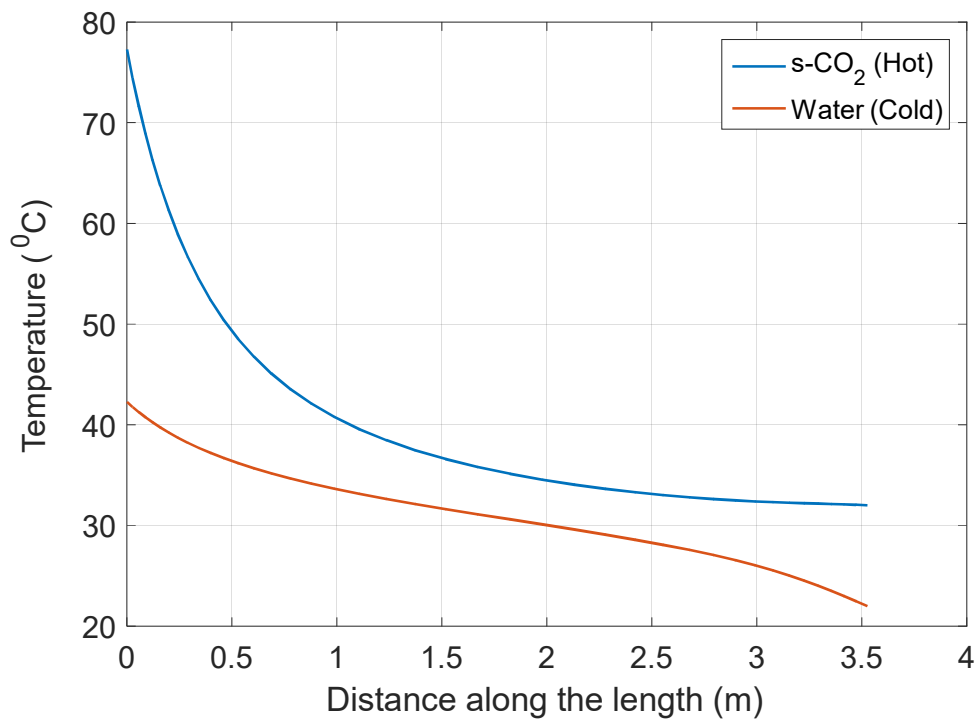


Figure 5-10 Precooler hot and cold streams temperature profile

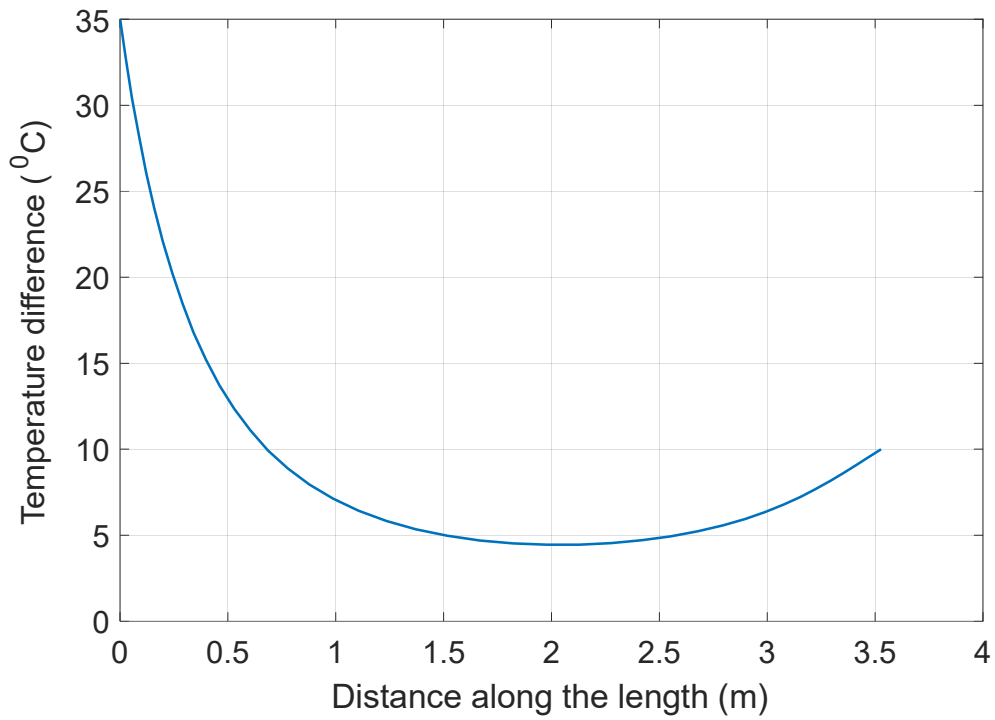


Figure 5-11 Temperature difference between the hot and cold stream within the pre-cooler

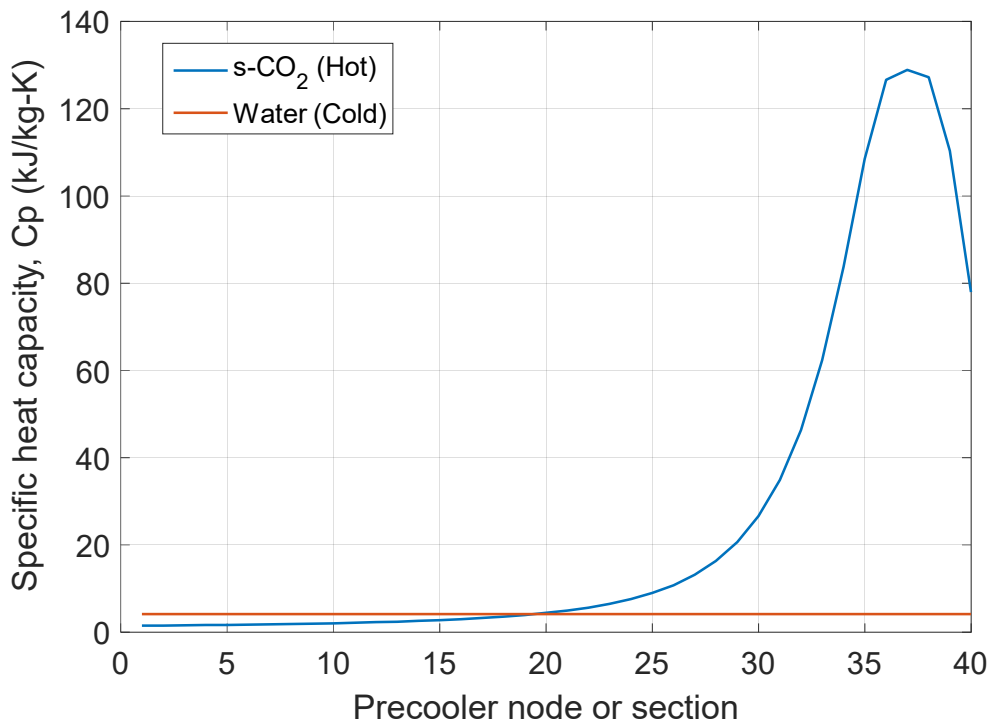


Figure 5-12 Hot and cold stream specific heat capacity values within the pre-cooler

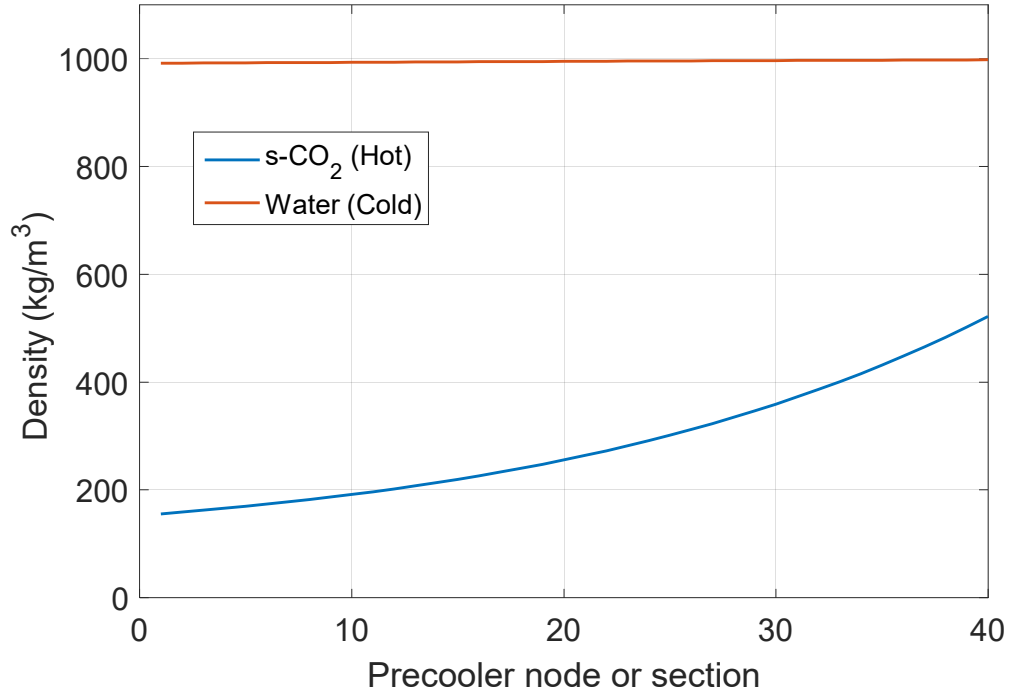


Figure 5-13 Hot and cold stream density values within the pre-cooler

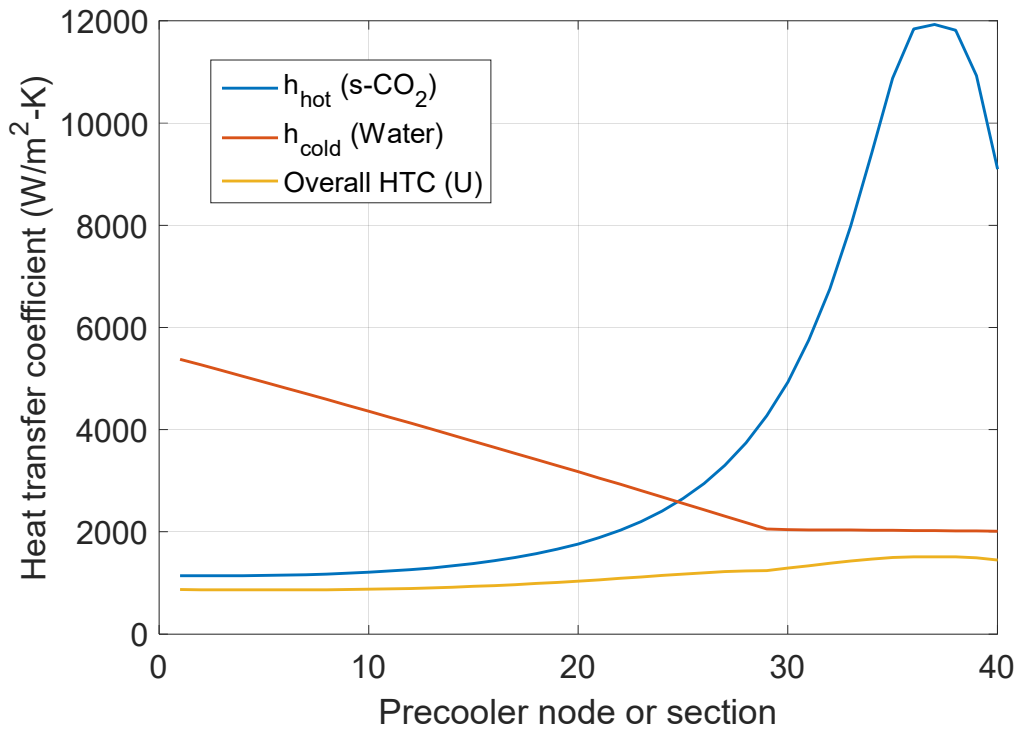


Figure 5-14 Variation of HTCs within the pre-cooler

5.3.2 Results of IHXs design

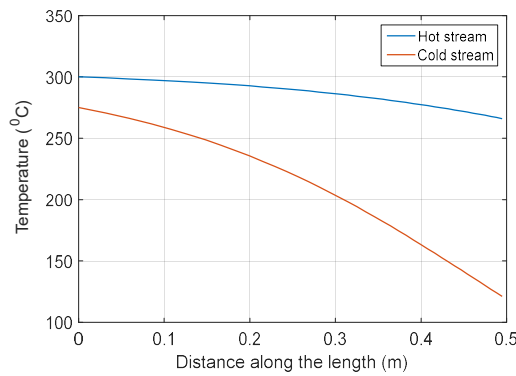
The IHX exchanges heat between the hot pressurised water leaving the reactor and cycle's s-CO₂ working fluid on the cold side. The pressurised water enters the IHX at 300 °C and heats the working fluid to the 275 °C temperature required at the turbine inlet. Table 5-3 shows the IHX conditions and design parameters for the simple cycle, recompression cycle and single recuperator recompression cycle layouts. Figure 5-15 shows the hot and cold stream temperature profiles while Figure 5-16 shows the HTCs in the IHXs. In the IHX, the CO₂ properties are relatively stable, thus the HTC remain almost constant.

Table 5-3 IHX conditions and design parameters for the simple, the recompression and the single recuperator recompression s-CO₂ cycle for SM-PWR application

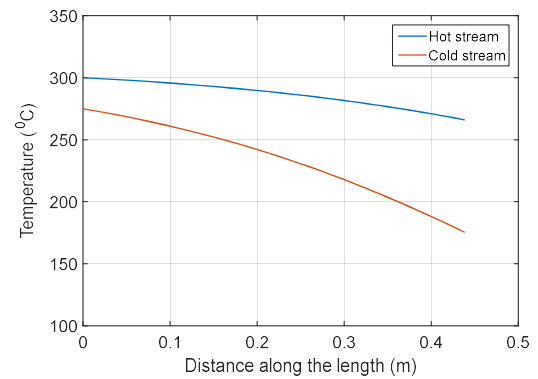
Description	Simple cycle	Recompression	New layout
Fluid, hot side/cold side	Pressurised water/s-CO ₂		
Hot side mass flow (kg/s)	2869.32	2869.26	2869.26
Cold side mass flow (kg/s)	2234.43	3759.42	3694.01
Hot side inlet pressure (bar)	155		
Hot side temperature, in/out (°C)	300/266		
Cold side inlet pressure (bar)	199.68	199.19	199.21
Cold side temperature, in/out (°C)	121.15/275	175.42/275	173.82/275
Heat transfer duty (MW)	501.43	501.42	501.42
Number of modules	23	30	30
Module height (mm)	865.83	892.35	878.18
Module length (mm)	495	438	440
Free flow area (m ²)	3.91	5.26	5.17
Surface area density (m ² /m ³)	714.11		
Thermal density (MW/m ³)	56.59	47.48	48.03
Effectiveness (%)	87.75	81	81.26
Average LMTD (°C)	90.55	59.36	60.22
Hot side average Re number	7172	5335	5421
Cold side average Re number	5411	7422	7393
Hot side velocity	0.97	0.72	0.73
Cold side velocity	2.12	3.02	3
Hot side pressure loss (kPa)	5.1	2.7	2.8
Cold side pressure loss (kPa)	10	14	13.9
Total core volume (m ³)	8.86	10.56	10.44
Total core mass (kg)	39972	47632	47086

The simple cycle IHX flow area is smaller than those of the recompression cycles because the s-CO₂ mass flow rate is smaller. Also, the pressure loss on the cold side is lesser for the simple

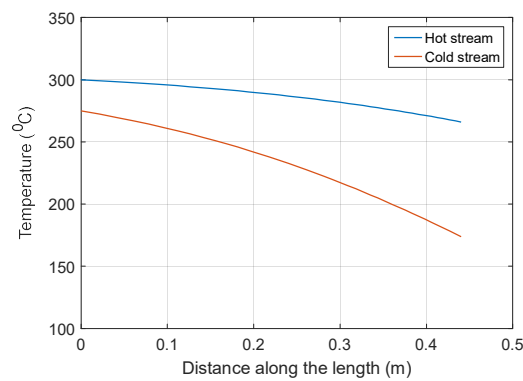
cycle. However, the pressure loss on the hot side is greater for the simple because of the smaller flow area. The average LMTD for the simple cycle IHX is higher, thus providing a higher driving force for heat transfer. Therefore, the volume of the simple cycle IHX is smaller, even though the HTC is slightly lower than those of the recompression cycles. The IHXs of the recompression cycle and the single recuperator recompression cycle have approximately the same pressure losses and volume.



(a) Simple cycle layout

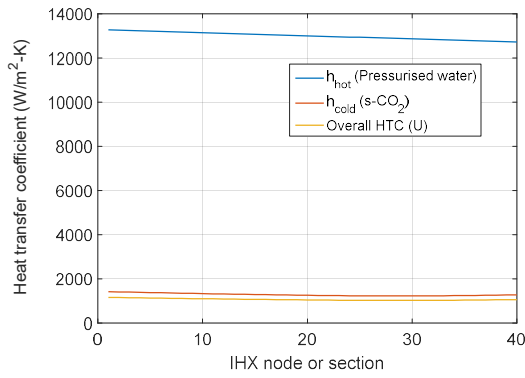


(b) Recompression cycle layout

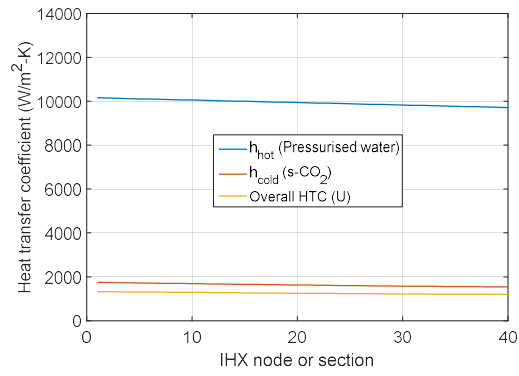


(c) Single recuperator recompression cycle layout

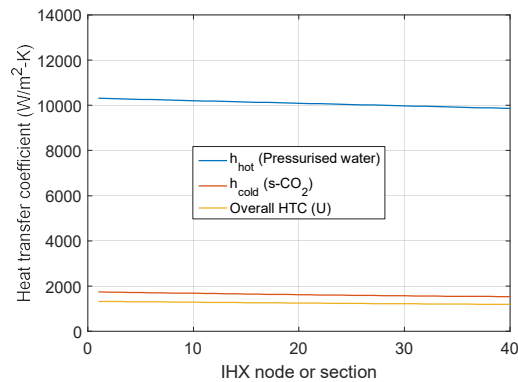
Figure 5-15 IHX hot and cold stream temperature profiles for the (a) simple cycle layout (b) recompression cycle layout and (c) single recuperator recompression cycle layout



(a) Simple cycle layout



(b) Recompression cycle layout



(c) Single recuperator recompression cycle layout

Figure 5-16 IHX hot and cold side HTC's and the overall HTC for the (a) simple cycle layout (b) recompression cycle layout and (c) single recuperator recompression cycle layout

5.3.3 Results of recuperators design

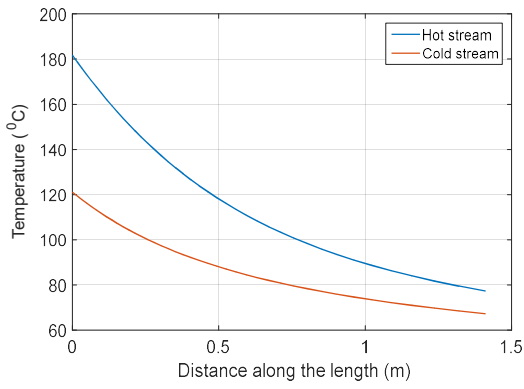
The recuperator exchange heat between the hot low pressure s-CO₂ leaving the turbine and the cold high pressure s-CO₂ leaving the compressor, thus reducing the required heat input. In the recompression cycle layout, the recuperator is separated into LTR and HTR. The other layouts have only one recuperator. Table 5-4 shows the recuperator conditions and design parameters for the simple cycle, recompression cycle and single recuperator recompression cycle layouts. Figure 5-17 shows the hot and cold stream temperature profiles while Figure 5-18 shows the HTC's in the recuperators.

The recompression cycles' recuperators have higher mass flow rates and heat transfer duty and lower average LMTD than the simple cycle recuperators. Therefore, the design of the recuperators for the recompression cycles is more challenging compared to the design of the simple cycle recuperator. The flow areas have been selected for all the recuperator to keep the s-CO₂ flow in the turbulence region while satisfying the pressure loss constraints. Higher pressure loss constraints have to be specified for the recompression cycle's LTR and the recuperator of the single recuperator recompression cycle due to their higher mass flow rate and duty. Overall, the recompression cycles recuperators hot side pressure loss is about five times the simple cycle

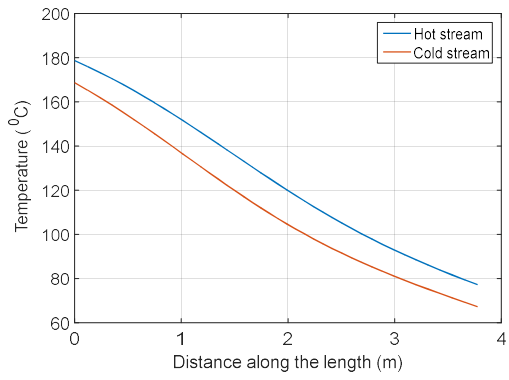
recuperator pressure loss. The cold side pressure loss is also higher for the recompression cycles. The recompression cycle's recuperator is about three times bigger than the simple cycle's recuperator. Therefore, even though recompression cycle permits high level of recuperation in the cycle but it comes at the expense of bigger recuperator size and higher cycle pressure loss. In the recuperators of the simple and single recuperator recompression cycle as well as the LTR of the recompression cycle, the HTCs on both sides decrease in a similar manner from the flow inlet to the outlet such that the overall HTC remains nearly constant. The HTR is farther away from the critical point; hence, there is almost no effect of CO₂ properties variation.

Table 5-4 Recuperator conditions and design parameters for the simple, the recompression and the single recuperator recompression s-CO₂ cycle for SM-PWR application

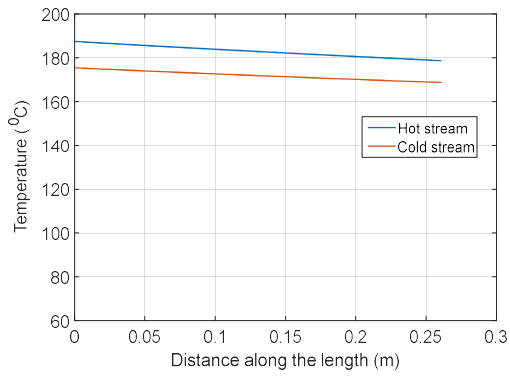
Description	Simple cycle	Recompression cycle		
		LTR	HTR	New layout
Fluid, hot side/cold side		s-CO ₂ /s-CO ₂		
Hot side mass flow (kg/s)	2234.43	3759.42	3759.42	3694.01
Cold side mass flow (kg/s)	2234.43	2209	3759.42	2209.99
Hot side inlet pressure (bar)	77.68	82.27	82.40	82.27
Hot side temperature, in/out (°C)	181.83/77.28	178.70/77.28	187.47/178.70	187.33/77.28
Cold side inlet pressure (bar)	200	200	199.24/	200
Cold side temperature, in/out (°C)	67.28/121.15	67.28/168.70	168.70/175.42	67.28/177.33
Heat transfer duty (MW)	287.78	463.63	37.82	492.28
Number of modules	14	17	35	17
Module height (mm)	895.05	888.63	896.92	891.52
Module length (mm)	1411	3776	261	3870
Free flow area (m ²)	2.46	2.97	6.16	2.98
Surface area density (m ² /m ³)		714.11		
Thermal density (MW/m ³)	18.09	9.03	5.13	9.33
Effectiveness (%)	89.22	93.39	46.46	93.90
Average LMTD (°C)	34.72	13.63	11.04	14.28
Hot side average Re number	12851	17521	10242	17462
Cold side average Re number	5892	5289	5450	5354
Hot side velocity	7.60	10.22	5.85	10.19
Cold side velocity	1.77	1.74	2.10	1.78
Hot side pressure loss (kPa)	116.5	576	12.4	576
Cold side pressure loss (kPa)	32.2	76.3	5.2	79.5
Total core volume (m ³)	15.91	51.34	7.37	52.79
Total core mass (kg)	71760	231520	33228	238060



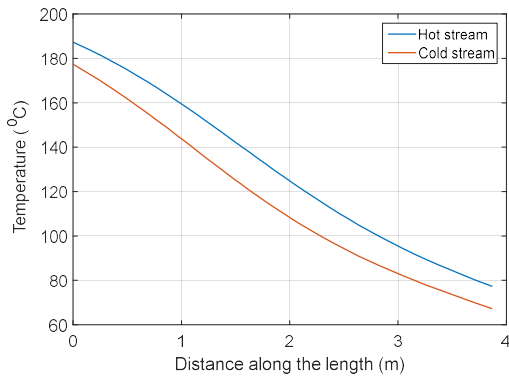
(a) Simple cycle



(b) Recompression cycle LTR

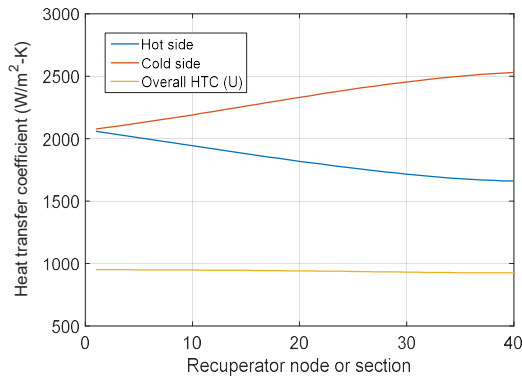


(c) Recompression cycle HTR

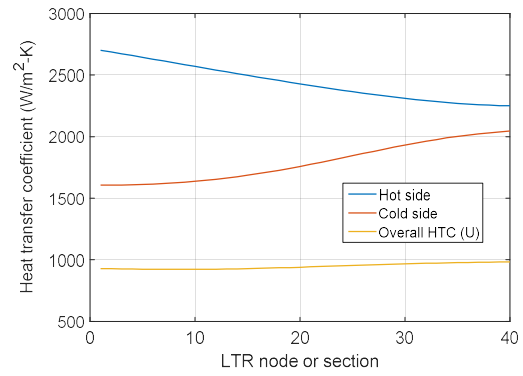


(d) Single recuperator recompression

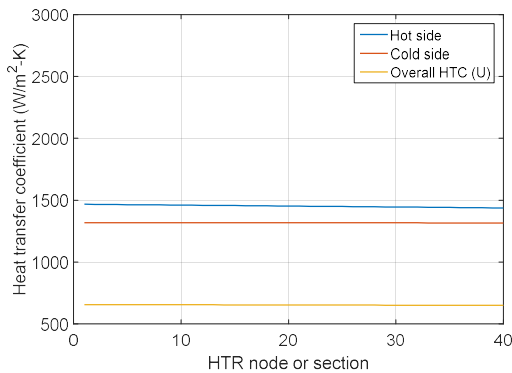
Figure 5-17 Recuperator hot and cold stream temperature profile for the (a) simple cycle layout (b) LTR of the recompression cycle layout (c) HTR of the recompression cycle layout and (d) single recuperator recompression cycle layout



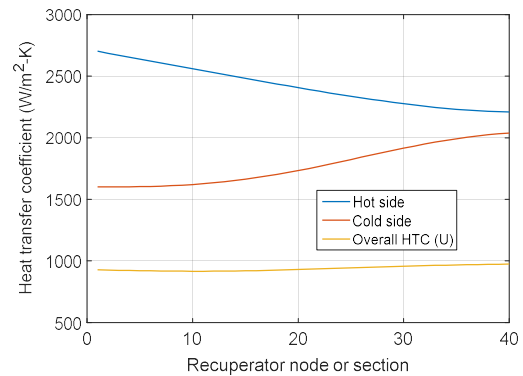
(a) Simple cycle



(b) Recompression cycle LTR



(c) Recompression cycle HTR



(d) Single recuperator recompression

Figure 5-18 Recuperator hot and cold sides HTC and the overall HTC for the (a) simple cycle layout (b) LTR of the recompression cycle layout (c) HTR of the recompression cycle layout and (d) single recuperator recompression cycle layout

5.3.4 Impact of heat exchanger design on plant performance and size

Figure 5-19 shows the total CO₂ pressure loss through the heat exchangers based on the preliminary design of the heat exchangers. The total pressure loss in the recompression cycle is more than 3 times higher than the simple cycle pressure loss. The pressure loss in the new cycle layout (single recuperator recompression) is a little less than the loss in the recompression cycle, primarily due to the elimination of the HTR. Cycle pressure loss has a significant effect on the plant thermal efficiency. Figure 5-20 compares the previous plant efficiency with that calculated with the actual pressure losses obtained from the preliminary design of the heat exchanger. The efficiency of the recompression cycle drops by about 2% point while the efficiency of the simple cycle remain relatively the same. The recompression cycle efficiency is now just about 0.86% point better than the simple cycle efficiency.

For SMR design, compactness can be a critical factor being that transportability of plant components and cost strongly depend on the size. Therefore, reducing the overall plant size can be one of the main design considerations. Figure 5-21 compares the total heat exchanger volumes comprising the recuperator, the IHX and the precooler for the different s-CO₂ cycle layouts. The total heat exchanger volume of the recompression cycles are higher than that of the simple cycle.

Though the volume of the precoolers and the IHXs are similar for the three cycles, the volume of the recuperators of the recompression cycles are larger than that of the simple cycle.

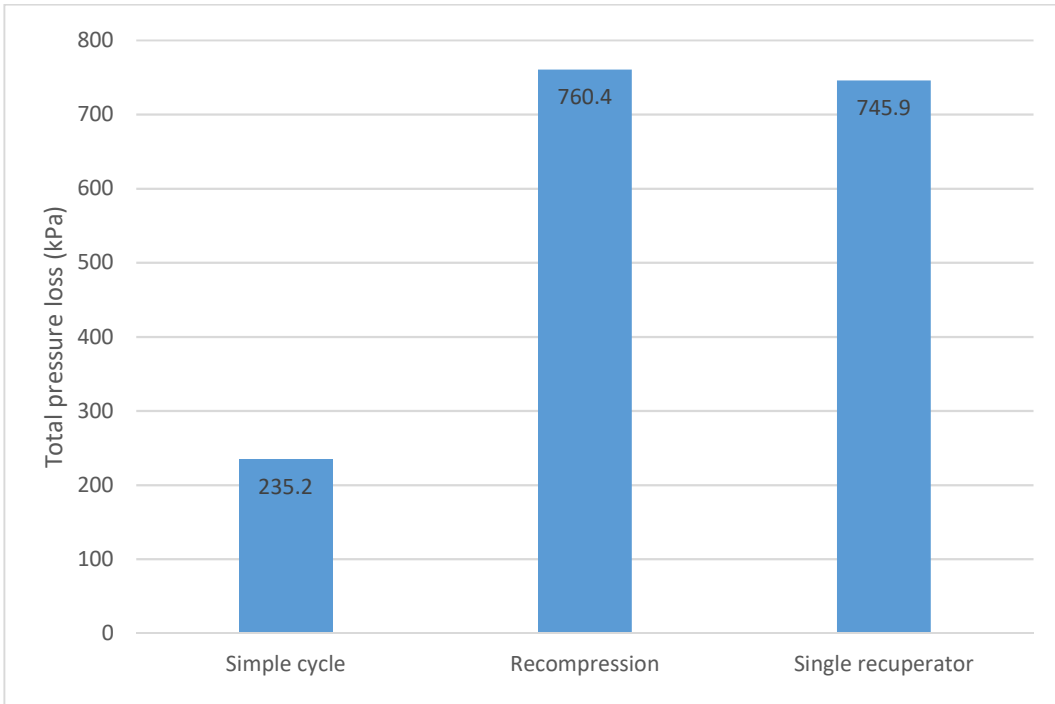


Figure 5-19 Comparison of total pressure losses for the simple, recompression and single recuperator recompression cycle

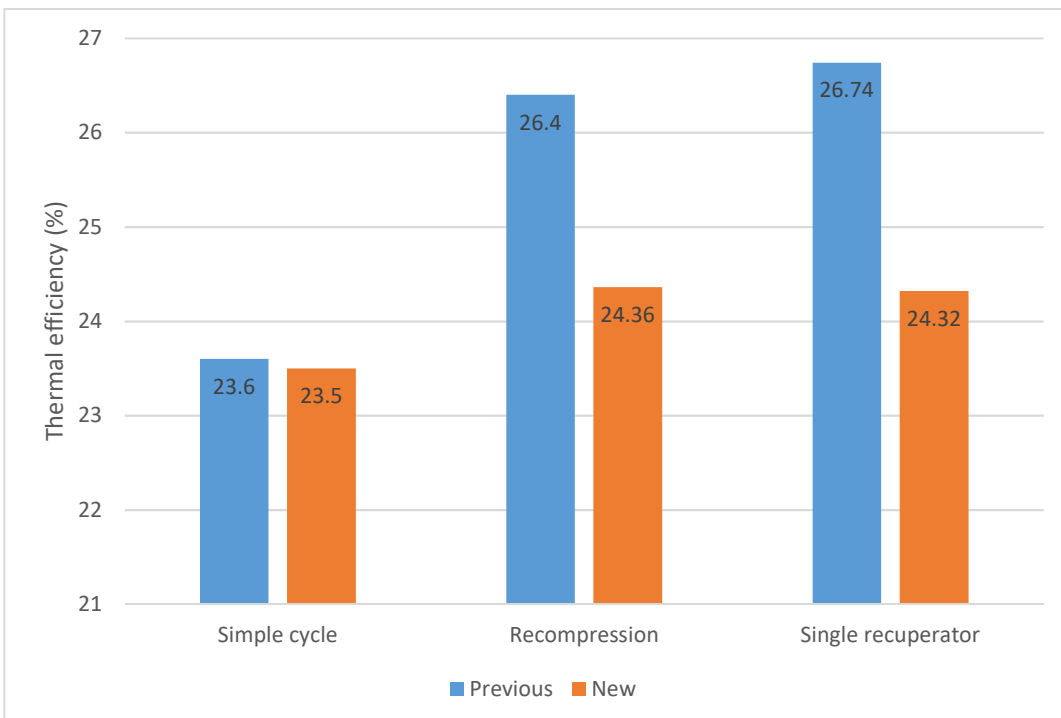


Figure 5-20 Comparison of the previous and the new thermal efficiency after heat exchanger design for the different s-CO₂ cycle layouts

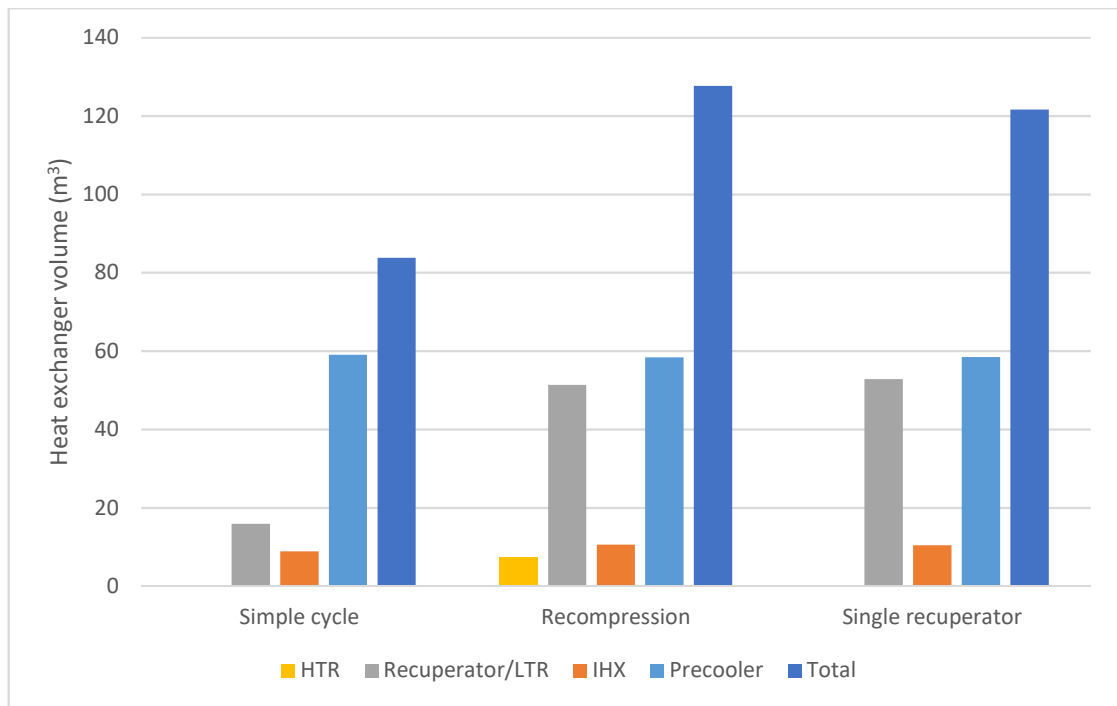


Figure 5-21 Comparison of the total heat exchanger volume including the volume of the recuperator, IHX and precooler for the different s-CO₂ cycle layouts

5.4 Parametric analysis of s-CO₂ Brayton cycles

5.4.1 Effect of precooler outlet conditions on thermal efficiency

Figure 5-22, Figure 5-23 and Figure 5-24 show the effects of changes in the precooler outlet temperature and pressure on the thermal efficiency of the simple, recompression and single recuperator recompression s-CO₂ Brayton cycles respectively. The TIT was kept at 275 °C and the maximum cycle pressure maintained at 200 bar. For the recompression cycles, optimum recompression fraction was selected. The efficiency is seen to increase with reduction in the precooler outlet temperature as expected. However, for each precooler outlet temperature, the efficiency is maximum at an optimum pressure. For precooler outlet temperature of 32 °C, the optimum pressure for the simple cycle is about 76 bar and about 81 bar for the recompression cycles. The optimum precooler outlet pressure is strongly coupled to the precooler outlet temperature. As the precooler outlet temperature increases from 32 °C to 52 °C, the optimum pressure increases from about 76 bar to about 110 bar.

At the optimum pressure, the recompression cycle gives the highest efficiency. The single recuperator recompression cycle gives efficiency value that is close to that of the recompression cycle. The efficiency of the simple cycle is about 2.3% point below that of the recompression cycle. Below 81 bar, the efficiency of the recompression cycle drops sharply. In reality, below 75 bar, the use of HTR becomes meaningless due to the reduced turbine outlet temperature.

A further rise in efficiency is noticed in the simple and single recuperator recompression cycle at precooler outlet pressure above 100 bar and at low temperature. However, these conditions cannot be selected, as the design of the recuperator and turbomachinery will be very challenging. For one, the cycle mass flow rate is very large due to the small pressure ratio for the same plant capacity. In addition, the lower temperature at the compressor outlet moves the conditions in the recuperator toward the critical region with a likelihood of pinch point problem in the recuperator. Cycles in this region are theoretically possible but cannot be realized in practice because the recuperator required would be impractically large (Bryant et al., 2011).

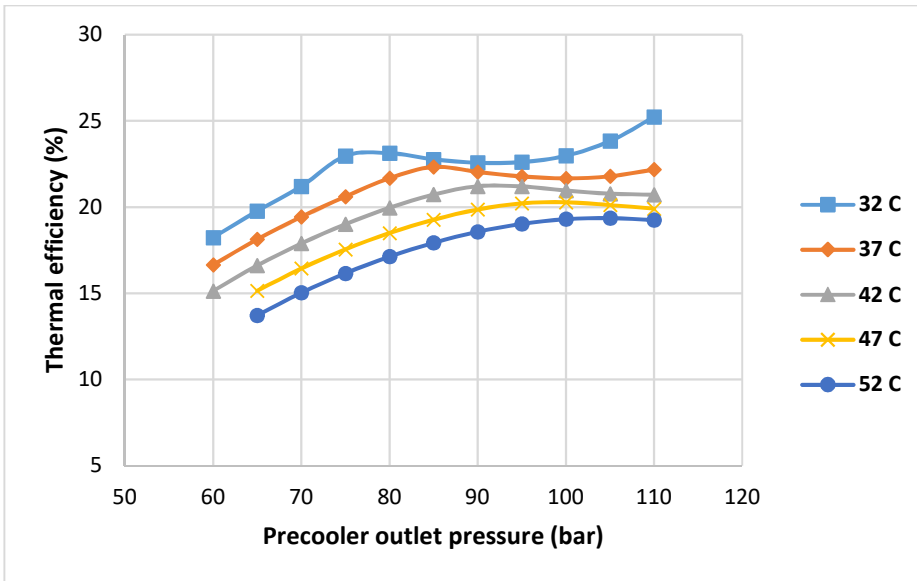


Figure 5-22 Effect of precooler outlet temperature and pressure on the thermal efficiency of simple s-CO₂ Brayton cycle

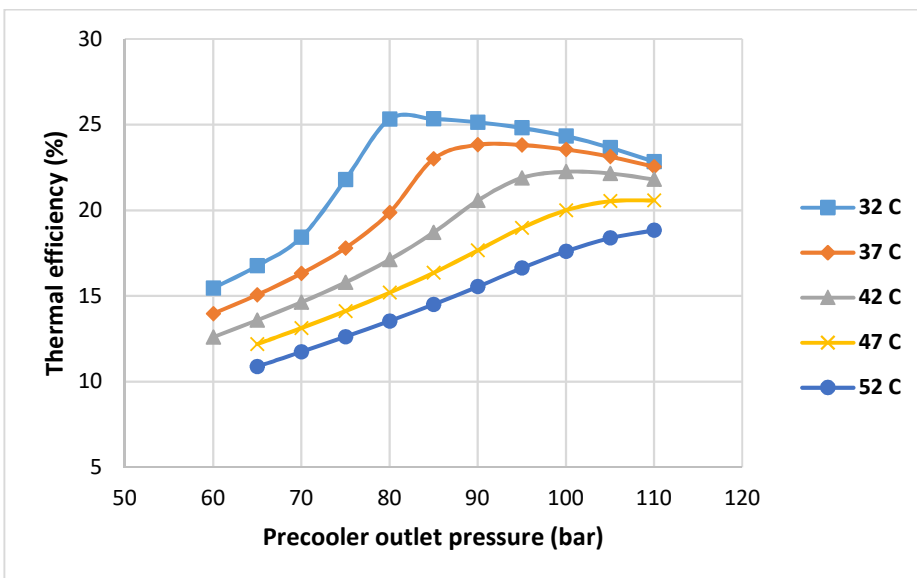


Figure 5-23 Effect of precooler outlet temperature and pressure on the thermal efficiency of recompression s-CO₂ Brayton cycle

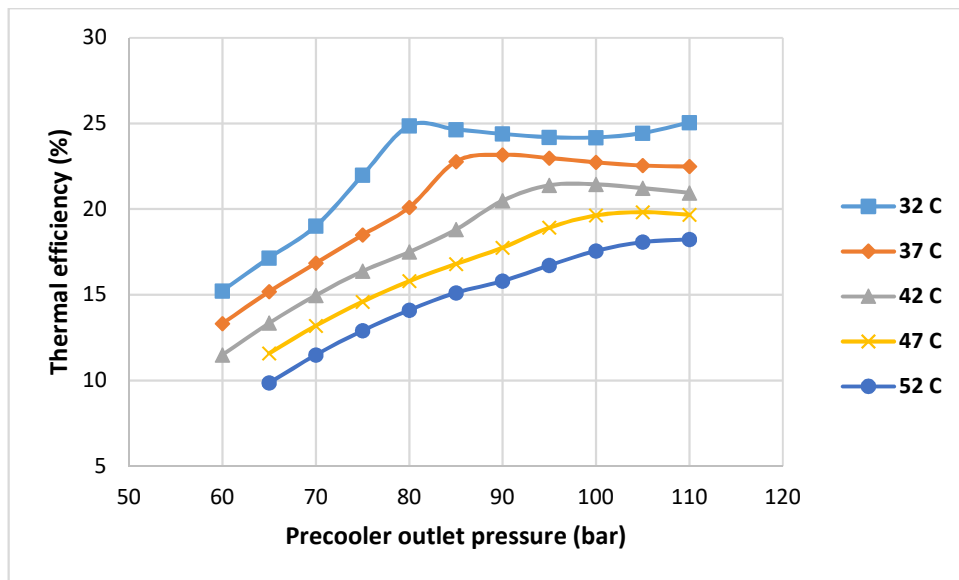


Figure 5-24 Effect of precooler outlet temperature and pressure on the thermal efficiency of single recuperator recompression s-CO₂ Brayton cycle

5.4.2 Effect of maximum operating pressure on thermal efficiency

Traditionally, the maximum cycle pressure for s-CO₂ cycle is usually chosen to be about 200 bar. This value has been viewed to offer a good compromise between cycle efficiency and material stresses (Gibbs, 2008). However, development in power generation technology has made pressures above 200 bar feasible. Supercritical steam power plant now operate at pressure above 250 bar. Figure 5-25 shows the effect of changes in maximum cycle pressure (i.e. compressor outlet pressure) on the thermal efficiency of the s-CO₂ Brayton cycles. The maximum cycle pressure was varied between 160 and 400 bar. The precooler outlet conditions were maintained at 32 °C temperature and corresponding optimum pressure. TIT remained at 275 °C.

The optimum maximum operating pressure are about 260 bar, 210 bar and 220 bar for the simple, recompression and single recuperator recompression cycle respectively. The higher optimum pressure for simple cycle would require greater thickness for pipes and heat exchangers, which could result in higher capital costs. At the optimum maximum cycle pressures, the recompression cycles have comparable efficiency (about 25.4% for recompression cycle and 25.2% for single recuperator). The simple cycle maximum efficiency is about 2% point lower than that of the recompression cycles.

As the maximum cycle pressure increases, the pressure ratio increases. Consequently, the turbine exit temperature reduces while the compressor outlet temperature increases. At a point, the temperature difference becomes so small that recuperation in HTR is no longer possible. For this reason, the recompression cycle cannot be implemented for maximum cycle pressure above 230 bar.

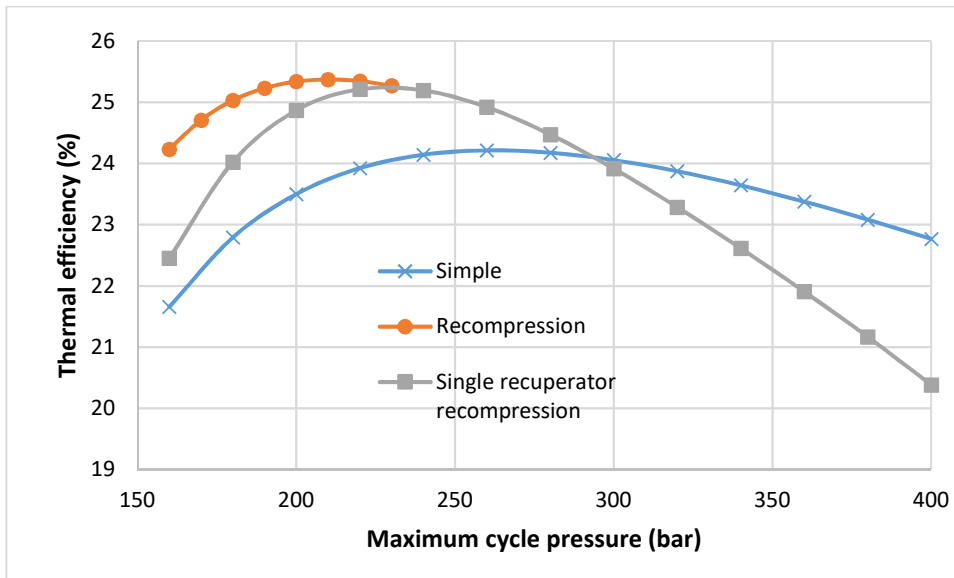


Figure 5-25 Effect of maximum cycle pressure on thermal efficiency for the simple, recompression and single recuperator s-CO₂ Brayton cycles

5.4.3 Effect of TIT on thermal efficiency

TIT is dependent on the reactor outlet temperature. In PWR, the design outlet temperature can be as high as 325 °C. Hence, the TIT can reach up to 315 °C for a s-CO₂ cycle with 10 °C minimum TTD. However, a generic heat source that is able to provide TIT from 240 °C to 700 °C was assumed in order to compare the cycles' performances over a wider range of temperature.

Figure 5-26 shows the effect of changes in TIT on the thermal efficiencies of the s-CO₂ Brayton cycles for a maximum cycle pressure of 200 bar and pre-cooler outlet temperature of 32 °C. With an increase in maximum operating temperature, the turbine inflow enthalpy increases and as a result the turbine work output increase as well. The effect on MC and RC work is not significant and hence the net work output of the cycle increases. Consequently, the thermal efficiency of the cycle increases with increase in maximum cycle temperature. In the temperature range applicable to PWR (below 300 °C), the newly proposed concept, single recuperator recompression cycle, give comparable performance to the recompression cycle. In the medium to high temperature range, the recompression cycle gives the highest efficiency as has been previously reported in the literature. Around the 240 °C temperature, the three cycle gives almost the same performance. This is because in order to continue to use the HTR in the recompression cycle, the flow has to be diverted from the RC to the MC with the cycle now operating almost like a simple cycle.

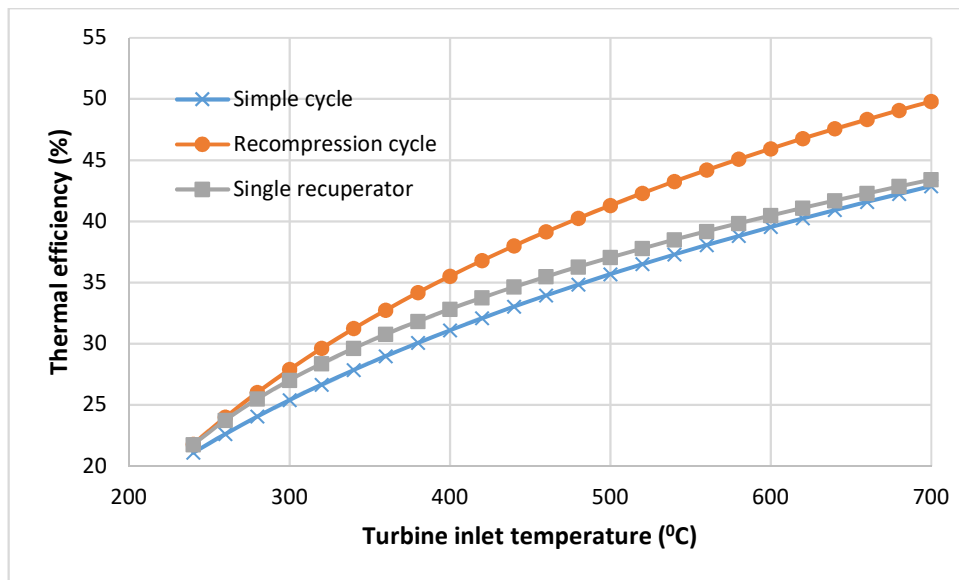


Figure 5-26 Effect of TIT on the thermal efficiency for the simple, recompression and single recuperator recompression s-CO₂ Brayton cycles

5.4.4 Effect of recuperator's minimum TTD

Even though the baseline minimum TTD for the recuperators has been chosen as 10 °C, lower values of about 5 °C has also been widely used in the literature. Reducing the minimum TTD will improve the thermal efficiency but at the expense of larger recuperator size. Hence, the effect of minimum TTD selection on the performance and recuperator volume was investigated by varying the minimum TTD from 5 to 20 °C. Recuperator effectiveness decreases with increase in minimum TTD as shown in Figure 5-27. Recuperator effectiveness for the recompression cycle has been obtained by taking the average of the LTR and HTR effectiveness. Figure 5-28 shows the effect of changes in recuperator's minimum TTD on the thermal efficiencies of the different layouts. The efficiency decreases linearly with increase in TTD.

Figure 5-29 shows the effect of changes in minimum TTD on the volume of the recuperators. Recuperator volume decreases with increase in TTD. With increase in TTD, the driving force for heat transfer is increased and thus smaller heat transfer area will be required for the same heat transfer duty. For the single recuperator recompression cycle, the volume increases rapidly as the minimum TTD decreases below 10 °C.

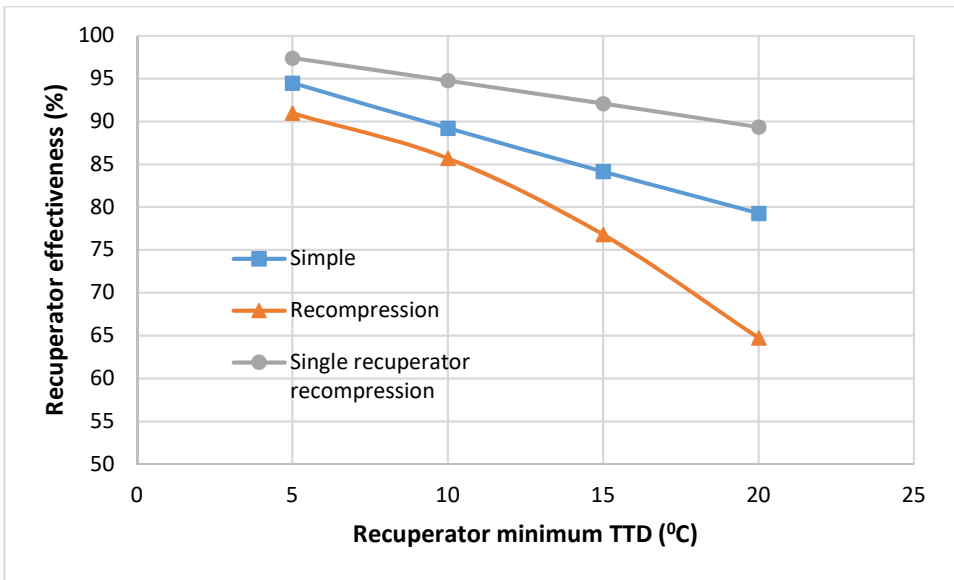


Figure 5-27 Effect of changes in recuperator minimum TTD on the recuperator effectiveness of the simple, recompression and single recuperator recompression cycles

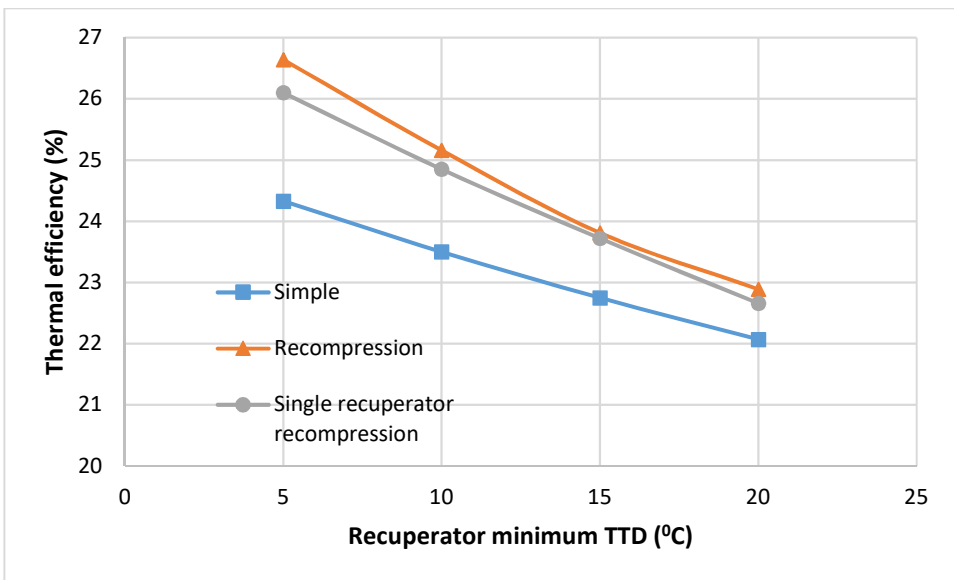


Figure 5-28 Effect of changes in recuperator minimum TTD on the thermal efficiencies of the simple, recompression and single recuperator recompression cycles

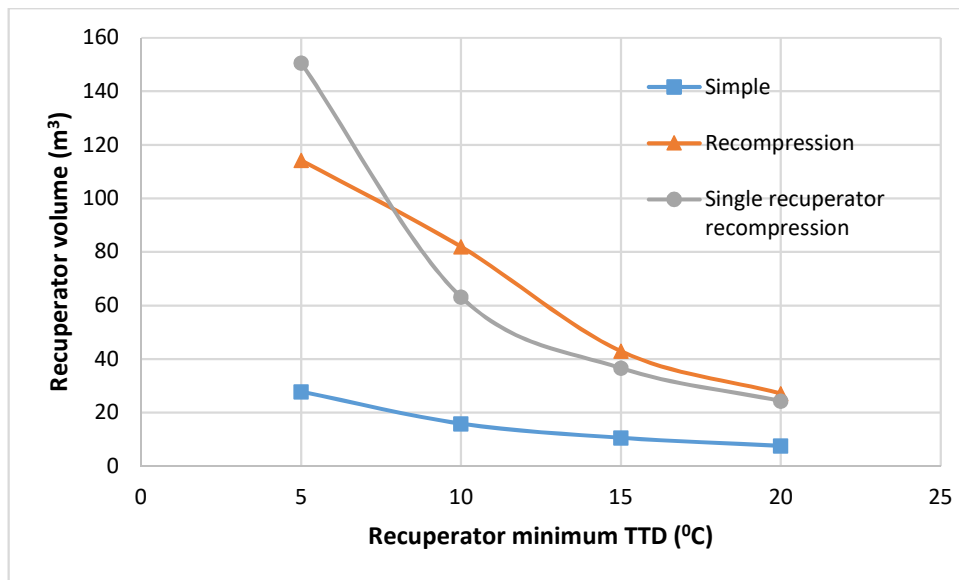


Figure 5-29 Effect of changes in recuperator minimum TTD on the recuperator volumes of the simple, recompression and single recuperator recompression cycles

5.5 Selection of suitable s-CO₂ Brayton cycle for PWR application

The newly proposed layout, the single recuperator recompression cycle, is considered suitable for PWR application based on the performance comparison and parametric analysis. It gives better efficiency than the simple cycle and gives performance comparable to that of the recompression cycle. The configuration is also simpler than the recompression cycle layout. In addition, under the PWR heat source condition, the operating range of recompression cycle layout is limited by the feasible values of maximum cycle pressure and minimum cycle pressure and temperature. At maximum cycle pressure above 230 bar or minimum cycle pressure below 75 bar, utilisation of HTR becomes impracticable for recompression cycle. This has the tendency to impede off design operation of recompression cycle for PWR application.

In order to optimise the performance and design of the single recuperator recompression cycle, the following boundary conditions were selected, based on the result of the parametric analysis:

- Reactor outlet temperature – 300 °C
- TIT – 290 °C
- MC outlet pressure – 220 bar
- Precooler outlet temperature – 32 °C
- Precooler outlet pressure – 81 bar
- Recuperator minimum TTD = 15 °C

By increasing the TIT from 275 to 290 °C, the performance of the plant improves but the volume of the IHX will increase due to reduction in TTD. Therefore, the recuperator's minimum TTD was increased to 15 °C to reduce the recuperator volume. The recuperator was then designed with reduced pressure loss by sacrificing a portion of the potential volume reduction.

Figure 5-30 shows the performance calculation results based on the selected boundary conditions. The results of preliminary design of the heat exchangers are shown in Table 5-5. The thermal efficiency increases by about 2.3% point on the efficiency before parametric analysis. The total heat exchanger volume also reduces by about 23%. This is majorly due to the reduction of the precooler volume as the s-CO₂ pressure in the precooler (about 81 bar) is now moved farther away for the critical point.

The performance reported by the industrial sponsor for the SM-PWR Alstom steam Rankine cycle benchmark gives a thermal efficiency of 30.5%, which reduces to net efficiency of about 26.8% with house loads. Even though the s-CO₂ cycle seems less efficient than the steam Rankine cycle, it may be more attractive due to the reduced footprint. The s-CO₂ cycle power plant is expected to be about 10 times smaller than steam Rankine cycle plant (Santini et al., 2016).

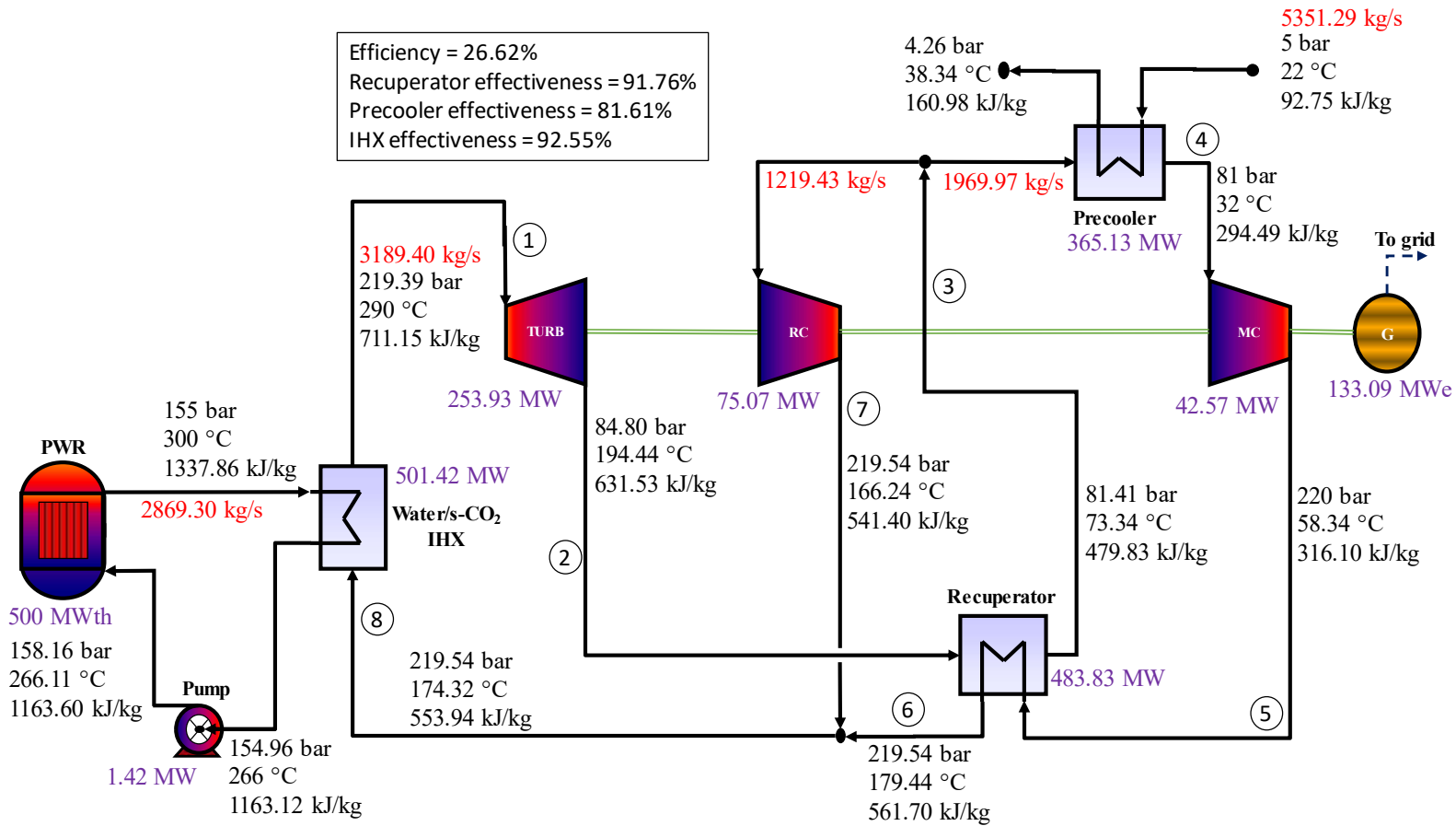


Figure 5-30 State point values and performance results of single recuperator recompression s-CO₂ Brayton cycle coupled to PWR based on the selected optimum boundary conditions

Table 5-5 Heat exchangers design result for the selected single recuperator recompression cycle for PWR application

Description	Precooler	Recuperator	IHX
Fluid, hot side/cold side	s-CO ₂ /Water	s-CO ₂ / s-CO ₂	Pressurised water/s-CO ₂
Hot side mass flow (kg/s)	1969.97	3189.40	2869.30
Cold side mass flow (kg/s)	5351.29	1969.97	3189.40
Hot side inlet pressure (bar)	81.41	84.80	155
Hot side temperature, in/out (°C)	73.34/32	194.44/73.34	300/266
Cold side inlet pressure (bar)	5	220	219.54
Cold side temperature, in/out (°C)	22/38.34	58.34/179.44	174.32/290
Heat transfer duty (MW)	365.13	483.83	501.42
Number of modules	18	18	30
Module height (mm)	882.48	884.03	890.57
Module length (mm)	2001	3406	669
Free flow area (m ²)	3.12	3.12	5.25
Surface area density (m ² /m ³)		714.11	
Thermal density (MW/m ³)	12.76	9.92	31.16
Effectiveness (%)	81.61	91.76	92.55
Average LMTD (°C)	13.40	17.59	52.69
Hot side average Re number	5332	13988	5346
Cold side average Re number	2645	4182	5959
Hot side velocity	2.10	7.94	0.72
Cold side velocity	1.72	1.35	2.37
Hot side pressure loss (kPa)	40.7	339	4.19
Cold side pressure loss (kPa)	74.2	45.95	15.37
Total core volume (m ³)	28.61	48.78	16.09
Total core mass (kg)	129020	219960	72568

5.6 Turbomachinery design for s-CO₂ Brayton cycle for SM-PWR

This section describes the turbomachinery design for the single recuperator recompression cycle for PWR application. The layout uses three turbomachinery: MC, RC and turbine. In the literature, both axial type machines and centrifugal/radial type machines have been suggested for s-CO₂ Brayton cycle power plants (Dostal, 2004; Yoon et al., 2012; Moisseytsev and Sienicki, 2007; Floyd et al., 2013; Cha et al., 2009; Gong et al., 2006; Lee et al., 2014). Axial turbomachinery is mostly utilised for large capacity power plants (> 125 MWe) while centrifugal turbomachinery is commonly designed for small power applications where the flow is too small to permit efficient use of axial blading (Dostal, 2004; Gibbs et al., 2006). Turbomachinery design for s-CO₂ cycle is an area of active research due to the unique behaviour of CO₂ around the critical point. Most

conventional turbomachinery design software, usually developed based on ideal gas assumption and normal fluid behaviour, cannot be employed for the design of s-CO₂ compressor. The reason is that convergence difficulties as well as real gas properties calculation is an issue due to rapid variation of CO₂ properties near the critical points (Carstens, 2007; Dostal, 2004). Also, ideal gas and constant specific heat capacity assumptions are not valid in the vicinity of the critical point.

In this study, axial flow turbomachinery is selected for the compressors and turbine. Compressors and turbine design were performed using the Matlab[®] codes presented in Chapter 3. CO₂ properties were obtained from NIST REFPROP property program, which is able to provide accurate CO₂ properties at conditions close to the critical point. In order to capture real gas property variations, turbomachinery design calculations were done in terms of enthalpy, pressure and entropy rather than pressure, temperature and constant specific heat capacity assumption, as is usually the case with conventional design software. Rotational speed of 3000 rpm is selected for the turbomachinery, in order to synchronise the shaft with the electric grid frequency.

Table 5-6 shows the design parameters obtained for the MC and the RC. A flow coefficient of 0.5 was assumed for the compressors. The designs were governed by the requirements to achieve stage loading of 0.3, stage reaction of 50% and hub to tip ratio between 0.75 and 0.9. The number of stages and blade speed were selected in order to respect these design constraints. Therefore, the MC has 8 stages while the RC is designed with 17 stages. The turbine design parameters are summarised in Table 5-7. For the turbine, a flow coefficient of 0.6 was assumed. The turbine design was guided by the need to maintain a stage loading of 1.08, reaction of 0.5 and hub to tip ratio between 0.75 and 0.9. This resulted in a turbine design with 3 stages. The detailed results of fluid properties, geometry and other parameters for the each stage of the turbomachinery are given in Appendix A.2. The main features of the turbomachinery include small blade heights, high hub to tip ratios, low blade speeds, low Mach numbers and gentle flow passage flares. The machines are compact. The total axial length is about 3.3m and the volume of all the turbomachinery is about 2 m³, which is only about 2% of the total heat exchanger volume.

Table 5-6 MC and RC design parameters and main features for the single recuperator recompression s-CO₂ cycle

Parameters	MC	RC
Number of stages	8	17
Flow coefficient	0.5	0.5
Stage loading coefficient	0.3	0.3
Reaction	0.5	0.5
Rotational speed, rpm	3000	3000
Maximum tip diameter, mm	639	761
Maximum tip speed, m/s	100	119
Mach (meanline maximum)	0.36	0.36
Blade height, mm (max/min)	34/29	60/31
Hub/Tip ratio (min/max)	0.89/0.90	0.84/0.91
Blade numbers, (1 st stage rotor/stator)	75/77	49/50
Blade chord, mm (1 st stage rotor/stator)	31/30	54/53
Axial length, mm	485	1430
Volume, m ³	0.15	0.62
Aspect ratio	1.1	1.1
Solidity	1.21	1.21
Pressure ratio (-)	2.72	2.70
Rated flow rate (kg/s)	1969.97	1219.43
Stage efficiency, %	89.34	89.14
de Haller number	0.74	0.74
Diffusion factor	0.4	0.4

Table 5-7 Turbine design parameters and main features for the single recuperator recompression s-CO₂ cycle

Parameters	Values
Number of stages	3
Flow coefficient	0.6
Stage loading coefficient	1.08
Reaction	0.50
Rotational speed, rpm	3000
Maximum tip diameter, mm	1107
Maximum tip speed, m/s	174
Mach (meanline maximum)	0.59
Blade height, mm (min/max)	52/109
Hub/Tip ratio (min/max)	0.80/0.90
Blade numbers, (1 st stage stator/rotor)	24/89
Blade chord, mm (1 st stage stator/rotor)	164/183
Axial length, mm	1403
Volume, m ³	1.28
Aspect ratio	3
Pressure ratio (-)	2.59
Rated flow rate (kg/s)	3189.4
Stage efficiency, %	92.54

5.7 Summary

This chapter describes the thermodynamic performance of s-CO₂ Brayton cycles for application to SM-PWR. S-CO₂ cycle achieve relatively higher efficiency compared to other CBC by keeping the compressor inlet conditions close to the critical point in order to reduce the compression work. Simple recuperated cycle, recompression cycle and newly suggested cycle, the single recuperator recompression cycle were compared in term of performance and heat exchanger design. Design of the heat exchangers showed that the recompression cycles suffer from higher pressure loss compared to the simple recuperated cycle. Parametric analysis was performed to investigate the effect of changes in precooler outlet conditions, maximum cycle pressure, TIT and recuperator minimum TTD on the performance of the plants. The single recuperator recompression cycle was considered the most suitable option of the three layouts for application to PWR. Design of the turbomachinery for the single recuperator recompression cycle showed that the turbine and compressors are very small in size compared to the heat exchangers.

In Chapter 7, the control system design for nuclear closed-cycle GT will be described while Chapter 9 will present the dynamic performance and automatic control configuration for the single recuperator recompression cycle coupled to SM-PWR.

6 Dynamic Model Development for Closed-Cycle GTs Coupled to Nuclear Reactors

6.1 Introduction

This chapter presents the mathematical model of the components of a typical closed-cycle GT coupled to nuclear reactor. In this thesis, the two plants modelled for dynamic performance investigation were: (1) the two-shaft nitrogen Brayton cycle receiving thermal input from a SM-SFR (2) the single recuperator recompression s-CO₂ Brayton cycle receiving thermal input from SM-PWR.

The complexity of the model was chosen to suit the purpose of studying the control schemes and dynamic behaviour of the nuclear power plants. The models are based on first principles (mass, energy and momentum conservation equations), thermodynamic laws and other constitutive equations with appropriate simplifications. Related work has been done by (Wang, 2009; Dostal, 2004; Carstens, 2007) at Massachusetts Institute of Technology (MIT) with other GT nuclear power plant systems. Hence these existing literatures and others on the modelling of GT cycles such as Ordys et al. (1994), Lee et al. (2011), Camporeale et al. (2000), Chacartegui et al. (2011b), Zhang et al. (2006), Gobran (2013), Flynn (2003) and Kaikko (1998) were widely consulted in the development and derivation of the dynamic models.

The heat balance (steady state) calculations were presented in the previous chapters. At the steady state/design calculation step, the input data for all components were assigned. These include the reactor outlet temperature, minimum cycle temperature, pressure ratio, turbomachinery efficiencies, maximum cycle temperature, maximum cycle pressure, thermal input, and pressure losses. The results of the steady state and component design calculations provide the physical parameters of the components as well as the design point values for the plant. Some of the steady state and design calculation values were transferred to the dynamic models where they were used as reference data and physical parameters for dynamic performance calculation. The dynamic model gives the plant transient performance based on these values. The operability of the plant can be evaluated by using the dynamic model. The following is a systematic presentation of the component dynamic models.

6.2 Plant components' dynamic model development

The model equations were grouped by components. The components modelled include nuclear reactors, coolant pumps, compressors, turbines, heat exchangers (IHX, precooler and recuperators), rotating shafts, generator, mixers, splitters, control valves, actuators and

controllers. The plants dynamic models were developed by modelling the performance of each component in the plant using mass and energy balances as well as the performance characteristics provided for each component. The necessary equations and data, including thermodynamic laws to describe the various components and processes and performance characteristics and working fluid data were developed. The characteristic curves representing turbomachinery performance like compressor ratio as a function of compressor speed and flow rate, were digitised and/or curve fitted. After the initial component-by-component modelling, the individual component models were later integrated into a complete system model. The model development for the components are described below.

6.2.1 Nuclear reactor model

The dynamics of the nuclear reactor was only required for simulating the relationship between the primary system and the CBC. Hence, only a simplified model of the reactor was considered because the aim is not a detailed study of the reactor transients, which usually requires a stand-alone reactor model with the core geometry parameters specified in detail (Wang, 2009). The reactor dynamic model consists of the point reactor kinetics model and the thermal-hydraulic model. The point kinetics model is used to predict both the time-dependent behaviour of the neutron population in the reactor core and the decay of the delayed neutron precursors. The thermal hydraulic model on the other hand determines the heat transfer within the reactor fuel core and coolant volume as a result of the generated fission power and the flow of the coolant into and out of the reactor. Thus, it gives the temperature of the reactor fuel and coolant.

Assuming six delayed neutron groups, the point reactor kinetics equations are (Thomas, 1999):

$$\frac{dn(t)}{dt} = \frac{\rho(t) - \beta}{\Lambda} n(t) + \sum_{i=1}^6 \lambda_i C_i(t) + S \quad (6-1)$$

$$\frac{dC_i(t)}{dt} = \frac{\beta_i}{\Lambda} n(t) - \lambda_i C_i(t) \quad (i = 1 \dots 6) \quad (6-2)$$

Reactivity, ρ , is a measure of the deviation of the core multiplication factor, k_e , from its critical value of unity

$$\rho = \frac{k_e - 1}{k_e} \quad (6-3)$$

The reactivity at any time will depend on the position of the control rod, the temperature of the core and the temperature of the coolant (Thomas, 1999). Therefore, the total reactivity, can be expressed as the sum of an external reactivity from the control rod, ρ_{rod} , and the inherent feedback reactivities from the core, ρ_f , and the coolant, ρ_c :

$$\rho(t) = \rho_{rod} + \rho_f + \rho_c \quad (6-4)$$

The feedback reactivities were expressed as a function of the average fuel and coolant temperatures (Han, 2000). The fuel reactivity is expressed as:

$$\rho_f = \alpha_f(T_f - T_{f,0}) \quad (6-5)$$

The coolant temperature reactivity is determined from:

$$\rho_c = \alpha_c(T_c - T_{c,0}) \quad (6-6)$$

Where α_f is the fuel reactivity coefficient, α_c is the coolant reactivity coefficient, T_f and T_c are the average fuel and coolant temperature respectively, and $T_{f,0}$ and $T_{c,0}$ are the steady state or initial fuel and coolant temperature respectively.

The six groups of delayed neutrons can be approximated by one effective group of delayed neutron, characterised by an effective yield fraction, β , and an effective decay constant, λ , as follow:

$$\beta = \sum_{i=1}^6 \beta_i \quad (6-7)$$

$$\lambda = \left[\frac{1}{\beta} \sum_{i=1}^6 \frac{\beta_i}{\lambda_i} \right]^{-1} \quad (6-8)$$

Therefore, the point reactor kinetic equations can be simplified and written in terms of the one effective delayed neutron group parameters and the fission thermal power, Q_f , as:

$$\frac{dQ_f}{dt} = \frac{\rho_t - \beta}{\Lambda} Q_f + \lambda C + S \quad (6-9)$$

$$\frac{dC}{dt} = \frac{\beta}{\Lambda} Q_f - \lambda C \quad (6-10)$$

Table 6-1 gives values of the reactivity coefficient, the prompt-neutron life time and the delayed neutron parameters adopted for the SFR reactor, while Table 6-2 gives the corresponding values for the PWR.

Table 6-1 Feedback reactivity coefficients, prompt-neutron life time and delayed neutron parameters for the SFR (Ragusa and Mahadevan, 2009)

Feedback reactivity coefficients: $\alpha_f = -0.8841 \text{ pcm}/^\circ\text{C}$; $\alpha_c = 0.1263 \text{ pcm}/^\circ\text{C}$		
Prompt-neutron lifetime: 3.2×10^{-7} seconds		
Delayed neutron parameters:		
Group	β_i	$\lambda_i(1/s)$
1	0.00009	0.0124
2	0.00087	0.0305
3	0.00070	0.111
4	0.00140	0.301
5	0.00060	1.14
6	0.00055	3.01
Overall	0.0042	0.0887

Table 6-2 Feedback reactivity coefficients, prompt-neutron life time and delayed neutron parameters for the PWR (Thomas, 1999; Naghedolfeizi, 1990)

Feedback reactivity coefficients: $\alpha_f = -1.1 \text{ pcm}/^\circ\text{C}$; $\alpha_c = -20 \text{ pcm}/^\circ\text{C}$		
Prompt-neutron lifetime: 1.79×10^{-5} seconds		
Delayed neutron parameters:		
Group	β_i	$\lambda_i(1/s)$
1	0.000266	0.0127
2	0.001492	0.0317
3	0.001317	0.115
4	0.002851	0.311
5	0.000897	1.40
6	0.000182	3.87
Overall	0.00700	0.0784

For the thermal hydraulic model, energy conservation equations were derived for the core fuel element and the coolant volume in the reactor core. The fission thermal energy is released in the fuel elements and transferred to the coolant by convection. The energy balance for the fuel is given by:

$$M_f C_p \frac{dT_f}{dt} = Q_f - Q_{fc} \quad (6-11)$$

The convective heat transfer between the fuel and the water or sodium coolant, Q_{fc} , can be determined by:

$$Q_{fc} = UA(T_f - T_c) \quad (6-12)$$

Where U is the convective HTC, A is the heat transfer area and T_c is the average coolant temperature.

The energy balance for the coolant passing through the reactor core is given by:

$$\rho_c V_c \frac{dh_o}{dt} = \dot{m}_i h_i - \dot{m}_o h_o + Q_{fc} \quad (6-13)$$

The coolant mass flow rates at the inlet and outlet of the reactor were assumed to be equal.

The coolant temperature may be obtained from the calculated enthalpy by using the coolant thermo-physical property function.

The average coolant temperature is given by:

$$T_c = \frac{T_i + T_o}{2} \quad (6-14)$$

The outlet pressure, P_o can be determined from:

$$P_o = P_i - \xi \frac{\dot{m}_i^2}{\rho_c} \quad (6-15)$$

The pressure loss coefficient, ξ , is initially calculated from the steady state values of P_i , P_o , \dot{m}_i and ρ_c .

6.2.2 Reactor coolant pump model

The reactor coolant pump is used to circulate the pressurised water or liquid sodium in the primary circuit through the reactor and the primary side of the IHX. The pump is a centrifugal type driven by an electric motor. The electric motor is not modelled but represented with its output, which is the delivered motor shaft power, W_m .

In order to force the coolant through the primary circuit components, the pump must produce enough pressure head to overcome the total frictional head loss in the primary circuit. Therefore, the momentum conservation equation for the primary system can be written as (Naghdolfeizi, 1990):

$$\frac{d}{dt}(MV) = \rho g A_{ef} \left(H_p - \sum H_{loss} \right) \quad (6-16)$$

The mass of coolant, M , is

$$M = \rho L A_{ef} \quad (6-17)$$

The flow velocity, V , is

$$V = \frac{\dot{Q}}{A_{ef}} \quad (6-18)$$

The total hydrodynamic head loss in the primary circuit, $\sum H_{loss}$, is proportional to the square of volumetric flow rate, \dot{Q}

$$\sum H_{loss} = K \dot{Q}^2 \quad (6-19)$$

Substituting Equation (6-17), (6-18) and (6-19) into Equation 6-16):

$$\frac{1}{g} \frac{L}{A_{ef}} \frac{d\dot{Q}}{dt} = H_p - K \dot{Q}^2 \quad (6-20)$$

Where g is the acceleration due to gravity, L is the effective length of the pipings in the primary circuit, A_{ef} is the effective area of piping in the primary circuit, H_p is the developed pump head and K is the friction factor coefficient.

The power balance equations for the motor-pump rotating assembly is:

$$I N \frac{dN}{dt} = W_m - W_h \quad (6-21)$$

Where I is the moment of inertia, N is the shaft rotational speed, W_m is the active power from the electric motor and W_h is the resistive hydraulic power applied by the fluid to the shaft

$$W_h = W_p / \eta_p \quad (6-22)$$

The pumping power, W_p , is given by

$$W_p = \dot{Q} \rho g H_p \quad (6-23)$$

The pump characteristic maps/equations relates the pump head, H_p and the resistive hydraulic power, W_h (or the pump efficiency, η_p) to the volumetric flow rate, \dot{Q} and shaft speed, N .

$$C_H = f_{H-map}(C_Q) \quad (6-24)$$

$$C_{P_D} = f_{P_D-map}(C_Q) \quad (6-25)$$

C_Q , C_H and C_{P_D} are the dimensionless flow coefficient, head coefficient and power coefficient respectively.

$$C_Q = \frac{\dot{Q}}{ND^3} \quad (6-26)$$

$$C_H = \frac{gH}{N^2D^2} \quad (6-27)$$

$$C_{P_D} = \frac{W_h}{\rho N^3 D^5} \quad (6-28)$$

Where D is pump impeller diameter,

The pump efficiency is expressed in terms of these coefficients as:

$$\eta_P = \frac{\dot{Q} \rho g H}{W_h} = \frac{C_H C_Q}{C_{P_D}} \quad (6-29)$$

The pump performance characteristic curves used in the model are shown in Figure 6-1 (taken from Walas (1990)). The performance curves are used in conjunction with affinity laws to determine the characteristics of the pump. The pump affinity relations are:

$$\frac{\dot{Q}_0}{N_0 D_0^3} = \frac{\dot{Q}_1}{N_1 D_1^3} = \text{constant} \quad (6-30)$$

$$\frac{H_0}{N_0^2 D_0^2} = \frac{H_1}{N_1^2 D_1^2} = \text{constant} \quad (6-31)$$

$$\frac{W_{h0}}{\rho_0 N_0^3 D_0^5} = \frac{W_{h1}}{\rho_1 N_1^3 D_1^5} = \text{constant} \quad (6-32)$$

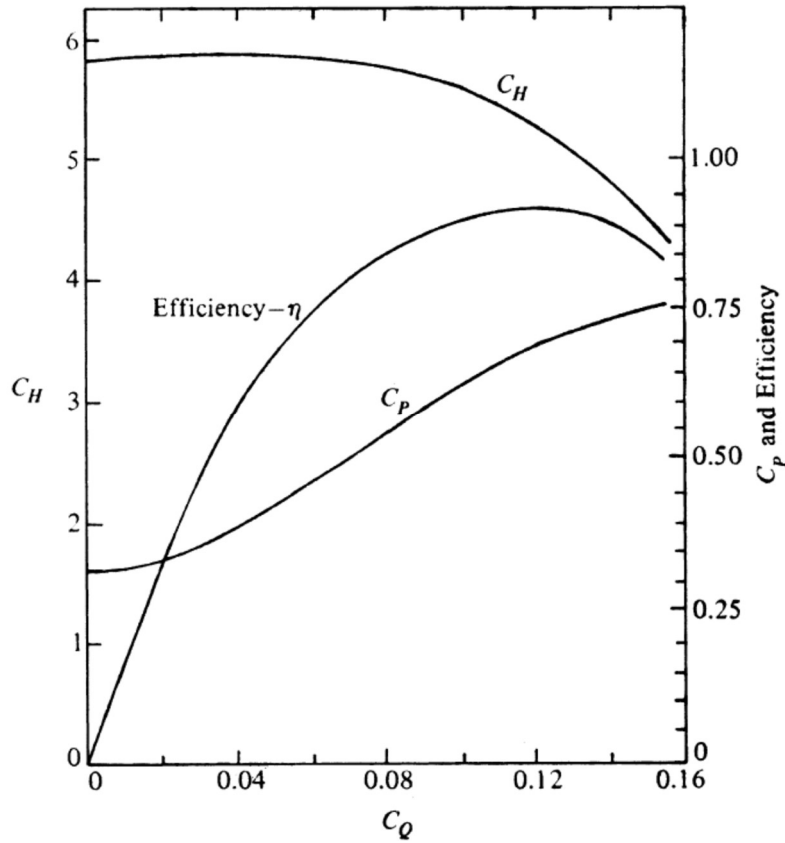


Figure 6-1 Dimensionless performance curves of pump (Walas, 1990)

Pump pressure rise is:

$$\Delta P = \rho g H_p \quad (6-33)$$

Hence, pump outlet pressure is

$$P_o = P_i + \Delta P \quad (6-34)$$

The accumulation of mass in the pump is negligible. Hence, the mass conservation equation gives:

$$\dot{m}_{p_i} = \dot{m}_{p_o} = \rho \dot{Q} \quad (6-35)$$

Where \dot{m}_{p_i} is the pump inlet mass flow rate and \dot{m}_{p_o} is the pump outlet mass flow rate

The pump outlet specific enthalpy is determined from the energy balance for the fluid volume, assuming negligible heat loss through the body of the pump:

$$W_h = \dot{m}(h_o - h_i) \quad (6-36)$$

The outlet temperature is then calculated from the specific enthalpy by using the coolant thermodynamic properties relation.

6.2.3 Compressor and turbine models

Though work has been carried out on the aerodynamic design of the turbomachinery to determine the compressors and turbines design parameters but their performance characteristic curve is yet to be generated. However, for nitrogen Brayton cycle, the industrial sponsor has separately carried out the design and generation of performance maps for the compressors and turbine. This data was utilised for the dynamic performance model of the compressors and turbine. For s-CO₂ turbomachinery, there are still uncertainties regarding the prediction of the performance. The unique real gas properties of CO₂ around the critical point gives challenges when designing or simulating turbomachinery performance. Hence existing performance curve obtained from other similar work reported in the literature will be adopted to estimate the performance of the s-CO₂ turbomachinery. The performance maps for the s-CO₂ cycle MC, RC and turbine were obtained from the work of Carstens et al. (2006).

In order to use these maps, they were scaled to generate new maps of normalised pressure ratios and normalised efficiencies as functions of normalised mass flow rates for a range of shaft speeds (all the normalisation was carried out with respect to design point). The use of performance maps rather than detailed calculations will reduce significantly the burden of such detailed computation in a dynamic model. Also, changes can be made easily to the turbomachinery performance model by simply switching the performance data. Therefore, as more realistic performance characteristic data becomes available from either experimental results or further aerodynamic design calculations they can be easily introduced into the model.

6.2.3.1 Compressor model

For s-CO₂ compressors, the most reliable way suggested for constructing a compressor map is using methods developed for incompressible turbomachinery (pumps). Hence, the pressure rise will be scaled with $U^2\rho$ to give the non-dimensional pressure ratio and the mass flow rate scaled with $U\rho$ to give the non-dimensional flow rate or flow coefficient (Gong et al., 2006). U is the impeller tip speed proportional to the rotational speed N , while ρ is the fluid density. Therefore, the compressor map describes the relations between the non-dimensional pressure ratio and the flow coefficient, and between the efficiency and the flow coefficient. The non-dimensional coefficients are also normalised to the reference/design point values.

Thus the flow coefficient is defined as (Trinh, 2009; Carstens, 2007):

$$\phi = \frac{\dot{m}}{\dot{m}_{ref}} \frac{\rho_{ref}}{\rho} \frac{N_{ref}}{N} \quad (6-37)$$

Ideal gas assumption is satisfactory for the compressors in the nitrogen cycle. Therefore, the mass flow rate can be corrected for changing inlet conditions by using the standard method for ideal gas turbomachinery and then normalised as follows:

$$\phi = \frac{\dot{m}}{\dot{m}_{ref}} \sqrt{\frac{T_i}{T_{ref}} \frac{P_{ref}}{P_i}} \quad (6-38)$$

The inputs to the compressor models are the mass flow rate, rotational speed and the fluid conditions (pressure, temperature and density) at the compressor inlet. With these inputs, the flow coefficient or corrected mass flow rate is calculated and the performance map is used to obtain corresponding values of non-dimensional pressure ratio and isentropic efficiency defined as:

$$\psi = \frac{\pi}{\pi_{ref}} \frac{\rho_{ref}}{\rho} \left(\frac{N_{ref}}{N} \right)^2 = f_{\pi-map}(\phi) \quad (6-39)$$

$$\eta_{nor} = \frac{\eta}{\eta_{ref}} = f_{\eta-map}(\phi) \quad (6-40)$$

Where ψ is the non-dimensional pressure ratio, π is the actual pressure ratio, η_{nor} is the normalised isentropic efficiency and η is the actual isentropic efficiency

The performance map is incorporated into the model by direct use of the data in a tabular form and table look-up algorithm as well as curve fitting the data with polynomial equations. Once the map data has been obtained, the compressor outlet conditions is computed as follows:

$$P_o = P_i \pi \quad (6-41)$$

$$h_o = h_i + \frac{h_{oi} - h_i}{\eta} \quad (6-42)$$

h_{oi} the enthalpy that would be at the outlet with an isentropic compression. It can be obtained from the fluid thermodynamic properties relations as a function of P_o and S_i (i.e. inlet entropy). Other discharge fluid properties such as outlet temperature, T_o can also be obtained from the fluid thermodynamic properties relations. That is,

$$T_o = f_{eos}(P_o, h_o) \quad (6-43)$$

The power consumption of the compressor, W_c is calculated as the product of the mass flow rate and enthalpy rise between the inlet and outlet section.

$$W_c = \dot{m}(h_o - h_i) \quad 6-44$$

The dynamic model of the turbomachinery assumes that the transport delay in the component are small and negligible.

6.2.3.2 Turbine model

The turbine model, similar to the compressor model, uses mass and energy conservation equation. It uses the equation of state of working fluid and the performance maps to provide constitutive relationships. The turbine produces mechanical energy from the thermal energy of the expanding working fluid. The produced mechanical energy is used to run the compressors and/or the electric generator.

The original turbine performance maps are transformed to provide relationship between non-dimensional pressure ratio and flow coefficient and between efficiency and flow coefficient at constant shaft speed parameter. Under turbine conditions, both the CO₂ and nitrogen working fluids were considered as ideal gas. Hence, the flow coefficient is as defined in equation (6-38). The other non-dimensional parameters normalised to their design point values utilised for map scaling are defined as (Carstens, 2007, Trinh, 2009, Gobran, 2013):

Non-dimensional shaft speed:

$$N_{nor} = \frac{N}{N_{ref}} \sqrt{\frac{T_{ref}}{T_i}} \quad (6-45)$$

Non-dimensional pressure ratio:

$$\psi(\phi, N_{nor}) = \frac{\pi - 1}{\pi_{ref} - 1} = f_{\pi-map}(\phi, N_{nor}) \quad (6-46)$$

Normalised isentropic efficiency:

$$\eta_{nor}(\phi, N_{nor}) = \frac{\eta}{\eta_{ref}} = f_{\eta-map}(\phi, N_{nor}) \quad (6-47)$$

These transformation of the characteristic map parameter will enable the use of the maps for turbine inlet fluid conditions and pressure ratios different from the original machine design values. The inputs to the turbine model are the inlet fluid conditions, mass flow rate and rotational speed. These input values are used to compute the flow coefficient and shaft speed parameters. The turbine characteristic maps are incorporated into the model in tabular form and in the form of equations. By using table look-up algorithm and solving the equations the normalised non-dimensional pressure ratio and isentropic efficiency can be obtained and used to determine the actual values as follows:

The actual pressure ratio is:

$$\pi = \psi(\pi_{ref} - 1) + 1 \quad (6-48)$$

Isentropic efficiency is:

$$\eta = \eta_{nor}\eta_{ref} \quad (6-49)$$

Thus, the exit pressure of the turbine is:

$$P_o = \frac{P_i}{\pi} \quad (6-50)$$

To determine other gas properties (e.g. temperature and enthalpy) at the turbine outlet, firstly the expansion process is considered isentropic with outlet enthalpy, h_{oi} . Then the actual turbine exit enthalpy and temperature are calculated as follows:

Turbine outlet enthalpy is:

$$h_o = h_i - \eta(h_i - h_{oi}) \quad (6-51)$$

Exit temperature is obtained from the fluid properties data:

$$T_o = f_{eos}(P_o, h_o) \quad (6-52)$$

The power delivered by the turbine, W_t is calculated as the product of the mass flow rate and enthalpy drop between the inlet and outlet section.

$$W_t = \dot{m}(h_i - h_o) \quad (6-53)$$

6.2.4 Heat exchanger model

The heat exchangers employed in the cycles are the IHX, the recuperators and the precoolers. They are included in the cycle in order to improve the performance of the cycle and for transferring the reactor heat to the PCS. A complex model of the heat exchangers will result in a computationally expensive simulation of the system. Whereas dynamic simulation for the purpose of studying the plant control schemes requires a very fast solution of the dynamic model. Therefore, the heat exchanger model must allow for a rapid computation of the dynamic behaviour of the heat exchangers. At the same time, the model must be reliable enough for accurate prediction of the overall transient response to changes in the operating conditions.

For the purpose of deriving the system of dynamic model equations, the counter-flow heat exchangers are divided into three regions (the hot stream, the cold stream and the metal wall) as shown in Figure 6-2. Equation of mass, energy and momentum conservation is used to build the models for the hot and cold stream regions, and energy conservation equation for the metal wall.

The conservation of mass for the hot stream control volume is:

$$V_H \frac{d\rho_H}{dt} = \dot{m}_{Hi} - \dot{m}_{Ho} \quad (6-54)$$

The energy conservation for the hot stream can be expressed as:

$$V_H \frac{d(\rho_H h_H)}{dt} = \dot{m}_{Hi} h_{Hi} - \dot{m}_{Ho} h_{Ho} - Q_{HW} \quad (6-55)$$

where Q_{HW} is the convective heat transferred from the hot stream to the metal wall.

The momentum conservation equation simplified to a quasi-static equation of pressure loss for the hot stream is (Ordys et al., 1994):

$$P_{Hi} - P_{Ho} = \frac{\dot{m}_H^2}{\rho_H} \xi \quad (6-56)$$

Similarly for the cold stream, the mass, energy and momentum conservation equations are:

$$V_C \frac{d\rho_C}{dt} = \dot{m}_{Ci} - \dot{m}_{Co} \quad (6-57)$$

$$V_C \frac{d(\rho_C h_C)}{dt} = \dot{m}_{Ci} h_{Ci} - \dot{m}_{Co} h_{Co} + Q_{WC} \quad (6-58)$$

$$P_{Ci} - P_{Co} = \frac{\dot{m}_C^2}{\rho_C} \xi \quad (6-59)$$

Where Q_{WC} is the convective heat transferred from the metal wall to the cold stream.

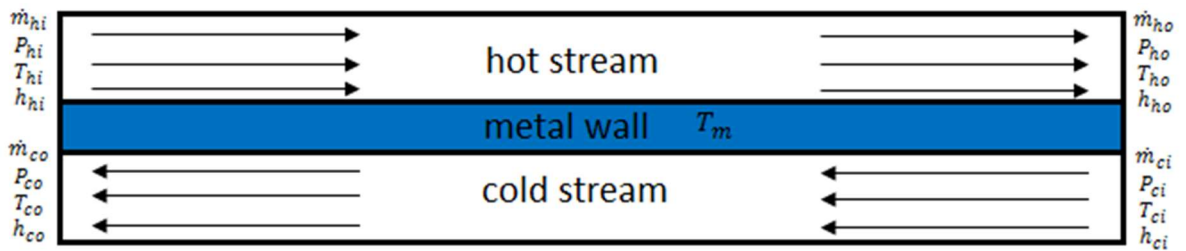


Figure 6-2 Heat exchanger regions

Changes in the inlet temperature of one of the stream do not reflect instantaneously in the outlet of the other stream. The lag is dependent on the thermal capacitances of the metal wall and the working fluid as well as the resistances to heat transfer (Wang, 2009). Therefore, the metal wall energy conservation equation is given as:

$$M_W C_W \frac{dT_W}{dt} = Q_{HW} - Q_{WC} \quad (6-60)$$

where M_W , C_W , and T_W , the mass of the metal wall, specific heat capacity of the metal and the metal mean temperature respectively.

Finally, a correlation for evaluating Q_{HW} and Q_{WC} is required (Ordys et al., 1994; Flynn, 2003):

$$Q_{HW} = K_{HW} \dot{m}_H^{0.8} (T_H - T_W) \quad (6-61)$$

$$Q_{WC} = K_{WC} \dot{m}_C^{0.8} (T_W - T_C) \quad (6-62)$$

6.2.5 Rotating shafts and generator model

The s-CO₂ recompression cycle considered in this study has two rotating shafts. The compressor turbine drives the MC and the RC and the power turbine drives the synchronous generator for electric energy production. An unbalance torque on the shaft during transient will cause the shaft to accelerate or decelerate. The transient behaviour of the shafts can be determined from the dynamic equation (Trinh, 2009):

$$\sum_j W_j = \sum_j I_j N \frac{dN}{dt} \quad (6-63)$$

Where W_j is the power on the shaft from the j^{th} component, I_j is the rotational moment of inertia of the j^{th} component and N is the angular speed of the shaft.

During normal operation, the shaft is assumed to rotate in positive direction. Therefore, turbines will exert positive torque while compressors and electric generator will exert negative torque. For the s-CO₂ Brayton cycle, with the MC, the RC and the turbine mounted on a single shaft, the shaft dynamic equation is:

$$(I_t + I_{mc} + I_{rc} + I_{gen}) N \frac{dN}{dt} = W_t - W_{mc} - W_{rc} - W_{gen} - W_{loss} \quad (6-64)$$

Similarly, for the two-shaft nitrogen Brayton cycle, the rotating mass of the generator shaft and the compressors shaft can be modelled as shown in equation (6-65) and equation (6-66):

$$(I_{fpt} + I_{gen})N \frac{dN}{dt} = W_{fpt} - W_{gen} - W_{loss} \quad (6-65)$$

$$(I_{cdt} + I_{lpc} + I_{hpc})N \frac{dN}{dt} = W_{cdt} - W_{lpc} - W_{hpc} - W_{loss} \quad (6-66)$$

Where I_{fpt} is the inertia of FPT, W_{fpt} is the power produced by the FPT, I_{cdt} is the inertia of the CDT, I_{lpc} is the inertia of the LPC, I_{hpc} is the inertia of the HPC, W_{cdt} is the power produced by the CDT, W_{lpc} is the power absorbed by the LPC and W_{hpc} is the power absorbed by the HPC.

The power delivered to the electric generator can be written as:

$$W_{gen} = \frac{W_L}{\eta_g} \quad (6-67)$$

Where W_L is the electric load demand and η_{gen} is the generator efficiency.

6.2.6 Control valve and actuator model

Valves are used for flow control in the cycle or for throttling flow to a desired pressure. Mass and energy storage in a control valve (Figure 6-3) can be considered negligible due to the small volume of the component.

Thus,

$$\dot{m}_o = \dot{m}_i = \dot{m} \quad (6-68)$$

$$h_o = h_i \quad (6-69)$$

The mass flow rate through the valve, \dot{m} , is dependent on the valve's upstream and downstream pressure, P_i and P_o , on the incoming fluid density, ρ_i , and on the fractional valve opening, y . This can be expressed by the algebraic equation (Thomas, 1999):

$$\dot{m} = C_v y \sqrt{P_i \rho_i \left(1 - P_o/P_i\right)} \quad (6-70)$$

Where C_v is the constant valve construction coefficient, which is usually provided by the manufacturer. The fractional valve opening or flow area, y , is defined as the ratio of valve's current flow area to its flow area when fully open. It will depend on the valve stem position, x , (also referred to as valve travel) and the valve flow characteristic dictated by the geometry of the valve. The three common valve characteristic are shown in Figure 6-4. It gives the relationship between valve travel and flow area, which can be represented mathematically as:

Linear valve characteristic:

$$y = x \quad (6-71)$$

Equal percentage or logarithmic characteristic:

$$y = R^{x-1}, \quad R = \text{Constant (between 20 and 50)} \quad (6-72)$$

Quick opening valve:

$$y = x^{\frac{1}{\delta}}, \quad \delta > 0 \quad (6-73)$$

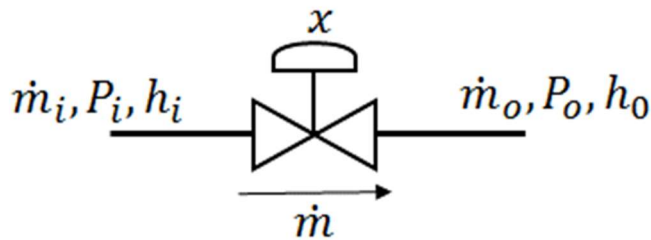


Figure 6-3 Control valve

A relative valve travel, x , of zero means that the valve is fully closed while a value of 1 means the valve is fully open. The valve travel position is usually determined by the actuator based on the signal from the controller. The actuator will drive the valve stem position, x , to its demanded position, x_d , specified by the controller output signal. It will take a certain amount of time for the actuator to move the stem position to the demanded value. Hence, the dynamics of the actuator plus valve can be modelled with a first order exponential lag as follows (Thomas, 1999):

$$\tau \frac{dx}{dt} = x_d - x \quad (6-74)$$

Where τ is the time constant associated with the actuator and x_d is the demanded valve travel.

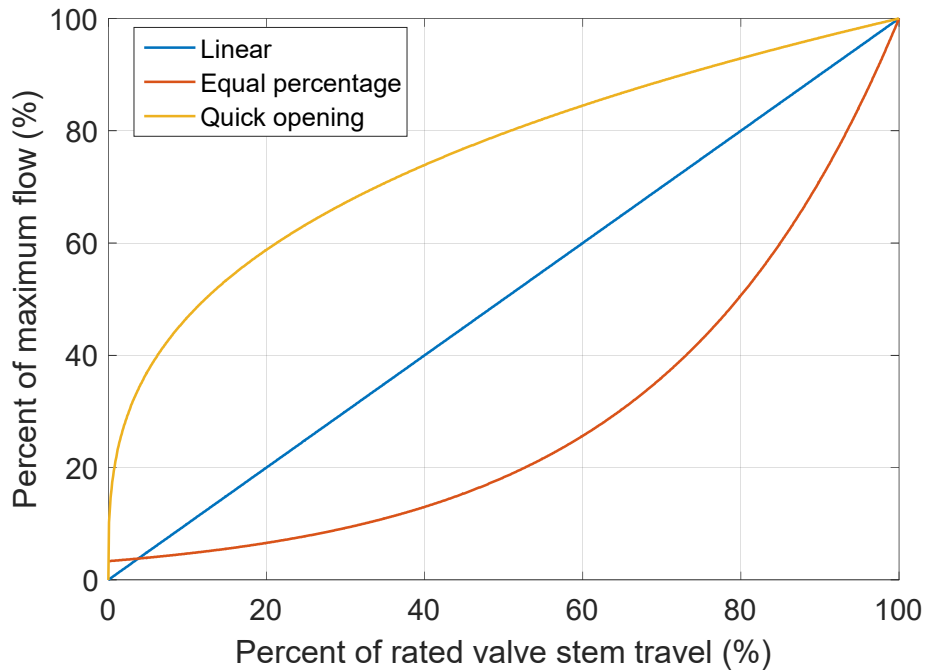


Figure 6-4 Linear, equal percentage and quick opening valve characteristics

6.2.7 Mixing junction model

The mixing junction has two incoming streams, 1 and 2, and an outgoing stream (Figure 6-5). Mass and energy storage in a mixing junction is neglected due to its small volume.

The mass conservation is:

$$\dot{m}_{1i} + \dot{m}_{2i} = \dot{m}_o \quad (6-75)$$

The energy conservation equation is:

$$\dot{m}_{1i}h_{1i} + \dot{m}_{2i}h_{2i} = \dot{m}_oh_o \quad (6-76)$$

Any imbalance in the incoming pressure is resolved by dropping one of the incoming stream pressure to the desired outlet pressure of the mixing junction.

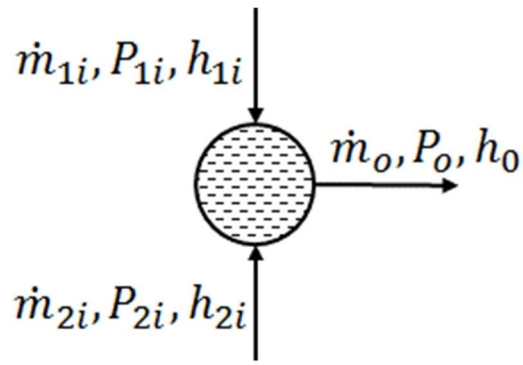


Figure 6-5 Mixing junction

6.2.8 Splitting junction model

A splitting junction has one inlet stream and two outlet stream (Figure 6-6). The mass conservation of the first outlet stream is:

$$\dot{m}_{1o} = y\dot{m}_i \quad (6-77)$$

For the second outlet stream:

$$\dot{m}_{2o} = (1 - y)\dot{m}_i \quad (6-78)$$

Where x is the flow split fraction, \dot{m}_{1o} is the first outlet stream mass flow rate, \dot{m}_{2o} is the second outlet stream mass flow rate and \dot{m}_i is the incoming fluid mass flow rate.

The two outgoing streams will have the same pressure and enthalpy as the incoming fluid such that:

$$h_{1o} = h_{2o} = h_i \quad (6-79)$$

$$P_{1o} = P_{2o} = P_i \quad (6-80)$$

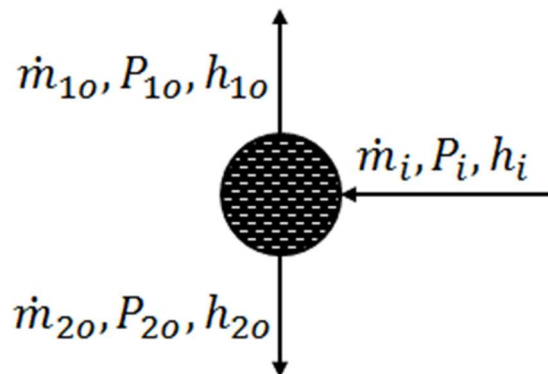


Figure 6-6 Splitting junction

6.2.9 PID controller model

The PID (Proportional-Integral-Derivative) controllers are designed to act on the error signals (i.e. difference between the measured value and the set point) to produce the control signals. The general function of the controller is to keep the controlled variable near its desired value. The control action of a PID is defined as:

$$u(t) = K_p e(t) + K_i \int_0^t e(t) d\tau + K_d \frac{de(t)}{dt} \quad (6-81)$$

Where K_p is the proportional gain, K_i is the integral gain and K_d is the derivative gain.

The three gains are the tuning parameters for the controller. The control signal, $u(t)$, is the summation of the three function of error, $e(t)$, from a specified set point. Proportional control has the effect of increasing the loop gain to make the system less sensitive to load disturbances, the integral of error is used to eliminate steady state error and the derivative term helps to improve closed loop stability.

6.3 Fluid thermodynamic properties for dynamic modelling

The PCS models must be able to simulate fluid properties of CO₂, nitrogen, water and liquid sodium. The fluid properties calculation is expected to be very accurate, able to calculate a wide variety of fluid properties and must be able to handle all the fluid type present in the cycle. In addition, the property calculation must be done in a way that minimise the computation time of the model. According to Carstens (2007), a typical global power plant model transient simulation may make thousands of property calculation at each time step. Therefore, in order to keep the overall cycle simulation time within reasonable limit it is very crucial that the property calculation routines run rapidly.

Simulating CO₂ properties is considerably more challenging due to the highly non-linear behaviour of CO₂ around the critical point which is a key region of operation of the plant. The fluid property source for this simulation is the NIST REFPROP program. A drawback of the REFPROP program is the slow runtime due its complexity. Using REFPROP directly in the Simulink model slowed down the simulation considerably. To overcome this problem, the fluid properties are pre-generated with the REFPROP code and stored in tabular forms as variables in Matlab[®] workspace. These property data variables are then entered into look-up tables in the Simulink model for calculating fluid properties. However, the steady state heat balance calculation for determining the design point conditions still utilises the NIST REFPROP program directly.

6.4 Model integration in Matlab®/Simulink®

The dynamic models of the power plant individual components were developed in Matlab®/Simulink®. Simulink® is a widely used software package for modelling, simulating and analysing dynamic systems. It is able to handle both linear and non-linear continuous time, discrete time and hybrid systems. With Simulink, the non-linear model can be linearized at the operating point for the purpose of control system design.

The dynamic behaviour of each component in Simulink® is described by the modelling equations and thermodynamic properties calculations presented in the previous sections. The component modules are then integrated to build the complete system model by connecting the outputs of the components to the inputs of the appropriate module. The Simulink connection of the power plant unit and the control system block can be found in Appendix B. Firstly, a Matlab® script is run to initialise the dynamic model at the design operating point. The Matlab® script loads the fluid property table, performs design point heat balance calculation and sets the component modelling parameters such as HTC's, friction coefficients and valve coefficients.

6.5 Summary

This chapter presents the dynamic model derivation and development for nuclear closed-cycle GT power plant. The dynamic model equations for the nuclear reactor, coolant pump, compressor, turbine, heat exchanger, rotating shaft and generator, control valve and actuator, mixing junction, splitting junction and PID controller were derived. The methodology adopted for determining the fluid thermodynamic properties was explained. The implementation and integration of the component models in Simulink® was described.

7 Control System Design

7.1 Introduction

Part-load operation and control is an area that needs to be proven in order to determine the overall success of the closed-cycle GTs coupled with nuclear reactors. The usual control methods employed in conventional GTs cannot be applied directly in closed-cycle GT plant. However, closed-cycle GTs present unique opportunities for part load operation and control of the plant. Firstly, in this chapter, the operation and control options that have been proposed in the literature for closed-cycle GTs were examined. The requirements and the objectives of the control systems were presented. Finally, the approach adopted for tuning the controllers were explained.

7.2 Control options for closed-cycle GTs coupled with nuclear reactors

7.2.1 Principles of closed-cycle GT control

According to Yan (1990) and Dostal (2004), reasonable insight into the possible operation and control methods for closed-cycle GT can be obtained by a simplified analysis of the PCS. The analysis assumed ideal gas properties for the working fluid. The cycle thermal efficiency can be defined as:

$$\eta_{th} = \frac{W_{net}}{Q_{in}} \quad (7-1)$$

Where P_{net} is the net mechanical power output and Q_{in} is the input thermal power.

The net power output can be define as (Yan, 1990; Dostal, 2004):

$$W_{net} = \dot{m}C_pT_{Ci} \left[\left(\eta_{T,is} \frac{T_{Ti}}{T_{Ci}} - \frac{\pi^{\frac{\gamma-1}{\gamma}}}{\eta_{C,is}} \right) \left(1 - \frac{1}{\pi^{\frac{\gamma-1}{\gamma}}} \right) \right] \quad (7-2)$$

Assuming a 100% effectiveness for the recuperator, the thermal power input is (Yan, 1990; Dostal, 2004):

$$Q_{in} = \eta_{T,is} \dot{m}C_pT_{Ti} \left(1 - \frac{1}{\pi^{\frac{\gamma-1}{\gamma}}} \right) \quad (7-3)$$

From equations (7-1) - (7-3), the parameters that can be used to control the power output of the plant can be identified. Considering equation (7-2) for instance, the power output is determined

by the mass flow rate, the compressor inlet temperature, the TIT, the turbomachinery efficiencies and the pressure ratio. However, a look at equation (7-1) indicates that the thermal efficiency depends on all these parameters except the mass flow rate of the working fluid. Thus, the mass flow rate can be used to vary the power output without corresponding loss of thermal efficiency. This is not exactly true for a real gas working fluid like s-CO₂ because a change in mass flow rate will affect the density in a non-linear manner and thus lead to a change in the velocity of the working fluid. These effects are not included in the highly idealized sets of equations above. Also, if pressure drops are taken into account, the density and velocity changed lead to a change in pressure drops which will leads to a change in plant efficiency. Nevertheless, the mass flow rate control is the most attractive control scheme for closed-cycle GT plant (Dostal, 2004). It is usually called inventory control or pressure control.

Equation (7-2) shows that the power output can be decreased by decreasing the TIT but this will result in reduction of plant efficiency. On the other hand, the compressor inlet temperature is relatively held constant during operation by the large thermal inertia in the precooler. Pressure ratio is another parameter that can be used for wide range power level control. However, it is better to operate the turbine and compressor at their optimum pressure ratio as much as possible. Adjusting the pressure ratio results in changes in aerodynamic characteristics within the turbomachinery, which leads to a decline in turbomachinery efficiency (Dostal, 2004).

The above-enumerated cycle parameters together with their effects on cycle thermal efficiency and power output formed the basis for the most commonly used control methods for closed-cycle GT power plants. In general, typical control options for modulating the power output of closed-cycle GT are inventory/pressure control, bypass control and reactor/temperature control.

7.2.2 Inventory/pressure control method

This method uses inventory tanks to store the working fluid (Figure 7-1). The working fluid is bled from the PCS at the compressor outlet into the inventory tanks when the output power is to be reduced. It is then injected back at the precooler inlet when output is to be increased. During power reductions, when the working fluid is removed from the CBC and stored in the inventory tank, the system pressure is reduced. This leads to a reduction in fluid density and mass flow rate. The mass flow rate is given as:

$$\dot{m} = \rho AV \quad (7-4)$$

The geometric design of the flow passage fix the cross section area, and as the flow velocity is constant, the mass flow rate is proportional to the density, which is also proportional to the absolute pressure. For an ideal gas working fluid, the thermal efficiency is independent of system pressure. The thermal efficiency is affected only by the increase in relative pressure drop at low

pressures (Dostal, 2004). Similarly, if the turbomachinery inlet temperatures and their speeds were kept constant, the turbomachinery efficiencies will remain practically unchanged since the pressure ratio remain unchanged (constant volumetric flow rates for ideal gas).

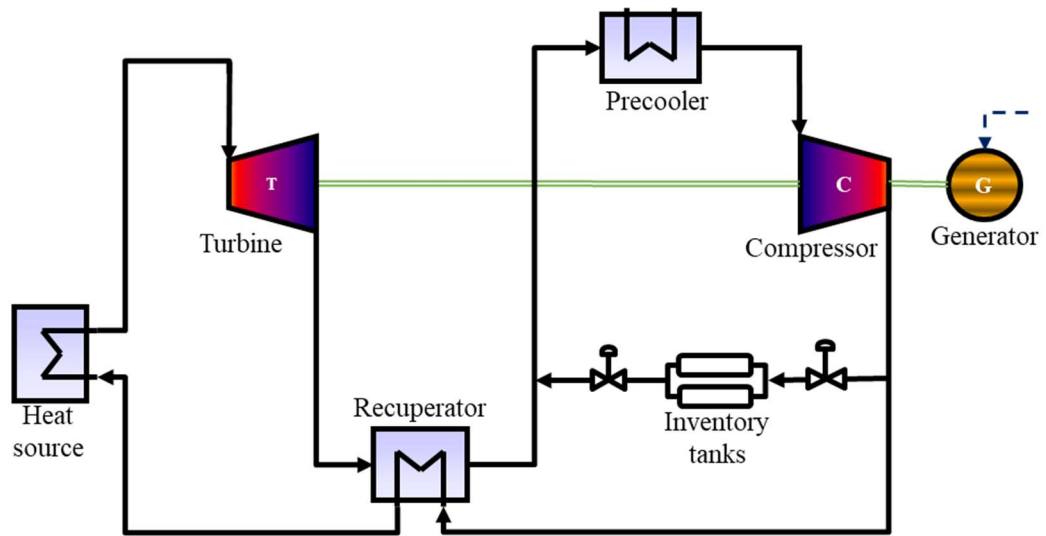


Figure 7-1 Simple CBC plant with inventory (pressure) control

A disadvantage of inventory control is that it requires an inventory tank whose size can be quite large depending on the plant capacity and the power range to be controlled. In addition, the rate of change of power level is very slow and is limited by the size of the control valves (Dostal, 2004; Yan, 1990). Hence, while small closed-cycle GT plants tends to utilise inventory control, the large plant usually do not use inventory control because of the large inventory of fluid that would be required and expected to be transferred between the tank and the power conversion circuit. For instance, the 25 MW Schleswig-Holstein nuclear power plant (KSH), which was developed as part of the European HTR programme, and the 50 MWe Oberhausen II plant both utilized inventory control (Yan, 1990). On the other hand, the large 800 MWe/2000 MWt GT-HTGR project developed by GA did not use inventory control. Instead, only bypass and temperature/reactor control were utilized for regulating the power output and shaft speed (Yan, 1990).

In this thesis, the reactors are of intermediate size (500 MWt) when compared to the above plants. Therefore, the feasibility of utilizing inventory control will still be investigated, though without detailed design and modelling of the inventory tanks.

7.2.3 Bypass control method

In bypass control, the power output is controlled by controlling the mass flow rate through the turbine (Dostal, 2004). Figure 7-2 shows bypass control scheme for CBC with three possible alternative locations of the bypass valve. Part of the high-pressure side working fluid is transferred

to the low-pressure side by regulating the bypass valve. This will result in reduction of the mass flow rate through the turbine as well as reduction of the turbine's pressure ratio and hence a reduction in the power output. For a constant speed machine, the turbine will operate away from its design velocity triangles and hence its efficiency will drop.

A significant advantage of bypass control over inventory control is its fast response to rapid changes in load demand. This is the only option available for fast transient demands in large closed-cycle GT plants since the tank and valves for inventory control would be too large (Dostal, 2004). In small plants, bypass control is used for very low power operation or in case of emergency such as loss of external load. It can satisfy a 10% load step change, which is one of the typical requirements on the control scheme. Hence, bypass control is always present in a closed-cycle GT because none of the other control options can satisfy such requirement (Dostal, 2004).

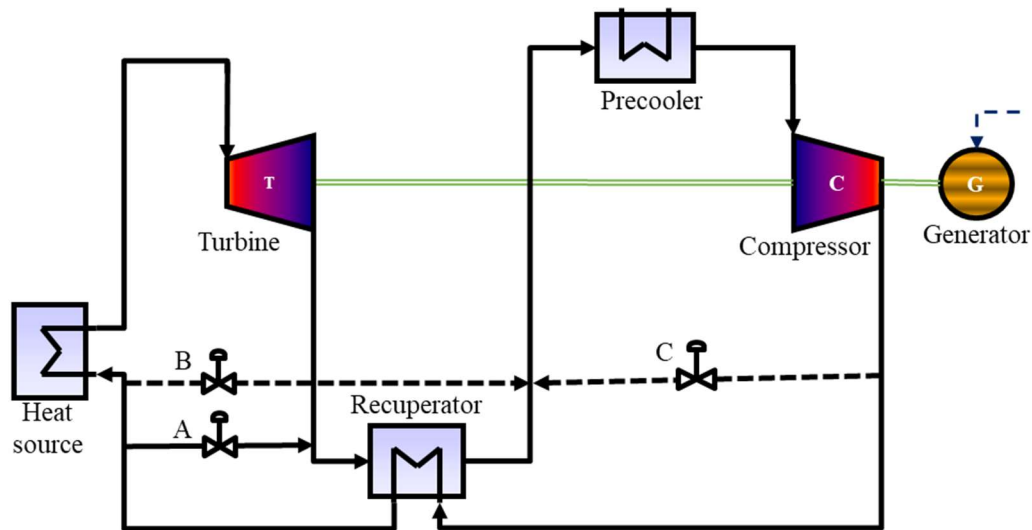


Figure 7-2 Simple CBC with bypass control method showing three possible location of the bypass valve (A, B or C)

7.2.4 Temperature/Reactor control method

As mentioned previously in Section 7.2.1, part load control of closed-cycle GT can be achieved by controlling the TIT. Temperatures around the cycle as well as pressures decrease as the TIT is reduced at part load. In nuclear reactor plants, temperature control is usually achieved by varying the amount of heat transferred to the working fluid in the IHX or reactor core. This is achieved through movement of the control rod and/or varying the torque (and thus speed) of the reactor coolant pump/circulator (Moisseytsev and Sienicki, 2010). The response of temperature control is usually very slow due to the large thermal inertia of the reactor. It is suitable mainly for those plants operating at base load (Dostal, 2004). However, in combination with bypass control, it can be used to control any closed-cycle GT.

According to Moisseytsev and Sienicki (2010), the three alternative schemes for controlling the reactor side of the plant are:

- **Active reactor control:** This option assumes that the reactor can be controlled through the movement of control rods and changing the speed of reactor coolant pump such that the coolant flow rate and its inlet temperature to the IHX remain unvarying. The coolant temperature at the IHX outlet then varies according to the heat removal capability of the closed GT cycle which also changes as the load demand from the electric grid changes.
- **Autonomous reactor control:** This allows the reactor core power and the coolant system pump flow rates to change autonomously in response to change in the heat removal conditions on the Brayton cycle by means of the internal reactivity feedbacks of the reactor core. A constant pump torque is maintained representing unchanging output from the pump electric motors. This option would be the closest equivalent of the active reactor control. There could be a slight increase in the coolant inlet temperature to the IHX. This temperature rise could presumably be precluded or significantly reduced through fine adjustment of the control rods and pump motors.
- **Direct reactor power and flow rate control:** The reactor core power and coolant system flow rates are ideally reduced linearly in a programmed fashion that instantaneously matches the prescribed load demand. The reactor power and flow rate are controlled through the coolant system pump torque. It was assumed that both the reactor power and pump torques vary linearly at the same rate as the grid demand. Theoretically, this approach would provide constant temperatures in the primary loop.

7.2.5 Comparison of the control options

A typical control scheme is usually made up of a combination of the above control methods. Bypass control is used for rapid changes in power demand, and inventory control for the slower transients, while preserving cycle efficiency. Comparing their response time, bypass control has the fastest response time followed by inventory control while temperature (reactor) control is the slowest.

Shown in Figure 7-3 is a comparison of the cycle efficiency as a function of the percentage of rated power for the different control methods (Yan, 1990). The figure is for an ideal gas Brayton cycle and therefore it would not be entirely similar for cycles that use real gases such as CO₂ (Dostal, 2004). For inventory control, the relation between efficiency and fractional power is relatively flat and a small fractional power output can be obtained by operating at low pressure.

In reality, the fluid frictional losses are slightly altered because the decreased density also decreases the flow Reynolds numbers. This increases the importance of viscous losses. The effect is that the efficiency reduces slightly as the power output is reduced because component efficiencies are reduced (Kumar et al., 2000). The serious degradation of efficiency with bypass control is regarded as a disadvantage in relation to inventory control. It should be noted, however, that the severity is important only if the fraction of time spent at less than full power is significant (Bammert and Krey, 1971).

The main features of these control methods are shown in Table 7-1 (Sánchez et al., 2011a). Concerning the operating range, it is worth noting that even if theoretically all the control methods should be able to control the full operating range, there are certain practical constraints that must be accounted for. For instance, widening the load range to be controlled by inventory is limited by the size and cost of the vessel where the working fluid is to be stored, and limits also arise for temperature control due to the thermal integration with the rest of the system. Finally, with respect to part load efficiency, the most effective control scheme is inventory since it is based on keeping the same cycle parameters, pressure ratio and TIT, but at a lower pressure level.

The following operation regimes and suggested control options can be identified for closed-cycle GT plant (Shin, 1975):

- Part-load following
 - Slow response – Inventory (pressure) control with reactor/temperature control
 - Rapid response – Bypass control
- Loss-of-load transient
 - Bypass control to limit shaft over-speeding
- Emergency shutdown
 - Shutdown bypass valve
- Normal start-up and shutdown
 - Starting motor with starting system electric power provided from the grid or emergency diesel generator

In this thesis, only the load following and loss of load transient will be studied.

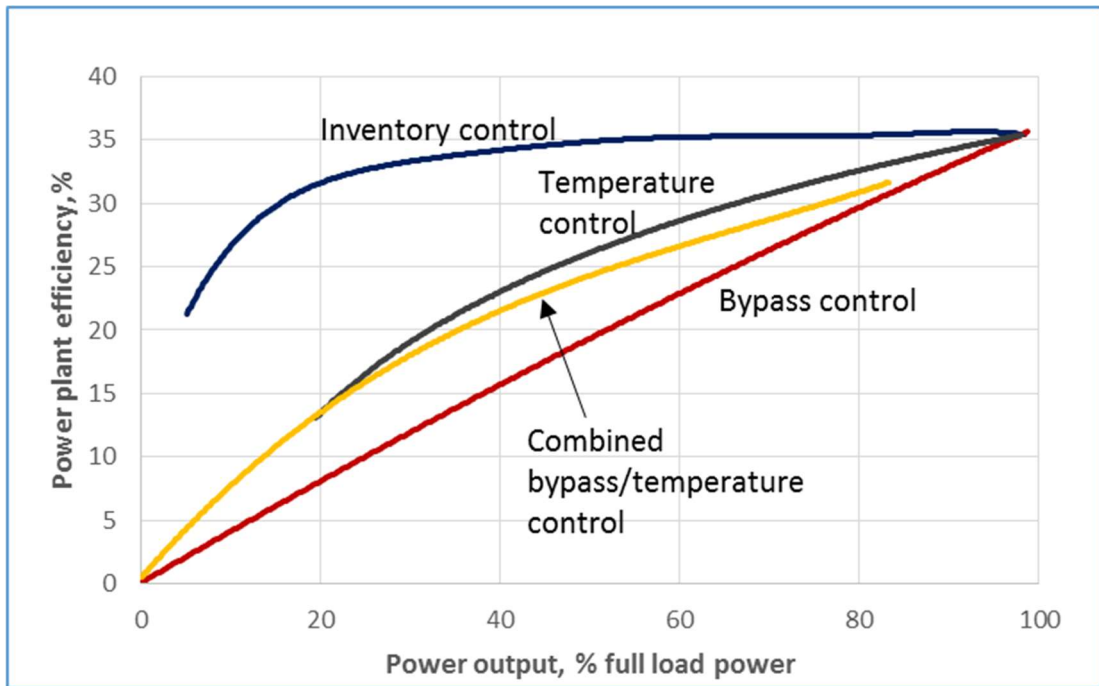


Figure 7-3 Effect of the different control methods on the cycle efficiency

Table 7-1 Features of the control methods

	Efficiency	Operating range	Response time
Inventory	Very good	Acceptable	Poor
Bypass	Poor	Good	Very good
Temperature	Poor	Acceptable	Poor

7.3 Control system requirements and objectives

The control system must be able to adjust the plant to the desired load level and maintain high cycle efficiency as much as possible while also complying with the utility requirements. The requirements of the control system design for this study are:

- Normal load-following of the electrical load between 100% and 50% at the rate of 9% of rated load per 133 seconds ($\sim\pm 4.06\%$ of rated load per minute). This has been specified in accordance with the French utility requirement because this research is part of an ongoing project in France to develop closed-cycle GT power plant. However, this is similar to the utility requirement of most other countries. US utility requires maximum rate of load change of $\pm 5\%$ of rated load per minute (Yan, 1990).
- Minimise generator shaft maximum over-speed following a 100% instantaneous loss of grid load event

The main target for the control system during normal operation is to keep the plant synchronised to the grid while smoothly supplying the electrical load demanded. If there is a mismatch between the frequency of the generated electricity and the grid frequency, the plant will be tripped and disconnected from the grid. Therefore, the generator shaft speed must be maintained within 99 to 101% of the synchronous speed (i.e. 50 ± 0.5 Hz or 3000 ± 30 rpm) by the control system in order to avoid grid separation (Wang, 2009).

During loss of grid load events, the generator is abruptly separated from the grid via opening of the breakers, resulting in an instantaneous 100% load rejection. This extreme stepwise disturbance to the plant leads to a rapid acceleration of the generator shaft. The control system must be able to control the over-speed of the generator shaft within the mechanical design limit of the turbomachines and generator. This is regarded as one of the most severe conditions for closed-cycle GTs as the turbine blade can break away from the rotor if the rotational speed becomes too high (Moisseytsev and Sienicki, 2008). The exact limit of the shaft speed is not available at this stage of the design; however, the control system will be expected to maintain the rotational speed below 120 % of the design value of 3000 rpm during loss of the external load (Wang, 2009).

Limiting the rate of temperature variation in the cycle is another consideration for the control system design. Rapid temperature variation results in thermal shock in the metal structure of the heat exchangers and pipes, which can lead to fatigue.

The objectives of the control system can be summarised as follows:

- To maintain high efficiency during part load operation
- To maintain the generator shaft rotational speed at 3000 ± 30 rpm during normal operation
- To limit the generator shaft over-speed below 120 % during loss of load events
- To minimise component thermal stress during load transient by limiting the rate of temperature variation
- To maintain the TIT at the design value (530 °C and 275 °C for the SM-SFR/Nitrogen and the SM-PWR/s-CO₂ plant respectively)
- To maintain the nuclear reactor core outlet temperature at the design value (545 °C and 300 °C for the SFR and PWR nuclear reactor respectively)
- To maintain the compressors' inlet temperature at the design value (27 °C and 32 °C for the nitrogen and s-CO₂ cycle respectively)
- To match the RC outlet pressure to the MC outlet pressure in the s-CO₂ cycle

7.4 Tuning of the PID controllers

The parameters will need to be tuned for the PID controllers to provide control actions satisfying the specific system requirements. The three constant parameters of the controllers to be tuned are the proportional gain, the integral time constant and the derivative time constant. The tuning of these controller parameters is vital to obtaining stable dynamic performance responses. The approach adopted for tuning of the controllers involve using the PID automatic tuning features in Simulink and an iterative adjustment of the controller parameters by rule of thumb. Each of the single-input-single-output (SISO) feedback loops is auto tuned one at a time with the interaction from other loops removed. Then by observing the dynamic response, the parameters are manually adjusted iteratively.

To start the tuning process, the Simulink PID Tuner interface is launched for the PID controller. Then the software will automatically computes a linear plant model from the Simulink model and design an initial controller. Further tuning is carried out by adjusting design criteria such as the response time and transient behaviour in the PID Tuner interface. The tuner computes PID parameters that stabilise the system based on the design criteria specified. The computed PID parameters are exported back to the PID controller block in the model. This process is repeated for each of the SISO feedback loops. All the feedback loops are then connected and their performances are verified. Due to interactions between the loops, the control system performance is usually not acceptable at this stage. Hence, the PID parameters are iteratively tweaked until an acceptable system response is achieved.

Obtaining a linear model of the plant is required for controller design in Simulink. However, the complexity of the developed model makes the linearization of the whole plant difficult for the Simulink linearization tool. It might be possible to ease the linearization process by system identification with the simulated response data. Furthermore, the control system scheme used in this study consist of multi-loop SISO feedback controls for changing power level and maintaining the plant variables within reasonable values. However, real life plant is regarded as a time variant nonlinear multi-input-multi-output (MIMO) system with strong interactions and coupling between the plant inputs and output variables. The interactions and coupling between the plant variables make tuning the controller parameters of the conventional SISO feedback loops non-trivial. Hence, the control systems can be improved by using advanced multivariable control design strategies such as Model Based Predictive Control (MBPC).

Since the focus of this conceptual study is on understanding the dynamic behaviour of the plant and the control system options during load-following operation and loss-of-load event, this controller tuning approach will suffice for the present. However, detailed and advanced controller

design approach can be attempted at later stage of the study when more data about the plant is available.

7.5 Summary

This chapter presents the general principles of control for closed-cycle GT and highlights the common control methods. The control system configuration is designed for the SM-SFR/Nitrogen nuclear plant and the SM-PWR/s-CO₂ nuclear plant. The approach adopted for the tuning of the PID controllers was explained. In the next two chapters, the results of the transient performance of the nuclear power plants under normal load-following and instantaneous loss of load using the control methods explained in this chapter will be presented.

8 Dynamic Performance Analysis of the SM-SFR Coupled with Nitrogen Cycle (SM-SFR/Nitrogen) Plant

8.1 Introduction

There exist substantial operation and control experience for the conventional nuclear steam Rankine cycle power plants. Hence, normal operation transients and sudden disconnection from the grid is unlikely to pose any major challenge for the operation of such plant. Conventional nuclear Rankine cycle power plants employ sophisticated, fast-acting and reliable bypass valves to avoid shaft over-speeding during loss-of-load transient. The initial shaft angular acceleration is dependent on the moment of inertia of the shaft and attached components. Turbomachinery for closed-cycle GT are smaller and thus the shaft and attached components have a much smaller inertia than steam cycle power plant. Therefore, operating a nuclear plant with closed-cycle GT raises concerns regarding the control of the PCS and of particular interest is the risk of turbomachine over-speeding beyond a safe limit during complete loss of load (Golovko et al., 2000).

Moreover, while the conventional nuclear power plants are large in capacity and are usually operated at base load, the SMRs with closed-cycle GT power plants will be expected to perform load-following operation. In addition, the proposed two-shaft configuration for the nitrogen cycle could make the operation and control more challenging compared to single-shaft arrangement. The shaft carrying only a turbine and a generator is more difficult to control for over-speed due to the smaller inertia and the absence of compressor work to slow the shaft.

The aim of this chapter is to discuss the results of the transient response of the two-shaft SM-SFR/Nitrogen nuclear power plant during normal load following and loss of load operation. The dynamic model development and derivation for nuclear plant with closed-cycle GT has been described in Chapter 6. The developed dynamic model will be simulated to analyse the transient behaviour and control characteristics of the plant during load following and 100% loss of grid load events. The transient simulations will demonstrate the interactions between the control systems and the PCS. This will be used to explore the controllability of the plant based on the operational requirements specified for normal load-following and sudden loss of load operating conditions.

In the next chapter, similar results will be discussed for the SM-PWR/sCO₂ closed-cycle GT plant.

8.2 Automatic control system configurations for the SM-SFR/Nitrogen nuclear power plant

In this section, a control system suitable for automatic operation of the nuclear plants is designed based on the principles of closed-cycle GT control discussed in Section 7.2. The adopted control strategy must aim to satisfy the control requirements and objectives highlighted in Section 7.3. Hence, the main functions of the automatic control system implemented in this study are:

- Control power output to match changes in load demand
- Control turbine-generator shaft speed and maintain synchronous speed (or grid frequency)
- Control reactor power and maintain the reactor outlet temperature
- Control primary side flowrate and maintain TIT
- Control cooling water flowrate and maintain compressor inlet temperature

Table 8-1 summarises the pairing of the manipulated inputs and the controlled outputs for automatic control of the nuclear closed-cycle GT plants.

Table 8-1 Pairing of the manipulated inputs and controlled output for plant automatic control system

Manipulated variable	Controlled variable	Comment on varied variables
Mass inventory of working fluid	Turbine output power	Working fluid pressures and mass flow rate change as inventory in cycle changes
Bypass valve stem position	Shaft rotational speed	Turbine output power varies as flow rate through the turbine varies
Control rod reactivity	Reactor core outlet temperature	Reactor fission power varies as the control rod position is varied
Reactor coolant pump torque	TIT	Flow rate of reactor coolant changes as the pump speed/torque changes
Cooling water pump	Compressor inlet temperature	Flow rate of water changes as the pump speed changes

The plant layout and the control scheme implementation for the SM-SFR/Nitrogen nuclear plant is shown in Figure 8-1 and the block diagram for each of the control system is shown in Figure 8-2. The implemented control methods are:

- **Inventory control:** The block diagram for the inventory control is shown in Figure 8-2(a). Detailed model of the inventory tank and the associated valves are not performed in this study. Instead, inventory regulation was achieved by assuming a direct regulation

of the mass of working fluid in the PCS. The mass inventory of nitrogen gas in the PCS is programmed as a function of the load demand, W_L . The inventory values are predetermined for operation at various power level and the interpolation of these values are stored inside the programmed block. Therefore, if the electric load demand changes, the required mass inventory of working fluid is calculated and used as the new mass inventory signal for the PCS. Consequently, the nitrogen gas density, pressure and mass flow rate would change leading to a change in mechanical power output delivered to the generator.

- **Bypass valve control:** The bypass valve is situated between the power turbine inlet and the recuperator hot inlet (Figure 8-1). The first bypass valve, V1, which is a linear valve, is used during normal load-following operation. The second valve, V2, which is a quick opening valve, is utilized during instantaneous loss of grid load. It is believed that the relatively low temperature of this plant will permit the use of conventional industrial valves at turbine inlet. This is unlike HTGR plant where the bypass valve have to be located before the reactor or the IHX due to the high temperature at turbine inlet. Locating the bypass valve close to the turbine will ensure a faster response to load change.

The block diagram of the feedback control loop for the bypass valve controller is shown in Figure 8-2(b). The bypass valve primarily control the turbine-generator shaft speed, N . Any imbalance between the load demand, W_L , and power output, W_o , will result in either acceleration or deceleration of the turbine-generator shaft speed. The measured turbine-generator shaft speed by the sensor is compared with the reference synchronous speed, N_0 , which is 3000 rpm in this case. The bypass valve controller then uses the error to produce a control signal based on the PI(D) algorithm. The control signal is sent to the bypass valve actuator to manipulate the valve stem position and thus the opening and closing of the valve. For instance, if the load demand decreases, the shaft speed accelerates, then the controller will act to open the bypass valve and divert part of the flow away from the turbine to the recuperator inlet immediately after the turbine outlet. The resulting lower flow through the turbine will lead to a decrease of the turbine pressure ratio. The combined effects of reduced mass flow rate and reduced enthalpy drop will result in a reduction of the power output to match the load demand. The turbine-generator shaft speed is then returned to the reference value. Bypass valve control is very useful for quick reduction of the power output especially when there is a sudden loss of electric load.

- **Control rod reactivity control:** The control rod system usually have a drive mechanism, which is able to move the rods in and out of the reactor core to alter the neutron flux density. The block diagram of the feedback control loop for the rod reactivity control is

shown in Figure 8-2(c). The control rod is utilized primarily to control the reactor core outlet temperature. However, manipulating the core outlet temperature as a means of actively controlling the reactor power to follow the load demand is difficult due to the large thermal inertia of nuclear reactor (Yan, 1990). Therefore, the objective of the control rod regulation in this study is to maintain a constant core outlet temperature at the design steady state value of 545 °C.

During part load operation of the plant, the reactor inlet condition is disturbed resulting in changes in the core outlet temperature. The difference between the core outlet temperature, T_{ro} , and the desired design temperature, $T_{ro,0}$, is fed into the rod reactivity controller. The controller then actuates the control rod drive mechanism, which varies the position of the control rods in the reactor core. The movement of the control rod in the core varies the inserted rod reactivity, ρ_{rod} , thus changing the reactor fission power until the actual core outlet temperature equals the desired set point value.

- **Pump torque control:** If the conditions of the liquid sodium and nitrogen gas at the inlets of the Na/N₂ IHX remain unaltered, the TIT will also remain unaltered. However, during changes in power level, the fluids conditions will change and so will the TIT. Any changes in the TIT can be offset by adjusting the liquid sodium flow rate in the primary circuit.

The block diagram of the feedback control loop for the pump torque controller is shown in Figure 8-2(d). The aim of the pump torque control is to maintain the TIT at its design value of 530 °C by adjusting the primary side flow rate. The pump circulates the liquid sodium coolant in the primary circuit. The mass flow rate of the liquid sodium is proportional to the pump speed, and thus to the torque supplied to the pump by an electric motor. Therefore, the pump torque can be manipulated to control the TIT.

- **Cooling water control:** The cooling water PID controllers (Figure 8-1 and Figure 8-2(e)) serves to maintained the compressors inlet temperatures at 27 °C. The conditions of the cooling water supplied to the cold side of the precooler and intercooler are boundary conditions to the PCS model. The controller controls the precooler and intercooler outlet temperatures, T_{ci} (i.e. LPC and HPC inlet temperatures) by manipulating the mass flow rates of the cooling water, \dot{m}_w .

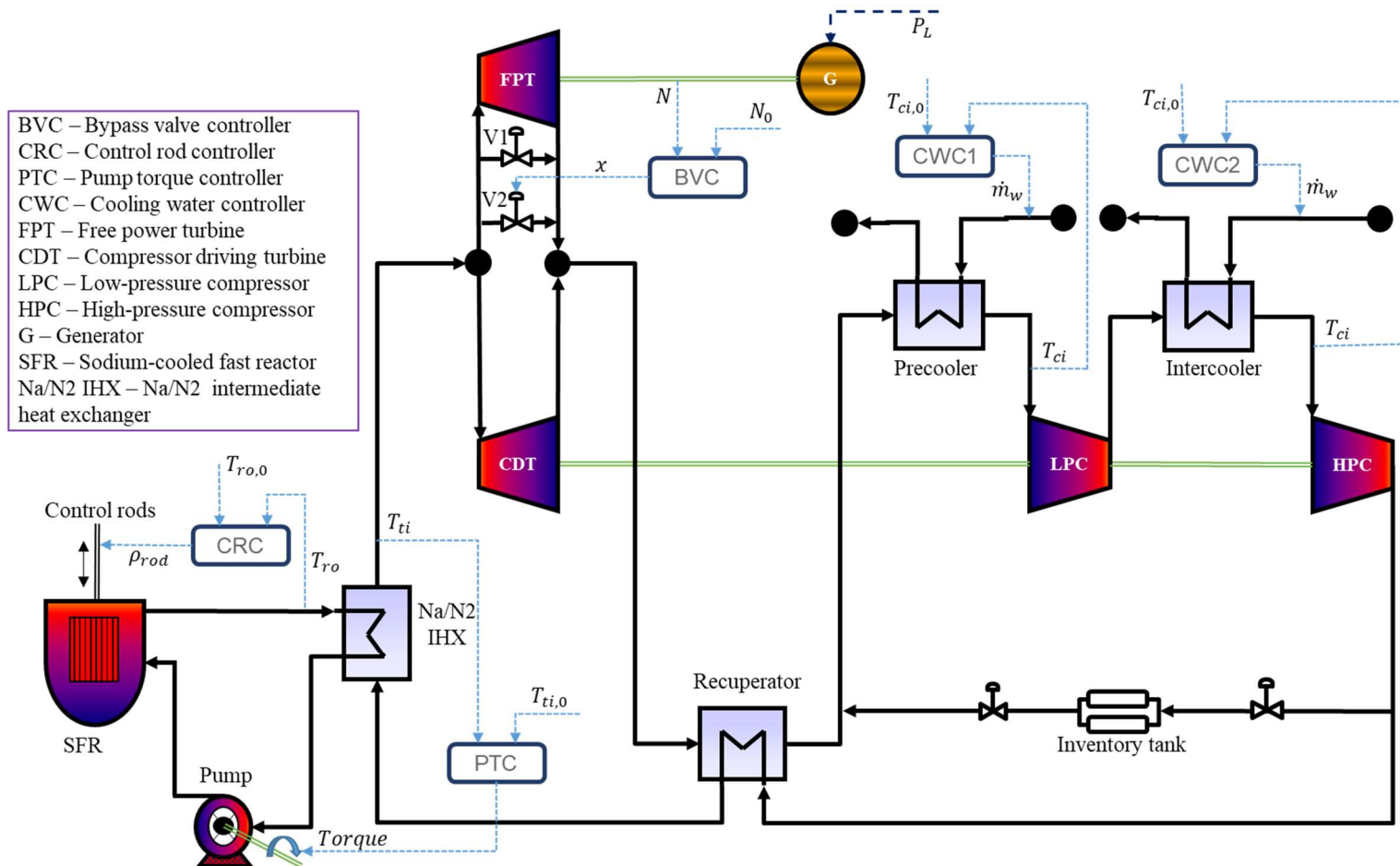
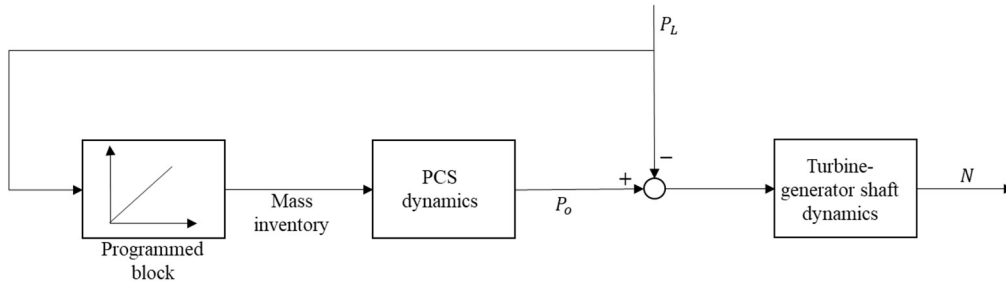
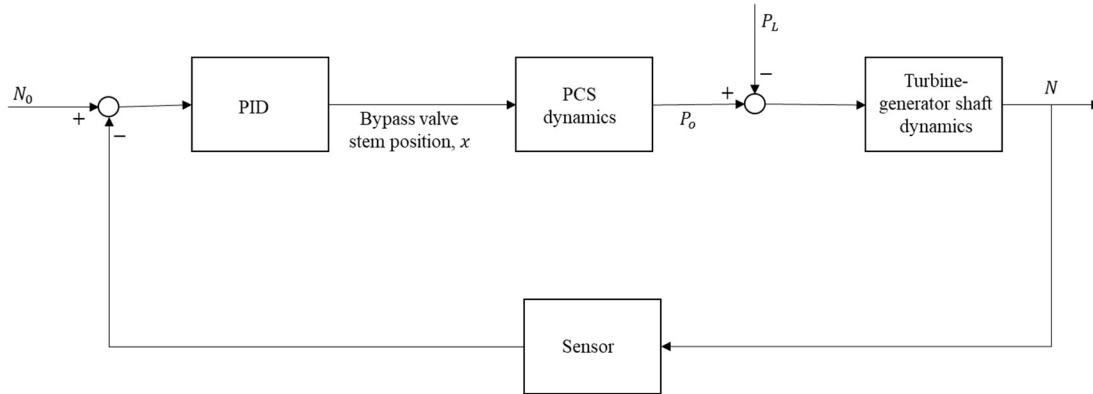


Figure 8-1 Control scheme for the SM-SFR/Nitrogen nuclear power plant

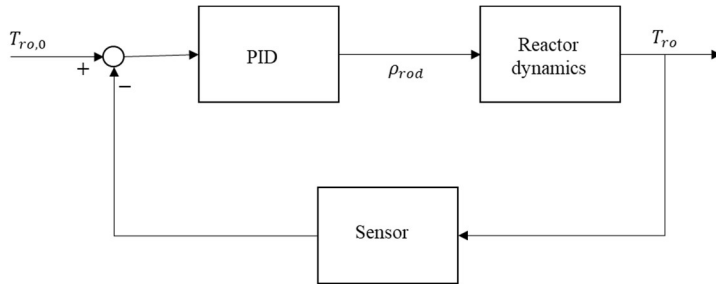
(a) Inventory regulation



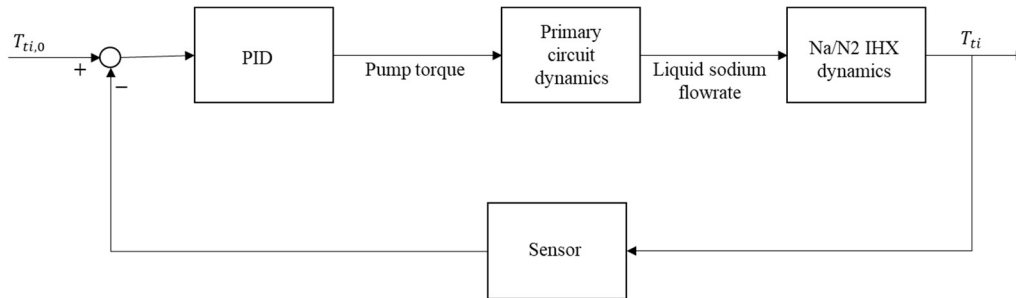
(b) Bypass valve control



(c) Control rod reactivity control



(d) Pump torque control



(e) Cooling water control

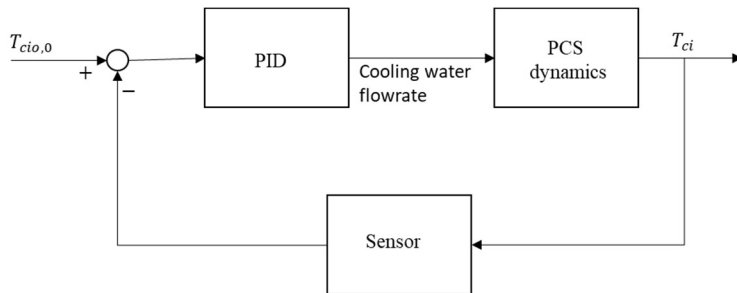


Figure 8-2 Block diagram of the implemented control methods

8.3 Plant's design point conditions and components parameters

The simulated nuclear nitrogen CBC power plant uses a Na/N₂ IHX to transfer the heat energy of the SM-SFR to the nitrogen PCS. The simulation included both the primary circuit (i.e. the reactor side) and the PCS. The proposed two-shaft layout of the PCS and the plant's design point conditions have been presented in Chapter 4. These values represent the full load steady state condition and are set as the initial values for the dynamic simulation. The design of the heat exchangers and turbomachinery have also been reported in Chapter 4. The industrial partner has provided the design of the pipes and the inertia of the rotating components. The plant's design point values and components parameters are summarised in Table 8-2.

With a 500 MWth reactor power and core outlet temperature of 545 °C, the turbines inlet temperature is 530 °C. The precooler and intercooler cooling water are provided at 20 °C. The recuperator is to recover the energy in the exhaust of the turbines. The CDT drives the LPC and the HPC. The compressor shaft rotates at 8000 rpm at the design operating point. The FPT-generator shaft rotates at 3000 rpm because the generator is synchronised with the grid at a frequency of 50 Hz. During part-load operation, the compressor shaft is allowed to vary while the FPT-generator shaft is maintained at the synchronous value with the aid of the control system.

Table 8-2 Summary of plant's design point conditions and parameters

Parameter	Value
Reactor thermal power	500 MWth
Reactor outlet temperature	545 °C
Turbines inlet temperature	530 °C
Cooling water supply temperature	20 °C
Compressors inlet temperature	27 °C
Maximum cycle pressure	180 bar
Total mass flowrate of nitrogen	3027.23 kg/s
Reactor side mass flowrate	4046.47 kg/s
Cooling water mass flowrate	Precooler: 1384.33 kg/s Intercooler: 1168.19 kg/s
FPT-generator shaft speed	3000 rpm
Compressors shaft speed	8000 rpm
Recuperator fluid volume (Hot or cold side)	27.6 m ³
Precooler fluid volume	3.9 m ³
Intercooler fluid volume	3.5 m ³
Na/N ₂ IHX fluid volume	4.8 m ³
Turbomachinery fluid volume	LPC: 2.5x10 ⁻² m ³ HPC: 4.2x10 ⁻² m ³ CDT: 4.4x10 ⁻² m ³ FPT: 0.46 m ³
Mass of heat exchangers metal	Recuperator: 508,080 kg Precooler: 79,954 kg Intercooler: 72,574 kg Na/N ₂ IHX: 99,736 kg
Electric power output	197.22 MWe
Efficiency	39.44%

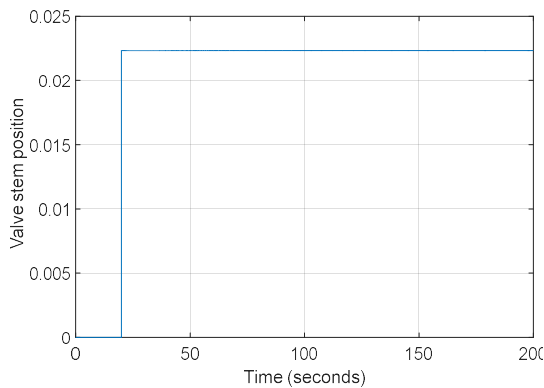
8.4 Open loop step response of the SM-SFR/Nitrogen plant model

The open loop response provides the normal dynamic response of the process by itself, with no control (Don and Robert, 2008). Therefore, the dynamic characteristics of the plant were observed by simulating the transient responses to step changes in the bypass valve stem position, mass inventory setting and control rod reactivity. These are the main manipulated inputs with potential for controlling the power output from the plant. The step changes were applied at time equal to 20 seconds and the amount of step changes were selected to achieve about 10% reduction in the output power supplied to the generator. However, the electrical load demand was kept at the full load design value. Therefore, the negative torque on the turbine generator shaft is expected to cause a reduction in the shaft speed. The simulations were carried out without any feedback

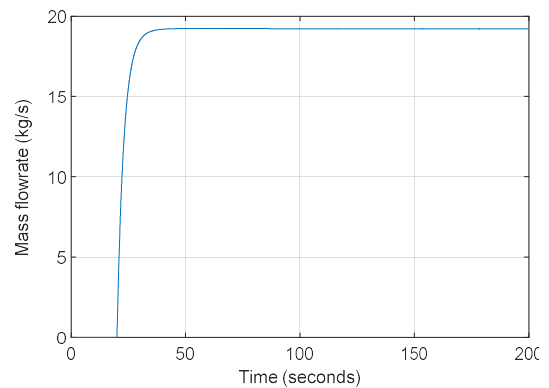
control action except for the case of mass inventory where the reactor side has to be controlled to prevent temperature cross over in the IHX.

Figure 8-3 shows the open loop transient responses to a step change in the bypass valve opening. The bypassed mass flow rate is seen to rise quickly from zero after the sudden opening of the valve (Figure 8-3(b)). Consequently, the power output and the shaft speed drop quickly to new levels (Figure 8-3(c) and (d)). The power output reduces to about 90% of full load value within 3 seconds of the step change in valve opening. Reactor power reduces only by about 3% mainly due to the negative reactive feedback (Figure 8-3(c)). Therefore, it is possible to change the power output quickly without having to actively control the reactor power by utilising bypass valve control.

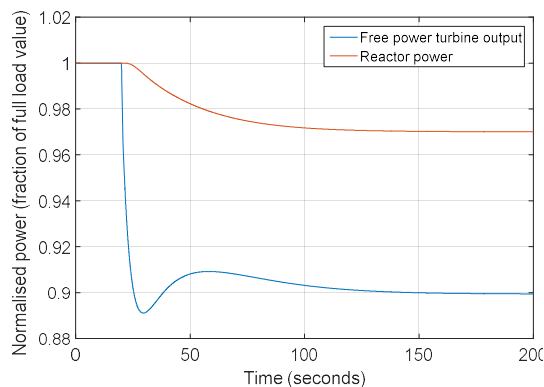
(a) Step change in bypass valve stem position



(b) Bypass valve mass flow rate



(c) Turbine power output and reactor power



(d) Turbine-generator shaft speed

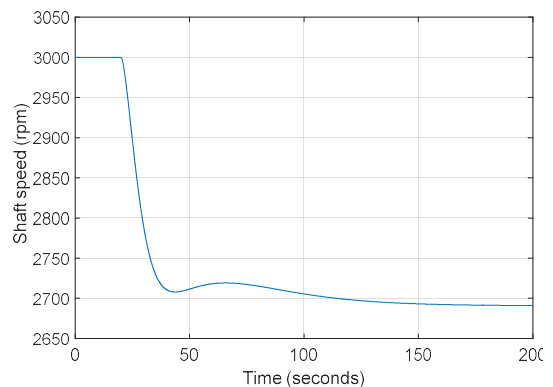
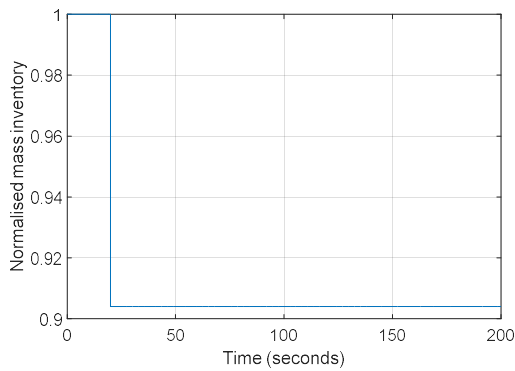


Figure 8-3 Plant's open loop transient response to step change in bypass valve opening showing the mass flow rate through the bypass valve, the free turbine power output supplied to the generator, the reactor fission power and the turbine-generator shaft speed

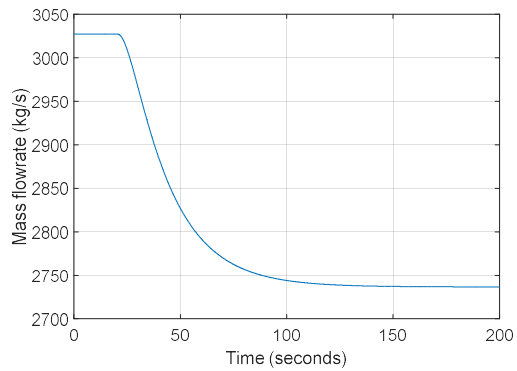
Transient responses to step change in mass inventory setting is shown in Figure 8-4. In response to the step reduction in mass inventory setting, the nitrogen gas mass flow rate and the system pressure are reduced. The power output also drops to new a new value due to the reduction in mass flow rate. The power output drops to 90% of the initial value about 100 seconds after the step change. Reducing the nitrogen gas mass flow rate in the PCS without any corresponding

change in the sodium coolant in the primary side can result in excessive heating of the nitrogen in the IHX. The nitrogen gas could be heated to the extent that the TIT equals the reactor outlet temperature. In order to avoid such situation, the TIT and reactor outlet temperatures were controlled to remain at the design values by manipulating the sodium mass flow rate and the control rod reactivity during inventory change. Figure 8-4(d) shows the turbine inlet and reactor outlet temperature as well as IHX nitrogen inlet and sodium outlet temperature transients during the step change in mass inventory with reactor side control.

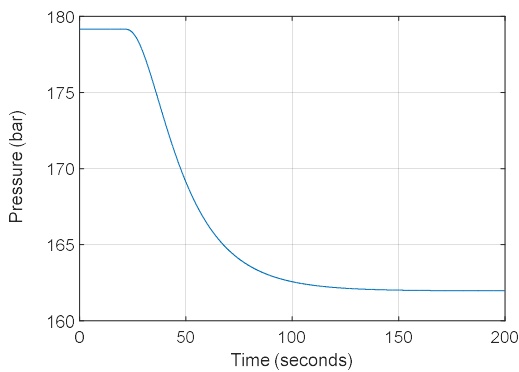
(a) Step change in mass inventory of nitrogen



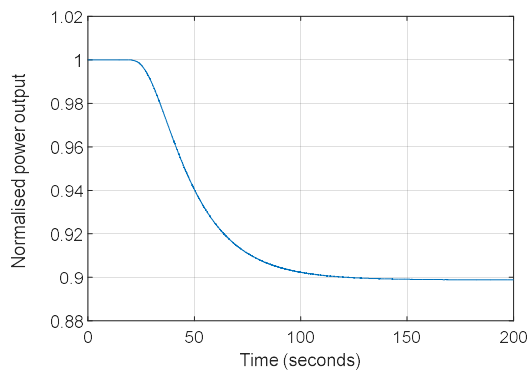
(b) Mass flow rate of nitrogen fluid



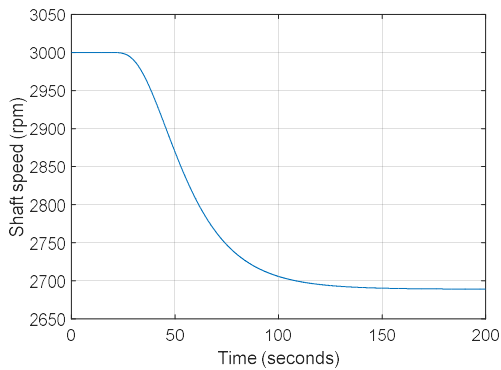
(c) TIP



(d) FPT output



(e) Turbine-generator shaft speed



(f) IHX temperature

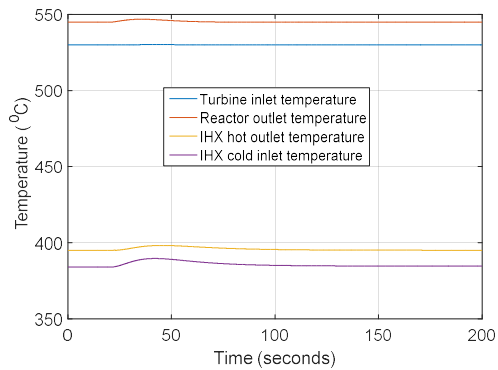


Figure 8-4 Plant's open loop transient response to step change in mass inventory setting showing the mass flow rate of nitrogen, the TIP, the FPT output supplied to the generator, the turbine-generator shaft speed and the IHX terminal temperatures

Figure 8-5 shows the open loop transient responses to step change in control rod reactivity. The insertion of negative rod reactivity results in reduction of reactor outlet and TITs (Figure 8-5(b)). The power output is reduced because of the drop in the TIT. It took about 130 seconds after the step change for the power output to drop to 90% of the initial value.

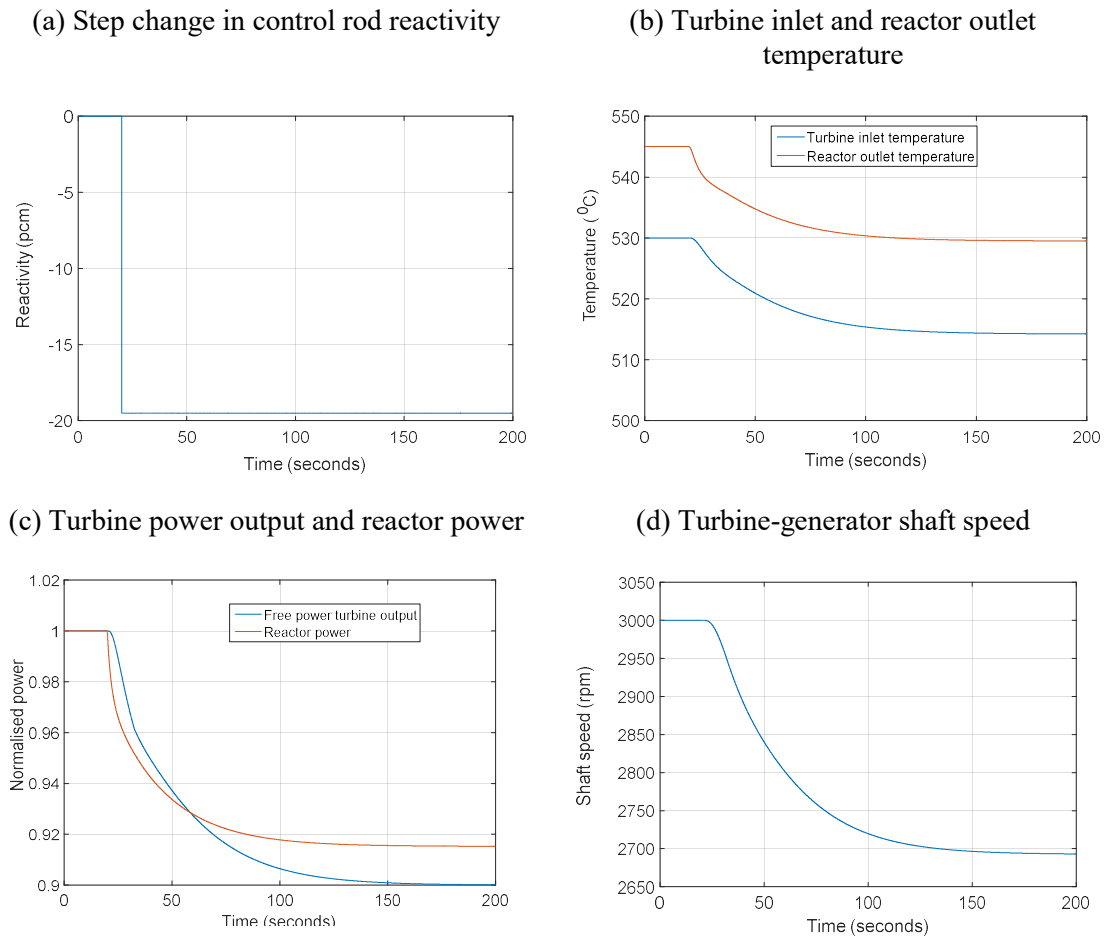


Figure 8-5 Plant's open loop transient response to step change in control rod reactivity showing the turbine inlet and reactor outlet temperatures, the FPT output supplied to the generator, the reactor fission power and the turbine-generator shaft.

For the purpose of plant control, bypass valve and inventory regulation were employed for power output/shaft speed control while control rod was used to maintain the reactor outlet temperature at the design value. The mass inventory is manipulated on a programmed basis without using any feedback measurement.

8.5 Normal load following between 100% and 50%

In this section, plant transient response to ramp load changes between 100% and 50% of full load at a rate of 9% per 133 seconds are simulated to study the dynamic behaviour of the plant during normal load following operation. Starting at 200 seconds the electric load demand decreases from 100% at a rate of 9% per 133 seconds as shown in Figure 8-6. At 939 seconds, the load reaches the 50% level and is maintained at this partial load until 3000 seconds. Then an up load from the

50% partial load back to the 100% level at a rate of 9% per 133 seconds follows. At 3739 seconds, the 100% load level is reached and is maintained until the end of the simulation at 6000 seconds.

The following control strategies were investigated: (1) Bypass valve control only (2) Bypass valve control with reactor side control (3) Inventory control with reactor control (4) Bypass valve and inventory control with reactor control. In all instances, the cooling water is regulated to maintain the compressors inlet temperatures at 27 °C. Typical values of the PID controller parameters obtained from the tuning process are shown in Table 8-3.

Table 8-3 Proportional, integral and derivatives gain parameters of the PID controllers

Controller	K_p	K_i	K_d
Bypass valve	-2×10^{-4}	-2×10^{-6}	-8×10^{-3}
Control rod reactivity	4.9×10^{-5}	2.1×10^{-7}	1.1×10^{-3}
Sodium pump torque	5×10^{-5}	1.5×10^{-6}	9×10^{-7}
Precooler cooling water	-3×10^2	-2×10^2	-
Intercooler cooling water	-3×10^2	-2×10^2	-

8.5.1 Control strategy 1: Bypass valve control only

This section will present the simulation results of load following operation engaging bypass valve control alone. That is, no inventory regulation and no reactor control (control rod position and reactor coolant pump torque are held constant). Cooling water control is used to maintain the compressor inlet temperature at design values. Figure 8-6 shows the load demand variation and the transient response of turbine power output and reactor fission power. The turbine output power is adjusted to follow the load demand smoothly by the bypass valve controller.

Figure 8-7 shows the FPT-generator shaft speed transient response. During the load reduction period between 200 seconds and 939 seconds, a positive torque is continuously present on the FPT-generator shaft due to excess power produced by the FPT. This leads to an increase of the shaft rotational speed away from the set point of 3000 rpm. The bypass valve controller, sensing the change in shaft speed, acts on the bypass valve actuator to open the bypass valve in order to return the shaft speed to the set point. As the bypass valve opens, the nitrogen flow bypasses the FPT. Hence, the FPT mass flowrate decreases from the initial value of 1442 kg/s to 1321 kg/s and the bypass mass flow rate increases from 0 to 121 kg/s as shown in Figure 8-8. The reduced mass flow rate through the FPT causes the outlet pressure of the turbine to increase and consequently the FPT pressure ratio reduces (Figure 8-9). The combined effects of the decrease in the turbine mass flow rate and pressure ratio lead to a decrease of the turbine output power as shown in Figure 8-6.

In the period between 939 seconds and 3000 seconds when the load demand is maintained at the 50% of full load value, the flow through the bypass valve and the flow through the FPT are maintained at their new values. The turbine output power is kept at 50% of the full load power, just like the electric load demand. The balance of the turbine power and load demand helps to maintain the FPT-generator shaft rotational speed at the reference value. During load increase from 50% to 100%, a negative torque is continuously present on the shaft, which leads to a decrease in the shaft speed. The bypass valve controller then acts to close the bypass valve resulting in an increase in FPT mass flow rate and power output. After the 100% load has been reached, the bypass valve is fully closed and all the other plant conditions return to their initial value. Throughout the load following operation, the deviation of the FPT-generator shaft speed from the set point is within ± 19 rpm. Hence, the rotational speed is maintained well within the target 3000 ± 30 rpm by the bypass valve controller.

Figure 8-10 shows the variation of the precooler and intercooler cooling water flowrates by the cooling water controllers. The compressors inlet temperatures are maintained at 27°C by the cooling water controllers (Figure 8-11). Figure 8-12 shows the temperature variations at reactor outlet, reactor inlet, turbine inlet, recuperator hot side inlet and Na/N₂ IHX cold side inlet. The reactor outlet temperature varies from 545°C to 556°C and back to 545°C during the transient because control rod has not been used to maintain it at the reference value. Similarly, the TIT varies between 530°C and 545°C since coolant flowrate is not been adjusted by the pump to maintain the TIT at the reference value. This variation of the TIT and the reduction of the FPT mass flowrate will shift the turbine operating points from the design point. The recuperator hot side inlet temperature increases from about 410°C to 449°C and decreases back to 410°C during the transient. The temperature rise can be attributed firstly to the rise in FPT outlet temperature as its operating points move from the design point and secondly due to mixing with a higher temperature bypass flow, which is diverted directly from the turbine inlet. The variation of the recuperator hot side inlet temperature results in the increase of the Na/N₂ IHX cold side inlet temperature from 384°C to 420°C and back to 384°C . Consequently, the heat removed from the primary loop through the Na/N₂ IHX is reduced during part-load operation and the reactor inlet temperature increases from 396°C to 433°C .

The increased reactor inlet temperature will result in changes in the average coolant and fuel temperature (Figure 8-13). The increased average coolant temperature produces a positive reactivity feedback while the increase fuel temperature produces a negative reactivity feedback as shown in Figure 8-14. The total core internal reactivity is negative during load reduction and positive during load rise. Hence, the reactor fission power reduces during load reduction and increases during load rise solely due to the effect of the reactivity produced by the change in fuel and coolant temperatures. At 50% load demand, the reactor power is about 86% of the full power

level (Figure 8-6). The rate of reduction of the reactor fission power is less than that of the load reduction during part load operation, which indicates a decrease in plant efficiency with bypass valve control as shown in Figure 8-15.

Figure 8-16 shows the variation of the power consumed by the LPC and HPC and the power delivered by the CDT and FPT during the load following transient. The CDT power increases from 222 MW to 243 MW and back to 222 MW due to the changes in TIT. Therefore, the compressor shaft speed increases from the nominal value of 8000 rpm to about 8230 rpm during the transient. Similarly, the LPC and HPC power increase by about 11 MW. The FPT power is reduced from 202 MW to 104 MW and increased back to the 202 MW through the action of the bypass valve controller.

The results of normal load following simulation with bypass valve control alone show that bypass valve control is capable of modulating the power output level to follow the load demand while maintaining the shaft speed within the required limit. However, the loss in thermal efficiency during part-load operation is about 16% point. Also, the recuperator hot side inlet temperature, the Na/N₂ IHX cold side inlet temperature, the reactor inlet temperature, the reactor outlet temperature and TIT increase by about 11 °C - 39 °C during the transient. The maximum temperature variation of 39 °C takes place at the recuperator hot side inlet. These temperature variations could cause thermal stresses on the heat exchangers and the reactor structures (Wang, 2009).

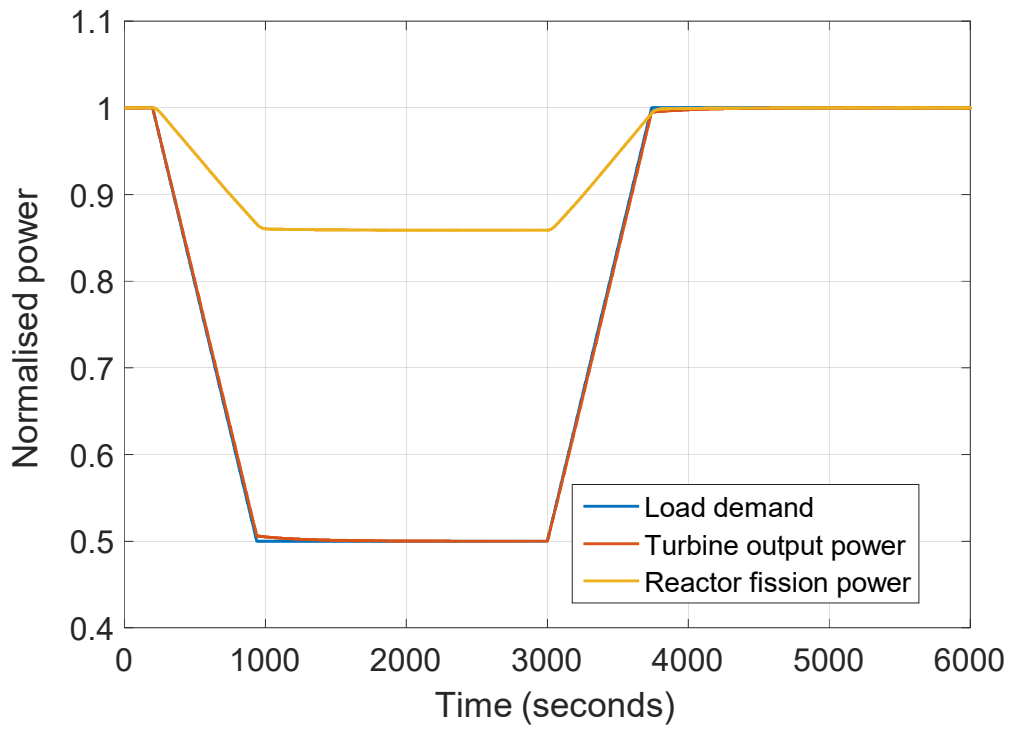


Figure 8-6 Load demand, turbine power output supplied to the generator and reactor fission power during normal load following with bypass valve control only

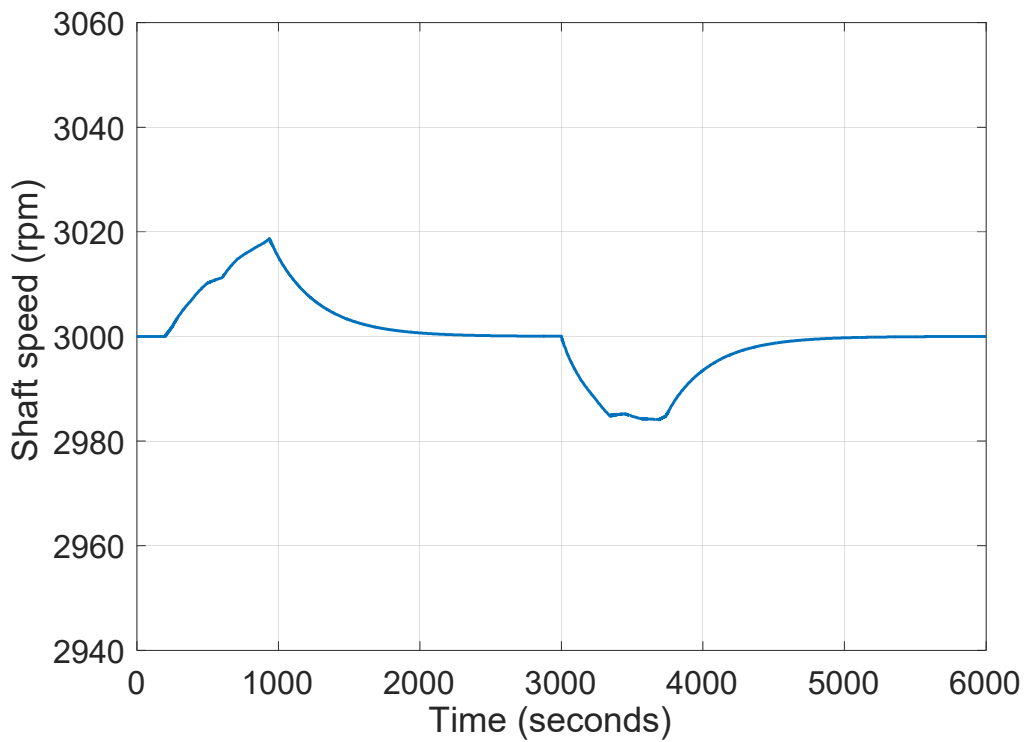


Figure 8-7 FPT-generator shaft speed during normal load following with bypass valve control only

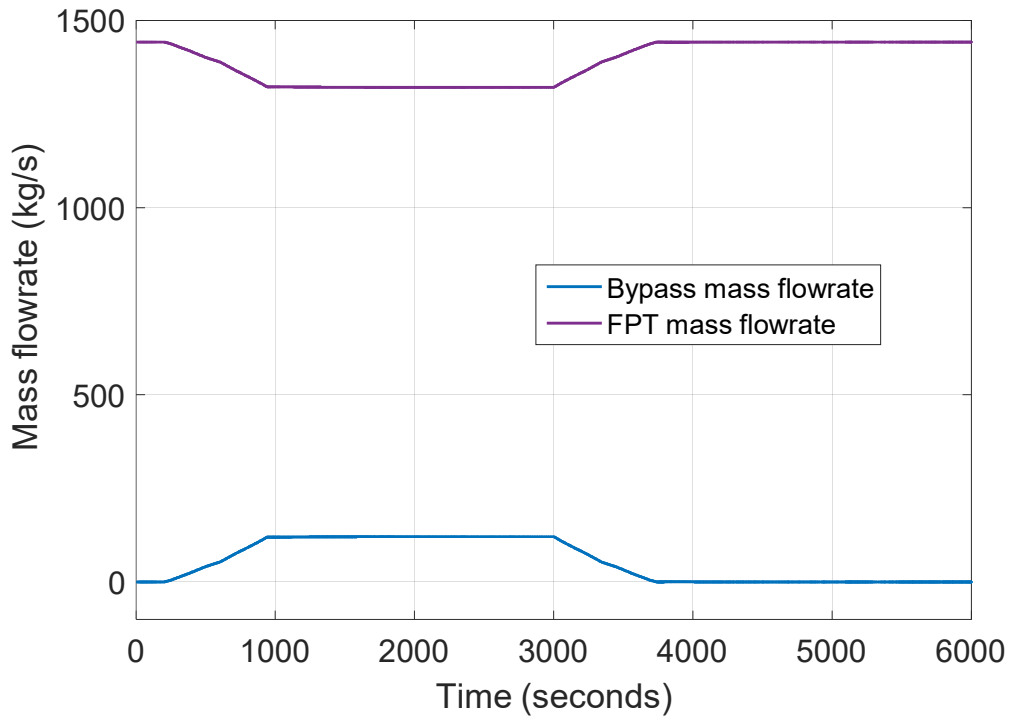


Figure 8-8 Bypass mass flowrate FPT mass flowrate during normal load following with bypass valve control only

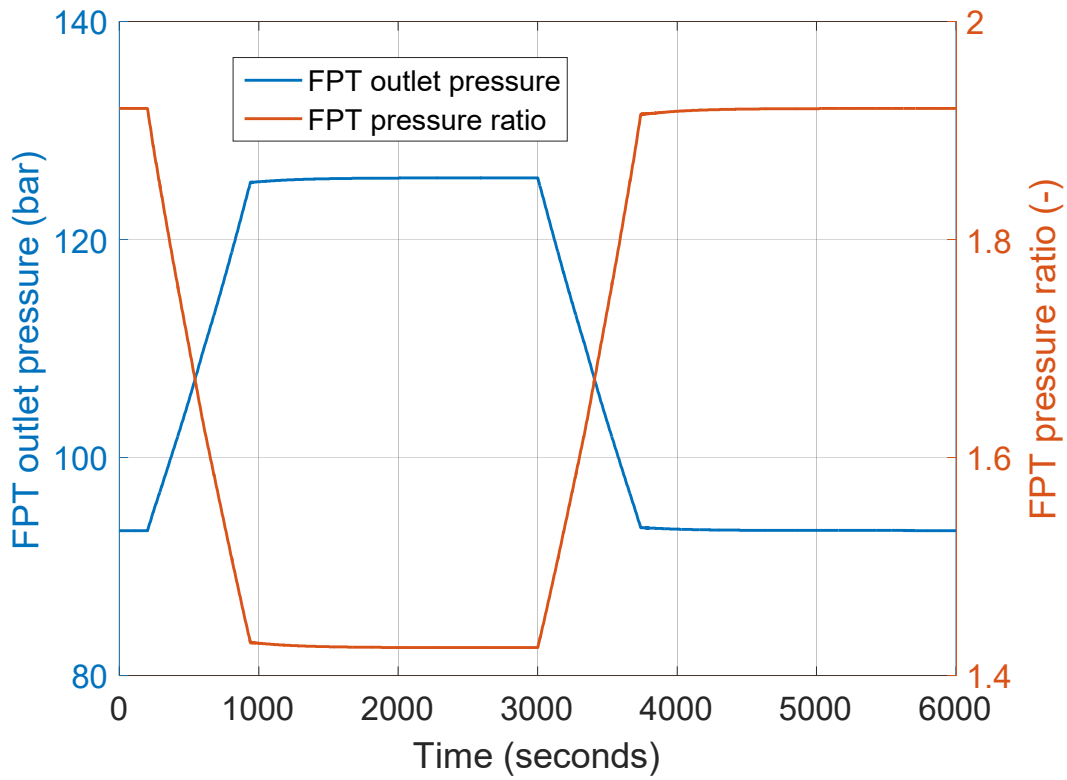


Figure 8-9 FPT outlet pressure and pressure ratio during normal load following with bypass valve control only

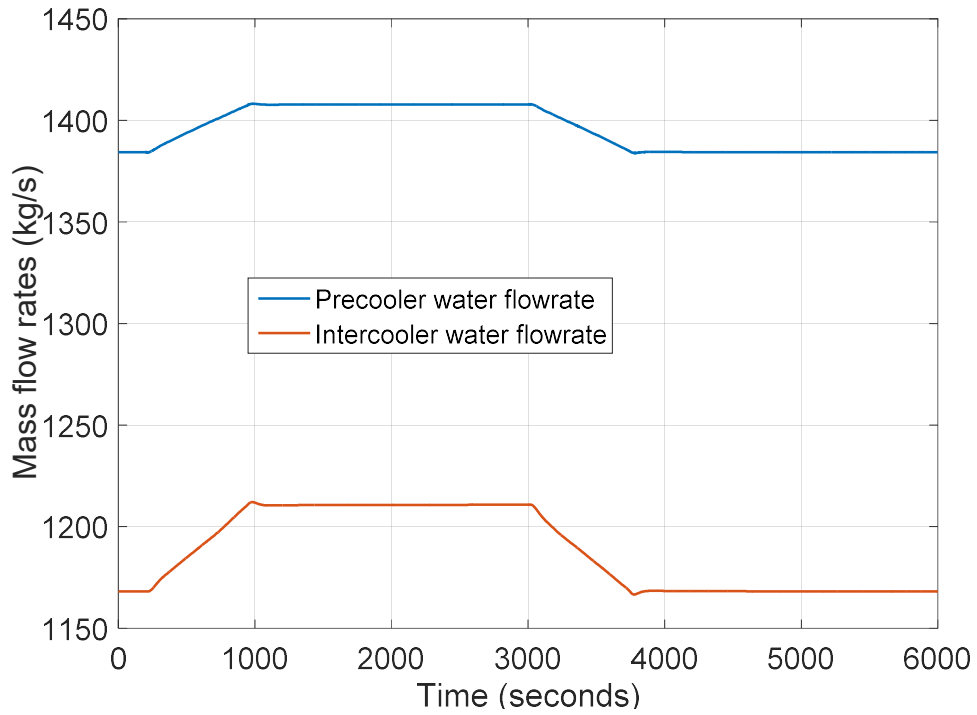


Figure 8-10 Precooler and intercooler cooling water flowrates manipulated by the cooling water controller during normal load following operation

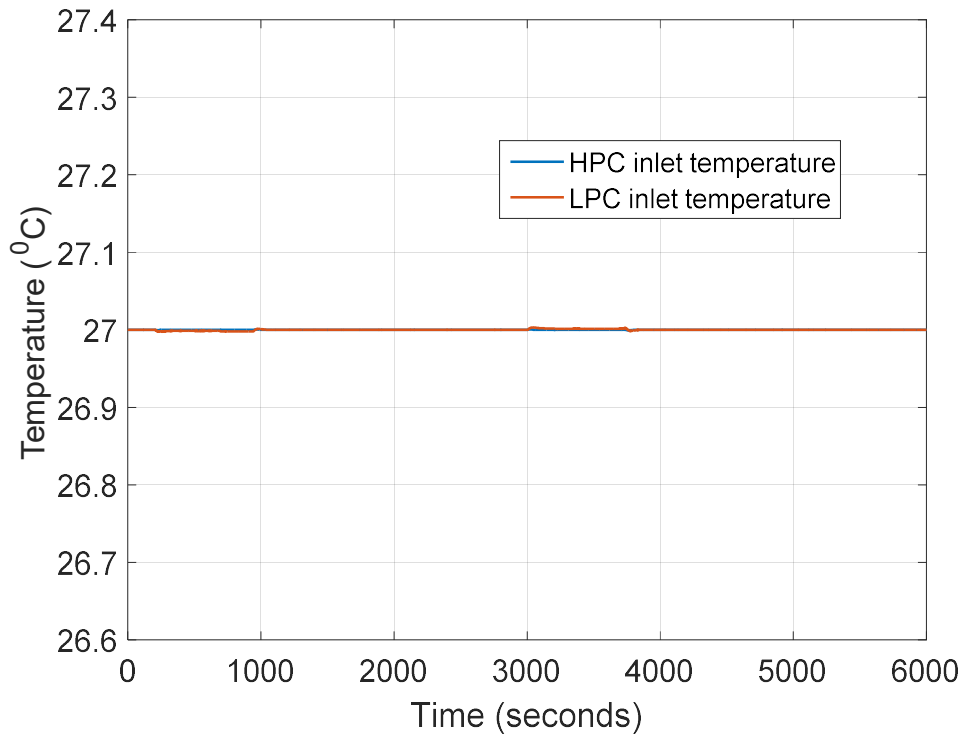


Figure 8-11 LPC and HPC inlet temperatures maintained at the design value by the cooling water controllers during load following operation

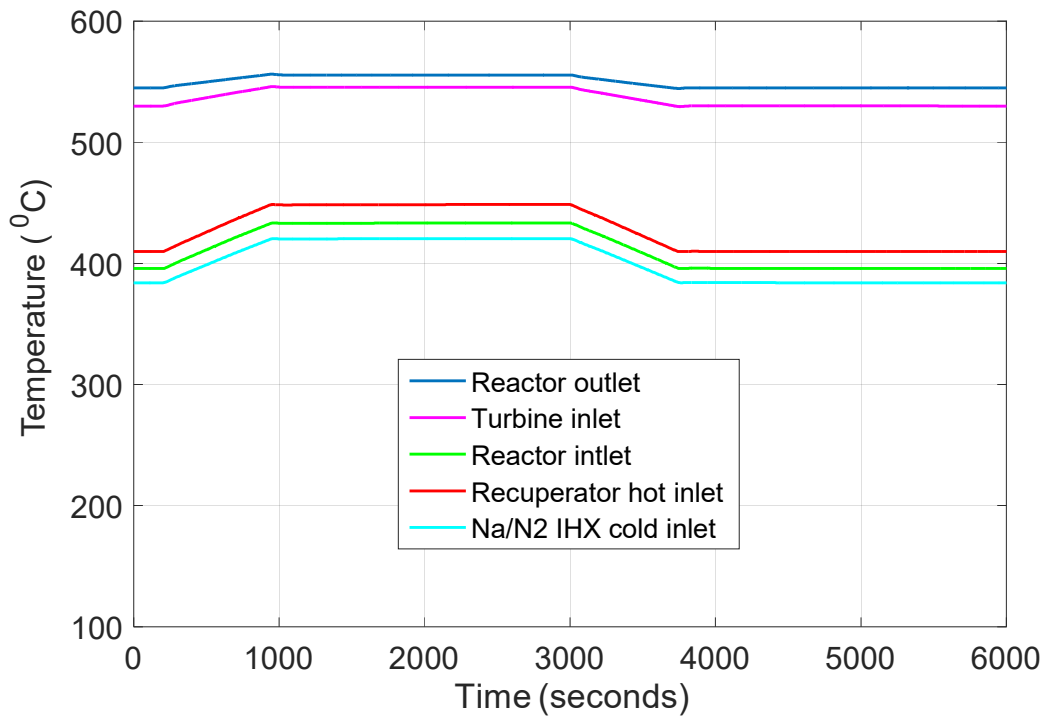


Figure 8-12 Temperature transients at reactor outlet, turbine inlet, recuperator hot side inlet, reactor inlet and Na/N2 IHX cold side inlet during load following with bypass valve control only

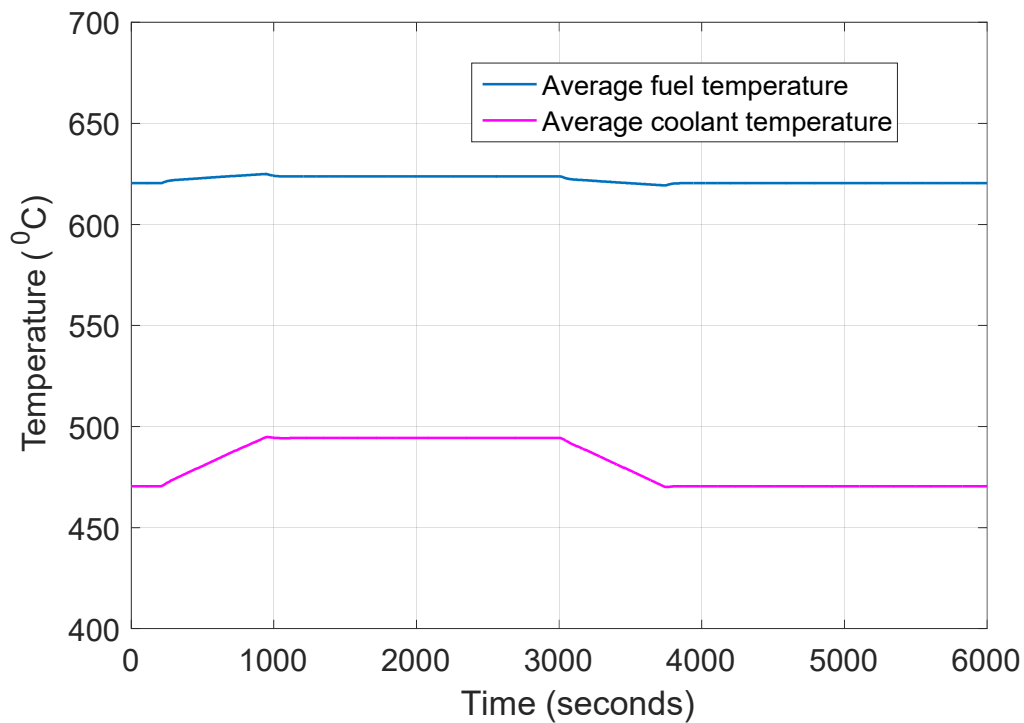


Figure 8-13 Average fuel and coolant temperature during load following operation with bypass valve control only

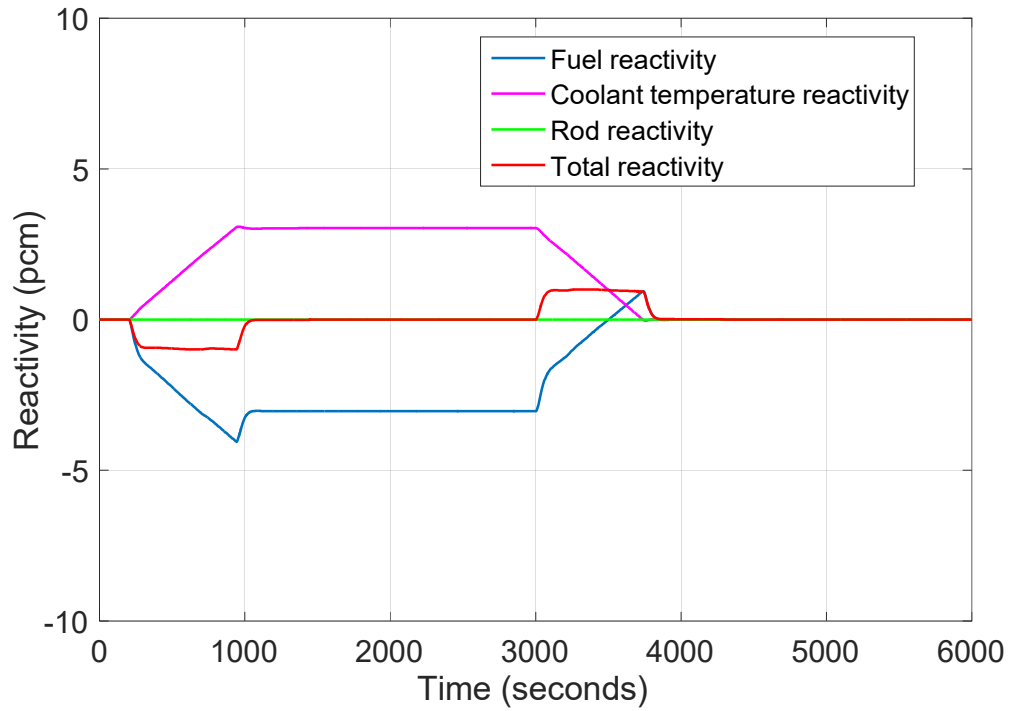


Figure 8-14 Changes in reactor reactivity during load following operation with bypass valve control only

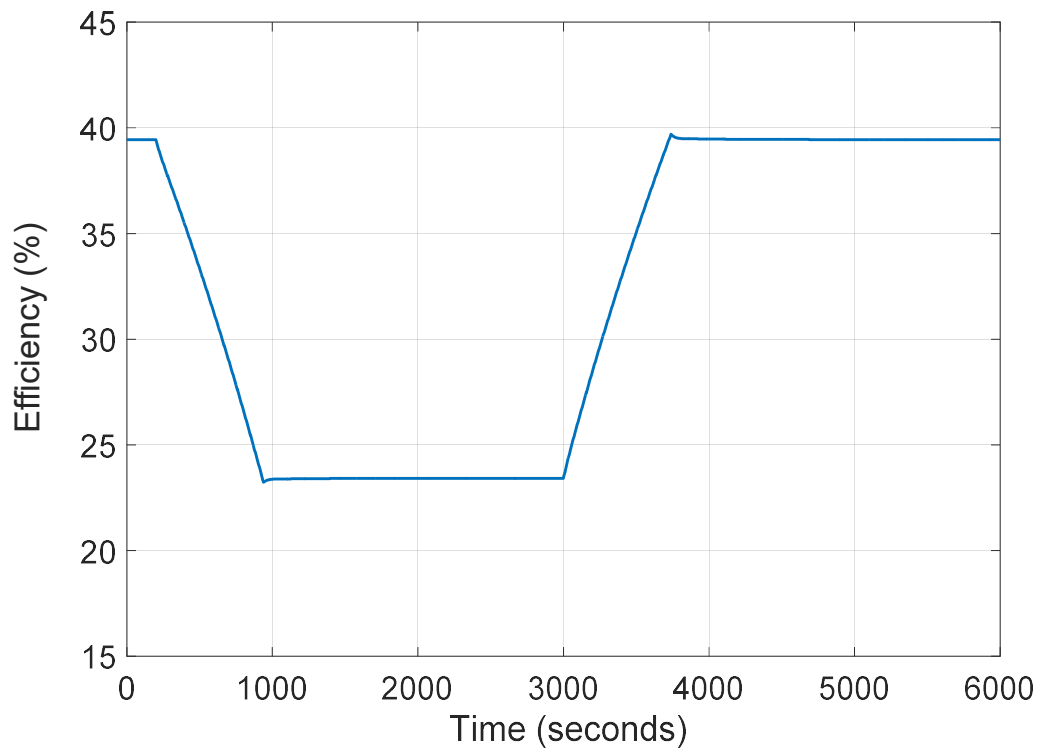


Figure 8-15 Variation of the plant efficiency during load following operation with bypass valve control only

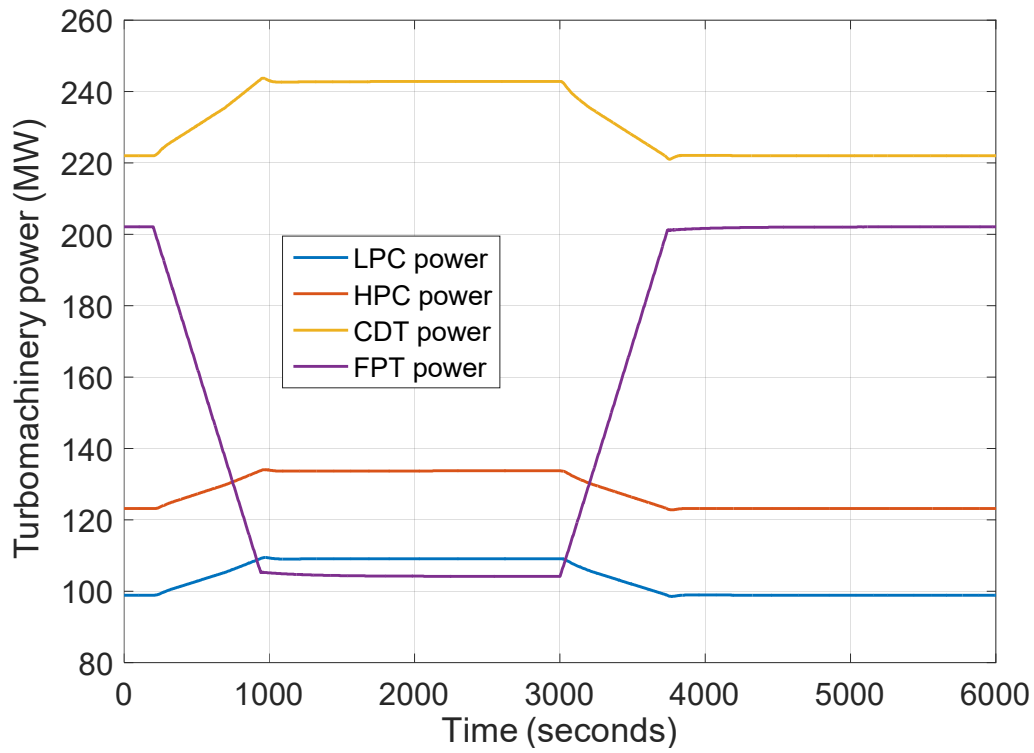


Figure 8-16 Turbomachinery power during load following operation with bypass valve control only

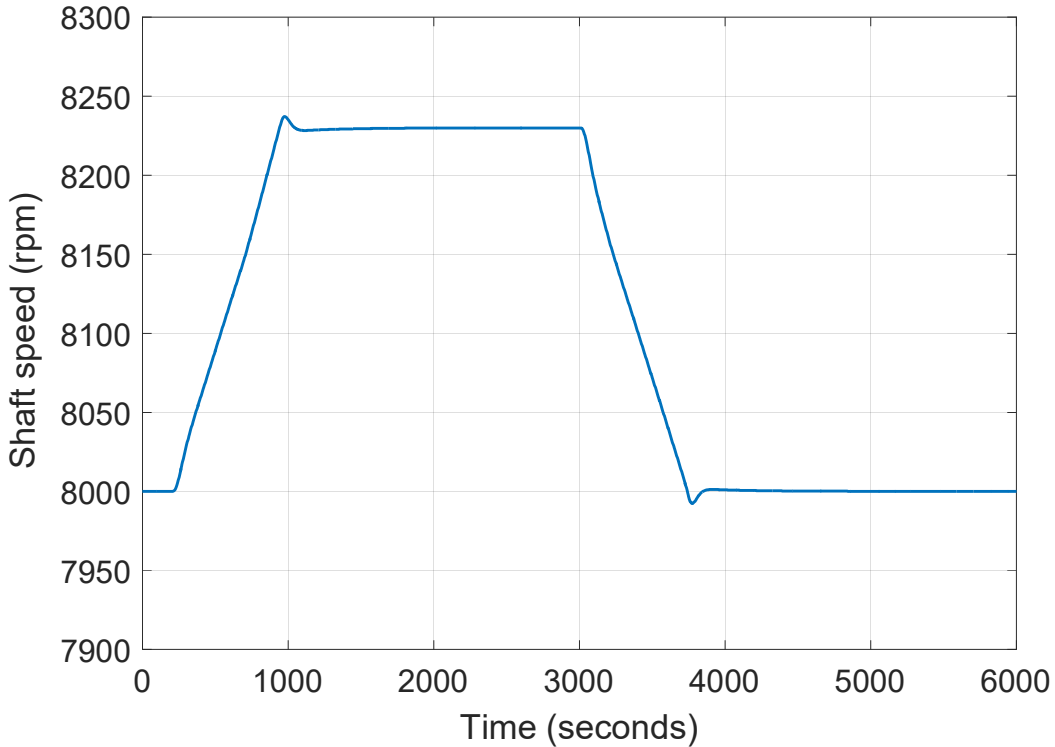


Figure 8-17 Compressor shaft speed variation during load following with bypass valve control only

8.5.2 Control strategy 2: Bypass valve control and reactor control

In this control strategy, reactor controls (i.e. control rod control and coolant pump control) are engaged, in addition to the bypass valve control, in order to maintain the reactor outlet temperature and TIT at the design values. The following control systems are used:

- Bypass valve control is used to maintain the FPT-generator shaft speed at 3000 rpm
- Control rod control is used to maintain the reactor outlet temperature at 545 °C
- Coolant pump torque control is used to maintain the TIT at 530 °C
- Cooling water controls are used to maintain the compressors inlet temperatures at 27 °C

Some results of the plant transient simulation are shown in Figure 8-18 to Figure 8-25.

Transient responses of the turbine power out and reactor fission power are shown in Figure 8-18. The reactor fission power level is about 82% at the 50% load demand, which means that the rate of reactor power reduction is still less than the rate of load reduction. Efficiency loss at 50% part-load operation is about 14.8% point (Figure 8-19). The bypass valve control maintains the FPT-generator shaft speed within ± 17 rpm of the nominal value (Figure 8-20). The control rod controller changes the reactor reactivity to vary the reactor power, which alters the amount of heat transferred to the sodium coolant and maintain the core outlet temperature at the design value. The control adjustment of the control rod reactivity along with the transient responses of the fuel and coolant temperature reactivity is shown in Figure 8-21. The TIT is controlled by regulating the reactor coolant mass flowrate in the primary loop. This is accomplished by the coolant pump torque controller, which uses the error between the actual TIT and the desired temperature to vary the pump torque and speed and thus control the coolant flowrate. The control variation of the pump torque as well as the transient responses of the pump speed and coolant mass flowrate is shown in Figure 8-22.

Figure 8-23 shows the temperature transient responses during the load following operation. It can be seen that the reactor outlet temperature and the TIT remain constant at 545 °C and 530 °C respectively throughout the transient period. However, temperature rise at recuperator hot side inlet, reactor inlet and Na/N₂ IHX cold side inlet are about 29, 23 and 27 °C respectively. As can be seen in Figure 8-24, the power delivered by the CDT and the compressors power are relatively constant throughout the simulation. Hence, compressors shaft speed changes only slightly by about ± 7 rpm as shown in Figure 8-25, which confirms that it is not necessary to have a separate control system for the compressor shaft speed.

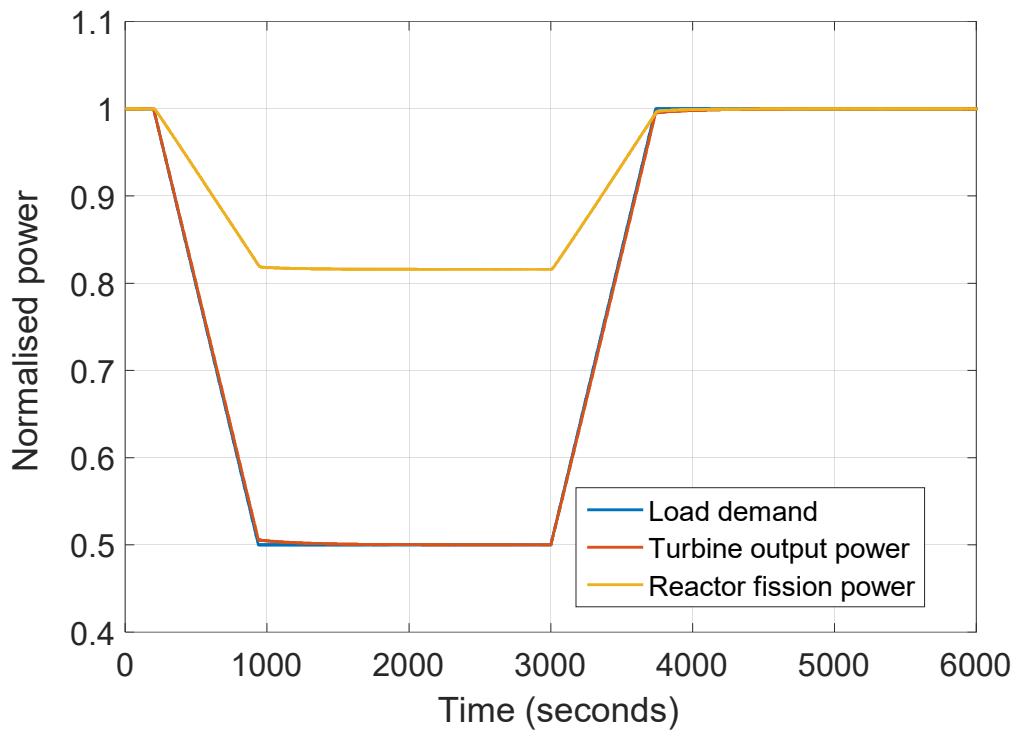


Figure 8-18 Load demand, turbine power output and reactor fission power during normal load following with bypass valve and reactor controls

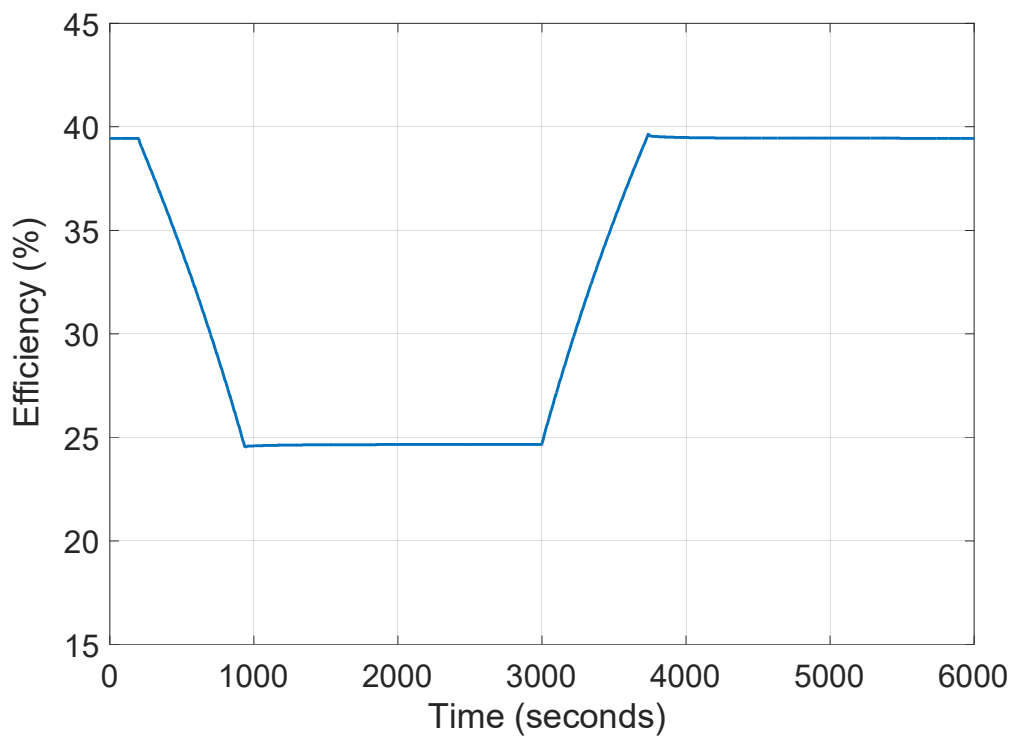


Figure 8-19 Variation of the plant efficiency during load following operation with bypass valve control and reactor control

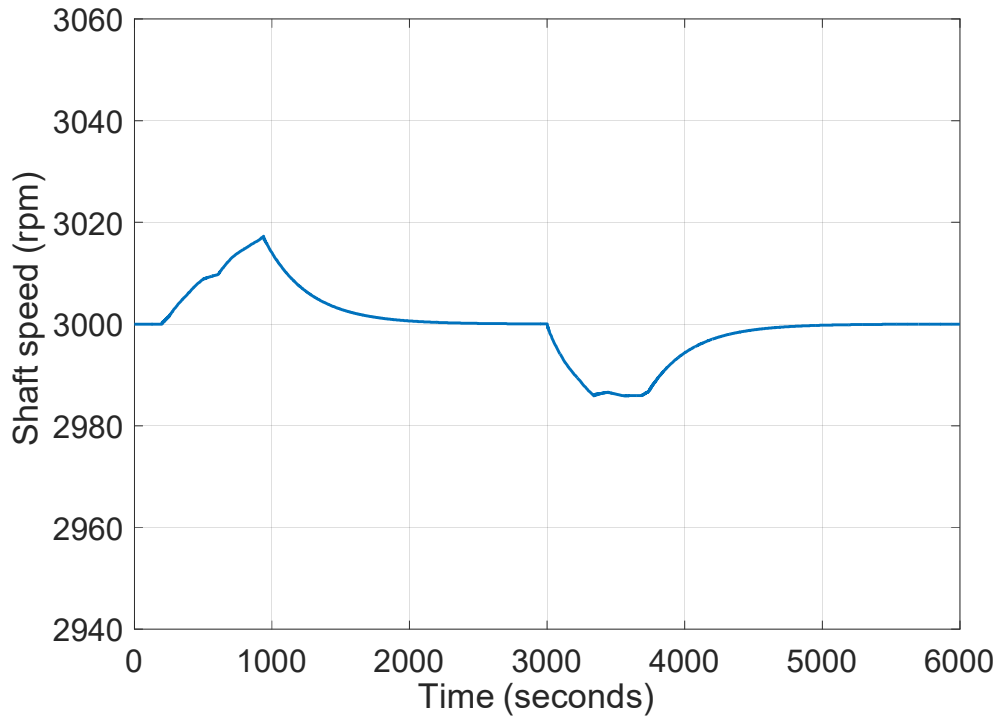


Figure 8-20 FPT-generator shaft speed during normal load following with bypass valve and reactor controls

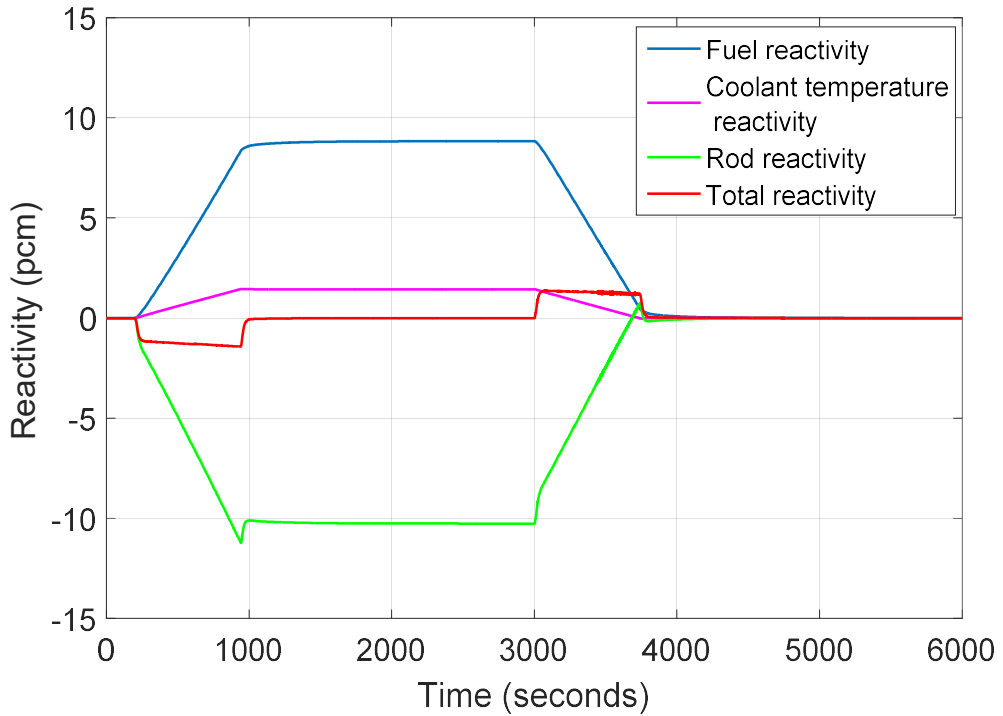


Figure 8-21 Control rod reactivity adjustment along with fuel and coolant reactivity during load following operation with bypass valve and reactor control

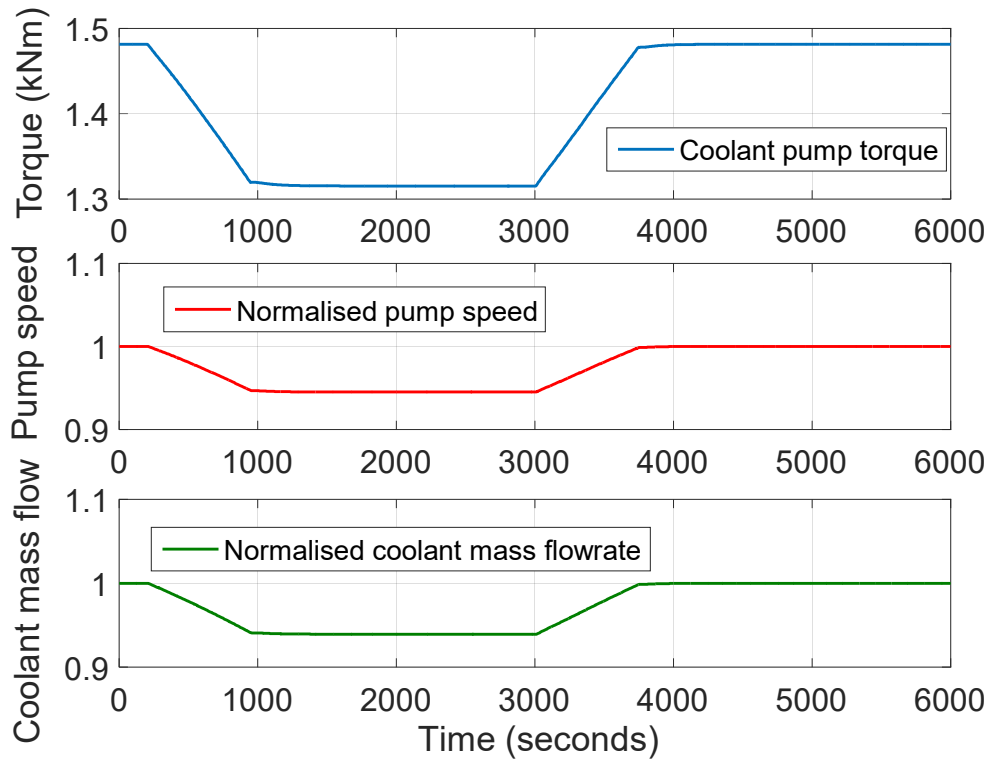


Figure 8-22 Adjustment of the coolant pump torque along with the variation of the pump speed and coolant mass flow rate during load following operation with bypass valve control and reactor control

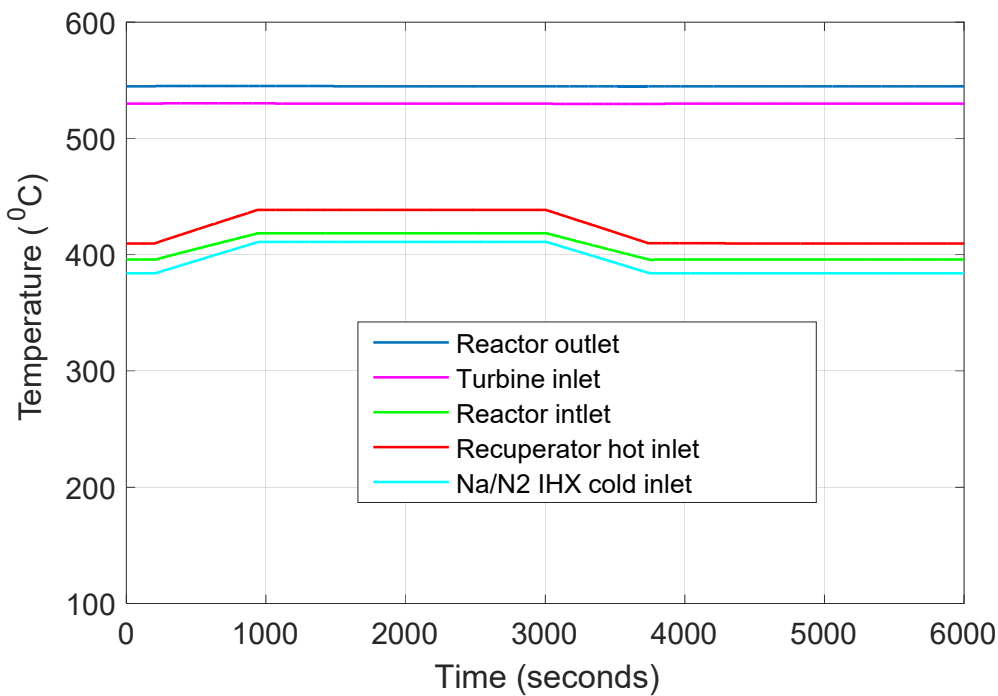


Figure 8-23 Temperature transients at reactor outlet, turbine inlet, recuperator hot side inlet, reactor inlet and Na/N2 IHX cold side inlet during load following with bypass valve control and reactor control

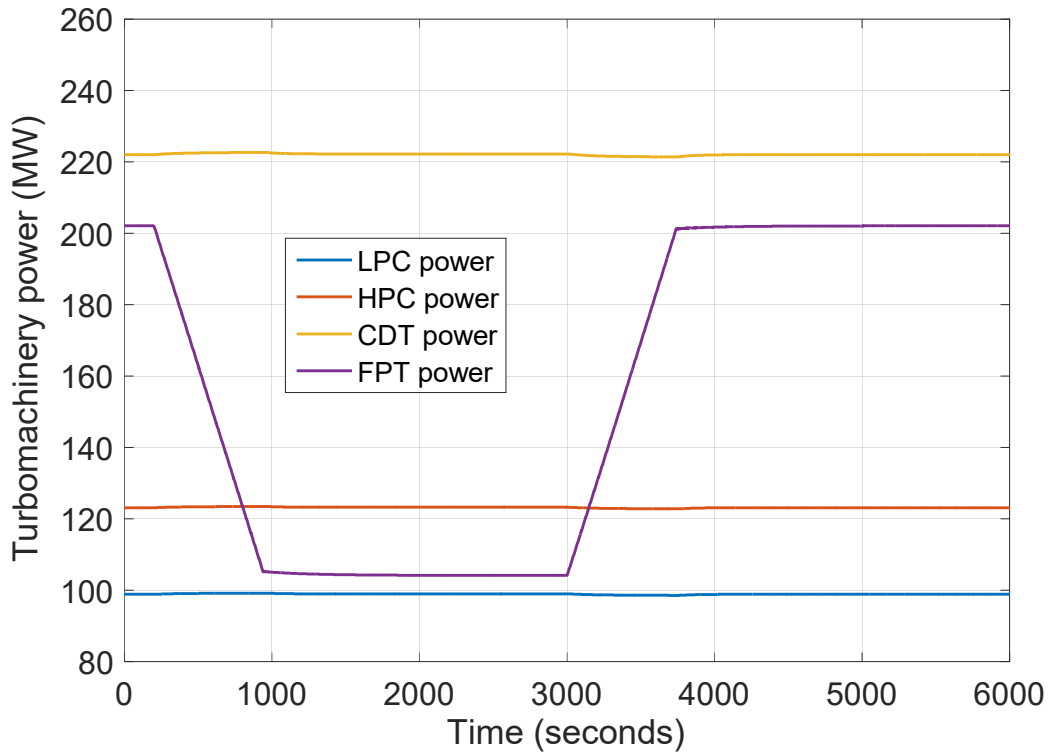


Figure 8-24 Turbomachinery power during load following operation with bypass valve control reactor control

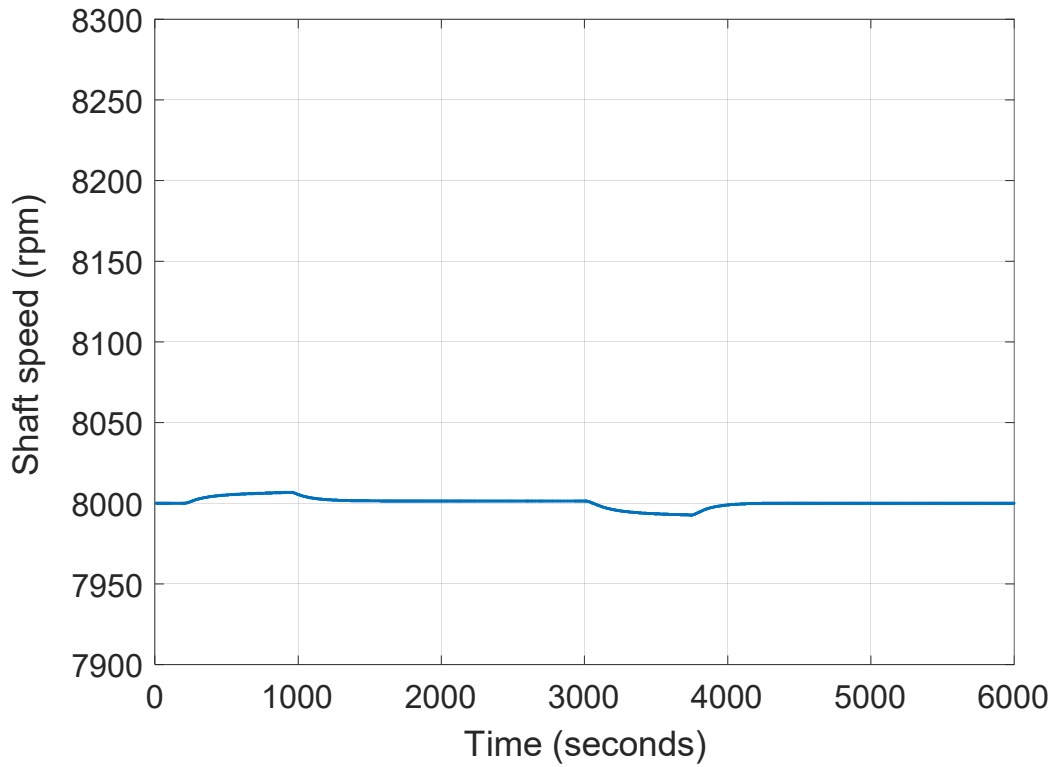


Figure 8-25 Compressor shaft speed variation during load following with bypass valve control and reactor control

8.5.3 Control strategy 3: Inventory regulation and reactor controls

Inventory control is investigated for maintaining high thermal efficiency as well as limiting the temperature increase and thermal stress on the components during part-load operation. The plant is controlled by the following control systems:

- Inventory control is used to regulate the nitrogen inventory in the PCS based on the load demand
- Control rod control is used to maintain the reactor outlet temperature at 545 °C
- Coolant pump torque control is used to maintain the TIT at 530 °C
- Cooling water controls are used to maintain the compressors inlet temperatures at 27 °C

The results of the simulation are shown in Figure 8-26 to Figure 8-35.

Figure 8-26 shows the transient responses of the turbine power output and reactor fission power to changes in the load demand. Reactor power changes at the same rate as the load demand, which implies a constant cycle thermal efficiency throughout the transient period as shown in Figure 8-27. As the load starts to decrease at 200 seconds, inventory regulation system withdraws nitrogen gas from the PCS as shown in Figure 8-28, in order to reduce the power output. Due to the nitrogen inventory removal from the PCS, the mass flowrate of nitrogen gas in the cycle is reduced at almost the same rate as the inventory reduction (Figure 8-29). Similarly, as shown in Figure 8-29, the sodium coolant mass flowrate and the cooling water mass flowrates are reduced at approximately the same rate to match the heat removal from the primary loop in the IHX and heat rejection in the coolers. These are achieved through the actions of the coolant pump controller and cooling water controller. When the load is raised again at 3000 seconds, the inventory regulation system responds by increasing the inventory of nitrogen in the PCS to raise the power output level and all the plant conditions are returned to their initial values.

As in the previous case, the reactor side controls adjust the rod reactivity and pump torque to keep the reactor outlet and TIT at the design value. Figure 8-30 shows the transient responses of the reactor reactivity while Figure 8-31 shown the coolant pump torque and speed control. Figure 8-32 shows that the pressure at turbine inlet (or high pressure side) and pressure at turbine outlet (or low pressure side) changes proportionally with inventory regulation. Thus, the cycle pressure ratio remains approximately constant at the design point value such that the turbomachinery are running close to their optimum operating point throughout the transient period (Figure 8-32). Figure 8-33 shows that the turbines and compressors power also changes at approximately the same rate as the load demand. Figure 8-34 shows the temperature transient responses at various

location during the load changes. The temperatures are relatively unchanged with inventory control.

The obvious advantage of inventory control is that it permits load following operation with virtually constant thermal efficiency and constant temperatures throughout the plant. However, the FPT-generator shaft speed varies by about ± 82 rpm during the transient period as shown in Figure 8-35. Therefore, inventory control cannot satisfy the utility requirement of maintaining the turbine-generator shaft speed within ± 30 rpm of the rated speed (3000 rpm) during loading following operation of this plant.

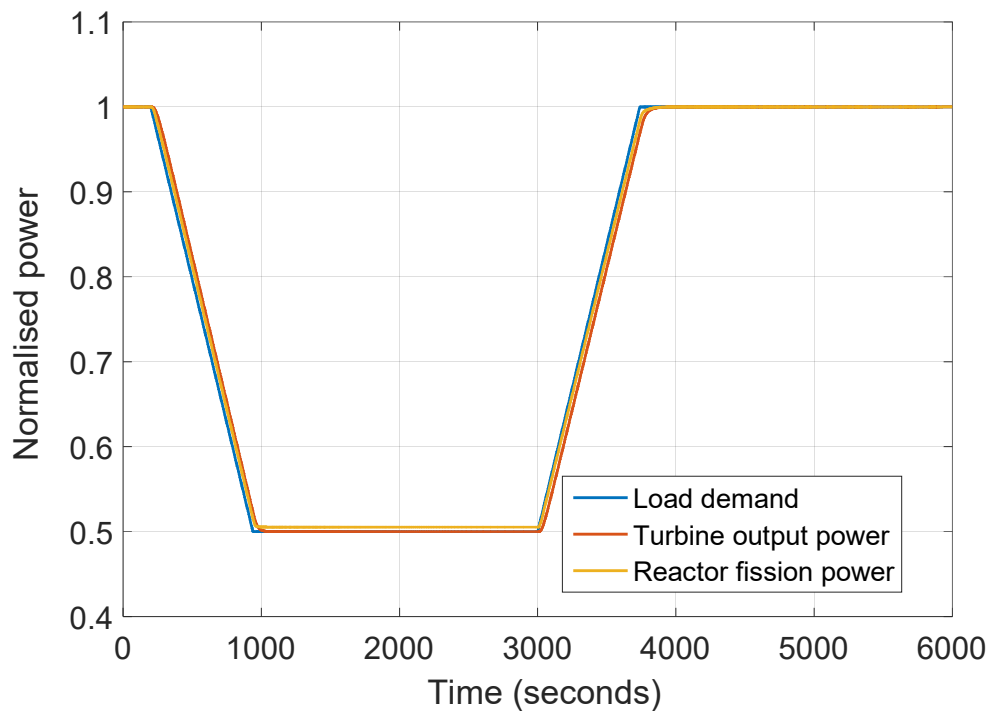


Figure 8-26 Load demand, turbine power output and reactor fission power during normal load following with inventory control and reactor controls

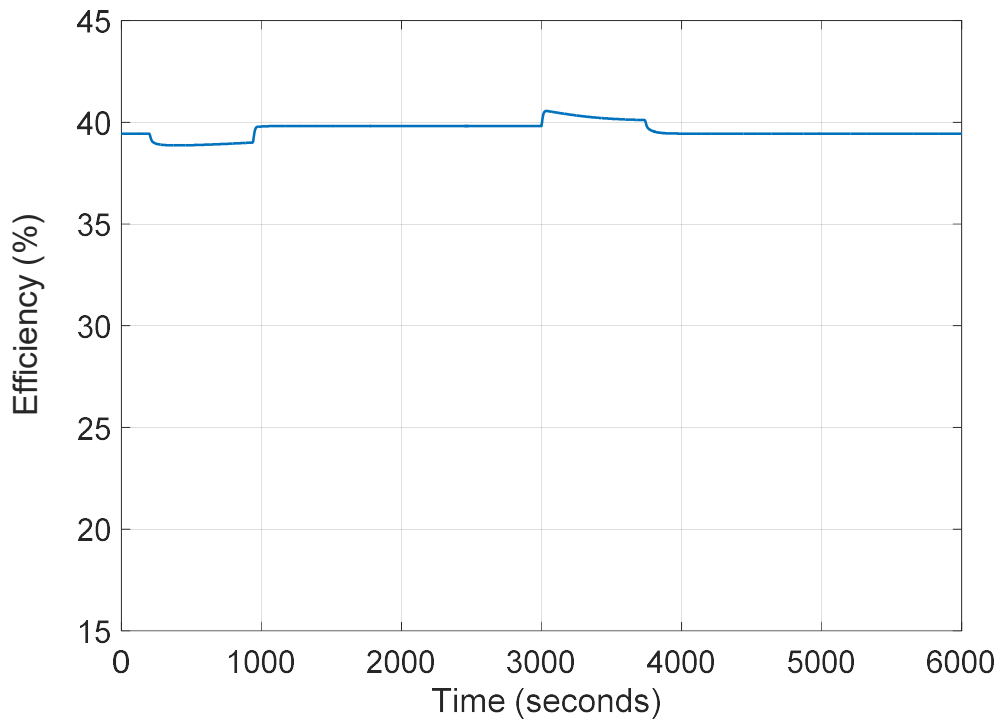


Figure 8-27 Plant efficiency during load following operation with inventory control and reactor controls

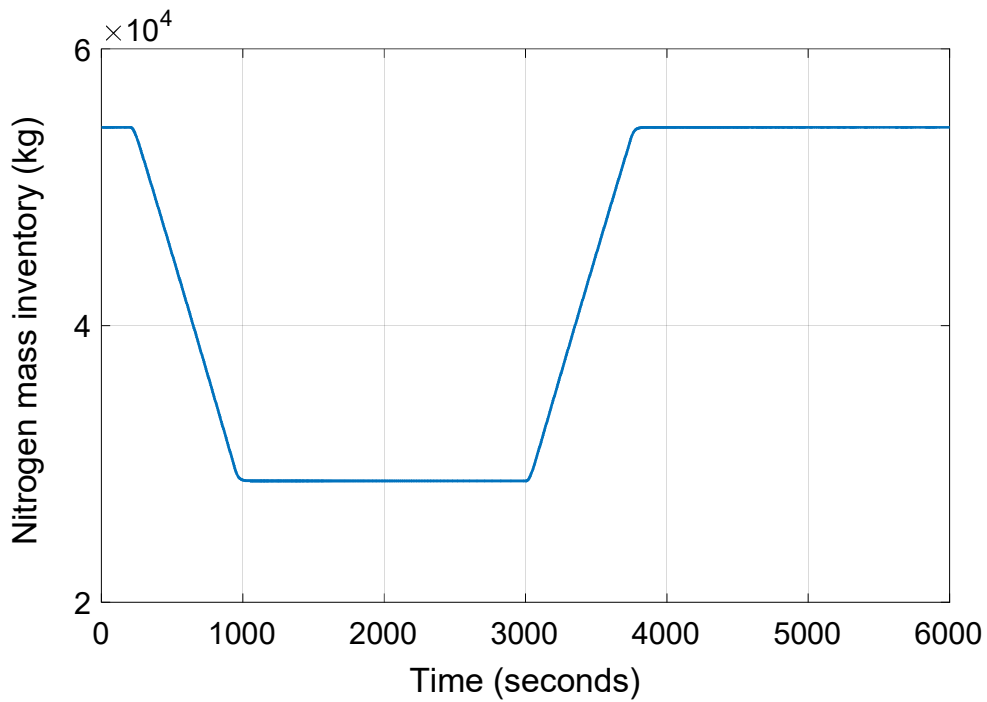


Figure 8-28 Mass inventory of nitrogen gas in the PCS during load following operation with inventory and reactor controls

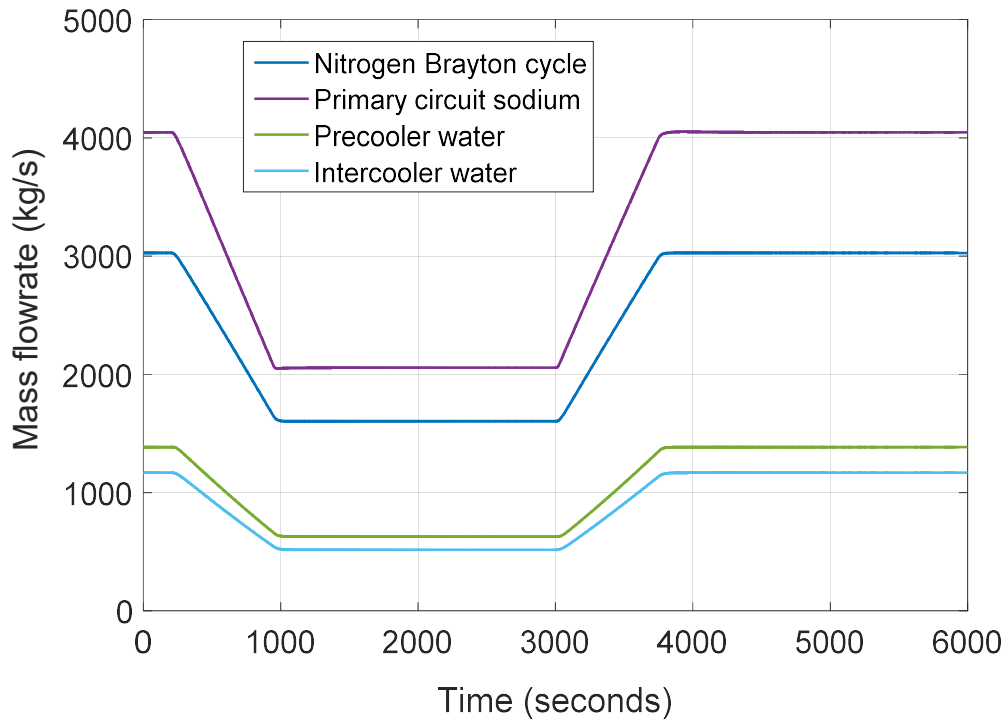


Figure 8-29 Transient responses of nitrogen, sodium and cooling water mass flowrate during load following operation with inventory control and reactor controls

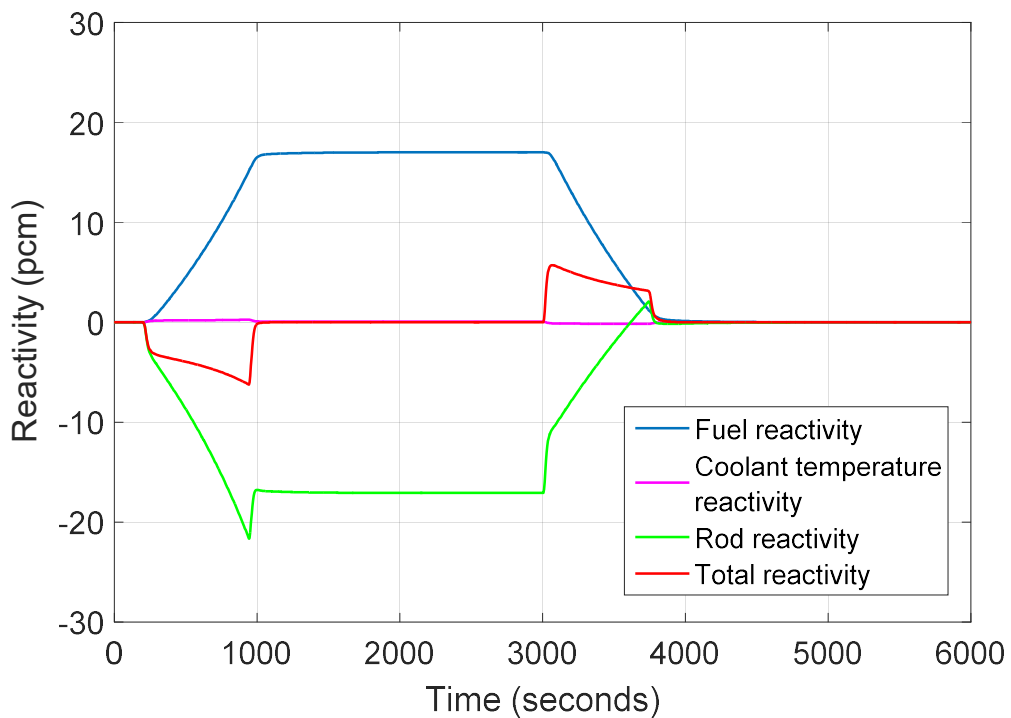


Figure 8-30 Control rod reactivity adjustment along with fuel and coolant reactivity during load following operation with inventory control and reactor control

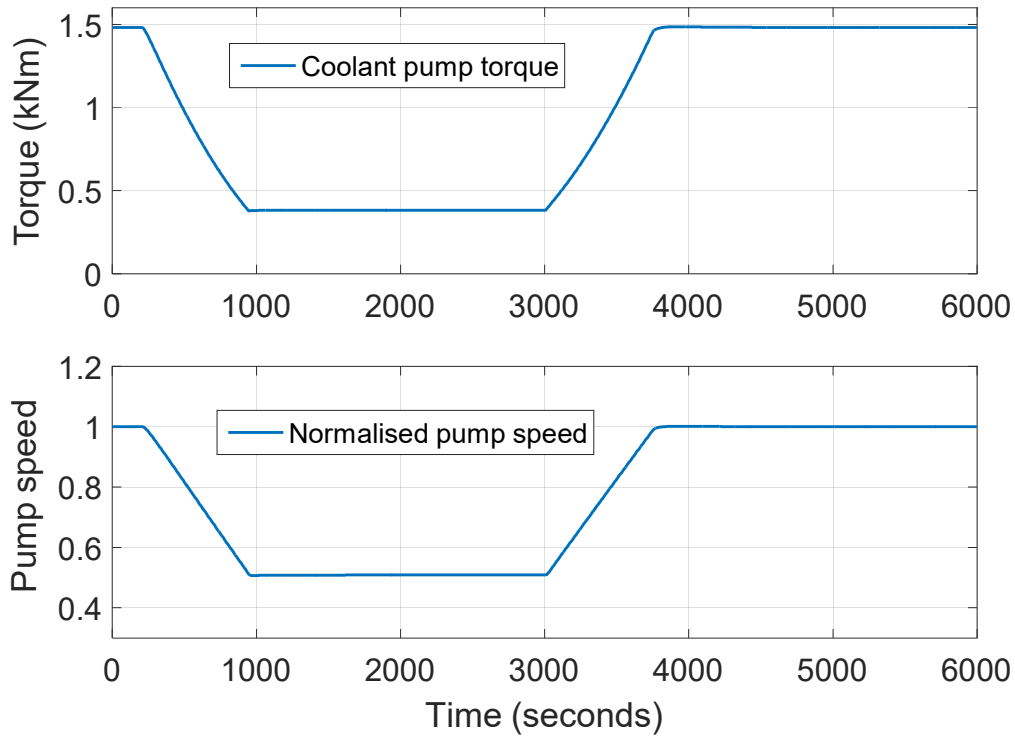


Figure 8-31 Control adjustment of the coolant pump torque and speed during load following operation with inventory control and reactor control

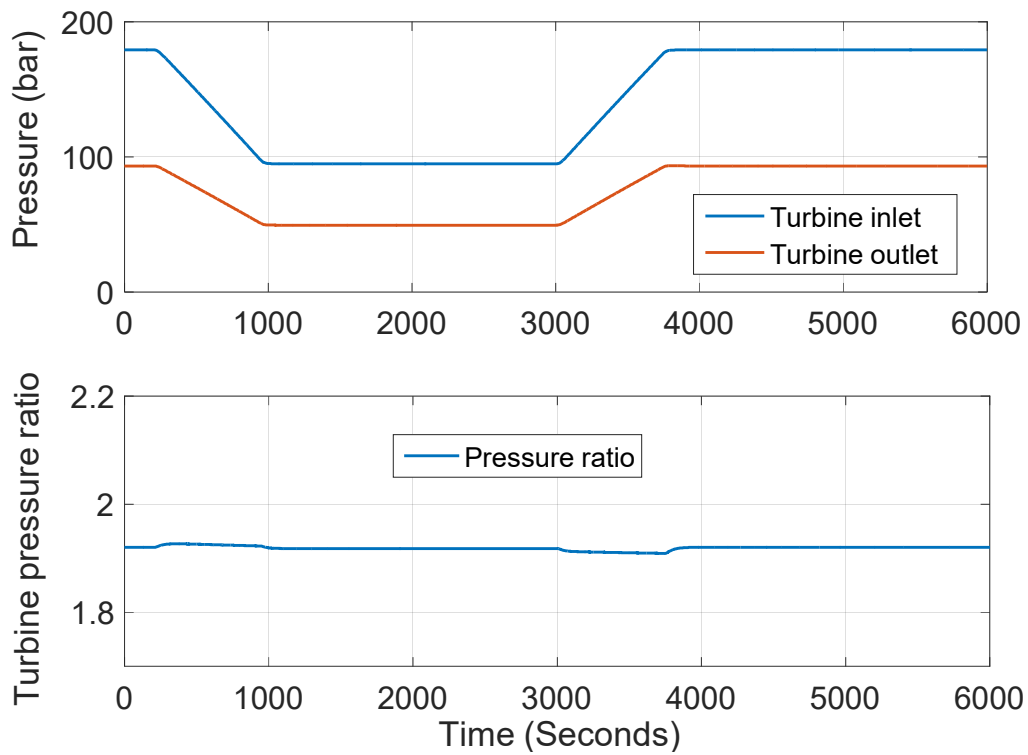


Figure 8-32 Variation of turbine inlet and outlet pressure and pressure ratio during load following operation with inventory control and reactor controls

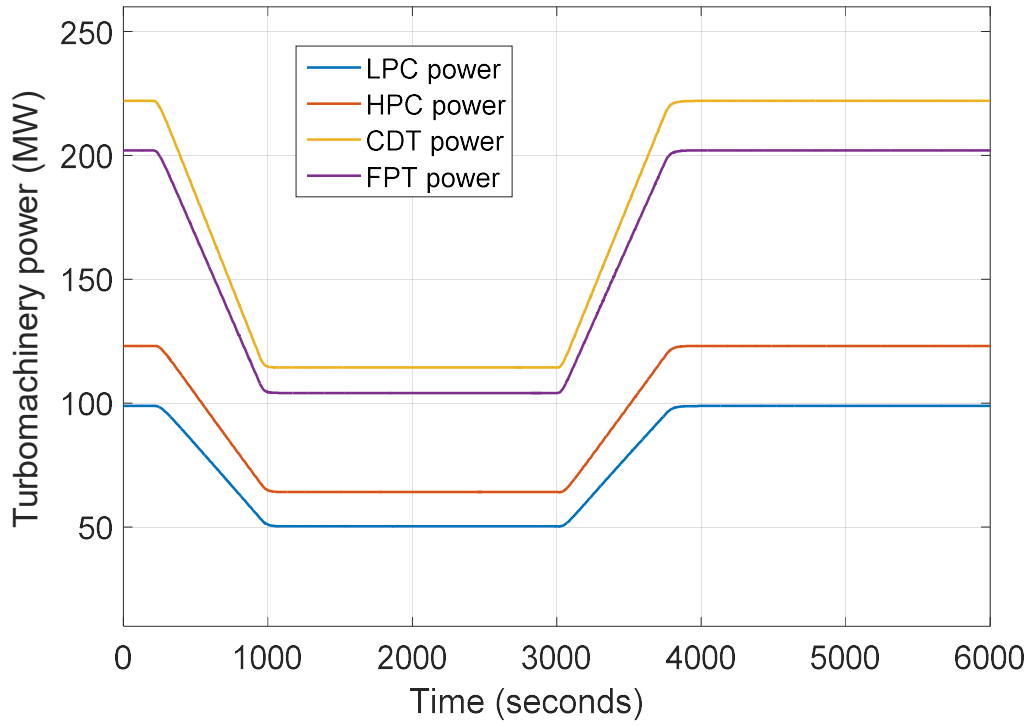


Figure 8-33 Variation of turbomachinery power during load following with inventory control and reactor controls

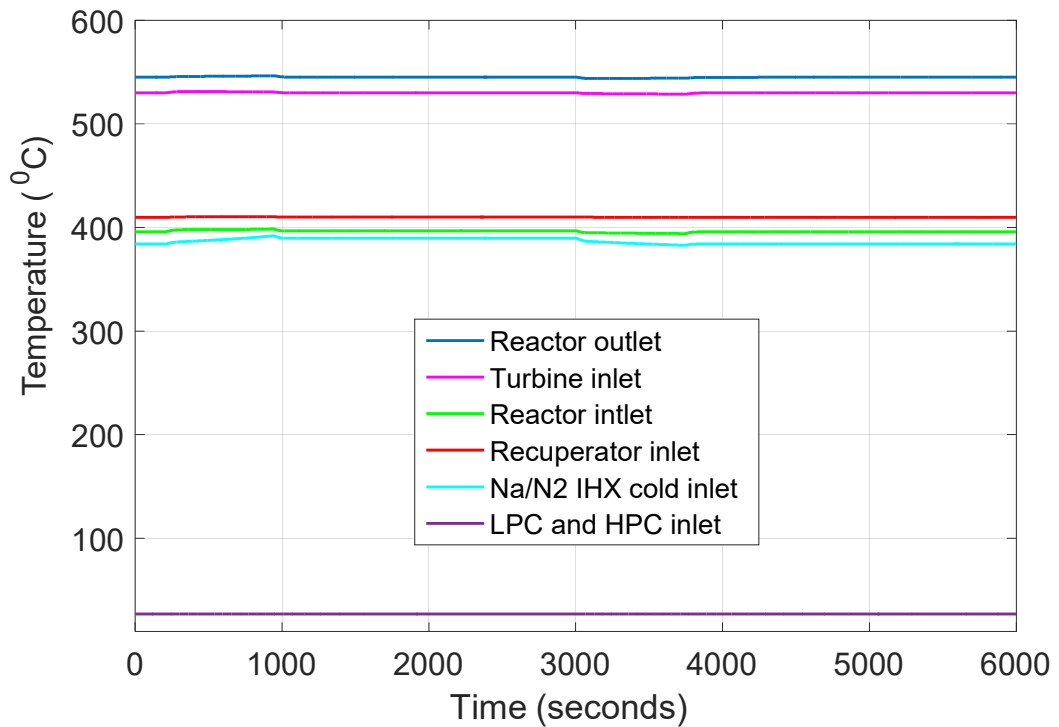


Figure 8-34 Temperature transient responses during load following with inventory control and reactor controls

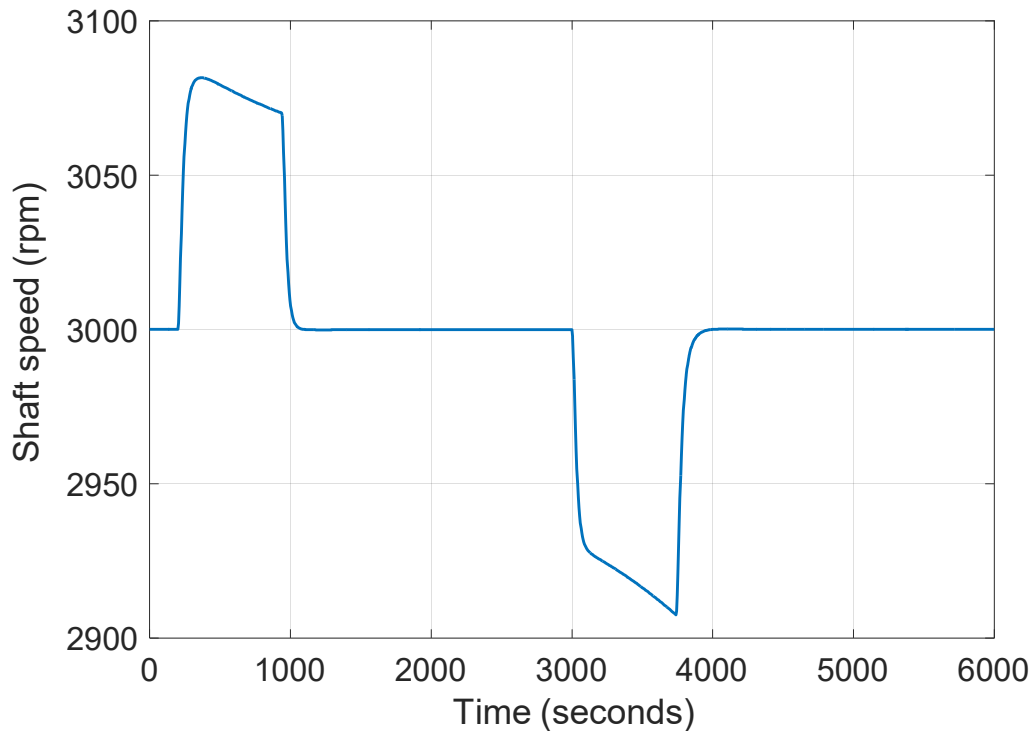


Figure 8-35 Transient response of FPT-generator shaft speed during load following operation with inventory control and reactor controls

8.5.4 Control strategy 4: Bypass valve control and inventory regulation with reactor control

This control strategy attempts to harness the benefits of bypass control and inventory control. This is accomplished by simultaneously engaging bypass valve control and inventory control for automatic control of the plant.

- Bypass valve control is used to maintain the FPT-generator shaft speed at 3000 rpm
- Inventory regulation is used to adjust the nitrogen inventory based on the load demand
- Control rod control is used to maintain the reactor outlet temperature at 545 °C
- Coolant pump torque control is used to maintain the TIT at 530 °C
- Cooling water controls are used to maintain the compressors inlet temperatures at 27 °C

Figure 8-36 shows that the turbine output power and reactor fission power follow the changes in load demand. The plant efficiency remains roughly the same during the transient period (Figure 8-37). During load reduction, the inventory control acts to remove nitrogen gas from the PCS and reduces cycle mass flowrate as shown in Figure 8-38. Since the inventory control is not fast enough to prevent acceleration of FPT-generator shaft speed, the bypass valve is open to divert part of the flow from the FPT (Figure 8-38). At the 50% load level, the nitrogen mass inventory

and flowrate is now at a new level corresponding to the load demand level, so that the FPT-generator shaft speed remains at 3000 rpm. Hence, the bypass valve controller closes the bypass valve completely, sensing no speed deviation. At 3000 seconds when the load demand starts to increase, the bypass valve control cannot be used to increase the output power because it is already closed. The power output response during this period will solely depend on how fast the inventory regulation system is able to refill the PCS with nitrogen. Hence, the FPT-generator shaft speed is outside the allowable maximum deviation during load demand increase as shown in Figure 8-39.

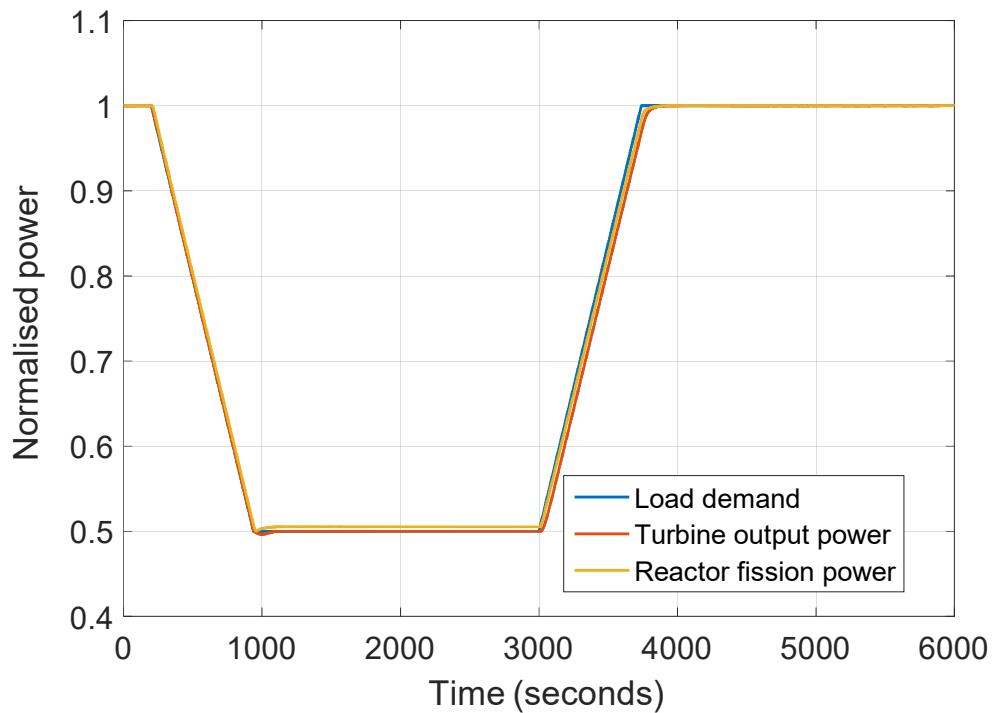


Figure 8-36 Responses of turbine output power and reactor fission power to load demand changes during load following operation with bypass valve control and inventory control

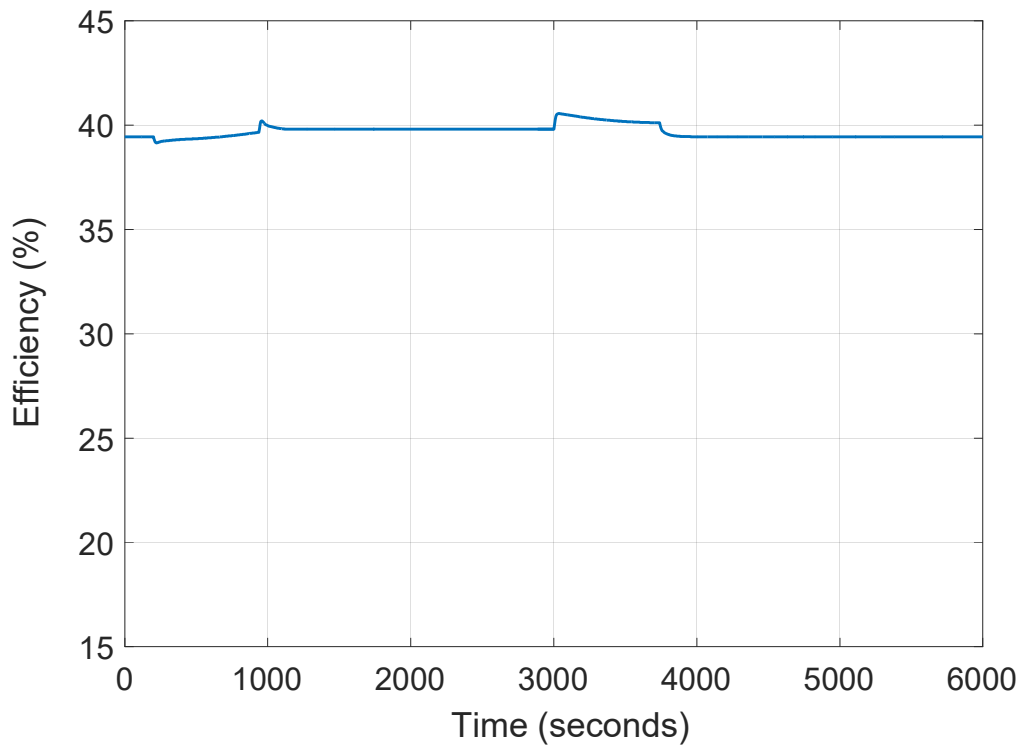


Figure 8-37 Plant efficiency during load following operation with bypass valve control and inventory control

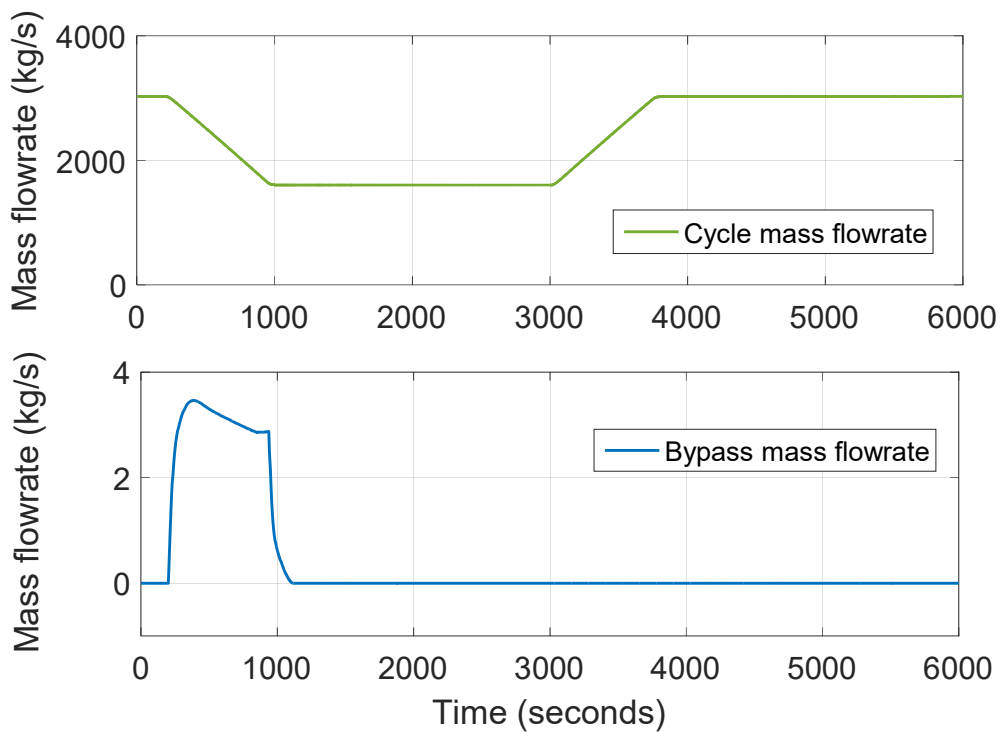


Figure 8-38 Total Brayton cycle and bypass valve mass flowrate during load following operation with bypass valve control and inventory control

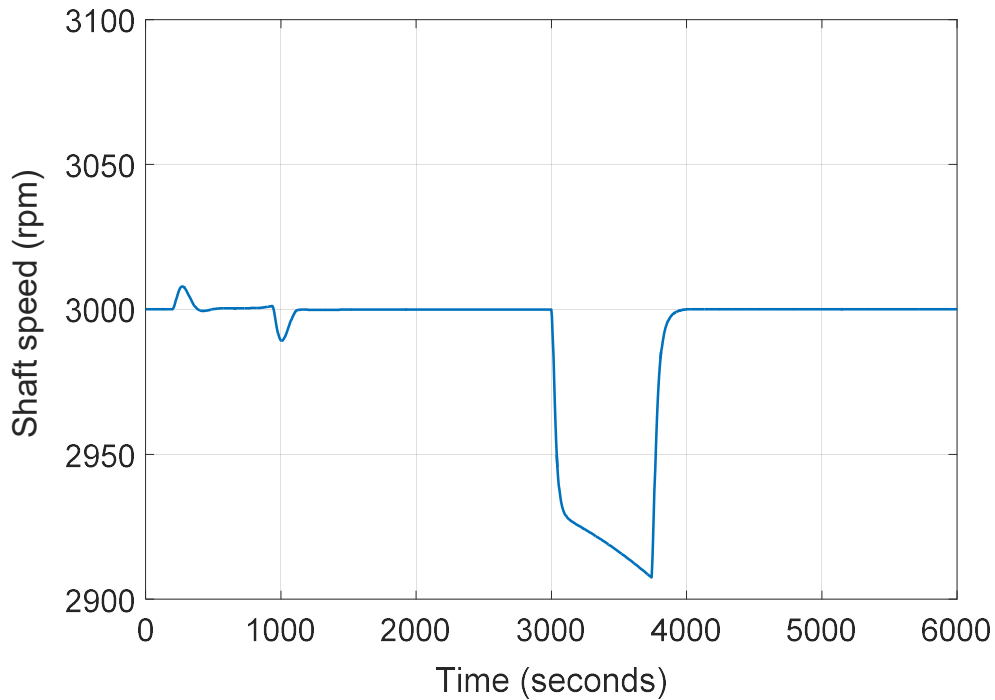


Figure 8-39 FPT-generator shaft speed during load following operation with bypass valve control and inventory control

8.6 100% instantaneous loss of grid load

Instantaneous reduction of grid load from full load value to zero load is simulated to study the plant transient behaviour during an abrupt separation from the grid. The grid load demand is suddenly reduced from full load to zero. The only load on the generator is the house (on site) load. Therefore, the FPT-generator shaft accelerates rapidly to higher speed due to the excess power delivered by the FPT. The objective of the control system during the loss of load event is to avoid over-speeding of the turbine-generator shaft by keeping the shaft speed below 120% of the nominal value.

The following control systems are employed:

- Bypass valve control is used to maintain the FPT-generator shaft speed at 3000 rpm
- Control rod control is used to maintain the reactor outlet temperature at 545 °C
- Coolant pump torque control is used to maintain the TIT at 530 °C
- Cooling water controls are used to maintain the compressors inlet temperatures at 27 °C

The transient responses of the plant are shown in Figure 8-40 to Figure 8-48.

After 20 seconds, the grid load is instantaneously reduced from 100% to 0% as seen in Figure 8-40. Figure 8-40 also shows the transient responses of the turbine power output and reactor fission power during the loss of load event. In order to achieve the control objective, a quick

opening (i.e. fast-acting) bypass valve is used instead of the usual linear valve employed for normal load following operation. The increased rotational speed of the turbine-generator shaft due to the loss of load causes the bypass valve to be rapidly opened by the controller. This will quickly divert flow away from the FPT and reduce the flow through the turbine as shown in Figure 8-41. The FPT mass flow rate is reduced to a level such that the turbine power delivered to the generator is just enough to supply the house load. The rapid reduction of the turbine power helps to prevent shaft over-speed and the rotational speed is returned to the nominal value after about 67 seconds as shown Figure 8-42. The peak over-speed is about 105% of the nominal speed. This is less than the 120% maximum limit defined in the control objectives.

The reactor outlet temperature is maintained at 545 °C by manipulation of the control rod reactivity. Figure 8-43 shows the transients responses of the reactor reactivity. Figure 8-44 shows the controller adjustment of the sodium coolant pump torque and the pump speed and coolant mass flowrates used to maintain the TIT at 530 °C. Figure 8-45 shows the regulation of the precooler and intercooler water flowrates to maintain the LPC and the HPC inlet temperature at 27 °C. The power delivered by the CDT and the power consumed by the LPC and the HPC is shown in Figure 8-46. The transient response of the compressor shaft speed is shown in Figure 8-47, the maximum speed increase is less than 1% of the nominal value.

Variation of the plant temperatures during loss of load is shown in Figure 8-48. It can be seen that the highest and the fastest temperature increase is at the recuperator hot side inlet. The temperature increases from 410 °C to about 470 °C in less than 11 seconds after the loss of load. This temperature increase is due to bypassing of the hot fluid at turbine inlet and mixing it with turbines outlet at the recuperator hot side inlet. At this stage of study, the thermal stress limit of the heat exchangers and the reactor structure is yet to be confirmed. Also, loss of load event is not expected to be a regular occurrence. However, if the temperature fluctuation becomes a concern then an alternative location for the bypass valve will be sought. The bypass valve could be located before the IHX or even before the recuperator to avoid heating of the bypassed nitrogen to high temperature. Nevertheless, placing the bypass valve close to the FPT will ensure a fast response to load change.

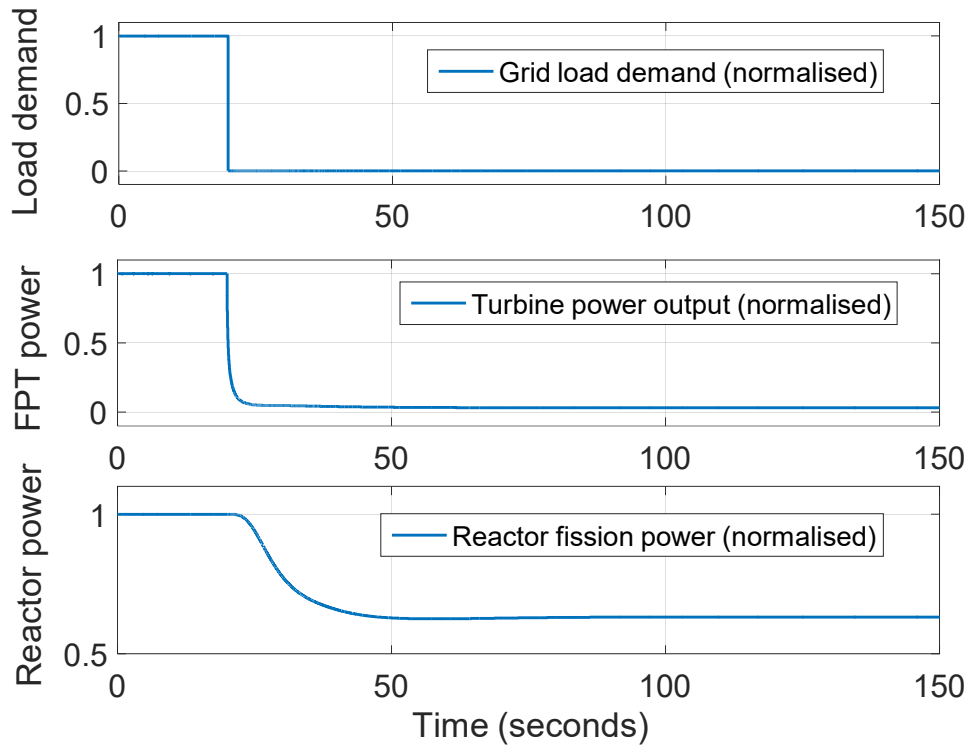


Figure 8-40 Grid load change from full load to zero and transient responses of the turbine power output and reactor fission power

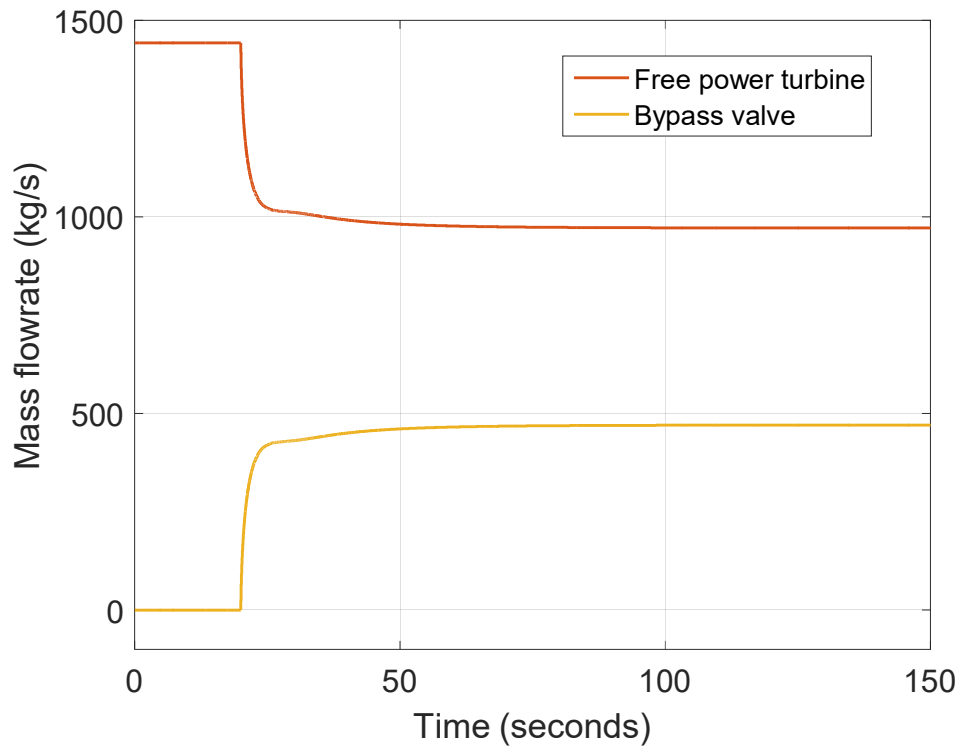


Figure 8-41 Transient responses of the bypass valve and FPT mass flowrates during loss of load event

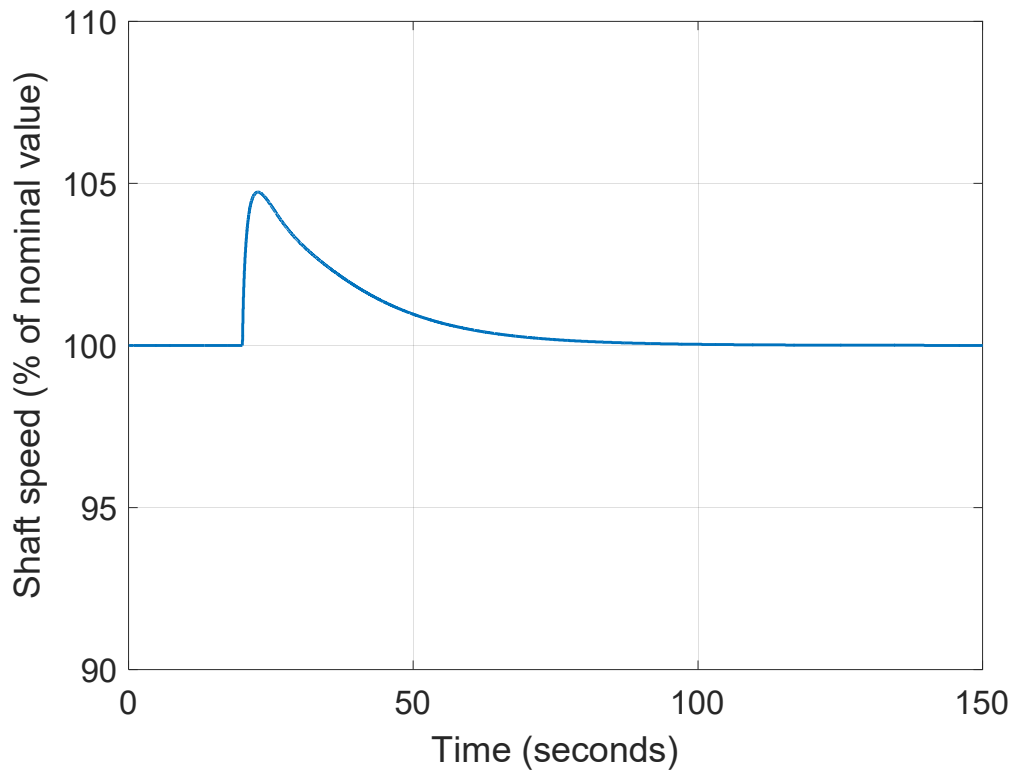


Figure 8-42 Transient response of the FPT-generator shaft rotational speed during loss of load event

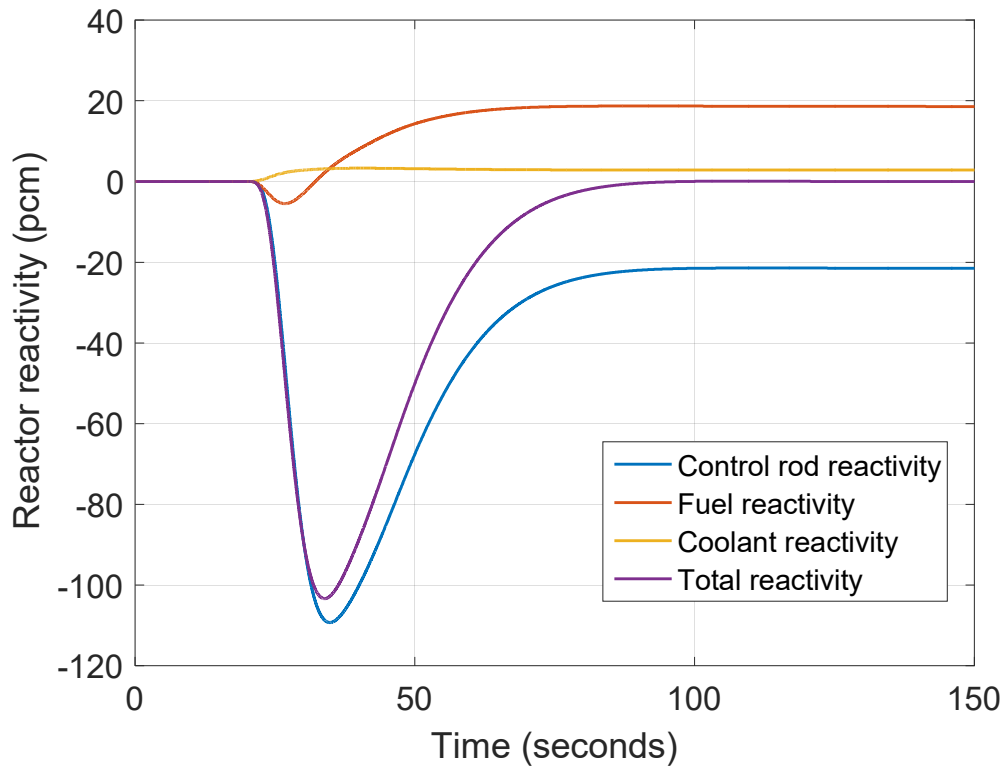


Figure 8-43 Transient responses of the reactor reactivity during loss of load event

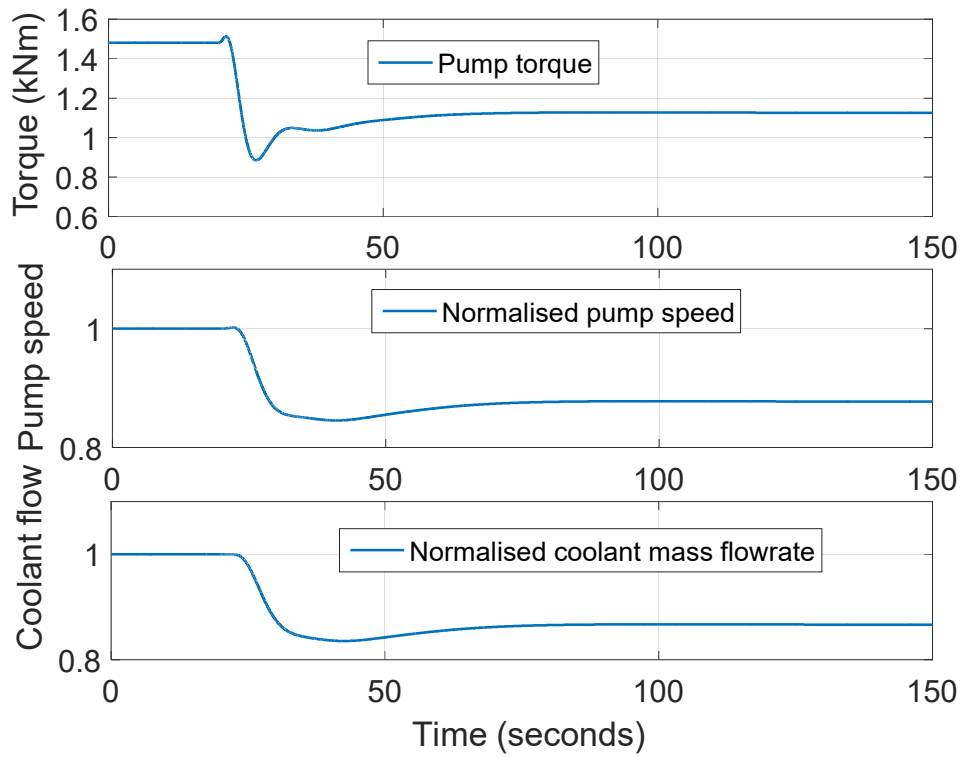


Figure 8-44 Control of the coolant pump torque along with the pump speed and coolant mass flowrate during loss of load event

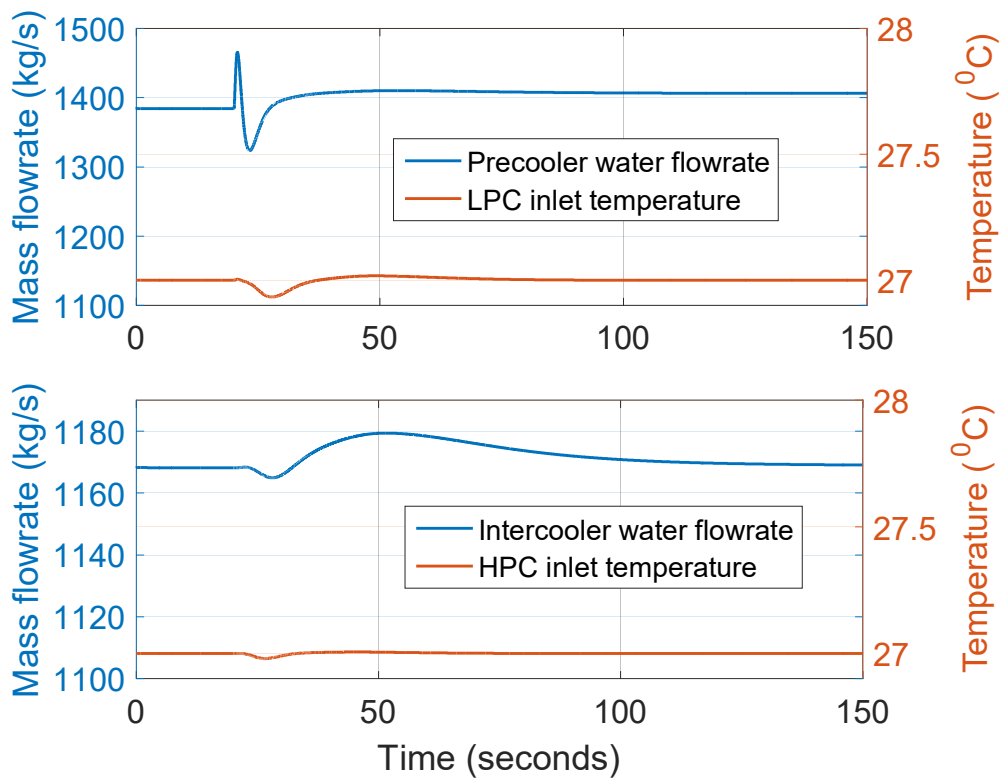


Figure 8-45 Transient responses of the precooler and intercooler water flowrates and the LPC and HPC inlet temperatures during loss of load event

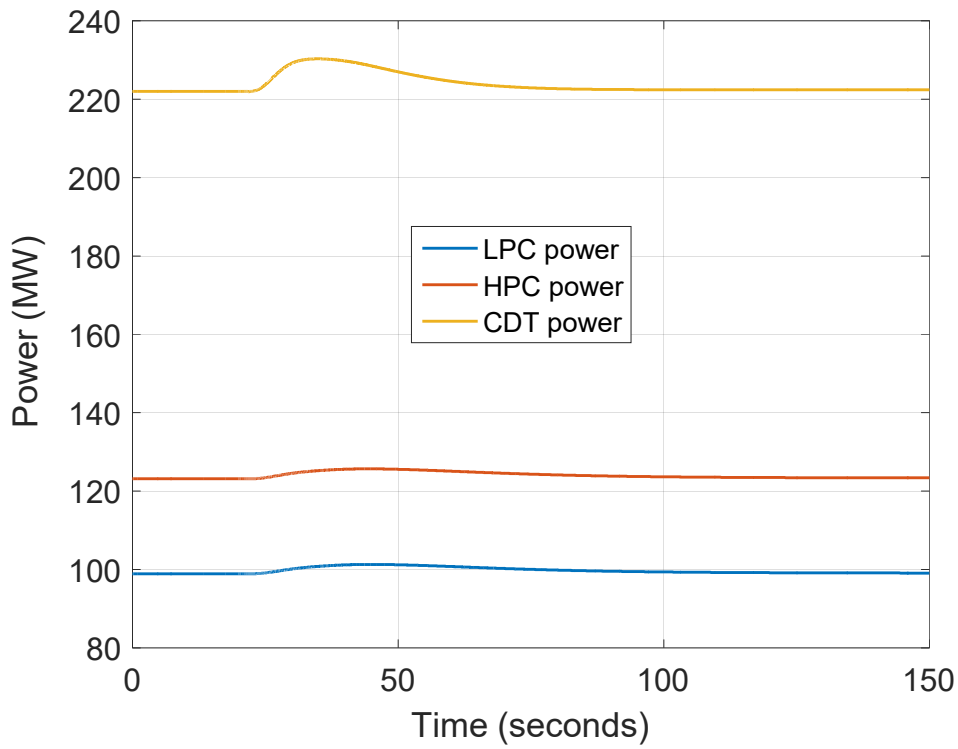


Figure 8-46 Variation of the CDT, the LPC and the HPC power during loss of load

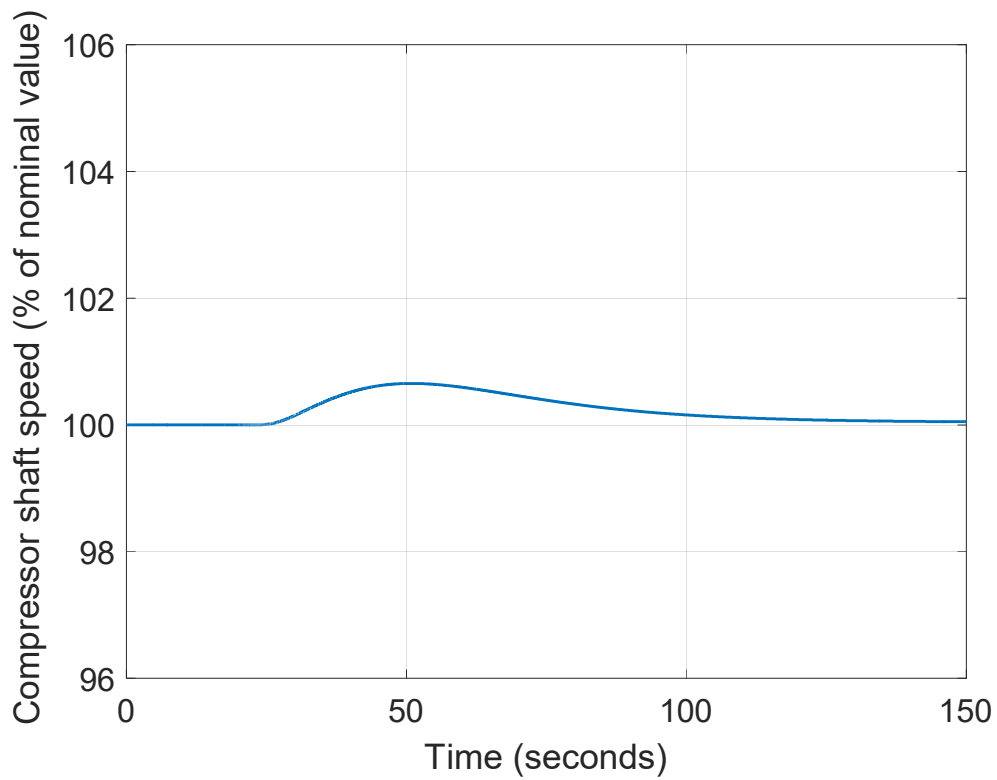


Figure 8-47 Transient response of compressor shaft rotational speed during loss of load

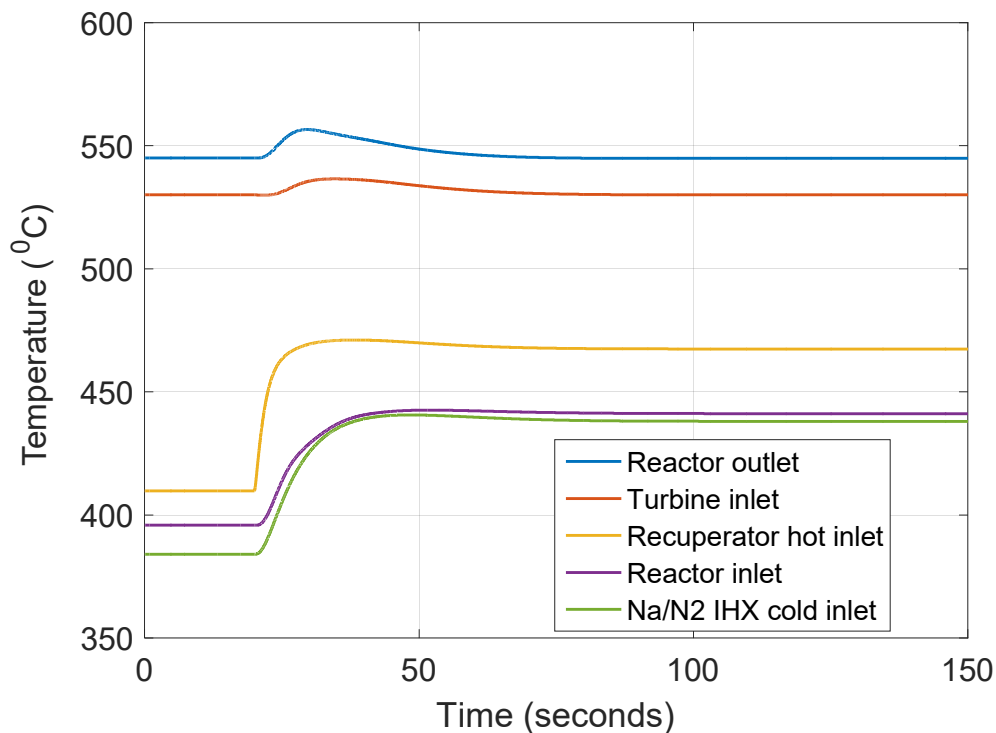


Figure 8-48 Transient responses of plant temperatures during loss of load

8.7 Summary

This chapter provided the dynamic simulation results for the two-shaft nitrogen CBC coupled to SM-SFR. Open loop dynamic characteristics of the plant were assessed by simulating plant transient responses to step change in bypass valve stem position, mass inventory and control rod reactivity without any feedback control loop. The turbine power output responds quickest to change in bypass valve opening, followed by change in inventory. Hence, bypass valve control and inventory control were investigated for power level control while control rod was utilised for keeping the reactor outlet temperature at the nominal value.

Plant dynamic behaviour under normal load following operation and loss of grid load scenario were studied. In order to satisfy the utility requirements, different control strategies were investigated. For load following operation, bypass valve control satisfies the utility requirements. Reactor side controls can be added to the bypass valve control to maintain the reactor outlet and TIT at the design value. For this plant, inventory control cannot meet the requirements of maintaining the turbine-generator shaft speed within ± 30 rpm of the rated speed during load following operation. During loss of load, a quick opening bypass valve is employed for shaft speed control.

Even though rise in recuperator hot side inlet temperature and reactor inlet temperature were observed, this is not considered excessive at this time. Further detailed design of the components would indicate the actual limit of temperature variation. In summary, stable control and operation of the two-shaft nitrogen cycle coupled with SM-SFR is feasible.

9 Dynamic Performance Analysis of the SM-PWR with s-CO₂ cycle (SM-PWR/s-CO₂) Plant

9.1 Introduction

In Chapter 5, the thermodynamic performance and preliminary design of s-CO₂ Brayton cycles coupled to SM-PWR were presented. However, besides the full load steady state performance studies of s-CO₂ cycle, one of the other technologies that need to be proven/developed relates to its operation and control. The dynamic behaviour of the cycle is relatively unknown. The dynamic performance and control of this PCS will have significant impact on its overall success. An understanding of the part-load behaviour is crucial for determining the plants operation and control schemes. Due to the real gas properties effects of CO₂, the operating conditions of s-CO₂ cycle strongly affect the cycle performance. Hence, the s-CO₂ cycle might require other control options apart from the strategies utilised for ideal gas closed cycle turbines. The aim of this chapter is to investigate the transient performance of the s-CO₂ cycle under normal load-following and sudden loss of load as well as the control schemes.

9.2 Operation, control and simulation challenges for s-CO₂ cycle

Dynamic operation, control and simulation of s-CO₂ Brayton cycle pose some unique challenges not seen in ideal gas cycles like the nitrogen cycle. This is due to its key features like the parallel operation of compressors, operating the MC inlet close to the critical point and rapid fluid property changes around the critical point. The phase diagram of CO₂ showing the critical region is given in Figure 9-1 while the rapid fluid property changes around the critical point is illustrated in Figure 9-2. The almost incompressible behaviour of CO₂ causes the power taken by the compressor to be low compared to an ideal gas. Though these are the key enabling features of the s-CO₂ recompression cycle unfortunately, they also present challenges for its operation, control and simulation as outlined below:

- **Precooler control issue:** An important non-ideal property is the large increase in specific heat capacity that occurs in the surroundings of the critical point. This increases the HTC because the heat transfer near the critical point is nearly a two-phase vaporization/condensation process and hence occurs very nearly at a constant temperature (Wright et al., 2010). This therefore causes a very low temperature drop in the hot side of the precooler despite the large amount of heat rejected. This results in some practical control issues for s-CO₂ plant because a small change in CO₂ temperature will require a very large amount of heat transfer in the precooler.

- Turbomachinery operation and system stability:** The use of inventory control during part-load operation will lead to the low pressure side of the cycle dropping below the critical pressure and the MC inlet density will drop significantly. This increases the compressor volumetric flow rate even though the mass flow rate also decrease with inventory control. It is unlikely for a compressor to operate with a volumetric flow rate much larger than its design value because turbomachine's performance is largely determined by the velocity triangles, which are dependent on the volumetric flow rate. It has been shown that the MC will drop its fluid density by over a factor of two if the mass flow rate drops by less than half, thus creating a limiting large volumetric flow rate in the MC (Carstens, 2007). Therefore, the MC would not be able to absorb extra flow, and by design, the RC cannot absorb as much flow as the MC. Also, a significant change in compressor performance due to the large density changes can create pressure spikes in the system (Trinh, 2009). This concern stems from the shock introduced to the system with a sudden drop in fluid density and the corresponding pressure changes moving through the closed cycle. The MC outlet pressure will decrease making the turbines to see an increased flow coefficient, $(\dot{m}\sqrt{T}/P)$, and thus decreased outlet pressure. The compressor sees the reduced pressure and the corresponding reduced density and reduces its pressure ratio further. This phenomenon may produce positive feedback, which could make the system unstable.
- Compressors in parallel:** Parallel operation of compressors is inherently more complex than single compressor operation. The outgoing outlet pressures of the compressors must match for stable operation. If the outlet pressures do not match and no active control actions are taken, then the lower pressure line will attempt to decrease its flow rate and divert more flow to the high pressure line until both compressor outlet pressures balance. When the density decreases by a large amount, the MC ability to raise the pressure decreases. Hence the mass flow rate to the MC will decrease, while flow to the RC increases to balance the outlet pressures. This will drive one or both of the compressors beyond available operating bounds and cause choke or stall (Trinh, 2009). The exact effects of these large non-linear changes on a compressor are complex and uncertain for now since most of the currently available performance maps are based on analytical models and numerical simulation (Carstens, 2007). Actual experimental data on compressor operating in the critical region will provide more information on the turbomachinery behaviour.
- S-CO₂ fluid properties calculation:** For modelling and simulation purposes as well as component design, the fluid properties calculation requirements for s-CO₂ are considerably more difficult than ideal gas cycles. One of the key challenges is that the

rapidly varying and non-linear changes in fluid properties makes solving the equation of state challenging. Also, the complexity of heat exchange with s-CO₂ might require detailed heat transfer and pressure drop calculations for the heat exchangers, this will prevent the use of simple but common relations like log-mean temperature (Carstens, 2007). Such detailed calculations will require thermodynamic transport properties such as thermal conductivity and viscosity. Finally, the CO₂ fluid properties have to be available above and below the critical pressure to allow for part-load operation. In a nutshell, the fluid properties calculations must be robust, very accurate, able to convert to and from a wide variety of properties and these requirements have to be met very quickly to minimise computation time (Carstens, 2007). In this study, the fluid property calculation requirements were satisfied by implementing a digitized form of NIST REFPROP property data as look-up tables in the Simulink models.

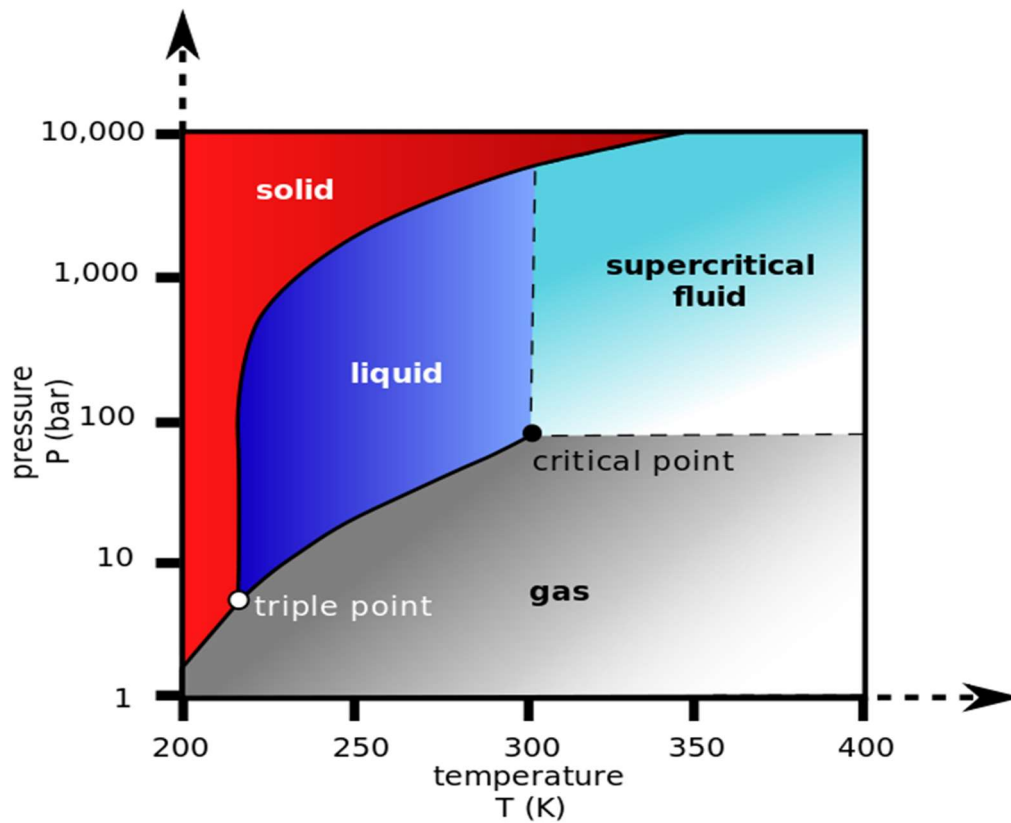


Figure 9-1 CO₂ phase diagram showing the critical point

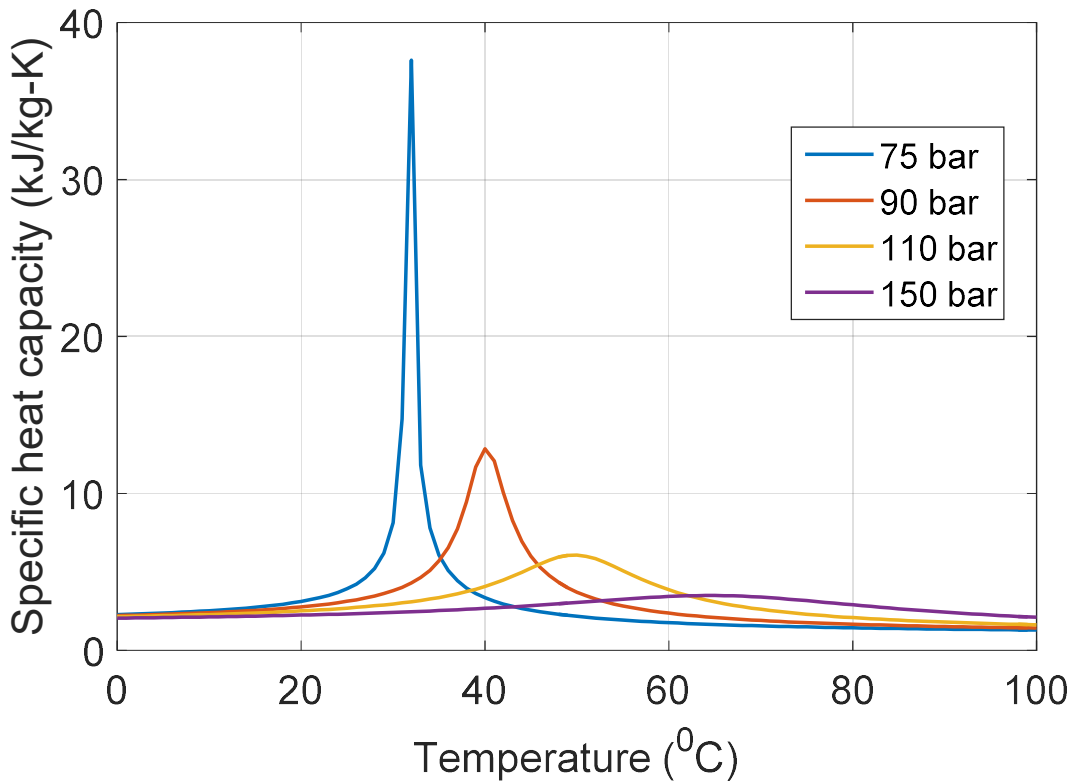


Figure 9-2 CO₂ isobaric specific heat capacity around the critical point

9.3 Design point conditions and components parameters for the SM-PWR/s-CO₂ cycle nuclear power plant

The simulated plant is the SM-PWR coupled to the newly proposed s-CO₂ Brayton cycle (i.e. the single recuperator recompression cycle). The steady state design point conditions and the preliminary design of the turbomachinery and heat exchanger have been reported in Chapter 5. Some of these values are set as the initial values for the dynamic simulation. Table 9-1 summarises the design point conditions and components parameters used for the simulation.

The thermal power of the reactor is 500 MWth and the core outlet temperature is 300 °C. The Water/s-CO₂ IHX is used to transfer the reactor heat energy to the s-CO₂ in the PCS. The TIT is 290 °C and the pre-cooler cooling water is provided at 22 °C. The turbomachinery-generator shaft rotates at 3000 rpm because the generator is assumed synchronised with the grid at a frequency of 50 Hz.

Table 9-1 Summary of design point conditions and parameters for the SM-PWR/s-CO₂ plant

Parameter	Value
Reactor thermal power	500 MWth
Reactor outlet temperature	300 °C
Turbines inlet temperature	290 °C
Cooling water supply temperature	22 °C
Compressors inlet temperature	32 °C
Maximum cycle pressure	220 bar
Total mass flowrate of CO ₂	3189.4 kg/s
Reactor side mass flowrate	2869.3 kg/s
Cooling water mass flowrate	5351.3 kg/s
Turbomachinery-generator shaft speed	3000 rpm
Recuperator fluid volume (Hot or cold side)	10.63 m ³
Precooler fluid volume	6.18 m ³
Water/s-CO ₂ IHX fluid volume	3.51 m ³
Turbomachinery fluid volume	MC: 3x10 ⁻² m ³
	RC: 3x10 ⁻² m ³
	Turbine: 0.35 m ³
Mass of heat exchangers metal	Recuperator: 219,740 kg
	Precooler: 127,830 kg
	Water/s-CO ₂ IHX: 72,493 kg
Electric power output	133.09 MWe
Efficiency	26.62%

9.4 Automatic control configuration for the SM-PWR/s-CO₂ nuclear power plant

S-CO₂ cycle power plant requires careful control to prevent system instability and turbomachinery performance failure. Figure 9-3 shows the possible placement of the control elements in the plant. No inventory/pressure control is implemented in order to avoid the problematic large variation of fluid properties at compressor inlets. In addition, flow split controller (FSC), RC variable throttle valve (V3) and low pressure side variable throttle valve (V4) have been added to the normal bypass valve, control rod and pump torque controller in order to effectively control the plant during part-load operation.

The flow split controller is used in conjunction with the RC throttle valve for turbomachinery matching and compressor surge/stall or choke prevention. A flow split that does not balance the compressor outlet pressures but keeps both compressors within allowable operating bounds is imposed by using the flow split valve to control the mass flowrate going into one of the compressors. This will cause the pressure rise across the RC to be higher than the MC pressure rise. Then by using the RC variable throttling valve, the RC outlet is throttled to match the MC

outlet pressure regardless of the incoming mass flowrate and fluid property changes. The turbine outlet and cycle low pressure side pressure is increased with bypass valve control. By using the low pressure side throttle valve, the compressors inlet pressures are kept at the design value.

This proposed control strategy aimed to satisfy the control requirements and objectives mentioned in Section 7.3.

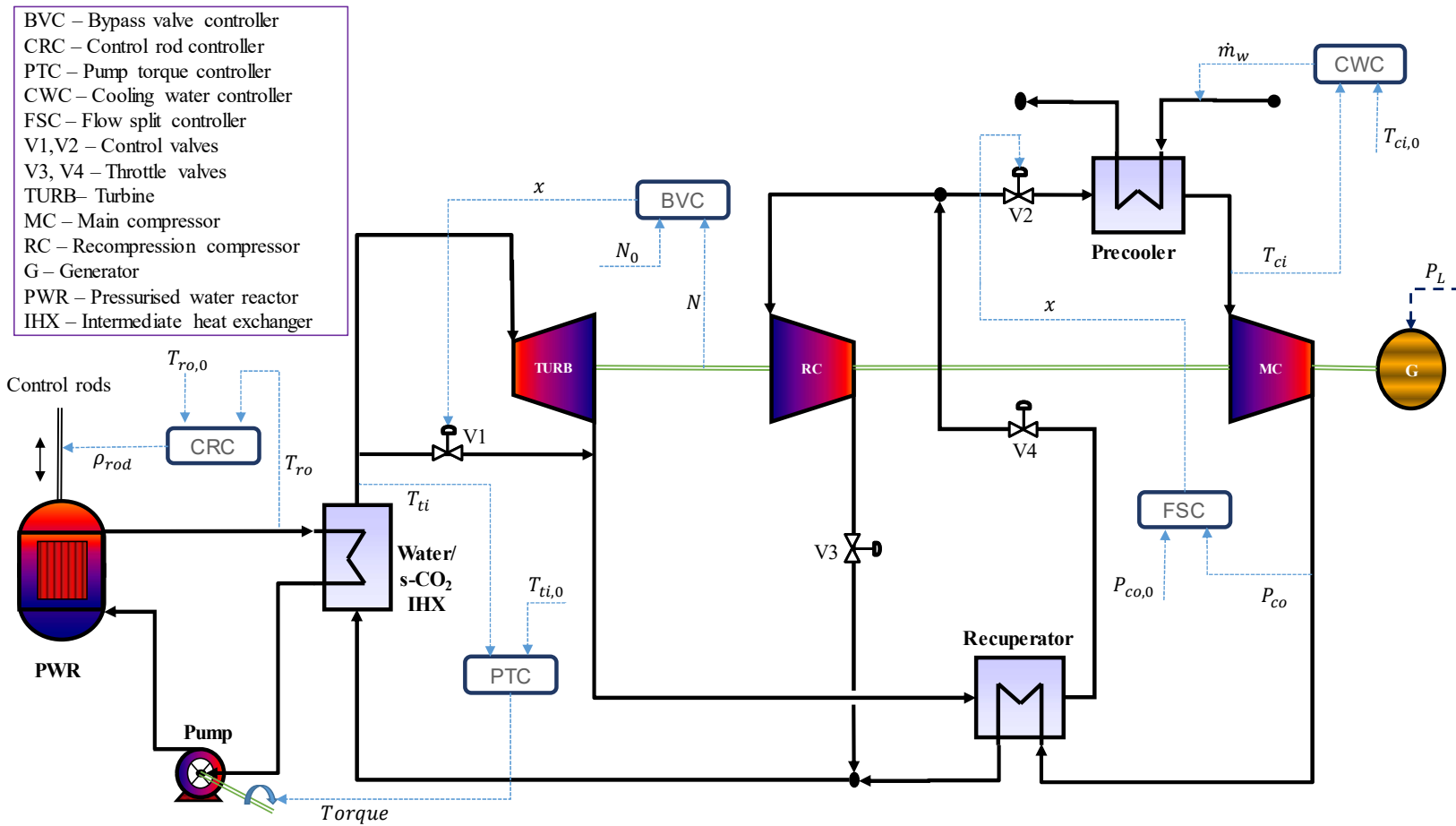


Figure 9-3 Control scheme for the SM-PWR/s-CO₂ cycle nuclear power plant

9.5 Normal load following between 100% and 50% of the SM-PWR/s-CO₂ plant

Load ramps between 100% and 50% of full load is simulated to study the normal load-following transients of the plant. Bypass valve controller is utilised to keep the shaft speed at the synchronous speed of 3000 rpm. Control rod controller is used to maintain the reactor outlet temperature at 300 °C while the coolant pump controller is used to keep the TIT at 290 °C. The cooling water controller is used to maintain the MC inlet temperature at 32 °C. The flow split controller is used to adjust the flow rate of the MC. In addition, the throttle valves are used to maintain the low pressure and high pressure values at compressor inlet and outlet respectively. The total mass flow rate will remain constant at 3189.4 kg/s since there is no inventory/pressure control. The transient response of the plant is shown in Figure 9-4 through Figure 9-15.

The maximum change in shaft speed is about ± 27 rpm, which is within the allowable value of ± 30 rpm (Figure 9-5). The plant efficiency drops to about 15% from 26.62% when the load is reduced to 50% of full load value (Figure 9-15).

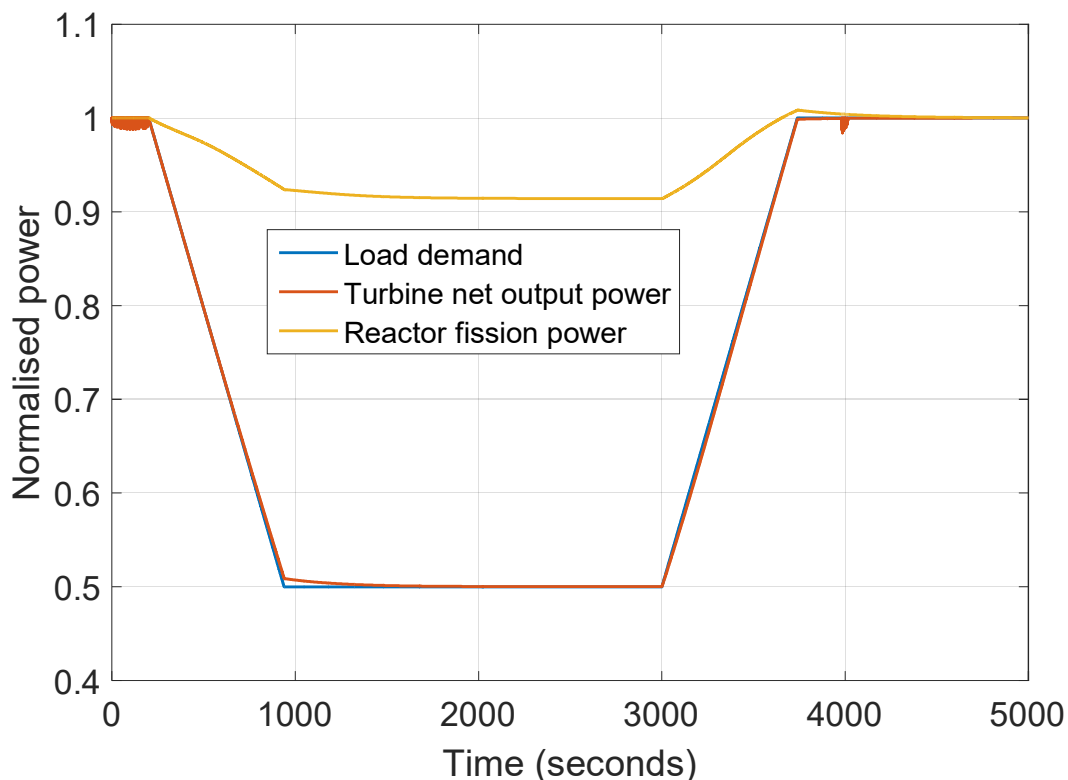


Figure 9-4 Load demand, turbine net power output and reactor power during normal load following of the SM-PWR/s-CO₂ plant

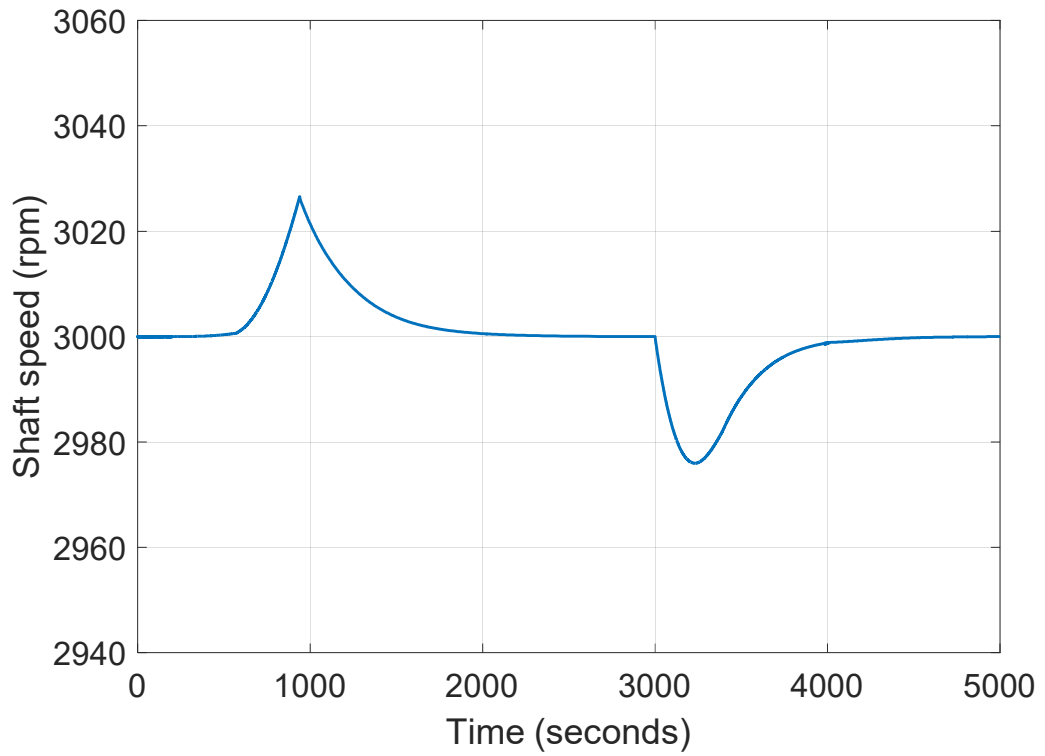


Figure 9-5 Shaft speed of the SM-PWR/s-CO₂ plant during normal load following transient

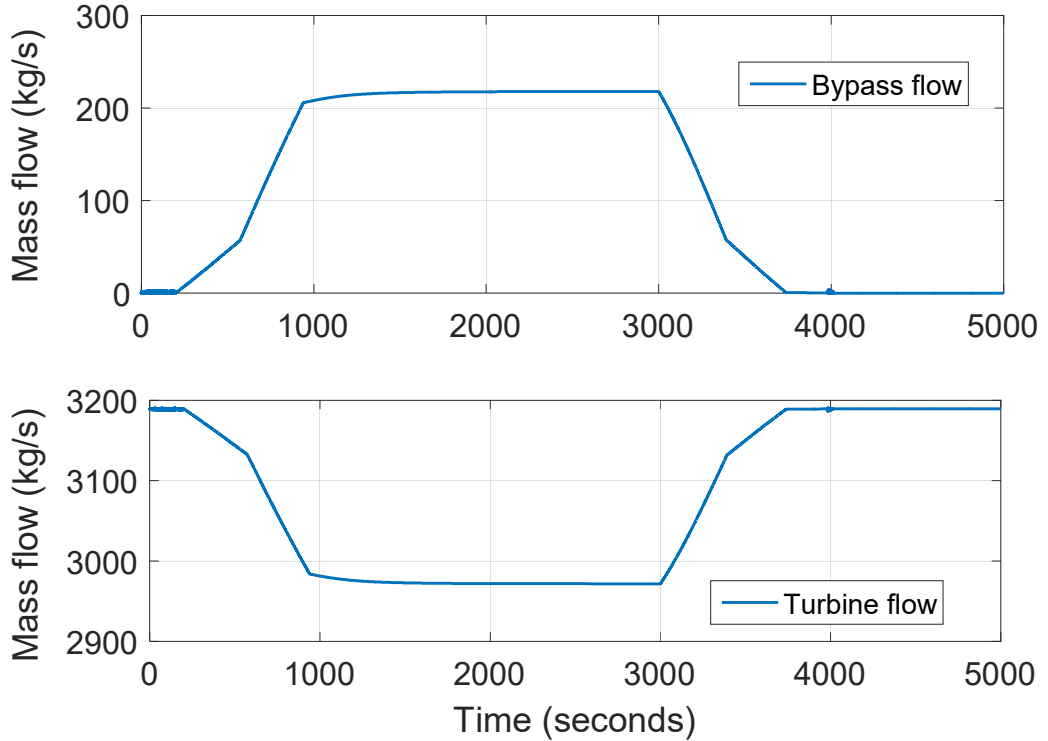


Figure 9-6 Bypass valve mass flow rate and turbine mass flow rate of the SM-PWR/s-CO₂ plant during normal load following operation

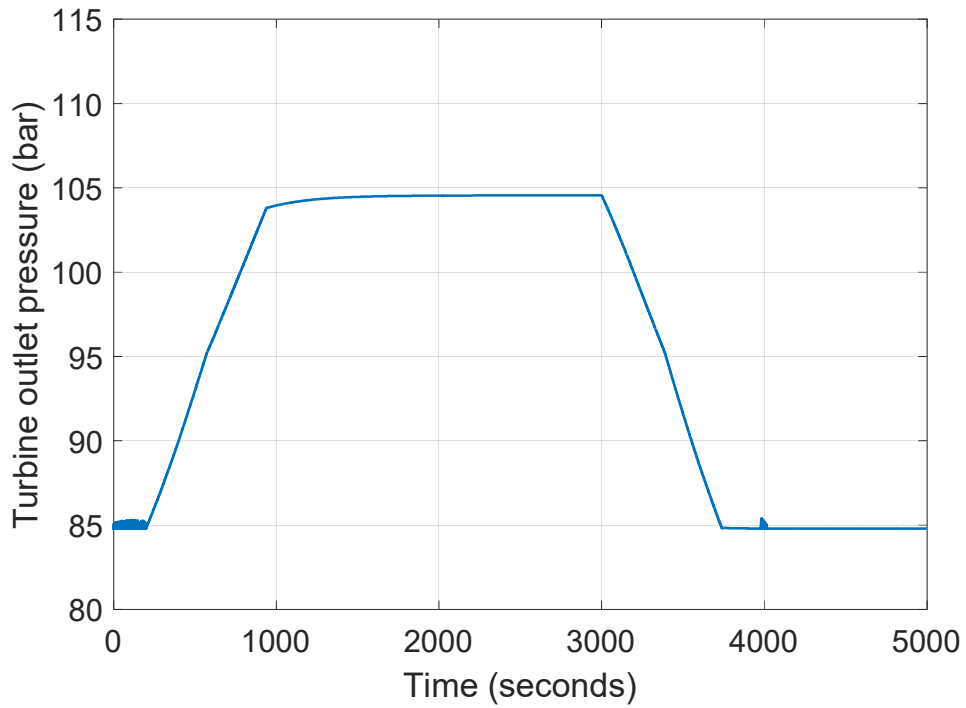


Figure 9-7 Turbine outlet pressure during normal load following operation of the SM-PWR/s-CO₂ plant

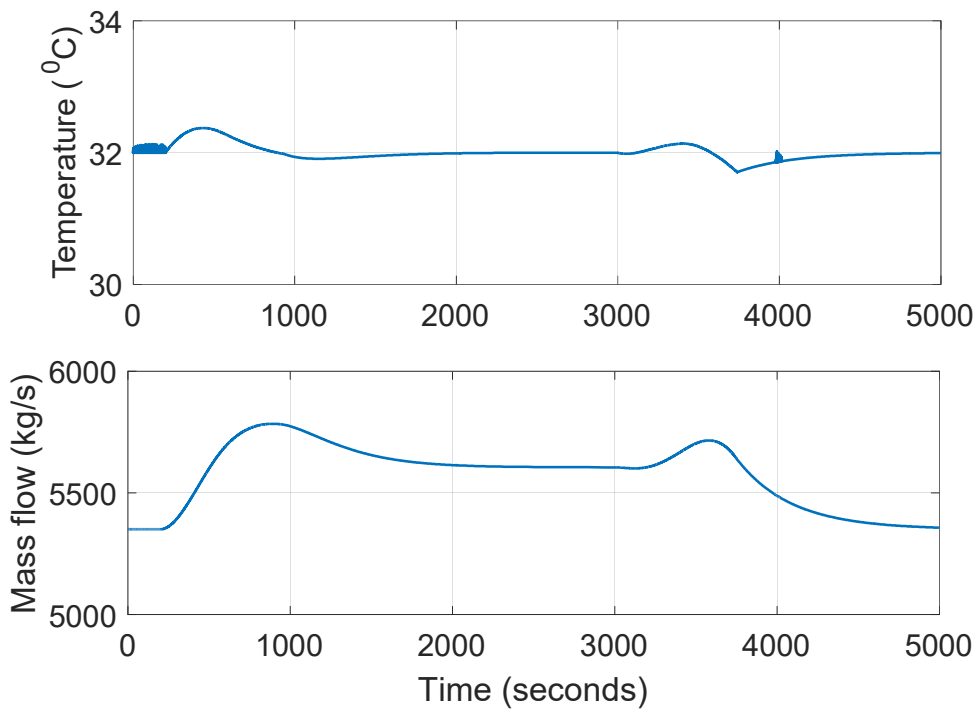


Figure 9-8 MC inlet temperature and adjustment of the cooling water mass flow rate during normal load following of the SM-PWR/s-CO₂ plant

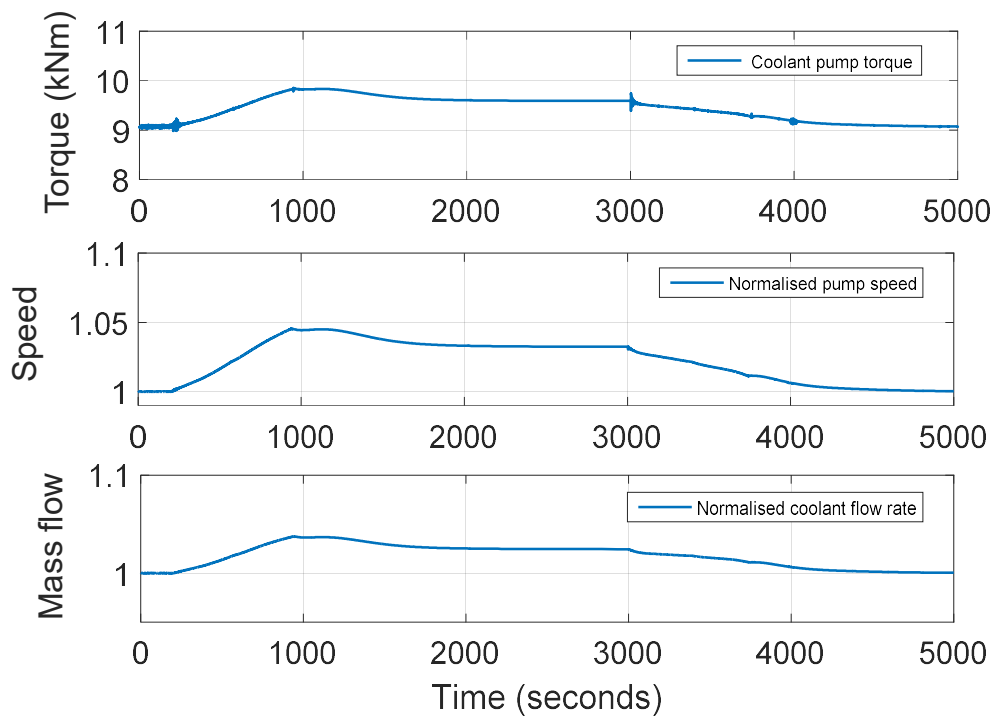


Figure 9-9 Adjustment of the coolant pump torque, speed and coolant mass flow rate to maintain the TIT at 290 °C during normal load following of the SM-PWR/s-CO₂ plant

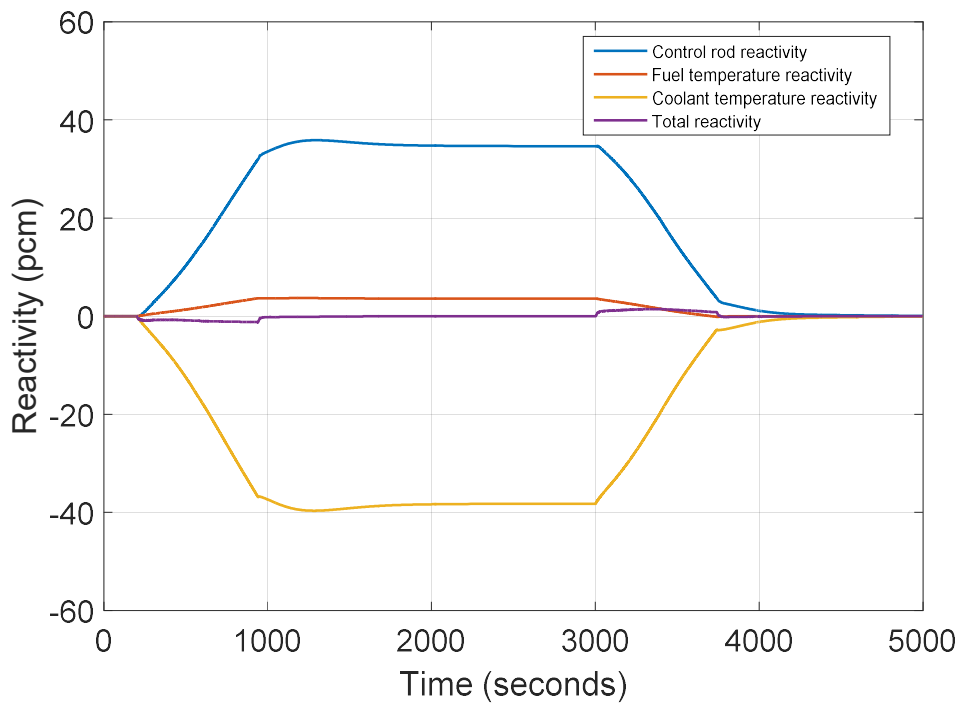


Figure 9-10 Fuel reactivity, coolant reactivity and modulation of control rod reactivity during normal load following of the SM-PWR/s-CO₂ plant

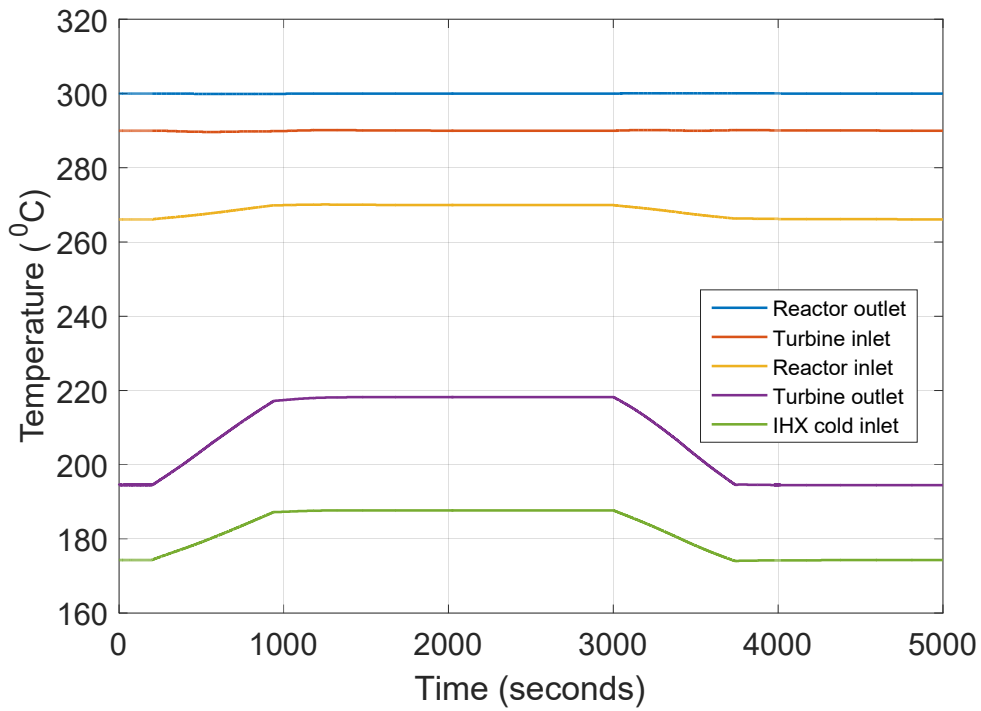


Figure 9-11 Reactor core outlet, turbine inlet, reactor inlet, turbine outlet/recuperator hot inlet and IHX cold inlet temperature during normal load following of the SM-PWR/s-CO₂ plant

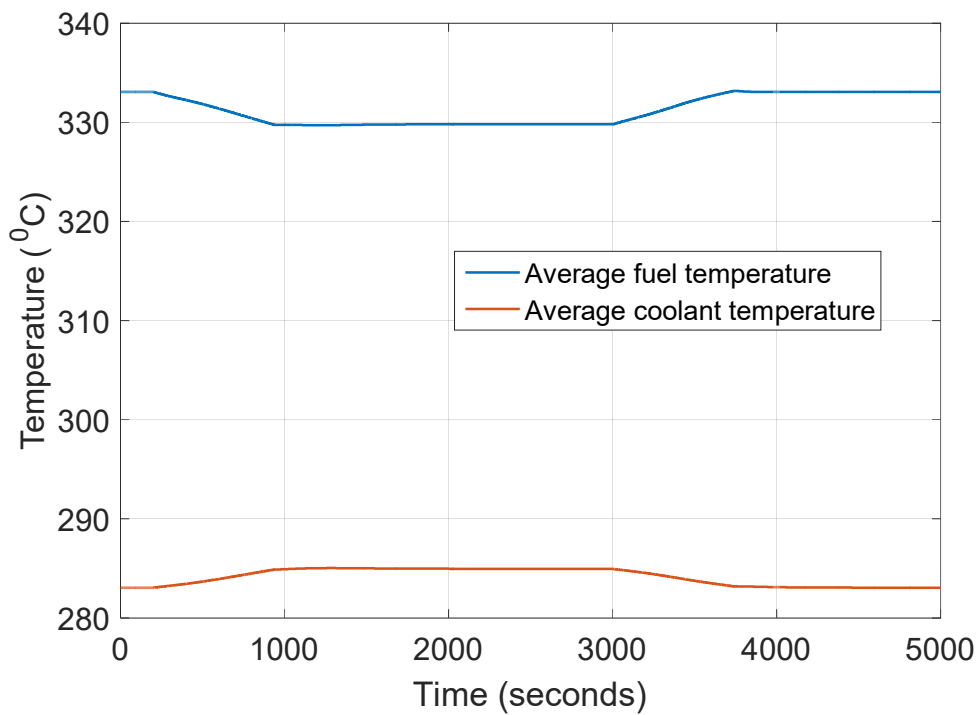


Figure 9-12 Average fuel temperature and average coolant temperature during normal load following of the SM-PWR/s-CO₂ plant

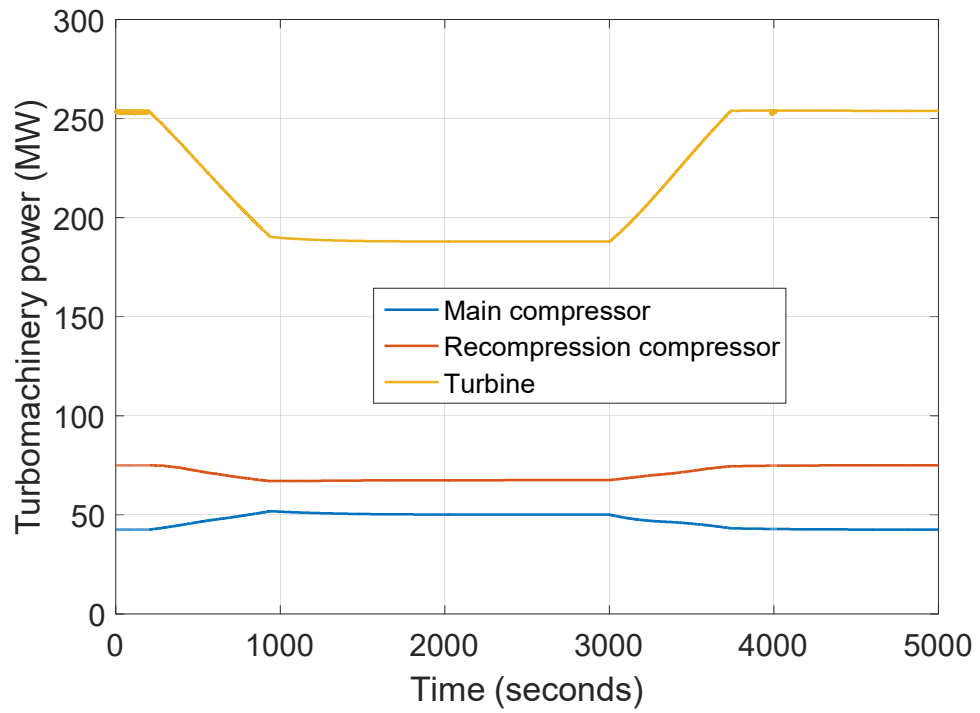


Figure 9-13 MC, RC and turbine power during normal load following of the SM-PWR/s-CO₂ plant

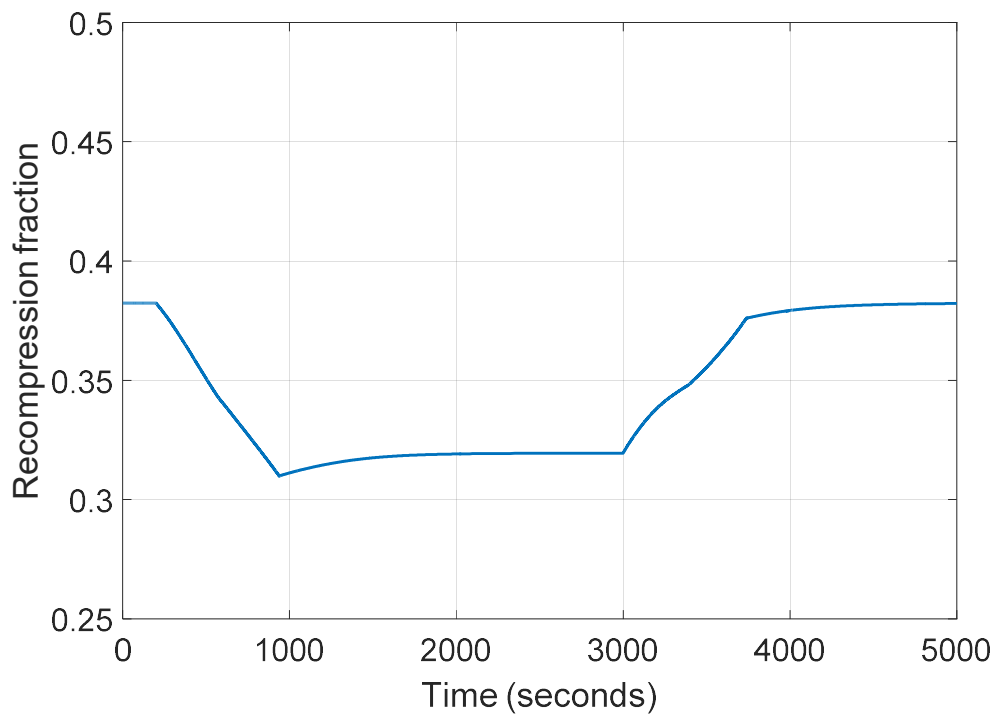


Figure 9-14 Adjustment of flow split fraction during normal load following of the SM-PWR/s-CO₂ plant

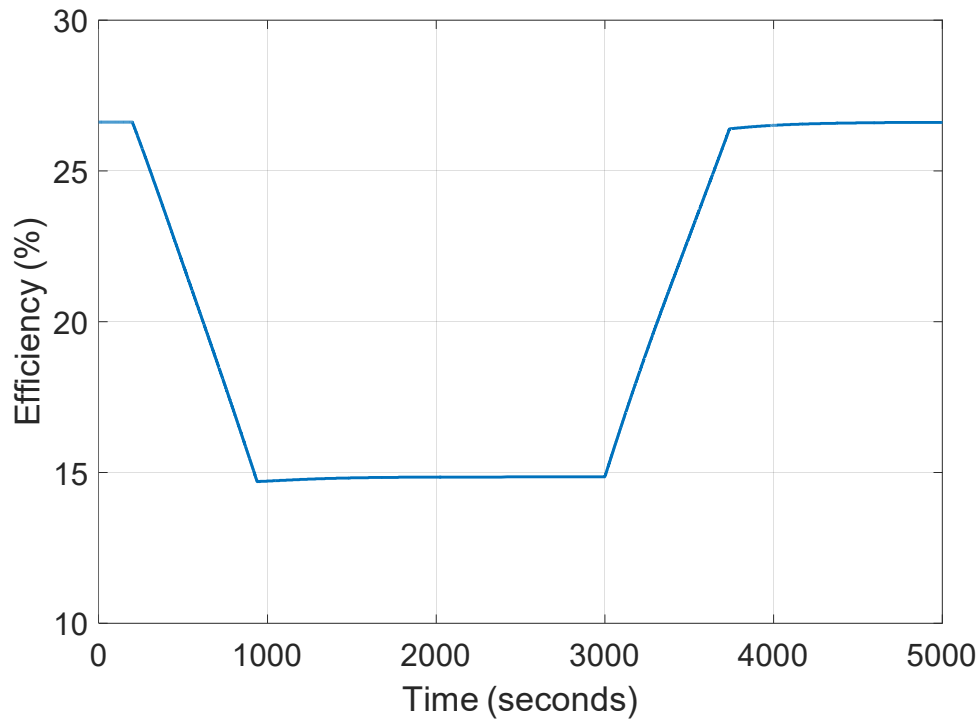


Figure 9-15 Variation of plant efficiency during normal load following of the SM-PWR/s-CO₂ plant

9.6 100% instantaneous loss of grid load of the SM-PWR/s-CO₂ plant

Instantaneous reduction of electric load demand from full load to zero load is simulated to study the plant transient behaviour during an abrupt separation from the grid. The objective of the control system during the loss of load event is to avoid over-speeding of the turbine-generator shaft by keeping the shaft speed below 120% of the nominal value. Quick opening bypass valve is used to avoid excessive over-speeding of the generator shaft during the loss of load event. Figure 9-16 to Figure 9-25 show the result of plant transient response to instantaneous loss of grid load. The highest over-speed is about 107% of the nominal speed. This is below the maximum allowable limit of 120% specified in the control objectives.

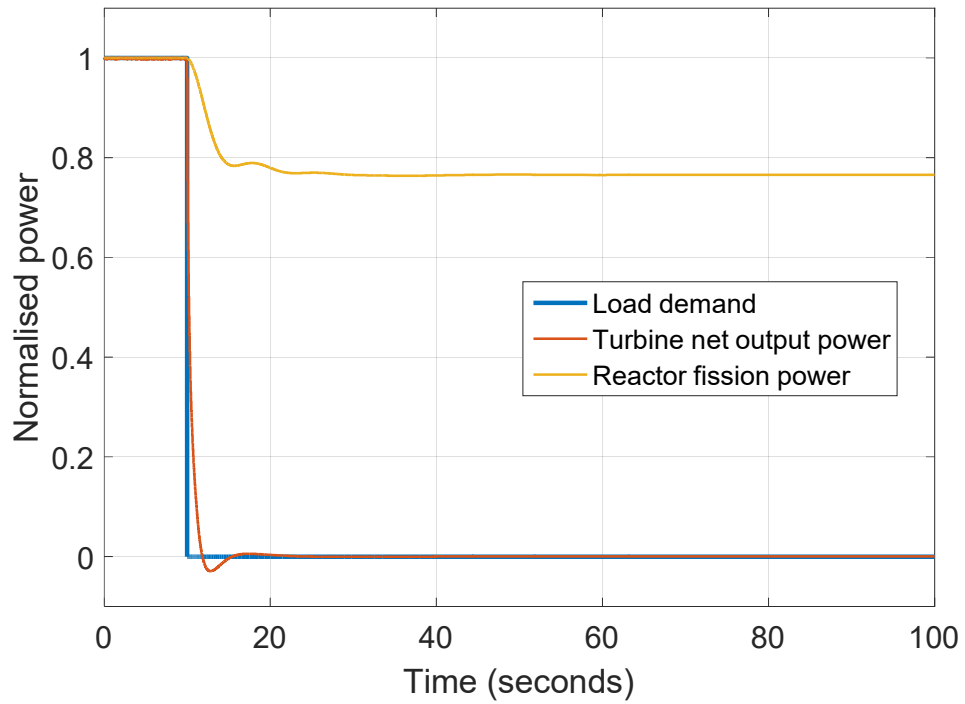


Figure 9-16 Grid load change from full load to zero and transient responses of the turbine net power output and reactor fission power of the SM-PWR/s-CO₂ plant

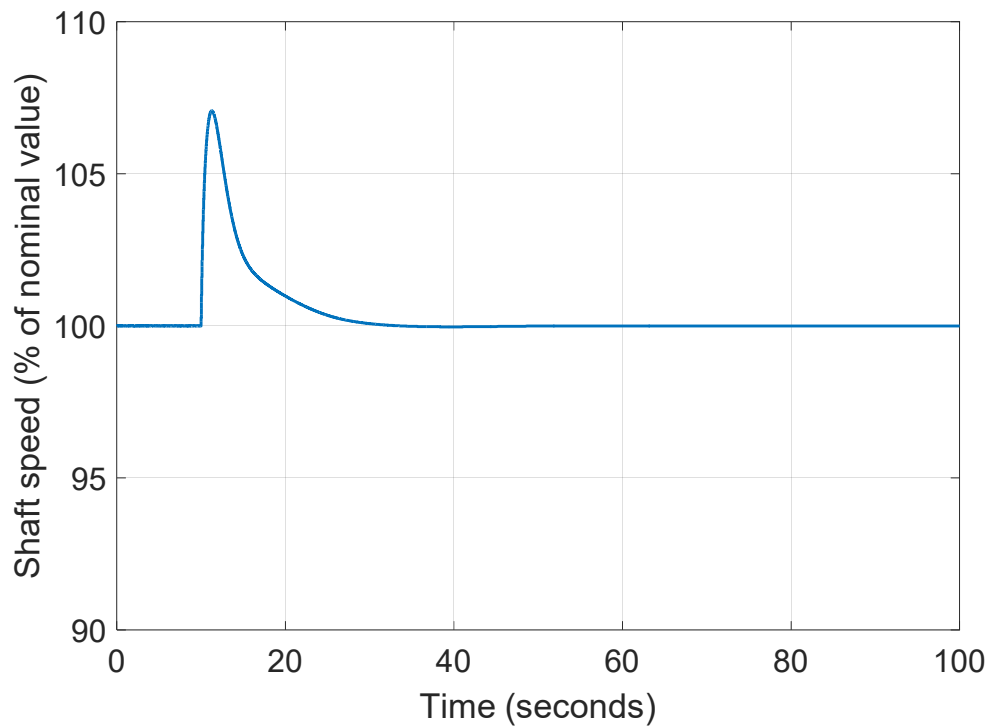


Figure 9-17 Transient response of the turbomachinery-generator shaft rotational speed during loss of load event of the SM-PWR/s-CO₂ plant

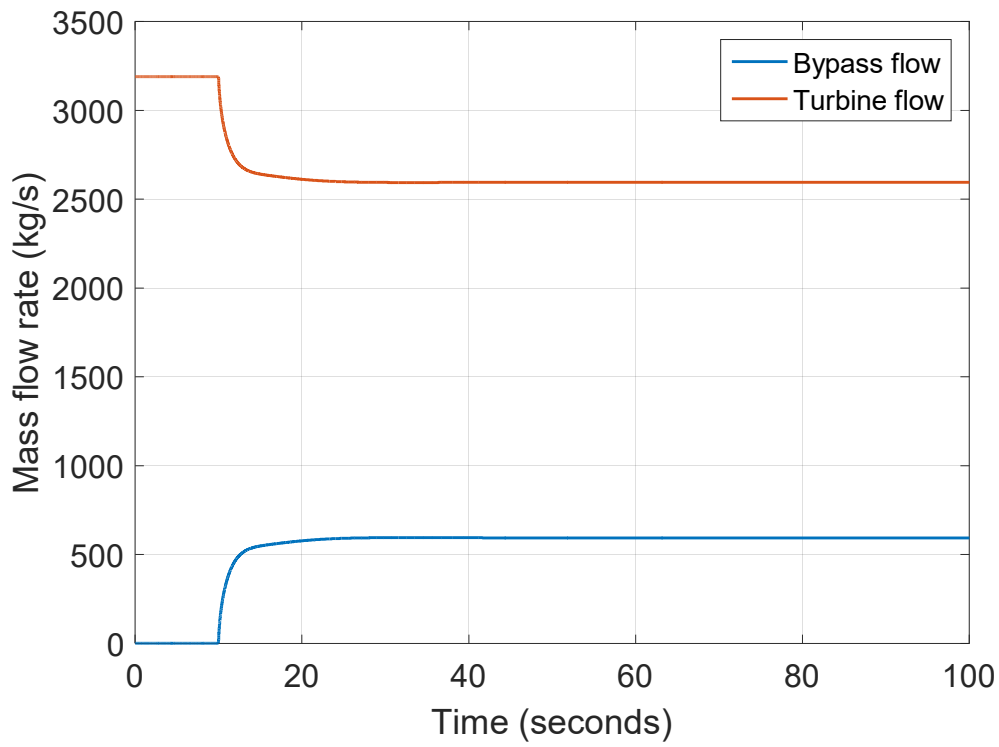


Figure 9-18 Transient responses of the bypass valve and turbine mass flowrates during loss of load event of the SM-PWR/s-CO₂ plant

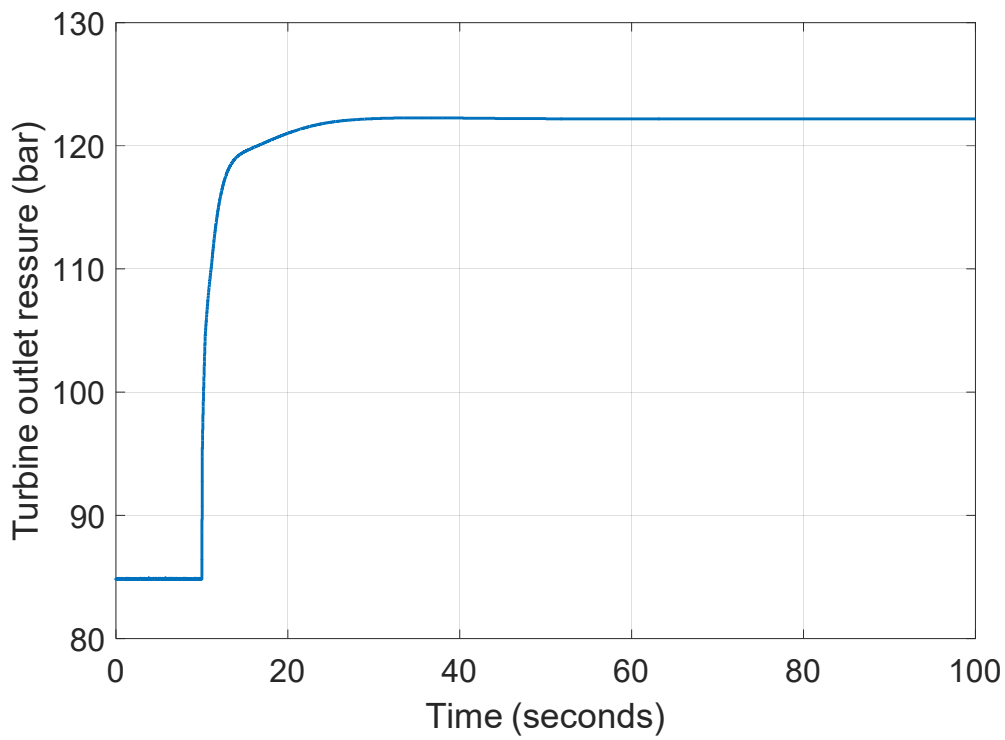


Figure 9-19 Turbine outlet pressure during loss of load event of the SM-PWR/s-CO₂ plant

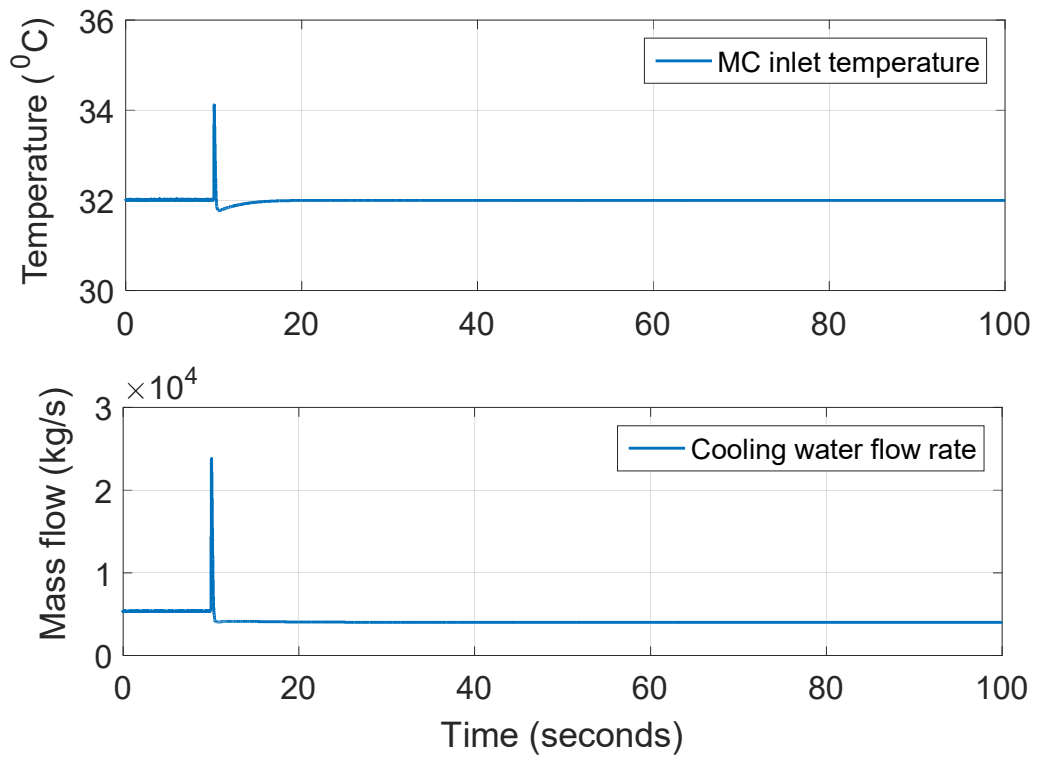


Figure 9-20 Transient responses of the MC inlet temperature and precooling water flowrates during loss of load event of the SM-PWR/s-CO₂ plant

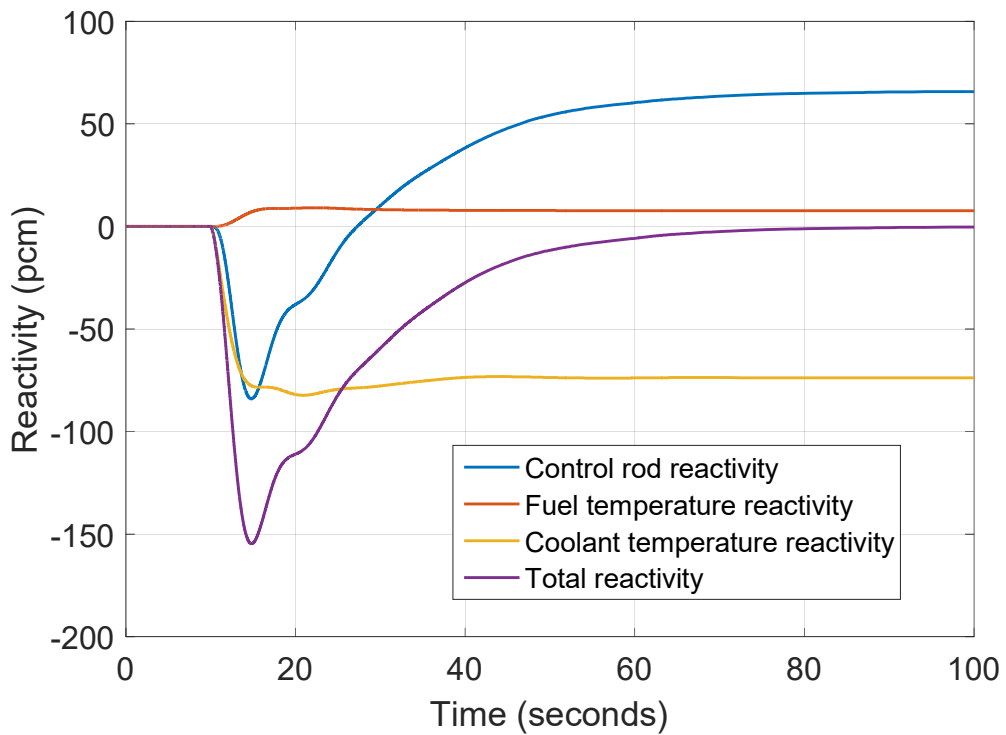


Figure 9-21 Transient responses of the reactor reactivity during loss of load event of the SM-PWR/s-CO₂ plant

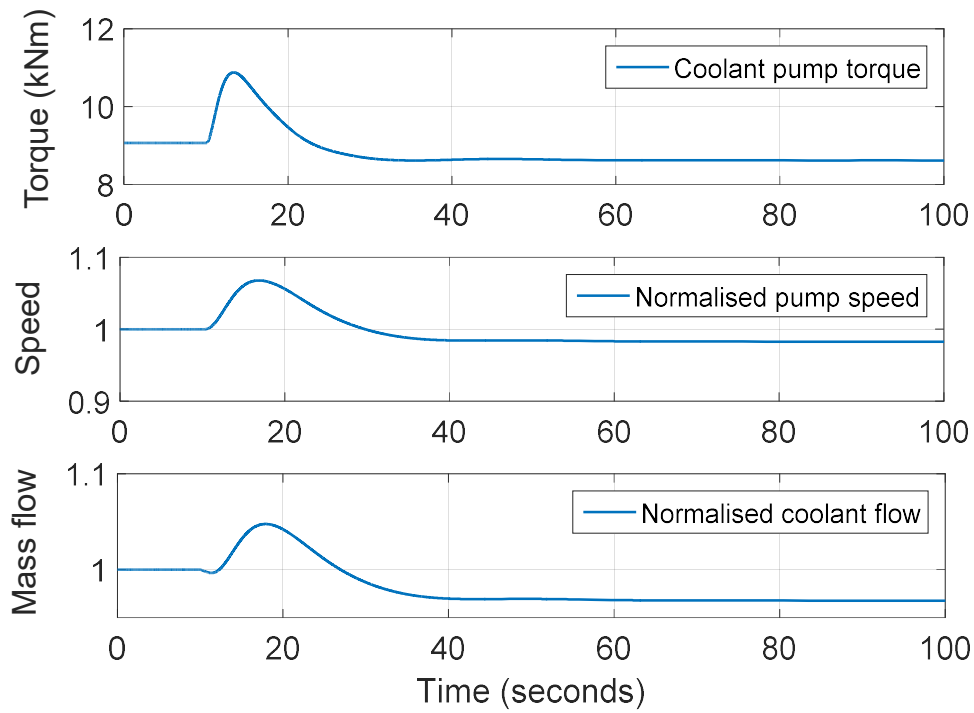


Figure 9-22 Control of the coolant pump torque along with the pump speed and coolant mass flowrate during loss of load event of the SM-PWR/s-CO₂ plant

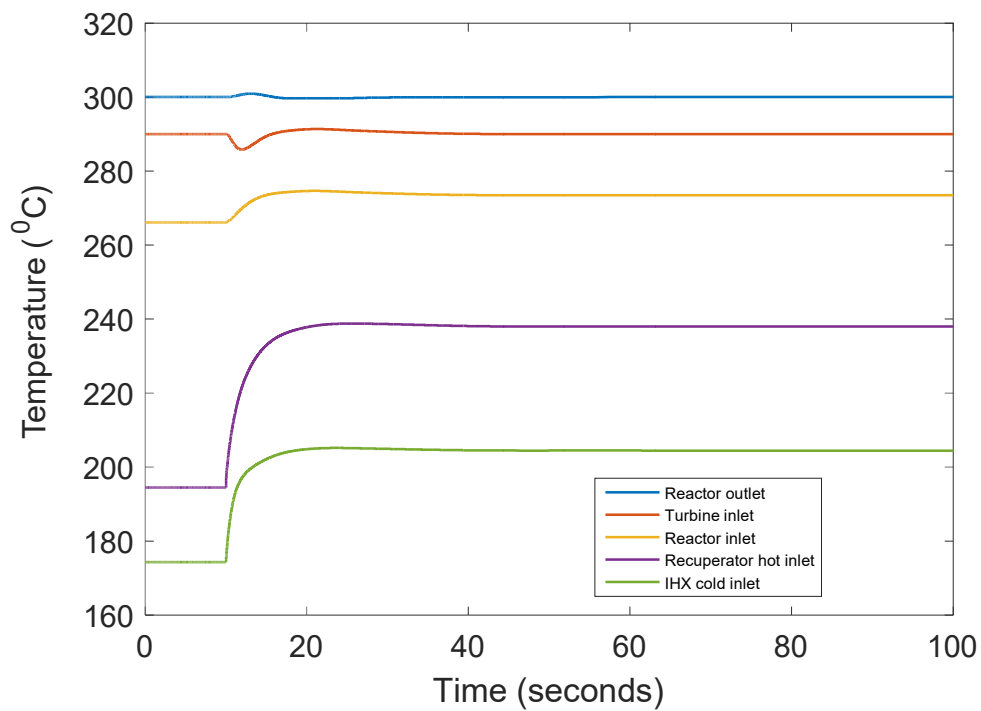


Figure 9-23 Transient response of reactor outlet, turbine inlet, reactor inlet, recuperator hot inlet and IHX cold inlet temperature during loss of load event of the SM-PWR/s-CO₂ plant

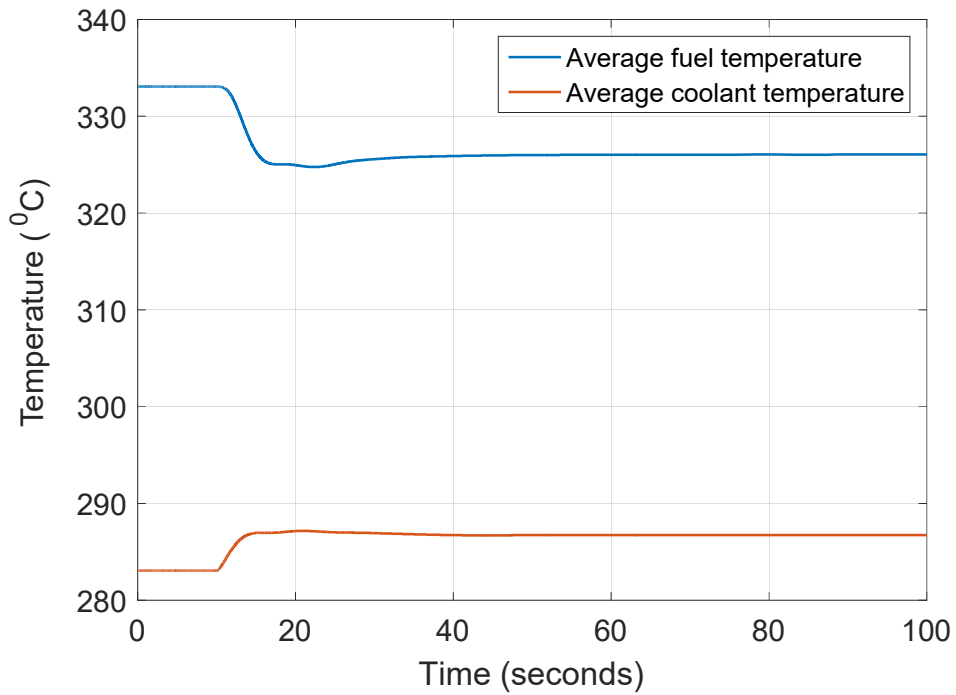


Figure 9-24 Transient response of average fuel and coolant temperature during loss of load event of the SM-PWR/s-CO₂ plant

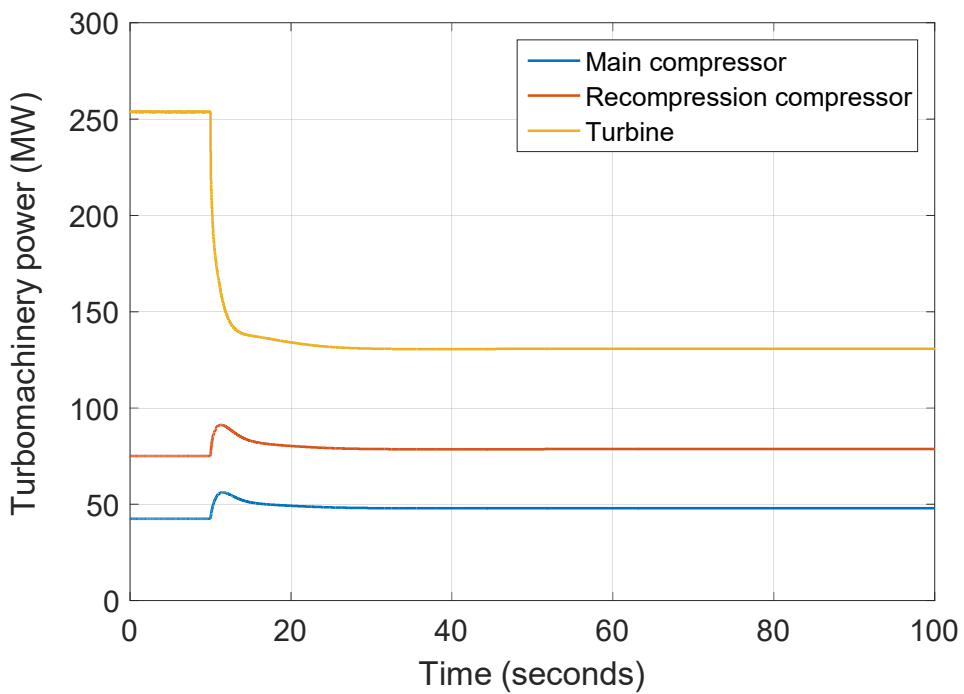


Figure 9-25 Transient response of the MC, RC and turbine power during loss of load of the SM-PWR/s-CO₂ plant

9.7 Summary

This chapter presents the dynamic performance analysis of the single recuperator recompression s-CO₂ cycle coupled to SM-PWR. The unique challenges for the operation, control and simulation of s-CO₂ cycle were enumerated. The automatic control configuration for the SM-PWR/s-CO₂ nuclear power plant was described. Inventory/pressure control was not investigated for the s-CO₂ cycle plant to avoid rapid fluid properties changes at the compressor inlet. Bypass valve control was used to control the power output and shaft speed. Flow split control and throttle valves were included to effectively control the plant. The control systems were able to maintain the shaft speed within ± 27 rpm during normal load following operation. Under loss-of-load scenario, the maximum shaft over-speed is about 107% of the synchronous speed.

10 Thermodynamic Performance Evaluation of Supercritical CO₂ CBC for Coal-Fired Power Generation with Solvent-based PCC⁴

10.1 Introduction

In recent times, the investigation of s-CO₂ closed-cycle GT as possible PCS for coal-based power plant is becoming popular. However, one problem of such application is the inefficient utilisation of the heat content of the flue gas leaving the furnace (Mecheri and Le Moullec, 2016; Hanak and Manovic, 2016; Le Moullec, 2013). The aim of this chapter is to evaluate the thermodynamic performance of coal-fired s-CO₂ Brayton cycle power plant that has been adapted for efficient utilisation of the flue gas heat by using a bottoming s-CO₂ Brayton cycle in conjunction with a main/topping s-CO₂ Brayton cycle.

So far, the use of s-CO₂ Brayton cycles as both topping cycle and bottoming cycle of a coal-fired power plant has not been explored in the literature. In this study, a single reheat s-CO₂ recompression cycle was considered as the topping cycle while three simpler s-CO₂ cycle were investigated as possible bottoming cycle for recovering the excess heat in the flue gas exiting the furnace. The investigated bottoming cycle options are simple recuperated cycle, partial heating cycle and the new concept proposed in Chapter 5, referred to as single recuperator recompression cycle. Performance evaluation was performed both for s-CO₂ cycle plants without CO₂ capture and for plants with CO₂ capture unit integrated. The performances of the different coal-fired s-CO₂ cycle configurations were compared with a reference supercritical steam cycle that was chosen as the benchmark. The most promising of the layouts was determined and the effects of cycle parameters such as TIT, precooler outlet temperature/pressure and recuperator's minimum TTD on the plant performance were investigated. The whole system comprising the coal-fired furnace, the s-CO₂ cycles and the MEA-based PCC plant were modelled and simulated with Aspen Plus[®] software.

⁴ Most of the results in this chapter have been presented at the 11th European Conference on Coal Research and Its Application (ECCRIA 11), 5-7 September 2016, Sheffield, UK.

10.2 Description of the supercritical CO₂ Brayton cycles for pulverised coal-fired application

10.2.1 Coal-fired furnace and the main s-CO₂ CBC

Integration of the main/topping s-CO₂ cycle with the coal-fired furnace is shown in Figure 10-1. A recompression s-CO₂ cycle was adopted due to its superior performance when compared to other s-CO₂ cycle layouts. The performance is further improved with a single stage of reheat. Hence, the turbine is divided into high-pressure (HP) and low-pressure (LP) turbine. Preheated CO₂ coming from the HTR entered the furnace at point T1 and exit at T2 after being heated to the maximum cycle temperature. The hot working fluid is expanded in the HP turbine and returned to the furnace at point T3 for reheating. The reheated CO₂ exiting the furnace at T4 is finally expanded in the LP turbine. During each pass through the furnace, the CO₂ working fluid is heated in three steps: convective economiser (ECOHT/ECORHT), radiant heater (RADHT/RADRHT) and final convective heater or reheater (CHT/CRHT).

Heat transfer in the furnace was either through radiation or convection. Radiant section of the furnace contains the two radiant heaters while the convective section contains the four convective heaters. Approximately half of the heat transferred to the CO₂ is through radiation from the flame to the radiant heaters. Combustion products rise to the top of the furnace and entered the convection zone at point A. The temperature of the hot flue gases at A was maintained at 1010 °C such that it was below ash softening temperature (Miller, 2011). As the flue gases flow through the convective section, they are first used for final heating of CO₂ to the required TIT in the convective heater and reheater. Then CO₂ leaving the HTR and HP turbine are heated in the economisers to the required radiant heaters inlet temperature. The flue gases leaves the furnace at point B. The CO₂ entering the furnace at T1 is at a higher temperature (about 465 °C) than the usual feedwater temperature in conventional coal-fired steam boiler (about 260 °C) (Fout et al., 2015). This is due to the high level of recuperation in recompression cycle. Consequently, the flue gases leave the furnace at relatively high temperature (about 495 °C) in the coal-fired s-CO₂ cycle power plant.

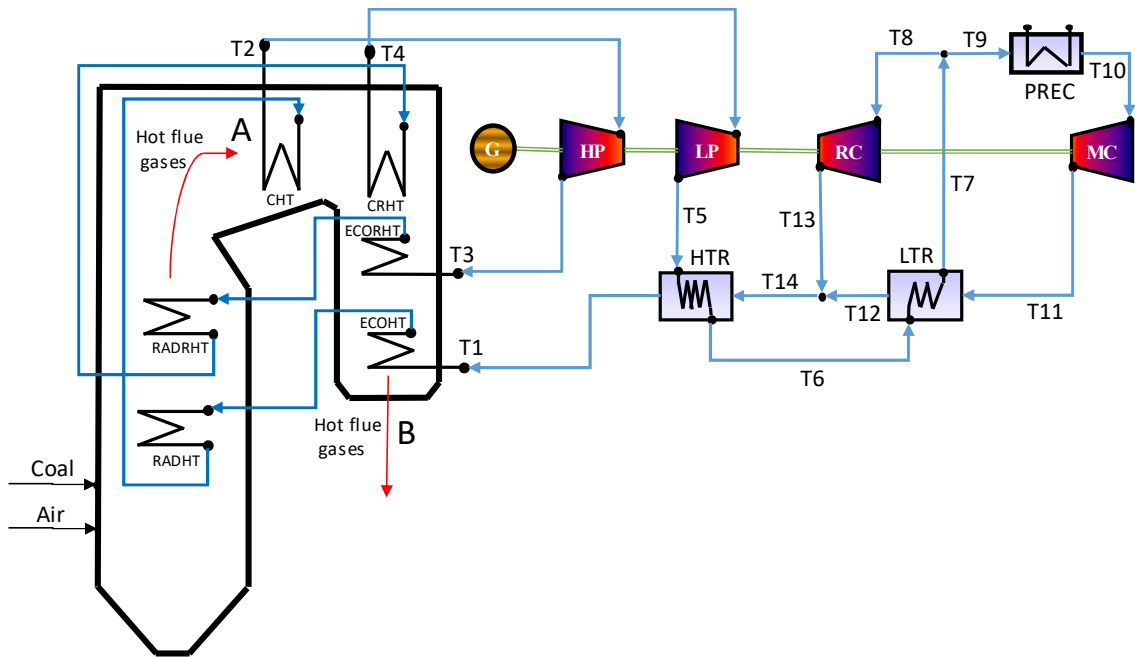


Figure 10-1 Main single reheat recompression cycle integration with coal-fired furnace

10.2.2 Utilisation of flue gases residual heat

A major drawback of coupling CBC to coal-fired furnace is the significant loss of heat through the hot flue gases leaving the furnace. If this exiting flue gases are not utilised, it will represent the main cause of inefficiency in the power plant (Miller, 2011). Several options exist for utilising waste heat of flue gases from combustion processes:

- The flue gases can be utilised to produce steam or hot water for industrial use or district heating in a combined heat and power (CHP) system. In fact, some of the early-operated coal-fired CBC plants such as the Oberhausen and Kashira plants were used to generate electricity as well as to produce heat for district heating (Olumayegun et al., 2016).
- Secondly, the hot flue gases can be used to preheat part or all of the cycle working fluid prior to the main heat addition in the furnace. Mecheri and Le Moullec (2016) employed this option by transferring the flue gases heat to a fraction of CO₂ flow that is extracted from the MC outlet.
- A third option is to add a bottoming cycle that uses the flue gases high-grade heat to generate additional electrical power (Kim et al., 2016; Manente and Lazzaretto, 2014). For instance, Echogen (USA) is in the process commercialising s-CO₂ bottoming power cycle utilising waste heat (Reuters, 2014).

- The final option is to use the flue gases to preheat the incoming combustion air. This is a common practice in conventional coal-fired power plants.

In this study, the use of bottoming cycle in conjunction with combustion air preheating was selected for improving the heat utilisation of the coal-fired s-CO₂ cycle power plant. In bottoming cycles, the net electric efficiency is a function of not just cycle efficiency (ratio of net electric power produced to heat transferred to the cycle) but also of the heat recovery factor (ratio of recovered heat to available heat in the flue gas) (Kim et al., 2016). Closed Brayton s-CO₂ cycle has favourable cycle efficiency. However, when used as a bottoming cycle the heat recovery in the heater is limited by the high temperature of CO₂ leaving the recuperator (Kim et al., 2016). However, the addition of air preheater downstream of the bottoming cycle will help to improve the plant's overall heat recovery factor. Recompression cycle was not used as bottoming cycle in this study. Cycles with simpler layouts and better heat recovery factor were favoured. Hence, the simple recuperated cycle, the partial heating cycle and the newly proposed single recuperator recompression cycle were considered as bottoming cycles in cascade with the main/topping single reheat recompression s-CO₂ cycle.

10.2.3 Overall plant configuration and integration with PCC

Three coal-fired s-CO₂ cycle configurations, representing the three different bottoming cycle choices, were investigated:

- Case A: the simple recuperated s-CO₂ cycle was selected as bottoming cycle as shown in Figure 10-2
- Case B: shown in Figure 10-3, the bottoming cycle is the partial heating s-CO₂ cycle
- Case C: the new concept, the single recuperator recompression s-CO₂ cycle was used as the bottoming cycle (Figure 10-4)

In all the cases, the topping cycle remains the single reheat recompression s-CO₂ cycle, which is integrated with coal-fired furnace. Coal is pulverised to fine powder in the mill. Secondary air, which is a large proportion of the incoming air, is sent to the forced draft (FD) fan while the remaining incoming air goes to the primary air (PA) fan. Air from the PA fan and FD fan is heated in the air preheater thereby recovering part of the remaining heat content of the flue gas exiting the bottoming cycle heater at point C. The heated primary air goes to the mill/pulveriser for drying and conveying the pulverised coal to the burners in the furnace. The heated secondary air is also introduced into the burners, where the coal and the air are mixed and combustion takes place. Heat released from the combustion is transferred to the CO₂ working fluid in the radiant and convective heaters.

The cooled flue gas leaving the air preheater passes through fabric filters or electrostatic precipitator (ESP) for particulate matters (majorly ash) removal. An induced draft (ID) fan

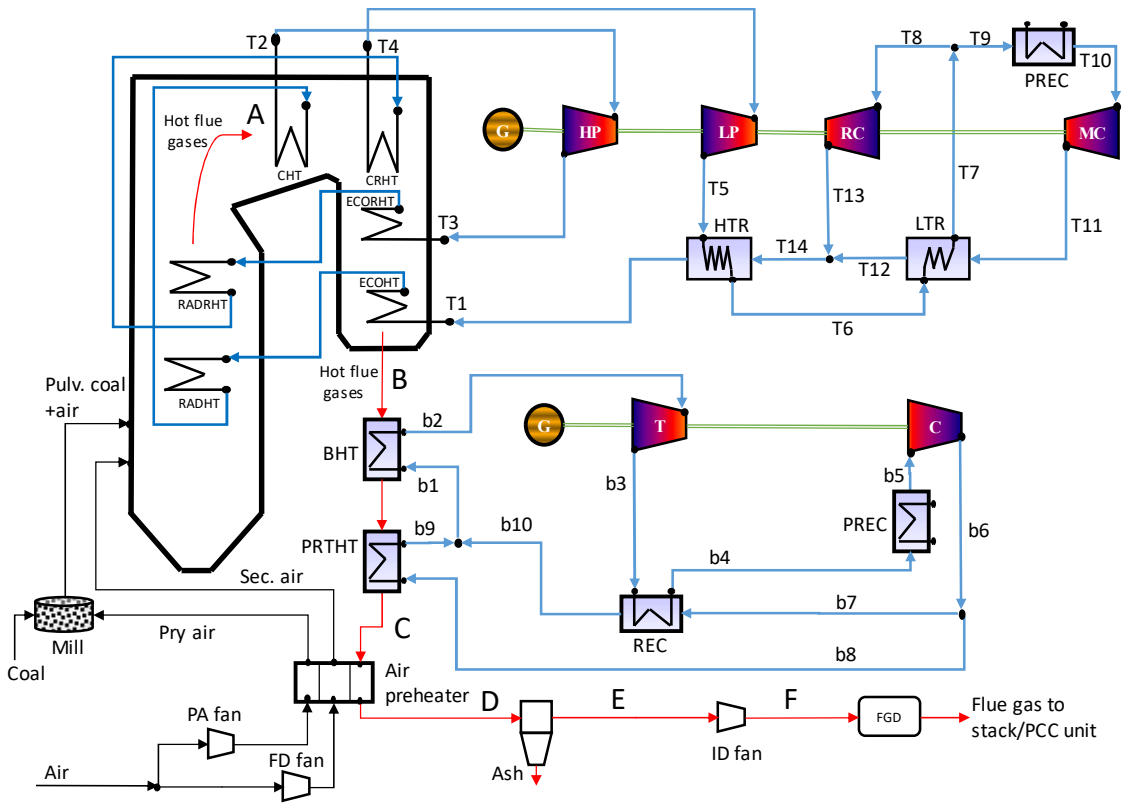


Figure 10-3 Case B - Partial heating bottoming cycle

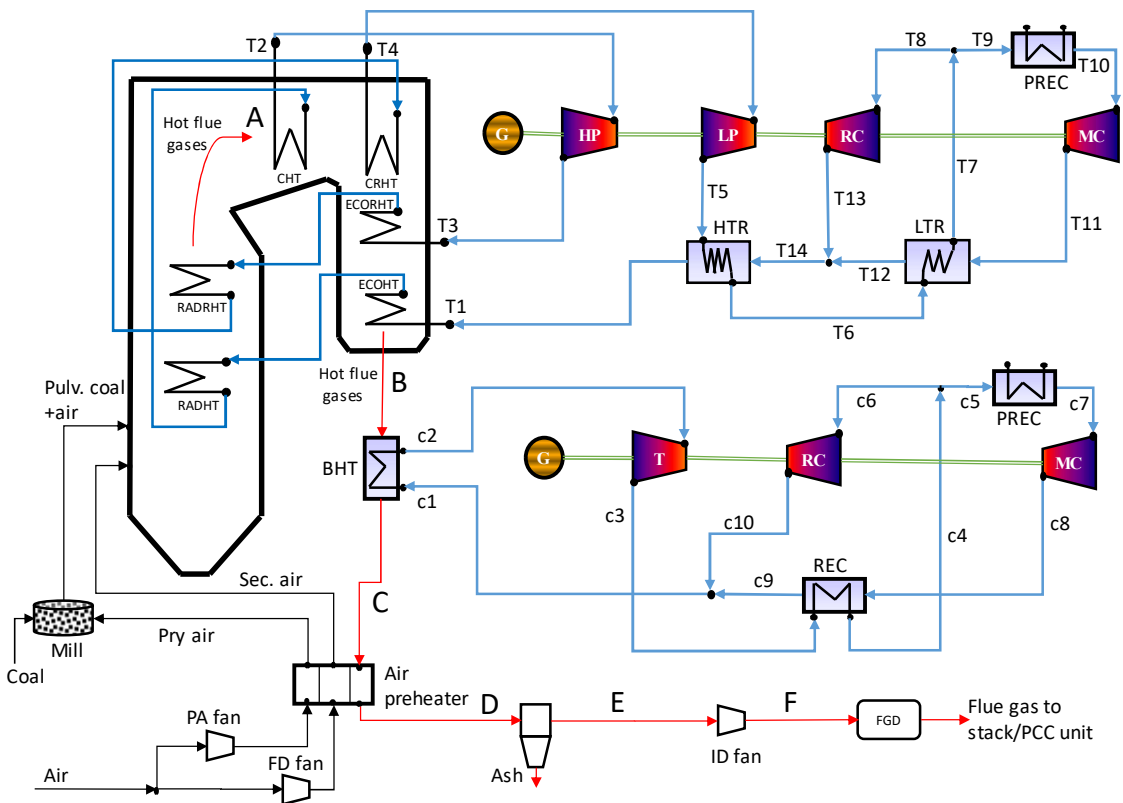


Figure 10-4 Case C - Single recuperator recompression bottoming cycle

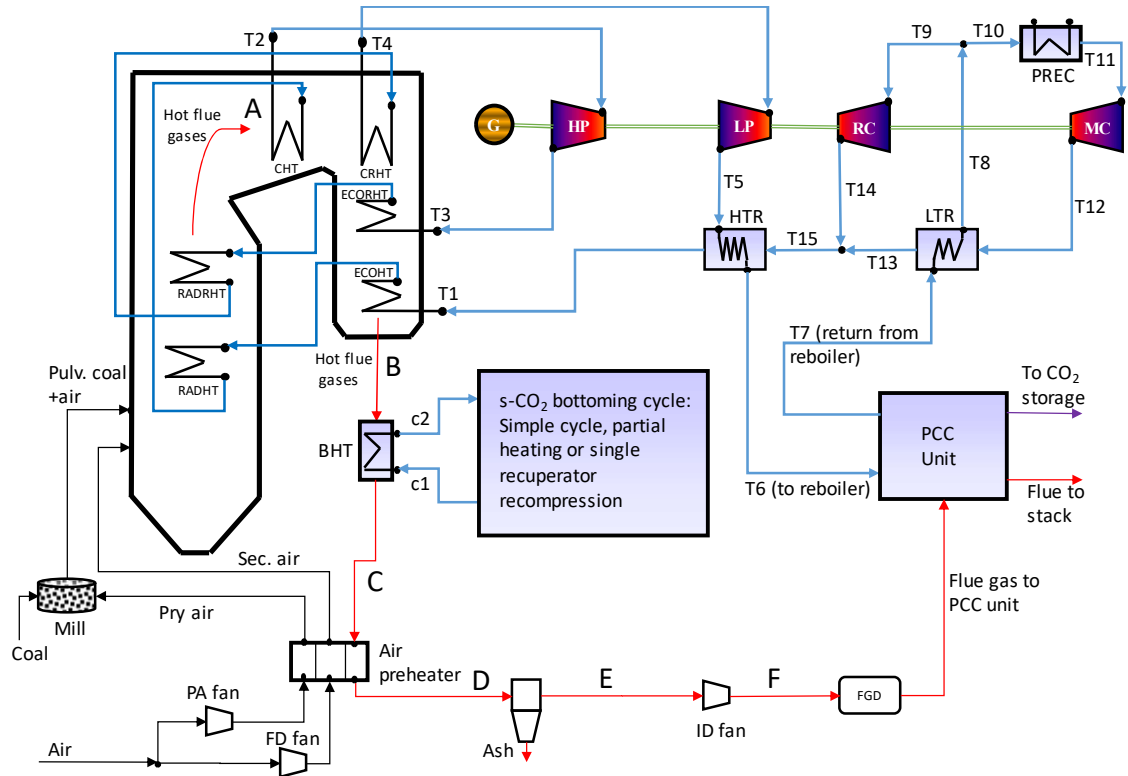


Figure 10-5 Integration of coal-fired s-CO₂ Brayton cycle with PCC unit

10.3 Steady state simulation of coal-fired s-CO₂ cycle power plant in Aspen Plus®

This section describes the methodology used to model and simulate the power plants comprising topping and bottoming s-CO₂ cycles fired by bituminous coal of known mass flow rate and combined with PCC. A model of the three cases of coal-fired s-CO₂ cycle power plant with PCC was developed for performance comparison among the cases as well as comparison with a benchmark coal-fired supercritical steam turbine power plant with 90% CO₂ capture reported in the literature (Olaleye et al., 2015). The benchmark plant was not modelled in this study but the performance results were obtained from Olaleye et al. (2015).

A simplified block diagram of the modelled coal-fired s-CO₂ cycle power plants is shown in Figure 10-6.

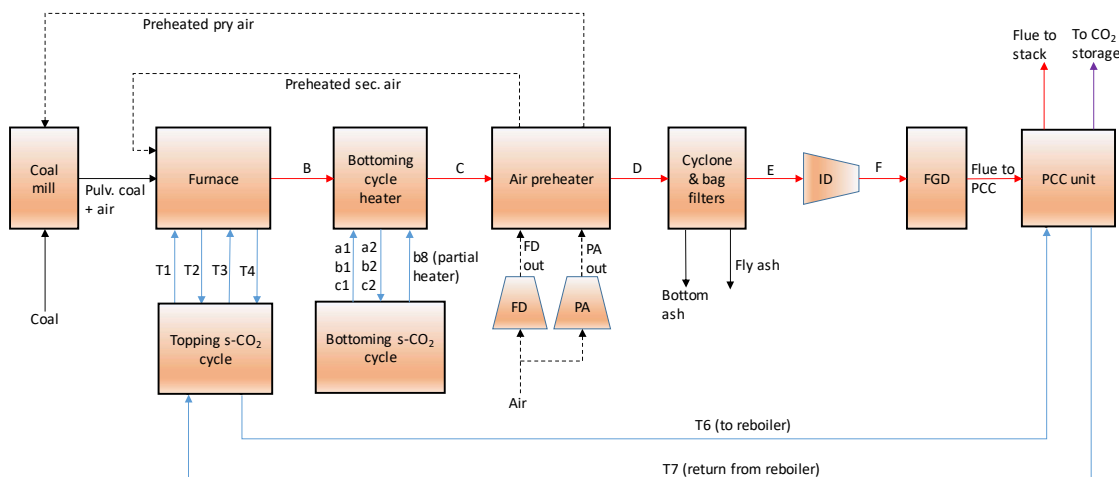


Figure 10-6 Simplified block diagram of the coal-fired s-CO₂ cycle power plants

10.3.1 Aspen Plus[®] software and thermo-physical property method

The steady state models were performed with Aspen Plus[®] V8.4 software to simulate the performance of the coal-fired s-CO₂ cycles power plants. The simulation environment is very flexible for describing the power plant components and connections. In Aspen Plus[®], unit operation blocks (crusher, screen, exchangers, pressure changers, mixer/splitters, reactors, separators, e.t.c.), combination of blocks, connection streams and user-defined calculations were used to model the power plant components and the complete process flowsheet. The plant components modelled include coal mill, fans, preheaters, pulverised coal-fired furnace, ash removal components, flue gas desulfurization and s-CO₂ cycle components like the external heat sources, turbine, compressor, recuperator and pre-cooler. Description of the PCC structure and its modelling are left until the next section.

Concomitant with process simulation is the need for accurate physical property data and models (Emun et al., 2010). Aspen Plus[®] contains extensive property calculation methods for the physical, chemical and thermodynamic properties of different solid, liquid and gaseous substances. In Aspen Plus[®], coal and ash were modelled as nonconventional solids. The HCOALGEN and the DCOALIGT physical property models were used to calculate the enthalpy and density of coal and ash (AspenTech, 2013). Peng-Robinson equation of state with Boston Mathias modification (PR-BM) was used to estimate the properties of air and combustion products. For the s-CO₂ properties, REFPROP property package in Aspen Plus[®] was used. REFPROP has been reported to be accurate and widely applicable to a variety of pure fluid and mixtures (Lemmon et al., 2013; Carstens, 2007).

10.3.2 Coal combustion and furnace simulation

The coal type fired is the Illinois No 6 bituminous coal. Details of the ultimate and proximate analysis of the coal are given in Table 10-1. The higher heating value (HHV) of the coal was calculated from the ultimate analysis by using the Dulong and Petit formula (Nag, 2008):

$$HHV \left(\frac{MJ}{kg} \right) = 33.83C + 144.45 \left(H - \frac{O}{8} \right) + 9.38S \quad (10-1)$$

Where C, H, O and S are mass fractions of carbon, hydrogen, oxygen and sulphur in coal respectively.

Table 10-1 Proximate and ultimate analysis of Illinois No 6 coal (Fout et al., 2015)

Parameter	Weight %
Proximate Analysis (as received)	
Moisture	11.12
Ash	9.70
Volatile matter	34.99
Fixed carbon	44.19
Total	100
Ultimate Analysis (as received)	
Moisture	11.12
Carbon	63.75
Hydrogen	4.50
Nitrogen	1.25
Chlorine	0.29
Sulphur	2.51
Ash	9.70
Oxygen	6.88
Total	100

Incoming air was assumed to consist of nitrogen (76.8% by weight) and oxygen (23.2% by weight) at 15 °C and 1.01 bar. Percent excess air supplied was specified to be 20%. A user-defined Fortran subroutine calculator was implemented to calculate the flow rate of air required for combustion based on the specified percent excess air, the coal flow rate and the coal characteristic. About 23.5% of the incoming air was sent to the PA fan while the rest was sent to the FD fan as secondary air. By specifying the isentropic efficiencies of the fan, the inlet conditions and the discharge pressure, Aspen Plus® determined the power required by the fans. Coal is dried with preheated primary air and grounded to fine powder in the coal mill. Volatile matter may be distilled off from the coal with moisture if the temperature of the primary air is too high, which may lead to fire hazard (Nag, 2008). Therefore, the primary air was only preheated to about 215 °C so that after drying the coal the temperature at pulveriser outlet was within the allowable pulveriser outlet temperature of 75 °C.

The drying process was modelled with RStoic block. Wet coal and hot primary air streams were fed to the RStoic block. The block was used to model drying by converting a portion of the coal to form water. The outlet, which is a stream of dried coal and moist air, is fed to the pulverising mill. The milling process was modelled with a combination of crusher and screen. The crusher was modelled by specifying the outlet particle size distribution (PSD) of coal. The screen block was used to separate the coarse material from the fine material. The coarse portion was returned to the crusher for further grinding. The PSD of the pulverised coal was specified such that about 70% of coal will pass through a 200-mesh screen and less than 1.3% retained on the 50 mesh. Pulverised coal is conveyed with the primary air to the furnace.

In the furnace, the pulverised coal and primary air are mixed with the heated secondary air for combustion. A sequence of RYield and RGibbs Aspen Plus[®] built-in models were used to simulate combustion of coal. RGibbs models chemical equilibrium and phase equilibrium by minimising the Gibbs free energy of the system. Therefore, there was no need to specify the reaction stoichiometry, only a list of possible products may be specified. However, Gibbs free energy can only be calculated for conventional components. Since coal was specified as a nonconventional component, it was first decomposed into its constituent elements by the RYield block. A calculator block was used to determine the actual yield distribution based on the inlet coal attributes. The products of the decomposition together with the heat of reaction associated with the decomposition was then passed to the RGibbs block.

During combustion, the chemical energy in the coal is converted to heat energy, which is transferred to the CO₂ working fluid. Heat radiation from the centre of the flame and absorption of the radiant heat by the working fluid were modelled with HEATER blocks. The radiant heat was divided in the ratio 0.65/0.35 between the main radiant heater and the reheat radiant heater. The exit of the radiant heat source corresponds to the top of the furnace and entrance to the convective zone where the flue gases temperature was maintained at 1010 °C. Convective heaters in this zone comprising of two final CO₂ heaters and two economisers were modelled with HEATX blocks with flue gases as the hot stream and CO₂ as the cold stream. For a given coal flow rate, a design specification was defined in Aspen Plus[®] to determine the topping cycle CO₂ flow rate required to cool the flue gases such that a 30 °C minimum TTD was maintained between the flue gases leaving the furnace at point B and CO₂ entering the furnace at point T1.

10.3.3 s-CO₂ CBCs simulation in Aspen Plus[®]

The topping and bottoming s-CO₂ cycles have the same maximum cycle pressure of 290 bar corresponding to the maximum cycle pressure of the benchmark supercritical steam turbine cycle (Olaleye et al., 2015). Similarly, the topping cycle HP and LP turbines inlet temperatures were fixed at 593 °C. Both topping and bottoming cycles' compressor inlet temperatures and pressure

were fixed just above the critical point at 31 °C and 76 bar. The bottoming cycle' TIT was fixed at 465 °C, which is 30 °C below the flue gas temperature entering the bottoming cycle heater. The values of recuperator's minimum TTD, compressor and turbine isentropic efficiencies, and heat exchanger pressure losses were selected based on values reported in the literature. Hence, a minimum TTD of 10 °C was specified for the recuperators (Mecheri and Le Moullec, 2016). MC, RC and turbine isentropic efficiencies were 90%, 89% and 93% respectively (Mecheri and Le Moullec, 2016). Heat exchanger relative pressure losses were fixed at 0.5% (Kim et al., 2016). For cycles with split flows, the split fractions could be independently adjusted to obtain optimum cycle efficiency.

Compressors and turbines were simulated in Aspen Plus® with COMPR block. Aspen Plus® calculates the power required (or delivered) based on the inlet conditions, discharge pressure and efficiency. Recuperators were modelled with HEATX block while precoolers were modelled with HEATER blocks. In the bottoming cycle, design specification was used to determine the needed CO₂ flow rate based on a minimum TTD of 30 °C between the flue gas leaving the bottoming cycle heater and the CO₂ entering the heater.

10.3.4 Preheater, ash removal and flue gas desulfurization simulation

Air preheater was modelled with MHeatX block, which represents heat transfer between the hot flue gases leaving the bottoming cycle heater and two cold streams (i.e. primary air and secondary air). Outlet specifications must be given for two of the three streams. Primary air and flue gas outlet temperatures were specified. Flue gas outlet temperature of 116 °C specified for the benchmark steam plant was assumed. Then, an overall energy balance determines the unspecified outlet temperature of the secondary air.

Ash removal from the flue gas was modelled with cyclone and bag filter blocks. 20% of ash was removed as bottom ash by the cyclone while the remaining 80% was removed as fly ash by bag filters. The ash-free flue gas is pushed through the FGD unit by ID fan. The power required by the fan was determined based on its discharge pressure and isentropic efficiency. The FGD removed sulphur oxide in the flue gas before entering the PCC unit.

10.3.5 Performance calculation

MS Excel™ spreadsheets were used to carry out the performance calculations. Therefore, MS Excel™ was linked with Aspen Plus® to access simulation results.

Two important performance indicators are the furnace (or heat recovery) efficiency and the cycle efficiency. The furnace efficiency is an indication of the ability of the power cycle to receive the heat available in the heat source while cycle efficiency indicates the ability to convert the received

heat into electrical power (Manente and Lazzaretto, 2014). The furnace efficiency, $\eta_{furnace}$ is calculated by taking the total amount of heat transferred to the s-CO₂ cycles and dividing it by the coal fuel power supplied to the plant.

$$\eta_{furnace} = \frac{(Q_{cycle})_{top} + (Q_{cycle})_{bottom}}{\dot{m}_{coal}(HHV)} \quad (10-2)$$

Where $(Q_{cycle})_{top}$ is the sum of the heat transferred to the topping s-CO₂ cycle through the economisers, radiant heaters and final convective heater/reheater, $(Q_{cycle})_{bottom}$ is the heat input from flue gases to the bottoming s-CO₂ cycle, \dot{m}_{coal} is the mass flow rate of coal fuel and HHV is the higher heating value of the supplied coal.

Cycle efficiency, η_{cycle} , is calculated by taking the electrical power output of the cycle and dividing by the heat transferred to the cycle. Hence, cycle efficiency for the topping cycle, $(\eta_{cycle})_{top}$, is

$$(\eta_{cycle})_{top} = \frac{(W_{elec})_{top}}{(Q_{cycle})_{top}} \quad (10-3)$$

Where $(W_{elec})_{top}$ is the topping cycle electrical power output given as:

$$\begin{aligned} (W_{elec})_{top} &= \left[\left(\sum W_t \right)_{top} - \left(\sum P_c \right)_{top} \right] \eta_{gen} \\ &= (W_{hpt} + W_{lpt} - W_{mc} - W_{rc}) \eta_{gen} \end{aligned} \quad (10-4)$$

$(\sum W_t)_{top}$ is the sum of topping cycle turbine power, $(\sum W_c)_{top}$ is the sum of topping cycle compressor power, W_{hpt} is the HP turbine power, W_{lpt} is the LP turbine power, W_{mc} is the MC power, W_{rc} is the RC power and η_{gen} is the electrical generator efficiency.

Cycle efficiency for the bottoming cycle is

$$(\eta_{cycle})_{bottom} = \frac{(W_{elec})_{bottom}}{(Q_{cycle})_{bottom}} = \frac{[(\sum W_t)_{bottom} - (\sum W_c)_{bottom}] \eta_{gen}}{(Q_{cycle})_{bottom}} \quad (10-5)$$

The overall cycle efficiency, $\eta_{overall\ cycle}$ is the ratio of the total electrical power output from the cycles, $(W_{elec})_{total}$ to the total heat transferred to the cycles, $(Q_{cycle})_{total}$.

$$\eta_{overall\ cycle} = \frac{(W_{elec})_{total}}{(Q_{cycle})_{total}} = \frac{(W_{elec})_{top} + (W_{elec})_{bottom}}{(Q_{cycle})_{top} + (Q_{cycle})_{bottom}} \quad (10-6)$$

The net power output of the plant, W_{net} is the total or gross power output from the topping and bottoming cycles, $(W_{elec})_{total}$ minus the auxiliary power consumption, W_{aux} in pumps, fans, coal mill e.t.c.:

$$W_{net} = (W_{elec})_{total} - W_{aux} \quad (10-7)$$

The plant net efficiency, η_{net} is defined as the ratio of the net power output to the coal fuel energy input to the plant:

$$\eta_{net} = \frac{W_{net}}{\dot{m}_{coal}(HHV)} \quad (10-8)$$

The three cases in this study with different bottoming cycle options will present different cycle efficiencies and furnace efficiencies. Therefore, the overall impact of the choice of power plant configurations on the plant net efficiency can only be determined through performance calculations and comparison among the cases.

10.4 Solvent-based post-combustion CO₂ capture

This section discusses the PCC, which is based on chemical absorption through MEA solvent. Benefits of MEA-based PCC include (1) high separation selectivity (2) It operates at atmospheric conditions (3) Experimental/pilot plant data are available.

10.4.1 Description of MEA-based CO₂ capture process

Figure 10-7 shows a simplified process flow diagram for a typical chemical absorption CO₂ capture process. The main components are absorber, a stripper with a reboiler and a condenser attached, direct contact cooler (DCC), rich MEA pump, lean MEA pump, lean/rich cross heat exchanger and lean MEA cooler.

Flue gas from the power plant's FGD unit is first cooled in the DCC to a suitable temperature for absorption (about 40 °C). The cooled flue gases are introduced into the absorber at the bottom while the lean MEA solvent solution enters the absorber at the top. The flue gases flow upward while the MEA solvent solution flows down under gravity through the absorber packed bed column. Chemical absorption of CO₂ in the flue gases by the MEA solvent takes place during the counter-current flow in the absorber. Cleaned flue gases leave the absorber at the top. Rich MEA solvent (i.e. with high loading of CO₂) leaves the absorber at the bottom. Its pressure is then increased by the rich MEA pump and heated in the lean/rich cross heat exchanger before entering the stripper at the top. In the stripper column, the rich MEA solvent is stripped of the CO₂ by the application of heat energy in the reboiler. The water vapour and CO₂ mixture released in the stripper is sent to the stripper condenser, which cools the mixture thereby turning most of the

water vapour to liquid water. The condensed water and CO₂ are separated in the flash drum. The condensed water is returned back to the stripper while the separated CO₂ leaves the stripper at the top. The resultant lean MEA solvent (i.e. with low loading of CO₂) exits the stripper at the bottom. The lean MEA solvent leaving the stripper is used to heat the rich MEA solvent in the cross heat exchanger and the temperature is further reduced in the lean MEA cooler before being returned to the absorber column at the top.

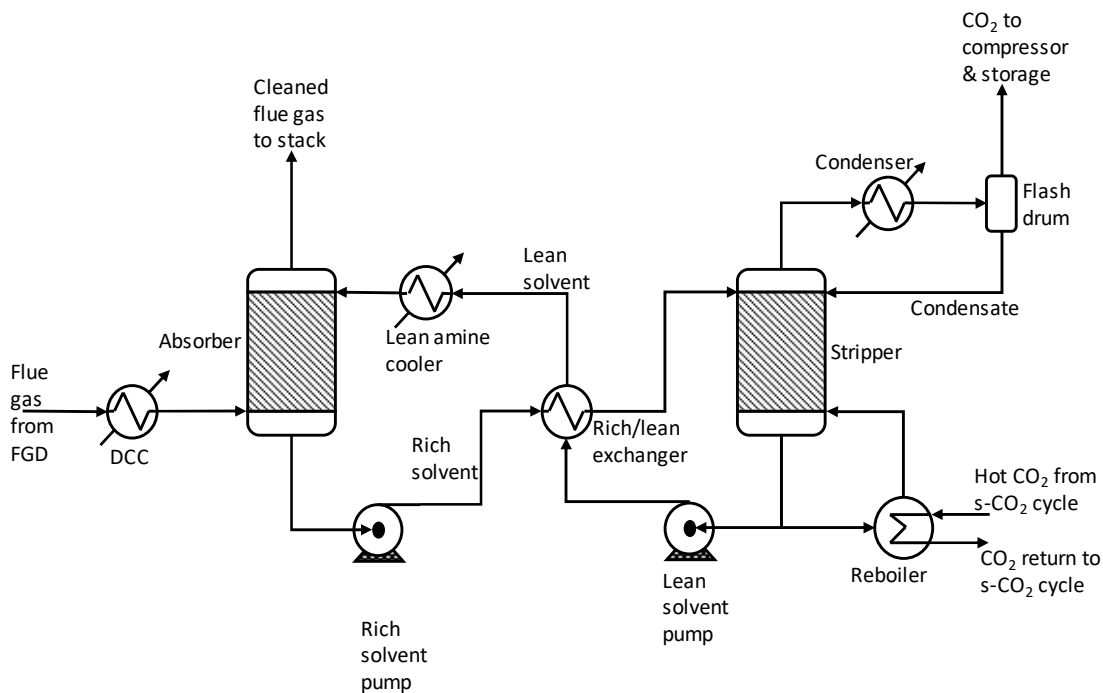


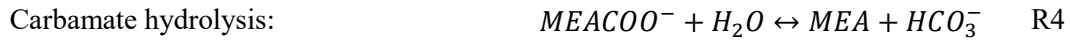
Figure 10-7 Simplified process flow diagram for MEA-based PCC unit (IPCC, 2005)

10.4.2 Rate-based simulation of the CO₂ capture system in Aspen Plus®

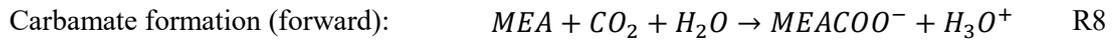
The MEA-based PCC was modelled and simulated in Aspen Plus® to determine the performance. The modelling was based on the parameters reported for the benchmark supercritical steam plant's PCC unit, which was validated with data from University of Kaiserslautern pilot plant (Olalaye et al., 2015). The PCC was modelled to capture 90% of the CO₂ in the flue gas using a 30%-wt MEA solvent solution. The temperature of the flue gas and the lean MEA entering the absorber was 40 °C. Absorber operating pressure was 1.013 bar. The rich MEA solvent solution was heated up to 106 °C in the cross heat exchanger. The stripper was operating at a pressure of 1.9 bar and the reboiler temperature was maintained at about 120 °C to avoid thermal degradation of the amine solvent. In Aspen Plus®, RadFrac block was used to model the absorber and the stripper. Koch FLEXIPAC® 1Y structured packing was selected for the absorber and stripper column. The design of the absorber and stripper arrived at four absorber columns with a diameter of 5.41m each and three stripper column with a diameter of 4.62m each in order to maintain the columns diameters

within the structural limit. Fifteen equilibrium stages were required for each of the absorber and the stripper column.

Modelling of the absorption and stripper columns in Aspen Plus® was through the use of rate-based models. Rate-based model provides a rigorous and good prediction of the simulation over a wide range of operating conditions unlike the traditional equilibrium-stage modelling approach (Zhang et al., 2009). The Electrolyte Non-Random-Two-Liquid (ElecNRTL) activity coefficient property package was selected to accurately predict the ionisation equilibrium and the heats of solution of the MEA-CO₂-H₂O system. The solution chemistry of the MEA-based chemical absorption process can be represented by the following equilibrium reactions (R1-R5) (Zhang and Chen, 2013):



Reaction models for the absorber and stripper consist of three equilibrium rate-based controlled reactions, R1, R3 and R5, in conjunction with the following kinetic rate-based controlled reactions (R6-R9) (Zhang and Chen, 2013):



The kinetic reaction rates, r , are described in Aspen Plus® by the power law expression:

$$r = kT^n \exp\left(-\frac{E}{RT}\right) \prod_{i=1}^N C_i^{a_i} \quad (10-9)$$

10.5 Verification of the Aspen Plus® model of the s-CO₂ Brayton cycle

The suitability of the Aspen Plus® model for simulating the performances of supercritical CO₂ Brayton cycles was investigated. An s-CO₂ recompression Brayton cycle was modelled for verifying the calculation. Independent results of numerical model reported by Dostal (2004) were compared with the Aspen Plus® simulation results. The input parameters were:

- Maximum cycle pressure - 200 bar
- TIT - 550 °C
- Precooler outlet temperature - 32 °C
- Precooler outlet pressure - 76.92 bar
- Mass flow rate - 3176.4 kg/s
- MC pressure ratio - 2.6
- Split flow fraction - 0.41
- Turbine isentropic efficiency - 90 %
- MC and RC efficiencies = 89 %

Comparison of the main simulation results against literature value is presented in Table 10-2. The temperature differences are within 0 – 2.26 °C and the maximum relative deviation is about 1.34%. The small differences in the result can be attributed to uncertainties in the pressure loss specifications and the round-off error in the input parameters. Otherwise, the simulation results agreed well with the literature values.

Table 10-2 Validation of s-CO₂ Brayton cycle model against literature value

Parameters	Literature value	Simulation value	Relative/absolute difference
Turbine outlet temperature	440.29 °C	440.29 °C	0 °C
MC outlet temperature	61.1 °C	61.11 °C	0.01 °C
RC inlet temperature	69.59 °C	71.34 °C	1.75 °C
RC outlet temperature	157.99 °C	160.25 °C	2.26 °C
Heater inlet temperature	396.54 °C	397.38 °C	0.84 °C
Thermal power	600 MWt	596.76 MWt	0.54%
Turbine work	383.71 MW	383.72 MW	0.003%
MC work	38.59 MW	38.57 MW	0.05%
RC work	74.84 MW	75.84 MW	1.34%
Net work output	270.28 MW	269.31 MW	0.36%
HTR duty	985.51 MW	977.49 MW	0.81%
LTR duty	398.8 MW	398.0 MW	0.2%
Precooler duty	328.38 MW	328.11 MW	0.08%
Cycle efficiency	45.05%	45.13 %	0.08% point

10.6 Baseline boundary conditions and design point parameters

Boundary conditions and design point parameters have to be specified in order to evaluate the thermodynamic performance of the coal-fired s-CO₂ cycle power plants. Therefore, the boundary conditions and parameters such as coal mass flow rate, combustion air conditions, percent excess air, flue gas stack temperature, maximum cycle pressure and turbines inlet temperature were selected based on the information published for the supercritical reheat steam cycle (Olaleye et al., 2015). This will ensure a fair comparison between the performances of the s-CO₂ cycle plants and the conventional supercritical steam plant. Other conditions and parameters like pressure losses and specifications of heat exchangers were selected based on similar studies of s-CO₂ power cycle reported in the literature (Kim et al., 2016; Mecheri and Le Moullec, 2016). A summary of the baseline boundary conditions and design point parameters is given in Table 10-3.

Table 10-3 Boundary conditions and design parameters

Parameter/variable	Value
Coal feed ($^{\circ}\text{C}/\text{bar}/(\text{kg}/\text{s})$)	15/1.01/51.82
Air ($^{\circ}\text{C}/\text{bar}$)	15/1.01
Excess air (%)	20
Maximum cycle pressure (bar)	290
HP & LP turbines inlet temperature ($^{\circ}\text{C}$)	593
Compressor inlet pressure (bar)	76
Compressor inlet temperature ($^{\circ}\text{C}$)	31
Gas-CO ₂ TTD ($^{\circ}\text{C}$)	30
Preheater hot outlet temperature ($^{\circ}\text{C}$)	116
Recuperator TTD ($^{\circ}\text{C}$)	10
Turbine isentropic efficiency (%)	93
MC isentropic efficiency (%)	90
RC isentropic efficiency (%)	89
Fan isentropic efficiency (%)	80
Generator efficiency (%)	98.4
Ash distribution, fly/bottom ash (%)	80/20

10.7 Performance comparisons among Case A, Case B and Case C of the coal-fired s-CO₂ Brayton cycle power plants

As far as possible, performance calculation for the s-CO₂ Brayton cycles should aim at achieving the maximum cycle efficiencies. Therefore, the flow split fraction (i.e. the fraction of the total flow that goes through the precooler/MC) should be adjusted such that the differences in the heat capacities between the hot streams and the cold streams in recuperators are minimised. This will improve heat transfer in the recuperators and thereby maximised cycle efficiency. Hence, the optimum flow split fraction that gives the maximum cycle efficiency needs to be determined for any selection of boundary conditions and parameters (Bae et al., 2014). Using the above baseline boundary conditions and parameters, the optimum flow split fractions for the topping cycle and the single recuperator recompression cycle (i.e. case C bottoming cycle) were investigated. Figure 10-8 shows the cycle efficiencies as a function of the flow split fractions. The optimum flow split fraction was found to be about 0.65 for the topping cycle while it was about 0.71 for the single recuperator recompression bottoming cycle.

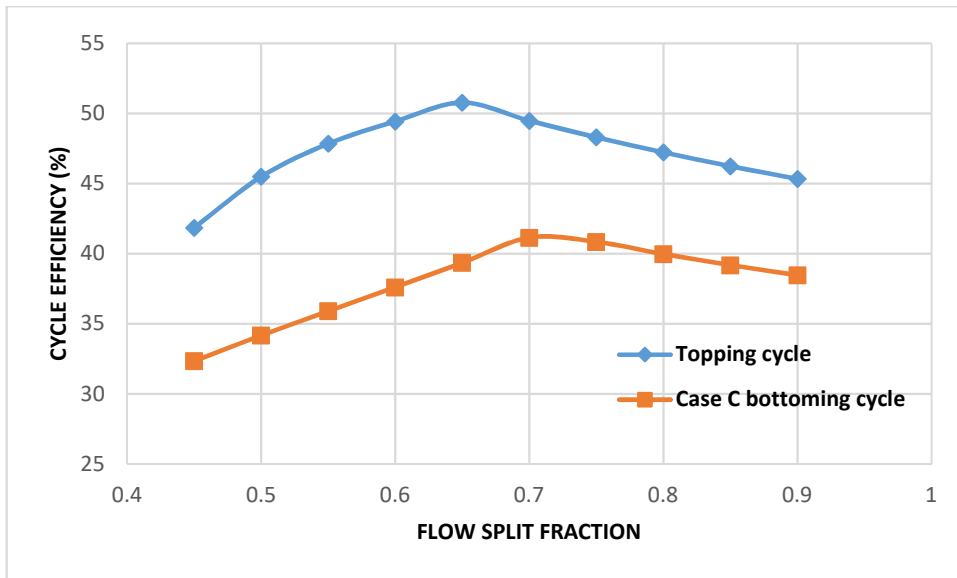
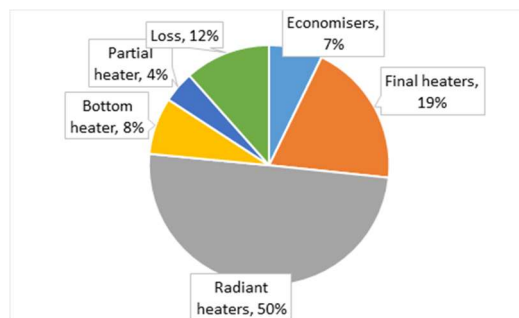
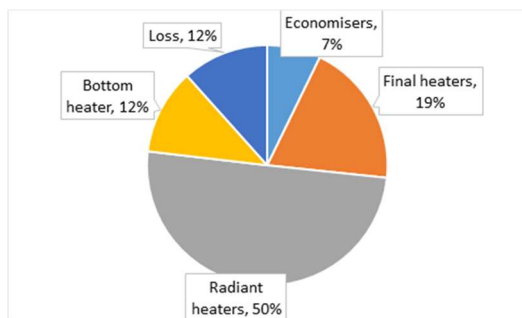


Figure 10-8 Cycle efficiencies of the topping cycle and Case C bottoming cycle as a function of the flow split fractions

In order to highlight the impact of integrating the coal-fired s-CO₂ power plants with the PCC unit, the performances of the power plants without carbon capture were first determined based the optimum flow split fractions, and the baseline boundary conditions and design parameters presented above. Table 10-4 shows the pressure, temperature and mass flow for the plants' main points. The stream nomenclature is based on Figure 10-2, Figure 10-3 and Figure 10-4. This was then followed by simulation and performance evaluation of the whole power plants, incorporating the PCC unit. The distribution of the fuel combustion heat energy among the different s-CO₂ heaters is shown in Figure 10-9. About 50% of the input heat energy was transferred by radiation to the s-CO₂ working fluid in the radiant heaters. The Case A and Case B bottoming cycles were able to recover about 12% of the total heat input, which otherwise would have been lost through the exhaust flue gas. In Case C, only about 9% was recovered but the unrecovered heat was utilised for preheating the secondary air to higher temperature level (258 °C) than Case A (177 °C) and Case B (165 °C). This then leads to higher heat transfer in the furnace for Case C. For the three cases, the heat losses were about 12%, that is, a furnace efficiency of approximately 88%. This value of furnace efficiency is comparable to the boiler efficiency obtainable in coal-fired steam power plants. Hence, the addition of the bottoming cycles and the combustion air preheaters enables efficient utilisation of the furnace heat.

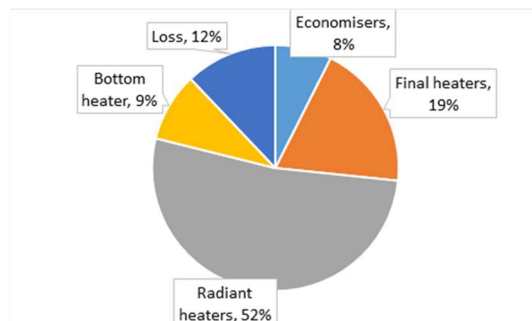
Table 10-4 Summary of the main stream values for the three cases calculated with baseline boundary conditions and design parameters

Stream	Case A			Case B			Case C		
	P (bar)	T (°C)	m (kg/s)	P (bar)	T (°C)	m (kg/s)	P (bar)	T (°C)	m (kg/s)
Coal	1.01	15	51.82	1.01	15	51.82	1.01	15	51.82
Air	1.01	15	540.88	1.01	15	540.88	1.01	15	540.88
Pry air	1.1	215	127.11	1.1	215	127.11	1.1	215	127.11
Sec. air	1.1	177.23	413.77	1.1	164.59	413.77	1.1	257.82	413.77
Pulv.Coal+air	1.09	75.28	178.93	1.09	75.28	178.93	1.09	75.28	178.93
A	1.09	1010	592.7	1.09	1010	592.7	1.09	1010	592.7
B	1.01	496	592.7	1.01	496	592.7	1.01	496	592.7
C	1.01	253.26	592.7	1.01	244.86	592.7	1.01	306.70	592.7
D	1.01	116	592.7	1.01	116	592.7	1.01	116	592.7
Flue to stack	1.01	56.67	585.08	1.01	56.67	585.08	1.01	56.67	585.08
T1	287.12	466	4052.52	287.12	466	4038.78	287.12	466	4163.13
T2	282.82	593	4052.52	282.82	593	4038.78	282.82	593	4163.13
T3	147.72	507.64	4052.52	147.72	507.64	4038.78	147.72	507.64	4163.13
T4	145.51	593	4052.52	145.51	593	4038.78	145.51	593	4163.13
a1,b1,c1	288.55	223.26	511.12	288.70	305.71	526.35	288.55	276.70	523.38
a2,b2,c2	287.25	466	511.12	287.25	466	526.35	287.25	466	523.38
b8	-	-	-	290	69.70	152.64	-	-	-



(a) Case A – Simple cycle bottoming

(b) Case B – Partial heating bottoming



(c) Case C – Single recuperator recompression bottoming

Figure 10-9 Distribution of the input heat value among the different heaters

Table 10-5 shows the performance result of the PCC unit that was integrated with the coal-fired s-CO₂ Brayton cycle power plants. Integration of the PCC to the plants penalised the net efficiency through (1) bleeding of CO₂ for solvent regeneration in reboiler, which resulted in lower cycle efficiency (2) additional auxiliary loads associated with the PCC units. Table 10-6 is a summary of the performance results for the three cases both without the PCC unit and with the PCC unit integrated. Interestingly, Case C (i.e. the single recuperator recompression bottoming cycle layout) gave the best overall plant net efficiency with or without PCC even though the bottoming cycle recovered the least amount of heat and thus produced the least power. The superior performance of Case C is due to better efficiency of the bottoming cycle. In contrast, Kim et al. (2016) concluded that power produced by bottoming cycle is a more important factor than the efficiency of bottoming cycle in determining the overall plant performance and therefore, did not recommend recompression cycle for bottoming cycle application despite having the best cycle efficiency. However, unlike our study, Kim et al. compared the performances of various s-CO₂ bottoming cycles without a downstream air preheater.

For a fixed coal fuel input, the plant overall performance depends on auxiliary loads, cycle efficiency and furnace efficiency. The cycle efficiency is majorly determined by the choice of cycle layout/configuration. Furnace efficiency, on the other hand, can be improved by heat recovery in the bottoming cycle and preheating of combustion air. In summary, the cycle layouts, the bottoming cycle heat recovery, the level of air preheating and the auxiliary loads will determine the plant net efficiency. Hence, for plants with similar auxiliary loads, plant net efficiency will be maximised by configurations with high cycle efficiency, good heat recovery in bottoming cycle and high level of air preheating. Unfortunately, good heat recovery in the bottoming cycle cannot be achieved simultaneously with a high level of air preheating. For instance, good heat recovery in the bottoming cycles of Case A and Case B meant that the temperature of the flue gas entering the air preheater was relatively low, limiting the amount of air preheating possible. On the other hand, Case C with the least heat recovery (or produced power) in bottoming cycle gave the highest air preheating duty (Table 10-6). Therefore, the poor heat recovery was somewhat compensated for by the added air preheater.

Table 10-5 Parameters and performance results of the PCC unit

Parameter	Value
CO ₂ removal percentage	90%
Flue gas absorber inlet temperature	40 °C
Lean solvent absorber inlet temperature	40 °C
MEA concentration	30%-wt
Absorber operating pressure	1.013 bar
Stripper operating pressure	1.9 bar
Lean solvent loading	0.29 mol CO ₂ /mol MEA
Rich solvent loading	0.53 mol CO ₂ /mol MEA
Reboiler temperature	120 °C
Condenser temperature	31.98 °C
Condenser duty	120.6 MW
Solvent circulation rate	18 m ³ /ton CO ₂
Thermal energy required	3.4 GJ/ton CO ₂

Table 10-6 Comparison of plant performances with and without PCC for Case A (simple recuperative cycle as bottoming cycle), Case B (partial heating cycle as bottoming cycle) and Case C (single recuperator recompression cycle as bottoming cycle)

Parameter	Case A		Case B		Case C	
	No PCC	With PCC	No PCC	With PCC	No PCC	With PCC
HHV, MJ/kg	27.05	27.05	27.05	27.05	27.05	27.05
Input heat value, MJ	1401.87	1401.87	1401.87	1401.87	1401.87	1401.87
Heat transferred to top cycle, MW	1077.49	1103.16	1072.8	1095.63	1106.01	1131.81
Heat transferred to bottom cycle, MW	161.46	161.46	167.03	149.57	126.75	106.56
Furnace efficiency, %	88.38	88.74	88.44	88.82	87.94	88.34
Preheater duty, MW	92.61	59.80	87.18	51.15	127.43	96.14
Top gross electric power, MWe	545.40	401.98	543.31	398.08	560	416.32
Bottom gross electric power, MWe	60.17	46.39	61.96	48.95	52.61	39.58
Top cycle efficiency, %	50.62	36.44	50.64	36.33	50.63	36.78
Bottom cycle efficiency, %	37.27	32.94	37.10	32.73	41.51	37.14
Overall cycle efficiency, %	48.88	36.04	48.82	35.90	49.69	36.81
Auxiliaries power, MW	10.38	10.7	10.38	10.7	10.39	10.7
Net electric power, MWe	595.19	437.67	594.90	436.33	602.22	445.19
CO ₂ specific emission, kg CO ₂ /MWh	714.69	98.05	715.04	98.35	706.35	96.39
Specific work output, kWh/m ³	5.28	5.24	5.26	5.23	5.16	5.10
Overall plant net efficiency, %	42.46	31.22	42.44	31.13	42.96	31.76

In Figure 10-10, the performances of the coal-fired s-CO₂ Brayton cycle power plants were compared with the state-of-the-art supercritical reheat steam power plant (Olaleye et al., 2015). The s-CO₂ Brayton cycle power plants, without CO₂ capture, was found to be about 3.34 - 3.86% point more efficient than the steam power plant. When the power plants were integrated with the PCC unit, the plant net efficiencies of the s-CO₂ power plants were about 0.68 – 1.31% point above the steam plant’s efficiency. Although the s-CO₂ Brayton cycle plants with CO₂ capture gave higher efficiency than steam cycle plant, the s-CO₂ cycle suffered more efficiency penalty (about 11.2%) than the steam plant (about 8.65%). This is probably due to the use of sensible heat of s-CO₂ working fluid to meet reboiler thermal requirement instead of low pressure condensing steam, as is usually the case in steam turbine power plant.

A comparison of the specific work output (i.e. the ratio of the generated power to the volumetric flow rate of the working fluid) of each cycle can give an indication of the relative size of plants and by extension the relative capital cost (Bae et al., 2014; Saravanamuttoo et al., 2009). Table 10-6 shows that the specific work outputs in all the three cases were comparable (approximately 5 kWh/m³). Case C shows a slightly lower specific work output but the difference is not considered significant. The specific work output of the s-CO₂ cycle is over 30 times more than that of the steam cycle. Therefore, the s-CO₂ cycle plant has the potential to be significantly smaller than the steam cycle plant. This is in good agreement with previous findings in the literature on the compactness of s-CO₂ cycle in comparison with steam cycle (Ishiyama et al., 2008; Dostal, 2004; Angelino, 1968; Olumayegun et al., 2016).

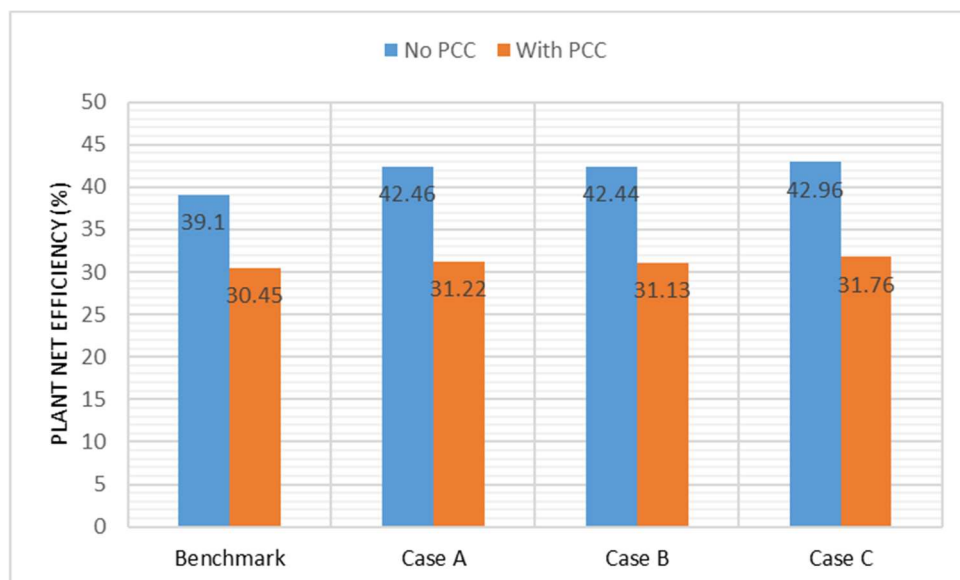


Figure 10-10 Comparison of the overall plant net efficiency of Case A (simple recuperative cycle as bottoming cycle), Case B (partial heating cycle as bottoming cycle) and Case C (single recuperator recompression cycle as bottoming cycle) with the supercritical steam plant (from Olaleye (2015)) as the benchmark

In this study, the cycle maximum pressure has been selected to match the maximum pressure in the steam cycle. However, a common feature of Brayton cycle is that there is an optimum pressure ratio (or cycle maximum pressure in our case) at which the efficiency has a peak value. Hence, the effect of cycle maximum pressure on plant performance was investigated by varying the pressure from 200 bar to 500 bar while the compressor inlet pressure was kept constant. Figure 10-11 shows the plant net efficiency as a function of cycle maximum pressure for the three configurations. Case C was found to maintain the best efficiency over the whole pressure range. Maximum efficiency occurred at an optimum pressure of about 400 bar. Currently, the choice of such a high pressure might not be feasible due to mechanical design considerations such as the maximum pressure limit of heat exchangers, turbomachinery seal solutions to prevent leakage and the need to avoid excessively small compressor blades. However, the USC steam plant with a maximum pressure of 350 bar and a TIT of 700 °C is expected to come into operation between 2020 and 2030 (Le Moullec, 2013). If the s-CO₂ cycle is operated at such maximum pressure (i.e. 350 bar), a net efficiency gain up to 4.24% above the current efficiency of steam turbine plant can be achieved without a corresponding increase in TIT to 700 °C as planned. Hence, the s-CO₂ plant has the advantage of increased efficiency at a lower temperature.

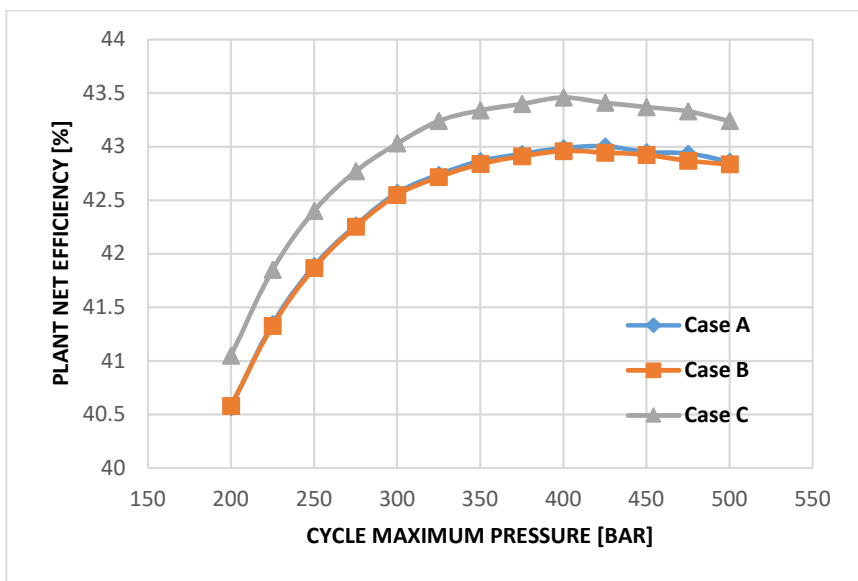


Figure 10-11 Plant net efficiency as a function cycle maximum pressure from 200 bar to 500 bar for the three configurations (Case A – simple recuperative cycle as bottoming cycle, Case B – partial heating cycle as bottoming cycle and Case C – single recuperator recompression cycle as bottoming cycle)

10.8 Choice of configuration and parametric study

In this study, the performance comparison was carried out for three potential s-CO₂ cycle configurations. The cycles were adapted for efficient utilisation of furnace heat similar to boiler heat utilisation in conventional steam turbine plant, albeit with bottoming cycles added. Operating

conditions (290 bar, 593 °C and single reheat) were chosen to match the current supercritical steam cycle conditions. Hence, current experience with material technology for pulverised coal-fired boiler and steam turbine could be applied to the development of the coal-fired s-CO₂ Brayton cycle power plant. The overall net efficiency of Case C option without CO₂ capture was 0.5% and 0.52% point over the efficiency of Case A and Case B respectively. With CO₂ capture, the efficiency gains were 0.54% and 0.63% above the efficiency of Case A and Case B. Therefore, of the three alternative configurations considered, Case C (with single recuperator recompression cycle as the bottoming cycle) is more attractive due to its better performance. It is also expected to be of similar size as the other two configurations considering the relative value of the specific work output and the component count. When compared with steam cycle plant, the net efficiency of Case C was higher than the efficiency of steam cycle plant by about 3.86% and 1.31% point without CO₂ capture and with CO₂ capture respectively.

Cycle efficiency is known to depend on the TIT, precooler outlet/MC inlet temperature and the recuperator minimum TTD. Hence, a parametric study was performed to investigate the effects of these parameters on the net efficiency of the chosen coal-fired s-CO₂ cycle power plant.

10.8.1 Effect of turbine inlet operation conditions

Figure 10-12 shows the effect of changes in TIT on the cycle performance for the single recuperator recompression bottoming cycle configuration without PCC unit and with PCC unit integrated. The figure was produced by varying the cycle maximum pressure from 200 bar to 500 bar for four different selection of TITs (600 °C, 650 °C, 700 °C and 750 °C). The cycle performance was calculated with the flow split fraction that gave the maximum efficiency for each data point while other cycle parameters were maintained at the baseline condition.

The result showed that the plant net efficiency increased with the rise in TIT. Also for each selection of TIT, there is an optimum cycle maximum pressure. The optimum cycle maximum pressure increase with an increase in TIT. With no PCC and at a TIT of 600 °C, the optimum cycle maximum pressure was about 400 bar, while at 650 °C, the optimum cycle maximum cycle pressure increased to about 450 bar and the trend continued with increase in TIT. At the operating conditions of the next USC steam turbine power plant (700 °C and 350 bar), the efficiency of the s-CO₂ cycle power plant is about 46.67%. This corresponds to about 7.57% point above the efficiency of the conventional supercritical steam plant.

From the foregoing, the adoption of the s-CO₂ cycle for coal-fired power plant application is promising. The s-CO₂ cycle achieved higher efficiency than steam cycle plant at similar operating conditions. Even for the advanced USC steam plant that is expected to achieve efficiency around 47%, this will be done with two or more reheat stages, three or more turbine modules and series

of feedwater heaters. However, with potentially smaller footprint and less complex configuration, similar efficiency can be achieved with coal-fired s-CO₂ Brayton cycle power plant investigated in this study.

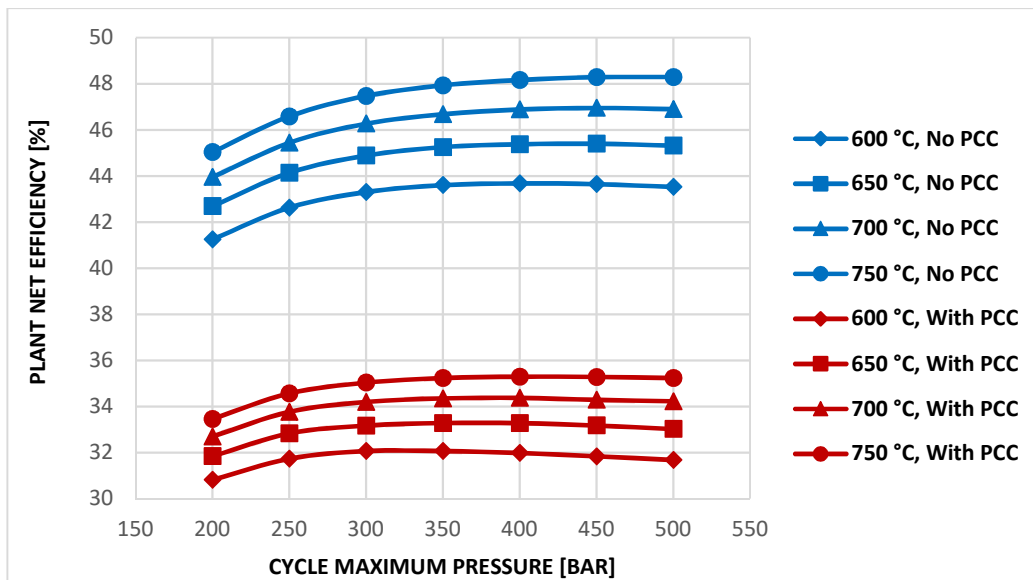


Figure 10-12 Plant net efficiency as a function of cycle maximum pressure at different TIT for the single recuperator recompression bottoming cycle configuration (i.e. Case C) with no carbon capture and with carbon capture integrated

10.8.2 Effect of precooler outlet/MC inlet operating conditions

The selection of precooler outlet temperature (or MC inlet temperature) is based on the ambient or heat sink temperature, which depends on location as well as the type of cooling (wet cooling or dry cooling). The effect of precooler outlet operating conditions on cycle performance was investigated by varying the precooler outlet pressure from 60 bar to 110 bar for four selections of precooler outlet temperature (31, 34, 37 and 40 °C). In order to keep the cycle supercritical at all times, only values of precooler outlet temperature above CO₂ critical temperature was considered. The cycle efficiency was optimised with the flow split fraction while other parameters were fixed at the baseline value. Figure 10-13 shows the plant net efficiency as a function of precooler outlet temperature and pressure.

The plant net efficiency decreases with rise in precooler outlet temperature. However, for each precooler outlet temperature, there is a corresponding pseudo-critical pressure at which the plant efficiency is maximum. For instance, the highest plant net efficiency for a precooler outlet temperature of 31 °C was achieved at a precooler outlet pressure of 76 bar. However, when the precooler outlet temperature was increased to 34 °C, the optimum precooler outlet pressure also increased to 81 bar. This trend continued with increase in precooler outlet temperature. This is due to rapid rise of the density of the CO₂ working around the pseudo-critical pressures associated

with the selected temperatures as shown in Figure 10-14. The increased density results in reduced compressor work and hence increased net work output or efficiency.

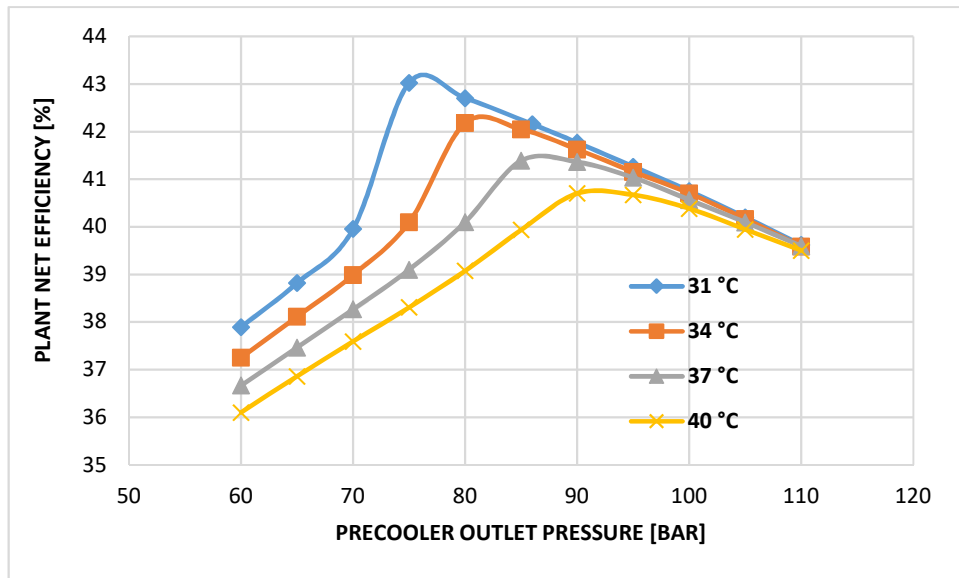


Figure 10-13 Effect of precooler outlet temperature on plant net efficiency of the single recuperator recompression bottoming cycle configuration with no carbon capture with precooler outlet pressure varying from 60 bar to 110 bar

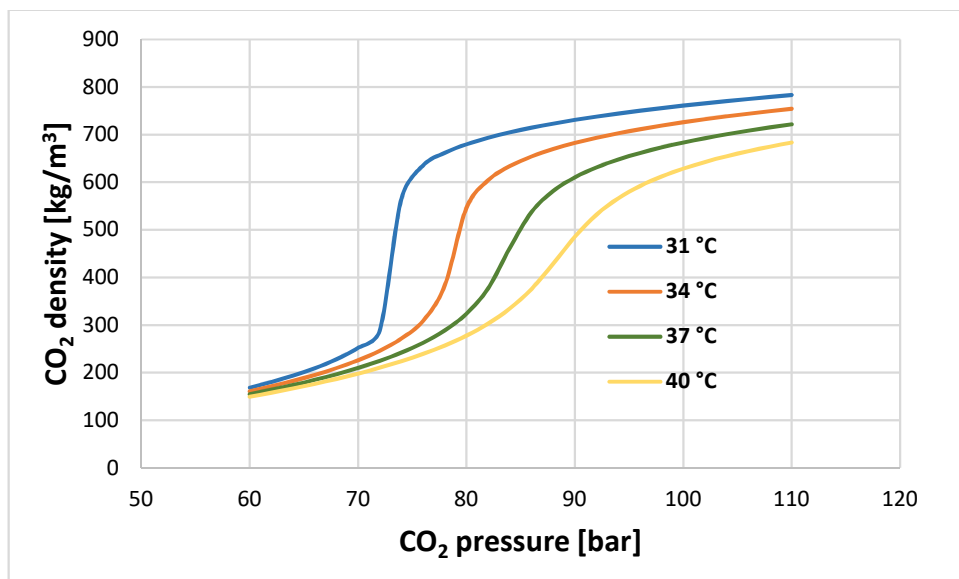


Figure 10-14 Plot of CO₂ pressure against density in the critical region showing the rapid rise in density at pseudo-critical pressures corresponding to different CO₂ temperatures

10.8.3 Effect of minimum TTD of the recuperators

The minimum TTD of the recuperators is considered to be the smallest temperature difference between the hot and the cold stream at either hot inlet/cold outlet end or cold inlet/hot outlet end of the heat exchanger. Supercritical CO₂ recuperator is known to have pinch-point problem in

which the smallest temperature difference occurs somewhere along the heat exchanger and not at the terminals (Mecheri and Le Moullec, 2016). The occurrence of pinch-point along the recuperator can be avoided by using recompression cycle and adjusting the flow split fractions to balance the heat capacities of the hot and cold stream. Therefore, minimum TTD will be the same as pinch-point temperature difference if the pinch-point is located at the terminal of the recuperators.

The selection of recuperator TTD or pinch-point temperature difference will influence the cycle efficiency and size of the recuperator (Mecheri and Le Moullec, 2016). Previous studies showed that the recuperator constituted the largest percentage of the size of CBC plant (Olumayegun et al., 2017; Hu et al., 2015). For the coal-fired s-CO₂ cycle plant with single recuperator recompression bottoming cycle, the effect of the recuperators' minimum TTD on the plant net efficiency is shown in Figure 10-15. The plant net efficiency decreased with increasing minimum TTD of the recuperators. For every 1°C increase in minimum TTD, the net efficiency was reduced by approximately 0.17% point. Hence, improved plant performance can be achieved by reducing the TTD between the hot and cold stream. This is because reducing the TTD will improve the effectiveness of the recuperator, and thus the plant performance. However, this will be at the cost of increased size of recuperator because more heat transfer area will be required.

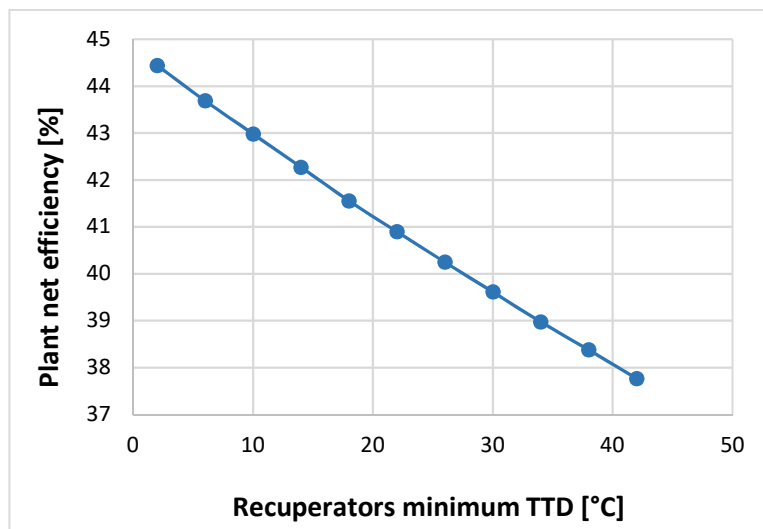


Figure 10-15 Plant net efficiency as a function of recuperators minimum TTD for the single recuperator recompression bottoming cycle s-CO₂ plant

10.9 Summary

In this chapter, s-CO₂ Brayton cycle has been proposed as a potential replacement for steam Rankine cycle of coal-fired power plant with 90% post-combustion CO₂ capture. Three cases representing three different s-CO₂ bottoming cycle options were considered. The investigated bottoming cycle options were simple recuperated cycle as Case A, partial heating cycle as Case

B and single recuperator recompression cycle (a newly proposed layout in this study) as Case C. In all the cases, the topping cycle was a single reheat s-CO₂ recompression cycle with the same main operating conditions as the reference supercritical steam Rankine cycle. Thermodynamic analysis and performance evaluation were performed for the three cases for situations without CO₂ capture and with CO₂ capture unit integrated. The integrated coal-fired furnace, s-CO₂ cycles and MEA-based CO₂ capture process were simulated in Aspen Plus[®].

11 Conclusions and Recommendations for Future Work

11.1 Conclusions

Closed-cycle GT has the potential for improved efficiency of electricity generation, compact and simple design, and reduced CO₂ emissions and therefore could complement conventional power generation plants. A state-of-the-art assessment of closed-cycle GT in this study recognises the need to demonstrate the integrity, operation and performance of the plant before commercial deployment. A systematic, full-scope study including the selection of plant design alternatives, design point thermodynamic performance analysis, preliminary design of major plant components, dynamic model development and simulation of plant transients, and implementation of control schemes has been performed for nitrogen and s-CO₂ CBCs for application to SM-SFR and SM-PWR respectively. In addition, performance evaluation was carried out for s-CO₂ Brayton cycles for application to coal-fired power generation with solvent-based PCC. These conceptual studies performed in this work may be significant as the design information about closed-cycle GT applications to SMR and coal-fired furnace could form the basis for the near-term demonstration of such technologies.

11.1.1 SM-SFR/nitrogen closed-cycle GT power plant

Study has been performed for a 500 MWth SM-SFR coupled to nitrogen CBCs. A reference single-shaft configuration and a proposed two-shaft configuration with parallel turbines were investigated. Thermodynamic performance assessment of the cycles, preliminary sizing of the heat exchangers and 2-D mean-line aerodynamic design of the turbomachinery were performed using models developed in Matlab[®]. As an outcome of this investigation the following main conclusions can be highlighted:

- Thermodynamic analysis of the cycles indicates that the proposed two shaft configuration with parallel turbines have the same cycle thermodynamic efficiency of 39.44% as the reference single shaft configuration. In contrast, two-shaft configuration with turbines in series is known to result in loss of cycle efficiency.
- Heat exchangers preliminary sizing shows that the recuperator constitute a major percentage of the total size. Therefore, any further effort to reduce the plant footprint should focus on the selection and design of the recuperator.
- As expected, cycle efficiency decreases almost linearly with increase in the minimum TTD of the recuperator while recuperator size decreases non-linearly with increase in TTD. Hence, any reduction in volume obtained by increasing the TTD will be at the cost

of reduced cycle efficiency. A TTD of 15 °C appears to be a good compromise between cycle efficiency and recuperator size.

- Preliminary design of the turbomachinery seems to reveal that the proposed two shaft configuration could favour simplification of the design and reduced size as well as increased cycle efficiency by improving the turbomachinery efficiency. The design of the LPC, the HPC and the CDT of the two shaft configuration can be optimised with the shaft rotational speed. An optimum compressors shaft speed of 8000 rpm is established. Total compressors volume is reduced from 1.16 m³ in the single shaft configuration to 0.2 m³ in the two shaft configuration while total turbine volume is reduced from 3.24 m³ to 2.2 m³.

Dynamic modelling, simulation and control of the SM-SFR/nitrogen cycle power plant with two-shaft configuration have also been performed using Matlab[®]/Simulink[®]. Transient responses of the plant under normal load following and 100% loss of grid load has been discussed. An automatic control scheme has been developed which enables the power plant to satisfy the operational requirements for the two load change scenarios. Automatic plant control is achieved by means of control actions to regulate: bypass valve opening to control generator shaft speed; inventory to control power output; control rod to control reactor core outlet temperature; coolant pump torque to control TIT; and cooling water to control compressor inlet temperature. For this plant, inventory control cannot satisfy the requirements to maintain the generator speed within ±30 rpm of the rated speed during load following operation. However, bypass valve control is able to keep the generator speed within ±17 rpm of the rated speed value. Under sudden loss of load condition, the generator shaft overspeed is about 105% of the rated speed, which is well below the specified 120% maximum limit. Hence, stable operation and control of the two-shaft SM-SFR/nitrogen closed-cycle GT plant is possible.

In the light of these findings, the proposed two-shaft CBC with nitrogen as working fluid could be a promising PCS for near-term demonstration of electricity generation from SFR. The current preliminary study neglected the impact of the pressure losses in the connecting pipes on the thermodynamic performance. Also the sizing of the heat exchangers is limited to the core, the sizes of the headers are not included. All this can be delayed until the detailed design phase. Nevertheless, this study provides considerable insight into the thermodynamic performance, preliminary sizing of heat exchangers and turbomachinery, and dynamic operation and control of nitrogen CBC coupled to SM-SFR.

11.1.2 SM-PWR/s-CO₂ closed-cycle GT power plant

Study has also been performed for a 500 MWth SM-PWR coupled to s-CO₂ CBCs. Performance analysis and preliminary components design were performed with the Matlab[®] models. The

thermodynamic performance and components design were carried out for three s-CO₂ cycle layouts: Simple recuperated cycle, recompression cycle and the newly proposed single recuperator recompression cycle layouts.

The performance assessment of the recompression s-CO₂ cycle for application to PWR shows that temperature of the turbine exhaust is too low to allow any meaningful recuperation in the HTR. Most of the recuperation takes place in the LTR. Hence, the single recuperator recompression cycle is suggested in which the HTR is removed leaving only one recuperator. The performance of the single recuperator recompression layout is comparable to that of the recompression cycle and higher than the efficiency of the simple recuperated cycle layout.

Heat exchanger designs were performed to determine the volume and the impact on the cycle performance through the pressure losses. The results of heat exchanger indicates that recompression cycle layouts have higher pressure losses than the simple cycle layout even though they allow higher level of recuperation. Therefore, if the pressure losses are taken into consideration, the recompression cycles might not be that superior to the simple cycle in term of performance. However, parametric analysis to determine the optimum minimum and maximum operation pressures shows that the single recuperator recompression layout is the most promising for application to PWR. Preliminary design of the turbomachinery for the single recuperator recompression cycle reveals that the machines are very compact (about 2% of the heat exchanger volume).

Dynamic modelling, simulation and control have also been performed for the single recuperator recompression coupled to SM-PWR. In order to avoid challenges associated with rapid variation s-CO₂ properties, no inventory/pressure control is implemented for the SM-PWR/s-CO₂ plant. Also, flow split control and throttle valves were added to the usual bypass valve, control rod, pump torque and cooling water control in order to effectively control the plant. The maximum variation of shaft speed during load following operation is about ± 27 rpm. Also, shaft over-speed is about 107% of the rated speed. All of this is within the allowable speed limit.

11.1.3 Coal-fired/s-CO₂ closed-cycle GT power plant

Study has been performed for a coal-fired s-CO₂ closed-cycle GT with solvent-based carbon capture process. Aspen Plus[®] was used to simulate the integrated coal-fired furnace, s-CO₂ cycles and MEA-based CO₂ capture process. Performance evaluation shows that the s-CO₂ Brayton cycle can be adapted for efficient utilisation of furnace and flue gases heat by using a topping s-CO₂ cycle and a bottoming s-CO₂ cycle in addition to combustion air preheating. The coal-fired s-CO₂ cycle is able to achieve furnace efficiency of about 88% in the three cases studied, which is comparable to the boiler efficiency of the conventional supercritical steam plant. The plant net

efficiency of the s-CO₂ Brayton cycle plant without CO₂ capture is about 3.34-3.86% above that of the supercritical steam plant. With CO₂ capture, the coal-fired s-CO₂ cycle suffers an efficiency penalty of about 11.2%, which is more than the efficiency penalty of the reference supercritical steam cycle plant (8.65%). Nevertheless, the plant net efficiency of the s-CO₂ cycle plant is still about 0.68-1.31% point more than that of the supercritical steam cycle with PCC. Of the three cases investigated, Case C (newly proposed single recuperator recompression s-CO₂ layout as bottoming cycle) is the most attractive configuration as it gives the highest plant net efficiency either without or with CO₂ capture. Also, comparison of the specific work outputs indicates that the size of the new concept is not expected to be significantly larger than those of Case A and Case B.

If the operating pressure expected for the next USC steam plant is adopted without any corresponding increase in TIT, the coal-fired s-CO₂ Brayton cycle could give about 4.24% point gain in efficiency over the current steam cycle plant. A further 3.33% point gain can be achieved if the TIT of the USC steam cycle plant is adopted as well. Parametric study with precooler outlet temperature shows that the plant net efficiency decreases with increase in precooler outlet temperature as expected but for each precooler outlet temperature value there is an optimum precooler outlet pressure.

Taken together, these findings suggests that cascaded s-CO₂ Brayton cycle is a promising PCS for coal-fired power plant application. The current study is conceptual in nature. Nevertheless, it provides considerable insight into the thermodynamic performance of s-CO₂ Brayton cycle adapted for coal-fired power plant, employing a topping reheat recompression s-CO₂ cycle and different options of bottoming s-CO₂ cycles. Operating conditions have been chosen to be similar to conditions obtainable in the current supercritical steam boiler so that the current experience with boiler material technology can be applied to the s-CO₂ furnace. Therefore, future development efforts can be focused on the s-CO₂ Brayton cycles.

11.2 Recommendations for future work

The following areas are recommended for further research in the study of closed-cycle GTs for power generation:

- 1) Currently, technical performance analysis is based on first-law efficiency. Exergetic analysis should be performed to locate exergy destruction, identify components to be prioritise for efficiency improvement and compare the plants to make design decisions.
- 2) Economic analysis should be performed to better assess the competitiveness of the different closed-cycle GT applications. In particular, detailed economic assessment is needed for the SM-PWR/s-CO₂ cycle plant with less efficiency than steam cycle option

to determine the true potential of the plant in comparison with conventional nuclear steam power.

- 3) The current study of coal-fired s-CO₂ power generation has been limited to steady state performance evaluation. Further work on the design of components, and dynamic performance and control is required.
- 4) Preliminary design of the PCHE heat exchanger has been performed with commonly available thermal-hydraulic correlations for heat exchangers. Experimental evaluation of the thermal-hydraulic performance of the heat exchangers would be required to confirm the design as well as provide a more reliable thermal-hydraulic correlation for PCHE.
- 5) Straight channels has been assumed for the heat exchanger. It is believed heat transfer could be improved with other channel shape such as wavy channels. Nevertheless, this might be at the expense of increased pressure loss. Future work should compare the design of PCHE with straight channel against other channel shape.
- 6) All exchanger has been assumed as PCHE. Future research should compare alternative CHE choices with potential to improve the compactness of the heat exchangers. Plate fin heat exchanger (PFHE) has been reported to be more compact than PCHE but this might pose more development risk than PCHE.
- 7) The volume of heat exchanger and the cycle efficiency are closely coupled with the pressure loss, length and number of channels (or flow area) of the heat exchangers. Optimisation of the heat exchanger design might be require to arrive at the best design parameters.
- 8) In this study, preliminary design of the heat exchanger only determine the core size and the thermal-hydraulic properties. Detailed design to determine the total size, which include the headers, as well as simulation of the stress, transients and fatigue have been left for future work.
- 9) All the turbomachinery has been design as axial type. However, centrifugal compressors have variously been suggested for the s-CO₂ cycle MC and RC. Future work on the design of centrifugal compressors for the s-CO₂ cycle should be carried out.
- 10) Future work should be done on detailed design of the turbomachinery to include span-line design, generation of performance maps for off design and dynamic modelling, and CFD analysis

- 11) Dynamic modelling, simulation and control have been performed for nuclear closed-cycle GTs under load following and loss of load conditions. Dynamic simulation and control for other operating conditions such as start-up and shutdown operations should be performed

- 12) The control systems have been implanted with PID controller. The controller parameters have been obtained largely by trial and error method due to the complexity of the first principle models which makes linearising the model difficult. In the future, system identification approach and advanced control strategies such as Model Predictive Control (MPC) and linear quadratic Gaussian(LQG) control should be investigated.

References

- Ablay, G. 2013. A modeling and control approach to advanced nuclear power plants with gas turbines. *Energy Conversion and Management*, 76(0), pp 899-909.
- Abram, T. & Ion, S. 2008. Generation-IV nuclear power: A review of the state of the science. *Energy Policy*, 36(12), pp 4323-4330.
- Ahn, Y., Bae, S. J., Kim, M., Cho, S. K., Baik, S., Lee, J. I. & Cha, J. E. 2015. Review of supercritical CO₂ power cycle technology and current status of research and development. *Nuclear Engineering and Technology*, 47(6), pp 647-661.
- Ahn, Y. & Lee, J. I. 2014. Study of various Brayton cycle designs for small modular sodium-cooled fast reactor. *Nuclear Engineering and Design*, 276(0), pp 128-141.
- Al-attab, K. A. & Zainal, Z. A. 2015. Externally fired gas turbine technology: A review. *Applied Energy*, 138(0), pp 474-487.
- Al-Sulaiman, F. A. & Atif, M. 2015. Performance comparison of different supercritical carbon dioxide Brayton cycles integrated with a solar power tower. *Energy*, 82(0), pp 61-71.
- Alpy, N., Cachon, L., Haubensack, D., Floyd, J., Simon, N., Gicquel, L., Rodriguez, G., Saez, M. & Laffont, G. 2011. Gas cycle testing opportunity with ASTRID, the French SFR prototype. In: *Supercritical CO₂ Power Cycle Symposium*, 24-25 May 2011, Boulder, Colorado. Available at: http://www.sco2powercyclesymposium.org/resource_center/system_concepts/gas-cycle-testing-opportunity-with-astrid-the-french-sfr-prototype [Accessed 11 April 2014].
- Angelino, G. 1968. Carbon dioxide condensation cycles for power production. *Journal of Engineering for Gas Turbines and Power*, 90(3), pp 287-295.
- Anheden, M. 2000. *Analysis of gas turbine systems for sustainable energy conversion*. PhD Thesis, Department of Chemical Engineering and Technology, Royal Institute of Technology.
- Arachchige, U. S. P. & Melaaen, M. C. 2012. Aspen Plus Simulation of CO₂ Removal from Coal and Gas Fired Power Plants. *Energy Procedia*, 23(0), pp 391-399.
- Armentrout, C. J. 2011. *Nuclear decisions 4 - What does it all mean?* [Online]. The Last Tech Age. Available at: <https://lasttechage.wordpress.com/2011/05/15/nuclear-decisions-4-%E2%80%93-what-does-it-all-mean/> [Accessed 02 May 2014].
- AspenTech. 2013. *Aspen Plus: Getting started modeling processes with solids*. Burlington, MA: Aspen Technology, Inc.
- Bae, S. J., Ahn, Y., Lee, J. & Lee, J. I. 2014. Various supercritical carbon dioxide cycle layouts study for molten carbonate fuel cell application. *Journal of Power Sources*, 270(0), pp 608-618.
- Bae, S. J., Lee, J., Ahn, Y. & Lee, J. I. 2015. Preliminary studies of compact Brayton cycle performance for Small Modular High Temperature Gas-cooled Reactor system. *Annals of Nuclear Energy*, 75(0), pp 11-19.
- Balje, O. 1981. *Turbomachines-A guide to Design, Selection and Theory*, New York: John Wiley and Sons.

- Bammert, K. & Groschup, G. 1977. Status report on closed-cycle power plants in the Federal Republic of Germany. *Journal of Engineering for Gas Turbines and Power*, 99(1), pp 37-46.
- Bammert, K. & Krey, G. 1971. Dynamic behavior and control of single-shaft closed-cycle gas turbines. *Journal of Engineering for Gas Turbines and Power*, 93(4), pp 447-453.
- Bammert, K. & Poesentrup, H. 1980. The behavior of a closed-cycle gas turbine with time dependent operating conditions. *Journal of Engineering for Gas Turbines and Power*, 102(3), pp 579-583.
- Banik, S., Ray, S. & De, S. 2016. Thermodynamic modelling of a recompression CO₂ power cycle for low temperature waste heat recovery. *Applied Thermal Engineering*, 107(0), pp 441-452.
- Bardia, A. 1980. Dynamics and control modeling of the closed-cycle gas turbine (GT-HTGR) power plant, Report no. GA-A15677, General Atomic Company, San Diego, CA.
- Barner, R. B. 2006. *Power conversion unit studies for the next generation nuclear plant coupled to a high-temperature steam electrolysis facility*. MSc Thesis, Texas A & M University.
- Batet, L., Alvarez-Fernandez, J. M., de les Valls, E. M., Martinez-Quiroga, V., Perez, M., Reventos, F. & Sedano, L. A. 2014. Modelling of a supercritical CO₂ power cycle for nuclear fusion reactors using RELAP5–3D. *Fusion Engineering and Design*, 89(4), pp 354-359.
- Bathie, W. W. 1996. *Fundamentals of gas turbines*, 2nd, New York: John Wiley and Sons.
- Baxi, C. B., Shenoy, A., Kostin, V. I., Kodochigov, N. G., Vasyaev, A. V., Belov, S. E. & Golovko, V. F. 2008. Evaluation of alternate power conversion unit designs for the GT-MHR. *Nuclear Engineering and Design*, 238(11), pp 2995-3001.
- Behar, O., Khellaf, A. & Mohammedi, K. 2013. A review of studies on central receiver solar thermal power plants. *Renewable and Sustainable Energy Reviews*, 23(0), pp 12-39.
- Bentivoglio, F., Tauveron, N., Geffraye, G. & Gentner, H. 2008. Validation of the CATHARE2 code against experimental data from Brayton-cycle plants. *Nuclear Engineering and Design*, 238(11), pp 3145-3159.
- Bhinder, F. S., Calay, R., Mustafa, M. Y., Al-Zubaidy, S. & Holdo, A. E. 2011. A hybrid power-plant to moderate carbon emissions. *International Journal of Research & Reviews in Applied Sciences*, 6(2), pp.
- Brenes, B. M. 2014. *Design of supercritical carbon dioxide centrifugal compressors*. PhD Thesis, The Thermal Power Group (GMTS, Grupo de Máquinas y Motores Térmicos), University of Seville.
- Brey, H. L. 2001. Development history of the gas turbine modular high temperature reactor. In: *IAEA Technical Committee Meeting on Gas Turbine Power Conversion Systems for Modular HTGRs*, 14-16 November 2000, Palo Alto, CA. Vienna, Austria: International Atomic Energy Agency (IAEA), pp 21-43.
- Bryant, J. C., Saari, H. & Zanganeh, K. 2011. An analysis and comparison of the simple and recompression supercritical CO₂ cycles. In: *Supercritical CO₂ Power Cycle Symposium*, 24-25 May 2011, Boulder, Colorado. Available at: http://www.sco2powercyclesymposium.org/resource_center/system_concepts/analysis-

[and-comparison-of-the-simple-and-recompression-supercritical-co2-cycles](#) [Accessed 05 Dec 2013]

- Cachon, L., Biscarrat, C., Morin, F., Haubensack, D., Rigal, E., Moro, I., Baque, F., Madeleine, S., Rodriguez, G. & Laffont, G. 2012. Innovative power conversion system for the French SFR prototype, ASTRID. In: *2012 International Congress on Advances in Nuclear Power Plants (ICAPP '12)*, 24-28 June 2012, Chicago, IL. Illinois: American Nuclear Society.
- Camporeale, S. M., Fortunato, B. & Dumas, A. 2000. Dynamic modelling of recuperative gas turbines. *Proceedings of the Institution of Mechanical Engineers, Part A: Journal of Power and Energy*, 214(3), pp 213-225.
- Carre, F., Yvon, P., Anzieu, P., Chauvin, N. & Malo, J.-Y. 2010. Update of the French R&D strategy on gas-cooled reactors. *Nuclear Engineering and Design*, 240(10), pp 2401-2408.
- Carstens, N. A. 2007. *Control Strategies for Supercritical Carbon Dioxide Power Conversion Systems*. PhD Thesis, Massachusetts Institute of Technology (MIT).
- Carstens, N. A., Hejzlar, P. & Driscoll, M. J. 2006. Control System Strategies and Dynamic Response for Supercritical CO₂ Power Conversion Cycles. Report no. MIT-GFR-038, Center for Advanced Nuclear Energy Systems, Nuclear Engineering Department, MIT.
- Casella, F. & Colonna, P. 2011. Development of a Modelica dynamic model of solar supercritical CO₂ Brayton cycle power plants for control studies. In: *Supercritical CO₂ Power Cycle Symposium*, 24-25 May 2011, Boulder, Colorado. Available at: http://www.sco2powercyclesymposium.org/resource_center/system_modeling_control/development-of-modelica-dynamic-model-of-solar-supercritical-co2-brayton-cycle-power-plants-for-control-studies [Accessed 15 Dec 2013].
- Cau, G., Tola, V. & Bassano, C. 2015. Performance evaluation of high-sulphur coal-fired USC plant integrated with SNO_x and CO₂ capture sections. *Applied Thermal Engineering*, 74(0), pp 136-145.
- CEA. 2012. 4th-Generation sodium-cooled fast reactor: The ASTRID technological demonstrator [Online]. French Alternative Energies and Atomic Energy Commission (CEA) Nuclear Energy Division (Paris). Available at: <http://www.cea.fr/multimedia/Documents/publications/rapports/rapport-gestion-durable-matieres-nucleaires/4th-generation-sodium-cooled-fast-reactors.pdf> [Accessed 10 November 2015]]
- Cha, J.-E., Lee, T.-H., Eoh, J.-H., Seong, S.-H., Kim, S.-O., Kim, D.-E., Kim, M.-H., Kim, T.-W. & Suh, K.-Y. 2009. Development of a supercritical CO₂ Brayton energy conversion system coupled with a sodium cooled fast reactor. *Nuclear Engineering and Technology*, 41(8), pp 1025-1044.
- Chacartegui, R., Muñoz de Escalona, J. M., Sánchez, D., Monje, B. & Sánchez, T. 2011a. Alternative cycles based on carbon dioxide for central receiver solar power plants. *Applied Thermal Engineering*, 31(5), pp 872-879.
- Chacartegui, R., Sánchez, D., Muñoz, A. & Sánchez, T. 2011b. Real time simulation of medium size gas turbines. *Energy Conversion and Management*, 52(1), pp 713-724.
- Cheang, V. T., Hedderwick, R. A. & McGregor, C. 2015. Benchmarking supercritical carbon dioxide cycles against steam Rankine cycles for Concentrated Solar Power. *Solar Energy*, 113(0), pp 199-211.

- Colebrook, C. F. 1939. Turbulent flow in pipes, with particular reference to the transition region between smooth and rough pipe laws. *Journal of the Institution of Civil Engineers*, 11(4), pp 133-156.
- Crespi, F., Gavagnin, G., Sánchez, D. & Martínez, G. S. 2017. Supercritical carbon dioxide cycles for power generation: A review. *Applied Energy*, 195(0), pp 152-183.
- Damiani, L., Prato, A. P. & Revetria, R. 2014. Innovative steam generation system for the secondary loop of “ALFRED” lead-cooled fast reactor demonstrator. *Applied Energy*, 121(0), pp 207-218.
- Dekhtiarev, V. L. 1962. On designing a large, highly economical carbon dioxide power installation. *Electrichenskie Stantskii*, 5(5), pp 1-6.
- Di Bella, F. A. 2011. Gas turbine engine exhaust waste heat recovery navy shipboard module development. In: *Supercritical CO₂ Power Cycle Symposium*, 24-25 May 2011, Boulder, Colorado. Available at: http://www.sco2powercyclesymposium.org/resource_center/system_concepts/gas-turbine-engine-exhaust-waste-heat-recovery-navy-shipboard-module-development [Accessed 09 December 2013].
- Dixon, S. L. 1998. *Fluid mechanics, thermodynamics of turbomachinery*, 5th, Oxford: Elsevier Inc.
- Don, W. G. & Robert, H. P. (eds.) 2008. *Perry's Chemical Engineers' Handbook*, USA: McGraw Hill Professional.
- Dostal, V. 2004. *A supercritical carbon dioxide cycle for next generation nuclear reactors*. PhD Thesis, Massachusetts Institute of Technology (MIT).
- Dostal, V., Todreas, N. E., Hejzlar, P. & Kazimi, M. S. 2001. Power Conversion Cycle Selection for the LBE Cooled Reactor with Forced Circulation. Report no. MIT-ANP-TR-085, Center for Advanced Nuclear Energy Systems, MIT.
- Driscoll, M. J. & Hejzlar, P. 2004. Topical report: 300 MWe Supercritical CO₂ Plant Layout and Design. Report no. MIT-GFR-014, Center for Advanced Nuclear Energy Systems, MIT (Cambridge, MA).
- du Toit, C. G., Rousseau, P. G. & Kgame, T. L. 2014. Separate effects tests to determine the thermal dispersion in structured pebble beds in the PBMR HPTU test facility. *Nuclear Engineering and Design*, 271(0), pp 437-443.
- Dupont, J. F., Jeanmonod, R. & Frutschi, H. U. 1977. Tugsim-10, a computer code for transient analysis of closed gas turbine cycles and specific applications. *Nuclear Engineering and Design*, 40(2), pp 421-430.
- Dyment, J. & Mantrala, V. 2015. *Jump Start: Getting Started with Aspen Plus® V8*. Aspen Technology, Inc.
- El-Genk, M. S. & Tournier, J.-M. 2008a. Noble gas binary mixtures for gas-cooled reactor power plants. *Nuclear Engineering and Design*, 238(6), pp 1353-1372.
- El-Genk, M. S. & Tournier, J.-M. 2008b. On the use of noble gases and binary mixtures as reactor coolants and CBC working fluids. *Energy Conversion and Management*, 49(7), pp 1882-1891.

- Emun, F., Gadalla, M., Majozi, T. & Boer, D. 2010. Integrated gasification combined cycle (IGCC) process simulation and optimization. *Computers & Chemical Engineering*, 34(3), pp 331-338.
- Eoh, J.-H., No, H. C., Lee, Y.-B. & Kim, S.-O. 2013. Potential sodium–CO₂ interaction of a supercritical CO₂ power conversion option coupled with an SFR: Basic nature and design issues. *Nuclear Engineering and Design*, 259(0), pp 88-101.
- Feher, E. G. 1966. *Supercritical cycle heat engine*. Patent US3237403.
- Feher, E. G. 1967. The supercritical thermodynamic power cycle. In: *IECEC Meeting*, Douglas Paper No. 4348, 13-17 August 1967, Miami Beach, Florida.
- Floyd, J., Alpy, N., Moisseytsev, A., Haubensack, D., Rodriguez, G., Sienicki, J. & Avakian, G. 2013. A numerical investigation of the sCO₂ recompression cycle off-design behaviour, coupled to a sodium cooled fast reactor, for seasonal variation in the heat sink temperature. *Nuclear Engineering and Design*, 260(0), pp 78-92.
- Flynn, D. 2003. *Thermal Power Plant Simulation and Control (IET Power and Energy Series 43)*, London: Institution of Engineering and Technology.
- Forsberg, C. W., Peterson, P. F. & Zhao, H. 2006. High-Temperature Liquid-Fluoride-Salt Closed-Brayton-Cycle Solar Power Towers. *Journal of Solar Energy Engineering*, 129(2), pp 141-146.
- Fourspring, P. M. & Nehrbauer, J. P. 2011. Heat exchanger testing for closed Brayton cycle using supercritical CO₂ as working fluid. In: *Supercritical CO₂ Power Cycle Symposium*, 24-25 May 2011, Boulder, Colorado. Available at: http://www.sco2powercyclesymposium.org/resource_center/fluid_mechanics/heat-exchanger-testing-for-closed-brayton-cycles-using-supercritical-co2-as-the-working-fluid [Accessed 05 December 2013]
- Fout, T., Zoelle, A., Keairnd, D., Turner, M., Woods, M., Kuehn, N., Shah, V., Chou, V., Hamilton, B. A. & Pinkerton, L. 2015. Cost and performance baseline for fossil energy plant (Volume 1a): Bituminous coal (PC) and natural gas to electricity (Revision 3). Report no. DOE/NETL-2015/1723, National Energy Technology Laboratory (NETL) (Pittsburgh, PA).
- Frutschi, H. U. 2005. *Closed-cycle gas turbines: Operating experience and future potential*, New York: ASME Press.
- Fuller, R. L. & Batton, W. 2009. Practical considerations in scaling supercritical carbon dioxide closed Brayton cycle power systems. In: *Supercritical CO₂ Power Cycle Symposium*, 29-30 April 2009, Troy, NY. Available at: http://www.sco2powercyclesymposium.org/resource_center/turbomachinery/practical-considerations-in-scaling-supercritical-carbon-dioxide-closed-brayton-cycle-power-systems [Accessed 05 December 2013]
- Garg, P., Kumar, P. & Srinivasan, K. 2013. Supercritical carbon dioxide Brayton cycle for concentrated solar power. *The Journal of Supercritical Fluids*, 76(0), pp 54-60.
- Gauthier, J.-C., Brinkmann, G., Copsy, B. & Lecomte, M. 2006. ANTARES: The HTR/VHTR project at Framatome ANP. *Nuclear Engineering and Design*, 236(5–6), pp 526-533.
- Geffraye, G., Antoni, O., Farvacque, M., Kadri, D., Lavialle, G., Rameau, B. & Ruby, A. 2011. CATHARE 2 V2.5_2: A single version for various applications. *Nuclear Engineering and Design*, 241(11), pp 4456-4463.

- Gibbs, J. P. 2008. *Power conversion system design for supercritical carbon dioxide cooled indirect cycle nuclear reactors*. MSc Thesis, Department of Nuclear Science and Engineering, MIT.
- Gibbs, J. P., Hejzlar, P. & Driscoll, M. J. 2006. Applicability of supercritical CO₂ power conversion systems to GEN IV reactors. Report no. MIT-GFR-037, Center for Advanced Nuclear Energy Systems, MIT (Cambridge, MA).
- GIF. 2014. Technology roadmap update for Generation IV nuclear energy systems [Online]. Gen IV International Forum (GIF) of Nuclear Energy Agency (NEA) of the Organisation for Economic Co-operation and Development (OECD) (Paris). Available at: <https://www.gen-4.org/gif/upload/docs/application/pdf/2014-03/gif-tru2014.pdf> [Accessed 06 May 2015]
- Gobran, M. H. 2013. Off-design performance of solar Centaur-40 gas turbine engine using Simulink. *Ain Shams Engineering Journal*, 4(2), pp 285-298.
- Gokhstein, D. P. & Verkhivker, G. P. 1971. Future Design of Thermal Power Stations Operating on Carbon Dioxide. *Thermal Engineering*, pp 36-38.
- Golovko, V. F., Dmitrieva, I. V., Kodochigov, N. G., Kuzavkov, N. G., Chudin, A. G. & Shenoy, A. 2001. Features of adapting gas turbine cycle and heat exchangers for HTGRs. In: *IAEA Technical committee meeting on gas turbine power conversion systems for modular HTGRs*, 14-16 November 2000, Palo Alto, CA. Vienna, Austria: International Atomic Energy Agency (IAEA), Report no. IAEA-TECDOC-1238, pp 63-74.
- Golovko, V. F., Kiryushin, A. I., Kodochigov, N. G. & Kuzavkov, N. G. 1995. State of HTGR development in Russia. In: *IAEA Technical committee meeting on design and development of gas cooled reactors with closed cycle gas turbines*, 30 Oct – 2 Nov 1995, Beijing, China. Report no. IAEA-TECDOC-899, pp 31-46.
- Gong, Y., Carstens, N. A., Driscoll, M. J. & Matthews, I. A. 2006. Analysis of Radial Compressor Options for Supercritical CO₂ Power Conversion Cycles. Report no. MIT-GFR-034, Center for Advanced Nuclear Energy Systems, Department of Nuclear Science and Engineering, and Gas Turbine Laboratory of the Department of Aeronautics and Astronautics Systems, MIT (Cambridge, MA).
- Gorla, R. S. R. & Khan, A. A. 2003. *Turbomachinery: design and theory*, New York: Marcel Dekker Inc.
- Han, G. Y. 2000. A mathematical model for the thermal-hydraulic analysis of nuclear power plants. *International Communications in Heat and Mass Transfer*, 27(6), pp 795-805.
- Hanak, D. P. & Manovic, V. 2016. Calcium looping with supercritical CO₂ cycle for decarbonisation of coal-fired power plant. *Energy*, 102(0), pp 343-353.
- Heatric. 2015. *Brayton Gas Cycle* [Online]. Poole, UK: Heatric - Division of Meggitt UK Ltd. Available: http://www.heatric.com/brayton_gas_cycle.html [Accessed 15 June 2015].
- Held, T. J. 2014. Initial test results of a megawatt-class supercritical CO₂ heat engine. In: *4th International Symposium on Supercritical CO₂ Power Cycles*, 9-10 September 2014, Pittsburgh, PA. Available at: <http://citeseerx.ist.psu.edu/viewdoc/download?doi=10.1.1.724.7458&rep=rep1&type=pdf> [Accessed 01 July 2015].
- Herranz, L. E., Linares, J. I. & Moratilla, B. Y. 2009. Power cycle assessment of nuclear high temperature gas-cooled reactors. *Applied Thermal Engineering*, 29(8-9), pp 1759-1765.

- Hesselgreaves, J. E. 2001. *Compact heat exchangers: selection, design and operation*, Oxford (UK): Elsevier Science Ltd.
- Hexemer, M. J. 2014. Supercritical CO₂ Brayton recompression cycle design and control features to support startup and operation. In: *4th International Symposium on Supercritical CO₂ Power Cycles*, 9-10 September 2014, Pittsburgh, PA. Available at: <http://www.sco2symposium.com/www2/sco2/papers2014/systemModelingControl/30-Hexemer.pdf> [Accessed 10 March 2015].
- Hexemer, M. J. & Rahner, K. 2011. Supercritical CO₂ Brayton cycle Integrated System Test (IST) TRACE model and control system design. In: *Supercritical CO₂ Power Cycle Symposium*, 24-25 May 2011, Boulder, Colorado. Available at: http://www.sco2powercyclesymposium.org/resource_center/system_modeling_control/supercritical-co2-brayton-cycle-integrated-system-test-ist-trace-model-and-control-system-design [Accessed 05 August 2014].
- Hoffmann, J. R. & Feher, E. G. 1971. 150 kwe supercritical closed cycle system. *Journal of Engineering for Gas Turbines and Power*, 93(1), pp 70-80.
- Hu, L., Chen, D., Huang, Y., Li, L., Cao, Y., Yuan, D., Wang, J. & Pan, L. 2015. Investigation on the performance of the supercritical Brayton cycle with CO₂-based binary mixture as working fluid for an energy transportation system of a nuclear reactor. *Energy*, 89(0), pp 874-886.
- IAEA. 2001. Current status and future development of modular high temperature gas cooled reactor technology. Report no. IAEA-TECDOC-1198, International Atomic Energy Agency (IAEA) (Vienna, Austria). Available at: http://www-pub.iaea.org/MTCD/Publications/PDF/te_1198_prn.pdf [Accessed 02 March 2014].
- IEA. 2016. Key world energy statistics [Online]. International Energy Agency (IEA) (Paris, France). Available at: <http://www.iea.org/publications/freepublications/publication/KeyWorld2016.pdf> [Accessed 15 March 2017].
- IPCC. 2005. Carbon Dioxide Capture and Storage [Online]. A Special Report of Working Group III of the Intergovernmental Panel on Climate Change (IPCC). Available at: <https://www.ipcc.ch/report/srccs/> [Accessed 10 February 2017]
- Ishiyama, S., Muto, Y., Kato, Y., Nishio, S., Hayashi, T. & Nomoto, Y. 2008. Study of steam, helium, and supercritical CO₂ turbine power generations in prototype fusion power reactor. *Progress in Nuclear Energy*, 50(2-6), pp 325-332.
- Iverson, B. D., Conboy, T. M., Pasch, J. J. & Kruijzena, A. M. 2013. Supercritical CO₂ Brayton cycles for solar-thermal energy. *Applied Energy*, 111(0), pp 957-970.
- Janse van Rensburg, J. J. & Kleingeld, M. 2011. CFD applications in the Pebble Bed Modular Reactor Project: A decade of progress. *Nuclear Engineering and Design*, 241(9), pp 3683-3696.
- Johnson, G. A., McDowell, M. W., O'Connor, G. M., Sonwane, C. G. & Subbaraman, G. 2012. Supercritical CO₂ Cycle Development at Pratt and Whitney Rocketdyne. In: *ASME Turbo Expo 2012: Turbine Technical Conference and Exposition*, 11-15 June 2012, Copenhagen, Denmark. American Society of Mechanical Engineers, pp 1015-1024.
- Johnson, P. K. & Hervol, D. S. 2006. Experimental validation of a closed Brayton cycle system transient simulation. In: *El-Genk, M. S., ed. AIP Conference Proceedings on Space Technology and Applications International FORUM (STAIF 2006)*, 12-16 February

- 2006, Albuquerque, New Mexico. American Institute of Physics (AIP) Publishing, pp 673-681.
- Kaikko, J. 1998. *Performance prediction of gas turbines by solving a system of non-linear equations*. PhD Thesis, Lappeenranta University of Technology.
- Kato, Y., Nitawaki, T. & Muto, Y. 2004. Medium temperature carbon dioxide gas turbine reactor. *11th International Conference on Nuclear Energy*, 230(1-3), pp 195-207.
- Kato, Y., Nitawaki, T. & Yoshizawa, Y. 2001. A carbon dioxide partial condensation direct cycle for advanced gas cooled fast and thermal reactors. In: *Global 2001 international conference on: "back-end of the fuel cycle: from research to solutions"*, 9-13 September 2001, Paris, France.
- Keller, C. 1978. Forty years of experience on closed-cycle gas turbines. *Annals of Nuclear Energy*, 5(8), pp 405-422.
- Kelly, J. E. 2014. Generation IV International Forum: A decade of progress through international cooperation. *Progress in Nuclear Energy*, 77(0), pp 240-246.
- Kikstra, J. F. 2001. *Modelling, Design and Control of a Cogenerating Nuclear Gas Turbine Plant*. PhD Thesis, Delft University of Technology.
- Kikstra, J. F. & Verkooijen, A. H. M. 2000. Dynamic modeling for an optimal design of a cogenerating nuclear gas turbine plant. *Computers & Chemical Engineering*, 24(2-7), pp 1737-1743.
- Kim, J. H., No, H. C., Kim, H. M. & Lim, H. S. 2008. Direct implementation of an axial-flow helium gas turbine tool in a system analysis tool for HTGRs. *Nuclear Engineering and Design*, 238(12), pp 3379-3388.
- Kim, J. H., No, H. C., Kim, H. M. & Lim, H. S. 2009. A system analysis tool with a 2D gas turbine modeling for the load transients of HTGRS. *Nuclear Engineering and Design*, 239(11), pp 2459-2467.
- Kim, M. S., Ahn, Y., Kim, B. & Lee, J. I. 2016. Study on the supercritical CO₂ power cycles for landfill gas firing gas turbine bottoming cycle. *Energy*, 111(0), pp 893-909.
- Kim, Y. M., Kim, C. G. & Favrat, D. 2012. Transcritical or supercritical CO₂ cycles using both low- and high-temperature heat sources. *Energy*, 43(1), pp 402-415.
- Kiryushin, A. I., Kodochigov, N. G., Kouzavkov, N. G., Ponomarev-Stepnoi, N. N., Gloushkov, E. S. & Grebennik, V. N. 1997. Project of the GT-MHR high-temperature helium reactor with gas turbine. *Nuclear Engineering and Design*, 173(1-3), pp 119-129.
- Kisohara, N., Kotake, S. & Sakamoto, T. 2008. Studies of super-critical CO₂ gas turbine power generation fast reactor. Report no. JAEA-Review 2008-040, Japan Atomic Energy Agency (JAEA) (Tokai, Ibaraki). Available at: <http://jairo.nii.ac.jp/0350/00001312> [Accessed 01 April 2014]
- Koster, A., Matzner, H. D. & Nicholisi, D. R. 2003. PBMR design for the future. *Nuclear Engineering and Design*, 222(2-3), pp 231-245.
- Kothandaraman, C. P. & Rudramoorthy, R. 2007. *Fluid mechanics and machinery*, 2nd edition, New Delhi: New Age International Limited.

- Kulhanek, M. & Dostal, V. 2011. Supercritical Carbon Dioxide cycles thermodynamic analysis and comparison. In: *Supercritical CO₂ Power Cycle Symposium*, 24-25 May 2011, Boulder, Colorado. Available at: http://www.sco2powercyclesymposium.org/resource_center/system_concepts/thermodynamic-analysis-and-comparison-of-supercritical-carbon-dioxide-cycles [Accessed 11 December 2013].
- Kumar, K. N. P., Turlidakis, A. & Pilidis, P. 2001. Performance review: PBMR closed cycle gas turbine power plant. In: *IAEA Technical Committee Meeting on Gas Turbine Power Conversion Systems for Modular HTGRs*, 14-16 November 2000, Palo Alto, CA. Vienna, Austria: International Atomic Energy Agency (IAEA), Report no. IAEA-TECDOC-1238, pp 99-112.
- Kunitomi, K., Katanishi, S., Takada, S., Takizuka, T. & Yan, X. 2004. Japan's future HTR—the GTHTTR300. *Nuclear Engineering and Design*, 233(1–3), pp 309-327.
- La Fleur, J. K. 1963. Description of an Operating Closed Cycle: Helium Gas Turbine. In: *ASME 1963 Aviation and Space, Hydraulic, and Gas Turbine Conference and Products Show*, 3-7 March 1963, Los Angeles, CA. American Society of Mechanical Engineer (ASME).
- Le Moulllec, Y. 2013. Conceptual study of a high efficiency coal-fired power plant with CO₂ capture using a supercritical CO₂ Brayton cycle. *Energy*, 49(0), pp 32-46.
- Le Pierres, R., Southall, D. & Osborne, S. 2011. Impact of mechanical design issues on printed circuit heat exchangers. In: *Supercritical CO₂ Power Cycle Symposium*, 24-25 May 2011, Boulder, Colorado. Available at: http://www.sco2powercyclesymposium.org/resource_center/materials/impact-of-mechanical-design-issues-on-printed-circuit-heat-exchangers [05 December 2013].
- Lee, J., Lee, J. I., Ahn, Y. & Choi, M. 2013. Preliminary study of helium Brayton cycle turbomachinery for small modular high temperature gas cooled reactor application. In: *2013 International Congress on Advances in Nuclear Power Plants (ICAPP'13)*, 14-18 April 2013, Jeju Island, Korea. Korea Nuclear Society.
- Lee, J., Lee, J. I., Yoon, H. J. & Cha, J. E. 2014. Supercritical Carbon Dioxide turbomachinery design for water-cooled Small Modular Reactor application. *Nuclear Engineering and Design*, 270(0), pp 76-89.
- Lee, J. C., Campbell, J. & Wright, D. E. 1981. Closed-cycle gas turbine working fluids. *Journal of Engineering for Gas Turbines and Power*, 103(1), pp 220-228.
- Lee, J. J., Kang, D. W. & Kim, T. S. 2011. Development of a gas turbine performance analysis program and its application. *Energy*, 36(8), pp 5274-5285.
- Lemmon, E. W., Huber, M. L. & McLinden, M. O. 2013. NIST Standard Reference Database 23: Reference Fluid Thermodynamic and Transport Properties-REFPROP. Version 9.1 ed. Gaithersburg: National Institute of Standards and Technology (NIST).
- Li, Q., Flamant, G., Yuan, X., Neveu, P. & Luo, L. 2011. Compact heat exchangers: A review and future applications for a new generation of high temperature solar receivers. *Renewable and Sustainable Energy Reviews*, 15(9), pp 4855-4875.
- Lienhard IV, J. H. & Lienhard V, J. H. 2008. *A heat transfer textbook*, 3rd edition, Cambridge, Massachusetts: Phlogiston Press.

- Linares, J. I., Herranz, L. E., Moratilla, B. Y. & Serrano, I. P. 2011. Power conversion systems based on Brayton cycles for fusion reactors. *Fusion Engineering and Design*, 86(9), pp 2735-2738.
- Ma, Z. & Turchi, C. 2011. Advanced supercritical carbon dioxide power cycle configurations for use in concentrating solar power systems. In: *Supercritical CO₂ Power Cycle Symposium*, 24-35 May 2011, Boulder, Colorado. Available at: http://www.sco2powercyclesymposium.org/resource_center/system_concepts/advanced-supercritical-carbon-dioxide-power-cycle-configurations-for-use-in-concentrating-solar-power-systems [Accessed 26 November 2013].
- Manente, G. & Lazzaretto, A. 2014. Innovative biomass to power conversion systems based on cascaded supercritical CO₂ Brayton cycles. *Biomass and Bioenergy*, 69(0), pp 155-168.
- MathWorks 2014. *Matlab*[®] *Primer*, Natick, MA: The MathWorks, Inc.
- MathWorks 2015. *Simulink*[®] *Getting Started Guide*, Natick, MA: The MathWorks, Inc.
- Mattingly, J. D. 2006. *Elements of gas turbine propulsion: Gas turbines and rockets*, Reston, VA: American Institute of Aeronautics and Astronautics (AIAA).
- McCann, L. D. 2007. Use of RELAP5-3D for dynamic analysis of a closed loop Brayton cycle coupled to a nuclear reactor. In: *El-Genk, M. S., ed. AIP Conference Proceedings on Space Technology and Applications International FORUM (STAIF 2007)*, 11-15 February 2007, Albuquerque, New Mexico. American Institute of Physics (AIP) Publishing, pp 541-550.
- McClung, A., Brun, K. & Chordia, L. 2014. Technical and economic evaluation of supercritical oxy-combustion for power generation. In: *4th International Symposium on Supercritical CO₂ Power Cycles*, 9-10 September 2014, Pittsburgh, PA. Available at: <http://www.sco2symposium.com/www2/sco2/papers2014/systemConcepts/40-McClung.pdf> [Accessed 16 March 2015].
- McDonald, C. F. 1985. Large Closed Cycle Gas Turbine Plants. In: Sawyer, J. W. (ed.) *Sawyer's Gas Turbine Engineering Handbook*. Norwalk, Con., USA: Turbomachinery International Publications.
- McDonald, C. F. 1994. Enabling technologies for nuclear gas turbine (gt-mhr) power conversion system. In: *ASME 1994 International Gas Turbine and Aeroengine Congress and Exposition*, 13-16 June 1994, The Hague, Netherlands. American Society of Mechanical Engineers (ASME).
- McDonald, C. F. 1995. The nuclear gas turbine - Towards realization after half a century of evolution. In: *ASME 1995 International Gas Turbine and Aeroengine Congress and Exposition*, 5-8 June 1995, Houston, Texas. The American Society of Mechanical Engineers (ASME).
- McDonald, C. F. 1997. Perspective on a Combustion-Free Gas Turbine to Meet Power Generation Needs in the 21st Century. In: *ASME 1997 International Gas Turbine and Aeroengine Congress and Exhibition*, 2-5 June 1997 Orlando, Florida. American Society of Mechanical Engineers (ASME).
- McDonald, C. F. 2012. Helium turbomachinery operating experience from gas turbine power plants and test facilities. *Applied Thermal Engineering*, 44(0), pp 108-142.

- McDonald, C. F. 2014. Power conversion system considerations for a high efficiency small modular nuclear gas turbine combined cycle power plant concept (NGTCC). *Applied Thermal Engineering*, 73(1), pp 82-103.
- Mecheri, M. & Le Moullec, Y. 2016. Supercritical CO₂ Brayton cycles for coal-fired power plants. *Energy*, 103(0), pp 758-771.
- Merk, B., Stanculescu, A., Chellapandi, P. & Hill, R. 2015. Progress in reliability of fast reactor operation and new trends to increased inherent safety. *Applied Energy*, 147(0), pp 104-116.
- Meter, J. V. 2008. *Experimental investigation of a printed circuit heat exchanger using supercritical carbon dioxide and water as heat transfer media*. MSc Thesis, Department of Mechanical and Nuclear Engineering, Kansas State University.
- Milani, D., Luu, M. T., McNaughton, R. & Abbas, A. 2017. A comparative study of solar heliostat assisted supercritical CO₂ recompression Brayton cycles: Dynamic modelling and control strategies. *The Journal of Supercritical Fluids*, 120(Part 1), pp 113-124.
- Miller, B. G. 2011. *Clean coal engineering technology*, Boston: Butterworth-Heinemann.
- Mohagheghi, M. & Kapat, J. 2014. Thermodynamic optimisation of recuperated S-CO₂ Brayton cycles for waste heat recovery applications. In: *4th International Symposium on Supercritical CO₂ Power Cycles*, 9-10 September 2014, Pittsburgh, PA. Available at: <http://www.swri.org/sites/default/files/thermodynamic-optimization-of-recuperated-s-co2-brayton-cycles-for-waste-heat-recovery-applications-mohagheghi.pdf> [Accessed 06 May 2015].
- Moisseytsev, A. & Sienicki, J. J. 2007. Development of a plant dynamics computer code for analysis of a supercritical carbon dioxide Brayton cycle energy converter coupled to a natural circulation lead-cooled fast reactor. Report no. ANL-06/27, Nuclear Energy Division, Argonne National Laboratories (ANL), Argonne, IL.
- Moisseytsev, A. & Sienicki, J. J. 2008. Transient accident analysis of a supercritical carbon dioxide Brayton cycle energy converter coupled to an autonomous lead-cooled fast reactor. *Nuclear Engineering and Design*, 238(8), pp 2094-2105.
- Moisseytsev, A. & Sienicki, J. J. 2009a. ANL Plant Dynamic Code and control strategy development for the supercritical carbon dioxide Brayton cycle. In: *S-CO₂ Power Cycle Symposium*, 29-30 April 2009, Troy, NY. Available at: http://www.sco2powercyclesymposium.org/resource_center/system_modeling_control/anl-plant-dynamics-code-control-strategy-development-for-the-supercritical-carbon-dioxide-brayton-cycle [Accessed 17 April 2014].
- Moisseytsev, A. & Sienicki, J. J. 2009b. Investigation of alternative layouts for the supercritical carbon dioxide Brayton cycle for a sodium-cooled fast reactor. *Nuclear Engineering and Design*, 239(7), pp 1362-1371.
- Moisseytsev, A. & Sienicki, J. J. 2010. Investigation of Plant Control Strategies for the Supercritical CO₂ Brayton Cycle for a Sodium-Cooled Fast Reactor using the Plant Dynamics Code. Report no. ANL-Gen IV-147, Argonne National Laboratory (ANL), Argonne, IL.
- Moisseytsev, A. & Sienicki, J. J. 2011. Validation of the ANL Plant Dynamics Code compressor model with SNL/BNI compressor test data. In: *Supercritical CO₂ Power Cycle Symposium*, 24-25 May 2011, Boulder, Colorado. Available at: http://www.sco2powercyclesymposium.org/resource_center/system_modeling_control/

[validation-of-the-anl-plant-dynamics-code-compressor-model-with-snl-bni-compressor-test-data](#) [Accessed 25 July 2014].

- Moisseytsev, A. & Sienicki, J. J. 2014. Recent developments in S-CO₂ cycle modelling and analysis at ANL. In: *4th International Symposium on Supercritical CO₂ Power Cycles*, 9-10 September 2014, Pittsburgh, PA. Available at: <http://www.swri.org/sites/default/files/recent-developments-in-s-co2-cycle-dynamic-modeling-and-analysis-at-anl-moisseytsev.pdf> [Accessed 03 August 2014].
- Munoz, d. E., Jose, M., Chacartegui, R., Sánchez, D. & Sánchez, T. 2011. The potential of the supercritical carbon dioxide cycle in high temperature fuel cell hybrid systems. In: *Supercritical CO₂ Power Cycle Symposium*, 24-25 May 2011, Boulder, Colorado. Available at: http://www.sco2powercyclesymposium.org/resource_center/system_concepts/potential-of-the-supercritical-carbon-dioxide-cycle-in-high-temperature-fuel-cell-hybrid-systems [Accessed 09 October 2014].
- Munroe, T. A., Zaccaria, M. A., Flaspohler, W. H., Pelton, R. J., Wygant, K. D. & Dubitsky, O. B. 2009. FLUENT CFD steady state predictions of a single stage centrifugal compressor with supercritical CO₂ working fluid. In: *Supercritical CO₂ Power Cycle Symposium*, 29-30 April 2009, Troy, NY. Available at: http://www.sco2powercyclesymposium.org/resource_center/turbomachinery/fluient-cfd-steady-state-predictions-of-single-stage-centrifugal-compressor-with-supercritical-co2-working-fluid [Accessed 29 December 2013].
- Muto, Y., Aritomi, M., Ishizuka, T. & Watanabe, N. 2014. Comparison of supercritical CO₂ gas turbine cycle and Brayton CO₂ gas turbine for solar thermal power plant. In: *4th International Symposium on Supercritical CO₂ Power Cycles*, 9-10 September 2014, Pittsburgh, PA. Available at: <http://citeseerx.ist.psu.edu/viewdoc/download?doi=10.1.1.705.6218&rep=rep1&type=pdf> [Accessed 10 May 2015].
- Muto, Y. & Kato, Y. 2008. Optimal cycle scheme of direct cycle supercritical CO₂ gas turbine for nuclear power generation systems. *Journal of Power and Energy Systems*, 2(3), pp 1060-1073.
- Nag, P. K. 2008. *Power plant engineering*, New Delhi: Tata McGraw-Hill.
- Naghdolfeizi, M. 1990. *Dynamic modeling of a pressurized water reactor plant for diagnostics and control*. MSc Thesis, University of Tennessee, Knoxville.
- Najjar, Y. S. H. & Zaaout, M. S. 1992. Comparative performance of closed cycle gas turbine engine with heat recovery using different gases. *Heat Recovery Systems and CHP*, 12(6), pp 489-495.
- Neises, T. & Turchi, C. 2014. A Comparison of Supercritical Carbon Dioxide Power Cycle Configurations with an Emphasis on CSP Applications. *Energy Procedia*, 49(0), pp 1187-1196.
- Nikiforova, A., Hejzlar, P. & Todreas, N. E. 2009. Lead-cooled flexible conversion ratio fast reactor. *Nuclear Engineering and Design*, 239(12), pp 2596-2611.
- No, H. C., Kim, J. H. & Kim, H. M. 2007. A review of helium gas turbine technology for high-temperature gas-cooled reactors. *Nuclear Engineering and Technology*, 39(1), pp 21.

- NRC. 2017. *The pressurised water reactor (PWR)* [Online]. Washington, DC: United States Nuclear Regulatory Commission (U.S.NRC). Available: <https://www.nrc.gov/reading-rm/basic-ref/students/animated-pwr.html> [Accessed 11 April 2017].
- Olaleye, A. K., Wang, M. & Kelsall, G. 2015. Steady state simulation and exergy analysis of supercritical coal-fired power plant with CO₂ capture. *Fuel*, 151(0), pp 57-72.
- Olumayegun, O., Wang, M. & Kelsall, G. 2016. Closed-cycle gas turbine for power generation: A state-of-the-art review. *Fuel*, 180(0), pp 694-717.
- Olumayegun, O., Wang, M. & Kelsall, G. 2017. Thermodynamic analysis and preliminary design of closed Brayton cycle using nitrogen as working fluid and coupled to small modular Sodium-cooled fast reactor (SM-SFR). *Applied Energy*, 191(0), pp 436-453.
- Ordys, A. J., Pike, A. W., Johnson, M. A., Katebi, R. M. & Grimble, M. J. 1994. *Modelling and simulation of power generation plants*, London ; New York: Springer-Verlag.
- Padilla, R. V., Soo Too, Y. C., Benito, R. & Stein, W. 2015. Exergetic analysis of supercritical CO₂ Brayton cycles integrated with solar central receivers. *Applied Energy*, 148(0), pp 348-365.
- Parma, E. J., Wright, S. A., Vernon, M. E., Rochau, G. E., Suo-Anttila, A. J., Al Rashdan, A. & Tsvetkov, P. V. 2011. Supercritical CO₂ Direct Cycle Gas Fast Reactor (SC-GFR) Concept. In: *Supercritical CO₂ Power Cycle Symposium*, 24-25 May 2011, Boulder, Colorado. Available at: http://www.sco2powercyclesymposium.org/resource_center/system_concepts/supercritical-co2-direct-cycle-gas-fast-reactor-sc-gfr-concept [Accessed 01 June 2014].
- Pasch, J. J., Conboy, T. M., Fleming, D. D. & Rochau, G. E. 2012. Supercritical CO₂ recompression Brayton cycle: completed assembly description. Report no. SAND2012-9546, Sandia National Laboratories (SNL), Albuquerque, CA.
- Pecnik, R., Rinaldi, E. & Colonna, P. 2012. Computational fluid dynamics of a radial compressor operating with supercritical CO₂. *Journal of Engineering for Gas Turbines and Power*, 134(12), pp 122301.
- Penfield Jr, S. R. & Rodwell, E. 2001. Auxiliary bearing design considerations for gas cooled reactors. In: *IAEA Technical Committee Meeting on Gas Turbine Power Conversion Systems for Modular HTGRs*, 14-16 November 2000, Palo Alto, CA. Vienna, Austria: International Atomic Energy Agency (IAEA). Report no. IAEA-TECDOC-1238, pp 193-208.
- Persichilli, M., Held, T., Hostler, S., Zdankiewicz, E. & Klapp, D. 2011. Transforming waste heat to power through development of a CO₂-based power cycle. In: *Electric Power Expo 2011*, 10-12 May 2011, Rosemount, IL.
- Pham, H. S., Alpy, N., Ferrasse, J. H., Boutin, O., Quenaut, J., Tohill, M., Haubensack, D. & Saez, M. 2015. Mapping of the thermodynamic performance of the supercritical CO₂ cycle and optimisation for a small modular reactor and a sodium-cooled fast reactor. *Energy*, 87(0), pp 412-424.
- Pérez-Pichel, G. D., Linares, J. I., Herranz, L. E. & Moratilla, B. Y. 2011. Potential application of Rankine and He-Brayton cycles to sodium fast reactors. *Nuclear Engineering and Design*, 241(8), pp 2643-2652.

- Pérez-Pichel, G. D., Linares, J. I., Herranz, L. E. & Moratilla, B. Y. 2012. Thermal analysis of supercritical CO₂ power cycles: Assessment of their suitability to the forthcoming sodium fast reactors. *Nuclear Engineering and Design*, 250(0), pp 23-34.
- Ragusa, J. C. & Mahadevan, V. S. 2009. Consistent and accurate schemes for coupled neutronics thermal-hydraulics reactor analysis. *Nuclear Engineering and Design*, 239(3), pp 566-579.
- Reuters. 2014. *Echogen Power Systems' waste heat recovery system available as turnkey solution* [Online]. Available at: <http://uk.reuters.com/article/2014/12/08/idUSnMKWcgTnHa+1ca+MKW20141208> [Accessed 08 February 2015].
- Rousseau, P. G. & Van Ravenswaay, J. P. 2003. Thermal-fluid comparison of three-and single-shaft closed loop brayton cycle configurations for HTGR power conversion. In: *2003 International congress on advances in nuclear power plants (ICAPP'03)*, 4-7 May 2003, Cordoba, Spain.
- Rousseau, P. G. & van Staden, M. 2008. Introduction to the PBMR heat transfer test facility. *Nuclear Engineering and Design*, 238(11), pp 3060-3072.
- Saez, M., Haubensack, D., Alpy, N., Gerber, A. & Daid, F. 2008. The use of gas based energy conversion cycles for sodium fast reactors. In: *2008 International Congress on Advances in Nuclear Power Plants (ICAPP'08)*, 8-12 June 2008, Anaheim, CA. Illinois: American Nuclear Society.
- Santini, L., Accornero, C. & Cioncolini, A. 2016. On the adoption of carbon dioxide thermodynamic cycles for nuclear power conversion: A case study applied to Mochovce 3 Nuclear Power Plant. *Applied Energy*, 181(0), pp 446-463.
- Saravanamuttoo, H. I. H., Rogers, G. F. C., Cohen, H. & Straznicky, P. 2009. *Gas Turbine Theory*, 6th, Essex (UK): Prentice Hall, Pearson Education.
- Sarkar, J. 2009. Second law analysis of supercritical CO₂ recompression Brayton cycle. *Energy*, 34(9), pp 1172-1178.
- Sarkar, J. & Bhattacharyya, S. 2009. Optimization of recompression S-CO₂ power cycle with reheating. *Energy Conversion and Management*, 50(8), pp 1939-1945.
- Seo, S. B., Seo, H. & Bang, I. C. 2016. Adoption of nitrogen power conversion system for small scale ultra-long cycle fast reactor eliminating intermediate sodium loop. *Annals of Nuclear Energy*, 87(Part 2), pp 621-629.
- Seong, S.-H., Lee, T.-H. & Kim, S.-O. 2009. Development of a simplified model for analyzing the performance of KALIMER-600 coupled with a supercritical carbon dioxide Brayton energy conversion cycle. *Nuclear Engineering and Technology*, 41(6), pp 785-796.
- Shah, R. K. & Sekulic, D. P. 2003. *Fundamentals of heat exchanger design*, New Jersey: John Wiley and Sons.
- Shin, J. I. 1975. *Conceptual design of an HTGR system for a total energy application*. MSc Thesis, Massachusetts Institute of Technology (MIT).
- Sienicki, J. J., Moisseytsev, A., Cho, D. H., Thomas, M., Wright, S. A., Pickard, P. S., Rochau, G., Rodriguez, G., Avakian, G. & Alpy, N. 2010. International collaboration on development of the supercritical carbon dioxide Brayton cycle for Sodium-cooled Fast Reactors under the Generation IV International Forum Component Design and Balance

of Plant project. In: *2010 International Congress on Advances in Nuclear Power Plants (ICAPP'10)*, 13-17 June 2010, San Diego. pp 392-399.

- Sienicki, J. J., Moisseytsev, A., Fuller, R. L., Wright, S. A. & Pickard, P. S. 2011. Scale dependencies of supercritical carbon dioxide Brayton cycle technologies and the optimal size for next-step supercritical CO₂ cycle demonstration. In: *Supercritical CO₂ Power Cycle Symposium*, 24-25 May 2011, Boulder, Colorado. Available at: http://www.sco2powercyclesymposium.org/resource_center/development_priorities/scale-dependencies-of-supercritical-carbon-dioxide-brayton-cycle-technologies-and-the-optimal-size-for-a-next-step-supercritical-co2-cycle-demonstration [Accessed 05 December 2013].
- Sienicki, J. J., Rodriguez, G., Kotake, S., Kisojara, N., Sakamoto, Y., Kim, J. B., Joo, Y.-S. & Cha, J. E. 2009. SFR component design and balance of plant project. In: *Generation IV International Forum (GIF) Symposium*, 9-10 September 2009, Paris, France. OECD Nuclear Energy Agency, pp 247-254.
- Singh, R., Rowland, A. S. & Jacobs, P. A. 2011. Dynamic characteristics and perspectives on control of a supercritical CO₂ closed Brayton cycle power loop in a geothermal power plant. In: *Supercritical CO₂ Power Cycle Symposium*, 24-25 May 2011, Boulder, Colorado. Available at: http://www.sco2powercyclesymposium.org/resource_center/system_modeling_control/dynamic-characteristics-and-perspectives-on-control-of-a-supercritical-co2-closed-brayton-cycle-power-loop-in-a-geothermal-power-plant [Accessed 23 October 2014].
- Sobolev, V. 2011. Database of thermophysical properties of liquid metal coolants for GEN-IV, Belgian Nuclear Research Centre (SCK.CEN) (Mol, Belgium).
- Span, R. & Wagner, W. 1996. A New Equation of State for Carbon Dioxide Covering the Fluid Region from the Triple-Point Temperature to 1100 K at Pressures up to 800 MPa. *Journal of Physical and Chemical Reference Data*, 25(6), pp 1509-1596.
- Strub, R. A. & Frieder, A. J. 1970. High pressure indirect CO₂ closed-cycle gas turbines. In: *International Conference on Nuclear Gas Turbines*, 8-9 April 1970, London. The British Nuclear Energy Society, pp 51-61.
- Sun, Y., Zhang, Y. & Xu, Y. 2001. Study on coupling a gas turbine cycle to HTR-10 test reactor. In: *IAEA Technical Committee Meeting on Gas Turbine Power Conversion Systems for Modular HTGRs*, 14-16 November 2000 Palo Alto, CA. Vienna, Austria: International Atomic Energy Agency (IAEA), Report no. IAEA-TECDOC-1238, pp. 45-51.
- Suo-Anttila, A. J. & Wright, S. A. 2011. Computational fluid dynamics code for supercritical fluids. In: *Supercritical CO₂ Power Cycle Symposium*, 24-25 May 2011, Boulder, Colorado. Available at: http://www.sco2powercyclesymposium.org/resource_center/fluid_mechanics/computational-fluid-dynamics-code-for-supercritical-fluids [Accessed 27 December 2013].
- Sánchez, D., Chacartegui, R., Muñoz de Escalona, J. M., Muñoz, A. & Sánchez, T. 2011a. Performance analysis of a MCFC & supercritical carbon dioxide hybrid cycle under part load operation. *International Journal of Hydrogen Energy*, 36(16), pp 10327-10336.
- Sánchez, D., Muñoz de Escalona, J. M., Chacartegui, R., Muñoz, A. & Sánchez, T. 2011b. A comparison between molten carbonate fuel cells based hybrid systems using air and supercritical carbon dioxide Brayton cycles with state of the art technology. *Journal of Power Sources*, 196(9), pp 4347-4354.

- Takada, S., Takizuka, T., Kunitomi, K., Xing, Y., Itaka, H., Mori, E., Takahashi, K. & Tanihira, M. 2003. The 1/3-scale aerodynamics performance test of helium compressor for GTHTR300 turbo machine of JAERI (step 1). In: *International Conference on Nuclear Engineering (ICONE'11)*, 20-23 April 2003, Tokyo. Tokyo: Japan Society of Mechanical Engineers, pp 3610.
- Takizuka, T. 2005. Reactor technology development under the HTTR project. *Progress in Nuclear Energy*, 47(1-4), pp 283-291.
- Takizuka, T., Takada, S., Yan, X., Kosugiyama, S., Katanishi, S. & Kunitomi, K. 2004. R&D on the power conversion system for gas turbine high temperature reactors. *Nuclear Engineering and Design*, 233(1), pp 329-346.
- Tarlecki, J., Lior, N. & Zhang, N. 2007. Analysis of thermal cycles and working fluids for power generation in space. *Energy Conversion and Management*, 48(11), pp 2864-2878.
- Tauveron, N. & Bentivoglio, F. 2012. Preliminary design and study of the indirect coupled cycle: CATHARE2 transient results. *Nuclear Engineering and Design*, 246(0), pp 233-244.
- Tauveron, N., Saez, M., Ferrand, P. & Leboeuf, F. 2007. Axial turbomachine modelling with a 1D axisymmetric approach: Application to gas cooled nuclear reactor. *Nuclear Engineering and Design*, 237(15-17), pp 1679-1692.
- Tauveron, N., Saez, M., Marchand, M., Chataing, T., Geffraye, G. & Bassi, C. 2005. Transient thermal-hydraulic simulations of direct cycle gas cooled reactors. *Nuclear Engineering and Design*, 235(23), pp 2527-2545.
- Thomas, P. 1999. *Simulation of industrial processes for control engineers*, Oxford: Butterworth-Heinemann.
- Thomas, S. 2011. The Pebble Bed Modular Reactor: An obituary. *Energy Policy*, 39(5), pp 2431-2440.
- Tochon, P., Mauget, C. & Pra, F. 2004. The use of compact heat exchangers technologies for the HTRs recuperator application per proper design. In: *2nd International Topical Meeting on High Temperature Reactor Technology*, 22-24 September 2004, Beijing.
- Traverso, A., Massardo, A. F. & Scarpellini, R. 2006. Externally Fired micro-Gas Turbine: Modelling and experimental performance. *Applied Thermal Engineering*, 26(16), pp 1935-1941.
- Trinh, T. Q. 2009. *Dynamic response of the supercritical CO₂ Brayton recompression cycle to various system transients*. MSc Thesis, Massachusetts Institute of Technology (MIT).
- Van Abel, E. N., Anderson, M. H. & Corradini, M. L. 2011. Numerical investigation of pressure drop and local heat transfer of supercritical CO₂ in printed circuit heat exchangers. In: *Supercritical CO₂ Power Cycle Symposium*, 24-25 May 2011, Boulder, Colorado. Available at: http://www.sco2powercyclesymposium.org/resource_center/fluid_mechanics/numerical-investigation-of-pressure-drop-and-local-heat-transfer-of-supercritical-co2-in-printed-circuit-heat-exchangers [Accessed 28 December 2013].
- van Ravenswaay, J. P., Greyvenstein, G. P., van Niekerk, W. M. K. & Labuschagne, J. T. 2006. Verification and validation of the HTGR systems CFD code Flownex. *Nuclear Engineering and Design*, 236(5-6), pp 491-501.

- Vega, J., Sonwane, C. & Eastland, T. 2014. Supercritical CO₂ turbomachinery configuration and controls for a zero emission coal fired power plant: System off design & control of system transients. In: *4th International Symposium on Supercritical CO₂ Power Cycles*, 9-10 September 2014, Pittsburgh, PA. Available at: <http://sco2symposium.com/www2/sco2/papers2014/systemModelingControl/76-Eastland.pdf> [Accessed 05 October 2015].
- Verkerk, E. C. & Kikstra, J. F. 2003. Comparison of two models for a high temperature reactor coupled to a gas turbine. *Nuclear Engineering and Design*, 220(1), pp 51-65.
- Verkerk, E. C. & Van Heek, A. I. 2001. Dynamics of a small direct cycle pebble bed HTR. In: *IAEA Technical Committee Meeting on Gas Turbine Power Conversion Systems for Modular HTGRs*, 14-16 November 2000, Palo Alto, CA. Vienna, Austria: International Atomic Energy Agency (IAEA), Report no. IAEA-TECDOC-1238, pp. 21-43.
- Vilim, R. B., Cahalan, J. E. & Mertyurek, U. 2004. GAS-PASS/H: A simulation code for gas reactor plant systems. In: *2004 International Congress on Advances in Nuclear Power Plants (ICAPP '04)*, 13-17 June 2004, Pittsburgh, PA. American Nuclear Society.
- Walas, S. M. 1990. *Chemical Process Equipment: Selection and Design*, Newton, MA: Butterworth-Heinemann.
- Walsh, P. P. & Fletcher, P. 2004. *Gas turbine performance*, 2nd, Oxford: John Wiley and Sons.
- Walter, A., Schulz, A. & Lohnert, G. 2006. Comparison of two models for a pebble bed modular reactor core coupled to a Brayton cycle. *Nuclear Engineering and Design*, 236(5-6), pp 603-614.
- Wang, C. 2009. *Balance of Plant Analysis for High Temperature Gas Cooled Reactors: Design and Optimization of Gas Turbine Power Conversion System, and Component Design of Turbo-Machinery for Modular Pebble Bed Reactor Plants*, Saarbrücken (Germany): Lambert Academic Publishing.
- Wang, J. & Gu, Y. 2005. Parametric studies on different gas turbine cycles for a high temperature gas-cooled reactor. *Nuclear Engineering and Design*, 235(16), pp 1761-1772.
- Wang, J., Sun, Z., Dai, Y. & Ma, S. 2010. Parametric optimization design for supercritical CO₂ power cycle using genetic algorithm and artificial neural network. *Applied Energy*, 87(4), pp 1317-1324.
- Wang, K., He, Y.-L. & Zhu, H.-H. 2017. Integration between supercritical CO₂ Brayton cycles and molten salt solar power towers: A review and a comprehensive comparison of different cycle layouts. *Applied Energy*, 195(819-836).
- Weisbrodt, I. A. 1996. Summary report on technical experiences from high-temperature helium turbomachinery testing in Germany. In: *Technical committee meeting on design and development of gas cooled reactors with closed cycle gas turbines*, 30 Oct - 2 Nov 1995, Beijing. Vienna, Austria: International Atomic Energy Agency (IAEA). Report no. IAEA-TECDOC-899, pp 177-248.
- Wenlong, L., Heng, X., Zuoyi, Z. & Yujie, D. 2012. Development and primary verification of a transient analysis software for high temperature gas-cooled reactor helium turbine power system. *Nuclear Engineering and Design*, 250(0), pp 219-228.
- WNA. 2015. *Small Nuclear Power Reactors* [Online]. London, UK: World Nuclear Association (WNA). Available at: <http://www.world-nuclear.org/info/nuclear-fuel-cycle/power-reactors/small-nuclear-power-reactors/> [Accessed 01 May 2015].

- Wright, S. 2012. Mighty mite: A turbine that uses supercritical carbon dioxide can deliver great power from a small package. *Mechanical Engineering-CIME*, 134(1), pp 40-43.
- Wright, S. A., Davidson, C. S. & Scammell, W. O. 2014. Bulk energy storage using a supercritical CO₂ waste heat recovery power plant. In: *4th International Symposium on Supercritical CO₂ Power Cycles*, 9-10 September 2014, Pittsburgh, PA. Available at: <http://citeseerx.ist.psu.edu/viewdoc/download?doi=10.1.1.707.7067&rep=rep1&type=pdf> [Accessed 11 November 2015].
- Wright, S. A., Fuller, R., Lipinski, R. J., Nichols, K. & Brown, N. 2005. Operational Results of a Closed Brayton Cycle Test-Loop. *AIP Conference Proceedings*, 746(1), pp 699-710.
- Wright, S. A., Radel, R. F., Vernon, M. E., Rochau, G. E. & Pickard, P. S. 2010. Operation and analysis of a supercritical CO₂ brayton cycle. Report no. SAND2010-0171, Sandia National Laboratories (SNL), Albuquerque, New Mexico.
- Wright, S. A. & Sanchez, T. 2005. Dynamic modelling and control of nuclear reactors coupled to closed loop Brayton cycle systems using SIMULINK. In: *El-Genk, M. S., ed. In: Space Technology and Applications International FORUM (STAIF 2005)*, 13-17 February 2005, Albuquerque, New Mexico. American Institute of Physics (AIP) Publishing, pp 991-1004.
- Wright, S. A., Vernon, M. E. & Pickard, P. S. 2006. Concept Design for a High Temperature Helium Brayton Cycle with Interstage Heating and Cooling. Report no. SAND2006-4147, Sandia National Laboratories (SNL), Albuquerque, New Mexico and Livermore, California.
- Wu, Z. & Yu, S. 2007. HTGR projects in China. *Nuclear Engineering and Technology*, 39(2), pp 103.
- Xie, H. 2011. Model development and simulation of transient behavior of helium turbine system. *Annals of Nuclear Energy*, 38(12), pp 2797-2805.
- Xu, Y., Hu, S., Li, F. & Yu, S. 2005. High temperature reactor development in China. *Progress in Nuclear Energy*, 47(1-4), pp 260-270.
- Yan, X. 1990. *Dynamic analysis and control system design for an advanced nuclear gas turbine power plant*. PhD Thesis, Department of Mechanical Engineering, Massachusetts Institute of Technology (MIT).
- Yan, X., Kunitomi, K., Nakata, T. & Shiozawa, S. 2003. GTHTR300 design and development. *Nuclear Engineering and Design*, 222(2-3), pp 247-262.
- Yan, X., Takizuka, T., Kunitomi, K., Itaka, H. & Takahashi, K. 2008. Aerodynamic design, model test, and CFD analysis for a multistage axial helium compressor. *Journal of Turbomachinery*, 130(3), pp 031018-1 - 031018-12.
- Yang, G., Shi, Z., Mo, N. & Zhao, L. 2014. Research on active magnetic bearing applied in Chinese modular high-temperature gas-cooled reactor. *Progress in Nuclear Energy*, 77(0), pp 352-360.
- Yang, X., Zhengang, S., Guojun, Y., Lei, Z. & Suyuan, Y. 2008. Design aspects and achievements of active magnetic bearing research for HTR-10GT. *Nuclear Engineering and Design*, 238(4), pp 1121-1128.

- Yoon, H. J., Ahn, Y., Lee, J. I. & Addad, Y. 2012. Potential advantages of coupling supercritical CO₂ Brayton cycle to water cooled small and medium size reactor. *Nuclear Engineering and Design*, 245(0), pp 223-232.
- Zhang, X., Li, J., Li, G. & Feng, Z. 2006. Dynamic modeling of a hybrid system of the solid oxide fuel cell and recuperative gas turbine. *Journal of Power Sources*, 163(1), pp 523-531.
- Zhang, Y. & Chen, C.-C. 2013. Modeling CO₂ Absorption and Desorption by Aqueous Monoethanolamine Solution with Aspen Rate-based Model. *Energy Procedia*, 37(0), pp 1584-1596.
- Zhang, Y., Chen, H., Chen, C.-C., Plaza, J. M., Dugas, R. & Rochelle, G. T. 2009. Rate-Based Process Modeling Study of CO₂ Capture with Aqueous Monoethanolamine Solution. *Industrial & Engineering Chemistry Research*, 48(20), pp 9233-9246.
- Zhao, H. & Peterson, P. F. 2008. Multiple reheat helium Brayton cycles for sodium cooled fast reactors. *Nuclear Engineering and Design*, 238(7), pp 1535-1546.

Appendices

Appendix A Turbomachinery Design Data

A.1 Turbomachinery design data for the SM-SFR/ Nitrogen plant

A.1.1 Turbomachinery design data for the single-shaft nitrogen cycle

Table A-1 Overall design requirements and parameters for the LPC of the single shaft nitrogen cycle

Parameter	
Working fluid	Nitrogen
Number of stages	3
Mass flow (kg/s)	3027.226
Pressure ratio	1.359128
Polytropic efficiency	0.893203
Isentropic efficiency	0.89
Power (MW)	98.88342
Torque (kNm)	314.7557
Rotor speed(rpm)	3000
Mean radius(m)	0.616779
Mean blade speed(m/s)	193.7669
Tip speed at inlet (m/s)	206.6345
Total enthalpy rise(kJ/kg)	32.6647
Stage enthalpy rise(kJ/kg)	10.88823
Axial length (m)	0.439724
Total volume (m3)	0.591001
Fluid volume (m3)	0.127106
Flow coefficient	0.5
Stage loading coefficient	0.29

Table A-2 Total/stagnation properties in the three stages of the LPC of the single-shaft nitrogen cycle

	Stage 1		Stage 2		Stage 3	
	Inlet	Exit	Inlet	Exit	Inlet	Exit
P(bar)	92.11	102.48	102.48	113.51	113.51	125.19
T(°C)	27.00	37.58	37.58	48.06	48.06	58.44
H(kJ/kg)	293.42	304.31	304.31	315.20	315.20	326.09

Table A-3 Static properties in the three stages of the LPC of the single shaft nitrogen cycle

	Stage 1		Stage 2		Stage 3	
	Inlet	Exit	Inlet	Exit	Inlet	Exit
P(bar)	85.63	95.57	95.57	106.16	106.16	119.48
T(°C)	20.60	31.24	31.24	41.79	41.79	53.92
H(kJ/kg)	286.99	297.88	297.88	308.77	308.77	321.40
Density(kg/m3)	98.43	105.10	105.10	111.82	111.82	119.87

Table A-4 Stage geometry and parameters for the LPC of the single-shaft nitrogen cycle

	STAGE 1			STAGE 2			STAGE 3		
	RLE	RTE/SLE	STE	RLE	RTE/SLE	STE	RLE	RTE/SLE	STE
Area (m2)	0.3175	0.3074	0.2973	0.2973	0.2884	0.2794	0.2794	0.2700	0.2607
Blade ht(m)	0.0819	0.0793	0.0767	0.0767	0.0744	0.0721	0.0721	0.0697	0.0673
Hub rad (m)	0.5758	0.5771	0.5784	0.5784	0.5796	0.5807	0.5807	0.5819	0.5831
Tip rad(m)	0.6577	0.6564	0.6551	0.6551	0.6540	0.6528	0.6528	0.6516	0.6504
Hub/Tip	0.8755	0.8792	0.8829	0.8829	0.8862	0.8896	0.8896	0.8931	0.8966
Reaction	0.55			0.55			0.47		
de Haller				0.75					
Press ratio	1.11			1.11			1.10		
Length(m)	0.156			0.146			0.137		
No of blade	Rotor-64 /Stator-66			68/70			73/75		

Table A-5 Overall design requirements and parameters for the HPC of the single shaft nitrogen cycle

Parameters	
Working fluid	Nitrogen
Number of stages	4
Mass flow (kg/s)	3027.226
Pressure ratio	1.443143
Polytropic efficiency	0.884624
Isentropic efficiency	0.88
Power (MW)	123.1367
Torque (kNm)	391.9564
Rotor speed(rpm)	3000
Mean radius(m)	0.596064
Mean blade speed(m/s)	187.2589
Tip speed at inlet (m/s)	197.4845
Total enthalpy rise(kJ/kg)	40.67642
Stage enthalpy rise(kJ/kg)	10.16911
Axial length (m)	0.460885
Total volume (m3)	0.566415
Fluid volume (m3)	0.101456
Flow coefficient	0.5
Stage loading coefficient	0.29

Table A-6 Total/stagnation properties in the four stages of the HPC of the single-shaft nitrogen cycle

	Stage 1		Stage 2		Stage 3		Stage 4	
	Inlet	Exit	Inlet	Exit	Inlet	Exit	Inlet	Exit
P(bar)	124.73	137.52	137.52	151.00	151.00	165.16	165.16	180.00
T(°C)	27.00	36.71	36.71	46.29	46.29	55.75	55.75	65.09
H(kJ/kg)	288.28	298.45	298.45	308.62	308.62	318.79	318.79	328.96

Table A-7 Static properties in the four stages of the HPC of the single shaft nitrogen cycle

	Stage 1		Stage 2		Stage 3		Stage 4	
	Inlet	Exit	Inlet	Exit	Inlet	Exit	Inlet	Exit
P(bar)	116.59	128.92	128.92	141.94	141.94	155.65	155.65	172.70
T(°C)	21.09	30.88	30.88	40.55	40.55	50.09	50.09	61.03
H(kJ/kg)	282.27	292.44	292.44	302.61	302.61	312.78	312.78	324.58
Density(kg/m3)	132.61	140.29	140.29	147.95	147.95	155.56	155.56	164.57

Table A-8 Stage geometry and parameters for the HPC of the single-shaft nitrogen cycle

	STAGE 1			STAGE 2			STAGE 3			STAGE 4		
	RLE	RTE	STE	RLE	RTE	STE	RLE	RTE	STE	RLE	RTE	STE
Area (m2)	0.244	0.237	0.230	0.230	0.224	0.219	0.219	0.213	0.208	0.208	0.202	0.196
Blade ht(m)	0.065	0.063	0.062	0.062	0.060	0.058	0.058	0.057	0.055	0.055	0.054	0.052
Hub rad(m)	0.564	0.564	0.565	0.565	0.566	0.567	0.567	0.568	0.568	0.568	0.569	0.570
Tip rad(m)	0.629	0.628	0.627	0.627	0.626	0.625	0.625	0.625	0.624	0.624	0.623	0.622
Hub/Tip	0.896	0.899	0.902	0.902	0.904	0.907	0.907	0.909	0.911	0.911	0.913	0.916
Reaction	0.55			0.55			0.55			0.47		
de Haller	0.75											
Press ratio	1.1			1.1			1.09			1.09		
Length(m)	0.125			0.118			0.112			0.106		
No of blades	Rotor-77/Stator-80			82/84			86/88			91/93		

Table A-9 Overall design requirements and parameters for the turbine of the single-shaft nitrogen cycle

Parameters	
Working fluid	Nitrogen
Number of stages	3
Mass flow (kg/s)	3027.23
Pressure ratio	1.920257
Polytropic efficiency	0.925967
Isentropic efficiency	0.93
Power (MW)	424.0741
Torque (kNm)	1349.87
Rotor speed(rpm)	3000
Mean radius(m)	0.661874
Mean blade speed(m/s)	207.934
Tip speed at exit (m/s)	229.1881
Total enthalpy rise(kJ/kg)	140.0865
Stage enthalpy rise(kJ/kg)	46.69551
Axial length (m)	2.008962
Total volume (m3)	3.244557
Fluid volume (m3)	0.920431
Flow coefficient	0.6
Stage loading coefficient	1.080001

Table A-10 Total/stagnation properties in the three stages nozzle leading (NLE), nozzle trailing edge (NTE) and rotor trailing edge (RTE) of the turbine of the single-shaft nitrogen cycle

	Stage 1			Stage 2			Stage 3		
	NLE	NTE	RTE	NLE	NTE	RTE	NLE	NTE	RTE
P(bar)	179.16	177.78	146.14	146.14	144.88	117.63	117.63	116.55	93.30
T(°C)	530.00	530.07	490.72	490.72	490.78	450.63	450.63	450.67	409.75
H(kJ/kg)	859.43	859.43	812.73	812.73	812.73	766.04	766.04	766.04	719.34

Table A-11 Static properties in the three stages nozzle leading (NLE), nozzle trailing edge (NTE) and rotor trailing edge (RTE) of the turbine of the single-shaft nitrogen cycle

	Stage 1			Stage 2			Stage 3		
	NLE	NTE	RTE	NLE	NTE	RTE	NLE	NTE	RTE
P(bar)	173.76	157.01	141.44	141.44	126.93	113.61	113.61	101.21	89.88
T(°C)	523.49	503.89	484.05	484.05	464.07	443.83	443.83	423.45	402.82
H(kJ/kg)	851.64	828.30	804.91	804.91	781.60	758.22	758.22	734.91	711.52
Density(kg/m3)	68.62	63.93	59.42	59.42	55.06	50.92	50.92	46.91	43.12

Table A-12 Stage geometry and parameters for the turbine of the single-shaft nitrogen cycle

	STAGE 1			STAGE 2			STAGE 3		
	NLE	NTE/RLE	RTE	NLE	NTE/RLE	RTE	NLE	NTE/RLE	RTE
Area (m ²)	0.354	0.380	0.408	0.408	0.441	0.477	0.477	0.517	0.563
Blade ht(m)	0.085	0.091	0.098	0.098	0.106	0.115	0.115	0.124	0.135
Hub rad(m)	0.619	0.616	0.613	0.613	0.609	0.605	0.605	0.600	0.594
Tip rad(m)	0.704	0.708	0.711	0.711	0.715	0.719	0.719	0.724	0.730
Hub/Tip	0.879	0.871	0.862	0.862	0.852	0.841	0.841	0.828	0.815
Reaction	0.50			0.50			0.50		
Press ratio	1.226			1.242			1.261		
Length(m)	0.594			0.690			0.810		
No of blade	Nozzle-20/Rotor-76			18/66			16/56		

A.1.2 Turbomachinery design data for the single-shaft nitrogen cycle

Table A-13 Overall design requirements and parameters for the LPC of the two-shaft nitrogen cycle

Parameters	
Working fluid	Nitrogen
Number of stages	1
Mass flow (kg/s)	3027.226
Pressure ratio	1.359128
Polytropic efficiency	0.89
Isentropic efficiency	0.89
Power (MW)	98.88342
Torque (kNm)	118.0334
Rotor speed(rpm)	8000
Mean radius(m)	0.40061
Mean blade speed(m/s)	335.6142
Tip speed at inlet (m/s)	368.7627
Total enthalpy rise(kJ/kg)	32.6647
Stage enthalpy rise(kJ/kg)	32.6647
Axial length (m)	0.140299
Total volume (m ³)	0.083886
Fluid volume (m ³)	0.025173
Flow coefficient	0.5
Stage loading coefficient	0.29

Table A-14 Total/stagnation properties in the one stage of the LPC of the two-shaft nitrogen cycle

	Stage 1	
	Inlet	Exit
P(bar)	92.11	125.19
T(°C)	27.00	58.44
H(kJ/kg)	293.42	326.09

Table A-15 Static properties in the one stage of the LPC of the two-shaft nitrogen cycle

	Stage 1	
	Inlet	Exit
P(bar)	75.16	108.55
T(°C)	9.49	44.81
H(kJ/kg)	275.91	312.01
Density(kg/m3)	90.56	112.99

Table A-16 Stage geometry and parameters for the LPC of the two-shaft nitrogen cycle

	STAGE 1		
	RLE	RTE/SLE	STE
Area (m2)	0.199	0.179	0.160
Blade height(m)	0.079	0.071	0.063
Hub radius (m)	0.361	0.365	0.369
Tip radius(m)	0.440	0.436	0.432
Hub/Tip	0.820	0.837	0.853
Reaction	0.55		
de Haller	0.75		
Press ratio	1.36		
Length (m)	0.14		
No of blades	Rotor-45/Stator-50		

Table A-17 Stage geometry and parameters for the LPC of the two-shaft nitrogen cycle

Parameters	
Working fluid	Nitrogen
Number of stages	2
Mass flow (kg/s)	3027.226
Pressure ratio	1.443143
Polytropic effic	0.883084
Isentropic effic	0.88
Power (MW)	123.1367
Torque (kNm)	146.9836
Rotor speed(rpm)	8000
Mean radius(m)	0.340461
Mean blade speed(m/s)	285.2242
Tip speed at inlet (m/s)	318.4826
Total enthalpy rise(kJ/kg)	40.67642
Stage enthalpy rise(kJ/kg)	20.33821
Axial length (m)	0.278576
Total volume (m3)	0.12365
Fluid volume (m3)	0.042205
Flow coefficient	0.5
Stage loading coefficient	0.25

Table A-18 Total/stagnation properties in the two stages of the HPC of the two-shaft nitrogen cycle

	Stage 1		Stage 2	
	Inlet	Exit	Inlet	Exit
P(bar)	124.73	151.00	151.00	180.00
T(°C)	27.00	46.29	46.29	65.09
H(kJ/kg)	288.28	308.62	308.62	328.96

Table A-19 Static properties in the two stages of the HPC of the two-shaft nitrogen cycle

	Stage 1		Stage 2	
	Inlet	Exit	Inlet	Exit
P(bar)	105.71	129.76	129.76	163.33
T(°C)	12.69	32.37	32.37	55.62
H(kJ/kg)	273.82	294.16	294.16	318.79
Density(kg/m3)	124.98	140.33	140.33	159.41

Table A-20 Stage geometry and parameters for the HPC of the two-shaft nitrogen cycle

	STAGE 1			STAGE 2		
	RLE	RTE/SLE	STE	RLE	RTE/SLE	STE
Area (m ²)	0.170	0.161	0.151	0.151	0.142	0.133
Blade height(m)	0.079	0.075	0.071	0.071	0.066	0.062
Hub radius (m)	0.301	0.303	0.305	0.305	0.307	0.309
Tip radius(m)	0.380	0.378	0.376	0.376	0.374	0.372
Hub/Tip	0.791	0.801	0.812	0.812	0.822	0.832
Reaction	0.55			0.45		
de Haller	0.78					
Press ratio	1.21			1.19		
Length(m)	0.148			0.131		
No of blades	Rotor-37/Stator-39			42/44		

Table A-21 Overall design requirements and parameters for the CDT of the two-shaft nitrogen cycle

Parameters	
Working fluid	Nitrogen
Number of stages	1
Mass flow (kg/s)	1584.8
Pressure ratio	1.920257
Polytropic efficiency	0.93
Isentropic efficiency	0.93
Power (MW)	222.0091
Torque (kNm)	265.0039
Rotor speed(rpm)	8000
Mean radius(m)	0.4299
Mean blade speed(m/s)	360.1524
Tip speed at exit (m/s)	387.9491
Total enthalpy rise(kJ/kg)	140.0865
Stage enthalpy rise(kJ/kg)	140.0865
Axial length (m)	0.304409
Total volume (m ³)	0.199573
Fluid volume (m ³)	0.044248
Flow coefficient	0.6
Stage loading coefficient	1.08

Table A-22 Total/stagnation properties in the one stage nozzle leading (NLE), nozzle trailing edge (NTE) and rotor trailing edge (RTE) of the CDT of the two-shaft nitrogen cycle

	Stage 1		
	NLE	NTE	RTE
P(bar)	179.16	174.72	93.3
T(°C)	530	530.23	409.75
H(kJ/kg)	859.43	859.43	719.34

Table A-23 Static properties in the one stage nozzle leading (NLE), nozzle trailing edge (NTE) and rotor trailing edge (RTE) of the CDT of the two-shaft nitrogen cycle

	Stage 1		
	NLE	NTE	RTE
P(bar)	163.30	118.43	83.32
T(°C)	510.40	450.60	388.91
H(kJ/kg)	836.08	766.04	695.89
Density(kg/m³)	65.79	52.49	40.92

Table A-24 Stage geometry and parameters for the CDT of the two-shaft nitrogen cycle

	STAGE 1		
	NLE	NTE/RLE	RTE
Area (m²)	0.111	0.140	0.179
Blade height(m)	0.041	0.052	0.066
Hub radius(m)	0.409	0.404	0.397
Tip radius(m)	0.451	0.456	0.463
Hub/Tip	0.91	0.89	0.86
Reaction	0.50		
Press ratio	1.92		
Length (m)	0.342		
No of blades	Nozzle-25/Rotor-79		

Table A-25 Overall design requirements and parameters for the FPT of the two-shaft nitrogen cycle

Parameters	
Working fluid	Nitrogen
Number of stages	4
Mass flow (kg/s)	1442.42
Pressure ratio	1.920257
Polytropic efficiency	0.925455
Isentropic efficiency	0.93
Power (MW)	202.0636
Torque (kNm)	643.1885
Rotor speed(rpm)	3000
Mean radius(m)	0.560375
Mean blade speed(m/s)	176.0471
Tip speed at exit (m/s)	190.0767
Total enthalpy rise(kJ/kg)	140.0865
Stage enthalpy rise(kJ/kg)	35.02163
Axial length (m)	1.784303
Total volume (m³)	1.996339
Fluid volume (m³)	0.457069
Flow coefficient	0.6
Stage loading coefficient	1.13

Table A-26 Total/stagnation properties in the four stages nozzle leading (NLE), nozzle trailing edge (NTE) and rotor trailing edge (RTE) of the FPT of the two-shaft nitrogen cycle

	Stage 1			Stage 2			Stage 3			Stage 4		
	NLE	NTE	RTE									
P(bar)	179.16	178.18	153.96	153.96	152.97	131.34	131.34	130.46	111.17	111.17	110.39	93.30
T(°C)	530.00	530.05	500.62	500.62	500.66	470.77	470.77	470.81	440.48	440.48	440.51	409.75
H(kJ/kg)	859.43	859.43	824.41	824.41	824.41	789.38	789.38	789.38	754.36	754.36	754.36	719.34

Table A-27 Static properties in the four stages nozzle leading edge (NLE), nozzle trailing edge (NTE) and rotor trailing edge (RTE) of the FPT of the two-shaft nitrogen cycle

	Stage 1			Stage 2			Stage 3			Stage 4		
	NLE	NTE	RTE									
P(bar)	175.28	163.08	150.39	150.39	139.43	128.15	128.15	118.37	108.34	108.34	99.66	90.80
T(°C)	525.33	511.32	495.77	495.77	481.65	465.86	465.86	451.52	435.49	435.49	420.95	404.70
H(kJ/kg)	853.85	837.11	818.70	818.70	802.09	783.68	783.68	767.07	748.66	748.66	732.05	713.63
Density(kg/m3)	69.02	65.63	62.02	62.02	58.80	55.43	55.43	52.40	49.23	49.23	46.39	43.42

Table A-28 Stage geometry and parameters for the FPT of the two-shaft nitrogen cycle

	STAGE 1			STAGE 2			STAGE 3			STAGE 4		
	NLE	NTE/RLE	RTE	NLE	NTE/RLE	RTE	NLE	NTE/RLE	RTE	NLE	NTE/RLE	RTE
Area (m2)	0.198	0.208	0.220	0.220	0.232	0.246	0.246	0.261	0.277	0.277	0.294	0.314
Blade ht(m)	0.056	0.059	0.063	0.063	0.066	0.070	0.070	0.074	0.079	0.079	0.084	0.089
Hub rad(m)	0.532	0.531	0.529	0.529	0.527	0.525	0.525	0.523	0.521	0.521	0.519	0.516
Tip rad(m)	0.588	0.590	0.592	0.592	0.593	0.595	0.595	0.597	0.600	0.600	0.602	0.605
Hub/Tip	0.905	0.900	0.894	0.894	0.889	0.882	0.882	0.876	0.869	0.869	0.861	0.852
Reaction	0.53			0.53			0.53			0.53		
Press ratio	1.16			1.17			1.18			1.19		
Length(m)	0.385			0.429			0.482			0.544		
No of blades	Nozzle-26/Rotor-103			25/92			23/82			20/73		

A.2 Turbomachinery design data for the single recuperator recompression s-CO₂ cycle

Table A-29 Overall design requirements and parameters for the MC of the single recuperator recompression s-CO₂ cycle

Parameters	
Working fluid	s-CO ₂
Number of stages	8
Mass flow (kg/s)	1969.97
Pressure ratio	2.716049
Polytropic efficiency	0.893354
Isentropic efficiency	0.89
Power (MW)	42.57125
Torque (kNm)	135.5085
Rotor speed(rpm)	3000
Mean radius(m)	0.302394
Mean blade speed(m/s)	95
Tip speed at inlet (m/s)	100.3287
Total enthalpy rise(kJ/kg)	21.6101
Stage enthalpy rise(kJ/kg)	2.701262
Axial length (m)	0.485246
Total volume (m ³)	0.154237
Fluid volume (m ³)	0.028925
Flow coefficient	0.5
Stage loading coefficient	0.299309

Table A-30 Total/stagnation properties in the eight stages of the MC of the single recuperator recompression s-CO₂ cycle

	Stage 1		Stage 2		Stage 3		Stage 4	
	Inlet	Exit	Inlet	Exit	Inlet	Exit	Inlet	Exit
P(bar)	81.00	97.24	97.24	113.90	113.90	130.91	130.91	148.22
T(°C)	32.00	36.26	36.26	40.08	40.08	43.58	43.58	46.86
H(kJ/kg)	294.49	297.19	297.19	299.89	299.89	302.59	302.59	305.29
	Stage 5		Stage 6		Stage 7		Stage 8	
	Inlet	Exit	Inlet	Exit	Inlet	Exit	Inlet	Exit
P(bar)	148.22	165.81	165.81	183.65	183.65	201.72	201.72	220.00
T(°C)	46.86	49.94	49.94	52.87	52.87	55.66	55.66	58.34
H(kJ/kg)	305.29	307.99	307.99	310.69	310.69	313.39	313.39	316.10

Table A-31 Static properties in the eight stages of the MC of the single recuperator recompression s-CO₂ cycle

	Stage 1		Stage 2		Stage 3		Stage 4	
	Inlet	Exit	Inlet	Exit	Inlet	Exit	Inlet	Exit
P(bar)	70.02	85.89	85.89	102.27	102.27	119.03	119.03	136.14
T(°C)	28.61	33.39	33.39	37.51	37.51	41.23	41.23	44.66
H(kJ/kg)	292.80	295.51	295.51	298.21	298.21	300.91	300.91	303.61
D(kg/m³)	643.45	667.97	667.97	686.12	686.12	701.08	701.08	714.11
A (m/s)	217.47	273.49	273.49	310.08	310.08	338.58	338.58	362.46
	Stage 5		Stage 6		Stage 7		Stage 8	
	Inlet	Exit	Inlet	Exit	Inlet	Exit	Inlet	Exit
P(bar)	136.14	153.54	153.54	171.20	171.20	189.11	189.11	211.43
T(°C)	44.66	47.88	47.88	50.92	50.92	53.81	53.81	57.16
H(kJ/kg)	303.61	306.31	306.31	309.01	309.01	311.71	311.71	314.97
Den(kg/m³)	714.11	725.77	725.77	736.38	736.38	746.13	746.13	757.33
Sonic sp.(m/s)	362.46	383.87	383.87	403.69	403.69	422.25	422.25	443.67

Table A-32 Stage geometry and parameters for the MC of the single recuperator recompression s-CO₂ cycle

	STAGE 1			STAGE 2			STAGE 3			STAGE 4		
	RLE	RTE/SLE	STE	RLE	RTE/SLE	STE	RLE	RTE/SLE	STE	RLE	RTE/SLE	STE
Area (m²)	0.064	0.063	0.062	0.062	0.061	0.060	0.060	0.060	0.059	0.059	0.059	0.058
Blade ht(m)	0.034	0.033	0.033	0.033	0.032	0.032	0.032	0.031	0.031	0.031	0.031	0.031
Hub rad (m)	0.285	0.286	0.286	0.286	0.286	0.286	0.286	0.287	0.287	0.287	0.287	0.287
Tip rad(m)	0.319	0.319	0.319	0.319	0.319	0.318	0.318	0.318	0.318	0.318	0.318	0.318
Hub/Tip	0.894	0.896	0.897	0.897	0.899	0.900	0.900	0.901	0.902	0.902	0.903	0.904
Reaction	0.50			0.50			0.50			0.50		
de Haller	0.74											
Press ratio	1.20			1.17			1.15			1.13		
Length(m)	0.066			0.063			0.062			0.061		
No of blades	Rotor-75/Stator-77			78/79			80/81			81/82		
	STAGE 5			STAGE 6			STAGE 7			STAGE 8		
	RLE	RTE/SLE	STE	RLE	RTE/SLE	STE	RLE	RTE/SLE	STE	RLE	RTE/SLE	STE
Area (m²)	0.058	0.058	0.057	0.057	0.057	0.056	0.056	0.056	0.056	0.056	0.055	0.055
Blade ht(m)	0.031	0.030	0.030	0.030	0.030	0.030	0.030	0.029	0.029	0.029	0.029	0.029
Hub rad (m)	0.287	0.287	0.287	0.287	0.287	0.288	0.288	0.288	0.288	0.288	0.288	0.288
Tip rad(m)	0.318	0.318	0.317	0.317	0.317	0.317	0.317	0.317	0.317	0.317	0.317	0.317
Hub/Tip	0.904	0.905	0.905	0.905	0.906	0.907	0.907	0.907	0.908	0.908	0.908	0.909
Reaction	0.50			0.50			0.50			0.42		
de Haller	0.74											
Press ratio	1.12			1.11			1.10			1.09		
Length(m)	0.060			0.059			0.058			0.057		
No of blades	Rotor-83/Stator-84			84/85			85/86			87/87		

Table A-33 Overall design requirements and parameters for the RC of the single recuperator recompression s-CO₂ cycle

Parameters	
Working fluid	s-CO ₂
Number of stages	17
Mass flow (kg/s)	1219.43
Pressure ratio	2.69672
Polytropic efficiency	0.891419
Isentropic efficiency	0.88
Power (MW)	75.06268
Torque (kNm)	238.9319
Rotor speed(rpm)	3000
Mean radius(m)	0.350141
Mean blade speed(m/s)	110
Tip speed at inlet (m/s)	119.4826
Total enthalpy rise(kJ/kg)	61.55554
Stage enthalpy rise(kJ/kg)	3.620914
Axial length (m)	1.429749
Total volume (m ³)	0.624761
Fluid volume (m ³)	0.143344
Flow coefficient	0.5
Stage loading coefficient	0.299249

Table A-34 Total/stagnation properties in the seventeen stages of the RC of the single recuperator recompression s-CO₂ cycle

	Stage 1		Stage 2		Stage 3		Stage 4	
	Inlet	Exit	Inlet	Exit	Inlet	Exit	Inlet	Exit
P(bar)	81.41	87.14	87.14	93.16	93.16	99.46	99.46	106.05
T(°C)	73.34	79.33	79.33	85.26	85.26	91.15	91.15	96.97
H(kJ/kg)	479.83	483.45	483.45	487.07	487.07	490.69	490.69	494.31
	Stage 5		Stage 6		Stage 7		Stage 8	
	Inlet	Exit	Inlet	Exit	Inlet	Exit	Inlet	Exit
P(bar)	106.05	112.95	112.95	120.14	120.14	127.63	127.63	135.44
T(°C)	96.97	102.74	102.74	108.44	108.44	114.07	114.07	119.63
H(kJ/kg)	494.31	497.93	497.93	501.55	501.55	505.17	505.17	508.79
	Stage 9		Stage 10		Stage 11		Stage 12	
	Inlet	Exit	Inlet	Exit	Inlet	Exit	Inlet	Exit
P(bar)	135.44	143.55	143.55	151.96	151.96	160.69	160.69	169.73
T(°C)	119.63	125.12	125.12	130.54	130.54	135.88	135.88	141.14
H(kJ/kg)	508.79	512.41	512.41	516.04	516.04	519.66	519.66	523.28
	Stage 13		Stage 14		Stage 15		Stage 16	
	Inlet	Exit	Inlet	Exit	Inlet	Exit	Inlet	Exit
P(bar)	169.73	179.08	179.08	188.73	188.73	198.70	198.70	208.97
T(°C)	141.14	146.32	146.32	151.42	151.42	156.44	156.44	161.38
H(kJ/kg)	523.28	526.90	526.90	530.52	530.52	534.14	534.14	537.76
	Stage 17							
	Inlet	Exit						
P(bar)	208.97	219.54						
T(°C)	161.38	166.23						
H(kJ/kg)	537.76	541.38						

Table A-35 Static properties in the seventeen stages of the MC of the single recuperator recompression s-CO₂ cycle

	Stage 1		Stage 2		Stage 3		Stage 4	
	Inlet	Exit	Inlet	Exit	Inlet	Exit	Inlet	Exit
P(bar)	77.58	83.12	83.12	88.93	88.93	95.03	95.03	101.43
T(°C)	69.31	75.32	75.32	81.29	81.29	87.22	87.22	93.08
H(kJ/kg)	477.57	481.19	481.19	484.81	484.81	488.44	488.44	492.06
Density(kg/m3)	166.94	175.47	175.47	184.17	184.17	193.05	193.05	202.07
	Stage 5		Stage 6		Stage 7		Stage 8	
	Inlet	Exit	Inlet	Exit	Inlet	Exit	Inlet	Exit
P(bar)	101.43	108.11	108.11	115.09	115.09	122.38	122.38	129.96
T(°C)	93.08	98.89	98.89	104.64	104.64	110.32	110.32	115.93
H(kJ/kg)	492.06	495.68	495.68	499.30	499.30	502.92	502.92	506.54
Density(kg/m3)	202.07	211.24	211.24	220.51	220.51	229.89	229.89	239.35
Sonic speed (m/s)	262.79	266.81	266.81	270.99	270.99	275.33	275.33	279.84
	Stage 9		Stage 10		Stage 11		Stage 12	
	Inlet	Exit	Inlet	Exit	Inlet	Exit	Inlet	Exit
P(bar)	129.96	137.86	137.86	146.06	146.06	154.57	154.57	163.39
T(°C)	115.93	121.47	121.47	126.94	126.94	132.33	132.33	137.65
H(kJ/kg)	506.54	510.16	510.16	513.78	513.78	517.40	517.40	521.02
Density(kg/m3)	239.35	248.87	248.87	258.43	258.43	268.02	268.02	277.62
	Stage 13		Stage 14		Stage 15		Stage 16	
	Inlet	Exit	Inlet	Exit	Inlet	Exit	Inlet	Exit
P(bar)	163.39	172.52	172.52	181.97	181.97	191.72	191.72	201.77
T(°C)	137.65	142.88	142.88	148.04	148.04	153.12	153.12	158.11
H(kJ/kg)	521.02	524.64	524.64	528.27	528.27	531.89	531.89	535.51
Density(kg/m3)	277.62	287.22	287.22	296.79	296.79	306.32	306.32	315.80
	Stage 17							
	Inlet	Exit						
P(bar)	201.77	214.55						
T(°C)	158.11	164.09						
H(kJ/kg)	535.51	539.87						
Density(kg/m3)	315.80	327.46						

Table A-36 Stage geometry and parameters for the RC of the single recuperator recompression s-CO₂ cycle

	STAGE 1			STAGE 2			STAGE 3			STAGE 4		
	RLE	RTE/SLE	STE	RLE	RTE/SLE	STE	RLE	RTE/SLE	STE	RLE	RTE/SLE	STE
Area (m2)	0.133	0.130	0.126	0.126	0.123	0.120	0.120	0.118	0.115	0.115	0.112	0.110
Blade ht(m)	0.060	0.059	0.057	0.057	0.056	0.055	0.055	0.053	0.052	0.052	0.051	0.050
Hub radius(m)	0.320	0.321	0.321	0.321	0.322	0.323	0.323	0.323	0.324	0.324	0.325	0.325
Tip radius(m)	0.380	0.380	0.379	0.379	0.378	0.378	0.378	0.377	0.376	0.376	0.376	0.375
Hub/Tip	0.841	0.845	0.848	0.848	0.852	0.855	0.855	0.858	0.861	0.861	0.864	0.867
Reaction	0.50			0.50			0.50			0.50		
de Haller	0.74											
Press ratio	1.07			1.07			1.07			1.07		
Length(m)	0.116			0.110			0.105			0.100		
No of blades	Rotor-49/Stator-50			52/53			54/55			57/58		
	STAGE 5			STAGE 6			STAGE 7			STAGE 8		
	RLE	RTE/SLE	STE	RLE	RTE/SLE	STE	RLE	RTE/SLE	STE	RLE	RTE/SLE	STE
Area (m2)	0.110	0.107	0.105	0.105	0.103	0.101	0.101	0.098	0.096	0.096	0.095	0.093
Blade ht(m)	0.050	0.049	0.048	0.048	0.047	0.046	0.046	0.045	0.044	0.044	0.043	0.042
Hub radius(m)	0.325	0.326	0.326	0.326	0.327	0.327	0.327	0.328	0.328	0.328	0.329	0.329
Tip radius(m)	0.375	0.375	0.374	0.374	0.373	0.373	0.373	0.373	0.372	0.372	0.372	0.371
Hub/Tip	0.867	0.870	0.872	0.872	0.875	0.877	0.877	0.880	0.882	0.882	0.884	0.887
Reaction	0.50			0.50			0.50			0.50		
de Haller	0.74											
Press ratio	1.06			1.06			1.06			1.06		
Length(m)	0.096			0.092			0.088			0.085		
No of blades	Rotor-59/Stator-61			62/63			65/66			67/69		
	STAGE 9			STAGE 10			STAGE 11			STAGE 12		
	RLE	RTE/SLE	STE	RLE	RTE/SLE	STE	RLE	RTE/SLE	STE	RLE	RTE/SLE	STE
Area (m2)	0.093	0.091	0.089	0.089	0.087	0.086	0.086	0.084	0.083	0.083	0.081	0.080
Blade ht(m)	0.042	0.041	0.040	0.040	0.040	0.039	0.039	0.038	0.038	0.038	0.037	0.036
Hub radius(m)	0.329	0.329	0.330	0.330	0.330	0.331	0.331	0.331	0.331	0.331	0.332	0.332
Tip radius(m)	0.371	0.371	0.370	0.370	0.370	0.370	0.370	0.369	0.369	0.369	0.369	0.368
Hub/Tip	0.887	0.889	0.891	0.891	0.893	0.895	0.895	0.896	0.898	0.898	0.900	0.901
Reaction	0.50			0.50			0.50			0.50		
de Haller	0.74											
Press ratio	1.06			1.06			1.06			1.06		
Length(m)	0.081			0.078			0.075			0.073		
No of blades	Rotor-70/Stator-72			73/74			76/77			78/80		
	STAGE 13			STAGE 14			STAGE 15			STAGE 16		
	RLE	RTE/SLE	STE	RLE	RTE/SLE	STE	RLE	RTE/SLE	STE	RLE	RTE/SLE	STE
Area (m2)	0.080	0.079	0.077	0.077	0.076	0.075	0.075	0.074	0.072	0.072	0.071	0.070
Blade ht(m)	0.036	0.036	0.035	0.035	0.035	0.034	0.034	0.033	0.033	0.033	0.032	0.032
Hub radius(m)	0.332	0.332	0.333	0.333	0.333	0.333	0.333	0.333	0.334	0.334	0.334	0.334
Tip radius(m)	0.368	0.368	0.368	0.368	0.367	0.367	0.367	0.367	0.367	0.367	0.366	0.366
Hub/Tip	0.901	0.903	0.905	0.905	0.906	0.908	0.908	0.909	0.910	0.910	0.912	0.913

Reaction	0.50	0.50	0.50	0.50
de Haller	0.74			
Press ratio	1.06	1.05	1.05	1.05
Length(m)	0.070	0.068	0.066	0.064
No of blades	Rotor-81/Stator-83	84/85	87/88	89/91
STAGE 17				
	RLE	RTE/SLE	STE	
Area (m2)	0.070	0.069	0.068	
Blade ht(m)	0.032	0.031	0.031	
Hub radius(m)	0.334	0.334	0.335	
Tip radius(m)	0.366	0.366	0.366	
Hub/Tip	0.913	0.914	0.916	
Reaction	0.50			
de Haller	0.74			
Press ratio	1.05			
Length(m)	0.062			
No of blades	Rotor-92/Stator-94			

Table A-37 Overall design requirements and parameters for the turbine of the single recuperator recompression s-CO₂ cycle

Parameters	
Working fluid	s-CO ₂
Number of stages	3
Mass flow (kg/s)	3189.4
Pressure ratio	2.587146
Polytropic efficiency	0.925443
Isentropic efficiency	0.93
Power (MW)	253.931
Torque (kNm)	808.2875
Rotor speed(rpm)	3000
Mean radius(m)	0.498986
Mean blade speed(m/s)	156.761
Tip speed at exit (m/s)	173.8127
Total enthalpy rise(kJ/kg)	79.61717
Stage enthalpy rise(kJ/kg)	26.53906
Axial length (m)	1.403015
Total volume (m3)	1.281104
Fluid volume (m3)	0.352539
Flow coefficient	0.6

Table A-38 Total/stagnation properties in the three stages of the turbine of the single recuperator recompression s-CO₂ cycle

	Stage 1			Stage 2			Stage 3		
	NLE	NTE	RTE	NLE	NTE	RTE	NLE	NTE	RTE
P(bar)	219.39	216.96	163.56	163.56	161.51	119.18	119.18	117.57	84.80
T(°C)	290.00	289.63	259.03	259.03	258.61	227.06	227.06	226.64	194.44
H(kJ/kg)	711.15	711.15	684.61	684.61	684.61	658.07	658.07	658.07	631.53

Table A-39 Static properties in the three stages of the turbine of the single recuperator recompression s-CO₂ cycle

	Stage 1			Stage 2			Stage 3		
	NLE	NTE	RTE	NLE	NTE	RTE	NLE	NTE	RTE
P(bar)	210.00	181.49	155.98	155.98	133.23	113.25	113.25	95.59	80.28
T(°C)	285.04	269.60	253.86	253.86	237.91	221.77	221.77	205.47	189.06
H(kJ/kg)	706.73	693.46	680.17	680.17	666.92	653.63	653.63	640.38	627.09
Density(kg/m3)	209.05	187.74	167.53	167.53	148.45	130.84	130.84	114.47	99.63

Table A-40 Stage geometry and parameters for the turbine of the single recuperator recompression s-CO₂ cycle

	STAGE 1			STAGE 2			STAGE 3		
	NLE	NTE/RLE	RTE	NLE	NTE/RLE	RTE	NLE	NTE/RLE	RTE
Area (m2)	0.162	0.181	0.202	0.202	0.228	0.259	0.259	0.296	0.340
Blade ht(m)	0.052	0.058	0.065	0.065	0.073	0.083	0.083	0.094	0.109
Hub rad(m)	0.473	0.470	0.467	0.467	0.463	0.458	0.458	0.452	0.445
Tip rad(m)	0.525	0.528	0.531	0.531	0.535	0.540	0.540	0.546	0.553
Hub/Tip	0.901	0.891	0.878	0.878	0.864	0.847	0.847	0.827	0.804
Reaction	0.50			0.50			0.50		
Press ratio	1.34			1.37			1.41		
Length (m)	0.376			0.476			0.617		
No of blades	Nozzle-24/Rotor-89			20/70			16/54		

Appendix B Integration of Plant Components Dynamic Models in Simulink

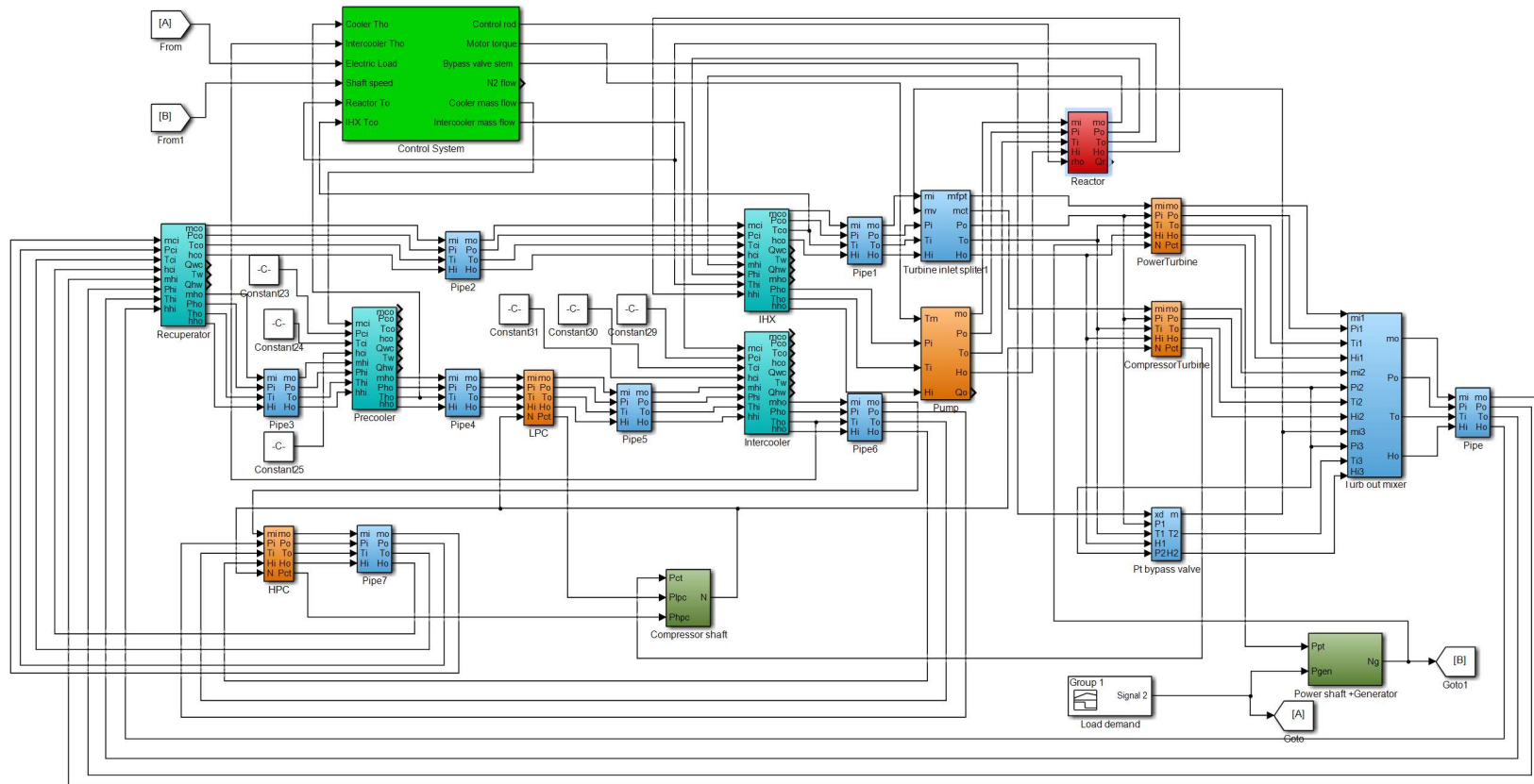


Figure B-1 Simulink integration of the dynamic models of the SM-SFR/nitrogen closed-cycle GT components (two-shaft parallel turbines layout)

